Biological and Medical Physics, Biomedical Engineering

Adam D. Douglass *Editor*

New Techniques in Systems Neuroscience

Springer

New Techniques in Systems Neuroscience

BIOLOGICAL AND MEDICAL PHYSICS, BIOMEDICAL ENGINEERING

The fields of biological and medical physics and biomedical engineering are broad, multidisciplinary and dynamic. They lie at the crossroads of frontier research in physics, biology, chemistry, and medicine. The Biological and Medical Physics, Biomedical Engineering Series is intended to be comprehensive, covering a broad range of topics important to the study of the physical, chemical and biological sciences. Its goal is to provide scientists and engineers with textbooks, monographs, and reference works to address the growing need for information.

Books in the series emphasize established and emergent areas of science including molecular, membrane, and mathematical biophysics; photosynthetic energy harvesting and conversion; information processing; physical principles of genetics; sensory communications; automata networks, neural networks, and cellular automata. Equally important will be coverage of applied aspects of biological and medical physics and biomedical engineering such as molecular electronic components and devices, biosensors, medicine, imaging, physical principles of renewable energy production, advanced prostheses, and environmental control and engineering.

For further volumes:
http://www.springer.com/series/3740

Adam D. Douglass
Editor

New Techniques in Systems Neuroscience

Springer

Editor
Adam D. Douglass
Dept. Of Neurobiology and Anatomy
University of Utah
Salt Lake City UT
Utah
USA

ISSN 1618-7210 ISSN 2197-5647 (electronic)
Biological and Medical Physics, Biomedical Engineering
ISBN 978-3-319-12912-9 ISBN 978-3-319-12913-6 (eBook)
DOI 10.1007/978-3-319-12913-6

Library of Congress Control Number: 2014954804

Springer Cham Heidelberg New York Dordrecht London

Printed on acid-free paper

Springer is part of Springer Science+Business Media (www.springer.com)

Preface

The human brain is a terrifically complicated structure. Nearly 100 billion neurons use trillions of synapses to communicate with one another, releasing a large and only partially catalogued variety of neurotransmitters that can exert very different effects depending on the neuroanatomical and physiological context. Activity in this network is driven by millisecond-duration action potentials, and the precise, relative timing of these events in different cells fundamentally determines the functional outcome. Even if we were able to account for all of these features, neuronal plasticity and regeneration would make any description we might derive only a snapshot of a temporally varying structure. Somehow, this mass of complexity allows us to perceive and interact with our environment in dynamic and appropriate ways. Systems neuroscientists, who seek to understand the cellular principles governing network function and behavior, have their work cut out for them.

The great technical difficulty in studying the brain, even in the simplified context of a model organism, has meant that insights into brain function often quickly follow technological advances. If that holds generally true, then we should expect the coming decade to be among the most illuminating periods in the history of neuroscience, as the last several years have seen an explosion of powerful new methods for studying the brain. The invention of optogenetics has given us a means to manipulate genetically defined populations of cells with a high degree of spatial and temporal precision and, in some cases, to do so without any invasive surgery. New microscopy techniques, coupled with an increasingly robust set of fluorescent calcium and voltage indicators, allow us to record activity in many cells simultaneously using a noninvasive optical readout. New ways to acquire and analyze electron microscopy data from large volumes of tissue are starting to provide complete physical wiring diagrams that will help constrain our models of circuit function. In addition, an ever-expanding set of molecular tools promises to help us identify molecular signatures of discrete neuronal subtypes, and to correlate those features with the cells' functional properties. In a very short period of time, the field has gained the ability to study how many identified single neurons work together in large groups to shape behavior.

While these new technical capabilities have already begun to provide important biological insight, there have also been significant lags in realizing their full

potential. There are two straightforward reasons for this. One is that it simply takes time for researchers to overcome the inevitable technical hurdles that accompany new methods, and the recent techniques, while powerful, also tend to be somewhat complex. The other reason derives from the sheer abundance of new tools. There are now dozens of optogenetic reagents and optical stimulation methods in the literature. The same goes for functional indicators and microscopy techniques. Predicting which tools will best address a particular biological question (or even which will do the job they are advertised to do) can be a daunting task, and often limits an investigator's willingness to adopt a new approach until a sufficiently large number of studies have shown it to be worthwhile.

This book addresses both of these issues while discussing the directions that several key technical areas are now moving in, and highlighting specific examples of how molecular and optical tools have helped us to understand neural circuit function. It is intended to form part of the ongoing discussion between tool-builders and other neuroscientists seeking to stay ahead of the curve in adopting new techniques. It should additionally serve as a useful, if dense, primer for students and other individuals looking to understand the methodological driving forces behind modern neuroscience.

In Chap. 1, Robert Marc and colleagues discuss progress in EM connectomics, where they and others are seeking to build high-resolution maps of neuronal connectivity that will be foundational to labs interested in physiology and behavior. In Chap. 2, Paul Bonthius and Chris Gregg examine the problem of heterogeneity in neuronal populations, with regard to the ways that new expression profiling techniques might help us to define and identify distinct subclasses of cells within complex tissues. Chapters 3–5 focus on the development of optical tools for fluorescently labeling neurons and recording calcium signals (Chap. 3), neuronal voltage imaging (Chap. 4), and manipulating neural activity with wavelength-shifted rhodopsin variants (Chap. 5). The following three chapters explore specific aspects of these methods in the context of three model organisms: Using optogenetics (and especially red-shifted optogenetic activators) to study physiology and behavior in *Drosophila melanogaster* (Chap. 6); using optical tools to monitor and manipulate neuronal activity in freely-behaving *C. elegans* (Chap. 7); and applying a variety of techniques to understand sensorimotor physiology and behavior in zebrafish (Chap. 8). Chapter 9, by Dinu Albeanu's group, discusses the principles behind methods for spatially structuring the illumination light used in optogenetics experiments, and Chap. 10, by Matt Smear, illustrates the unique insight into olfactory circuits that he and his colleagues have derived by combining functional imaging, optogenetics, and behavior.

The ongoing work of these authors and many other technical innovators will define the kinds of experiments we do for years to come. I hope it inspires the reader to take advantage of the incredible opportunities we now have to understand the brain.

September 19, 2014 Adam D. Douglass

Contents

Contributors

Dinu F. Albeanu Cold Spring Harbor Laboratory, Cold Spring Harbor, NY, USA

Watson School of Biological Sciences, Cold Spring Harbor, NY, USA

James R. Anderson Department of Ophthalmology, University of Utah School of Medicine, Salt Lake City, UT, USA

Francesca Anselmi Cold Spring Harbor Laboratory, Cold Spring Harbor, NY, USA

Arkarup Banerjee Cold Spring Harbor Laboratory, Cold Spring Harbor, NY, USA

Watson School of Biological Sciences, Cold Spring Harbor, NY, USA

Paul J. Bonthuis Department of Neurobiology and Anatomy, University of Utah School of Medicine, Salt Lake City, UT, USA

Robert E. Campbell Department of Chemistry, University of Alberta, Edmonton, AB, Canada

Adam D. Douglass Department of Neurobiology and Anatomy, University of Utah School of Medicine, Salt Lake City, UT, USA

Romain Franconville Howard Hughes Medical Institute, Janelia Farm Research Campus, Ashburn, VA, USA

Christopher Gregg Department of Neurobiology and Anatomy, University of Utah School of Medicine, Salt Lake City, UT, USA

Vivek Jayaraman Howard Hughes Medical Institute, Janelia Farm Research Campus, Ashburn, VA, USA

Bryan W. Jones Department of Ophthalmology, University of Utah School of Medicine, Salt Lake City, UT, USA

Sung Soo Kim Howard Hughes Medical Institute, Janelia Farm Research Campus, Ashburn, VA, USA

Steven Knafo Institut du Cerveau et de la Moelle épinière (ICM), 83 boulvard de l'hopital, Paris, France

Per M. Knutsen Department of Physics, Section of Neurobiology, University of California, San Diego, CA, USA

J. Scott Lauritzen Department of Ophthalmology, University of Utah School of Medicine, Salt Lake City, UT, USA

John Y. Lin University of Tasmania, Hobart, Tasmania, Australia

Linjiao Luo Key Laboratory of Modern Acoustics, Ministry of Education, Department of Physics, Nanjing University, Nanjing, China

Robert E. Marc Department of Ophthalmology, University of Utah School of Medicine, Salt Lake City, UT, USA

Arnaud Muller Department of Physics, Section of Neurobiology, University of California, San Diego, CA, USA

Aravinthan D. T. Samuel Department of Physics and Center for Brain Science, Harvard University, Cambridge, MA, USA

Crystal Sigulinsky Department of Ophthalmology, University of Utah School of Medicine, Salt Lake City, UT, USA

Matthew C. Smear Institute of Neuroscience, University of Oregon, Eugene, OR, USA

Dan Turner-Evans Howard Hughes Medical Institute, Janelia Farm Research Campus, Ashburn, VA, USA

Quan Wen Department of Neurobiology and Biophysics, School of Life Sciences, University of Science and Technology of China, Hefei, Anhui Province, China

Claire Wyart Institut du Cerveau et de la Moelle épinière (ICM), 83 boulvard de l'hopital, Paris, France

Yongxin Zhao Department of Chemistry, University of Alberta, Edmonton, AB, Canada

Chapter 1
High-Resolution Synaptic Connectomics

Robert E. Marc, Bryan W. Jones, Crystal Sigulinsky, James R. Anderson and J. Scott Lauritzen

Abstract High-speed, high-resolution connectomics enables unambiguous mapping of synapses, gap junctions, adherens junctions, and other forms of adjacency among neurons in complex neural systems such as brain and retina. This chapter reviews the motivations for generating complete network architectures; the technologies available for large-scale network acquisition, visualization, and analysis; the fusion of molecular markers with a high-resolution ultrastructure; new networks and organelles discovered by ultrastructural connectomics; and new technological advances needed to expand the applications of connectomics.

1.1 Motivations for Ultrastructural Connectomics

A connectome is the complete set of cellular partners and connections for a neural region. It can be executed on the mesoscale (spatial resolution of magnetic resonance imaging or even conventional optical imaging) to map fiber networks or on the nanoscale (spatial resolution of electron imaging) to map synaptic networks. This review addresses our experience with high-resolution synaptic connectomics based on automated transmission electron microscope (ATEM) imaging.

The notion of using computational methods to accelerate ultrastructural analysis is at least three decades old [92]. Even so, computational imaging for electron microscopy did not become a mainstream strategy until recently. There were three reasons for this: slow acquisition speed, expensive storage, and weak analytical scale. Film-based imaging followed by high-performance digitization [40] or even digital camera acquisition followed by analysis was so slow that it had no competitive advantage. Second, data storage at the resolution required for synaptic identification and quantification was prohibitively expensive, especially for NIH-funded investigators. The third reason is less obvious: no formal rationale existed to motivate large-scale acquisitions.

R. E. Marc (✉) · B. W. Jones · C. Sigulinsky · J. R. Anderson · J. S. Lauritzen
Department of Ophthalmology, University of Utah School of Medicine, Salt Lake City, UT 84132, USA
e-mail: robert.marc@hsc.utah.edu

A. D. Douglass (ed.), *New Techniques in Systems Neuroscience,* Biological and Medical Physics, Biomedical Engineering, DOI 10.1007/978-3-319-12913-6_1

These problems were addressed in unrelated ways. The physical acquisition problem was solved by (1) ablation sectioning and surface imaging using secondary electron imaging and (2) true sectioning with automated primary electron imaging. Both create large digital datasets that can be navigated with computational tools and analyzed by teams. NIH and NSF initiatives to develop software for acquiring and managing these datasets were critical in making practical image volumes (e.g., 74, 95]. Further, image pyramid strategies (e.g., [33]) played a fundamental role in structuring applications for navigating and annotating these large volumes [4]. The storage problem was solved by the hardware market when the price of hard drive storage dropped below 0.10 USD/gigabyte in 2009.

Previous transmission electron microscope (TEM) reconstructions were case driven: explorations of the synaptic connectivity of specific small cells or small regions of cell networks. Sampling complete networks was not possible nor did appropriate analytical tools exist. No framework for analysis emerged that addressed neuronal population size and diversity, cell and process patterning, constraints of mapping network topologies, or specifying sampling protocols. How much data would be necessary for a real query? Nevertheless, the small-scale studies that were accomplished were of exceptional quality and very high resolution (e.g., [93–94]). We shall return to this point, because many current efforts fall far short of the required resolution for complete connectomics analysis.

But finally, the analytical motivations for large-scale connectomics evolved in parallel with network theories of systems [99, 102]. The proper motivation for connectomics is graph theory: the analysis of network connection patterns and how signals travel through networks [72]. Formal schemas for exploring network topologies and their component motifs (i.e., stereotyped components) can scale to massive levels.

1.1.1 Network Topologies and Ground Truth

A fundamental concept in remote sensing is *ground truth*. The reliability of any remote system of detection and classification (e.g., imaging and tracing processes and synapses) is gauged by its performance on ground truth signatures collected on-site from a validated target. The reliability of a remote platform such as TEM or scanning electron microscope (SEM) and associated algorithms in locating similar targets requires statistical definition. For biological neural networks, there is some debate about the nature of ground truth. We have made the argument that ground truth datasets for testing imaging and algorithms ought to come from neural TEM samples with Nyquist-compliant resolutions [72]: images with resolutions superior to the structures being resolved. For synapses, gap junctions, adherens junctions, endocytosis sites, and discovery of new cell contact features, that means 2 nm pixel sizes or smaller [4]. Previous reviews specify a 10-nm scale for connectivity analysis [49], but that is incorrect as we show below. Once sufficient numbers of connection motifs are sampled [3], it becomes possible to test biological variations in those

motifs in development and disease. A weaker concept is the *gold standard*, which is the best reference that can be achieved under certain limitations. Arguably, once 2-nm datasets exist with appropriate instances of 0.25-nm validation [3, 43], lower resolution gold standard sets are of limited value.

1.1.2 Graph Theory and Networks

Graph theory provides a framework for discovering, describing, and analyzing networks of all types, including neural networks [12, 25]. Neurons that integrate signals from other cells are *graph vertices*, and the individual connections they form via synapses, gap junctions, or other spatially discrete signaling modalities are *graph edges* [72]. While classical approaches treat networks as electrical circuits, they are not loop circuits at all, but rather flow systems. Indeed, the father of classical circuitry analysis, Gustav Kirchoff, also developed many critical aspects of network graph theory for analyzing flow. More importantly, graph theory allows robust descriptions of large-scale network organization. With high neuronal diversity and both dense and sparse components, it appears that biological systems-level networks such as retina and brain [83] are small-world networks [7–8]. Such networks contain essential features of local-scale disordered Watts–Strogatz networks [101], but in other cases, show evidence of highly connected hubs, e.g., retinal AII amacrine cells [4]. Hubs are characteristic of random systems like the World Wide Web [6], but the connectivity of retinal hubs is definitely not random. The problem of uncovering these topologies in detail falls under the field of *graph enumeration*, but the implication of high diversity was anticipated by Barmpoutis and Murray [7] who note that in determining the range of short distance/large clustering graph distributions, there are many graphs with short ranges but less than maximal clustering. Since there is no known evolutionary selector for maximal network clustering, this means that local network topologies cannot be inferred.

1.1.3 Network Enumeration

A major contribution made by graph theory to connectomics is a concrete definition of network diversity. In connectomics, we equate cells with graph vertices and their functional connections (synapses and gap junctions) with graph edges. Graph enumeration theory describes the possible network forms of any given system [35]. Figure 1.1 illustrates three relations for network diversity using a simple three-vertex example. A simple undirected network (a network with bidirectional edges) with three nodes admits eight different network connections. Allowing mixed (directed + undirected) connections admits $D_8 = 64$ configurations. Allowing each node to possess reentrant-directed connections expands the topology space to 512 options. And this does not consider connection weight diversity. No physiological or modeling effort has proven capable of resolving even this limited diversity.

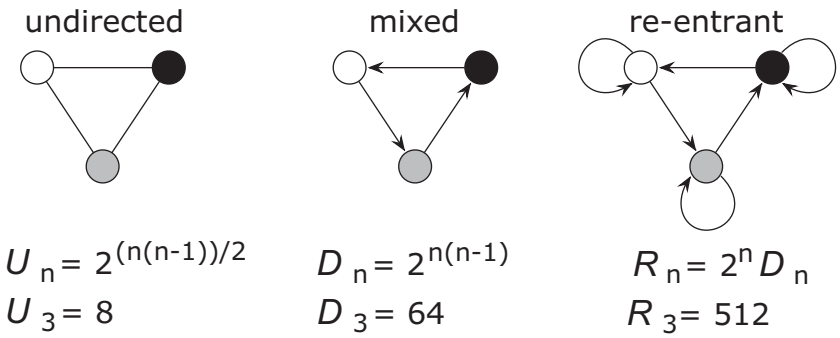

Fig. 1.1 Key network enumeration relations illustrated for a simple 3-vertex cluster connected in undirected (U_n *left*), mixed (D_n *center*, directed and undirected), and reentrant (R_n *right*) configurations, where n is the number of vertices (cells)

In the face of real biological complexity, the challenge is beyond resolution by any inverse solution approach. In the vertebrate retina, with ≈70 cell classes [63], $D_{70} = 9 \times 10^{1473}$. In the primate brain, based on known neuronal diversity and the estimated 250 distinct brain regions, 200 of which are cortical [100], we can estimate that at least 1000 classes of neurons exist. So for brain, $D_{1000} = 9 \times 10^{300728}$ [71]. How big is this number? The estimated number of atoms in the observable universe is 10^{80} and the time since the Big Bang is 4.3×10^{17} s [9]. Thus, even a universal computer running since the beginning of time could not parse a brain. This has distinct implications for each branch of neuroscience. Physiological mapping, even with multielectrode or optogenetics approaches [24], cannot uniquely specify correct topologies because *system transfer functions do not uniquely map onto network topologies*. This is a fundamental limitation of all inverse solution approaches [5]. For computing, and especially large-scale modeling [36, 39], sorting topologies is computationally intractable: It is the clique discovery problem, one of the best-known NP-complete problems [48]. Even simplifying concepts such as the common neighbor rule [83] do not significantly ease the topology discovery problem. Previous modeling efforts in simple invertebrate networks [84] have been argued as evidence that morphologic topology may be neither stable nor definitive and that different individual network weights in *each different animal* may lead to similar network performance. In this view, connectomics is not a viable effort. Morgan and Lichtman [81] give a strong defense of connectomics on this point, but it can be further argued that the high diversity of modeling solutions obtained by Prinz et al. [84] means that network topology and synaptic weights *must both* be demonstrably constrained to develop a functioning system of repeating units known to underlie vertebrate brain and retinal organization [72]. Ultimately, due to the massive diversity of neuronal classes, classical TEM sampling has been unable to completely specify any outflow module in the retina, much less than any other complex brain region. However, discrete, complete topologies can be discovered by connectomics.

1.2 Technologies

1.2.1 Biological Motivations for High-Resolution Ultrastructure

A complete connectomics map requires being able not only to simply detecting the easiest or most common motifs, but also to trace all neurogliovascular associations of brain and retina. Among sets of neurons, this includes connection types and *nonconnections*. The occurrence of a connection between a pair of cells (an edge between vertices) is a nominal proof of its typological existence, and its expected density can be computed from spatial dimensions of the chosen canonical field. Evidence of a nonconnection, however, is statistical, as one can only assert the absence of a connection over a sampled field, compared to realized connections. There are two types of nonconnections: those arising from (1) spatial separation where two kinds of cells never touch and, more importantly, (2) *touches*: contacts that form no connections despite opportunity. The latter implies deterministic rather than strictly probabilistic events in network assembly. There are five types of cell adjacency: touches, adherens, synapses + adherens, gap junctions + adherens, and synapses + gap junctions + adherens. Synapses and gap junctions never appear without nearby adherens complexes (Fig. 1.2).

The task of completely specifying the network associations of a cell depends on the reliability of discriminating contact types in a full 3D setting, which includes both ideal transverse and nonideal oblique sections through synapses, gap junctions, adherens junctions, and other paramembrane specializations. Bluntly, SEM imaging has never been competitive with TEM imaging for connectivity analysis. Indeed, after a half century of technical development, SEM still cannot provide the resolution of even the earliest TEM studies for synaptic analysis [22], and has never been the platform of choice. The question at hand is whether connectivity analysis by new SEM imaging is as reliable or complete as ATEM analysis. Part of the argument for SEM imaging is that it may visualize synapses adequately, even if not optimally.

While some presynaptic and postsynaptic features are supraoptical (>200 nm), most are not. Figure 1.2 shows a complex glutamate synapse in rabbit retina between an ON cone bipolar cell and two targets at a classical bipolar cell dyad. While the presynaptic ribbon is just at the limit of optical resolution, the postsynaptic densities (PSDs) of the ganglion and amacrine cell targets are both far smaller, on the order of 100 nm. Similarly, the entire gap junction is suboptical.

Definitive gap junction mapping requires picoscale imaging (Fig. 1.3). The spot adherens (Fig. 1.2a) is less than 30 nm in extent. This is nontrivial, as adherens junctions likely mediate protein delivery to and turnover of gap [58–59] and synaptic junctions [10, 79, 82]. Identifying contacts of these dimensions requires ground truth quality imagery, not 10–16-nm scale imaging typical of SEM data. Figure 1.2a–e shows the progressive degradation in image quality associated with 2-nm ATEM imaging (Fig. 1.2c), nominal 10-nm imaging (e.g., [49]), and 16-nm

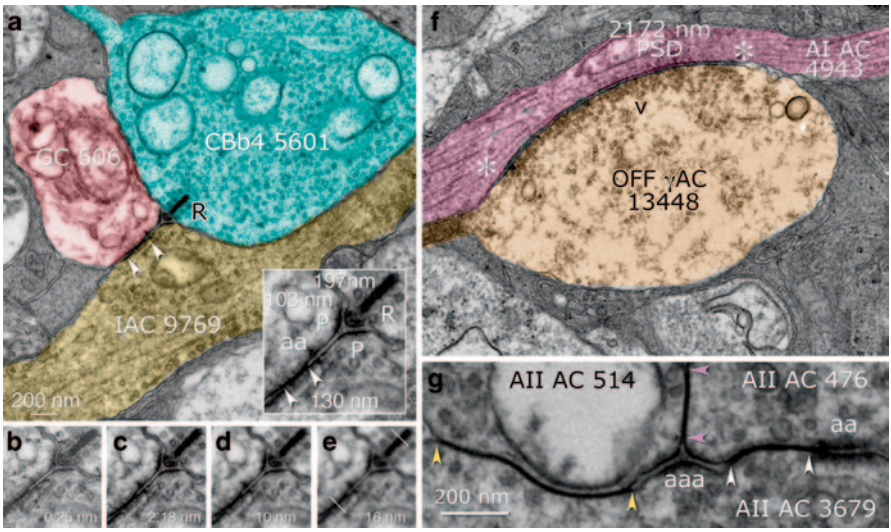

Fig. 1.2 Cell associations imaged with high-resolution ATEM. *A* A complex synapse involving excitatory ribbon drive from a glutamatergic bipolar cell (*CBb4 5601*) targeting a ganglion cell (*GC 606*) and a GABAergic amacrine cell (*IAC 9769*), and direct gap junction coupling between cells 606 and 9769. The insert marks a presynaptic ribbon (*R)* 197-nm long, a postsynaptic density (*P*) in ganglion cell 606 (103 nm) and amacrine cell 9769, the gap junction (*bracket by arrowheads*) between cells 606 and 9769, and a focal adherens junction (*aa*). *B* The inset region reimaged by goniometric tilt TEM with a resolution of 0.25 nm/pixel and a tilt of 5° from planar. *C* The primary image captured by ATEM with a resolution of 2.18 nm/pixel. *D* A simulated 10-nm/pixel resolution capture using a boxcar blur. *E* A simulated 16-nm/pixel resolution capture using a boxcar blur. The length and nominal position of scan paths used to profile the synaptic ribbon and gap junction are shown as *lines*. *F* A giant conventional form inhibitory synapse between an *OFF* cone pathway GABAergic amacrine cell (*γAC*) 13488 and a rod pathway *AI AC 4943*. *G* Three gap junctions between three different *AII ACs (476, 514, and 3679)* bracketed by 2-cell (*aa*) and 3-cell (*aaa*) adherens complexes. All data from the open-access RC1 connectome

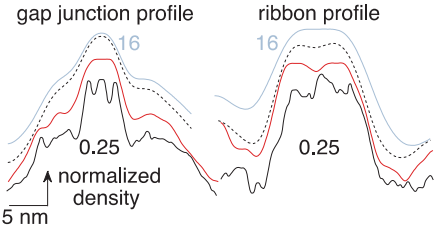

Fig. 1.3 Pixel density scans of a gap junction and synaptic ribbon shown in Fig. 1.2 at varying resolutions in nm/pixel: 0.25 (*black*), 2.18 (*red*), 10 (*dotted*), and 16 (*grey*). Imaging at 0.25 nm reveals the characteristic profiles of both structures. Resolutions used for connectomics lose details but 2-nm resolution retains enough high-frequency components to distinguish them

imaging characteristic of much published serial bloc-face (SBF) SEM imaging. Indeed the degradation at 16 nm is so marked that no validated gap junctions or bipolar cell synapses have yet been illustrated as part of any SBF connectomics analysis [14, 15, 38]. In contrast, 2-nm resolution ATEM easily detects all synapses and gap junctions, as well as validates noncontacts [2, 55, 71, 72]. The quality of these images is compared by density scans of critical features such as ribbons and gap junctions (Fig. 1.3), both of which are easily confused with PSDs and adherens junctions in automated detection systems, but are readily marked correctly by human annotators. Importantly, the severe blurring of gap junctions, synaptic ribbons, and PSDs at SBF scales makes these structures effectively indistinguishable. While the ability of ATEM to track these small contacts is critical to complete analysis, so too is ongoing validation by reimaging at ground truth level. We have found that selective homocellular gap junctions coupling cone bipolar cells to class-specific sheets [56] are extremely small (60–90 nm), formed by small processes of similar diameter. Validating these and similar contacts requires a ground truth resolution of smaller than half the size of the smallest structure that serves as a discriminator. In this case, the discriminant would be the gap between the outer leaflets of the coupled membranes. In retinal gap junctions, especially those involving amacrine cells, the feature would be the 1.8-nm gap [67]. If we modeled that gap as a three-segment trapezoid profile, each segment would have to be 0.6 nm and the sampling resolution would need to be 0.3 nm/pixel, which is why we have chosen 0.25 nm as our ground truth resolution. We have discovered that even with 2-nm ATEM resolution, gap junctions of less than 90 nm in planar extent and oblique tilt of $\geq 45°$ cannot be discriminated from similar-sized adherens junctions. Indeed our success rate is exactly 50%. Thus, as these specific contacts are identified, it is essential that many be validated by reimaging at ground truth resolution. So far, only ATEM methods have proven capable of reimaging ultrastructural features [4].

1.2.2 Samples, Ablation Sectioning, True Sectioning, and Imaging

Conventional fixation with mixed aldehydes, osmium en bloc staining, and optional en bloc uranyl acetate for electron imaging is optimal for ATEM. We use a Karnovsky's variant with light osmication. We do not use ferrocyanide staining as iron atoms cannot be removed for postembedding immunocytochemistry, which is one of our major tools. In contrast, SEM methods require a substantial enhancement of membranes for tracking and synapse identification and the use of osmium-thiocarbohydrazide-osmium and ferrocyanide is common. Since these metallization approaches cannot be reversed, SBF/FIB imaging is, so far, incompatible with molecular markers.

There are three sectioning technologies under exploration. Ablation methods use physical sectioning with an automated microtome, such as in vacuo SBF sectioning [14, 37] or surface ablation via in vacuo field ion beam (FIB) milling [50,

80], followed by SEM or scanning TEM (STEM) imaging of secondary electrons (surface-backscattered electrons). Ablation techniques require very thin sectioning steps [11] as secondary electrons are surface reflections of the sample and do not penetrate deeply. This surface imaging approach leads to excellent binarization of membrane images for tracing, but is quite sensitive to skips in data. It also limits resolution because electron beams can only be reduced to nanometer scale widths, and acquisition times can be quite long for large sample fields. Ablation methods are also incompatible with en bloc molecular markers for proteins and small molecules, so far. However, these are superb methods for wide-field connectomics: getting the broad-brush view of connectivity, which high-resolution connectomics can then refine.

Manual ultramicrotomy using existing platforms remains a reasonable alternative to specialized ablation systems [2, 13]. Microtomists can produce hundreds to thousands of serial sections with minor errors and much less time than required for TEM acquisition. Sections are placed on monomolecular films, followed by conventional metal staining and ATEM [2, 4]. Primary electron projection images of sections 50–70-nm thick can be used as 2D pages in a 3D volume or assembled as true 3D datasets. Because the data are projection images, they can be further refined by goniometric reimaging. In addition, intercalated thin sections are placed on slides for computational molecular phenotyping every 20–30 TEM sections, permitting the insertion of molecular data into the connectome (Fig. 1.4). Finally, robotic sectioning onto Kapton® films [49] is a new but not readily usable option. Hopefully, that technology will advance to the point of enabling more efficient use of existing TEMs by using electron-transparent films.

1.2.3 Molecular markers and Classification

The synaptic resolution of electron optical imaging comes at a significant price: the restricted ability to use typical macromolecular markers to classify cells. Neuronal classification has been based on Golgi impregnation or dye marking of cells, and more recently, by the expression of genetic markers. All these approaches led to consistent estimates of cell diversity in the retina [60, 61, 87]. Morphologic features have not proven useful for extending these classifications (e.g., cell diameters, Scholl rings, fractal analysis of dendritic arbors). An alternative approach, computational molecular phenotyping (CMP), developed by Marc et al. [47, 64, 65, 69, 70] allows fusions of structural and molecular profiling using pattern recognition, yielding neuron classification equivalent to prior anatomic studies. Based on formal theories of unsupervised multidimensional classification derived in remote sensing [23, 62] and clustering algorithms such as the K-means and isodata methods, CMP led to robust classifications, but achieved them in single retinas instead of hundreds [47, 64, 65, 69, 70]. CMP is compatible with ATEM [66]. The superiority of multivariate small molecule signatures over other TEM visualization methods also comes from its coverage. While there are over 60–70 classes of cells in mammalian retina (neurons, glia, microglia, vascular cells), and some are identifiable with antibodies

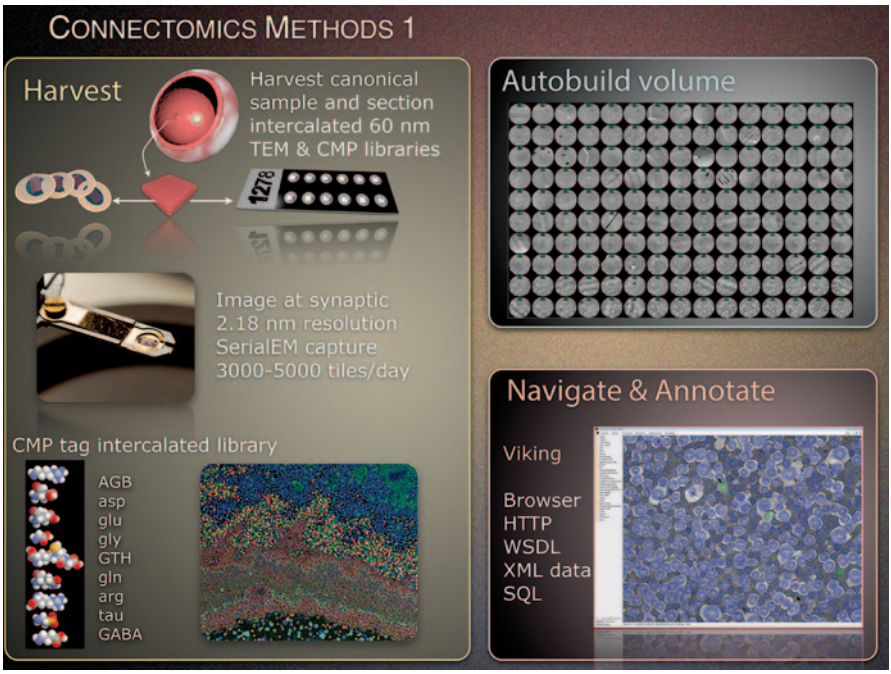

Fig. 1.4 Workflow for building connectomics volumes. Samples containing a canonical field are fixed for *TEM*, embedded and serially sectioned onto *TEM* grids with intercalated computational molecular phenotyping (*CMP*) sections placed on array slides. Fields are imaged at synaptic resolution and captured using SerialEM automation. Slides are probed for an array of small molecules that give a complete cellular coverage and high levels of classification. About 1000 *TEM* image tiles are mosaicked into single-image slices and slices registered into aligned volumes that can be visualized in the Viking navigation and annotation environment

targeting macromolecules, most are not TEM compliant and such univariate markers have very narrow coverage. Even with a theoretical experiment involving eight macromolecular tags, far less than 10% fraction of any neural system is classified. Conversely, small molecule tags such as glutamic acid embedded in a CMP schema quantitatively discriminate many classes of cells [21, 47, 64, 65, 68, 69]. CMP places multiple signals in every cell in a TEM dataset, so that even if a biologically ultimate class cannot be extracted for each, at least a very well-defined superclass cohort can be specified.

1.2.4 Computational TEM: Fast High-Resolution Acquisition

Each slice of a connectome volume is composed of > 1000 image tiles and can contain 100s to 1000s of slices (Figs. 1.4 and 1.5). This means that capturing needs to be high speed and automated. For our version of ATEM, individual grids are loaded manually into a goniometric holder and imaged at ≈ 5000× magnification in a grid

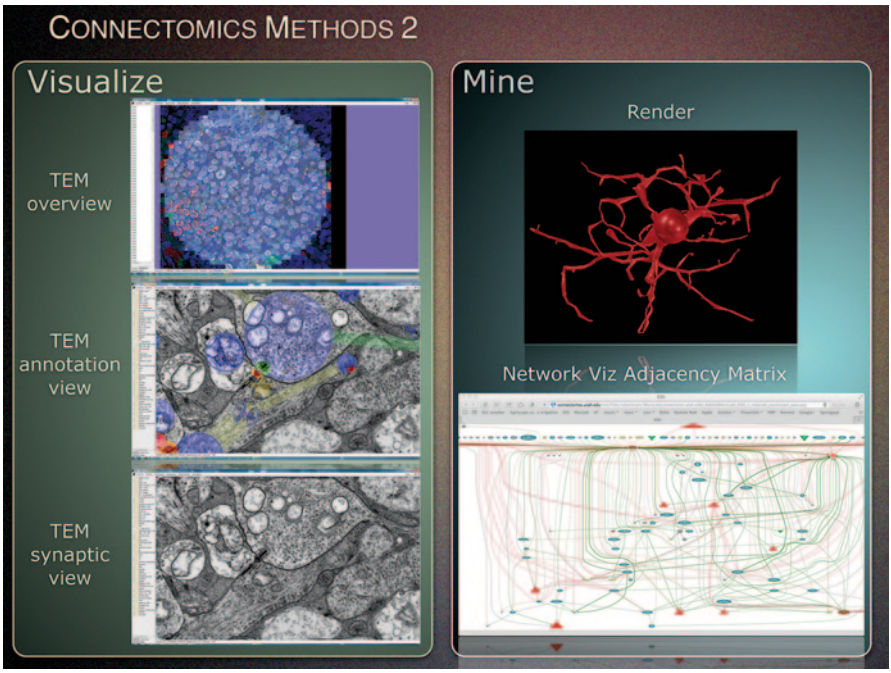

Fig. 1.5 Workflow elements for analyzing high-resolution connectomics volumes. Volumes are navigated at any desired resolution and annotated using the Viking navigator and annotation client. Individual synaptic fields can be rendered for image publication within Viking. Viking disk annotations contain all the information necessary to build accurate 3D cell volumes and visualize complete networks. Vikingplot is a MatLab® application that queries the SQL database to provide 3D rendering of individual cells or even all cells in the volume as individual images, stereo images, or fly-through movies. Network Viz is a graphing client that visualizes adjacency matrices of connected cells in a volume and allows queries of Viking

pattern with roughly 12 % edge overlap using a JEOL JEM 1400 TEM and a Gatan Ultrascan phosphorimaging camera [2, 3, 4, 95]. In the rabbit retinal connectome RC1 [4], each image slice (the digital transform of a physical section) contains a canonical field of 0.243-mm diameter and, at a resolution of 2.18 nm/pixel, requires 950–1100 individual images. Stage motion, focus, and image capture are achieved by SerialEM, developed by David Mastronarde at the University of Colorado, Boulder [74]. Modifications to SerialEM also allow sections to be preheated in a wide beam for film stabilization and complex patterns of image acquisition.

1.2.5 Image Volume Visualization and Annotation

Conventional imaging tools are incapable of visualizing datasets as large as a connectome or navigating them in a structured way. New tools are required [3, 28, 37, 44]. By using image pyramid sets [3, 78], web applications can readily view,

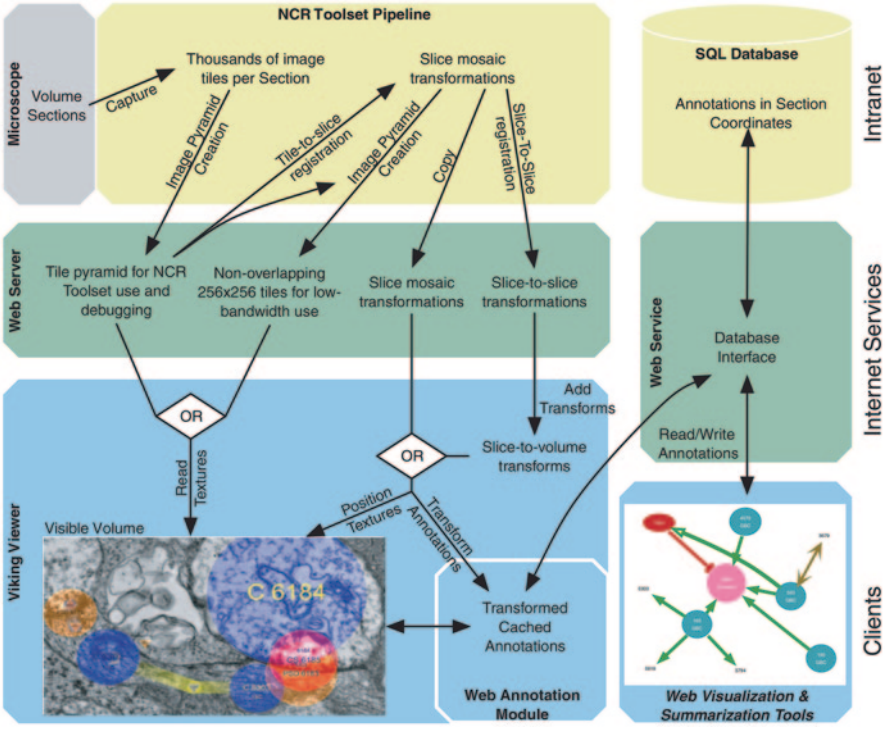

Fig. 1.6 Overview of the integrated image transform-Viking functions. Viking is a scalable annotation environment, based on a three-tier architecture. Tier 1 processes the TEM image data and maintains the *SQL* database maintenance in a secure environment isolated from the Internet. Tier 2 servers form the Web services definition language (WSDL) interface whereby transfers images, transforms, and annotations are negotiated between clients and Tier 1. Tier 3 is composed of our Viking viewing/annotation client and Viz analytics tools. Method calls between layers are stateless, and the tiered architecture permits independent tier modification. (From Anderson et al. [3] by permission of the authors)

transform, and annotate connectomes. Anderson et al. [3] have developed Viking to address these needs. Viking has a three-tier architecture in which Tier 3 viewer and analysis clients use HTTP to communicate with Tier 2 image and Web services definition language (WSDL)-compliant Web servers which, in turn, query the Tier 1 image library and populate annotations in a Tier 1 SQL database (Fig. 1.6). Viking operates by HTTP and supports concurrent multiuser, collaborative annotation. By demarcating viewing and analysis from data collection and hosting, this architecture allows independent tier specialization. Most importantly, it is capable of applying image transformations in real time for high-speed visualization. Human operators use disc-based annotation, centering an appropriately sized disc in every neural profile, which Viking links into a network of graphs (Figs. 1.5 and 1.6), 3D navigational skeletons, databases, and 3D renderings in multiple formats at 2 nm or better resolution. Presynaptic ribbons, patterned densities, vesicle clouds, PSDs, gap junctions, and adherens junctions are all characterized by their connectome

physical locations, dimensions, and parent structures, allowing the assembly of formal adjacency matrices.

1.2.6 Analysis: Automated Versus Authenticated Synapse Tracing

Retinal connectome RC1 is a connectome in an advanced state of annotation with ≈ 900,000 embedded annotations. RC1 is an open-data resource. The entire volume, all of its imagery, and all of its annotations are publicly available [4, 55], and any portion of it may be reproduced under a Creative Commons Attribution-NonCommercial 4.0 International License. No imagery or data from RC1 can be restricted by publication copyright. Even though it contains over 300 bipolar cells (BCs), 300 Müller cells (MCs), 39 AII ACs, over 100 ACs, and 20 ganglion cells (GCs), and includes a full set of small molecule markers for classification, it is far from complete. A spectrum of solutions has been proposed to complete the annotation set, ranging from automated detection schemas [43] to high-density crowdsourcing [15, 38). We were one of the earliest proponents of crowdsourcing [2] and have retreated from that position somewhat to advocate an executive annotator + team format. One of the major problems of automated and crowdsourcing approaches is resolving contact error detection and correction. The ease with which both software and novice annotators confuse oblique synapses, adherens junctions, and gap junctions, demands a ready-correction schema. In theory, any automated system must be tested against a ground truth dataset [43], but no one has proven that any automated system can discriminate these components. We have three practical solutions. First, errors in identification create violations of well-known connectivity rules: e.g., retinal ganglion cells are always postsynaptic, bipolar cells are never presynaptic to each other, rod bipolar cells form no gap junctions, OFF cone bipolar cells form no heterocellular gap junctions (so far), and ON bipolar cells are not coupled to ganglion cells. Any such aberrant contacts in a network build can be readily flagged by database queries for reconciliation by an experienced analyst. Second, albeit slower, goniometric reimaging can validate or reject unusual contacts. Third, our annotation training is intense. All new annotators serve an apprenticeship directed by a proven low-error annotator. Finally, as the entire volume is open access, any error can be corrected by later annotators.

1.3 Discovery

A key objective in developing high-resolution connectomics technologies arose directly from our own prior work identifying a broad array of complex-nested amacrine cell networks that have yet to be explained in any retina [66]. Analysis of RC1 has subsequently discovered new motifs and synaptic/coupling architectures. Here, we present a selection of those discoveries.

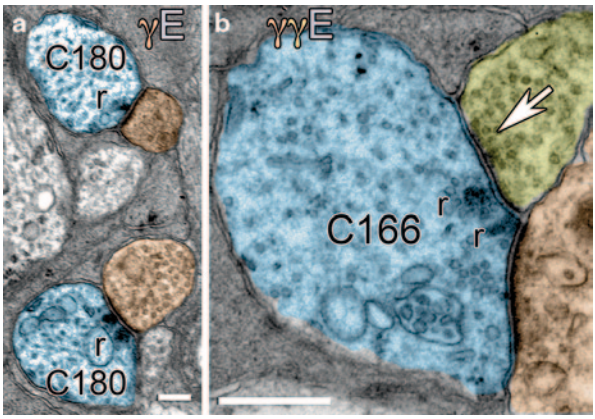

Fig. 1.7 Axonal ribbons made by ON bipolar cells in RC1. (*A*) Axonal ribbons (*r*) at mid-axon (*blue*) from ON cone bipolar cell 180 to AC targets (*orange*) in the OFF sublayer. Cell 180 splits high in the OFF sublayer and makes axonal ribbons immediately after the split. (*B*) Axonal ribbons from ON cone bipolar cell 166 to two different targets (*orange, yellow*), one of which makes a feedback synapse (*arrow*). Note the distinctive postsynaptic densities in the targets. Scales, 500 nm. *γ* GABA, *E* glutamate. (Recomposed from Anderson et al. [4] by permission of the authors)

1.3.1 Novel Networks Refactor the Retinal Inner Plexiform Layer

In the process of tracing rod–cone pathways, we noted two abundant suboptical architectures that changed the expected patterning of signals in the mammalian inner plexiform layer: nanoscale ON bipolar cell axonal synaptic ribbons (Fig. 1.7) and nanoscale descending axonal processes in OFF bipolar cells. By annotating all bipolar cells in RC1 (≈300), we defined rod bipolar cells and two superclasses of cone bipolar cells: ON (CBb) and OFF (CBa). CBa and CBb cells are fully distinguished by three features: (1) CBa cells terminate primarily in sublayer **a** with fine processes into the upper sublayer **b**, while CBb cells terminate primarily in sublayer **b** with axonal outputs in sublayer **a**; (2) CBa cells are both presynaptic and postsynaptic to AII amacrine cells, while CBb cells are instead coupled to AII amacrine cells by large gap junctions; and (3) CBa cells have a strong primary glutamate signature while CBb cells have a mixed glutamate–glycine signature due to coupling with glycinergic AII amacrine cells. Complete annotation allows further refinement of cone bipolar cells into ultimate classes including six OFF (CBa1, CBa1w, CBa1–2i, CBa2, CBa2w; CBab2) and six ON (CBb3, CBb3–5-4i, CBb4w, CBb5w, CBb6, and CBb7) cone bipolar cells, where the number indicates a progressively more proximal stratification, **i** denotes an interlaced axonal pattern, and **w** denotes wide-field axonal arbors. In the process of this complete annotation, we found abundant suboptical (<100 nm) synaptic ribbons and vesicle assemblies in the axons of CBb cells [5]. Upon reconstruction, we showed that these represented a novel ON pathway input to the OFF layer of the inner plexiform layer [55], verifying the optical

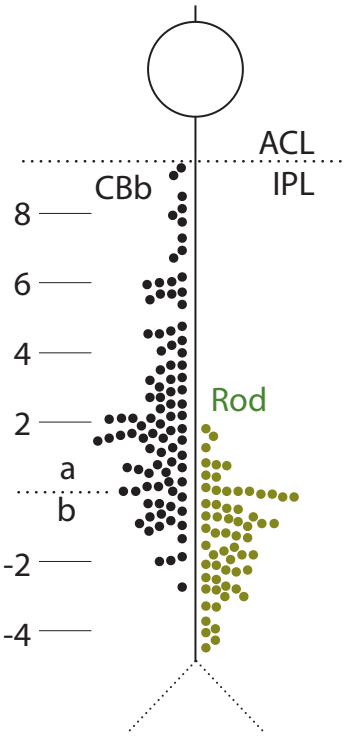

Fig. 1.8 Axonal ribbons. The distribution of 160 axonal ribbons in 54 ON cone bipolar cells and 63 of the highest ribbons in 63 of 104 rod bipolar cells in connectome RC1. Ribbon positions are measured relative to the sublayer *a*/*b* border, defined as the proximal face of the nearest AII AC lobule. ON cone bipolar cell axonal ribbons are distributed throughout sublayer *a*. Rod bipolar cell axonal ribbons are excluded from 80% of sublayer *a*. (From Lauritzen et al. [55], by permission)

immunocytochemical visualization of synaptic ribbon proteins [26, 42]. High-resolution connectomics then enabled a complete connectivity analysis. Connectomics of RC1 [55] showed that (1) 36% of CBb cells form OFF layer axonal ribbons (Figs. 1.7 and 1.8); (2) all classes of CBb cells contribute to this motif, targeting ON ganglion cells that arborize in the OFF sublayer, e.g., intrinsically photosensitive ganglion cells and bistratified diving ganglion cells; and (3) specific glycinergic and GABAergic amacrine cells engaged in ON → OFF crossover signaling were targeted. These data completely revise the notion that amacrine cell and ganglion cell stratification patterns alone control access to ON and OFF inputs. More detailed discussion of the implications of this motif is available in Marc et al. [72]. No SEM schema has detected these motifs.

Similarly, the ON sublayer of the inner plexiform layer is not a pure ON signal domain. Lauritzen et al. recently discovered that the upper half of the ON layer contains significant numbers of ribbon outputs arising from fine descending processes of OFF cone BCs, forming a large band of commingled CBa and CBb cell inputs in IPL sublayers 3–5. These processes are usually < 100 nm in diameter and

synaptically target amacrine cells. Once again, these are processes that have been missed by lower resolution technologies such as SBF SEM [38]. This branching permits intermixed ON class and OFF class processes to target single glycinergic and GABAergic amacrine cells, generating ON–OFF functions. These new sets of bipolar cells are termed CBab cells. They are, nevertheless, classical OFF cone BCs as their primary arbors are in the OFF layer; they are coupled to other OFF bipolar cells in homocellular arrays; they are presynaptic and postsynaptic to AII amacrine cell lobules; and they are glycine negative. The diversity of contacts is as complex as for axonal ribbons. CBab cells provide a direct ribbon drive to at least one ganglion cell class in the ON layer and synapse onto amacrine cells throughout the nominal ON layer of the inner plexiform layer, creating ON–OFF amacrine cells that likely drive all ON bipolar cell surrounds. Thus, CBab cells form specific ON–OFF subnetworks that could not otherwise be constructed. These unpredicted network topologies may underlie widespread ON–OFF signaling in the retina.

These new findings suggest a revision of the traditional view of inner plexiform layer organization in the mammalian retina. First, there is no pure OFF layer as it is completely patterned with ON inputs from axonal ribbons. Second, the central region of the inner plexiform layer is composed of mixed ON and OFF cone bipolar cells whose surrounds are ON–OFF, since they are driven by GABAergic and glycinergic amacrine cells that collect inputs from both ON CBb and OFF CBab cells. Finally, the “pure” ON zone is restricted to a thin layer of rod bipolar cells and wide-field ON cone bipolar cells. This refactoring implies that multistratified amacrine and ganglion cells cannot be assumed to be ON–OFF in polarity and that monostratified amacrine and ganglion cells cannot be assumed to be pure OFF or pure ON. Complete connectivity maps must be derived for every cell class.

1.3.2 Bipolar Cell Coupling Arrays

Homocellular coupling between neurons such as horizontal cells or AII amacrine cells, and heterocellular coupling between ON cone bipolar cells and AII amacrine cells (using the notation CBb::AII) has long been known [27, 51–53, 85]. These gap junctions are often large and/or abundant. However, the neural retina contains numerous classes of highly branched cells, such as cone bipolar cells, and tracing their processes has heretofore proven challenging. Even markers selective for single classes do not allow tracing of suboptical processes nor visualization of suboptical gap junctions [57]. By tracing every class of cone bipolar cell, we discovered an extensive axonal coupling within but not between CBa and CBb superclasses [56]. Within each superclass, both in-class (homocellular, e.g., CBb4w::CBb4w) coupling sheets and cross-class (heterocellular, e.g., CBb3::CBb3–4i::CBb4w) coupling tiers exist. Cross-class coupling occurs between neighboring CBb pairs because their stratifications overlap vertically and laterally. As many CBb cells appear to express Cx36 [34], this may explain in-class and cross-class coupling. These networks are sparse: Five CBb5w bipolar cells (Fig. 1.9) coupled at five loci

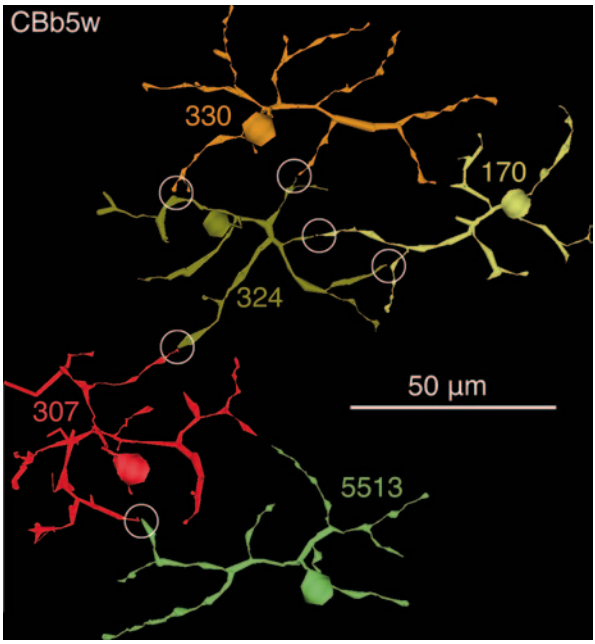

Fig. 1.9 Homocellular bipolar cell coupling. A coupled sheet of *CBb5w* cells viewed in the XY plane (the retinal image plane). Each color denotes a different cell of the same class and circles mark points of coupling. Vikingplot rendering of data from the open access connectome *RC1*. Lauritzen, unpublished

represent a cellular volume spanning > 39,000 distinct high-resolution images. The probability of finding any of these gap junctions randomly by TEM is far less than 1 in 10,000 image sessions. Without 3D tracing, it is impossible to define the cell of origin. It is only through connectomics that we find biological relationships that are sparse, yet pervasive. Further, the largest dimension of the gap junction at one locus between cells is ≈ 140 nm, far below the limit of optical imaging. Tiered coupling in the ON pathway (e.g., CBb3::CBb4::CBb5) excludes CBa or rod bipolar cells. The physiological implications are unclear. It is possible that cone bipolar cells use coupling to smooth signaling transitions across classes with different dynamic ranges, or smooth inhibition across patches of cells. CBa::CBa coupling is also extensive. Coupling may play a role in the development of cone bipolar cell terminal tiling.

1.3.3 Advanced Networks: Rod–Cone Suppression, Nested Feedback

Inhibitory networks dominate the retina. Over 90 % of the mass of the vertebrate inner plexiform layer is made of GABAergic neurons. The most common synapses

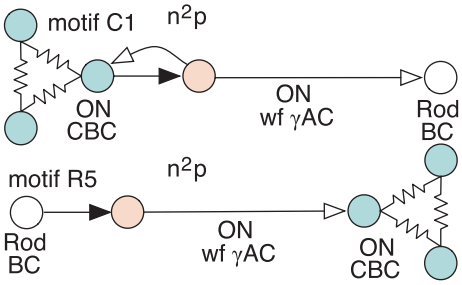

Fig. 1.10 Two of the eight rod–cone decision networks discovered in open-access connectome RC1. In motif *C1*, couple patches of *ON* cone bipolar cells (*ON CBC*) drive wide-field feedback/feedforward *ON* GABAergic amacrine cells (*ON wf γAC*) that inhibit rod BCs. In motif *R5*, rod BCs drive feedforward *ON wf γACs* that inhibit *ON CBCs*

are amacrine cell synapses. The most common motifs are amacrine-to-amacrine synapses [66]. Yet, there are no models that require or explain this attribute. By mining the *complete* connectivities of certain cells, we have been able to extract key architectures such as decision networks. We have also been able to define participants in serial amacrine cell motifs, some of which represent nested feedback and feedforward architectures introduced by Marc and Liu [66]. These networks could not have been identified by statistical methods.

Inhibitory decision networks are the essential components of sensory "trigger features," such as motion. Similar decision processes have been implicated in rod–cone interactions by psychophysical analyses [16, 18, 30, 32, 54, 89, 90, 96–98]. Such interactions are surprisingly fast and often involve small spatial fields [17–19, 96]. Rods can also induce a variety of chromatic effects in cone pathways [89]. What are the pathways underlying these operations?

Connectomics analysis of RC1 shows that at least eight unique suppression motifs exist between rod bipolar cells and cone bipolar cells [72] and that these are mediated by several different sets of amacrine cells (Fig. 1.10). Cone pathway suppression of rod pathways is mediated by five distinct motifs initiated in all cone bipolar cell classes. Rod bipolar cells receive inhibition by ON cone bipolar cells via motifs C1 and C2; and inhibition by OFF cone bipolar cells via motifs C3, C4, and C5. Rod pathway suppression of cone pathways is mediated by three distinct motifs targeting all cone bipolar cell classes. ON cone bipolar cells receive a powerful suppression via motifs R1 and R3, while motif R2 suppresses OFF cone bipolar cells. These motifs are consistent with a range of psychophysical results and show that there is a complete suppressive crossover between all cone bipolar cells and rod bipolar cells. This was not known prior to high-resolution connectomics.

While amacrine cell serial synapses have been described for over half a century, their role has been completely unknown, even though they are the most common synapses in the inner plexiform layer [65]. Marc and Liu [66], using limited series of TEM sections, showed that nested feedback was a dominant motif in the vertebrate inner plexiform layer, but could not identify all the partners. Using comprehensive connectomics, it has now been possible to show that all cone bipolar cell

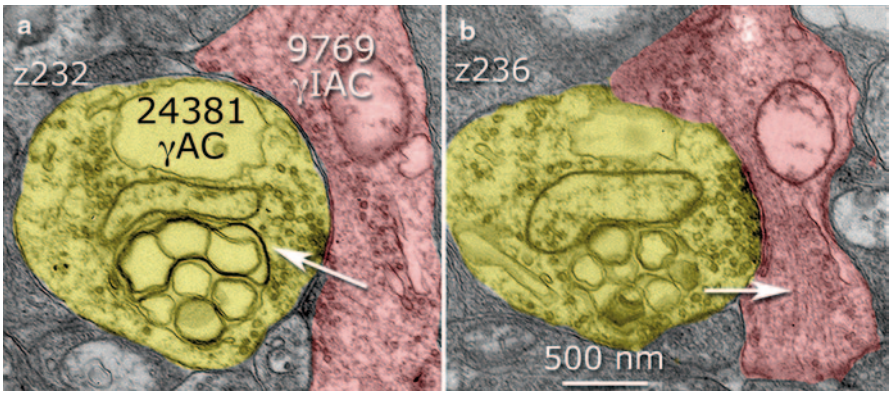

Fig. 1.11 Nested inhibition between different classes of amacrine cells. *A* Wide-field GABAergic feedback amacrine cell *24381* is postsynaptic to GABAergic feedforward interstitial amacrine cell *9769* (*arrow*) at slice *z232* in retinal connectome RC1. *B* Cell *24381* is presynaptic to cell *9769* (*arrow*) at slice *z236*

feedback amacrine cells engaged in a variety of nested topologies. Indeed, there is no simple first-order feedback. There are a large number of possible nesting topologies and several have been documented. One example is multichannel nesting where a pure feedforward GABAergic interstitial amacrine cell collects signals from several classes of ON cone bipolar cells (IAC, cell 9769, Fig. 1.11) and is both presynaptic and postsynaptic to a different wide-field GABAergic amacrine cell (wf AC, cell 24381, Fig. 1.11) that itself is a part of a more different ON cone bipolar cell feedback network. This reciprocal relationship simultaneously creates both nested feedback to bipolar cells through the CBb>IAC>i fw AC>i CBb and nested feedforward to target ganglion cells CBb>wf AC>i IAC>i GC.

The advantage of nesting low-gain inhibition (i.e., feedback networks inhibiting themselves as well as their targets) is that it is the *simplest form of network tuning possible*. The concept is realized in many forms in modern electronics, such as nested transconductance amplifiers, where the depth, polarity, and strength of nesting shapes the frequency response of the network [103]. Marc and Liu [66] described how such a network could improve the bandpass of bipolar cell output (Fig. 1.12) by increasing both the system corner frequency and bandwidth. Of course, this is only a simple linear systems analysis, and in spiking networks, these attributes can be even more potent, forming critical timing networks.

1.3.4 New Structures

Since the 1960s, ultrastructural analysis of brain and retina has depended on known morphologies: chemical synapses, gap junctions, and adherens junctions. In analyzing connectome RC1, especially during a complete neuronal mapping, new contact

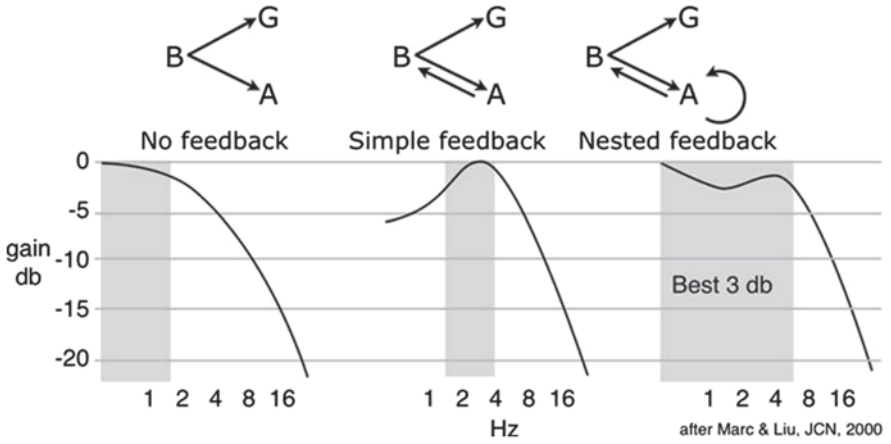

Fig. 1.12 The effect of nested inhibition on network properties as modeled by Marc and Liu [66]. The *top row* illustrates the topologies of networks among bipolar (*B*), amacrine (*A*), and ganglion cells (*G*) with no feedback, simple first-order feedback, or nested feedback. The *bottom panels* illustrate the frequency response properties (ordinate in db, decibels; abscissa in *Hz*, cycles per second) of bipolar cell output under three conditions. Simple feedback classically increases the corner frequency from a simple roll-off (*left*) to a bandpass form (*middle*) at the expense of low-frequency roll-off. Nested feedback attenuates the roll-off and essentially spreads the bandwidth (the best 3 db range) two- to threefold

architectures were discovered [72]. Their full description is outside the scope of this review, but they are examples of the power of high-resolution 3D mapping.

Cistern contacts were first found between ON cone bipolar cell axons and amacrine cells [4, 55]. They are characterized by postcistern density that resembles a conventional PSD. The precistern structure is smooth endoplasmic reticulum (SER) loop.

Rough endoplasmic reticulum (RER) contacts resemble cistern contacts and appear to be initiated by amacrine cells in most cases. Two or flattened SER cisterns on the pre-RER side are capped by a loop of RER, and the opposing processing displays a PSD similar to a conventional excitatory synapse. RER contacts can originate both in and far from neuronal somas, and we envision the contact using a signaling peptide requiring local synthesis.

Bipolar cell conventional (BCC) synapses are large synapses found in bipolar cells that resemble conventional brain glutamate synapses. First described in human retinas [1], they have been completely ignored since. Normally, bipolar cells are defined as cells that use synaptic ribbon complexes for glutamate signaling. However, cone bipolar cells (not rod bipolar cells) can also display synapses without synaptic ribbons and target cells that use very large PSDs. Interestingly, some BCC synapses target only specific cells (including directionally selective ganglion cells). We hypothesize that BCC synapses drive transient events while ribbon synapses drive sustained signaling.

Keyholes are unusual and rare structures formed mostly by CBb3 ON bipolar cells and CBa2 OFF bipolar cells. Keyholes are loops formed by bipolar cell axon terminal tendrils recurving to contact the parent terminal with a gap junction. In the process, they surround fine amacrine cell processes, some as small as 30 nm. We do not know whether keyholes are functional. If so, they may act as low-gain ephaptic signaling sites.

Plaques are large, dense, osmiophilic cisterns formed at the plasmalemma by ganglion cells primarily in their somas or proximal dendrites, adjacent to Müller cells but not adjacent to any neurons. This is yet another structure that has not been previously described, yet is quite readily detected in the RC1 volume. While we do not know the function of this organelle, its association with neurons known to use TRP-style channels is intriguing.

New Network Concepts: Sparseness and Joint Distributions Despite the very high density of connections in the retina, most occur largely as widely spaced singlets (very much like brain), especially in terms of amacrine cell inputs to ganglion cells. Understanding the relationships between neuronal sets requires knowing the full shape of the dendritic/axonal field and the patterning of synaptic inputs. The notion that one can summarize cell networks statistically is not supported by connectomics analysis of retinal connectivity. For example, there has been a debate about whether retinal AII amacrine cells have significant outflow to retinal ganglion cells [53, 94]. In line with both analyses (1) the scales of sampling are too small and (2) the assumption that sampling will be uniform across cells is wrong. Sampling is a joint distribution J_{AB} of the physical intersections between two arbors A_{XYZ} and B_{XYZ} in 3D space: $J_{AB}=A_{XYZ} \cap B_{XYZ}$. Individual cell classes differ widely in neurite patterning [86], so J will depend on the individual elements [55]. The axonal ribbons of ON cone bipolar cells are a perfect example. In a random instance of one ON bipolar cell class, the most probable outcome will be that no axonal ribbons will be observed. Does this not mean that axonal ribbons are some statistical fluke? Not at all. It means that the distribution of targets that prefer ON bipolar cell input in the OFF sublayer is sparse, with a surfeit of axons but a deficit of targets. Importantly, every time a target encounters an ON bipolar cell axon, it does make a synapse. Thus, the sampling by the target is perfect, but the statistics of the source appears variable. The latter is an illusion, and the former is the result of joint distribution sampling. The same is true of the synapses of AII amacrine cells onto the dendrites of ganglion cells in the OFF layer [4, 73]. Again, sources far outnumber targets. AII ACs have large Hausdorff dimensions (they are highly space filling) and form far more output neurites than are required to completely target all the ganglion cells dendrites in the OFF volume. However, OFF alpha ganglion cell dendrites traversing the OFF layer receive input from every AII amacrine cell they encounter, again with perfect efficiency. This means that the classical practice of measuring output percentages from an afferent and computing synaptic variances has little meaning for network analysis.

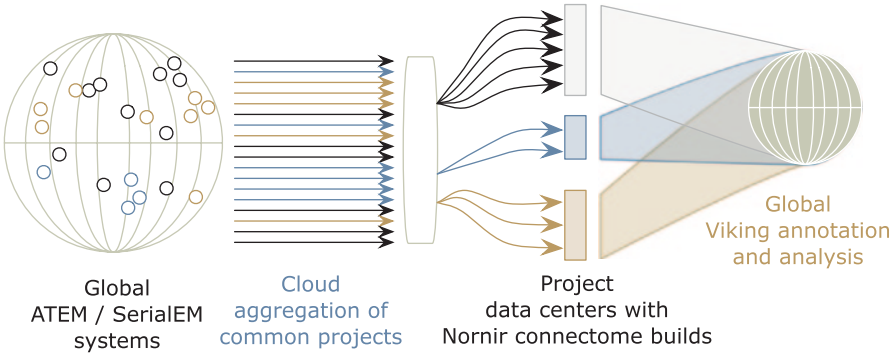

Fig. 1.13 Massively scaling connectomics. Global collections of ATEM systems independently acquire large datasets for multiple projects. These are aggregated by cloud-based storage resources into common project datasets and distributed to data centers charged with their builds. All build becomes globally available via Viking-like Web tools for annotation and analysis

1.4 Future Directions

1.4.1 Faster Connectome Builds

Completeness is a new objective in neuroanatomy. Deciphering the individual motifs of brain and retinal networks requires the discovery all cell classes, all contacts, and contact patterns. Every network we have explored shows new, unexpected motifs [4, 55, 71], and this goal is strongly justified. But the practice of high-resolution connectomics is not easily expanded. Our current build of mouse retina based on 1400 serial sections and large scale (0.28 mm diameter) is taking roughly 12 months. To do comparative studies of wiring differences across individuals, strains, species, etc., we need faster connectome builds (threefold or more), especially if we are to explore a large-scale neural reorganization in disease, development, and learning–memory transitions. No current platform is adequate. The simplest solution is building more platforms, of any type, and running them continuously. ATEM systems have two advantages in that they can be re-purposed from existing TEMs with appropriate software enhancements, and all acquisition can be asynchronous. Unlike SBF SEM or FIB SEM/STEM, a connectome acquisition on ATEM systems can be easily interspersed with other projects. Thus, ATEM systems are superb for core ultrastructural services. An ideal scheme for high-throughput connectomics would be a global build system (Fig. 1.13) that would require no new infrastructure. Existing arrays of TEM can be coordinated with image sets of grids for multiple projects, and all data can be moved to cloud storage for project-specific aggregation and queuing to distributed data centers for connectome builds and database instantiation. Importantly, Viking is a Web client with very low bandwidth demands, which means that annotation and analysis are fully open and distributed, and thousands of analysts can develop and refine connectomes simultaneously. We estimate that such

a network of existing TEMs based on SerialEM acquisition, our new open source Nornir build system (available at GitHub), and Viking annotation, can accelerate connectome assembly and use by over 100-fold. Indeed, new initiatives, such as the Open Connectome Project [20], inspire the idea that significant advances in analytical speed can be had as well. In contrast, single system enhancements via faster cameras and more stable scanning stages may yield improvements 2–3 ×.

1.4.2 Improved Molecular Markers

We need expanded libraries of molecular markers that are intrinsically compatible with electron imaging. Small molecule markers are ideal for ultrastructural imaging without compromising TEM contrast [45, 55, 66, 71], but it is also important to exploit key macromolecules in connectivity mapping to differentiate synaptic partners such as in array tomography [75–77]. So far, it has not been possible to merge the power of array tomography (which allows single-synapse molecular profiling) with electron imaging. There are two primary reasons for this. First, most antibodies against macromolecules were developed under conditions optimal for native or denatured protein detection, e.g., in western blots, but not for highly modified epitopes generated by TEM fixation. When such antibodies are found, they are happy accidents. A major advance would be the development of designed TEM-compliant antibodies. The second reason for limited use of protein markers is expression level: cell class-specific variations in total protein and variations in distribution. While the total amount of protein such as connexin 36 may be low, virtually all of it is located in transmembrane rafts of protein with approximate center-to-center spacing of 10 nm [91], which corresponds to an effective concentration of 1–3 mM in epitope presentation. Another protein expressed at similar levels may be distributed uniformly throughout the cytoplasm of a cell with a mean nanomolar concentration and completely undetectable by conventional TEM immunocytochemistry.

1.5 Neural Dynamics, Development, and Disease

A serious limitation of high-resolution connectomics is the inability to perform large-scale statistical comparisons. While highly focused studies have enabled detailed descriptions of small-scale plasticity changes in neural architecture driven by different conditions [13, 29, 88], scaling up such efforts to analyze complete network variations in genetic and disease models is beyond current architectures. Early connectomics studies may help define canonical fields more precisely and support statistical studies on smaller volumes. For example, in advanced retinal degenerations, key neurons such as bipolar cells lose their dendrites and rewire in the inner plexiform layer [45, 46], but the scope of that rewiring remains unknown. Rather than building an entire connectome containing over 100 rod bipolar cells

(in 3–5 months), one could build and analyze 10 different connectomes of 10 rod bipolar cells each at the same time. But if one does not know the spatial domain of a target system, larger scale sampling will be critical and speeding up connectomics is a major objective.

Modeling What do we want to do with these complex network diagrams and lists of features? Clearly, one goal is to generate rich models that allow parametric exploration of large-scale systems [36, 39, 83]. The connectomics community will be responsible for exporting structural and network data in appropriate modeling formats such as variants of NEURON [41] and NeuroML [31]. We are currently developing such tools using Python scripting with open access in the GitHub repository. One challenge is to exploit full 3D cell descriptors and spatial distributions of connections for modeling cells as noncompact entities. At present, Viking-based cellular elements are more richly defined than most modeling environments can accommodate, and modeling networks on multihop scales involving dozens of cells classes and thousands of copies demands advanced computational tools [39].

Acknowledgments We thank the National Institutes of Health (EY02576, EY015128, and EY014800), National Science Foundation (0941717), the Thome Foundation, and Research to Prevent Blindness for support. We also thank Shoeb Mohammed for software development, and Hope Morrison, John Vo Hoang, and Noah Nelson for annotation.

References

1. Allen, R. A. (1969). The retinal bipolar cells and their synapses in the inner plexiform layer. *UCLA Forum Medical Sciences, 8,* 101–143.
2. Anderson, J. R., Jones, B. W., Yang, J.-H., Shaw, M. V., Watt, C. B., Koshevoy, P., Spaltenstein, J., Jurrus, E., UV, K., Whitaker, R., Mastronarde, D., Tasdizen, T., & Marc, R. E. (2009). A computational framework for ultrastructural mapping of neural circuitry. *PLoS Biology, 7*(3), e1000074.
3. Anderson, J. R., Grimm, B., Mohammed, S., Jones, B. W., Spaltenstein, J., Koshevoy, P., Tasdizen, T., Whitaker, R., & Marc, R. E. (2011a). The Viking viewer: Scalable multiuser annotation and summarization of large connectomics datasets. *Journal of Microscopy, 241,* 13–28. doi:10.1111/j.1365-2818.2010.03402.x
4. Anderson, J. R., Jones, B., Watt, C., Shaw, M. V., Yang, J.-H., DeMill, D., Lauritzen, J. S., Lin, Y., Rapp, K. D., Mastronarde, D., Koshevoy, P., Grimm, B., Tasdizen, T., Whitaker, R., & Marc, R. E. (2011b). Exploring the retinal connectome. *Molecular Vision, 17,* 355–379.
5. Aster, R., Borchers, B., & Thurber, C. (2005). *Parameter estimation and inverse problems*. New York: Academic Press
6. Barabási, A.-L., & Albert, R. (1999). Emergence of scaling in random networks. *Science, 286,* 509–512.
7. Barmpoutis, D., & Murray, R. M. (2010). Networks with the smallest average distance and the largest average clustering. arXiv 1007.4031.
8. Barthelemy, M., & Amaral, L. A. N. (1999). Small-world networks: Evidence for a crossover picture. *Physical Review Letters, 82,* 3180–3183.
9. Bennett, C. L., Larson, D., Weiland, J. L., Jarosik, N., Hinshaw, G., Odegard, O., Smith, K. M., Hill, R. S., Gold, B., Halpern, M., Komatsu, E., Nolta, M. R., Page, L., Spergel, D. N., Wollack, E., Dunkley, J., Kogut, A., Limon, M., Meyer, S. S., Tucker, G. S., & Wright, E. L.

(2013). Nine-year Wilkinson Microwave Anisotropy Probe (WMAP) observations: Final maps and results. arXiv 1212.5225v3 [astro-ph.CO]
10. Benson, D. L., & Huntley, G. W. (2012). Building and remodeling synapses. *Hippocampus, 22,* 954–968.
11. Boergens, K. M., & Denk, W. (2013). Controlling FIB-SBEM slice thickness by monitoring the transmitted ion beam. *Journal of Microscopy, 252,* 258–262.
12. Bollobás, B. (1998). *Modern graph theory*. New York: Springer.
13. Bourne, J. N., & Harris, K. M. (2011). Nanoscale analysis of structural synaptic plasticity. *Current Opinion in Neurobiology, 22,* 1–11. doi:10.1016/j.conb.2011.10.019.
14. Briggman, K. L., & Denk, W. (2006). Towards neural circuit reconstruction with volume electron microscopy techniques. *Current Opinion in Neurobiology, 16,* 562–570.
15. Briggman, K. L., Helmstaedter, M., & Denk, W. (2011). Wiring specificity in the direction-selectivity circuit of the retina. *Nature, 471,* 138–188.
16. Brill, M. H. (1990). Mesopic color matching: Some theoretical issues. *Journal of the Optical Society of America A. Optics and Image Science, 7,* 2048–2051.
17. Buck, S. L. (1997). Influence of rod signals on hue perception: Evidence from successive scotopic contrast. *Vision Research, 37,* 1295–3101.
18. Buck, S. L. (2004). Rod-cone interactions in human vision. In: L. M. Chalupa & J. Werner (Eds.) Visual neurosciences (Vol. 1, pp. 863–878). MIT Press, Cambridge
19. Buck, S. L., Stefurak, D. L., Moss, C., & Regal, D. (1984). The time-course of rod-cone interaction. *Vision Research, 24,* 543–548.
20. Burns, R., Roncal, W. G., Kleissas, D., Lillaney, K., Manavalan, P., Perlman, E., Berger, D. R., Bock, D. D., Chung, K., Grosenick, L., Kasthuri, N., Weiler, N. C., Deisseroth, K., Kazhdan, M., Lichtman, J., Reid, R. C., Smith, S. J., Szalay, A. S., Vogelstein, J. T., & Vogelstein, R. J. (2013). The open connectome project data cluster: Scalable analysis and vision for high-throughput neuroscience. *Science Statistics Database Management*. doi: 10.1145/2484838.2484870.
21. Chua, J., Nivison-Smith, L., Tan, S. S., & Kalloniatis, M. (2013). Metabolic profiling of the mouse retina using amino acid signatures: Insight into developmental cell dispersion patterns. *Experimental Neurology, 250,* 74–93.
22. Cohen, A. I. (1965). Some electron microscopic observations on inter-receptor contacts in the human and macaque retinae. *Journal of Anatomy, 99,* 595–610.
23. Cover, T. M., & Hart, P. E. (1967). Nearest neighbor pattern classification. *IEEE Transactions on Information Theory IT, 13,* 21–27.
24. Deisseroth, K. (2011). Optogenetics. *Nature Methods, 8,* 26–29.
25. Diestel, R. (2005). *Graph theory* (3rd edn.). Heidelberg: Springer-Verlag.
26. Dumitrescu, O. N., Pucci, F. G., Wong, K. Y., & Berson, D. M. (2009). Ectopic retinal ON bipolar cell synapses in the OFF inner plexiform layer: Contacts with dopaminergic amacrine cells and melanopsin ganglion cells. *Journal of Comparative Neurology, 517,* 226–244.
27. Famiglietti, E. V. J., & Kolb, H. (1975). A bistratified amacrine cell and synaptic circuitry in the inner plexiform layer of the retina. *Brain Research, 84,* 293–300.
28. Fiala, J. C. (2005). Reconstruct: A free editor for serial section microscopy. *Journal of Microscopy, 218,* 52–61.
29. Fiala, J. C., Spacek, J., & Harris, K. M. (2002). Dendritic spine pathology: Cause or consequence of neurological disorders? *Brain Research Reviews, 39,* 29–54.
30. Frumkes, T. E., & Eysteinsson, T. (1988). The cellular basis for suppressive rod-cone interaction. *Visual Neuroscience, 1,* 263–273.
31. Gleeson, P., Crook, S., Cannon, R. C., Hines, M. L., Billings, G. O., Farinella, M., Morse, T. M., Davison, A. P., Ray, S., Bhalla, U. S., Barnes, S. R., Dimitrova, Y. D., & Silver, R. A. (2010). NeuroML: A language for describing data driven models of neurons and networks with a high degree of biological detail. *PLoS Computational Biology, 6,* e1000815.
32. Goldberg, S. H., Frumkes, T. E., & Nygaard, R. W. (1983). Inhibitory influence of unstimulated rods in the human retina: Evidence provided by examining cone flicker. *Science, 221,* 180–182.

33. Google. (2010). KML Reference—KML—Google Code. Google, Inc.
34. Han, Y., & Massey, S. (2005). Electrical synapses in retinal ON cone bipolar cells: Subtype-specific expression of connexins. *Proceedings of the National Academy of Sciences of the United States of America, 102,* 13313–13318.
35. Harary, F., & Palmer, E. M. (1973). *Graphical enumeration*. New York: Academic Press.
36. Hay, E., Hill, S., Schürmann, F., Markram, H., & Segev, I. (2011). Models of eocortical Lalyer 5b pyramidal cells capturing a wide range of dendritic and perisomatic active properties. *PLoS Computational Biology, 7,* e1002107.
37. Helmstaedter, M., Briggman, K. L., & Denk, W. (2008). 3D structural imaging of the brain with photons and electrons. *Current Opinion in Neurobiology, 18,* 633–641.
38. Helmstaedter, M., Briggman, K. L., Turaga, S. C., Jain, V., Seung, H. S., & Denk, W. (2013). Connectomic reconstruction of the inner plexiform layer in the mouse retina. *Nature, 500,* 168–174.
39. Hendrickson, P. J., Yu, G. J., Robinson, B. S., Song, D., & Berger, T. W. (2012). Towards a large-scale biologically realistic model of the hippocampus. Conference proceedings:... Annual International Conference of the IEEE Engineering in Medicine and Biology Society. IEEE Engineering in Medicine and Biology Society. Conference, 2012, pp. 4595–4598.
40. Heuser, J. (2000). How to convert a traditional electron microscopy laboratory to digital imaging: Follow the 'Middle Road'. *Traffic (Copenhagen, Denmark), 1,* 614–621.
41. Hines, M. L., & Carnevale, N. T. (2001). NEURON: A tool for neuroscientists. *The Neuroscientist, 7,* 123–135.
42. Hoshi, H., Liu, W.-L., Massey, S. C., & Mills, S. L. (2009). ON inputs to the OFF layer: Bipolar cells that break the stratification rules of the retina. *Journal of Neuroscience, 29,* 8875–8883. doi:10.1523/jneurosci.0912-09.2009.
43. Jagadeesh, V., Manjunath, B. S., Anderson, J. R., Jones, B. W., Marc, R. E., & Fisher, S. K. (2013). Robust segmentation based tracing using an adaptive wrapper for inducing priors. *IEEE Trans Image Process, 22,* 4952–2063.
44. Jeong, W., Beyer, J., Hadwiger, M., Blue, R., Law, C., Vazquez, A., Reid, C., Lichtman, J., & Pfister, H. (2010). SSECRETT and NeuroTrace: Interactive visualization and analysis tools for large-scale neuroscience datasets. *IEEE Computer Graphics and Applications, 30,* 58–70.
45. Jones, B. W., Watt, C. B., Frederick, J. M., Baehr, W., Chen, C. K., Levine, E. M., Milam, A. H., LaVail, M. M., & Marc, R. E. (2003). Retinal remodeling triggered by photoreceptor degenerations. *The Journal of Comparative Neurology, 464,* 1–16.
46. Jones, B. W., Kondo, M., Terasaki, H., Watt, C. B., Rapp, K., Anderson, J. R., Lin, Y., Shaw, M. V., Yang, J. H., & Marc, R. E. (2011). Retinal remodeling in the Tg P347 Lrabbit, a large-eye model of retinal degeneration. *The Journal of Comparative Neurology, 519,* 2713–2733.
47. Kalloniatis, M., Marc, R. E., & Murry, R. F. (1996). Amino acid signatures in the primate retina. *The Journal of Neuroscience: The Official journal of the Society for Neuroscience, 16,* 6807–6829.
48. Karp, R. M. (1972). Reducibility among combinatorial problems. In R. E. Miller & J. W. Thatcher (Eds.), *Complexity of computer computations* (pp. 85–103). New York: Plenum.
49. Kleinfeld, D., Bharioke, A., Blinder, P., Bock, D. D., Briggman, K. L., Chklovskii, D. B., Denk, W., Helmstaedter, M., Kaufhold, J. P., Lee, W. C., Meyer, H. S., Micheva, K. D., Oberlaender, M., Prohaska, S., Reid, R. C., Smith, S. J., Takemura, S., Tsai, P. S., & Sakmann, B. (2011). Large-scale automated histology in the pursuit of connectomes. *The Journal of Neuroscience: The Official Journal of the Society for Neuroscience, 31,* 16125–16138.
50. Knott, G., Marchman, H., Wall, D., & Lich, B. (2008). Serial section scanning electron microscopy of adult brain tissue using focused ion beam milling. *The Journal of Neuroscience: The Official Journal of the Society for Neuroscience, 28,* 2959–2964.
51. Kolb, H. (1977). The organization of the outer plexiform layer in the retina of the cat: Electron microscopic observations. *Journal of Neurocytology, 6,* 131–153.
52. Kolb, H., & Famiglietti, E. V. (1974a). Rod and cone pathways in the inner plexiform layer of cat retina. *Science, 186,* 47–49.

53. Kolb, H., & Famiglietti, E. V. J. (1974b). Rod and cone pathways in the retina of the cat. *Invest Ophthal, 15,* 935–946.
54. Lange, G., Denny, N., & Frumkes, T. E. (1997). Suppressive rod-cone interactions: Evidence for separate retinal (temporal) and extraretinal (spatial) mechanisms in achromatic vision. *Journal of the Optical Society of America. A, Optics, Image Science, and Vision, 14,* 2487–2498.
55. Lauritzen, J. S., Anderson, J. R., Jones, B. W., Watt, C. B., Mohammed, S., Hoang, J. V., & Marc, R. E. (2012). ON cone bipolar cell axonal synapses in the OFF inner plexiform layer of the rabbit retina. *The Journal of Comparative Neurology, 521,* 977–1000.
56. Lauritzen, J. S., Hoang, J. V., Sigulinsky, C., Jones, B. W., Anderson, J. R., Watt, C. B., Mohammed, S., & Marc, R. E. (2013). Tiered cross-class bipolar cell gap junctional coupling in the rabbit retina. *Invest Ophthal, 54,* 1754.
57. Lee, S. C., Cowgill, E. J., Al-Nabulsi, A., Quinn, E. J., Evans, S. M., & Reese, B. E. (2011). Homotypic regulation of neuronal morphology and connectivity in the mouse retina. *The Journal of Neuroscience: The Official Journal of the Society for Neuroscience, 31,* 14126–14133.
58. Li, X., Kamasawa, N., Ciolofan, C., Olson, C. O., Lu, S., Davidson, K. G. V., Yasumura, T., Shigemoto, R., Rash, J. E., & Nagy, J. I. (2008). Connexin45-containing neuronal gap junctions in rodent retina also contain connexin36 in both apposing hemiplaques, forming bihomotypic gap junctions, with scaffolding contributed by zonula occludens-1. *The Journal of Neuroscience: The Official Journal of the Society for Neuroscience, 28,* 9769–9789.
59. Lynn, B. D., Li, X., & Nagy, J. I. (2012). Under construction: Building the macromolecular superstructure and signaling components of an electrical synapse. *The Journal of Membrane Biology, 245,* 303–317.
60. MacNeil, M. A., Heussy, J. K., Dacheux, R. F., Raviola, E., & Masland, R. H. (1999). The shapes and numbers of amacrine cells: Matching of photofilled with Golgi-stained cells in the rabbit retina and comparison with other mammalian species. *The Journal of Comparative Neurology, 413,* 305–326.
61. MacNeil, M. A., Heussy, J. K., Dacheux, R. F., Raviola, E., & Masland, R. H. (2004). The population of bipolar cells in the rabbit retina. *The Journal of Comparative Neurology, 472,* 73–86.
62. MacQueen, J. (1967). Some methods for classification and analysis of multivariate observations. In: *Proc. 5th Berkeley Symposium* (pp. 281–297)
63. Marc, R. E. (2010). Synaptic organization of the retina. In L. A. Levin, S. F. E. Nilsson, J. Ver Hoeve, S. M. Wu, P. L. Kaufman, & A. Alm (Eds.), *Adler's physiology of the eye* (pp. 443–458). Elsevier.
64. Marc, R. E., & Cameron, D. A. (2001). A molecular phenotype atlas of the zebrafish retina. *Journal of Neurocytology, 30,* 593–654.
65. Marc, R. E., & Jones, B. W. (2002). Molecular phenotyping of retinal ganglion cells. *The Journal of Neuroscience: The Official Journal of the Society for Neuroscience, 22,* 412–427.
66. Marc, R. E., & Liu, W. (2000). Fundamental GABAergic amacrine cell circuitries in the retina: Nested feedback, concatenated inhibition, and axosomatic synapses. *The Journal of Comparative Neurology, 425*(4), 560–582.
67. Marc, R. E., Liu, W. L., & Muller, J. F. (1988). Gap junctions in the inner plexiform layer of the goldfish retina. *Vision Research, 28*(1), 9–24.
68. Marc, R. E., Liu, W. L., Kalloniatis, M., Raiguel, S. F., & van Haesendonck E. (1990). Patterns of glutamate immunoreactivity in the goldfish retina. *The Journal of Neuroscience: The Official Journal of the Society for Neuroscience, 10*(12), 4006–4034.
69. Marc, R. E., Murry, R. F., & Basinger, S. F. (1995). Pattern recognition of amino acid signatures in retinal neurons. *The Journal of Neuroscience: The Official Journal of the Society for Neuroscience, 15*(7 Pt 2), 5106–5129.
70. Marc, R. E., Murry, R. F., Fisher, S. K., Linberg, K. A., Lewis, G. P., & Kalloniatis, M. (1998). Amino acid signatures in the normal cat retina. *Investigative Ophthalmology & Visual Science, 39*(9), 1685–1693.

71. Marc, R. E., Jones, B. W., Lauritzen, J. S., Watt, C. B., & Anderson, J. R. (2012). Building retinal connectomes. *Current Opinion in Neurobiology, 22,* 568–574.
72. Marc, R. E., Anderson, J. R., Jones, B. W., Watt, C. B., & Lauritzen, J. S. (2013). Retinal connectomics: Towards complete, accurate networks. *Progress in Retinal and Eye Research, 37,* 141–162.
73. Marc, R. E., Anderson, J. R., Jones, B. W., Sigulinsky, C., Watt, C. B., & Lauritzen, J. S. (2014). The aII amacrine cell connectome: A dense network hub. *Front Neural Circuits*. doi: 10.3389/fncir.2014.00104.
74. Mastronarde, D. N. (2005). Automated electron microscope tomography using robust prediction of specimen movements. *Journal of Structural Biology, 152,* 36–51.
75. Micheva, K. D., & Bruchez, M. P. (2011). The gain in brain: Novel imaging techniques and multiplexed proteomic imaging of brain tissue ultrastructure. *Current Opinion in Neurobiology*. doi:10.1016/j.conb.2011.08.004.
76. Micheva, K. D., & Smith, S. J. (2007). Array tomography: A new tool for imaging the molecular architecture and ultrastructure of neural circuits. *Neuron, 55,* 25–36.
77. Micheva, K. D., Busse, B., Weiler, N. C., O'Rourke, N., & Smith, S. J. (2010). Single-synapse analysis of a diverse synapse population: Proteomic imaging methods and markers. *Neuron, 68,* 639–653.
78. Mikula, S., Trotts, I., Stone, J. M., & Jones, E. G. (2007). Internet-enabled high-resolution brain mapping and virtual microscopy. *Neuroimage, 35*(1), 9–15. doi:S1053-8119(06)01176-1 [pii]. 10.1016/j.neuroimage.2006.11.053.
79. Mizoguchi, A., Nakanishi, H., Kimura, K., Matsubara, K., Ozaki-Kuroda, K., Katata, T., Honda, T., Kiyohara, Y., Heo, K., Higashi, M., Tsutsumi, T., Sonoda, S., Ide, C., & Takai, Y. (2002). Nectin: An adhesion molecule involved in formation of synapses. *The Journal of Cell Biology, 156,* 555–565.
80. Morales, J., Rodríguez, A., Rodríguez, J. R., Defelipe, J., & Merchán-Pérez, A. (2013). Characterization and extraction of the synaptic apposition surface for synaptic geometry analysis. *Front Neuroanatomy, 7,* 20. doi:10.3389/fnana.2013.00020.
81. Morgan, J. L., & Lichtman, J. W. (2013). Why not connectomics. *Nature Methods, 10,* 494–500.
82. Ogita, H., Ritake, Y., Miyoshi, J., & Takai, Y. (2010). Cell adhesion molecules nectins and associating proteins: Implications for physiology and pathology. *Proceedings. Japan Academy, 86,* 621–629.
83. Perin, R., Telefont, M., & Markram, H. (2013). Computing the size and number of neuronal clusters in local circuits. *Front Neuroanatomy, 7,* 1–10.
84. Prinz, A. A., Bucher, B., & Marder, E. (2004). Similar network activity from disparate circuit parameters. *Nature Neuroscience, 7,* 1345–1352.
85. Raviola, E., & Gilula, N. B. (1975). Intramembrane organization of specialized contacts in the outer plexiform layer of the retina. A freeze-fracture study in monkeys and rabbits. *The Journal of Cell Biology, 65,* 192–222.
86. Reese, B. E. (2008). Mosaics, tiling and coverage by retinal neurons. In: R. H. Masland & T. Albright (Eds.), *The senses* (Vol. 1, pp. 439–456). Academic Press, San Diego
87. Rockhill, R. L., Daly, F. J., MacNeil, M. A., Brown, S. P., & Masland, R. H. (2002). The diversity of ganglion cells in a mammalian retina. *Journal of Neuroscience, 22,* 3831–3843.
88. Sorra, K. E., & Harris, K. M. (2000). Overview on the structure, composition, function, development, and plasticity of hippocampal dendritic spines. *Hippocampus, 10,* 501–511.
89. Stabell, B., & Stabell, U. (1998). Chromatic rod-cone interaction during dark adaptation. *Journal of the Optical Society of America. A, Optics, Image Science, and Vision, 15,* 2809–2815.
90. Stabell, B., & Stabell, U. (2002). Effects of rod activity on color perception with light adaptation. *Journal of the Optical Society of America. A, Optics, Image Science, and Vision, 19,* 1249–1258.
91. Staehelin, L. A. (1972). Three types of gap junctions interconnecting intestinal epithelial cells visualized by freeze-etching. *Proceedings of the National Academy of Sciences of the United States of America, 69,* 1318–1321.

92. Stevens, J. K., Davis, T. L., Friedman, N., & Sterling, P. (1980). A systematic approach to reconstructing microcircuitry by electron microscopy of serial sections. *Brain Research, 2,* 265–293.
93. Strettoi, E., Dacheux, R. F., & Raviola, E. (1990). Synaptic connections of rod bipolar cells in the inner plexiform layer of the rabbit retina. *The Journal of Comparative Neurology, 295,* 449–466.
94. Strettoi, E., Raviola, E., & Dacheux, R. F. (1992). Synaptic connections of the narrow-field, bistratified rod amacrine cell (AII) in the rabbit retina. *The Journal of Comparative Neurology, 325,* 152–168.
95. Tasdizen, T., Koshevoy, P., Grimm, B., Anderson, J. R., Jones, B. W., Whitaker, R., & Marc, R. E. (2010). Automatic mosaicking and volume assembly for high-throughput serial-section transmission electron microscopy. *Journal Neuroscience Methods, 193,* 132–144.
96. Thomas, L. P., & Buck, S. L. (2006). Foveal and extra-foveal influences on rod hue biases. *Visual Neuroscience, 23,* 539–542.
97. Trezona, P. W. (1970). Rod participation in the 'blue' mechanism and its effect on colour matching. *Vision Research, 10,* 317–332.
98. Trezona, P. W. (1973). The tetrachromatic colour match as a colorimetric technique. *Vision Research, 13,* 9–25.
99. van den Heuvel, M. P., & Sporns, O. (2011). Rich-club organization of the human connectome. *Journal of Neuroscience, 31*(44), 15775–15786. doi:10.1523/jneurosci.3539–11.2011.
100. Van Essen, D. C., Glasser, M. F., Dierker, D. L., Harwell, J., & Coalson, T. (2011). Parcellations and hemispheric asymmetries of human cerebral cortex analyzed on surface-based atlases. *Cerebral Cortex, 22,* 2241–2262. doi:10.1093/cercor/bhr291.
101. Watts, D. J., & Strogatz, S. H. (1998). Collective dynamics of 'small- world' networks. *Nature, 393,* 440–442.
102. Wong, E., Baur, B., Quader, S., & Huang, C.-H. (2012). Biological network motif detection: Principles and practice. *Briefings in Bioinformatics, 13,* 202–215. doi:10.1093/bib/bbr033.
103. Xie, X., Schnieder, M. C., Sánchez-Sinencio, E., & Embabi, S. H. K. (1999). Sound design of low power nested transconductance-capacitance compensation amplifiers. *IEEE Electronics Letters, 35,* 956–958.

Chapter 2
Decoding the Transcriptome of Neuronal Circuits

Paul J. Bonthuis and Christopher Gregg

Abstract Genomics is fostering broad discoveries across biological disciplines, including the neurosciences. However, the analysis of gene expression and gene regulation in the brain is complicated by the extraordinary cellular heterogeneity, complex connectivity, and dynamic physiology of the tissue. Indeed, one of the great challenges of modern neuroscience involves the functional and molecular classification of cells in the brain within the context of network connectivity. In parallel, a major area of focus in the field of genomics involves the development of technologies that can profile the transcriptome of single or small numbers of cells [38]. Thus, major objectives in these two fields are well aligned. Here, we review modern approaches for the analysis of gene expression at the cellular level in the brain. As detailed below, these new technologies involve both ex vivo genomics approaches and new and emerging technologies for *in situ* and *in vivo* imaging of molecules in the brain.

2.1 Introduction

Brain functions and behaviors emerge through the coordinated responses and activity of different neurons organized into networks. Neural networks are composed of neurons with unique molecular features such as the expression of specific neurotransmitters, neuropeptides, ion channels, receptors, and transcription factors. Neurons are typically classified based on the expression of one or a few molecular markers. However, these broad classifications fail to capture the complexity of network connectivity and functionality. For example, a heavily studied neuron population in the arcuate nucleus that plays a role in feeding behavior has been defined by its expression of agouti-related peptide (AgRP). Yet, optogenetic studies have revealed that AgRP neurons are functionally heterogeneous and only a specific subpopulation controls the drive to feed. The subset of AgRP neurons that drive hunger have been shown to interact with cells in the paraventricular nucleus that express

P. J. Bonthuis (✉) · C. Gregg
Department of Neurobiology and Anatomy, University of Utah School of Medicine, Salt Lake City, UT, USA
e-mail: Paul.Bonthuis@neuro.utah.edu

A. D. Douglass (ed.), *New Techniques in Systems Neuroscience,* Biological and Medical Physics, Biomedical Engineering, DOI 10.1007/978-3-319-12913-6_2

oxytocin, thyrotropin-releasing hormone, and pituitary adenylate cyclase-activating polypeptide [3, 35]. Currently, the gene expression programs that define the unique connectivity patterns and functions of AgRP neuron subpopulations are unknown. Subpopulations of neurons can be defined based on connectivity patterns for every major, molecularly defined class of neuron in the brain. Recent collaborative efforts have begun to define wiring diagrams (connectomes) in mouse and human brains at the macro-, meso- and microscales (http://www.humanconnectome.org; http://www.mouseconnectome.org; https://www.alleninstitute.org). The studies reveal extraordinary complexity and cellular diversity in terms of connection patterns [54, 93]. Further, efforts to classify neurons based on morphological and physiological criteria are underway and the number of defined different cell types is constantly growing. In addition to the 85 billion neurons that are estimated to exist in the human brain, there are even more glial cells, which also perform essential supporting functions. Underlying the formation and function of all these cells is the transcriptome.

The transcriptome was once thought to be largely composed of ribosomal RNA, transfer RNA, and a small number of protein-coding messenger RNAs (~ 2% of the total). However, it is now clear that transcription is pervasive in the genome and that ~ 75% of the genome is transcribed [15]. In most cases, the function of these transcripts is unknown. GENCODE estimates that the human genome (version 19) contains 57,820 genes that give rise to 196,520 different transcripts (http://www.gencodegenes.org/stats.html). In total, 20,345 protein-coding genes have been identified, each of which gives rise to ~ 3 different transcripts due to the effects of alternative promoters, polyadenylation sites, and exon splicing. Different transcript isoforms from a given gene can have very different functions, and their highly regulated expression can change in response to different stimuli in a developmental stage and cell-type-specific manner. The noncoding portion of the human transcriptome includes 13,870 long noncoding RNAs and 9013 small noncoding RNAs. Noncoding RNA species range from small noncoding RNAs, such as microRNAs (1973 in total), endogenous small-interfering RNAs (siRNAs), small nucleolar RNAs (snoRNAs, 1530 in total), small nuclear RNA (snRNA, 1383 in total), and piwi-interacting RNAs (piwiRNAs), to long noncoding RNAs that are between 200 bp and several kilobases in length. The functions of most features of the transcriptome are poorly defined.

It has been estimated that 86% of all human genes are expressed in the brain, and most of these are differentially localized to different brain regions and/or different developmental stages [33, 50]. In addition, 90% of all genes expressed in the brain exhibit differential exon usage between brain regions and/or developmental stages [33, 50]. Thus, the brain transcriptome is dynamic and extremely complex. Some features of gene expression appear to be unique to the brain. For example, 3′ untranslated regions (3′UTRs) are generally longer for transcripts in the brain compared to peripheral tissues [88]. These sequences can be over 10 kb in length and are known to contain binding sites for miRNAs and regulatory proteins, which could make transcript regulation through the 3′UTR especially complex in the brain. In addition to differences between brain regions and developmental stages, expression levels and isoform usage can change in response to metabolic changes, hormonal

changes, neuronal activity, circadian rhythms, and other events. Some isoforms contain signal sequences that result in their transport specifically into dendrites, while others are localized to axons or specific organelles, or are retained in the nucleus [7, 30]. Thus, the transcriptome of the brain is not a disorganized cloud of RNA molecules but rather a highly regulated system of transcripts that arise under specific conditions and are trafficked to precise locations for local translation or other functions. Understanding these processes is central to the greater goal of understanding the mechanisms that underlie specific brain functions.

For the most part, our understanding of the brain transcriptome arises from studies of discrete regions: microdissected chunks of brain, which is composed of hundreds of different cell types. Since brain functions arise through the activities of thousands of different cell types organized into different circuits, this level of analysis generally fails to capture the complex relationship between the transcriptome and circuit physiology. Encouragingly, emerging approaches are beginning to allow accurate measurements of gene expression at the cellular level in the brain. Defining the gene expression programs that establish the morphological, anatomical, and physiological traits of specific cell types is becoming a realistic undertaking. Further, we are gaining access to cell type-specific transcriptional programs that respond to changes in neuronal activity, disease, and other events.

In this chapter, we describe established and emerging techniques for measuring the transcriptome in specific neuronal populations. We cover the following topics: (1) how different cell types are defined and identified; (2) techniques and technologies to label and isolate RNA selectively from a desired cell type; (3) methods to detect and quantify RNA transcripts from a small number of cells of a specific type or from single cells; and finally, (4) quantitative *in vivo* and *in situ* analyses to measure both the location and expression levels of genes in individual cells. Although newer techniques are constantly emerging and not all of them can be comprehensively described here, it is our aim to discuss the benefits and limitations of some of the most widely used and potentially impactful approaches available.

2.2 Cell Type Identification and Labeling

Brain cells are categorized by anatomical location and characteristic features. The broadest intrinsic characteristic is whether a cell is neuronal or glial. Central nervous system glia consist of astrocytes that perform homeostatic functions, myelin-producing oligodendrocytes, ventricular ependymal cells that secrete cerebrospinal fluid and form the blood–brain barrier, and phagocytic microglia differentiated from hematopoietic stem cells. Neurons are polarized cells that send and receive electro-chemical information through synaptic connections with other neurons. A typical neuron receives numerous excitatory and inhibitory inputs onto its dendritic processes, and if excited above a threshold electrical potential, it fires depolarizing action potentials that trigger the release of small molecule and/or peptide neurotransmitters from their axon terminals. Anatomical location, morphology (e.g., soma size and shape, dendritic arborization, axon length), electrophysiological

properties, connectivity, neurotransmitter content, and molecular marker expression are common ways to differentiate neuronal cell types [52]. For example, two major classes of neurons are pyramidal shaped, long-distance projecting, glutamatergic excitatory neurons, and γ-aminobutyric acid (GABAergic), inhibitory interneurons; however, classifying subtypes of these two classes is difficult [76]. One way to identify neural subtypes is through electrophysiological characteristics. These can include properties of intrinsic firing, responses to neurotransmitters, and electrical conductance through the composition of ion channels [19].

Transgenic technologies for labeling specific cell types based on molecular expression patterns are particularly useful in organisms where these tools are well advanced, such as mice. Typical transgenic labeling tools include CRE recombinase and fluorescent reporter proteins acquired from bioluminescent organisms, such as green fluorescent protein (GFP) derived from jellyfish. Old methods for molecular reporter labeling genetically engineered GFP fused to the amino- or carboxy-terminal end of a gene of interest, and transgenic knock-in insertion by homologous recombination replaced the endogenous gene with the protein-fusion reporter. However, recombinant fusion proteins can be problematic if the conjugated reporter perturbs the function of the endogenous protein. Fluorescent proteins can also be cloned into bacterial artificial chromosomes (BACs) such that their expression is controlled by several kilobases of the transcriptional regulatory element from an endogenous gene of interest. Ideally, when the BAC construct is inserted into the genome following pronuclear injection, the reporter is only expressed in the cell types that express the endogenous gene [25, 44, 85]. In practice, however, BAC transgenics often have off-target labeling due to positional effects related to the site of genomic integration. Further, one must often screen several founder lines in order to identify a line in which the correct cells are labeled. In model organisms where homologous recombination can be utilized for gene targeting, many labs have turned to modified, knock-in strategies. For example, a CRE recombinase allele or fluorescent reporter of interest can be engineered with an upstream internal ribosome entry sequence (IRES) and targeted to the 3′UTR region of the endogenous gene of interest [71, 82]. In this approach, a bicistronic transcript is generated under the control of the endogenous enhancer and promoter elements. Thus, the expression of the CRE allele or reporter matches the endogenous transcript.

CRE lines can be crossed to floxed reporter lines, where expression of the reporter is conditional upon a CRE recombination event in order to label specific cell types. A challenge for conditional reporter lines is often that the intensity of the fluorescent label is weak, limited to a subset of cells and/or variegated. To address these issues in mice, Liqiun Lou's laboratory developed an approach to increase expression by knocking the reporter gene into the permissive *ROSA26* locus in the mouse genome under the control of a strong and ubiquitous promoter, such as CAG [51, 94]. CAG is a synthetic sequence composed of a cytomegalovirus enhancer, the chicken beta-actin promoter, and the splice acceptor site of the rabbi beta-globin gene [53]. Subsequently, the Allen Institute for Brain Science used this approach to generate robust conditional reporter lines with three spectrally distinct fluorescent proteins: EYFP, ZsGreen, and tdTomato [46]. The reporters were engineered with a woodchuck hepatitis virus post-transcriptional regulatory element that is added to

the end of the transcript to increase mRNA stability. Numerous CRE driver lines are now available from the Allen Brain Institute and other public repositories (GENSAT or Jackson Laboratory) for use with these reporter lines, and the expression patterns of different CRE drivers are being characterized and made publically available at http://transgenic-mouse.alleninstitue.org. These are outstanding resources to begin studying the transcriptome of specific cell types in the brain.

Ideally, one would be able to purify subtypes of cells from the brain not just on the basis of the expression of a single marker gene, but also based on connectivity patterns and physiological properties. Currently, we have limited approaches to integrate all of these features. In principle, fluorescent retrograde tracers can be used in combination with reporter mice to label specific subpopulations of molecularly defined neurons for purification. This approach would allow for the isolation of neurons based on both connectivity patterns and molecular markers. A pioneering study by Arlotta and colleagues previously employed retrograde fluorescent tracers to define and purify motor neurons in the developing cortex for transcriptome analysis [2]. Virus-based approaches to label specific circuits have also been developed [8, 43, and 57]. However, these labeling methods are not ideal for transcriptome analysis, since they influence the health of the infected cells and can change gene expression. Sugino et al. [76] were able to characterize 12 distinct populations of both GABA and glutamate neurons, as distinguished by a combination of factors including anatomical location, transgene expression, and by connectivity using a retrograde tracer.

Approaches to isolate cells based on their activity patterns are very limited. Immediate early gene expression can be used as a proxy for neuronal activity. Recent studies exploited this by expressing a destabilized fluorescent reporter under the control of enhancers from the immediate early genes c-fos and arc [10]. These reporters have been used to label cells that respond to fear conditioning [63], oriented visual stimuli [89], and motor learning [65]. Cells labeled in this way could be purified for transcriptome analysis within a functionally related group of cells. In principle, this approach could be used in combination with other reporter lines and/or neuron tracing strategies to further enhance specificity. An alternative approach, involving activity-dependent ribosomal protein phosphorylation, is detailed below.

2.3 Cell Type and RNA Isolation Strategies

The strategy chosen to capture and isolate RNA from specific cell types is intrinsically linked to the methods used to identify or label the cell types of interest. Laser-capture microdissection (LCM) isolates brain regions or specific cell types under a microscope from thin cryosections of frozen or fixed tissue based on anatomical location, morphology, and molecular marker expression [26, 45, 52, 72]. LCM can attain two types of samples: whole tissue from a well-outlined and defined brain region, or single cells of a specifically labeled type. These methods offer improved accuracy, precision, and selectivity compared to manual dissection of fresh whole tissue. One issue with standard LCM is that the wide cuts that are generated (~ 7.5 μm) cannot dissect fine cell contours, such as neuronal processes, and

material from these compartments are lost. However, laser-directed microdissection (LDM) systems make narrow cuts (~ 0.5 μM) that can trace the shape of the cell [56, 66]. Both LCM and LDM require cryosectioning of either fresh-frozen or fixed tissue; therefore, the RNA might be more degraded as compared to RNA extracted directly from live tissue.

For higher quality RNA and less contamination from surrounding tissue, live cells expressing a molecular reporter can be purified for RNA extraction by enzymatically dissociating tissue into single cells and then picking the labeled cells under a fluorescent microscope. In this approach, live tissue vibratome sections are prepared (~ 400 μM) and transferred into oxygenated artificial cerebral spinal fluid (ACSF), as would be done for electrophysiological recordings [29]. The slice preparation, or a microdissected portion thereof, is then dissociated by protease digestion and gentle mechanical trituration while keeping the cells alive and intact. Unfortunately, these procedures tear off neural processes, leaving the contents of axonal and dendritic compartments behind after cell sorting. Once the tissue is dissociated, individual cells are sorted by their expression of molecular (i.e., fluorescent) markers. Manually sorting live cells is a labor-intensive, yet highly accurate method for purifying individual cell types. Fluorescently labeled neurons are manually sorted in a culture dish by scanning for labeled cells under a dissecting microscope, and healthy cells are picked using a pulled glass mouth pipette and deposited into a lysis buffer for RNA extraction [29]. Manual sorting is convenient and useful when a highly pure sample of ~ 30–100 cells is sufficient [52, 56, 76].

A high-throughput purification approach to isolate dissociated cells involves fluorescent-activated cell sorting (FACS). In FACS, live cells are streamed single file through a narrow nozzle, as a detector measures their fluorescence. As the single cells exit the bottom of the nozzle, different electrostatic charges are applied to them before they pass through an electric field that deflects and sorts them into separate receptacle tubes based upon fluorescence [84]. This approach has been used in numerous gene expression-profiling studies [11, 17, 44].

A final method to sort live, dissociated cells, which does not need a transgenic organism or other means of fluorescent labeling, is called immunopanning (PAN) [6]. This technique uses antibody-covered culture plates to separate different cell types based on their expression of cell-surface proteins. Cells are placed into the immunolabeled plates over a period of time to allow antibody binding, and unbound cells that do not present the conjugate surface antigen are washed away from the adherent cells. By using a series of plates with antibodies against unique antigens, cells are separated according to specific protein expression profiles. Unfortunately, empirical evidence indicates that PAN induces immediate early, stress, and apoptosis genes, likely because the process takes a relatively long period of time and exposes the cell surfaces to antibodies [55]. Once cells of a desired type are acquired by any of the methods above, RNA is extracted from the purified live-cell population.

While the methods described above are common, they have major limitations. The axonal and dendritic processes are stripped away, yet these cellular compartments contain a large portion of the transcriptome due to local translation at synapses, growth cones, and other sites [48]. In addition, the cells are extensively manipulated and separated from their *in vivo* environment, which presumably leads to

dramatic changes to physiological gene expression. Generally, these purification approaches are appropriate for discovering cell type-specific marker genes that distinguish one cell type from another, but are not ideal for studying endogenous gene expression programs. The limitations of these methods have led to the development of other strategies for RNA purification from defined cell populations.

RNA-tagging methods avoid the need for tissue dissociation and cell screening steps. In these approaches, transgenic organisms express epitope-tagged RNA-binding proteins in a cell type-specific manner. Antibodies against the epitope tags are used to immunoprecipitate mRNA-protein complexes from whole-tissue homogenates, and then the RNA is extracted from the immunoprecipitate. Approaches of this type include poly-A-binding protein (PABP) purification, translating ribosome affinity purification (TRAP), and RiboTag [55]. As the name implies, PABP binds to the poly-A tail of mRNA transcripts and stabilizes eukaryotic initiation factor (EIF) subunit binding to the 5′-cap of mRNA. Protein–protein interactions between PABP and EIF complexes promotes mRNA circularization, enhances mRNA stability, and increases protein translation presumably due in part to increased ribosome reinitiation [21]. Since PABP naturally binds to poly-A tails (i.e., mRNA), cell type-specific mRNA isolation is made possible with a recombinant FLAG-tagged PAPB expressed under the control of a cell-specific promoter [36, 47, 67, 92]. RNA is fixed to RNA-binding proteins *in situ* with formaldehyde, and total cell homogenates are then immunoprecipitated with FLAG-antibody conjugated beads. After washing away the rest of the cellular content, including RNA not captured by the FLAG beads, poly-A mRNA fixed to FLAG-tagged PABP is reverse-crosslinked and eluted. Thus, PABP technology captures all polyadenylated RNA in a cell type-specific manner, including many untranslated RNAs.

Translated RNA can be purified from untranslated RNA by exploiting the fact that actively translated mRNA is loaded with ribosomes. In TRAP technology, EGFP is fused to the N-terminus of the large ribosomal-subunit L10a and is expressed in transgenic organisms under the control of a cell type-specific promoter [16, 28]. The EGFP-L10a fusion protein integrates into polysome complexes, and immunoprecipitation with an EGFP antibody enriches for actively translated RNA from the targeted cells. In contrast to PABP isolation, TRAP does not involve fixation of RNA-protein complexes prior to immunoprecipitation, but it does require rapid dissection and homogenization in lysis buffer supplemented with magnesium and cycloheximide. The lysis buffer performs several functions, including keeping ribosomes bound to polysomal RNA and solubilizing rough endoplasmic reticulum. High-affinity EGFP antibodies that can withstand high salt washes are conjugated to magnetic beads and used for the immuno-isolation [28]. The RiboTag method is similar to TRAP in that it purifies cell type-specific polyribosomal mRNA. The strategy uses Cre-lox technology to conditionally knock-in a c-terminally hemagglutinin (HA)-tagged version of ribosomal protein subunit *Rpl22* exon4, which is transgenically inserted just downstream of the endogenous exon 4 [68]. Cell type-specific expression of CRE removes the endogenous exon 4 by recombination and puts the HA-tagged exon 4 in frame to express HA-tagged RPL22 protein ($RPL22^{HA}$). This versatile strategy can be combined with many existing cell type-specific CRE driver lines. Finally, phosphorylated ribosome capture is a variation of TRAP that is

specifically geared toward neuroscience applications, and selectively purifies RNA from neurons based upon changes in firing activity rather than on *a priori* selected molecular markers [34]. This approach depends upon the fact that the S6 subunit of the ribosome is phosphorylated by the PI3-K/mTOR, MAPK, and PKA signaling pathways in activated neurons [34]. An antibody specific for the phosphorylated epitope of S6 subunit is used to pull down RNA undergoing translation within the activated cells. This technique provides a powerful new method to study activity-induced gene expression profiles in cells that fire under specific conditions. Overall, ribosomal-tagging methods are powerful for studying actively translated, coding RNAs, but they are not applicable for noncoding RNAs.

A cell type-specific RNA-tagging approach that does not depend upon mRNA-binding proteins, and can capture all RNA species including noncoding RNA, is the thiouracil RNA-tagging (TU-tagging) method. In TU tagging, CRE-lox technology is used to conditionally express a heterologous thiouracil phosphoribosyltransferase (UPRT) enzyme derived from *Taxoplasma gondii* [49] in specific cell types of interest. Next, 4-thiouracil (TU), which is incorporated into actively transcribed RNA, is injected into the UPRT transgenic organism. Only cells that express the UPRT transgene will incorporate TU into the transcriptome [24]. RNA is then purified from whole-tissue dissections, and TU-incorporated RNAs within the pool of total RNA are chemically conjugated to biotin via the thiol group of TU. Streptavidin beads are then used to purify biotin-conjugated, TU-tagged RNA for downstream profiling by RNASeq. This method provides temporal information, since the TU injection allows for pulse labeling of newly transcribed RNAs. Overall, the immunoprecipitation and TU-tagging methods are powerful, but suffer from high background. The ongoing efforts are focused on improving purification chemistries to address this problem.

The choice of which method to use must be guided by the central goals of the experiment. For example, if the goal is to identify cell type-specific marker genes, then cell dissociation and purification-based strategies should work well. If the goal is to study endogenous gene expression programs in disease models or under different experimental conditions, then other purification strategies might more effectively represent the physiological state. Empirical evidence shows that only 30–60 cells are needed to get consistently reproducible results in the number of RNA transcripts detected from cell type-specific pools [56]. Unfortunately, none of these methods are universally optimal and new strategies with improved efficiencies are greatly needed.

2.4 Single Cell Transcriptomics

Analyzing the transcriptome from several cells provides an averaged readout of gene expression at the cellular level. The genomics and neuroscience communities have sought to accurately profile gene expression at the single cell level for over two decades. The pioneering study that first achieved this feat was performed by Catherine Dulac and led to the discovery of chemoreceptors in the vomeronasal organ of the mouse in 1994 [18]. However, subsequent attempts to profile the entire transcriptome of a single cell achieved limited success. Encouragingly, advances in

single cell genomics are now occurring at a rapid rate [72]. An ideal application for this technology would involve the integration of electrophysiological methods, such as patch clamp, with gene expression profiling on the same neuron to learn how physiological properties relate to gene expression [61].

To perform single cell transcriptome analysis, new technologies are being developed to isolate and process many single cells using microfluidic chambers. For example, the C1 Single-Cell Auto Prep System (Fluidigm, South San Francisco, CA) isolates 96 cells into individual chambers within a microfluidic chip and automatically performs lysis, cDNA synthesis, and amplification [80]. The single cell cDNA samples can then be used for qPCR analysis of targeted genes or made into libraries for next-generation sequencing. Since loading the chip only requires pipetting a single sample, hands-on time and chances for technical errors and contamination artifacts are greatly reduced. A direct comparison of single cell RNAseq libraries constructed at the nanoliter scale in C1 microfluidic devices, to libraries constructed at the microliter scale in tubes, found the C1-generated libraries performed better in regard to sensitivity, accuracy, and false positives [91]. Moreover, combining the data from all 96 single cells processed in the C1 device quantitatively recapitulates measurements from a bulk RNA sample RNAseq experiment, giving high confidence that the single cell measurements were accurate. These results demonstrated the ability to differentiate discrete cell identities and/or physiologies within tissues by individually assessing the transcriptomes of single cells. The nanoliter volumes used in microfluidic devices not only improve single cell sequencing quality, but also reduce the cost of consumable reagents.

2.5 Amplification of Low Input RNA

After separating a pool of cell type-specific live cells, RNA-tagged molecules, or individual single cells from the surrounding tissue, the resulting RNA isolation yields are usually low and need to be amplified before transcriptome measurement. New methods for amplifying different amounts of starting material into cDNA libraries usable for transcriptome measurement are being created at a rapid rate. Each method has inherent strengths, weaknesses, limitations, and biases [1, 72], and so, investigators must chose which amplification method will best be suited to their particular question.

In vitro transcription (IVT) has been in use for over three decades to linearly amplify an RNA sample [86], and IVT is often used to amplify and convert an RNA sample into labeled cRNA for microarray analysis. IVT starts by reverse-transcribing an RNA sample. The oligo dT primer used in this reaction contains a 5′ leader overhang encoding a T7-transcriptional promoter sequence (Fig. 2.1). The oligo dT sequence nonselectively anneals to polyA-tailed mRNA, while the 5′ overhang introduces a T7 RNA-polymerase loading site into each cDNA. Subsequent IVT with a T7 RNA polymerase is used to make copy RNA (cRNA). A second round of reverse transcription and IVT from the first round cRNA may be performed to amplify the library and label the cRNA for microarray hybridization. This approach

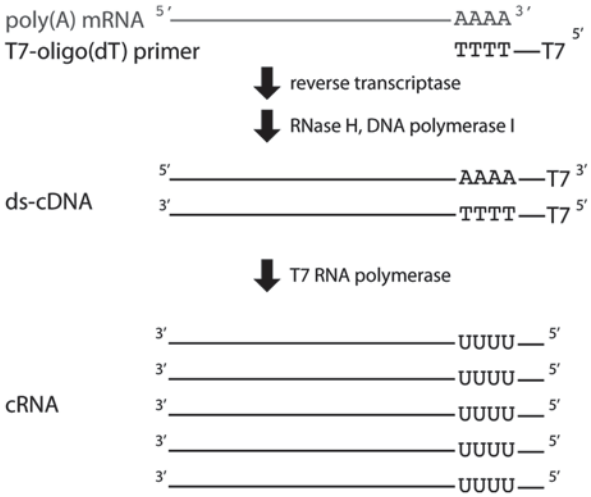

Fig. 2.1 In vitro transcription (*IVT*). Polyadenylated total mRNA (*polyA mRNA*) is selectively reverse-transcribed to copy-DNA (*cDNA*) with an oligo(dT) primer carrying a T7 RNA polymerase binding site on the 5′-end (**T7-oligo(dT) primer**). After reverse transcription, the cDNA:mRNA duplexes are converted to double-stranded cDNA (**ds-cDNA**) by the addition of **RNase H**, to cleave the mRNA into short sequences, and **DNA polymerase I** uses the cleaved mRNA to prime synthesis of second-strand cDNA. The ds-cDNA, with a T7 site, is then used as template for in vitro transcription with **T7 RNA polymerase** to synthesize several molecules of copy-RNA (**cRNA**). A second round of IVT, using the cRNA as starting template, may be used to further amplify and label the library for transcriptome measurement (e.g., microarray analysis). RNA sequence is depicted in *grey letters and lines*, and DNA in *black letters and lines*. (Figure was adapted from [86])

has been successfully used to amplify a range of RNA starting concentrations acquired by several isolation methods. For example, RNA isolated from 5000 to 10,000 FACS purified EGFP positive cells (yielding 3–10ngs of total RNA; [44]), RNA isolated from ~ 30 to 50 cells acquired by manual sorting (yielding 0.25–1 ng of total RNA [76]), TRAP-purified RNA from pooled tissue of several (3–7) mice [16, 28], and even RNA isolated from single cells after electrophysiological recording [17]. Since IVT is a process of linear amplification, artifacts due to exponential amplification (e.g., PCR) are avoided [19].

Like IVT, RNA single primer isothermal amplification (Ribo-SPIA) by NuGEN is a linear amplification technology [12, 37]. NuGEN (San Carlos, CA) has several products to generate libraries for different applications. The first step in Ribo-SPIA is to reverse-transcribe mRNA into cDNA using a 5′-RNA-DNA-3′ hybrid reverse transcription primer (RT primer). The 3′-DNA ends of the RT primers anneal to the mRNA template and prime first-strand cDNA synthesis with reverse transcriptase. The reverse transcription reaction can either use RT primers that all have a 3′-DNA poly-(T) sequence for 3′-biased mRNA amplification, or use a mixture RT primers with both poly-(T) and random nucleotide 3′-DNA sequence for whole of transcriptome amplification. The 5′ ends of the RT primers are composed of a single

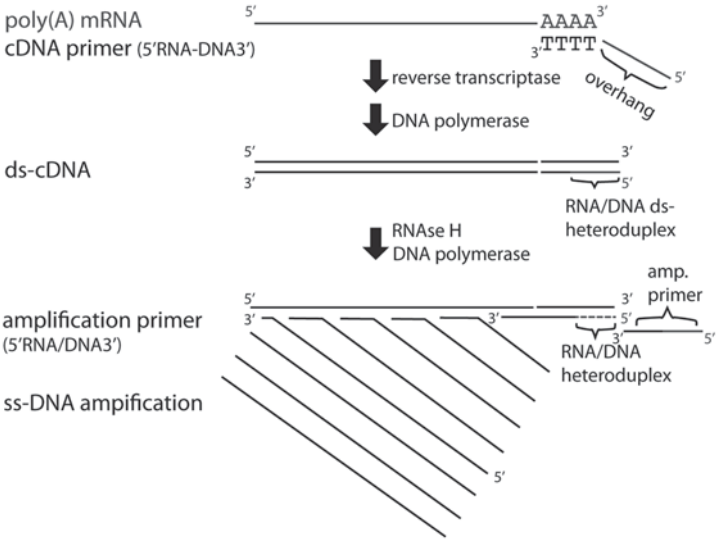

Fig. 2.2 Single-primer isothermal amplification. Polyadenylated total mRNA (polyA mRNA) is selectively reverse-transcribed to copy-DNA (cDNA) with a chimeric RNA–DNA hybrid primer (**cDNA primer**) consisting of DNA oligo (dT) sequence on the 3′-end and a unique RNA sequence on the 5′-end **(overhang)**. The RNA 5′-end overhang encodes a primer-binding site for subsequent amplification steps, but is not complementary to any mRNA template sequence. Second-strand cDNA synthesis, with DNA polymerase, creates a double-stranded cDNA (**ds-cDNA**) with an RNA–DNA double-stranded heteroduplex (**RNA–DNA ds-heteroduplex**) on the cDNA primer side. The addition of **RNase H** cleaves the RNA side of the **RNA–DNA heteroduplex** to allow annealing of a chimeric RNA–DNA **amplification primer** to the ds-cDNA library. A strand displacing **DNA polymerase** is used to extend the amplification primer to make single-stranded copies of the library. Under isothermic conditions, repeated cycles of RNase H cleavage of the RNA portion of the RNA–DNA heteroduplexes, annealing of additional RNA–DNA chimeric amplification primers, and extension by strand-displacing DNA polymerase generate a single-stranded DNA amplification (**ssDNA amplification**) of the cDNA library. The DNA portion of the amplification primer can consist of oligo (dT) sequence to anneal and amplify the 3′-end of the transcriptome, or of random sequence to randomly anneal and amplify the whole transcriptome. RNA sequence is depicted in *grey letters and lines*, and DNA in *black letters and lines*. RNase-digested RNA is depicted by *dashed grey lines*. (Figure was adapted from [37])

unique primer sequence. First- and second-strand cDNA synthesis incorporates an RNA–DNA hetero-duplex amplification primer-binding site at the extreme 5′ end of the complement strand (Fig. 2.2). The addition of RNAse-H degrades the RNA side of the hetero-duplex and clears the way for a 5′-RNA–DNA-3′ hybrid amplification primer to anneal to the second-strand cDNA and initiate polymerase extension by a strand-displacing polymerase. Thus, isothermic linear amplification is achieved by sequential cycles of RNAse-H hetero-duplexed RNA cleavage, RNA–DNA hybrid amplification primer binding, and polymerase extension by strand displacement (Fig. 2.2). Nugen's Ovation RNA Amplification System, which uses Ribo-SPIA technology, was the method used to amplify the cDNA sample for microarray analysis of phosphorylated ribosome capture described above [34].

Exponential amplification methods (i.e., PCR) have also been developed to amplify low-abundance mRNA samples, including those derived from single cells. An individual cell has picogram concentrations of RNA, and constructing cDNA libraries for single cell RNAseq requires careful handling to avoid amplification of contaminating nucleotides. Tang et al. employed a homopolymer tailing method to exponentially amplify mRNA isolated from single mouse blastomere cells [79, 77]. Their method manually selects and lyses single cells directly in PCR buffer containing RNAse inhibitors and reagents for reverse transcription using an oligo-(dT) RT primer with a unique 5′-overhang sequence for subsequent amplification [78]. After reverse transcription, free RT primer is removed by Exonuclease I digestion. The cDNA is then homopolymer tailed with poly-(dA) nucleotides by terminal deoxynucleotide transferase (TdT), while the mRNA template is digested with RNAse H (Fig. 2.3). A second oligo-(dT) primer with a 5′-overhang encoding a second unique primer sequence is then used with a DNA polymerase to make double-stranded cDNA. The double-stranded cDNA is exponentially amplified with primers that anneal to the flanking sequence introduced by the 5′-overhangs on the first- and second-strand cDNA synthesis primers. The amplified cDNA is then purified, sheared into ~ 100 bp fragments, and the fragments are enzymatically end-repaired for blunt-end ligation to adaptors used for RNA sequencing platforms. The Tang et al. protocol [78] is quite complicated in that it requires several purification steps, including gel purification and tube transfers, to prevent and remove amplification byproducts produced from the oligonucleotides used in constructing the sequencing library. Quartz-Seq is a simplified homopolymer tailing method where all steps of the process can be carried out in a single tube [69]. Improvements introduced by Quartz-Seq to eliminate oligonucleotide amplification byproducts include minimized concentration of reverse transcription primer, use of suppression PCR that occludes primer dimer amplification, and reduced homopolymer tail length [69]. Since homopolymer tailing methods use oligo-(dT) for reverse transcription to selectively capture mRNA, the low processivity inherent to reverse transcriptases leads to a somewhat 3′-biased representation of the transcriptome.

To alleviate the 3′-bias in cDNA library construction, template-switching methods are designed to selectively amplify only a full-length cDNA that includes the 5′-end of mRNA transcripts. Like homopolymer-tailing, SMART (Switching Mechanism At 5′ End of RNA Transcript) technology uses an oligo-dT reverse transcription primer with a 5′-overhang that introduces a unique primer site to the 5′-end of first-strand cDNA [70]. When the SMARTScribe Reverse Transcriptase reaches the 5′-terminus of an mRNA, the enzymes terminal transferase activity adds overhanging polycytosine extensions to the 3′ end of the full-length cDNA (Fig. 2.4). A second oligonucleotide with complementary polyguanines, and a 5′ primer sequence overhang, anneals with the cDNA polycytosine extensions. The transcriptase then switches templates to fill in a primer-binding site sequence encoded by the 5′-overhang of the polyguanine oligonucleotide. Thus, primer-binding sites that are used for exponential PCR amplification flank the resulting full-length cDNA. The terminal-transferase activity is inefficient when the reverse transcriptase does not reach the 5′ end of the mRNA; therefore, truncated cDNA extensions are selected against PCR

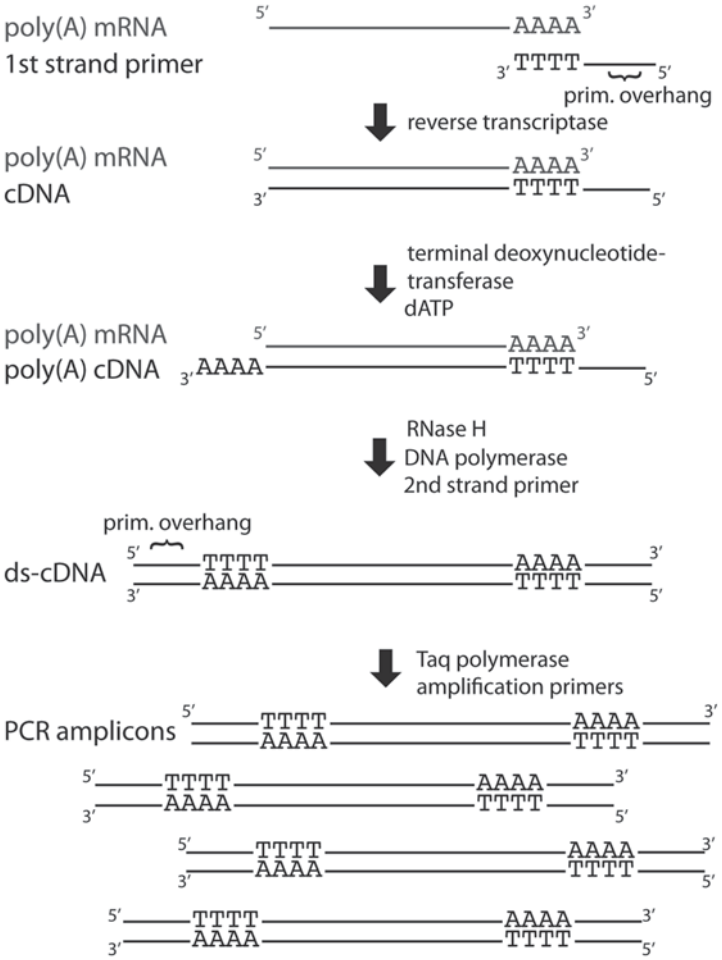

Fig. 2.3 Homopolymer tailing amplification. Polyadenylated total mRNA (**polyA mRNA**) is reverse-transcribed to copy-DNA (cDNA) with a first-strand cDNA primer (**first-strand primer**) consisting DNA oligo (dT) sequence on the 3′-end and a unique sequence encoding a primer-binding site overhang (**prim. overhang)**. After clearing the reaction of free primers with exonuclease I, the first-strand cDNA is then homopolymer tailed with dA residues on the 3′-end with **terminal deoxynucleotide transferase** and dATP. **RNase H**, **DNA polymerase**, and an oligo-(dT) primer with a second unique overhang sequence (**second-strand primer**) **are** used to make double-stranded cDNA (**ds-cDNA**). The ds-cDNA is then amplified by PCR using **Taq polymerase** and **amplification primers** that anneal to the binding-site overhangs introduced to the library by the first- and second-strand cDNA synthesis primers. RNA sequence is depicted in *grey letters and lines*, and DNA in *black letters and lines*. (Figure was adapted from [77])

amplification. However, terminal-transferase activity does add nucleotides to the cDNA when it reaches the end of fragmented RNA, so high-quality, intact RNA is imperative for long-distance PCR to include the 5′-end of mRNA transcripts. Moreover, extremely long transcripts may be underrepresented in the amplified library

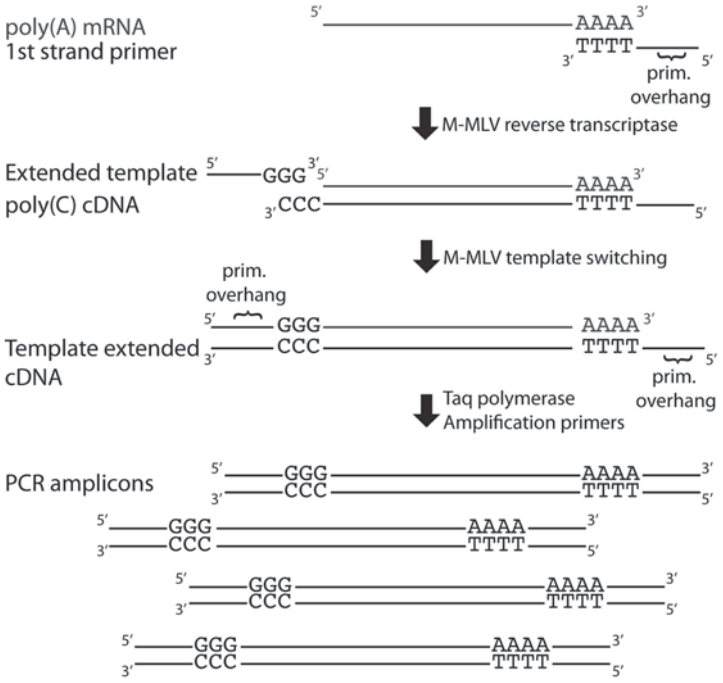

Fig. 2.4 Template-switching amplification. Polyadenylated total mRNA (**polyA mRNA**) is reverse-transcribed to copy-DNA (cDNA) with a **M-MLV reverse transcriptase** and a **first strand primer** consisting oligo (dT) sequence on the 3′-end and a unique sequence encoding a primer-binding site overhang (**prim. overhang)**. When M-MLV reaches the 3′-end of a mRNA template, it adds a poly-(dCT) stretch with endogenous, template-independent terminal transferase activity; terminal transferase activity of M-MLV is inefficient when it prematurely terminates reverse transcription before the 5′-end of the mRNA template. Upon adding a poly (dC) stretch to the end of a full-length cDNA, a second oligonucleotide with a poly(dG) sequence on the 3′-end can anneal and provide an **extended template** for the reverse transcriptase. The M-MLV reverse transcriptase then switches templates to fill in the 5′-end of the extended template with complementary sequence. The 5′-end of the extended template encodes a primer-binding site that is incorporated onto the 3′-end of the first-strand cDNA when M-MLV fills in the extended template. After extended template switching and fill-in synthesis, primer-binding sites, which are used for PCR exponential amplification, flank the resulting full-length cDNA molecules. RNA sequence is depicted in *grey letters and lines*, and DNA in *black letters and lines*. (Figure was adapted from [64])

if the reverse transcriptase frequently does not reach the 5′-end of the mRNA transcript. SMART methodology has been adapted for single cell transcriptome analysis by next generation sequencing in a technique called SmartSeq [64]. Patch-aspiration and the SMARTer Ultra Low RNA Kit (Clonetech #634935) were successfully used to amplify cDNA from single hippocampal primary cells, and *in situ* single neurons from live tissue slices, for Illumina RNAseq analysis [61]. A direct performance comparison between SMART and NuGEN found that each had specific advantages over the other. For example, SMART yielded significant less rRNA than NuGEN

(5.5 vs. 28.7%), NuGEN had more even coverage 5′ to 3′, and SMART had a poor correlation of expression for high GC content genes [1]. Single cell-tagged reverse transcription (STRT) is another template-switching method that multiplexes amplification and sequencing through the use of barcodes [31]. STRT begins by allocating single cells into individual wells of a 96-well plate for reverse transcription and template switching. Each well, containing the transcriptome of a single cell, also contains a template-switching oligonucleotide that introduces a unique barcode sequence to the 5′ end of the cDNA-coding strand. The barcoded cDNA is then pooled from all 96 wells for PCR amplification and RNAseq on a single lane. Since the barcoded region is on the 5′ end of the second-strand cDNA (i.e., coding strand), this method allows for strand-specific identification by RNAseq analysis, but the transcriptome measurement is inherently 5′-position biased [72].

A concern of the homopolymer tailing and template switching methods for single cell RNAseq is that bias introduced by exponential PCR amplification may not accurately represent the relative abundance of different transcripts within the transcriptome. Cell Expression by Linear amplification and Sequencing (CEL-seq), combines barcoded multiplexing and IVT to linearly amplify the transcriptomes of several individual cells [27]. Similar to the STRT strategy, single cells are reverse-transcribed in individual wells, but the reverse transcription primer is composed of 3′-poly-(dT) to select mRNA, a unique barcode, the 5′ Illumina sequencing adaptor, and a T7 promoter on the 5′-end. After reverse transcription of many cells, cDNAs are pooled to increase the total amount to a level suitable for a single round of reproducible IVT. IVT is then used to linearly amplify cRNA with cell-identifying barcodes and the Illumina 5′-adaptor. The amplified cRNA is fragmented and ligated to the 3′ Illumina adaptor. Finally, the fragmented cRNA is converted to cDNA, and molecules with both the 5′ and 3′ Illumina adaptors are selected by PCR amplification. Harshimshony et al. directly compared their CEL-seq method to the PCR-based multiplexing STRT method [31] and found that the expression-level correlations in CEL-seq were superior to those of STRT [27]. This method enables a highly accurate measurement of transcript expression levels and is strand-specific, but has a strong 3′-positon bias [72].

2.6 RNAseq Technology and Limitations

RNAseq transcriptome measurement is a revolutionary technological advancement, but the library preparation methods and short read lengths of common second-generation sequencing platforms do have limitations to overcome. Almost all library preparations involve many enzymatic and physical manipulations. These include reverse transcriptase conversion of RNA to cDNA, mechanical or chemical fragmentation of RNA or cDNA and fragment size selection, enzymatic blunt-ended fragment cleanup and ligation of adapters, and PCR amplification. Since ~ 80% of total RNA is rRNA, a poly-(A) selection of mRNA or rRNA removal step is required before library construction so that the majority of reads are meaningful. Every step

in the preparation pipeline has the potential to introduce biased and stochastic selection that increases the variance and lowers the reproducibility of RNAseq, thus lowering the fidelity of the sequenced library to represent the transcriptome [72]. Estimates indicate that less than 6 of every 1000 (~ 0.5%) individual transcript molecules in the starting sample are captured and represented in an RNAseq library prepared with standard methodology [22, 72]. Moreover, the short read lengths of second-generation sequencing make it difficult to unambiguously discern transcript variant structures and their abundances. Variants from a single gene can be formed from alternative transcription start-and-stop sites, alternative exon splice junctions, and intergene fusion products. These structures can be found with methods such as serial analysis of gene expression (SAGE), polyadenylation site (PAS) identification [74, 87], cap analysis of gene expression (CAGE) [13, 75], and exon–exon junction reads [32]; however, it is impossible to assign short variant reads to an individual transcript structure without some level of uncertainty [14, 59].

Another obstacle with RNAseq is to identify transcript strandedness from the sequenced read, since strand information is lost during exponential amplification of the fragmented libraries. First-strand cDNA sequencing, ligation of 5′ and 3′ orientation-specific adapters to RNA or first-strand cDNA, chemical bisulfite conversion of mRNA cytosines to uracils (C to U), and second-strand cDNA synthesis with dUTP are all used to maintain strand information during RNAseq [41]. However, the DNA-dependent DNA polymerase (DDDP) activity of reverse transcriptases during cDNA synthesis is a significant source of antisense DNA artifacts in the sequencing library. DDDP activity can generate spurious second-strand cDNA products from hairpin-folded first-strand cDNA [14, 41]. Furthermore, DDDP activity combined with template switching can make a contiguous sequence from separate transcripts, which can confound the identification of true gene fusion products.

2.7 Direct RNA Sequencing

Direct RNA sequencing (DRS) technology that does not rely upon reverse transcriptase conversion of RNA to cDNA could eliminate many of the biases introduced during the steps of RNAseq library construction and reduce the amount of RNA needed in a sample for sequencing. Helicose Biosciences (Cambridge, MA) developed a DRS platform that performs sequence-by-synthesis on single poly-(A)-tailed RNA molecules with an optimized polymerase and fluorescent nucleotide analogues called virtual terminator (VT) nucleotides [60]. The VT nucleotides are conjugated with fluorescent dyes and blocking groups that inhibit polymerase extension until they are chemically cleaved. The RNAs to be sequenced are 3′-end poly-(A) tailed with *E. coli* poly-(A) polymerase I (PAPI) to a length of about 150 nucleotides. The poly-(A)-tailed RNAs are then captured by annealing them to a solid-substrate array conjugated with oligo-(dT) polynucleotides. The oligo-(dT) serves as a primer for RNA single molecule sequence-by-synthesis. The first step in the reaction is to fill in the complement strand with normal dTTPs, and a single

cognate VT nucleotide (either vt-ATP, vt-CTP, or vt-GTP) that terminates the extension of the nascent, cognate copy strand at the first RNA nucleotide immediately 5′ of the poly-A tail. Fluorescent imaging of the single incorporated VTs on the nascent complement strands then marks the position of each single RNA molecule on the array. The fluorescent labels and blocking groups are then chemically liberated, thus removing the label and unblocking the 3′-end of the VT for polymerase extension of the next cognate VT base in the sequence. Cycles of adding one VT base species at a time, imaging the fluorescent nucleotide extensions, and liberating the dye label and blocking groups for sequencing subsequent nucleotides are repeated in the same alternating nucleotide order to obtain the RNA sequence [60]. Since the Helicose platform sequences single RNA molecules, the technology eliminates all the biases introduced during library construction and amplification, and the strand of the sequenced transcript is known [59]. Naturally polyadenylated mRNA molecules do not even need in vitro enzymatic tailing in order to be sequenced. However, the short read length combined with sequencing reads starting at the end of the poly-A tail means that coverage is 3′-biased. To get a complete transcriptome coverage, RNA would need to be fragmented and poly-(A)-tailed in vitro before hybridization to the array, which has the potential to introduce small sequencing biases of its own. In addition, by fragmenting the RNA, the abundance and structure of different transcript isoforms from the same gene cannot be determined with absolute certainty.

2.8 Long-Read Sequencing

The short read length of most second-generation sequencing technologies means that variant transcript isoform structures and their abundances must be computationally inferred from the number of reads that span exon–exon boundaries, the number of reads within individual exons, and transcript and exon lengths [59]. Paired-end sequencing is able to provide more information about transcript structure. In paired-end sequencing, a library is constructed with fragments much larger than can be sequenced with an end-to-end contiguous read. Instead, short reads are made from both terminal ends of each library fragment; and from these reads, the length of the whole molecule, and genome annotations, the entire fragment structure and sequence can be inferred.

In contrast with short-read and paired-end sequencing, full-length transcript sequencing can unambiguously identify the absolute structure of every individual transcript. Pacific Biosciences (Menlo Park, CA) has generated a single molecule real-time (SMRT) sequencing platform that can perform reads up to 30 kb in length [14]. Furthermore, this platform does not require library amplification, thus eliminating one source of read bias. Sequence-by-synthesis reactions are performed on SMRT cells fabricated to contain 150,000 zero-mode waveguides (ZMWs), which are nanostructure wells ~ 100 nm in diameter [20]. Single polymerases bound to individual cDNA molecules are immobilized on the bottom of the ZMWs. Sequencing is achieved by imaging nucleotide analogues linked with spectrally distinct

fluorophores at their terminal phosphates as they enter the polymerase during phosphodiester bond formation. The small diameter of the ZMWs only allows the fluorescence excitation light to penetrate a very short distance into the ZMW. The excitation volume in this configuration is on the order of zeptoliters (10^{-21} l) and is occupied on average by one or fewer dNTP molecules, even when the dNTP concentration is high enough for fast and accurate DNA polymerase activity [20]. When a cognate fluorescent dNTP pairs to the base of the template DNA within the polymerase, it is held in the ZMW excitation zone much longer than are free nucleotides, which transiently increases fluorescence intensity during nucleotide incorporation. Once the phosphodiester bond is formed, the fluorophore is liberated and diffuses away from the excitation zone, and the next base in the template is available for pairing with a cognate fluorescent dNTP. Since the rate of real-time sequencing reads is very fast and set by the kinetics of the polymerase, variable durations of individual base additions to the nascent strand lead to variable fluorescent pulse widths and low-quality base call reads. To compensate for the high base call error rates associated with the fast kinetics of real-time sequencing, the PacBio system generates a DNA template library with "dumbbell-shaped" molecules that are amenable to rolling-circle amplification. PacBio "SMRTbell" DNA library structures are constructed by ligating single-stranded hairpin adapters onto both ends of double-stranded DNA inserts, making a contiguous, circular piece of DNA. A primer that anneals to the loop of one of the hairpin adapters initiates extension by a strand-displacing DNA polymerase. A single pass through the template generates reads from both the plus and minus strands, giving twofold read coverage of the double-stranded template. Depending on the size of the template, rolling-circle amplification makes several passes over the insert during a single continuous long read (CLR). Since the base call errors of low-quality reads appear to be random and not base or template context specific, a highly accurate circular consensus (CCS) read can be deduced from the CLR. The consensus sequence between the two known adaptor sequences represents the library insert molecule.

Sharon et al. [73] applied the PacBio real-time sequencing platform to obtain long reads from the human transcriptome. SMARTbell libraries were made from polyA+ human RNA reverse transcribed with an oligo-dT primer. The authors generated and analyzed 476,000 CCS reads of cDNA inserts that averaged 1 kb in length. It was found that most CCS reads with an insert of under 1.5 kb in length contained the structure of a complete transcript, but less than half of the inserts over 2.4 kb were of complete transcripts. Together with the fact that the average CLR was much longer than the average CCS, this indicated that the major limitation of PacBios SMRT technology is the processivity of reverse transcriptases [14, 73]. This work also estimated that 14.5% of reads from spliced and genome mapable RNA molecules were of transcript variants that are not annotated in the GENCODE project. Most of the unannotated transcript reads were splice variants of known protein-coding genes; many others were of long noncoding RNAs. A follow-up study by this group used the PacBio real-time platform to sequence the transcriptome of lymphoblastoid cells derived from a female subject and her two parents [81]. Utilizing single nucleotide variations (SNVs) between gene alleles, they were

able to determine which inherited allele encoded a particular transcript read and from which parent she inherited the allele [81]. These studies indicate that long-read technologies will be needed to determine the true structure and abundance of various transcripts, and the effects of different alleles on the transcriptome. The major drawback of the Pac-Bio SMRT platform is that it only obtains about 50,000 reads per cell, which is over an order of magnitude less than the short-read platforms.

The development of nanopore sequencing technology also has the potential to generate long reads of the transcriptome, with minimal sample preparation, low cost, and fast speeds. Simplistically stated, the principle of nanopore sequencing is to apply an electric potential to drive a single-stranded DNA molecule across a pore with a diameter just large enough for ssDNA to pass through it, and measure the nucleotide sequence one base at a time as it passes single file through the pore. Many different strategies have been proposed to realize nanopore sequencing, but all are in various stages of development to overcome technical obstacles [5]. For the first time during two decades of research into this technology, Laszlo et al. [39] recently demonstrated the ability to sequence naturally occurring, complex DNA molecules with a nanopore technology. Their setup involved using Phi29 DNA polymerase to separate the strands of dsDNA molecules, and slowly control the speed of ssDNA movement through a *Mycobacterium smegmatis* porin A (MspA) protein channel suspended in a lipid bilayer, and record the reduction in current that passes through the channel as it is occluded by the polynucleotide. MspA is short and constricted such that only four bases (quadromers) of a single-stranded polynucleotide span the length of the channel at any one time, and each possible quadromer reduces the current by a predictable amount. They first calibrated their setup by using synthetic oligonucleotides with sequences arranged such that all 256 possible four nucleotide (A, G, C, and T) quadromer permutations were represented ($4^4 = 256$), and measured the current levels associated with each quadromer in the channel. They used this information to predict the pattern of changing current levels over time when passing phi X 174 genomic sequence through the channel, and were able to show that their prediction matched the empirical result with high accuracy. However, they also noted from measuring the naturally occurring phi X 174 DNA molecules that the current levels associated with each quadromer were significantly affected by the surrounding sequence; therefore, de novo sequencing and alignment without the aid of genomic annotation would not be possible. Despite this limitation, the technology was still able to correctly identify a molecule of phi X 174 genomic sequence by comparing experimental values with a database of over 5000 viral genome predictions. They also produced proof-of-concept SNP detection algorithms. Furthermore, the median sequence length of linearized phi X 174 genomic DNA molecules was over 1000 bp, and the longest read was up to 4500 bp [39]. The main advantage of nanopore sequencing is that no library preparation beyond RNA isolation would be needed. Thus amplification biases and library construction chemistries would be eliminated, which would both increase the fidelity and decrease the cost of sequencing. Further improvements and adaptation for RNA could make nanopore sequencing a viable and cheap option for transcriptome assessment in the future.

2.9 Quantitative Gene Expression *In Situ*

All of the RNAseq methods described here suffer from the limitation that the localization of any identified RNA molecule cannot be determined with a precision that is finer than the size of the dissected tissue. Subcellular resolution is not possible even when extracting cellular content from single cells. *In situ* hybridization (ISH) is a popular technique for neuroscientists to identify the anatomical location, distribution, and number of cells in the brain that express a particular gene. As commonly practiced, ISH involves cryosectioning thin slices of tissue onto microscope slides, fixing the RNA to the tissue, and hybridizing labeled antisense nucleotide probes that are complementary to the transcript of interest. Detection methods require conjugating the probe with radionucleotides, biological affinity labels, enzymatic tags, and fluorescent molecules. These standard ISH techniques are excellent for identifying cells that express the gene of interest, but are only semi-quantitative when attempting to measure gene expression levels.

Radioactivity exposure of X-ray films and densitometry measurement is the gold standard method for quantitative ISH [58]. Typically, oligonucleotide probes are tailed with [$\alpha-^{35}$S]dATP or [$\alpha-^{33}$P]dATP using a terminal deoxynucleotide transferase (TdT) reaction. ^{35}S and ^{33}P are used in part because their β-particle maximum energies are sufficiently low to avoid saturating the detector, but sufficiently high to allow relatively low exposure time. The characteristics of the X-ray film are also an important resolution factor. Since the signal produced by radioactivity on X-ray film is not linear, standard samples prepared with known amounts of radioactivity need to be exposed to the film along with the radioactive probe-labeled ISH samples. Exposure time is determined empirically so that there is sufficient signal for densitometery measurement, but the optical density must not exceed the linear range of detection (~1 OD). Therefore, it may be necessary to expose multiple films to obtain the optimal exposure time, which can be between a few days and up to six weeks [58]. Once a good exposure is acquired, an image analysis system is used to measure the optical densities of samples and standards. The researcher outlines a defined region of the sample, and the signal in that region is interpolated from the standards. Both optical density and area can be used to quantify relative expression levels.

Despite the large amount of work and time required, X-ray film exposure only quantifies relative expression at regional, not cellular, level resolution. To obtain gene expression values at the cellular level, a much more involved process of nuclear emulsion radiography is used. Briefly, slides are dipped in a photographic emulsion solution after probe hybridization, then the emulsion is dried and exposed for 4–8 weeks. After exposure, slides are weakly counterstained to identify cell bodies. Images are then captured with brightfield or darkfield microscopy, and the number of visible silver gains above individual cells is counted manually or with an image analysis software. By reducing background signal through better probe preparation and using high stringency conditions during hybridization and the post-hybridization wash steps, Liu et al. [42] optimized these procedures in order to quantify RNA from fixed, post-mortem human brain tissue.

The downside of using autoradiography for *quantitative* ISH is its extreme labor-intensiveness, and the necessity of using "hot" radioactive isotopes. A "cold" alternative uses antisense probes conjugated with multiple fluorophores to increase the signal from individual RNA target molecules. Under sparse labeling conditions, the resulting high-intensity, punctate signals represent single molecules that can be counted. This approach can either use a few (~ 5) heavily labeled probes (~ 5 fluorochromes per probe) that hybridize to adjacent sequences on the RNA [21, 83], or many (48) singly labeled probes [62]. Z-plane image stacks of cells or tissues with heavily labeled RNA molecules are deconvolved to remove background signal and projected in Z to render the data as a two-dimensional image. A minimum-intensity threshold is then applied to remove background. The method of using multiple singly labeled probes has been demonstrated in several biological samples, including cultured hippocampal neurons [62]. Although these methods achieve subcellular resolution, their capacity to detect different RNAs species in the same sample is limited by the number of spectrally discernable fluorescent reporters to approximately four.

A new technology called RNAscope (Advanced Cell Diagnostics, Inc.) detects RNA in fresh-frozen or formalin-fixed and paraffin-embedded tissues. The design of RNAscope amplifies signal and reduces background [90]. RNAscope uses sets of duplicate probes that hybridize to juxtaposed sequences of the target RNA molecule. When juxtaposed, the duplicate probe sets provide an annealing site for a preamplifier molecule. Nonspecific binding of a single probe fails to provide an annealing site for the preamplifier, thus eliminating background. Ten to twenty probe sets are made to hybridize to various positions along the RNA molecule. Each bound preamplifier contains 20 binding sites for amplifier molecules, and each amplifier molecule in turn provides 20 binding sites for label probes. Label probes can be conjugated to HRP or AP enzymes for chromogenic detection with brightfield microscopy, or fluorescent probes for epifluorescence microscopy. The signal amplification (up to 8000 label probes per RNA) allows for punctate single-molecule detection and quantification, and multiplexing for different target molecules with the use of different fluorescent labels [90]. Automated quantitative analysis (AQUA; [9]) was used with RNAscope to quantify Esr1 transcript levels in breast cancer tissue samples [4]. RNAscope was also used to determine the percentage of excitatory and inhibitory cells of the rat cortex that express different NRG1 isoforms [42]. Like the multiple-probe methods described above, RNAscope is multiplexing-limited and not capable of unbiased measurement of the whole transcriptome.

Fluorescent *in situ* sequencing (FISSEQ) is a newly published method that has the capacity to quantitate the entire transcriptome in an unbiased way, as well as to measure the positions of individual RNA molecules at subcellular resolution [40]. In FISSEQ, RNA is reverse-transcribed *in situ* with random hexamers, containing a 5′-overhang for primer annealing, in fixed cells or tissues. Aminoallyl dUTP is used in the reverse transcription reaction so that the cDNA incorporating this modified base can be fixed to the cellular protein matrix with bis-N-succinimidyl (pentaethylene glucol) ester [BS(PEG)9] linker. The cDNA is then circularized with circular ligase, amplified by rolling circle amplification using Phi29 DNA polymerase, and

the tandem amplicons are cross-linked together with BS(PEG)9 to form an amplified, three-dimensional cDNA library for RNA sequencing. RNAseq is performed with SOLiD sequence-by-ligation technology. SOLiD technology uses a set of fluorescently labeled probes that compete for annealing to the template and ligation to the sequencing primer. Incorporation of a particular probe is determined by complementarity of a di-base region with the template sequence, and probe signal is acquired by fluorescence microscopy. Successive cycles of sequencing-by-ligation that covers a set length of the template identify the nucleotide sequence and position of RNA molecules. Since FISSEQ uses nucleotide sequencing-based detection, it is an unbiased approach that can quantify all transcripts of the whole transcriptome, and it does not require signal intensity cutoff thresholding to distinguish signal from noise. By sequencing individual RNA molecules *in situ*, FISSEQ not only quantitates the transcriptome expression levels in specific individual cells, it also determines the subcellular location of each molecule of a particular RNA transcript.

2.10 Discussion and Outlook

Billions of cells and trillions of synaptic connections develop into an abundance of distinct and integrated neural structures that form the circuitry of the human brain. It is largely unknown to what degree individual neurons actually represent functionally distinct cell types. Variability in single cell transcriptomes suggests a potentially enormous degree of functional heterogeneity among neurons. The combined use of molecular markers, mammalian model organisms, mouse genetics, and next generation sequencing has made it possible to begin exploring this heterogeneity. The ongoing technological developments are continuing to improve the fidelity of quantitative transcriptome measurement with longer reads and more accurate representation of the full complement of transcripts. Moreover, the ability of *in situ* methods to provide unambiguous anatomical information could make technologies like FISSEQ the future of unbiased transcriptome sequencing for complex tissues. Leveraging the ability to detect changes in immediate early gene expression in these experiments may give additional insight into network connectivity. It is well within reach to characterize functional circuits by identifying specific cells based on their gene expression profiles.

The major limitation of all current transcriptome measurements is that they only provide a single snapshot of expression at a given time. It is not yet possible to track temporal changes over the course of development, or during behavior, within a single individual. In fact, it is hard to even imagine a future technology that could perform such a feat *in vivo*. Dynamic information on gene expression is typically inferred by using multiple subjects in a well-controlled time-course experiment and cannot be performed at cellular resolution due to the complexity and variability of the mammalian brain. *In vivo* two-photon imaging of an activity-induced gene engineered with a fluorescent reporter is the best that has been achieved in regard to following gene expression within a single cell over time [10]. Wang et al. [89]

used a transgenic mouse line expressing GFP under the control of the endogenous promoter of the immediate-early-gene Arc and made optical windows through their skulls to image Arc-GFP expression within the superficial layers of the visual cortex using a two-photon microscope. They were able to track cellular expression of Arc-GFP, a proxy for high levels of neuronal activity, over the course of several days, and identify cells affected by visual experience. Although useful for analyzing a particular candidate gene, *in vivo* two-photon imaging is limited to recording perhaps a few spectrally discrete fluorescent reporters at once and is obviously not applicable to unbiased transcriptome profiling. A system for dynamic measurement of the transcriptome *in vivo* would be a truly transformative technology.

Perhaps a second-best solution to dynamic *in vivo* transcriptome profiling is to take an intersectional approach. For example, a mouse could be exposed to a particular sensory stimulus or environmental condition. Neurons responding to that experience could then be identified microscopically using immediately early gene (IEG) fluorescent reporters. At the end of the *in vivo* experiment, electrophysiological and morphological properties of responsive (IEG^+) neurons could be compared to nonactivated (IEG^-) neurons. Ren et al. [65] used this approach to measure Arc-dependent electrophysiological changes in the persistent firing patterns of neurons in the frontal cortex. In the future, after the electrophysiological measurement, the contents of individual cells could be acquired by patch-aspiration and processed for RNAseq and proteome analysis [61]. Alternatively, if the electrophysiological recording methods maintain cell integrity, the slice preparations could be fixed and processed for *in situ* RNA sequencing and immunohistochemistry [40]. Defining the cell physiology and other properties immediately before capturing the RNA would aid in assessing the relationship between neuronal activity and the transcriptome.

Understanding the functions of neural circuits in the brain at the cellular level is one of biology's most difficult problems. Fortunately, genomics is blazing a trail for the neurosciences to negotiate the hurdles associated with cellular profiling, large datasets, and vastly interconnected networks. In turn, the large number of cell types and signaling mechanisms in the brain, and their interactions with sensory inputs, should provide ample opportunity for novel discoveries about the interactions between the transcriptome and the environment.

References

1. Adiconis, X., et al. (2013). Comparative analysis of RNA sequencing methods for degraded or low-input samples. *Nature Methods, 10*(7), 623–629.
2. Arlotta, P., et al. (2005). Neuronal subtype-specific genes that control corticospinal motor neuron development in vivo. *Neuron, 45*(2), 207–221.
3. Atasoy, D., et al. (2012). Deconstruction of a neural circuit for hunger. *Nature, 488*(7410), 172–177.
4. Bordeaux, J. M., et al. (2012). Quantitative in situ measurement of estrogen receptor mRNA predicts response to tamoxifen. (G. E. Woloschak, ed.) *PloS One, 7*(5), e36559.

5. Branton, D., et al. (2008). The potential and challenges of nanopore sequencing. *Nature Biotechnology, 26*(10), 1146–1153.
6. Cahoy, J. D., et al. (2008). A transcriptome database for astrocytes, neurons, and oligodendrocytes: A new resource for understanding brain development and function. *The Journal of Neuroscience, 28*(1), 264–278.
7. Cajigas, I. J., et al. (2012). The local transcriptome in the synaptic neuropil revealed by deep sequencing and high-resolution imaging. *Neuron, 74*(3), 453–466.
8. Callaway, E. M. (2008). Transneuronal circuit tracing with neurotropic viruses. *Current Opinion in Neurobiology, 18*(6), 617–623.
9. Camp, R. L., Chung, G. G., & Rimm, D. L. (2002). Automated subcellular localization and quantification of protein expression in tissue microarrays. *Nature Medicine, 8*(11), 1323–1328.
10. Cao, V. Y., et al. (2013). In vivo two-photon imaging of experience-dependent molecular changes in cortical neurons. *Journal of Visualized Experiments,* (71), e50148, doi:10.3791/50148.
11. Chiu, I. M., et al. (2013). A neurodegeneration-specific gene-expression signature of acutely isolated microglia from an amyotrophic lateral sclerosis mouse model. *CellReports, 4*(2), 385–401.
12. Dafforn, A., et al. (2004). Linear mRNA amplification from as little as 5 ng total RNA for global gene expression analysis. *BioTechniques, 37*(5), 854–857.
13. de Hoon, M., & Hayashizaki, Y. (2008). Deep cap analysis gene expression (CAGE): Genome-wide identification of promoters, quantification of their expression, and network inference. *BioTechniques, 44*(5), 627–632.
14. de Klerk, E., Dunnen, den, J. T. & t Hoen, P. A. C. (2014). RNA sequencing: From tag-based profiling to resolving complete transcript structure. *Cellular and Molecular Life Sciences, 71*(18), 3537–3551.
15. Djebali, S., et al. (2012). Landscape of transcription in human cells. *Nature, 489*(7414), 101–108.
16. Doyle, J. P., et al. (2008). Application of a translational profiling approach for the comparative analysis of CNS cell types. *Cell, 135*(4), 749–762.
17. Draper, S., et al. (2010). Differential gene expression between neuropeptide Y expressing neurons of the dorsomedial nucleus of the hypothalamus and the arcuate nucleus: Microarray analysis study. *Brain Research, 1350*(C), 139–150.
18. Dulac, C., & Axel, R. (1995). A novel family of genes encoding putative pheromone receptors in mammals. *Cell, 83*(2), 195–206.
19. Eberwine, J., et al. (1992). Analysis of gene expression in single live neurons. *Proceedings of the National Academy of Sciences, 89*(7), 3010–3014.
20. Eid, J., et al. (2009). Real-time DNA sequencing from single polymerase molecules. *Science, 323*(5910), 133–138.
21. Femino, A. M., et al. (1998). Visualization of single RNA transcripts in situ. *Science, 280*(5363), 585–590.
22. Fu, G. K., et al. (2014). Molecular indexing enables quantitative targeted RNA sequencing and reveals poor efficiencies in standard library preparations. *Proceedings of the National Academy of Sciences, 111*(5), 1891–1896.
23. Gallie, D. R. (1998). A tale of two termini. *Gene, 216*(1), 1–11.
24. Gay, L., et al. (2013). Mouse TU tagging: A chemical/genetic intersectional method for purifying cell type-specific nascent RNA. *Genes & Development, 27*(1), 98–115.
25. GENSAT. (2014). The gene expression nervous system atlas (GENSAT) project. New York: NINDS Contracts N01NS02331 & HHSN271200723701 C to The Rockefeller University. gensat.org. http://www.gensat.org/index.html. Accessed 27 Aug 2014.
26. Grison, A., et al. (2014). Mesencephalic dopaminergic neurons express a repertoire of olfactory receptors and respond to odorant-like molecules. *BMC Genomics, 15*(1), 729.
27. Hashimshony, T., et al. (2012). CEL-seq: Single-cell RNA-seq by multiplexed linear amplification. *CellReports, 2*(3), 666–673.
28. Heiman, M., et al. (2008). A translational profiling approach for the molecular characterization of CNS cell types. *Cell, 135*(4), 738–748.

29. Hempel, C. M., Sugino, K., & Nelson, S. B. (2007). A manual method for the purification of fluorescently labeled neurons from the mammalian brain. *Nature Protocols, 2*(11), 2924–2929.
30. Holt, C. E., & Schuman, E. M. (2013). The central dogma decentralized: New perspectives on RNA function and local translation in neurons. *Neuron, 80*(3), 648–657.
31. Islam, S., et al. (2011). Characterization of the single-cell transcriptional landscape by highly multiplex RNA-seq. *Genome Research, 21*(7), 1160–1167.
32. Jiang, H. & Wong, W. H., (2009). Statistical inferences for isoform expression in RNA-Seq. *Bioinformatics, 25*(8), 1026–1032.
33. Kang, H. J. et al. (2011). Spatio-temporal transcriptome of the human brain. *Nature, 478*(7370), 483–489.
34. Knight, Z. A. et al. (2012). Molecular profiling of activated neurons by phosphorylated Ribosome capture. *Cell, 151*(5), 1126–1137.
35. Krashes, M. J. et al. (2014). An excitatory paraventricular nucleus to AgRP neuron circuit that drives hunger. *Nature, 507*(7491), 238–242.
36. Kunitomo, H. et al. (2005). Identification of ciliated sensory neuron-expressed genes in Caenorhabditis elegans using targeted pull-down of poly(A) tails. *Genome biology, 6*(2), R17.
37. Kurn, N. et al. (2005). Novel isothermal, linear nucleic acid amplification systems for highly multiplexed applications. *Clinical Chemistry, 51*(10), 1973–1981.
38. Lasken, R. S. (2013). Single-cell sequencing in its prime. *Nature Biotechnology, 31*(3), 211–212.
39. Laszlo, A. H. et al. (2014). Decoding long nanopore sequencing reads of natural DNA. *Nature biotechnology, 32*(8), 829–833.
40. Lee, J. H. et al. (2014). Highly multiplexed subcellular RNA sequencing in situ. *Science, 343*(6177), 1360–1363.
41. Levin, J. Z. et al. (2010). Comprehensive comparative analysis of strand-specific RNA sequencing methods. *Nature methods, 7*(9), 709–715.
42. Liu, C.-Q. et al. (2010). A quantitative in situ hybridization protocol for formalin-fixed paraffin-embedded archival post-mortem human brain tissue. *Methods, 52*(4), 359–366.
43. Lo, L. & Anderson, D. J. (2011). A Cre-dependent, anterograde transsynaptic viral tracer for mapping output pathways of genetically marked neurons. *Neuron, 72*(6), 938–950.
44. Lobo, M. K. et al. (2006). FACS-array profiling of striatal projection neuron subtypes in juvenile and adult mouse brains. *Nature Neuroscience, 9*(3), 443–452.
45. Luo, L. et al. (1999). Gene expression profiles of laser-captured adjacent neuronal subtypes. *Nature Medicine, 5*(1), 117–122.
46. Madisen, L. et al. (2010). A robust and high-throughput Cre reporting and characterization system for the whole mouse brain. *Nature Neuroscience, 13*(1), 133–140.
47. Maret, S. et al. (2007). Homer1a is a core brain molecular correlate of sleep loss. *Proceedings of the National Academy of Sciences of the United States of America, 104*(50), 20090–20095.
48. Martin, K. C. & Zukin, R. S. (2006). RNA trafficking and local protein synthesis in dendrites: An overview. *The Journal of Neuroscience, 26*(27), 7131–7134.
49. Miller, M. R. et al. (2009). TU-tagging: Cell type-specific RNA isolation from intact complex tissues. *Nature Methods, 6*(6), 439–441.
50. Miller, J. A. et al. (2014). Transcriptional landscape of the prenatal human brain. *Nature, 508*(7495), 199–206.
51. Muzumdar, M. D. et al. (2007). A global double-fluorescent Cre reporter mouse. *Genesis, 45*(9), 593–605.
52. Nelson, S. B., Sugino, K. & Hempel, C. M. (2006). The problem of neuronal cell types: A physiological genomics approach. *Trends in Neurosciences, 29*(6), 339–345.
53. Niwa, H., Yamamura, K. & Miyazaki, J. (1991). Efficient selection for high-expression transfectants with a novel eukaryotic vector. *Gene, 108*(2), 193–199.
54. Oh, S.W. et al. (2014). A mesoscale connectome of the mouse brain. *Nature, 508*(7495), 207–214.

55. Okaty, B. W., Sugino, K. & Nelson, S. B. (2011a). A quantitative comparison of cell-type-specific microarray gene expression profiling methods in the mouse brain J. Kelso, ed. *PloS ONE, 6*(1), e16493.
56. Okaty, B. W., Sugino, K. & Nelson, S. B. (2011b). Cell type-specific transcriptomics in the brain. *The Journal of Neuroscience, 31*(19), 6939–6943.
57. Osakada, F. et al. (2011). New rabies virus variants for monitoring and manipulating activity and gene expression in defined neural circuits. *Neuron, 71*(4), 617–631.
58. O'Shea & Gundlach (1994). In situ hybridization protocols for the brain. In Wisden and Morris, eds. New York: Academic.
59. Ozsolak, F. & Milos, P. M., (2011). RNA sequencing: Advances, challenges and opportunities. *Nature Reviews. Genetics, 12*(2), 87–98.
60. Ozsolak, F. et al. (2009). Direct RNA sequencing. *Nature, 461*(7265), 814–818.
61. Qiu, S. et al. (2012). Single-neuron RNA-Seq: Technical feasibility and reproducibility. *Frontiers in Genetics, 3,* 1–8.
62. Raj, A. et al. (2008). Imaging individual mRNA molecules using multiple singly labeled probes. *Nature Methods, 5*(10), 877–879.
63. Ramirez, S. et al. (2013). Creating a false memory in the hippocampus. *Science, 341*(6144), 387–391.
64. Ramsköld, D. et al. (2012). Full-length mRNA-Seq from single-cell levels of RNA and individual circulating tumor cells. *Nature Publishing Group, 30*(8), 777–782.
65. Ren, M. et al. (2014). Arc regulates experience-dependent persistent firing patterns in frontal cortex. *The Journal of Neuroscience, 34*(19), 6583–6595.
66. Rossner, M. J. et al. (2006). Global transcriptome analysis of genetically identified neurons in the adult cortex. *The Journal of Neuroscience, 26*(39), 9956–9966.
67. Roy, P. J. et al. (2002). Chromosomal clustering of muscle-expressed genes in Caenorhabditis elegans. *Nature, 418*(6901), 975–979.
68. Sanz, E. et al. (2009). Cell-type-specific isolation of ribosome-associated mRNA from complex tissues. *Proceedings of the National Academy of Sciences, 106*(33), 13939–13944.
69. Sasagawa, Y. et al. (2013). Quartz-Seq: A highly reproducible and sensitive single-cell RNA sequencing method, reveals non-genetic gene-expression heterogeneity. *Genome Biology, 14*(4), R31.
70. Schmidt, W. M. & Mueller, M. W. (1999). CapSelect: A highly sensitive method for 5′ CAP-dependent enrichment of full-length cDNA in PCR-mediated analysis of mRNAs. *Nucleic Acids Research, 27*(21), e31.
71. Shah, N. M. et al. (2004). Visualizing Sexual Dimorphism in the Brain. *Neuron, 43*(3), 313–319.
72. Shapiro, E., Biezuner, T. & Linnarsson, S., (2013). Single-cell sequencing-based technologies will revolutionize whole-organism science. *Nature Reviews Genetics, 14*(9), 618–630.
73. Sharon, D. et al. (2013). A single-molecule long-read survey of the human transcriptome. *Nature Biotechnology, 31*(11), 1009–1014.
74. Shepard, P. J. et al. (2011). Complex and dynamic landscape of RNA polyadenylation revealed by PAS-Seq. *RNA, 17*(4), 761–772.
75. Shiraki, T. et al. (2003). Cap analysis gene expression for high-throughput analysis of transcriptional starting point and identification of promoter usage. *Proceedings of the National Academy of Sciences, 100*(26), 15776–15781.
76. Sugino, K. et al. (2005). Molecular taxonomy of major neuronal classes in the adult mouse forebrain. *Nature Neuroscience, 9*(1), 99–107.
77. Tang, F. et al. (2009). mRNA-Seq whole-transcriptome analysis of a single cell. *Nature Methods, 6*(5), 377–382.
78. Tang, F. et al. (2010). RNA-Seq analysis to capture the transcriptome landscape of a single cell. *Nature Protocols, 5*(3), 516–535.
79. Tang, F. et al. (2011). Deterministic and Stochastic Allele Specific Gene Expression in Single Mouse Blastomeres M. Pesce, ed. *PloS ONE, 6*(6), e21208.

80. Taylor, P. (2013). Analytical and preparative instrumentation. *Journal of Biomolecular Screening, 18*(1), 143–145.
81. Tilgner, H. et al. (2014). Defining a personal, allele-specific, and single-molecule long-read transcriptome. *Proceedings of the National Academy, 111*(27), 9869–9874.
82. Tong, Q. et al. (2008). Synaptic release of GABA by AgRP neurons is required for normal regulation of energy balance. *Nature Neuroscience, 11*(9), 998–1000.
83. Trcek, T. et al. (2012). Single-mRNA counting using fluorescent in situ hybridization in budding yeast. *Nature Protocols, 7*(2), 408–419.
84. Tung, J.W. et al. (2007). Modern flow cytometry: A practical approach. *Clinics in Laboratory Medicine, 27*(3), 453-68-v.
85. van den Pol, A. N. et al. (2009). Neuromedin B and gastrin-releasing peptide excite arcuate nucleus neuropeptide Y neurons in a novel transgenic mouse expressing strong Renilla green fluorescent protein in NPY neurons. *The Journal of Neuroscience, 29*(14), 4622–4639.
86. Van Gelder, R. N., et al. (1990). Amplified RNA synthesized from limited quantities of heterogeneous cDNA. *Proceedings of the National Academy of Sciences, 87*(5), 1663–1667.
87. Velculescu, V. E. et al. (1995). Serial analysis of gene expression. *Science, 270*(5235), 484–487.
88. Wang, L. & Yi, R. (2014). 3′UTRs take a long shot in the brain. *BioEssays, 36*(1), 39–45.
89. Wang, K.H. et al. (2006). In vivo two-photon imaging reveals a role of arc in enhancing orientation specificity in visual cortex. *Cell, 126*(2), 389–402.
90. Wang, F. et al. (2012). RNAscope: A novel in situ RNA analysis platform for formalin-fixed, paraffin-embedded tissues. *The Journal of Molecular Diagnostics: JMD, 14*(1), 22–29.
91. Wu, A. R. et al. (2013). Quantitative assessment of single-cell RNA-sequencing methods. *Nature Methods, 11*(1), 41–46.
92. Yang, Z., Edenberg, H. J. & Davis, R. L., (2005). Isolation of mRNA from specific tissues of Drosophila by mRNA tagging. *Nucleic Acids Research, 33*(17), e148-e148.
93. Zingg, B. et al. (2014). Neural networks of the mouse neocortex. *Cell, 156*(5), 1096–1111.
94. Zong, H. et al. (2005). Mosaic analysis with double markers in mice. *Cell, 121*(3), 479–492.

Chapter 3
Fluorescent Proteins for Neuronal Imaging

Yongxin Zhao and Robert E. Campbell

Abstract Over the past two decades, the growing selection of engineered fluorescent proteins have helped drive a revolution in the ability of researchers to image protein localization and biochemical dynamics in live cells in real time. Although the fluorescent proteins were long preceded by other fluorophores compatible with live cell imaging, the fact that fluorescent proteins are fully genetically encoded has enabled them to be applied in applications that would not otherwise be possible. In particular, fluorescent proteins have enabled the creation of transgenic animals in which specific neuronal cell types are uniquely and fluorescently labeled. Furthermore, through the use of highly engineered fluorescent proteins that change their fluorescence in response to a change in calcium ion concentration or membrane potential, fluorescent proteins have enabled high resolution minimally invasive imaging of neuronal activity in model organisms. In this chapter we will provide an overview of fluorescent protein technology and detail the technological developments that have made such experiments possible. Particular emphasis will be placed on the development of strategies for engineering Ca^{2+} and voltage indicators, and the latest breakthroughs in these directions will be highlighted.

3.1 Introduction to Fluorescent Proteins

Since the first fluorescent protein (FP) was discovered in *Aequorea victoria* by Shimomura et al. in the 1960s [1], FPs have become one of the most thoroughly studied and exploited classes of proteins in cell biology and have revolutionized the way we observe the biological world. *Aequorea victoria* green FP (avGFP) and its homologues are now well established as indicators for monitoring protein localization, small molecule dynamics, enzyme activities, the interactions between

Y. Zhao (✉) · R. E. Campbell
Department of Chemistry, University of Alberta, 11227 Saskatchewan Drive, T6G 2G2 Edmonton, AB, Canada
e-mail: yongxin2@ualberta.ca

R. E. Campbell
e-mail: robert.e.campbell@ualberta.ca

A. D. Douglass (ed.), *New Techniques in Systems Neuroscience,* Biological and Medical Physics, Biomedical Engineering, DOI 10.1007/978-3-319-12913-6_3

biomolecules, and physiological changes in living tissues. Due to their importance as biological tools, FPs and FP-based indicators have been subjected to extensive engineering efforts. Compiling a complete list of every FP and FP-based indicator would be a daunting task. Rather than attempt to provide an exhaustive compilation of every example, this chapter aims to provide an overview of current FP technology with a focus on the development of FP-based indicators and the breakthroughs in engineering improved Ca^{2+} and voltage indicators for neuroimaging. We expect that the principles and representative examples provided here will serve as a sufficient foundation to enable a novice user to venture into the primary literature and find the FP-based neuronal imaging tool that is best suited to their research application.

3.1.1 FP Structure

All FPs possess a β-barrel structure consisted of 11 β-strands, with an α-helix through the central axis of the cylinder (Fig. 3.1) [2, 3]. The α-helix contains the chromophore and is buried in the center of the β-barrel, which is conventionally called a β-can. Although naturally occurring FPs have now been discovered in a wide variety of marine animal species, the β-can structure is highly conserved. Once the β-can is properly folded, the chromophore can be autonomously formed from a specific tripeptide sequence and exhibits visible wavelength fluorescence [4]. This feature makes FPs exceptionally useful genetically encoded markers, as introduction of an appropriate FP-encoding gene into almost any organism will result in

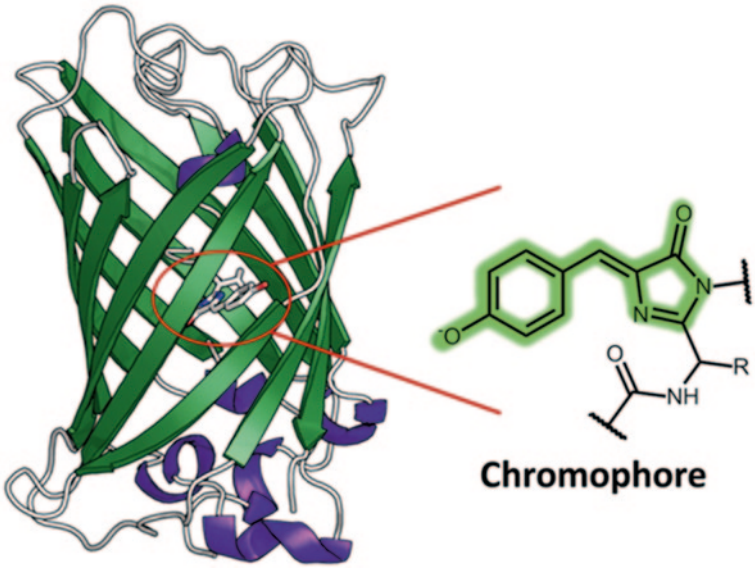

Fig. 3.1 Structure of avGFP and its intrinsic chromophore (PDB ID 1EMA) [3]

the appearance of fluorescence [5, 6]. More importantly, it is convenient to modify FP genes using standard molecular biology tools, which facilitates the creation of recombinant fusion proteins or FPs with modified properties. These FP-containing constructs have proven to be nontoxic to living organisms, allowing the creation of transgenic fluorescent animals to become a standard endeavor. In this way, fluorescent labeling of almost any protein of interest in living organisms can be achieved, including a variety of mammals that could not otherwise be labeled using traditional synthetic fluorophores.

3.1.2 FP Colors and Chromophores

3.1.2.1 FP Colors

Improved versions of GFP with better brightness and folding efficiency were developed soon after the first demonstration of its heterogeneous expression in a model organism [7–9]. It was also found that the fluorescent color of GFP could be altered to blue or yellow emission by introducing mutations into or near the chromophore-forming residues [4]. Despite the tremendous success in engineering avGFP for improved photophysical properties and altered hues, some developments have remained elusive. Despite extensive efforts, the emission wavelength of avGFP has not been extended above 530 nm effectively. Only one engineered avGFP variant was reported with partial red emission at 585 nm [10]. Fortunately, this engineering problem has been solved by nature. FPs with yellow (YFP), orange (OFP), and red (RFP) fluorescent emission were later discovered in reef corals and anemones [11, 12]. The first reported RFP, DsRed from *Discosoma sp*., is also the one that has received the most attention to date and seen the broadest use in imaging applications.

Red-shifted fluorescence wavelengths provide a major advantage for biological imaging, because they minimize the autofluorescence and scattering problems of tissues, which is more significant with the blue/green/yellowish fluorescence of avGFP homologues. At shorter wavelengths light is strongly absorbed by endogenous pigments, such as melanin or hemoglobin, and optical scattering and phototoxicity are more severe. Accordingly more red-shifted FPs are generally preferable relative to more blue-shifted FPs [13]. This trend remains true through wavelengths of about 1000 nm, beyond which the absorbance of water becomes the limiting factor. For these reasons, the optimal wavelength range for exciting and detecting the emission of fluorescent probes (often referred to as the “optical window”) runs from approximately 650 to 1000 nm in biological tissues [13–15]. To better use the optical window for fluorescence imaging *in vivo*, much effort has been invested in engineering FPs with ever more red-shifted wavelengths and pushing both their excitation and emission wavelengths into the near-infrared [16–19]. An alternative approach is to use near-infrared 2-photon (2P) excitation to excite FPs that fluoresce at visible wavelengths [20, 21].

3.1.2.2 Chromophore Structures

The chromophore structure of avGFP was first determined over three decades ago [22]. The mechanism by which avGFP's chromophore matures has been extensively studied and the overall series of transformations is reasonably well understood. Following folding into a nearly native conformation, residues 65–67 are transformed into the chromophore through a series of autogenic reactions. Evidence supports a mechanism in which nucleophilic attack of the amide nitrogen of Gly67 on the carbonyl carbon of Ser65 leads to the formation of an imidazolinone ring. This is followed by oxidation by molecular oxygen, and finally a dehydration step [4, 23–29] (Fig. 3.2). Although some exceptions exist, the majority of FPs have a chromophore in the *Z* (also referred to a *cis*) conformation [30]. Oxidation is the rate-limiting step [27], and oxygen is the only nonprotein component that is required for chromophore

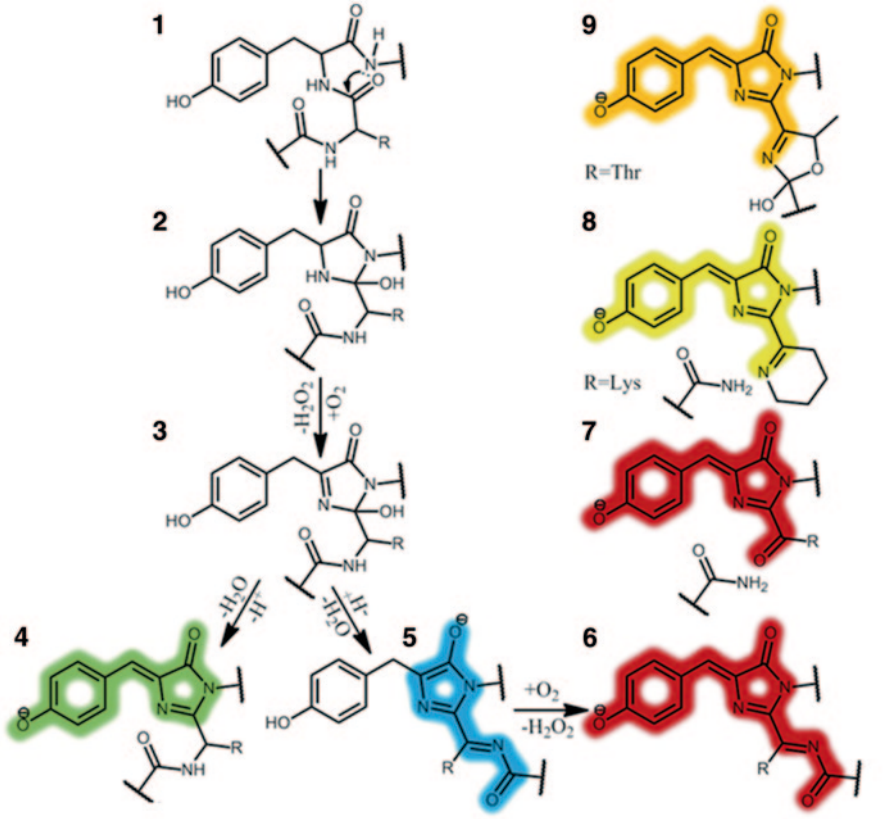

Fig. 3.2 Proposed maturation mechanisms for FP chromophores. The starting material is a tripeptide *1*. The avGFP *green* chromophore *4* is formed via the pathway *1-2-3-4*. The *DsRed*-like chromophore *6* matures via the *blue*-emitting intermediate *5*. Chromophore and environment modification leads to a range of different chromophores *7–9*. (Adapted from Dedecker et al. [40])

formation. Depending on the FP, this process generally takes minutes to hours to complete.

The steps leading to formation of further extended RFP chromophores are less understood, and there remains some debate regarding the mechanistic details [26, 31, 32]. DsRed, the prototypical RFP, possesses a GFP-like chromophore with an acylimine extension that elongates the conjugated system (Fig. 3.2) [33]. Most other OFPs, RFPs, and some YFPs are thought to have chromophore structures that are closely related to, or further modified versions of, the DsRed chromophore. The chemistry of RFP chromophore formation is complex, and several competing mechanisms have been proposed [26, 31, 34–36]. It is generally accepted that most RFPs mature via a common DsRed-like pathway. Previous studies suggested that the DsRed chromophore forms via a green fluorescent intermediate [33], but there is increasing evidence suggesting that the maturation occurs via an unusual blue intermediate (Fig. 3.2) [26, 35]. The blue-to-red chromophore conversion can be disrupted with certain mutations, resulting in a blue FP [37]. The maturation of red fluorescence is often incomplete, and a significant fraction of proteins become trapped in a green-emissive state via the competing avGFP-type chromophore formation pathway (Fig. 3.2). The presence of this green "contamination" for many RFPs can lead to experimental complications [38].

FPs with a variety of different chromophore structures have been discovered (Fig. 3.2), though the GFP-like green chromophore and DsRed-like red chromophore seem to occur most frequently in nature. Yet other chromophore structures have been artificially created by substituting the residues in the chromophore-forming tripeptide. For example, substitution of the central tyrosine in the GFP chromophore with various aromatic amino acids results in violet-, cyan-, and blue-emitting FPs [4, 39].

3.1.2.3 Chromophore Environment and Fluorescence Emission

The structure of FP chromophores determines only part of the spectroscopic properties; interactions with surrounding amino acid residues and highly ordered water molecules inside the barrel are also important. Single mutations in the FP barrel can significantly influence the spectroscopic properties of the protein or even render it nonfluorescent [4]. Owing to the protection of the coupled network provided by the barrel, FPs are remarkably resistant to chemically or heat-induced denaturation, and even proteolysis [41].

Synthetic analogues of the FP chromophore have been extensively used for studying the effect of the chromophore environment on fluorescence emission [42, 43]. One typical synthetic analogue is 4′-hydroxybenzilidene-2,3-dimethylimidazolinone (HBDI; Fig. 3.3). Relative to avGFP (quantum yield about 0.8), HBDI is very weakly fluorescent (fluorescent quantum yield 10^{-4}) in aqueous solution at room temperature [44]. Ultrafast spectroscopy of HBDI reveals that highly efficient internal conversion occurs in a wide range of solvents leading to deactivation of the excited state on a subpicosecond time scale, which is too short

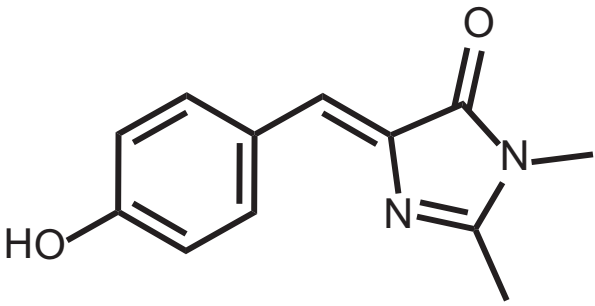

Fig. 3.3 Structure of 4′- hydroxybenzilidene-2,3-dimethylimidazolinone (HBDI), a synthetic analogue of the avGFP chromophore

for fluorescence to be a competitive process [45–47]. In contrast, avGFP displays excited-state lifetimes of about 3 ns. The fluorescence of HDBI appears when the temperature is below the glass transition temperature of the solvent [44, 46, 48]. Although there is still debate about the mechanism associated with this fast internal conversion, the current consensus attributes it to flexibility or rotation along one of the bonds adjacent to the methylene bridge [42, 43]. The chromophore environment in FPs has evolved to prevent this internal conversion from occurring and thus lead to high fluorescence quantum yields.

The chromophore of an FP can be either protonated or deprotonated depending on the pH of the solution [4, 49]. This fact is important since many spectroscopic properties of the protein, and the responses of many FP-based indicators, can be explained in terms of protonation. The deprotonated anionic state absorbs at about 470 nm in avGFP, while a protonated neutral state absorbs at about 390 nm [44]. Analogous observations can be made for almost all known FPs (although the wavelengths may be different) as long as there is a titratable group in the chromophore, with few exceptions [50]. In avGFP, excitation of the anionic state results in green fluorescence with a maximum at about 505 nm. Excitation of the neutral form of avGFP at 395 nm also results in the emission of green fluorescence, similar to that observed for excitation of the anionic state. Studies reveal that the mechanism behind this phenomenon is fast excited-state proton transfer (ESPT) [51] through an internal proton wire [52]. ESPT is not common among FPs, but it can be exploited for engineering FPs that display very large apparent Stokes shifts [17, 53, 54].

3.1.3 FPs as Imaging Tools: Practical Considerations

FPs are a very powerful toolset for imaging of biological activities. However, naturally occurring FPs from marine species evolved to optimize the survival of those animals. Therefore, in practice, FPs are not necessarily optimal for the experimental imaging conditions that researchers are most interested in. Accordingly, researchers expend a tremendous amount of effort to optimize FPs for experimental applications. Fortunately, because FPs are genetically encoded, their properties can be readily manipulated using the standard tools of molecular biology. Furthermore,

their relatively good expression in *Escherichia coli* facilitates screening for desirable fluorescence phenotypes. In this section, we will discuss several practical aspects of FPs and efforts to engineer improved variants.

3.1.3.1 Oligomerization

Most natural FPs exhibit a moderate to strong tendency to form quaternary (oligomeric) structures. For instance, avGFP and its derivatives tend to dimerize at high concentrations, FPs isolated from *Renilla* sea pansies form dimers, and all the wild type yellow, orange, and red FPs isolated from reef corals and anemones are tetramers [55, 56]. Unfortunately, FP oligomerization is problematic for many applications in cell imaging. In particular, when FPs are fused to a host protein for targeting to specific organelles or studying the protein–protein interactions of the host protein [57–59], the oligomeric structure can contribute to mislocalization of the fusion protein.

To address the problem of oligomerization, Campbell et al. successfully engineered a monomeric RFP (mRFP1) from DsRed, by sequential introduction of repulsive residue interactions [60]. This innovation has enabled red fluorescence labeling experiments that were otherwise impossible with DsRed, and served as a template for engineering many additional monomeric OFPs and RFPs [61–63]. Similar strategies have been exploited to convert other naturally tetrameric FPs into monomeric FPs [64, 65].

In addition to oligomerization, some FPs can also undergo higher order aggregation, leading to mislocalization and increased cytotoxicity. To date, little is known about the mechanism of FP aggregation. One hypothesis is that aggregation may be due to nonspecific oligomerization triggered by electrostatic or hydrophobic interactions between FP copies. A study on DsRed supports the role of electrostatic interaction in aggregation [66]. Yanushevich et al. analyzed the crystal structure of DsRed and speculated that DsRed tetramers possess a negatively charged protein surface while each DsRed copy contains four positively charged residues in its N-terminus. The positively charged N-terminus can serve as salt bridges with adjacent DsRed tetramers that eventually form a stable net-like “polymeric” structure (i.e., the aggregates). Based on this rationale, Yanushevich et al. reported the nonaggregating DsRed2 mutant by substitution of Lys and Arg residues near the N-terminus with negatively charged or neutral residues [66].

3.1.3.2 Photostability

The photostability of a FP determines how much illumination it can tolerate before it irreversibly photobleaches. This is a key consideration when choosing an FP, since it influences how much fluorescent output can be detected in practice. Photostability is particularly important for long-term imaging, for imaging of weak fluorescent signals from proteins expressed at low levels, and for quantitative measurements.

Some wild-type FPs possess reasonably high photostability; however, no natural FPs have evolved to endure the very high light levels used in typical microscopy experiments. Some engineered FP variants do preserve the good photostability of their corresponding wild-type FP, as does EGFP which is derived from avGFP [4, 67]. However, it is more typical for an engineered FP to have worse photostability than the corresponding wild-type protein.

Only a few research efforts dedicated to improving the photostability of FPs have been reported to date [63, 64, 68], owing to a poor general understanding of the photodestruction mechanism and the lack of appropriate methods to evaluate the complex photostability of FPs comprehensively. In some literature reports, photostability has been defined as the time required to reach 50% of an initial emission rate of 1000 photons/s for each FP [61, 63, 69]. However, the photostability of any given FP depends on many experimental parameters in addition to the obvious one of illumination intensity. The type of light source used, delivery as continuous or pulsed light, frequency of pulses, and excitation wavelengths could all have strong influences on the observed rate of photobleaching. For example, TagRFP-T was engineered for improved photostability using colony-based screening [63] at relatively low intensities of light, but is actually less photostable than its predecessor TagRFP under laser illumination [70]. Similarly, mPlum is more photostable than mRaspberry in wide-field imaging but less stable in confocal imaging [71]. To make matters even more complicated, the phenomenon of FP photobleaching is often confused with reversible photochromism [72, 73] or irreversible photoconversion that causes a shift in fluorescent spectra [74–77].

We recommend that researchers consider the complex nature of FP photostability when choosing a photostable FP. However, the numbers provided in the literature can only provide a general guide and may not be applicable to the particular experimental conditions of interest. Parallel experiments with more than one photostable FP and careful evaluation using the actual experiment setup are recommended.

3.1.4 Methods of FP Engineering

In the previous section, we discussed some practical issues regarding the use of FPs for live cell imaging, which are emblematic of the challenges faced in FP development. In the past two decades, extensive efforts to engineer improved FPs using both rational design and high throughput screening led to a dramatic expansion of the inventory of useful FPs for fluorescence imaging. In this section, we will briefly overview the current methods and challenges in the development of FPs, which are also applicable to FP-based indicators. A detailed protocol for engineering and characterizing improved FPs has recently been published [78].

Typically, the first step is often rational or semirational design guided by an X-ray crystal structure or homology model of the FP of interest [37]. A successful rational design requires an insightful analysis of the structure of an FP. For example, such analysis could be based on knowledge of the interacting residues at the

interfaces between two FP copies in a native FP oligomer. The experimenter could rationally introduce mutations that are designed to disrupt the key interactions and decrease oligomerization [60, 64, 65]. Such approaches have been fairly successful for addressing some challenges such as FP monomerization and creating blue-shifted fluorescent hues [4, 50, 61]. However, these rational changes are essentially always accompanied with undesirable effects on other FP properties. Even in cases where only one mutation is introduced, other important parameters of the resultant FP variant are likely to deteriorate if no further engineering effort is undertaken.

Prototype FPs generated by rational design often require further optimization by a process called directed evolution. Directed evolution iteratively selects variants with improved properties of interest from a library containing hundreds to thousands of randomly mutated FP variants. An advantage of this approach is that a comprehensive understanding of the function-structure relation of the FP is not required, as long as the screening method can effectively identify and collect mutants with improved properties, such as folding efficiency [79], fluorescence brightness [7], or other photophysical properties [63, 80, 81].

There are several platforms for directed evolution of FPs. Colony on-plate screening selects FP variants based on fluorescent images of *E. coli* colonies on a nutrient agar plate. Currently, this remains the most successful approach due to its robustness, flexibility for customization, and low cost [60, 64, 65, 76, 82]. Fluorescence-activated cell sorting (FACS) provides much higher throughput to screen FP-expressing cells for brightness [7] and different colors [61]. The higher throughput of FACS significantly reduces the labor and time needed to find improved variants compared to colony on-plate screening. However, FACS also requires expensive instrumentation and maintenance and allows limited customization. The recent advance of microfluidic technologies enables new platforms that potentially can combine the merits of both colony on-plate screening and FACS. Unlike FACS, microfluidic chips are cost-effective and amenable to customization for screening specific fluorophore properties. They are also capable of automatic high-throughput screening that saves much time and effort compared to a colony on-plate screen. For example, droplet-based microfluidic chips have been used for directed evolution of enzymes with improved catalytic rate [83, 84]. Recently, Jimenez and coworkers reported a microfluidic platform that is capable of screening FP variants for improved photostability [85, 86]. We have recently reported a microfluidic FACS device for assisting the directed evolution of a yellow fluorescent FP-based Ca^{2+} indicator [87].

3.2 FP-Based Indicators and their Design Principles

Fluorescent indicators based on engineered FPs are very powerful tools for visualizing the dynamics of biological processes and providing insight into complex cellular mechanisms. By virtue of their surrounding protein shell, the chromophores of FPs are protected from their environment. This is advantageous when an FP is used

as a “passive” marker of protein expression, localization, and organelle structure (which are still the most common applications of FP). In these applications, the observed brightness at a certain point in a tissue should be proportional to only the local concentration of the FP, and not influenced by its environment. In contrast, the protected nature of the chromophore is a disadvantage in applications where visualizing dynamic biochemical changes is the goal.

To use an FP as an “active” marker of biochemical changes, the protein must be engineered such that the fluorescence responds to a change in the external environment. FPs have been engineered to probe numerous biochemical and physiological changes in cells, such as the concentration of secondary messengers, membrane potential, protein–protein interactions, cellular signaling, and many others [88]. Generally speaking, FP-based indicators are multidomain fusion proteins consisting of a sensor domain (a protein that can respond to a biological parameter of interest) and a reporter domain (usually consisting of one or two FPs). The sensor domain responds to a change in the environment and induces a molecular conformational change that, in turn, modulates the photophysical properties of the reporter domain [88]. This could include a change in the fluorescent brightness at one wavelength, or a ratiometric change phenomenon where the fluorescence changes differentially at two wavelengths.

The key challenge of developing FP-based indicators is to transduce a molecular conformation change within the sensor domain into a change of a fluorescent property of the reporter domain. Several transduction mechanisms have been developed for converting a wide variety of biophysical or biochemical changes into either intensiometric or ratiometric changes in FP fluorescence readout. Traditional mechanisms include: Förster resonance energy transfer (FRET) between two FPs [89]; bimolecular fluorescence complementation (BiFC) [90–92]; and modulation of the chromophore environment of a single FP [92–95]. More recently, two new mechanisms have been developed: bioluminescence resonance energy transfer (BRET) from a luciferase to a FP [96]; and dimerization-dependent FPs (ddFPs) [97, 98]. We can group all five mechanisms into three categories: indicators based on energy transfer (FRET and BRET); indicators based on complementation (BiFC and ddFPs); and single FP-based indicators.

3.2.1 Indicators Based on Energy Transfer

FRET is a phenomenon that involves radiationless energy transfer between two chromophores [99]. When a donor chromophore possesses a fluorescent emission that overlaps spectrally with the absorption of an acceptor chromophore, the excited state of the donor may transfer the energy to the acceptor via nonradiative dipole–dipole coupling. The efficiency of FRET is inversely proportional to the sixth power of the distance between the donor and acceptor, and thus very sensitive to small changes in distance.

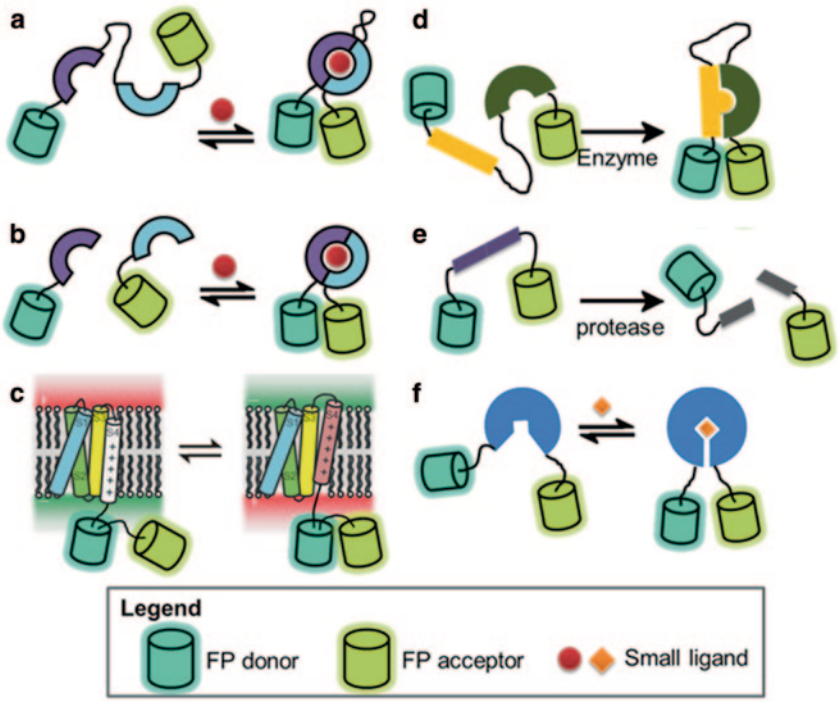

Fig. 3.4 Design principles for FP-based FRET reporters. **a** Intramolecular FRET reporters of small molecules [89]. **b** Intermolecular FRET reporters of small molecules [101]. **c** Reporters of voltage-dependent intramolecular rearrangements [102]. **d** Reporters of enzymatic activity [103, 104]. **e** Protease reporters [82]. **f** Allosteric "clam-shell" reporters [105]. (Adapted from [88])

FRET is the most broadly useful mechanism for designing FP-based indicators. In most cases, a standard pair of donor and acceptor FPs is chosen without requirement for further engineering, and this pair is then strategically fused to the termini of the sensing protein. This fusion is done in such a way that the expected conformational change, associated with the biological process of interest, will modulate the FRET efficiency between the donor FP and acceptor FP. There are many design strategies available for constructing FRET-based FP indicators (Fig. 3.4). An important advantage of this approach is that the ratio of the fluorescence intensities in the donor and acceptor channels allows internal calibration for quantitative microscopic imaging. Generally speaking, ratiometric imaging cancels out many sources of measurement variability arising from differential protein expression in different cells, uneven illumination, slight changes in focus, and motion artifacts [100].

One of the major disadvantages of FRET-based FP indicators is that they require two color channels, which complicates their use in multiparameter imaging [88]. One way to circumvent this problem is to substitute the donor FP with a self-illuminating protein reporter (i.e., a luciferase) and exploit BRET, which is similar to FRET except that the bioluminescent donor is excited via a chemical reaction

instead of light absorption [96]. This approach does not require the excitation of the donor FP and therefore frees up spectral bandwidth. The major drawback of BRET-based indicators is that they are generally dimmer than regular FRET-based indicators due to the lower photon flux, as the brightest luciferase only emits around one-hundredth as many photons as a typical FP [106].

3.2.2 Indicators Based on Complementation

3.2.2.1 Bimolecular Fluorescence Complementation

FPs can be genetically split into two nonfluorescent fragments that assemble into the native fluorescent structure when they are brought sufficiently close to each other [90, 91] (Fig. 3.5). This bimolecular fluorescence complementation (BiFC) phenomenon can be used as a design strategy to construct indicators for visualizing protein–protein interactions in living cells. Potentially interacting protein partners can be genetically fused to each of the split FP fragments. When the partners interact, the two split FP fragments are brought into close proximity and combine to form an intact FP. Because there is essentially no fluorescence prior to protein-protein interaction, this approach generates higher fluorescent contrast compared to other types of FP-based indicators. BiFC can be applied with FPs with different

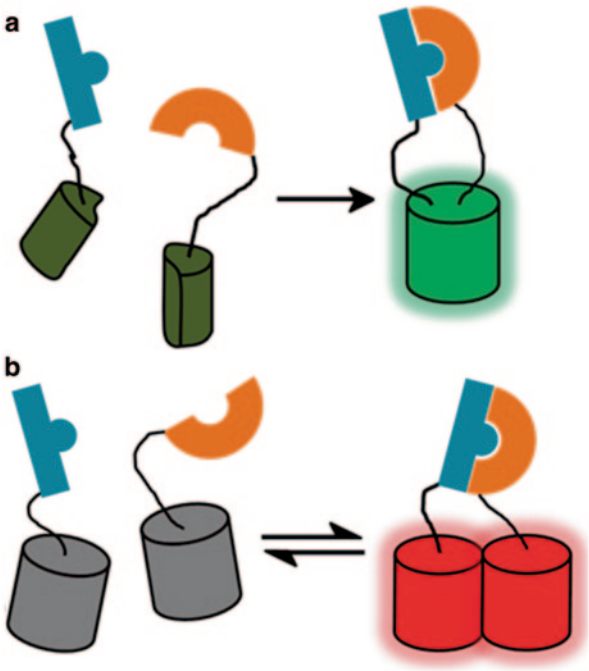

Fig. 3.5 Complementation-based strategies. **a** Bimolecular fluorescence complementation. **b** Dimerization-dependent FPs

hues ranging from blue to far red [107–111]. The disadvantages of BiFC includes slow kinetics and the irreversible nature of the reconstitution due to very high affinity between the two complement split fragments, which prevents this approach from being useful for probing dynamic and reversible biological events [90].

3.2.2.2 Dimerization-Dependent FPs

To overcome certain limitations of the BiFC approach, Alford et al. developed a novel strategy for engineering FP-based indicators, which shares similar concepts with both the split-FP strategy and the FRET-based strategy [97, 98]. The key to this strategy is an engineered pair of dimerization-dependent FPs (ddFPs): FPs that are dimly fluorescent in the monomeric state but exhibit significantly brighter fluorescence upon dimerization (Fig. 3.5). Because intact and fully folded FPs are used in the ddFP strategy, the complementation process is fully reversible. The ddFP approach is conceptually similar to the FRET-based approach as the fluorescence signal depends on bringing the two FP partners into close proximity. However, a critical difference is that the two FP partners of ddFPs have moderate affinity for each other and will spontaneously dimerize at high concentrations while this is less of a concern for most monomeric FP FRET pairs.

3.2.3 Single FP-Based Indicators

As their name implies, single FP-based indicators only utilize a single engineered FP that has been engineered to be sensitive to the analyte of interest. Although most of these probes generate an intensiometric signal (i.e., single color), there are examples of single FP-based indicators with ratiometric responses [87, 92, 112]. In general, single FP-based indicators generate larger fluorescent signals than other types of reversible indicator. On the other hand, it is often difficult to engineer a practically useful single FP-based indicator since it requires relatively sophisticated protein design and extensive modification of the FP β-barrel.

Single FP-based indicators can be divided into two subclasses based on whether or not an external sensing domain is employed. In the first subclass, the FP serves as both the sensor and the fluorescent reporter unit. This is usually achieved by utilizing either an intrinsic or engineered molecular recognition site within the FP β-barrel. Generally speaking, the intrinsic recognition sites only bind to small analytes such as H^+ [113], Cl^- [114], or metal ions [115]. A broader range of sensor specificities can be achieved by introducing additional molecular recognition sites on the surface of the β-barrel such as a disulfide bonds for redox sensing [116–118] or a Ca^{2+} binding site [119]. Alternatively, the chromophore itself can be modified by introducing unnatural amino acids with distinct chemical reactivity [120, 121]. The major limitation of single FP-based indicators that lack an external sensing domain is that the scope of analytes that are amenable to detection by this approach is relatively small.

The second subclass overcomes the major limitation of the FP-only approach by introducing a second sensing domain. This domain undergoes a conformational change that results in modulation of the fluorescence of the attached FP when responding to a specific biological event. In this way, the potential applications of the single FP-based design are greatly expanded. In most cases, this design requires partial exposure of the FP chromophore to the environment to maximize the transduction efficiency of the sensor domain. Chromophore exposure can be achieved by either directly inserting the sensor domain at a position near the chromophore, or by using a technique called circular permutation, in which the original N- and C-termini are fused together with a polypeptide linker and new N- and C-termini are created at a site on the β-barrel near the phenolate group of the chromophore [94, 122].

The prototypical examples of single FP-based indicators using an external sensing domain are Ca^{2+} indicators that rely on Ca^{2+} -dependent conformational changes in calmodulin (CaM). In the first demonstration of such a design, Baird et al. engineered a low affinity Ca^{2+} indicator (called camgaroo) [94, 123] by inserting CaM at position 145 of the yellow FP EYFP. The most popular design for a single FP-based Ca^{2+} indicator was pioneered in parallel by two groups [92, 95]. In this design, the new N- and C- termini of a circularly permutated FP (cpFP) were fused to the CaM-binding domain M13 and to CaM itself, respectively (see Fig. 3.6b). Structural analysis has revealed that Ca^{2+} induces a substantial conformational change of M13 and CaM, which in turn modulates the chromophore environment and alters the fluorescence of the FP domain [124, 125]. This type of FP-based Ca^{2+} indicator will be discussed in more detail in the following sections.

3.3 Genetically Encoded Indicators for Neuroimaging

Monitoring spatiotemporal activity patterns in neural circuits is a critical technique for understanding complex brain functions. The continuing advance of various fluorescence microscopy technologies and genetic labeling techniques heralds a growing prominence for these techniques in neural circuit analysis [126–128]. The development of genetically encoded indicators contributes to this field by providing fluorescent probes capable of reporting key biochemical and physiological events in the brain. Compared to traditional synthetic dyes, genetically encoded indicators can be introduced into neural cells in a much less invasive manner, through viral infection and the creation of transgenic animals. In addition, they can be expressed in specific cell types and subcellular compartments over long periods of time. These features enable one to monitor activity within a specific subset of neurons in intact tissues as well as chronic imaging of circuit dynamics.

Genetically encoded indicators of neuronal activity require the conversion of a relevant biochemical or physiological parameter into fluorescence readout. Some physiological changes relevant to neuronal activity are summarized in Table 3.1. Among these, membrane potential, ion concentrations, second messenger concentrations, and various neurotransmitters are important and feasible targets for

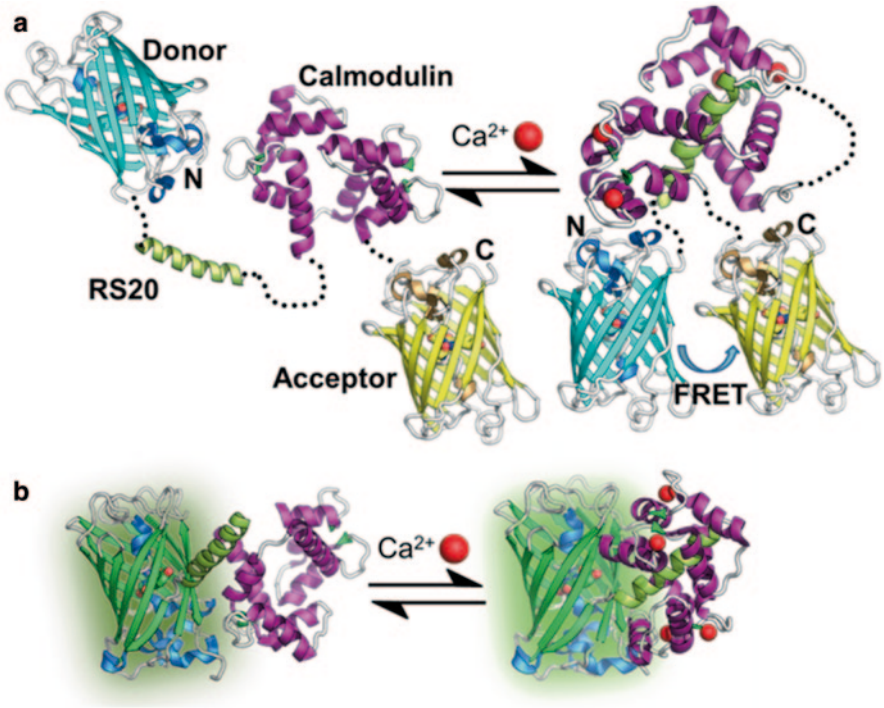

Fig. 3.6 Schematic demonstrations of genetically encoded Ca^{2+} indicators. **a** A model of a cameleon-type FRET-based Ca^{2+} indicators based on Ca^{2+} -binding domains M13 and calmodulin. **b** A model of a single FP-based Ca^{2+} indicator, based on the crystal structure of GCaMP2 (PDB ID 3EK8 and 3EKU) [125]

Table 3.1 Biochemical changes associated with neuronal activities

Neuronal activity	Biochemical change	Key participating ions, small molecules, and proteins
Action potential	Intracellular ion concentrations; membrane potential	Na^+; K^+; Cl^-; Ca^{2+}
Synaptic transmission	Vesicle fusion and release	Soluble NSF attachment protein (SNAP); SNAP receptor (SNARE); pH
	Release of neurotransmitters	Glutamate; gamma-aminobutyric acid (GABA); dopamine; histamine; noradrenaline; serotonin; acetylcholine; numerous peptides; many others
	Activation of postsynaptic signaling pathways	G_q protein–coupled receptors (GPCRs); Ca^{2+}, inositol trisphosphate (IP3); diacylglycerol (DAG); calmodulin-dependent protein kinase II (CaMKII); among others

interrogation of neuronal activities. Sensor proteins that bind and/or respond to these targets are available in nature and can be engineered in such a way as to modulate the fluorescence of an attached fluorophore. A corollary is that, if a protein that responds to a particular target molecule or activity with a change in conformation is not known in nature, there is little chance that a FP-based indicator could be engineered for that same target.

Genetically encoded fluorescent indicators that can respond to changes in Ca^{2+}, membrane potential, glutamate, and pH have been developed with advanced protein engineering techniques [92–95, 112, 113, 129–137].Ca^{2+} indicators have so far been the most successful owing to their large fluorescence changes and high signal-to-noise ratio (SNR) [112, 136, 138]. Furthermore, the diverse roles of Ca^{2+} in cell signaling and neuronal activity have meant that these indicators are useful to a broad range of researchers. Indicators for specific neurotransmitters and pH are also important tools for monitoring synaptic transmission [113, 131]. Although the overall performance of voltage indicators is relatively poor compared to Ca^{2+} indicators, development of voltage indicators has recently been accelerated. Membrane potential is a direct measure of neural activity and can provide temporal resolution in the millisecond range, whereas Ca^{2+} signals are usually a hundred times slower.

3.3.1 Ca^{2+} Indicators for Imaging of Neuronal Activities

For the last three decades, molecular tools for imaging free intracellular Ca^{2+} concentration have attracted an ever-increasing level of attention in neuroscience. Ca^{2+} is a ubiquitous intracellular second messenger and plays critical roles in various neuronal functions, such as synaptic transmission, neuronal development, and plasticity. Spikes in cytosolic Ca^{2+} concentration are an indirect measure of electrical activity. When a neuron fires an action potential, its voltage-gated Ca^{2+} channels open in response to membrane depolarization and lead to an increase of intracellular Ca^{2+} concentration within a few milliseconds [139–141].

Traditionally, optical recordings of intracellular Ca^{2+} fluctuations were achieved using synthetic dyes that exhibit Ca^{2+} -dependent fluorescence changes. This field was largely initiated by the breakthrough work of Roger Y. Tsien and coworkers who developed a series of synthetic Ca^{2+} indicator dyes with nearly ideal fluorescence properties [100]. Tsien and coworkers also invented a noninvasive way to load synthetic dyes into the cells using acetoxymethyl ester. Since then, synthetic dye-based Ca^{2+} indicators have remained indispensable tools used by neuroscientists to optically record neuronal activity in ex vivo tissues or within the brain of a living animal [142–144].

Synthetic Ca^{2+} indicators are inarguably powerful and versatile tools, but their use in intact brain tissues is limited. In some cases it is difficult to load cells with acetoxymethyl ester-modified indicators, a problem that is particularly acute in some model organisms such as *Caenorhabditis elegans* or the fruit fly *Drosophila melanogaster* [144]. Synthetic dyes also tend to leak out of the cells during long

term imaging. Finally, there is essentially no subcellular targeting specificity with synthetic dyes, and therefore subcellular labeling in individual pre- or postsynaptic sites is currently impossible. Notably, cell type-specific loading has been achieved using cleverly designed synthetic dyes that specifically bind to a particular genetically encoded peptide sequence. For example, Tour et al. effectively targeted the calcium green Ca^{2+} indicator to a genetically modified α_{1C} channel in order to probe the activities of Ca^{2+} nanodomains [145]. This genetic targeting was achieved using the very specific interaction between a bisarsenic-modified version of the synthetic dye and a small peptide containing a tetracysteine motif [146–148].

To address the shortcomings of synthetic dyes in neuroimaging, the Tsien lab introduced the "cameleons" in 1997, the first example of a genetically encoded Ca^{2+} indicator (GECI) [89]. The advent of this tool was an important milestone in the field of bioimaging. As a family, GECIs offer a number of advantages compared to synthetic Ca^{2+} indicators. First, the genetic encoding of these probes allows GECIs to be introduced into the preparation using various molecular approaches that make invasive microinjection unnecessary. Second, GECIs can be conveniently targeted to specific subcellular compartments as well as to specific cell types. Third, GECIs exhibit low cytotoxicity and permit Ca^{2+} imaging over longer time periods compared to synthetic Ca^{2+} indicators. Finally, because they are genetically encoded, GECI properties such as Ca^{2+} affinity, fluorescence response dynamic range, and response kinetics can be modified by protein engineering to improve or customize the performance for specific applications.

Although a variety of design strategies have been reported for GECIs [89, 92, 94, 95, 97, 149], only two sensing mechanisms have been widely used. These are based on FRET (i.e., cameleons [89] and TN-XXL [150]) and Ca^{2+} -dependent modulation of chromophore pK_a within a single FP (i.e., GCaMP [95], pericam [92], and genetically encoded calcium indicators for optical imaging (GECOs) [112]). Development and application of GECIs based on these two design mechanisms are discussed in the following sections.

3.3.1.1 FRET-Based Ca^{2+} Indicators

Cameleons, the first generation of GECIs [89], are chimeric proteins that, in their original iteration, were composed of a blue or cyan FP as a FRET donor and a green or yellow FP as a FRET acceptor. The two FPs are connected by CaM and its binding partner M13 (the CaM-binding domain of myosin light chain kinase) (Fig. 3.6a). A similar design with only the CaM-binding domain was also reported in 1997 [149]. When the CaM domain of a cameleon binds to Ca^{2+}, it changes its conformation and sequentially binds to M13, which results in a more compact conformation that decreases the distance between the FRET donor and acceptor. This decreased distance causes an increase in FRET efficiency that manifests itself as a decrease in donor intensity and an increase in acceptor intensity. It is standard practice to divide the intensity in the acceptor channel by the intensity in the donor channel to provide a ratiometric signal that is proportional to Ca^{2+} concentration.

A drawback of the first generation cameleon (cameleon-1) is that it only exhibited a 70% change in emission ratio upon binding to Ca^{2+}, which limited the signal-to-noise ratio and fidelity for detecting Ca^{2+} dynamics. In 1999, Miyawaki et al. developed an improved version of cameleon with larger Ca^{2+} response and less pH sensitivity [151]. These improved cameleons could be used to image Ca^{2+} dynamics in hippocampal neurons. In 2004, Nagai et al. further improved cameleon's Ca^{2+} response by optimizing the relative orientation of the two chromophores using circularly permuted YFPs (cpYFPs). The best variant, termed yellow-cameleon 3.6 (YC3.6), is more efficient at accepting excited state energy from CFP in the Ca^{2+} -bound state, thereby increasing the ratiometric Ca^{2+} -dependent fluorescence response to nearly 600% [152]. In the same work, the authors also generated a transgenic mouse line expressing YC3.6, in which YC3.6 could be used to detect stimulated neural activities, although with reduced dynamic range relative to in vitro experiments. To date, YC3.6 remains one of the most popular GECIs for neural imaging. In 2010, Nagai and coworkers engineered a series of high Ca^{2+} affinity versions of cameleon called YC-nano with K_d values ranging from 15 to 140 nM and up to a 1450% Ca^{2+} dependent change in emission ratio [153]. Compared to traditional GECIs with lower Ca^{2+} affinities, YC-nano variants perform better in cells where the resting intracellular Ca^{2+} concentration is low. Accordingly, they are capable of detecting subtle Ca^{2+} transients associated with intercellular signaling dynamics and neuronal activity.

Interference from intracellular proteins is a potential problem for GECIs based on CaM, because CaM is a ubiquitous signaling protein that interacts with many kinases, phosphatases, and ion channels. The presence of endogenous interaction partners may interfere with GECI function and lead to reduced or diminished dynamic range [144]. In 2004, Griesbeck and coworkers engineered a new type of FRET-based GECI, called TN-L15, by replacing calmodulin with troponin C (TnC) which interacts with fewer endogenous proteins [154]. In 2006, Mank et al. reported further improvements in the dynamic range and kinetics of TnC-based indicators by engineering the magnesium- and calcium-binding properties within the C-terminal lobe. The best variant to arise from that work, TN-XL, exhibits a highly reproducible fluorescence signal with fast rise and decay times, as demonstrated in the presynaptic motor neurons of transgenic flies [155]. By deletion of low affinity N-terminal lobes, the same group obtained a further improved version of TnC-based GECIs, designated TN-XXL, with higher affinity to Ca^{2+}. They demonstrated the usefulness of TN-XXL for the chronic imaging in mouse brain *in vivo* [150]. Very recently, Thestrup et al. developed a new FRET-based indicator "Twitch," based on *Opsanus* troponin C, with reduced number of Ca^{2+} -binding sites compared to TN-XXL [137]. They optimized the indicator by combining a large functional screen in bacteria with a secondary screen in rat hippocampal culture. The optimized version of Twitch performs comparably to the synthetic organic Ca^{2+} indicator dye Oregon Green BAPTA-1-AM, and enables detection of action potentials in neurons and functional recordings from highly mobile T lymphocytes [137].

3.3.1.2 Single FP-Based Ca^{2+} Indicators

In 1999, Baird et al. reported an interesting new approach for generating GECIs [94]. In this work, they inserted calmodulin at position 145 of an enhanced version of yellow FP (EYFP) and found that the resulting hybrid, dubbed "camgaroo1," is a viable Ca^{2+}indicator for use in live cells. Camgaroo1 was the first example of a GECI based on a single FP. Two years later, Griesbeck et al. engineered camgaroo2 based on a YFP variant (Citrine) with improved folding and reduced chloride and pH sensitivity [123].

Camgaroos are not useful for neural imaging since their Ca^{2+} affinity (as represented by the effective dissociation constant (K_d)~7 μM) is outside the normal physiological range (50–5000 nM [140]). Although camgaroos were not ideal tools for neural imaging, the idea of converting a Ca^{2+}-induced conformational change into a change in chromophore environment was an important one that proved influential. In 2001, two research groups in Japan independently reported a variation on the camgaroo design that consisted of a FP, circularly permutated at position 148, with CaM and M13 fused at the C- and N-termini, respectively (Fig. 3.6b). The resulting constructs, designated pericam [92], and GCaMP1 [95], both exhibited larger dynamic range and higher affinity to Ca^{2+} relative to camgaroos.

Compared to FRET-based cameleons, GECIs based on single FPs are generally less amenable to modification due to the fact that the sensing mechanism is derived from the close coupling of the CaM domain and the FP. For FRET-based GECIs, dynamic range and affinity can be tuned by swapping in alternative FRET donors or acceptors, adjusting linker length, and mutating CaM. In tools like camgaroo and GCaMP, the calcium-binding and FP domains are intimately connected and modification of one tends to produce unpredictable, and often undesirable, changes in the other domain. Accordingly, single FP-based indicators lack the "modularity" of FRET-based probes and are not as amenable to having particular portions of the protein swapped out or otherwise modified.

Despite the difficulties inherent in engineering improved single FP-based indicators, slow and steady progress continues through the present day. In 2005, Reiff et al. briefly mentioned improved GCaMP1.3 and GCaMP1.6 variants in their comparative study on the *in vivo* performance of available GECIs for probing neural activity in flies [156]. They found that the response characteristics of all tested indicators differed considerably. GCaMP1.6 exhibited the largest and fastest fluorescence response and was capable of reporting high rates of neural activity, but suffered from faster photobleaching. On the other hand, GCaMP1.3 exhibited fairly linear changes in fluorescence intensity and SNR that were proportional to the frequency of electric field-stimulated action potentials in neurons. Also in 2005, the second generation of GCaMP, termed GCaMP2, was developed and reported to be functional in transgenic mice [157]. To gain insight into the Ca^{2+}-sensing mechanism of GCaMP2, Wang et al. and Akerboom et al. determined its X-ray crystal structure [124, 125]. Briefly, in the Ca^{2+} -bound state, the key residue R377 of CaM is positioned near the fluorophore and stabilizes it in a brightly fluorescent deprotonated state. Presumably, this interaction is not present in the Ca^{2+}-free state, and

the chromophore is therefore non-fluorescent and protonated. The insight provided by this structure, and those of related variants, has greatly assisted the engineering of improved GCaMPs. In 2009, guided by the crystal structure of GCaMP2, Lin et al. engineered the third generation of GCaMP, GCaMP3 [158]. Compared to other GECIs of that time, GCaMP3 exhibited several fold better Ca^{2+} responses for imaging of neural activities in worms, flies and mice [158].

Although GECIs have long provided multiple practical advantages, their sensitivity has only recently compared well to that of commonly used synthetic Ca^{2+} indicators, such as Oregon Green BAPTA-1-AM and fluo-4 [159]. In 2013, GCaMP6, which made dramatic improvements in signal magnitude and SNR in neuron, was reported by Chen et al. [136]. The authors presented compelling evidence that GCaMP6 is the first GECI to surpass the performance of synthetic Ca^{2+} indicators for *in vivo* imaging.

Single FP-based GECIs have also started to narrow the gap with synthetic reporters in terms of their kinetics. Synthetic Ca^{2+} indicators generally have fluorescence changes with response time constants less than 1 ms, which is much faster than GECIs. The relatively slow kinetic response of GECIs limits their capacity for resolving high-frequency neuronal Ca^{2+} oscillation. To address this shortcoming, Sun et al. developed fast versions of GCaMPs, based on GCaMP3, which possess up to 20-fold accelerated off-responses [160]. Fast GCaMPs have better performance for tracking Ca^{2+} spikes in *Drosophila* auditory neurons responding to natural courtship songs and observing rapid Ca^{2+} responses in mammalian neurons compared to GCaMP3 and GCaMP5G [160].

One area where single FP-based GECIs lagged behind their synthetic counterparts was in the area of color selection. While blue, green, orange, and red fluorescent synthetic Ca^{2+} indicators have been available for some time, a decade after the introduction of single FP-based GECIs, only green fluorescent variants were available. This lack of color diversity meant that Ca^{2+} imaging was essentially a monochromic endeavor, which limited the range of applications that these tools could be applied to. The complex mechanism of GCaMP revealed by structural analysis [124, 125], suggested that it would likely be difficult to engineer different colors of GCaMP based on different FP scaffolds using rational approaches.

To address this engineering challenge, Zhao et al. developed a high throughput colony-based screening method for directed evolution of single FP-based GECIs [112]. The key concept of this approach was to target mutants into the periplasmic space of *E. coli*, where Ca^{2+} concentration can be manipulated by changing the Ca^{2+} concentration in the environment. This approach enables rapid evaluation of mutants and facilitates high throughput screening. This work resulted in expansion of the palette of single FP-based GECIs from blue to red. In addition, an unexpected new type of ratiometric indicator, with a novel Ca^{2+} -sensing mechanism and unprecedentedly large dynamic range (11,000% change in emission ratio), was discovered [112]. This new palette of GECIs (designated as GECOs), opened the door to multicolor Ca^{2+} imaging. Introduction of the red fluorescent GECI, R-GECO1, should enable deeper Ca^{2+} imaging in tissue, due to less scattering and lower autofluorescence when using red-shifted excitation and emission wavelengths.

Improved versions of R-GECO and other types of single RFP-based GECIs have since followed [138, 161, 162]. In principle, R-GECO1 could be used in combination with blue light-activatable optogenetic actuators (i.e., channelrhodopsin-2 [163]) to enable simultaneous activation and optical recording of Ca^{2+} dynamics in the same cell. However, studies found that R-GECO1 and its descendants exhibit complex photochromism and the red emission intensity can artificially increase under strong blue light illumination [138, 162], which limit their utility in optogenetic applications. Another type of red GECIs utilizing a cp version of mRuby as the fluorescent reporter, termed RCaMP, does not exhibit complex photoisomerization and could be better suitable for optogenetic experiments, but its dynamic range is smaller than that of the R-GECO variants [162].

Although several effective screening methods for improving GECIs have been reported [112, 137, 164], the screening process tends to be time-consuming and laborious. To accelerate the development of genetically encoded Ca^{2+} indicators, Zhao et al. designed and built a μ FACS for screening GECIs with improved properties [87].Their results indicate that a μ FACS-aided directed evolution approach can identify superior variants with less effort, compared to the manual, on-plate screening approach [112]. In addition, Zhao et al. engineered a novel yellow FP-based Ca^{2+} indicator based on mPapaya [65], termed Y-GECO. The μ FACS-aided directed evolution approach was used to pre-screen libraries of around 10^6 variants of Y-GECO with up to 300 cells/s throughput, while the manual screening approach screened only up to 10^4 variants per round. Owing to the high throughput power of μ FACS aided directed evolution approach, the researchers successfully evolved the brightness and Ca^{+} response of Y-GECO with higher efficiency compared to a manual screening approach conducted in parallel [87].

3.3.1.3 Applications of Ca^{2+} Indicators for Neuronal Imaging

Transgenic Animals Expressing GECIs

GECIs have unique advantages for targeting and imaging neurons in live, behaving animals. Most importantly, GECIs can be introduced by minimally invasive approaches, such as virus injection, in utero electroporation, or the generation of transgenic animals. The first GECI-based Ca^{2+} imaging in behaving animals was done in 2000 by Kerr et al. using *C. elegans* [141] expressing a cameleon construct. The indicator faithfully responded to evoked Ca^{2+} transients in individual *C. elegans* neurons. In 2002, Fiala et al. reported the use of cameleon 2.1 [151] in the *Drosophila* brain [165], and successfully measured odorant-evoked intracellular Ca^{2+} dynamics in selectively labeled olfactory projection neurons [165]. In 2003, Yu et al. expressed two versions of camgaroo [94] in *Drosophila* mushroom bodies [94, 166]. Wang et al. reported a sensitive two-photon microscopy system for imaging of GCaMP in the *Drosophila* brain [167]. Liu et al. studied the function of thermosensory neurons in *Drosophila* larvae using a yellow cameleon 2.1 (YC2.1) [168].

In 2003, the first example of using GECIs in neural imaging in vertebrates was done in a stable transgenic line of zebrafish expressing cameleon YC2.1 [169]. Up to that point, GECIs had been used for Ca^{2+} imaging only in worms and flies, and the use of GECIs to detect Ca^{2+} transients in normally behaving vertebrates had not been demonstrated. In 2004, Hasan et al. reported the detection of neural activities in the brains of transgenic mouse lines expressing camgaroo2 or a pericam-variant [170]. Later, mouse lines expressing GCaMP2 [157] and YC3.6 [152] were also reported. A number of transgenic animal lines expressing GECIs are now available to the research community. There are several public resources for interested users, including the Jackson laboratory (http://www.jax.org/index.html) and the Janelia farm GENIE project (http://research.janelia.org/genie/).

Neuronal Circuit Mapping and Dynamics Monitoring in Defined Cell Classes
Fluorescence imaging using GECIs is a powerful approach for mapping neural connections and monitoring circuit dynamics in anatomical space [171]. Using specific promoters, GECIs can be genetically targeted to a subset of the neuronal population, which allows researchers to identify subpopulations of neurons with specific functions and define their organization. For example, an improved transgenic mouse line expressing GCaMP2 in cerebellar granule cells was reported in 2007 by Díez-García et al. [172] and used to characterize the function of synapses by parallel fibers in the cerebellum [173, 174]. In a more recent study, a zebrafish line expressing GCaMP3 specifically in the spinal motor neurons was used to study the development of central pattern generators [175].

Genetically encoded indicators that are targeted to specific cell types can also help to reveal the maps in overlaid or intermingled neural circuits. For example, Fletcher et al. used GCaMP2 to image macroscopic pre- and postsynaptic sensory maps of the mouse olfactory bulb [176, 177]. In the studies, they used synaptopHluorin [130], an FP-based indicator of synaptic release, to image the presynaptic activity of olfactory nerve terminals. Simultaneous fluorescence imaging of GCaMP2-expressing neurons that can be synaptically excited by olfactory nerves provided postsynaptic odor maps of the olfactory bulb [176, 177].

GECIs also enable monitoring neural circuit dynamics. Recently, Harvey et al. used GCaMP3 and imaging at single-cell resolution to reveal the choice-specific sequences of neuron activation in the posterior parietal cortex [178].

Previous techniques only enable interrogation of neural circuits in a very small region of the brain, which are unlikely to reveal correlation of populations of neurons in distant regions. To properly understand the brain functions and behaviors, we need to examine neural activities in the intermediate or higher level of organization. Recording neuronal activities in the whole brain with single-cell resolution has been one of the most challenging objectives of modern neuroscience. Early in 2013, Ahrens et al. moved a big step toward this goal with the advance of light sheet microscopy technology [179]. Using a Ca^{2+} indicator known as GCaMP5G [180], they successfully recorded neural activities from the whole brain of the larval zebrafish *in vivo*, and identified two populations of neurons in distant regions with correlated activity patterns and likely have important roles in swimming [179].

Chronic Imaging of Neuronal Activities

Unlike synthetic dyes that leak out of cells over time after injection, the expression of GECIs can be stable for weeks to months or can even last the complete lifetime of a transgenic animal. This feature makes GECIs suitable for chronic imaging *in vivo*. For FRET-based GECIs, TN-XXL has been used for long-term *in vivo* imaging of Ca^{2+} response from visually stimulated layer 2/3 cortical neurons in mice [150]. Virally expressed YC3.6 in mice was reported to successfully detect visual response from the same neurons during behavior response over 1 month [181]. Similarly, YC3.6 was also used for mapping sensory response in mouse somatosensory cortex over several weeks [182]. Studies have demonstrated the usefulness of single FP-based GECIs for long term *in vivo* imaging of neuronal activities in mouse brain such as mouse motor cortex [158] and CA1 neurons from the hippocampus [183] using GCaMP3. Long-term imaging of GCaMP3 has revealed learning-related circuit changes [184]. GCaMP6, the most state-of-the-art GECI reported to date, was used for long term imaging to monitor the organization and dynamic of neural circuit in mouse visual cortex [136].

3.3.2 Voltage Indicators for Imaging of Neuronal Activities

3.3.2.1 FP-Based Voltage Indicators

Genetically encoded voltage indicators (GEVIs) directly measure the most fundamental neuron signal, the action potential. In contrast, GECIs provide a measure of the slow Ca^{2+} signals that lag behind action potentials. In addition, GEVIs can, in principle, measure subthreshold membrane potential fluctuations and hyperpolarization, which do not lead to any change in Ca^{2+} concentration. Despite these important advantages, in practice, GECIs are more widely used for imaging of neuronal activities, whereas GEVIs are rarely used. Similarly, synthetic organic Ca^{2+} indicators are also more widely used compared to synthetic organic voltage indicators. The challenge of using GEVIs for neuroimaging is twofold. First, from the perspective of the probe molecules themselves, the currently available GECIs are generally more sensitive and brighter than GEVIs. In addition, since the plasma membrane has a much smaller volume than the cytosol, the total amount of GEVI per cell dramatically constrained, and the fluorescent signals are correspondingly dimmer. The membrane-tethered nature of GEVIs also makes them notoriously difficult to engineer. Second, from an instrumental point of view, voltage imaging requires a very restricted integration time as membrane potentials generally rise within milliseconds, which significantly limits the available photons for each frame of acquisition and requires a more expensive microscope system and camera compared to Ca^{2+} imaging. In the following section, we discuss the engineering of GEVIs, some applications thereof, and future directions for the field.

The first GEVI, FlaSh [93], was reported in 1997, the same year as the first GECI cameleon. In the next 5 years, SPARC [185], VSFP [186] and improved FlaSh [187]

were developed. They all belong to the first class of GEVIs, which utilize FPs as the fluorescence reporter. The early versions of this class utilize either the intact K^+ or Na^+ channels, or just the voltage-sensing domain of one of these channels, as the voltage-sensing unit. Much like with the single FP-based GECIs, the conformation change in the voltage-sensing domain was coupled to the modulation of fluorescence of a genetically fused FP. Unfortunately, these early designs did not gain widespread acceptance, largely because of the issues of poor membrane trafficking and cytotoxicity in neurons [188].

Knöpfel and coworkers reported an improved second generation of VSFP, VSFP2, in 2007 [133]. VSFP2 uses the voltage sensing domain of the sea squirt *Ciona intestinalis* voltage sensor-containing phosphatase to modulate FRET between donor and acceptor FPs and displays excellent membrane trafficking in mammalian cells. Although the dynamic range for voltage sensing is fairly small, VSFP2 was capable of monitoring electrical events in neurons, a critical milestone in the field of GEVIs. VSFP2 was followed by a number of further improved versions of FRET-based and single FP-based VSFPs [102, 134, 189–191], though the improvements in the signal magnitude and SNR remained modest.

The small signal magnitudes and slow kinetics of most VSFP-type GEVIs has limited their applications for monitoring neuronal electrical activity. In 2012, Pieribone and coworkers reported a new version of a VSFP-type GEVI, ArcLight, which exhibited large changes in fluorescence intensity in response to voltage changes [192]. ArcLight uses super ecliptic pHluorin as the FP domain. Strikingly, a single point mutation A227D dramatically improves the dynamic range for voltage sensing by five times. Although ArcLight exhibits slow kinetics, its large signal magnitude allows reliable detection of single action potentials and excitatory potentials in individual neurons and dendrites, thus becomes currently one of the most promising GEVIs for *in vivo* imaging. Swapping of the voltage-sensing domain has led to faster versions of ArcLight, though with diminished fluorescence response [193].

Very recently, St-Pierre et al. developed a new VSFP-type GEVI by inserting a circularly permuted green FP in an extracellular loop of a voltage-sensing domain [194]. This design, called ASAP1, renders much faster fluorescence response (~2 ms on and off kinetic) to membrane potential compared to ArcLight. With bright fluorescence and large dynamic range, ASAP1 can reliably detect single action potentials and subthreshold potential changes.

The second class of GEVIs are hybrid voltage sensor (hVOS) indicators [195] consisting of a membrane-targeted GFP and a fluorescence quencher dipicrylamine (DPA). The fluorescence of membrane targeted GFP is modulated by FRET between the FP and the DPA that migrates through the membrane bilayer depending on voltage. Strictly speaking, hVOS is not completely genetically encoded since it requires a supplement of DPA, which is toxic to cells in high dosage. In addition, the distribution of DPA in tissue is difficult to control, and hence the applications of hVOS-type GEVIs are limited [196].

3.3.2.2 Microbial Opsin-Based Voltage Indicators

Recently, Cohen and coworkers reported a third class of GEVIs based on microbial rhodopsins [132, 197]. Microbial rhodopsins are integral membrane proteins consist of seven transmembrane alpha helixes. A retinal molecule binds to the apoprotein by forming a Schiff base linkage with a lysine residue at the core of the protein, which constitutes the fluorescent chromophore. Cohen and coworkers discovered that the microbial rhodopsins proteorhodopsin and archaerhodopsin-3 (Arch) exhibit voltage-dependent changes in retinal fluorescence and, in the case of Arch. The mechanism of these GEVIs appears to be an electric field-dependent modulation of the pK_a of the Schiff base that leads to a change of the fluorescence intensity. Arch-based fluorescent voltage indicators can be functionally expressed in the plasma membrane of mammalian cells and are capable of resolving neuronal action potentials with high sensitivity and high SNR [132].

The first generation of Arch-based voltage indicators was associated with several important disadvantages. First, illumination of the wild-type protein generated a hyperpolarizing photocurrent, as the wild-type protein is a light-driven proton pump. A mutant Arch that does not generate photocurrent (Arch D95N) exhibited substantially slower kinetics. Yet another drawback was that both Arch and Arch D95N were dim, with the brightness increasing as a nonlinear function of illumination intensity [198]. In addition, neither protein was trafficked efficiently to the plasma membrane. Gong et al. later reported nonpumping mutants Arch EEN and Arch EEQ with improved voltage sensitivity, but the issues of dim fluorescence and slow kinetics remained [199].

To overcome the multiple critical issues of Arch-based voltage indicators, Hochbaum et al. [200] developed a hierarchic screening approach and successfully produced two variants, known as QuasAr1 and QuasAr2, with improved brightness and membrane trafficking, large voltage sensitivities, and fast kinetics. In addition, QuasAr1 and QuasAr2 do not generate photocurrent, and therefore, do not perturb membrane potential during illumination. By combining the QuasAr proteins with a novel channelrhodopsin actuator CheRiff, Hochbaum et al. engineered coexpression constructs, designated Optopatch, that enable the genetically targeted all-optical electrophysiology in dissociated neuron culture, human stem cell-derived neurons, and intact brain slice tissues.

Although QuasAr1 and QuasAr2 have been engineered for improved brightness, their fluorescence brightness is still not comparable to GEVIs based on conventional FPs. To combine the voltage sensitivity and speed of QuasArs and the brightness and spectral range of conventional FPs, Peng et al. reported a palette of GEVIs based on voltage-dependent electrochromic FRET (eFRET) from an FP donor to a QuasAr acceptor [201]. In this design, a FP is fused to QuasAr2, and voltage-induced changes in the absorption spectrum of QuasAr2 lead to voltage-dependent nonradiative quenching of the appended FP. The FRET efficiency was optimized by screening linker sequences between QuasAr2 and a FP. These eFRET-based constructs report single action potentials in cultured rat hippocampal neurons with a modest single-trial SNR at a 1 kHz acquisition frequency. Owing to the brightness

of FPs, the illumination intensity required for imaging eFRET constructs is much lower than QuasAr1 and QuasAr2. In a similar approach, Schnitzer and coworkers reported a construct with FPs fused to a mutant of nonfluorescent microbial opsin Mac [202]. These constructs exhibit faster kinetics and more robust detection of neural spiking compared to ArcLight. With these FRET-based opsin voltage indicators, they imaged neural spiking and subthreshold membrane voltage dynamics in cultured neurons, in pyramidal cells within neocortical tissue slices, and in cerebellar Purkinje neurons *in vivo*. A drawback of these FRET-based opsin indicators is the generation of transient excitatory photocurrent at the onset of illumination, which potentially can perturb neuronal activities.

3.3.2.3 *In vivo* Applications of Voltage Indicators

Voltage imaging using GEVIs has been considered a promising approach to study neuronal activities at high spatial and temporal resolution in the era of light-based electrophysiology [203]. However, few applications have been demonstrated to date, owing to the lack of GEVIs with optimal properties. Knöpfel and coworkers were the first to demonstrate the feasibility of using GEVIs in the brain of mice *in vivo* [135]. VSFP-based imaging successfully resolved synaptic potentials and action potentials from individual cells in cortical brain slices in single trials, with low SNRs [135]. In the follow-up work, they developed VSFP-butterfly with maximum voltage sensitivity tuned around the resting potential of neurons. Using VSFP-butterfly, they were able to detect synaptic potentials from individual cells *in vivo* with higher SNR compared to previous generations of VSFP. Soon after the development of ArcLight, Cao et al. [204] reported a landmark work in optical *in vivo* voltage recordings. Using ArcLight, they successfully imaged the electrical activity of genetically targeted neurons at single cell level in the intact brain of a living *Drosophila* fruit fly [204]. ArcLight provides a robust signal with sufficient SNR to decipher *in vivo* single electrical events, such as action potentials and hyperpolarization events in neurons, which are critical to understand neural computation processes.

3.3.3 Other Indicators for Imaging of Neuronal Activities

Synaptic transmission is essential for neurons to communicate with each other and process information flow in a neural network, and it is widely believed that synaptic changes play an important role in formation of memory [205]. Just as FP-based indicators have enabled the visualization of Ca^{2+} concentration and membrane potential in neurons, FP-based indicators could, in principle, be used to convert the processes of synaptic transmission into changes of fluorescent signal. The importance of indicators of synaptic transmission is widely recognized, and several strategies for fluorescence imaging of neurotransmission have been developed. The most straightforward strategy aims to directly probe the concentration change of

neurotransmitters during neurotransmission. Other strategies include coupling neurotransmitter binding events to other optical readouts, and detection of pH changes in synaptic clefts associated with synaptic vehicle fusion.

3.3.3.1 Neurotransmitter Indicators

Neurotransmitters are endogenous chemical compounds that transmit neural signals from one neuron to another. Many neurotransmitters are amino acids, such as glutamate, glycine, and GABA, or biogenic amines, such as dopamine and serotonin, or even peptides and proteins, such as somatostatin and substance P [206]. Binding of neurotransmitters may either inhibit or excite the postsynaptic neurons. Among the numerous neurotransmitters, glutamate is the major excitatory amino acid neurotransmitter in mammalian neural systems [207]. The first genetically encoded neurotransmitter for glutamate was reported in 2005 [208]. Upon binding to glutamate, the indicator converts the allosteric change of a bacterial glutamate binding protein ybeJ (also known as GltI) into change of FRET signal [208]. That same year, Tsien and coworkers reported a similarly designed glutamate indicator (GluSnFR) [209]. In 2008, Hire et al. optimized the performance of GluSnFR by systematic optimization of the linker and adjustment of the glutamate affinity. The end product, SuperGluSnFR, was capable of quantitative real-time optical measurements of synaptic glutamate release, spillover, and reuptake in dissociated hippocampal neurons with centisecond temporal, and spine-sized spatial, resolution [131]. In 2013, Marvin et al. reported the first single FP-based glutamate indicator iGluSnFR [210]. IGluSnFR was engineered in vitro for maximized fluorescence response, and it could robustly detect glutamate release events with sufficient SNR and kinetics for *in vivo* imaging in worms, zebrafish, and mice [210]. Notably, bacteria express a variety of periplasmic binding proteins including ones for GABA, acetylcholine, glycine, and other small molecules that serve as neurotransmitters in the brain [196]. A design principle similar to that used for iGluSnFR may one day produce a series of genetically encoded indicators for probing various neurotransmitters with spine-sized spatial resolution.

Instead of probing the neurotransmitters directly, one could probe the neurotransmitter binding events by coupling it to a different optical readout using a multi-component system. Nguyen et al. described a multi-component system, called cell-based neurotransmitter fluorescent engineered reporters (CNiFERs), to monitor *in situ* neurotransmitter receptor activation [211]. CNiFERs are engineered cultured cells that stably express an M1 acetylcholine receptor and the GECI TN-XXL. The system utilizes the GPCR cascade to convert receptor activity into a rise in cytosolic Ca^{2+} which is reported by TN-XXL. Nguyen et al. injected CNiFERs in the frontal cortex of the adult rat and used CNiFERs to probe the change of cholinergic signaling induced by an atypical neuroleptic drug [211]. Substitution of the M1 receptor with other Cys-loop receptors produced various versions of CNiFERs for serotonin and other neurotransmitters [212]. The advantages of this system include modular design and signal amplification through coupling to Ca^{2+}, but this system is not able

to detect neurotransmission in spine-size spatial resolution and is relatively slow due to the nature of the multicomponent signaling cascade [196]. Another drawback of this system is the need to implant exogenous cultured cells into the rodent brain, which may alter the function of neurons near the site of injection.

3.3.3.2 pH Indicators

Another strategy for visualization of neurotransmission is to exploit the acidic pH inside secretory vesicles to visualize vesicle exocytosis and recycling in the synaptic clefts [213]. In 1998, Miesenböck et al. generated pH-sensitive mutants of GFP ("pHluorins") by structure-guided combinatorial mutagenesis. The authors fused pHluorins to the vesicle membrane protein synaptophysin in order to target pHluorins to secretory and synaptic vehicles. The targeted pHluorin, termed synapto-pHluorin, successfully reported transmission events at individual synaptic boutons, as well as secretion and fusion of single secretory granules [113]. In 2002, Miesenböck and coworkers targeted synapto-pHluorin to the fly antennal lobe, where it enabled functional imaging of olfactory circuits in *Drosophila* [214]. In 2004, Bozza et al. used transgenic mice expressing synapto-pHluorin to report on synaptic vesicle fusion in olfactory sensory neurons. Furthermore, synapto-pHluorin selectively labeled presynaptic terminals of sensory neurons in glomeruli of the olfactory bulb and enabled the studies of neuronal populations that were previously inaccessible and chronic imaging from genetically defined neurons *in vivo* [130]. Recently, Li et al. developed a red fluorescent analogue of synapto-pHlourin, designated sypH-Tomato, for imaging of neurotransmission [215]. Combined with the green GECI GCaMP3, sypHTomato permits simultaneous imaging of Ca^{2+} and neurotransmitter release in neural networks.

3.3.3.3 Chloride Indicators

Chloride ions (Cl^-) regulate multiple physiological functions, including control of cell volume, fluid secretion, cellular pH, and maintenance of the resting membrane potential [114]. For the perspective of neurotransmission, Cl^- is essential for inhibitory transmission as presynaptic release of GABA activates postsynaptic GABA receptors, leading to Cl^- fluxes that underlie synaptic inhibition. In 2000, Kuner et al. developed the first generation of genetically encoded chloride indicator, Clomeleon [114]. Clomeleon is a fusion protein consisting of a Cl^--sensitive YFP and Cl^--insensitive CFP. YFP contains a Cl^- binding site close to the chromophore and has decreased fluorescent intensity upon binding to Cl^-. Therefore, Cl^- binding to YFP alters the FRET between CFP donor and YFP acceptor, which enables ratiometric imaging of intracellular Cl^- in neurons [114] and brain tissues [216]. However, it is challenging to use Clomeleon to image GABA-induced Cl^- fluxes, as the affinity of Clomeleon (~100 mM) is far beyond the typical physiological range of intracellular Cl^- (~5~6 mM) and extracellular Cl^- in the synaptic cleft (as high as

4 mM) for postsynaptic inhibitory transmission [216]. To solve this issue, Grimley et al. tuned the halide affinity and fluorophore characteristics of YFP to develop a second generation of Cl^- indicator, SuperClomeleon [217]. SuperClomeleon has a Cl^- affinity of 8.1 mM and can be used in mouse neurons to images changes in Cl^- concentration associated with exogenously applied GABA or inhibitory synaptic activity [217].

3.4 Perspective and Future Challenges

Optical interrogation of neuronal activities *in vivo* using genetically encoded indicators is a potentially revolutionary technology for neuroscientists who study neural circuits. However, practical issues and numerous hurdles have slowed the transition from initial proof of concept experiments to robust *in vivo* demonstrations and widespread acceptance. One major hurdle is the highly multidisciplinary knowledge base that is required to undertake such experiments. Early adaptors require not only the traditional skill sets of tissue culture, neuroanatomy, and electrophysiology, but also must be experts in molecular biology and cutting edge fluorescence imaging technology. Fortunately, this issue is being overcome by a growing number of resources that are helping to increase the accessibility of these techniques. Specifically, there is a rapidly growing selection of transgenic animal lines expressing various genetically encoded indicators, as well as by commercial virus production services, which release researchers from the tedious and time-consuming processes for making their own transgenic animal lines or preparing virus for gene delivery.

The ultimate test of any genetically encoded indicator is to be useful in a living animal, ideally a mouse. However, a fundamental challenge for all optical imaging modalities is scattering of light as it penetrates deeper into opaque tissues. This issue could be partially addressed through the development indicators with excitation and emission wavelengths in the near-infrared region and/or instrumental strategies that sidestep the scattering problems [218]. Some of these instrumental strategies include: miniaturized optical devices embedded near the brain region of interest [219–221], multiphoton imaging [21], and online inversion of the scattering matrix [222]. Even in small transparent organisms like the zebrafish embryo, it is challenging to image neuronal activities in a large volume of brain tissue with single-cell spatial resolution and millisecond acquisition speed. Hopefully, this goal can be achieved using improved imaging modalities, such as digital light sheet microscopy [179, 223], aberration-corrected multifocus microscopy [224], or spatial light modulator microscopy [225]. Additional progress towards this goal will be made through the availability of faster and more sensitive cameras, new excitation sources, and improved imaging software.

Despite the rapid progress of this field, particularly in the area of GECI technology, it is clear that the overall performance of many of the genetically encoded indicators falls short of the needs and demands of many practicing neuroscientists. Fortunately, the very nature of genetically encoded indicators means that further

improvements are guaranteed to come. GECIs, GEVIs and various other variants with improved brightness, response kinetics and magnitude, photostability and selectivity, are sure to be discovered, by applying the powerful approach of laboratory directed evolution. The major hurdle in achieving this goal is simply the investment in infrastructure and manpower required to set up high throughput screening systems that can identify rare improved variants from libraries of thousands. Ultimately, genetically encoded indicators will surpass the performance of established synthetic organic indicators and usher in a new era where *in vivo* optical imaging stands next to electrophysiology as a core technology of neuroscience.

References

1. Shimomura, O., Johnson, F. H., & Saiga, Y. (1962). Extraction, purification and properties of aequorin, a bioluminescent protein from luminous hydromedusan, *Aequorea*. *Journal of Cellular and Comparative Physiology, 59,* 223–239.
2. Yang, F., Moss, L. G., & Phillips, G. N. J. (1996). The molecular structure of green fluorescent protein. *Nature Biotechnology, 14,* 1246–1251.
3. Ormö, M., Cubitt, A. B., Kallio, K., et al. (1996). Crystal structure of the *Aequorea victoria* green fluorescent protein. *Science, 273,* 1392–1395.
4. Tsien, R. Y. (1998). The green fluorescent protein. *Annual Review of Biochemistry, 67,* 509–544.
5. Chalfie, M., Tu, Y., Euskirchen, G., et al. (1994). Green fluorescent protein as a marker for gene-expression. *Science, 263,* 802–805.
6. Inouye, S., & Tsuji, F. I. (1994). *Aequorea* green fluorescent protein expression of the gene and fluorescence characteristics of the recombinant protein. *FEBS Letters, 341,* 277–280.
7. Cormack, B. P., Valdivia, R. H., & Falkow, S. (1996). FACS-optimized mutants of the green fluorescent protein (GFP). *Gene, 173,* 33–38.
8. Crameri, A., Whitehorn, E. A., Tate, E., & Stemmer, W. P. (1996). Improved green fluorescent protein by molecular evolution using DNA shuffling. *Nature Biotechnology, 14,* 315–319.
9. Heim, R., Cubitt, A. B., & Tsien, R. Y. (1995). Improved green fluorescence. *Nature, 373,* 663–664.
10. Mishin, A. S., Subach, F. V., Yampolsky, I. V., et al. (2008). The first mutant of the *Aequorea victoria* green fluorescent protein that forms a red chromophore. *Biochemistry, 47,* 4666–4673.
11. Matz, M. V., Fradkov, A. F., Labas, Y. A., et al. (1999). Fluorescent proteins from nonbioluminescent Anthozoa species. *Nature Biotechnology, 17,* 969–973.
12. Wiedenmann, J., Schenk, A., Rocker, C., et al. (2002). A far-red fluorescent protein with fast maturation and reduced oligomerization tendency from *Entacmaea quadricolor* (Anthozoa, Actinaria). *Proceedings of the National Academy of Sciences of the United States of America, 99,* 11646–11651.
13. Deliolanis, N. C., Kasmieh, R., Wurdinger, T., et al. (2008). Performance of the red-shifted fluorescent proteins in deep-tissue molecular imaging applications. *Journal of Biomedical Optics, 13,* 044008.
14. Weissleder, R. (2001). A clearer vision for in vivo imaging. *Nature Biotechnology, 19,* 316–317.
15. Ntziachristos, V. (2006). Fluorescence molecular imaging. *Annual Review of Biomedical Engineering, 8,* 1–33.
16. Davidson, M. W., & Campbell, R. E. (2009). Engineered fluorescent proteins: Innovations and applications. *Nature Methods, 6,* 713–717.

17. Shcherbakova, D. M., Subach, O. M., & Verkhusha, V. V. (2012). Red fluorescent proteins: Advanced imaging applications and future design. *Angewandte Chemie* (*International ed. in English*)*, 51,* 10724–10738.
18. Shcherbo, D., Shemiakina, I. I., Ryabova, A. V., et al. (2010). Near-infrared fluorescent proteins. *Nature Methods, 7,* 827–829.
19. Shcherbakova, D. M., & Verkhusha, V. V. (2013). Near-infrared fluorescent proteins for multicolor in vivo imaging. *Nature Methods, 10,* 751–754.
20. Drobizhev, M., Makarov, N. S., Tillo, S. E., et al. (2011). Two-photon absorption properties of fluorescent proteins. *Nature Methods, 8,* 393–399.
21. So, P. T. C., Dong, C. Y., Masters, B. R., & Berland, K. M. (2000). Two-photon excitation fluorescence microscopy. *Annual Review of Biomedical Engineering, 2,* 399–429.
22. Shimomura, O. (1979). Structure of the chromophore of *Aequorea* green fluorescent protein. *FEBS Letters, 104,* 220–222.
23. Lemay, N. P., Morgan, A. L., Archer, E. J., et al. (2008). The role of the tight-turn, broken hydrogen bonding, Glu222 and Arg96 in the post-translational green fluorescent protein chromophore formation. *Chemical Physics, 348,* 152–160.
24. Heim, R., Prasher, D. C., & Tsien, R. Y. (1994). Wavelength mutations and posttranslational autoxidation of green fluorescent protein. *Proceedings of the National Academy of Sciences of the United States of America, 91,* 12501–12504.
25. Cubitt, A. B., Heim, R., Adams, S. R., et al. (1995). Understanding, improving and using green fluorescent proteins. *Trends in Biochemical Sciences, 20,* 448–455.
26. Wachter, R. M., Watkins, J. L., & Kim, H. (2010). Mechanistic diversity of red fluorescence acquisition by GFP-like proteins. *Biochemistry, 49,* 7417–7427.
27. Reid, B. G., & Flynn, G. C. (1997). Chromophore formation in green fluorescent protein. *Biochemistry, 36,* 6786–6791.
28. Barondeau, D. P., Putnam, C. D., Kassmann, C. J., et al. (2003). Mechanism and energetics of green fluorescent protein chromophore synthesis revealed by trapped intermediate structures. *Proceedings of the National Academy of Sciences of the United States of America, 100,* 12111–12116.
29. Rosenow, M. A., Huffman, H. A., Phail, M. E., & Wachter, R. M. (2004). The crystal structure of the Y66L variant of green fluorescent protein supports a cyclization-oxidation-dehydration mechanism for chromophore maturation. *Biochemistry, 43,* 4464–4472.
30. Petersen, J., Wilmann, P. G., Beddoe, T., et al. (2003). The 2.0-angstrom crystal structure of eqFP611, a far red fluorescent protein from the sea anemone *Entacmaea quadricolor*. *The Journal of Biological Chemistry, 278,* 44626–44631.
31. Subach, F. V., & Verkhusha, V. V. (2012). Chromophore transformations in red fluorescent proteins. *Chemical Reviews, 112,* 4308–4327.
32. Miyawaki, A., Shcherbakova, D. M., & Verkhusha, V. V. (2012). Red fluorescent proteins: Chromophore formation and cellular applications. *Current Opinion in Structural Biology, 22,* 679–688.
33. Gross, L. A., Baird, G. S., Hoffman, R. C., et al. (2000). The structure of the chromophore within DsRed, a red fluorescent protein from coral. *Proceedings of the National Academy of Sciences of the United States of America, 97,* 11990–11995.
34. Verkhusha, V. V., & Lukyanov, K. A. (2004). The molecular properties and applications of Anthozoa fluorescent proteins and chromoproteins. *Nature Biotechnology, 22,* 289–296.
35. Strack, R. L., Strongin, D. E., Mets, L., et al. (2010). Chromophore formation in DsRed occurs by a branched pathway. *Journal of the American Chemical Society, 132,* 8496–8505.
36. Pletnev, S., Subach, F. V., Dauter, Z., et al. (2010). Understanding blue-to-red conversion in monomeric fluorescent timers and hydrolytic degradation of their chromophores. *Journal of the American Chemical Society, 132,* 2243–2253.
37. Subach, O. M., Patterson, G. H., Ting, L. M., et al. (2011). A photoswitchable orange-to-far-red fluorescent protein, PSmOrange. *Nature Methods, 8,* 771–777.
38. Cotlet, M., Hofkens, J., Habuchi, S., et al. (2001). Identification of different emitting species in the red fluorescent protein DsRed by means of ensemble and single-molecule spectros-

copy. *Proceedings of the National Academy of Sciences of the United States of America, 98,* 14398–14403.
39. Tomosugi, W., Matsuda, T., Tani, T., et al. (2009). An ultramarine fluorescent protein with increased photostability and pH insensitivity. *Nature Methods, 6,* 351–353.
40. Dedecker, P., De Schryver, F. C., & Hofkens, J. (2013). Fluorescent proteins: Shine on, you crazy diamond. *Journal of the American Chemical Society, 135,* 2387–2402.
41. Bokman, S. H., & Ward, W. W. (1981). Renaturation of *Aequorea* gree-fluorescent protein. *Biochemical and Biophysical Research Communications, 101,* 1372–1380.
42. Meech, S. R. (2009). Excited state reactions in fluorescent proteins. *Chemical Society Reviews, 38,* 2922–2934.
43. Tolbert, L. M., Baldridge, A., Kowalik, J., & Solntsev, K. M. (2012). Collapse and recovery of green fluorescent protein chromophore emission through topological effects. *Accounts of Chemical Research, 45,* 171–181.
44. Niwa, H., Inouye, S., Hirano, T., et al. (1996). Chemical nature of the light emitter of the *Aequorea* green fluorescent protein. *Proceedings of the National Academy of Sciences of the United States of America, 93,* 13617–13622.
45. Litvinenko, K. L., Webber, N. M., & Meech, S. R. (2001). An ultrafast polarisation spectroscopy study of internal conversion and orientational relaxation of the chromophore of the green fluorescent protein. *Chemical Physics Letters, 346,* 47–53.
46. Webber, N. M., Litvinenko, K. L., & Meech, S. R. (2001). Radiationless relaxation in a synthetic analogue of the green fluorescent protein chromophore. *Journal of Physical Chemistry B, 105,* 8036–8039.
47. Vengris, M., van Stokkum I. H., He, X., et al. (2004). Ultrafast excited and ground-state dynamics of the green fluorescent protein chromophore in solution. *Journal of Physical Chemistry A, 108,* 4587–4598.
48. Stavrov, S. S., Solntsev, K. M., Tolbert, L. M., & Huppert, D. (2006). Probing the decay coordinate of the green fluorescent protein: Arrest of cis-trans isomerization by the protein significantly narrows the fluorescence spectra. *Journal of the American Chemical Society, 128,* 1540–1546.
49. Ward, W. W., Prentice, H. J., Roth, A. F., et al. (1982). Spectral perturbations of the *Aequorea* green-fluorescent protein. *Photochemistry and Photobiology, 35,* 803–808.
50. Ai, H., Shaner, N. C., Cheng, Z., et al. (2007). Exploration of new chromophore structures leads to the identification of improved blue fluorescent proteins. *Biochemistry, 46,* 5904–5910.
51. Chattoraj, M., King, B. A., Bublitz, G. U., & Boxer, S. G. (1996). Ultra-fast excited state dynamics in green fluorescent protein: Multiple states and proton transfer. *Proceedings of the National Academy of Sciences of the United States of America, 93,* 8362–8367.
52. Brejc, K., Sixma, T. K., Kitts, P. A., et al. (1997). Structural basis for dual excitation and photoisomerization of the *Aequorea victoria* green fluorescent protein. *Proceedings of the National Academy of Sciences of the United States of America, 94,* 2306–2311.
53. Kogure, T., Kawano, H., Abe, Y., & Miyawaki, A. (2008). Fluorescence imaging using a fluorescent protein with a large Stokes shift. *Methods* (*San Diego, California*)*, 45,* 223–226.
54. Piatkevich, K. D., Hulit, J., Subach, O. M., et al. (2010). Monomeric red fluorescent proteins with a large Stokes shift. *Proceedings of the National Academy of Sciences of the United States of America, 107,* 5369–5374.
55. Baird, G. S., Zacharias, D. A., & Tsien, R. Y. (2000). Biochemistry, mutagenesis, and oligomerization of DsRed, a red fluorescent protein from coral. *Proceedings of the National Academy of Sciences of the United States of America, 97,* 11984–11989.
56. Yarbrough, D., Wachter, R. M., Kallio, K., et al. (2001). Refined crystal structure of DsRed, a red fluorescent protein from coral, at 2.0-Å resolution. *Proceedings of the National Academy of Sciences of the United States of America, 98,* 462–467.
57. Lauf, U., Lopez, P., & Falk, M. M. (2001). Expression of fluorescently tagged connexins: A novel approach to rescue function of oligomeric DsRed-tagged proteins. *FEBS Letters, 498,* 11–15.

58. Gavin, P., Devenish, R. J., & Prescott, M. (2002). An approach for reducing unwanted oligomerisation of DsRed fusion proteins. *Biochemical and Biophysical Research Communications, 298,* 707–713.
59. Soling, A., Simm, A., & Rainov, N. (2002). Intracellular localization of Herpes simplex virus type 1 thymidine kinase fused to different fluorescent proteins depends on choice of fluorescent tag. *FEBS Letters, 527,* 153–158.
60. Campbell, R. E., Tour, O., Palmer, A. E., et al. (2002). A monomeric red fluorescent protein. *Proceedings of the National Academy of Sciences of the United States of America, 99,* 7877–7882.
61. Shaner, N. C., Campbell, R. E., Steinbach, P. A., et al. (2004). Improved monomeric red, orange and yellow fluorescent proteins derived from *Discosoma* sp. red fluorescent protein. *Nature Biotechnology, 22,* 1567–1572.
62. Shaner, N. C., Steinbach, P. A., & Tsien, R. Y. (2005). A guide to choosing fluorescent proteins. *Nature Methods, 2,* 905–909.
63. Shaner, N. C., Lin, M. Z., McKeown, M. R., et al. (2008). Improving the photostability of bright monomeric orange and red fluorescent proteins. *Nature Methods, 5,* 545–551.
64. Ai, H., Henderson, J. N., Remington, S. J., & Campbell, R. E. (2006). Directed evolution of a monomeric, bright and photostable version of *Clavularia* cyan fluorescent protein: Structural characterization and applications in fluorescence imaging. *The Biochemical Journal, 400,* 531–540.
65. Hoi, H., Howe, E. S., Ding, Y., et al. (2013). An engineered monomeric zoanthus sp yellow fluorescent protein. *Chemistry & Biology, 20,* 1296–1304.
66. Yanushevich, Y. G., Staroverov, D. B., Savitsky, A. P., et al. (2002). A strategy for the generation of non-aggregating mutants of Anthozoa fluorescent proteins. *FEBS Letters, 511,* 11–14.
67. Patterson, G. H., & Lippincott-Schwartz, J. (2002). A photoactivatable GFP for selective photolabeling of proteins and cells. *Science, 297,* 1873–1877.
68. Shaner, N. C., Lin, M. Z., McKeown, M. R., et al. (2009). Evaluating and improving the photostability of fluorescent proteins. *Proceedings of the SPIE, 7191,* 719105.
69. Shaner, N. C., Patterson, G. H., & Davidson, M. W. (2007). Advances in fluorescent protein technology. *Journal of Cell Science, 120,* 4247–4260.
70. Lubbeck, J. L., Dean, K. M., Ma, H., et al. (2012). Microfluidic flow cytometer for quantifying photobleaching of fluorescent proteins in cells. *Analytical Chemistry, 84,* 3929–3937.
71. Shcherbo, D., Murphy, C. S., Ermakova, G. V., et al. (2009). Far-red fluorescent tags for protein imaging in living tissues. *The Biochemical Journal, 418,* 567–574.
72. Ando, R., Mizuno, H., & Miyawaki, A. (2004). Regulated fast nucleocytoplasmic shuttling observed by reversible protein highlighting. *Science, 306,* 1370–1373.
73. David, C. C., Dedecker, P., Cremer, G. D., et al. (2012). Spectroscopic characterization of Venus at the single molecule level. *Photochemical & Photobiological Sciences: Official Journal of the European Photochemistry Association and the European Society for Photobiology, 11,* 358–363.
74. Marchant, J. S., Stutzmann, G. E., Leissring, M. A., et al. (2001). Multiphoton-evoked color change of DsRed as an optical highlighter for cellular and subcellular labeling. *Nature Biotechnology, 19,* 645–649.
75. Bogdanov, A. M., Mishin, A. S., Yampolsky, I. V., et al. (2009). Green fluorescent proteins are light-induced electron donors. *Nature Chemical Biology, 5,* 459–461.
76. Hoi, H., Shaner, N. C., Davidson, M. W., et al. (2010). A monomeric photoconvertible fluorescent protein for imaging of dynamic protein localization. *Journal of Molecular Biology, 401,* 776–791.
77. Kremers, G. J., Hazelwood, K. L., Murphy, C. S., et al. (2009). Photoconversion in orange and red fluorescent proteins. *Nature Methods, 6,* 355–358.
78. Ai, H. W., Baird, M. A., Shen, Y., et al. (2014). Engineering and characterizing monomeric fluorescent proteins for live-cell imaging applications. *Nature Protocols, 9,* 910–928.
79. Pedelacq, J. D., Cabantous, S., Tran, T., et al. (2006). Engineering and characterization of a superfolder green fluorescent protein. *Nature Biotechnology, 24,* 79–88.

80. Goedhart, J., van Weeren L., Hink, M. A., et al. (2010). Bright cyan fluorescent protein variants identified by fluorescence lifetime screening. *Nature Methods, 7,* 137–139.
81. Grotjohann, T., Testa, I., Leutenegger, M., et al. (2011). Diffraction-unlimited all-optical imaging and writing with a photochromic GFP. *Nature, 478,* 204–208.
82. Ai, H., Hazelwood, K. L., Davidson, M. W., & Campbell, R. E. (2008). Fluorescent protein FRET pairs for ratiometric imaging of dual biosensors. *Nature Methods, 5,* 401–403.
83. Esvelt, K. M., Carlson, J. C., & Liu, D. R. (2011). A system for the continuous directed evolution of biomolecules. *Nature, 472,* 499–503.
84. Agresti, J. J., Antipov, E., Abate, A. R., et al. (2010). Ultrahigh-throughput screening in drop-based microfluidics for directed evolution. *Proceedings of the National Academy of Sciences of the United States of America, 107,* 4004–4009.
85. Lubbeck, J. L., Dean, K. M., Davis, L. M., et al. (2011). A microfluidic cell sorter for directed evolution of fluorescent proteins based on dark-state conversion and photobleaching. *Biophysical Journal, 100,* 175a.
86. Davis, L. M., Lubbeck, J. L., Dean, K. M., et al. (2013). Microfluidic cell sorter for use in developing red fluorescent proteins with improved photostability. *Lab on a Chip, 13,* 2320–2327.
87. Zhao, Y., Abdelfattah, A. S., Zhao, Y., et al. (2014). Microfluidic cell sorter-aided directed evolution of a protein-based calcium ion indicator with an inverted fluorescent response. *Integrative Biology, 6,* 714–725.
88. Alford, S. C., Wu, J., Zhao, Y., et al. (2013). Optogenetic reporters. *Biology of the Cell, 105,* 14–29.
89. Miyawaki, A., Llopis, J., Heim, R., et al. (1997). Fluorescent indicators for Ca^{2+} based on green fluorescent proteins and calmodulin. *Nature, 388,* 882–887.
90. Kerppola, T. K. (2008). Bimolecular fluorescence complementation (BiFC) analysis as a probe of protein interactions in living cells. *Annual Review of Biophysics, 37,* 465–487.
91. Ghosh, I., Hamilton, A. D., & Regan, L. (2000). Antiparallel leucine zipper-directed protein reassembly: Application to the green fluorescent protein. *Journal of the American Chemical Society, 122,* 5658–5659.
92. Nagai, T., Sawano, A., Park, E. S., & Miyawaki, A. (2001). Circularly permuted green fluorescent proteins engineered to sense Ca^{2+}. *Proceedings of the National Academy of Sciences of the United States of America, 98,* 3197–3202.
93. Siegel, M. S., & Isacoff, E. Y. (1997). A genetically encoded optical probe of membrane voltage. *Neuron, 19,* 735–741.
94. Baird, G. S., Zacharias, D. A., & Tsien, R. Y. (1999). Circular permutation and receptor insertion within green fluorescent proteins. *Proceedings of the National Academy of Sciences of the United States of America, 96,* 11241–11246.
95. Nakai, J., Ohkura, M., & Imoto, K. (2001). A high signal-to-noise Ca^{2+} probe composed of a single green fluorescent protein. *Nature Biotechnology, 19,* 137–141.
96. Saito, K., Chang, Y. F., Horikawa, K., et al. (2012). Luminescent proteins for high-speed single-cell and whole-body imaging. *Nature Communications, 3,* 1262.
97. Alford, S. C., Abdelfattah, A. S., Ding, Y., & Campbell, R. E. (2012). A fluorogenic red fluorescent protein heterodimer. *Chemistry & Biology, 19,* 353–360.
98. Alford, S. C., Ding, Y., Simmen, T., & Campbell, R. E. (2012). Dimerization-dependent green and yellow fluorescent proteins. *ACS Synthetic Biology, 1,* 569–575.
99. Forster, T. (1959). Transfer mechanisms of electronic excitation. *Discussions of the Faraday Society, 27,* 7–17.
100. Grynkiewicz, G., Poenie, M., & Tsien, R. Y. (1985). A new generation of Ca^{2+} indicators with greatly improved fluorescence properties. *The Journal of Biological Chemistry, 260,* 3440–3450.
101. Zaccolo, M., De Giorgi, F., Cho, C. Y., et al. (2000). A genetically encoded, fluorescent indicator for cyclic AMP in living cells. *Nature Cell Biology, 2,* 25–29.
102. Akemann, W., Mutoh, H., Perron, A., et al. (2012). Imaging neural circuit dynamics with a voltage-sensitive fluorescent protein. *Journal of Neurophysiology, 108,* 2323–2337.

103. Zhang, J., Ma, Y., Taylor, S. S., & Tsien, R. Y. (2001). Genetically encoded reporters of protein kinase A activity reveal impact of substrate tethering. *Proceedings of the National Academy of Sciences of the United States of America, 98,* 14997–15002.
104. Ting, A. Y., Kain, K. H., Klemke, R. L., & Tsien, R. Y. (2001). Genetically encoded fluorescent reporters of protein tyrosine kinase activities in living cells. *Proceedings of the National Academy of Sciences of the United States of America, 98,* 15003–15008.
105. Fehr, M., Frommer, W. B., & Lalonde, S. (2002). Visualization of maltose uptake in living yeast cells by fluorescent nanosensors. *Proceedings of the National Academy of Sciences of the United States of America, 99,* 9846–9851.
106. Wu, C., Mino, K., Akimoto, H., et al. (2009). In vivo far-red luminescence imaging of a biomarker based on BRET from *Cypridina* bioluminescence to an organic dye. *Proceedings of the National Academy of Sciences of the United States of America, 106,* 15599–15603.
107. Chu, J., Zhang, Z., Zheng, Y., et al. (2009). A novel far-red bimolecular fluorescence complementation system that allows for efficient visualization of protein interactions under physiological conditions. *Biosensors & Bioelectronics, 25,* 234–239.
108. Fan, J. Y., Cui, Z. Q., Wei, H. P., et al. (2008). Split mCherry as a new red bimolecular fluorescence complementation system for visualizing protein-protein interactions in living cells. *Biochemical and Biophysical Research Communications, 367,* 47–53.
109. Jach, G., Pesch, M., Richter, K., et al. (2006). An improved mRFP1 adds red to bimolecular fluorescence complementation. *Nature Methods, 3,* 597–600.
110. Ohashi, K., Kiuchi, T., Shoji, K., et al. (2012). Visualization of cofilin-actin and Ras-Raf interactions by bimolecular fluorescence complementation assays using a new pair of split Venus fragments. *Biotechniques, 52,* 45–50.
111. Shyu, Y. J., Liu, H., Deng, X., & Hu, C. D. (2006). Identification of new fluorescent protein fragments for bimolecular fluorescence complementation analysis under physiological conditions. *Biotechniques, 40,* 61–66.
112. Zhao, Y., Araki, S., Wu, J., et al. (2011). An expanded palette of genetically encoded Ca^{2+} indicators. *Science, 333,* 1888–1891.
113. Miesenböck, G., De Angelis, D. A., & Rothman, J. E. (1998). Visualizing secretion and synaptic transmission with pH-sensitive green fluorescent proteins. *Nature, 394,* 192–195.
114. Kuner, T., & Augustine, G. J. (2000). A genetically encoded ratiometric indicator for chloride: Capturing chloride transients in cultured hippocampal neurons. *Neuron, 27,* 447–459.
115. Eli, P., & Chakrabartty, A. (2006). Variants of DsRed fluorescent protein: Development of a copper sensor. *Protein Science: A Publication of the Protein Society, 15,* 2442–2447.
116. Hanson, G. T., Aggeler, R., Oglesbee, D., et al. (2004). Investigating mitochondrial redox potential with redox-sensitive green fluorescent protein indicators. *The Journal of Biological Chemistry, 279,* 13044–13053.
117. Dooley, C. T., Dore, T. M., Hanson, G. T., et al. (2004). Imaging dynamic redox changes in mammalian cells with green fluorescent protein indicators. *The Journal of Biological Chemistry, 279,* 22284–22293.
118. Ostergaard, H., Henriksen, A., Hansen, F. G., & Winther, J. R. (2001). Shedding light on disulfide bond formation: Engineering a redox switch in green fluorescent protein. *The EMBO Journal, 20,* 5853–5862.
119. Tang, S., Wong, H.-C., Wang, Z.-M., et al. (2011). Design and application of a class of sensors to monitor Ca^{2+} dynamics in high Ca^{2+} concentration cellular compartments. *Proceedings of the National Academy of Sciences of the United States of America, 108,* 16265–16270.
120. Chen, S., Chen, Z. J., Ren, W., & Ai, H. W. (2012). Reaction-based genetically encoded fluorescent hydrogen sulfide sensors. *Journal of the American Chemical Society, 134,* 9589–9592.
121. Chen, Z. J., Ren, W., Wright, Q. E., & Ai, H. W. (2013). Genetically encoded fluorescent probe for the selective detection of peroxynitrite. *Journal of the American Chemical Society, 135,* 14940–14943.

122. Topell, S., Hennecke, J., & Glockshuber, R. (1999). Circularly permuted variants of the green fluorescent protein. *FEBS Letters, 457,* 283–289.
123. Griesbeck, O., Baird, G. S., Campbell, R. E., et al. (2001). Reducing the environmental sensitivity of yellow fluorescent protein. Mechanism and applications. *The Journal of Biological Chemistry, 276,* 29188–29194.
124. Wang, Q., Shui, B., Kotlikoff, M. I., & Sondermann, H. (2008). Structural basis for calcium sensing by GCaMP2. *Structure* (*London, England: 1993*)*, 16,* 1817–1827.
125. Akerboom, J., Rivera, J. D., Guilbe, M. M., et al. (2009). Crystal structures of the GCaMP calcium sensor reveal the mechanism of fluorescence signal change and aid rational design. *The Journal of Biological Chemistry, 284,* 6455–6464.
126. Helmchen, F., & Denk, W. (2005). Deep tissue two-photon microscopy. *Nature Methods, 2,* 932–940.
127. Miesenböck, G., & Kevrekidis, I. G. (2005). Optical imaging and control of genetically designated neurons in functioning circuits. *Annual Review of Neuroscience, 28,* 533–563.
128. Svoboda, K., & Yasuda, R. (2006). Principles of two-photon excitation microscopy and its applications to neuroscience. *Neuron, 50,* 823–839.
129. Marcaggi, P., Mutoh, H., Dimitrov, D., et al. (2009). Optical measurement of mGluR1 conformational changes reveals fast activation, slow deactivation, and sensitization. *Proceedings of the National Academy of Sciences of the United States of America, 106,* 11388–11393.
130. Bozza, T., McGann, J. P., Mombaerts, P., & Wachowiak, M. (2004). In vivo imaging of neuronal activity by targeted expression of a genetically encoded probe in the mouse. *Neuron, 42,* 9–21.
131. Hires, S. A., Zhu, Y., & Tsien, R. Y. (2008). Optical measurement of synaptic glutamate spillover and reuptake by linker optimized glutamate-sensitive fluorescent reporters. *Proceedings of the National Academy of Sciences of the United States of America, 105,* 4411–4416.
132. Kralj, J. M., Douglass, A. D., Hochbaum, D. R., et al. (2012). Optical recording of action potentials in mammalian neurons using a microbial rhodopsin. *Nature Methods, 9,* 90–95.
133. Dimitrov, D., He, Y., Mutoh, H., et al. (2007). Engineering and characterization of an enhanced fluorescent protein voltage sensor. *PLoS ONE, 2,* e440.
134. Tsutsui, H., Karasawa, S., Okamura, Y., & Miyawaki, A. (2008). Improving membrane voltage measurements using FRET with new fluorescent proteins. *Nature Methods, 5,* 683–685.
135. Akemann, W., Mutoh, H., Perron, A., et al. (2010). Imaging brain electric signals with genetically targeted voltage-sensitive fluorescent proteins. *Nature Methods, 7,* 643–649.
136. Chen, T. W., Wardill, T. J., Sun, Y., et al. (2013). Ultrasensitive fluorescent proteins for imaging neuronal activity. *Nature, 499,* 295–300.
137. Thestrup, T., Litzlbauer, J., Bartholomäus, I., et al. (2014). Optimized ratiometric calcium sensors for functional in vivo imaging of neurons and T lymphocytes. *Nature Methods 11,* 175–182.
138. Wu, J., Liu, L., Matsuda, T., et al. (2013). Improved orange and red Ca^{2+} indicators and photophysical considerations for optogenetic applications. *ACS Chemical Neuroscience, 4,* 963–972.
139. Berridge, M. J. (1998). Neuronal calcium signaling. *Neuron, 21,* 13–26.
140. Berridge, M. J., Lipp, P., & Bootman, M. D. (2000). The versatility and universality of calcium signalling. *Nature Reviews. Molecular Cell Biology, 1,* 11–21.
141. Kerr, R., Lev-Ram, V., Baird, G., et al. (2000). Optical imaging of calcium transients in neurons and pharyngeal muscle of C elegans. *Neuron, 26,* 583–594.
142. Garaschuk, O., Milos, R.-I., Grienberger, C., et al. (2006). Optical monitoring of brain function in vivo: From neurons to networks. *Pflügers Archiv European Journal of Physiology, 453,* 385–396.
143. Göbel, W., & Helmchen, F. (2007). In vivo calcium imaging of neural network function. *Physiology, 22,* 358–365.

144. Mank, M., & Griesbeck, O. (2008). Genetically encoded calcium indicators. *Chemical Reviews, 108,* 1550–1564.
145. Tour, O., Adams, S. R., Kerr, R. A., et al. (2007). Calcium green FlAsH as a genetically targeted small-molecule calcium indicator. *Nature Chemical Biology, 3,* 423–431.
146. Griffin, B. A., Adams, S. R., & Tsien, R. Y. (1998). Specific covalent labeling of recombinant protein molecules inside live cells. *Science, 281,* 269–272.
147. Adams, S. R., Campbell, R. E., Gross, L. A., et al. (2002). New biarsenical ligands and tetracysteine motifs for protein labeling in vitro and in vivo: Synthesis and biological applications. *Journal of the American Chemical Society, 124,* 6063–6076.
148. Gaietta, G., Deerinck, T. J., Adams, S. R., et al. (2002). Multicolor and electron microscopic imaging of connexin trafficking. *Science, 296,* 503–507.
149. Romoser, V. A., Hinkle, P. M., & Persechini, A. (1997). Detection in living cells of Ca^{2+}-dependent changes in the fluorescence emission of an indicator composed of two green fluorescent protein variants linked by a calmodulin-binding sequence A new class of fluorescent indicators. *The Journal of Biological Chemistry, 272,* 13270–13274.
150. Mank, M., Santos, A. F., Direnberger, S., et al. (2008). A genetically encoded calcium indicator for chronic in vivo two-photon imaging. *Nature Methods, 5,* 805–811.
151. Miyawaki, A., Griesbeck, O., Heim, R., & Tsien, R. Y. (1999). Dynamic and quantitative Ca^{2+} measurements using improved cameleons. *Proceedings of the National Academy of Sciences of the United States of America, 96,* 2135–2140.
152. Nagai, T., Yamada, S., Tominaga, T., et al. (2004). Expanded dynamic range of fluorescent indicators for Ca^{2+} by circularly permuted yellow fluorescent proteins. *Proceedings of the National Academy of Sciences of the United States of America, 101,* 10554–10559.
153. Horikawa, K., Yamada, Y., Matsuda, T., et al. (2010). Spontaneous network activity visualized by ultrasensitive $Ca(^{2+})$ indicators, yellow Cameleon-Nano. *Nature Methods, 7,* 729–732.
154. Heim, N., & Griesbeck, O. (2004). Genetically encoded indicators of cellular calcium dynamics based on troponin C and green fluorescent protein. *The Journal of Biological Chemistry, 279,* 14280–14286.
155. Mank, M., Reiff, D. F., Heim, N., et al. (2006). A FRET-based calcium biosensor with fast signal kinetics and high fluorescence change. *Biophysical Journal, 90,* 1790–1796.
156. Reiff, D. F., Ihring, A., Guerrero, G., et al. (2005). In vivo performance of genetically encoded indicators of neural activity in flies. *The Journal of Neuroscience: The Official Journal of the Society for Neuroscience, 25,* 4766–4778.
157. Díez-García, J., Matsushita, S., Mutoh, H., et al. (2005). Activation of cerebellar parallel fibers monitored in transgenic mice expressing a fluorescent Ca^{2+} indicator protein. *The European Journal of Neuroscience, 22,* 627–635.
158. Tian, L., Hires, S. A., Mao, T., et al. (2009). Imaging neural activity in worms, flies and mice with improved GCaMP calcium indicators. *Nature Methods, 6,* 875–881.
159. Gee, K. R., Brown, K. A., Chen, W. N. U., et al. (2000). Chemical and physiological characterization of fluo-4 Ca^{2+}-indicator dyes. *Cell Calcium, 27,* 97–106.
160. Sun, X. R., Badura, A., Pacheco, D. A., et al. (2013). Fast GCaMPs for improved tracking of neuronal activity. *Nature Communications*, *4* Article number: 2170.
161. Ohkura, M., Sasaki, T., Kobayashi, C., et al. (2012). An improved genetically encoded red fluorescent Ca^{2+} indicator for detecting optically evoked action potentials. *PLoS ONE, 7,* e39933.
162. Akerboom, J., Calderón, N. C., Tian, L., et al. (2013). Genetically encoded calcium indicators for multi-color neural activity imaging and combination with optogenetics. *Frontiers in Molecular Neuroscience, 6,* 2.
163. Boyden, E. S., Zhang, F., Bamberg, E., et al. (2005). Millisecond-timescale, genetically targeted optical control of neural activity. *Nature Neuroscience, 8,* 1263–1268.
164. Wardill, T. J., Chen, T. W., Schreiter, E. R., et al. (2013). A neuron-based screening platform for optimizing genetically-encoded calcium indicators. *PLoS ONE, 8,* e77728.

165. Fiala, A., Spall, T., Diegelmann, S., et al. (2002). Genetically expressed Cameleon in *Drosophila melanogaster* is used to visualize olfactory information in projection neurons. *Current Biology: CB, 12,* 1877–1884.
166. Yu, D., Baird, G. S., Tsien, R. Y., & Davis, R. L. (2003). Detection of calcium transients in *Drosophila* mushroom body neurons with camgaroo reporters. *The Journal of Neuroscience: The Official Journal of the Society for Neuroscience, 23,* 64–72.
167. Wang, J. W., Wong, A. M., Flores, J., et al. (2003). Two-photon calcium imaging reveals an odor-evoked map of activity in the fly brain. *Cell, 112,* 271–282.
168. Liu, L., Yermolaieva, O., Johnson, W. A., et al. (2003). Identification and function of thermosensory neurons in *Drosophila* larvae. *Nature Neuroscience, 6,* 267–273.
169. Higashijima, S.-I., Masino, M. A., Mandel, G., & Fetcho, J. R. (2003). Imaging neuronal activity during zebrafish behavior with a genetically encoded calcium indicator. *Journal of Neurophysiology, 90,* 3986–3997.
170. Hasan, M. T., Friedrich, R. W., Euler, T., et al. (2004). Functional fluorescent Ca^{2+} indicator proteins in transgenic mice under TET control. *PLoS Biology, 2,* e163.
171. Knöpfel, T. (2012). Genetically encoded optical indicators for the analysis of neuronal circuits. *Nature Reviews. Neuroscience, 13,* 687–700.
172. Díez-García, J., Akemann, W., & Knöpfel, T. (2007). In vivo calcium imaging from genetically specified target cells in mouse cerebellum. *NeuroImage, 34,* 859–869.
173. Qiu, D.-L., & Knöpfel, T. (2007). An NMDA receptor/nitric oxide cascade in presynaptic parallel fiber—Purkinje neuron long-term potentiation. *The Journal of Neuroscience: The Official Journal of the Society for Neuroscience, 27,* 3408–3415.
174. Qiu, D.-L., & Knöpfel, T. (2009). Presynaptically expressed long-term depression at cerebellar parallel fiber synapses. *Pflügers Archiv—European Journal of Physiology, 457,* 865–875.
175. Warp, E., Agarwal, G., Wyart, C., et al. (2012). Emergence of patterned activity in the developing zebrafish spinal cord. *Current Biology: CB, 22,* 93–102.
176. Fletcher, M. L., Masurkar, A. V., Xing, J., et al. (2009). Optical imaging of postsynaptic odor representation in the glomerular layer of the mouse olfactory bulb. *Journal of Neurophysiology, 102,* 817–830.
177. Fletcher, M. L. (2011). Analytical processing of binary mixture information by olfactory bulb glomeruli. *PLoS ONE, 6,* e29360.
178. Harvey, C. D., Coen, P., & Tank, D. W. (2012). Choice-specific sequences in parietal cortex during a virtual-navigation decision task. *Nature, 484,* 62–68.
179. Ahrens, M. B., Orger, M. B., Robson, D. N., et al. (2013). Whole-brain functional imaging at cellular resolution using light-sheet microscopy. *Nature Methods, 10,* 413–420.
180. Akerboom, J., Chen, T. W., Wardill, T. J., et al. (2012). Optimization of a GCaMP calcium indicator for neural activity imaging. *The Journal of Neuroscience: The Official Journal of the Society for Neuroscience, 32,* 13819–13840.
181. Andermann, M. L., Kerlin, A. M., & Reid, R. C. (2010). Chronic cellular imaging of mouse visual cortex during operant behavior and passive viewing. *Frontiers in Cell Neuroscience, 4,* 3.
182. Minderer, M., Liu, W., Sumanovski, L. T., et al. (2012). Chronic imaging of cortical sensory map dynamics using a genetically encoded calcium indicator. *The Journal of Physiology, 590,* 99–107.
183. Dombeck, D. A., Harvey, C. D., Tian, L., et al. (2010). Functional imaging of hippocampal place cells at cellular resolution during virtual navigation. *Nature Neuroscience, 13,* 1433–1440.
184. Huber, D., Gutnisky, D. A., Peron, S., et al. (2012). Multiple dynamic representations in the motor cortex during sensorimotor learning. *Nature, 484,* 473–478.
185. Ataka, K., & Pieribone, V. A. (2002). A genetically targetable fluorescent probe of channel gating with rapid kinetics. *Biophysical Journal, 82,* 509–516.

186. Sakai, R., Repunte-Canonigo, V., Raj, C. D., & Knöpfel, T. (2001). Design and characterization of a DNA-encoded, voltage-sensitive fluorescent protein. *The European Journal of Neuroscience, 13,* 2314–2318.
187. Guerrero, G., Siegel, M. S., Roska, B., et al. (2002). Tuning FlaSh: Redesign of the dynamics, voltage range, and color of the genetically encoded optical sensor of membrane potential. *Biophysical Journal, 83,* 3607–3618.
188. Baker, B. J., Lee, H., Pieribone, V. A., et al. (2007). Three fluorescent protein voltage sensors exhibit low plasma membrane expression in mammalian cells. *Journal of Neuroscience Methods, 161,* 32–38.
189. Lundby, A., Mutoh, H., Dimitrov, D., et al. (2008). Engineering of a genetically encodable fluorescent voltage sensor exploiting fast Ci-VSP voltage-sensing movements. *PLoS ONE, 3,* e2514.
190. Jin, L., Baker, B., Mealer, R., et al. (2011). Random insertion of split-cans of the fluorescent protein venus into Shaker channels yields voltage sensitive probes with improved membrane localization in mammalian cells. *Journal of Neuroscience Methods, 199,* 1–9.
191. Barnett, L., Platisa, J., Popovic, M., et al. (2012). A fluorescent, genetically-encoded voltage probe capable of resolving action potentials. *PLoS ONE, 7,* e43454.
192. Jin, L., Han, Z., Platisa, J., et al. (2012). Single action potentials and subthreshold electrical events imaged in neurons with a fluorescent protein voltage probe. *Neuron, 75,* 779–785.
193. Han, Z., Jin, L., Platisa, J., et al. (2013). Fluorescent protein voltage probes derived from ArcLight that respond to membrane voltage changes with fast kinetics. *PLoS ONE, 8,* e81295.
194. St-Pierre, F., Marshall, J. D., Yang, Y., et al. (2014). High-fidelity optical reporting of neuronal electrical activity with an ultrafast fluorescent voltage sensor. *Nature Neuroscience, 17,* 884–889.
195. Chanda, B., Blunck, R., Faria, L. C., et al. (2005). A hybrid approach to measuring electrical activity in genetically specified neurons. *Nature Neuroscience, 8,* 1619–1626.
196. Looger, L. L., & Griesbeck, O. (2012). Genetically encoded neural activity indicators. *Current Opinion in Neurobiology, 22,* 18–23.
197. Kralj, J. M., Hochbaum, D. R., Douglass, A. D., & Cohen, A. E. (2011). Electrical spiking in *Escherichia coli* probed with a fluorescent voltage-indicating protein. *Science, 333,* 345–348.
198. Maclaurin, D., Venkatachalam, V., Lee, H., & Cohen, A. E. (2013). Mechanism of voltage-sensitive fluorescence in a microbial rhodopsin. *Proceedings of the National Academy of Sciences of the United States of America, 110,* 5939–5944.
199. Gong, Y., Li, J. Z., & Schnitzer, M. J. (2013). Enhanced archaerhodopsin fluorescent protein voltage indicators. *PLoS ONE, 8,* e66959.
200. Hochbaum, D. R., Zhao, Y., Farhi, S. L., et al. (2014). All-optical electrophysiology in mammalian neurons using engineered microbial rhodopsins. *Nature Methods, 11,* 825–833.
201. Zou, P., Zhao, Y., Douglass, A. D., et al. (2014). Bright and fast multi-colored voltage reporters via electrochromic FRET (eFRET). *Nature Communications* (In press).
202. Gong, Y., Wagner, M. J., Zhong Li, J., & Schnitzer, M. J. (2014). Imaging neural spiking in brain tissue using FRET-opsin protein voltage sensors. *Nature Communications, 5* Article number: 3674.
203. Pastrana, E. (2011). Light-based electrophysiology. *Nature Methods, 9,* 38–38.
204. Cao, J., Arha, M., Sudrik, C., et al. (2013). Light-inducible activation of target mRNA translation in mammalian cells. *Chemical Communications* (*Cambridge*)*, 49,* 8338–8340.
205. Lynch, M. A. (2004). Long-term potentiation and memory. *Physiological Reviews, 84,* 87–136.
206. Snyder, S. H., & Innis, R. B. (1979). Peptide neurotransmitters. *Annual Review of Biochemistry, 48,* 755–782.
207. Cotman, C. W., & Monaghan, D. T. (1986). Anatomical organization of excitatory amino acid receptors and their properties. *Advances in Experimental Medicine and Biology, 203,* 237–252.

208. Okumoto, S., Looger, L. L., Micheva, K. D., et al. (2005). Detection of glutamate release from neurons by genetically encoded surface-displayed FRET nanosensors. *Proceedings of the National Academy of Sciences of the United States of America, 102,* 8740–8745.
209. Tsien, R. Y. (2005). Building and breeding molecules to spy on cells and tumors. *FEBS Letters, 579,* 927–932.
210. Marvin, J. S., Borghuis, B. G., Tian, L., et al. (2013). An optimized fluorescent probe for visualizing glutamate neurotransmission. *Nature Methods, 10,* 162–170.
211. Nguyen, Q.-T., Schroeder, L. F., Mank, M., et al. (2010). An in vivo biosensor for neurotransmitter release and in situ receptor activity. *Nature Neuroscience, 13,* 127–132.
212. Yamauchi, J. G., Nemecz, Nguyen, Q. T., et al. (2011). Characterizing ligand-gated ion channel receptors with genetically encoded Ca^{2+} sensors. *PLoS ONE, 6,* e16519.
213. Sudhof, T. C. (1995). The synaptic vesicle cycle: A cascade of protein–protein interactions. *Nature, 375,* 645–653.
214. Ng, M., Roorda, R. D., Lima, S. Q., et al. (2002). Transmission of olfactory information between three populations of neurons in the antennal lobe of the fly. *Neuron, 36,* 463–474.
215. Li, Y., & Tsien, R. W. (2012). pHTomato, a red, genetically encoded indicator that enables multiplex interrogation of synaptic activity. *Nature Neuroscience, 15,* 1047–1053.
216. Berglund, K., Schleich, W., Krieger, P., et al. (2006). Imaging synaptic inhibition in transgenic mice expressing the chloride indicator, Clomeleon. *Brain Cell Biology, 35,* 207–228.
217. Grimley, J. S., Li, L., Wang, W., et al. (2013). Visualization of synaptic inhibition with an optogenetic sensor developed by cell-free protein engineering automation. *The Journal of Neuroscience: The Official Journal of the Society for Neuroscience, 33,* 16297–16309.
218. Marblestone, A. H., Zamft, B. M., Maguire, Y. G., et al. (2013). Physical principles for scalable neural recording. *Frontiers in Computional Neuroscience, 7,* 137.
219. Caravaca-Aguirre, A. M., Niv, E., Conkey, D. B., & Piestun, R. (2013). Real-time resilient focusing through a bending multimode fiber. *Optics Express, 21,* 12881–12887.
220. Zorzos, A. N., Boyden, E. S., & Fonstad, C. G. (2010). Multiwaveguide implantable probe for light delivery to sets of distributed brain targets. *Optics Letters, 35,* 4133–4135.
221. Zorzos, A. N., Scholvin, J., Boyden, E. S., & Fonstad, C. G. (2012). Three-dimensional multiwaveguide probe array for light delivery to distributed brain circuits. *Optics Letters, 37,* 4841–4843.
222. Conkey, D. B., Caravaca-Aguirre, A. M., & Piestun, R. (2012). High-speed scattering medium characterization with application to focusing light through turbid media. *Optics Express, 20,* 1733–1740.
223. Keller, P. J., Schmidt, A. D., Wittbrodt, J., & Stelzer, E. H. (2008). Reconstruction of zebrafish early embryonic development by scanned light sheet microscopy. *Science, 322,* 1065–1069.
224. Abrahamsson, S., Chen, J., Hajj, B., et al. (2013). Fast multicolor 3D imaging using aberration-corrected multifocus microscopy. *Nature Methods, 10,* 60–63.
225. Quirin, S., Peterka, D. S., & Yuste, R. (2013). Instantaneous three-dimensional sensing using spatial light modulator illumination with extended depth of field imaging. *Optics Express, 21,* 16007–16021.

Chapter 4
The Voltage Imaging Frontier

Adam D. Douglass

Abstract Methods for optically recording the electrical activity in neurons have existed for nearly half a century, and yet these techniques remain extremely limited in their practical application. During the last few years, new classes of genetically encoded voltage indicators and innovative new microscopy techniques have put us tantalizingly close to making voltage imaging—in large networks, with the temporal resolution and sensitivity of electrode-based recordings—commonplace. This chapter discusses the history of voltage imaging in neuroscience with a view to understanding the enormous technical barriers that have made this field slow to develop. It also identifies significant issues that remain to be dealt with, and considers how the specific demands posed by different biological questions weigh the relative advantages and disadvantages of optical voltage readouts versus calcium imaging and electrodes.

4.1 Introduction

A fundamental, technical goal of neuroscience during the last half-century has been to record electrical activity in single neurons noninvasively, without the use of electrodes. From the very beginning, efforts to develop such techniques have relied on different forms of light microscopy, which has the properties needed to enable simultaneous recordings from multiple neurons in parallel and to do so without undue perturbation of the sample. Pioneering work done in the late 1960s validated this strategy by showing that neuronal firing elicits optical changes in nerve tissues that can be detected even without an exogenous probe [1]. These early efforts offered hope that voltage imaging would soon become commonplace. Somehow, though, the necessary techniques have failed to mature to a stage that would allow widespread adoption.

The last 15 years of technical innovation in neuroscience provide emphatic support for the general idea of using optical approaches to study the brain. Optogenetic

A. D. Douglass (✉)
Department of Neurobiology and Anatomy, University of Utah School of Medicine, Salt Lake City, UT, USA
e-mail: adam.douglass@neuro.utah.edu

A. D. Douglass (ed.), *New Techniques in Systems Neuroscience,* Biological and Medical Physics, Biomedical Engineering, DOI 10.1007/978-3-319-12913-6_4

techniques for manipulating neuronal activity with light transitioned from proof-of-principle experiments [2, 3] to near-universal adoption [4] with blinding speed. The palette of optogenetic tools now enables not only the excitation and inhibition of genetically defined neurons, but also allows one to use a variety of wavelengths of light to independently manipulate different cell populations in a single experiment [5–7] and to evoke either chronic [8] or acute [9] changes in neuronal activity. Efforts to engineer improved genetic tools [10, 11] and better instrumentation [12] continue to expand the range of ways to experimentally manipulate the brain.

Functional imaging has experienced similar success in the development of fluorescent, genetically encoded calcium indicators (GECIs). Following the invention of the first such sensor [13], the GCaMP family of GECIs was developed based on a similar principle, and rapidly improved through a series of mutagenesis and targeted engineering efforts [14]. The last year has seen a new generation of these tools that have the temporal resolution and sensitivity needed to report single action potentials under certain biological conditions [15]. Parallel efforts are underway to increase the spectral diversity of calcium reporters and appear destined to have similar success [16, 17]**.** While calcium imaging suffers from using an indirect measure of neuronal firing as a surrogate for the underlying electrical activity, the mature and highly favorable optical characteristics of GECIs have made them a standard way of probing brain activity.

It has also become possible to measure much more specific aspects of neuronal activity. Miesenböck and colleagues created a pH-sensitive variant of green fluorescent protein (GFP) that, when tethered to the luminal domain of a synaptic vesicle, reports the increase in pH that is the hallmark of vesicle fusion [3]. Fluorescent reporters for certain intracellular signaling events [18] and the local release of specific neurotransmitters [19, 20] have also appeared and allow one to mount very detailed investigations of circuit physiology using standard microscopy techniques.

There is no doubt that these approaches are fulfilling their promise. These massive efforts to build better optical probes and methodologies have, in just a few short years, dramatically reduced the use of electrodes for recording and manipulating neuronal activity in many experimental contexts, and enable sophisticated analyses of the relationship between physiology and behavior that account for the influence of cell type and ensemble firing patterns in heterogeneous neuronal networks [12, 21–23]. Optogenetics and calcium imaging have proven to be robust methods in virtually every experimental preparation.

Why, then, can we still not use a microscope to reliably measure the most defining aspect of neuronal activity? It is not for lack of trying. Over the last 50 years, several labs have created a series of elegant, optical methods for measuring voltage and recording activity in neurons. While many of these methods allowed optical identification of action potentials in a limited number of typically reduced preparations, none have constituted the breakthrough the field has been waiting for. The reason these techniques have not seen widespread use is intimately related to the nature of the action potential itself. As a highly transient event that occurs over the narrow dimensions of the plasma membrane, the action potential is temporally and spatially difficult to resolve [24]. The difficulty in accurately quantifying a

phenomenon that might last for less than a millisecond was historically convolved with the more general problems of creating molecular reporters of cellular phenomena and developing microscopy techniques that are capable of resolving individual cells within complex tissues. Now that optogenetics and calcium imaging have motivated such spectacular progress on these latter issues, we find ourselves much better positioned to return to our original goal of recording electrical activity with light, in whatever preparation we choose.

Very recent developments in indicator design and microscopy appear probably to motivate a revolution in voltage imaging. This chapter will place those emerging methods within the context of the history of voltage imaging in order to highlight not only how we have arrived at this point, but also to emphasize the technical challenges that remain. We will discuss the ongoing work that seeks to achieve a complete optical description of electrical activity in large ensembles of neurons, and consider the advantages that remain in using a true voltage readout now that calcium indicators are already so robust.

4.2 Early Approaches

4.2.1 Intrinsic Signals

While the development of voltage imaging techniques has become inextricably linked with the chemistry and molecular biology required to create new, voltage-sensitive fluorophores, the first optical measurements of electrical activity in neurons involved very little biological engineering. As early as the 1940s, a number of researchers had attempted to detect changes in the intrinsic opacity and birefringence of nerve tissue in response to electrical stimulation. Hill and Keynes [25] were the first to succeed. Stimulation of crab walking nerves was shown to cause an increase in their opacity, an effect that was apparent only upon averaging the signals from many repetitions, and which the authors were unable to explain. Much later, in a series of spectacularly insightful experiments, Larry Cohen and his colleagues investigated changes in light scattering and optical birefringence caused by electrical stimulation of different neuronal tissues. These included crab motor nerves, *Electrophorus* electric organs, and, crucially, individual squid giant axons [1, 26]. The authors demonstrated that changes in both scattering and birefringence could be detected at the single-cell level, though the response magnitudes were extremely small (in the order of 10^{-5} for the giant axon) and required averaging of thousands of recordings to achieve a satisfactory signal-to-noise ratio (SNR) (Fig. 4.1).

Several biophysical phenomena appear to give rise to these optical signals. First, the authors speculated that small changes in cell volume accompanying the action potential could affect light scattering. The hypothesized volume changes were difficult to demonstrate directly, but were later verified in experiments that measured mechanical deflections of the cell surface during the action potential using atomic

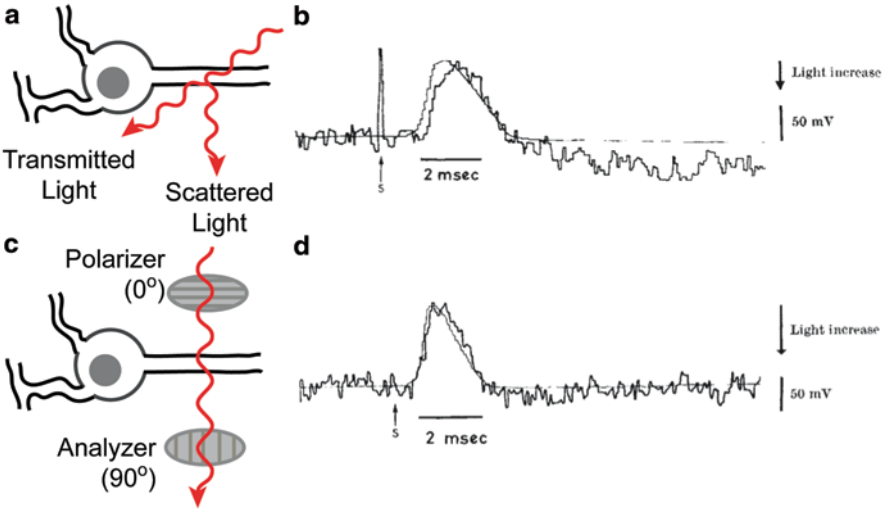

Fig. 4.1 Transmembrane potential affects intrinsic optical signals measured in squid giant axons. Cohen et al. [1] measured membrane potential using two different modalities. **a** In light scattering mode, a *white light* source incident on a single, isolated axon is either transmitted or scattered by the sample in different directions. A detector placed at different angles relative to the illumination axis recorded the amount of scatter over time. **b** With the detector positioned at 45°, action potentials were observed as a transient decrease in light scattering, with a fractional magnitude of roughly 3×10^{-6}. 3000–20,000 spikes were averaged to facilitate detection. *Thick* trace represents the optical signal, and *thin* trace shows the simultaneous intracellular recording. **c** In birefringence mode, the light intensity passing through a pair of crossed polarizers with the axon at 45° was measured. **d** Averaging multiple action potentials as in **b**, the authors demonstrated a fractional decrease of roughly 8×10^{-6} in transmitted light intensity, showing that membrane birefringence also decreases during depolarization. Panels **b** and **d** are reproduced from Cohen et al. [1]

force microscopy [27]. Second, a change in the refractive index of the cell surface was also thought to contribute to scattering. Third, birefringence changes were attributed to an electrically induced realignment of cell surface components during the spike. This sort of induced change in optical axis is referred to as the Kerr effect and has been hypothesized to occur in a number of biological contexts [28]. While none of these phenomena have been explained in much greater detail, intrinsic optical changes do seem to arise in a variety of preparations. Recent work has identified changes in light scattering as a consequence of activity in the neurohypophysis and pituitary pars intermedia of mammals. These experiments further decomposed the response waveform into temporal components that correlate with the action potential, calcium entry and vesicle fusion, and a lower magnitude but persistent aftereffect termed the "R-wave" [29, 30].

The goals of these early instances of voltage imaging were descriptive in nature. The authors were interested in using optical changes that occur during the action potential as a means of understanding the cellular consequences of these events. The measurements were considered advantageous in that they provided information

about the system independent of electrical recordings [1] and were not intended to replace electrode-based methods. While a fuller understanding of the origins of these intrinsic signals might aid the present search for a robust means of imaging voltage, such recordings hold limited promise in their rawest form. The extremely small magnitude of the voltage-evoked response typically requires extensive averaging across trials, preventing measurements of spontaneous activity. And because these techniques have not been developed to incorporate optical sectioning, it is impossible to record specifically from individual neurons in complex tissues. These landmark experiments did, however, essentially create functional imaging, and motivated a number of groups to explore this approach in the coming decades.

4.2.2 Synthetic Voltage-Sensitive Dyes

The signal amplification and optical sectioning enabled by fluorescence readouts made them an obvious target for further development. Many fluorophores are sensitive to local variations in pH, viscosity, hydrophobicity, and other physical parameters. Because these properties were known or suspected to change in the neuronal cell membrane during an action potential, it was assumed that many membrane-bound dyes would serve as voltage indicators. This assumption was surprisingly well borne out. Tasaki et al. [31] were the first to demonstrate modulation of an exogenous fluorophore during an action potential, by loading crustacean motor nerves with dye 8-anilinonaphthalene-1-sulfonic acid (ANS). Fractional changes in fluorescence signal in the order of $\sim 10^{-4}$ were observable upon averaging several trials. Given the large amount of effort that has subsequently gone into developing fluorescent voltage indicators, the number of dyes that exhibit voltage-dependent signals without any engineering whatsoever is truly stunning. Subsequent work showed that dozens of fluorophores modulate their fluorescence during the action potential, including compounds as mundane as fluorescein isothiocyanate, acridine orange, and rhodamine B [32], or as exotic and seemingly irrelevant as lysergic acid diethylamide (LSD) [33] (Fig. 4.2a, b). The physical origins of these effects are still not well characterized, but their manifestation in such chemically diverse molecules suggests that several different types of modulation could be at work [32].

The search for better dyes led to a group of merocyanine compounds (Fig. 4.2c) that, in 1973, were used to report single action potentials in squid giant axons, without averaging [34]. This landmark achievement was then reproduced in smaller cells from a leech sensory ganglion, which afforded a more difficult target owing to their dramatically smaller size [35]. The fractional fluorescence changes in these experiments were small—just 10^{-3} over the range of an action potential—but sufficient to achieve a relatively high SNR (10:1 in the case of the giant axon). Soon afterward, it was shown that the voltage sensitivity of these dyes is conferred by multiple processes acting in parallel, including dissociation from the cell, reorientation of the molecular dipole, and changes in oligomerization [36]. These studies were the first to offer a realistic hope that single-cell, single-trial detection of action potentials by fluorescence imaging might become a broadly viable technique.

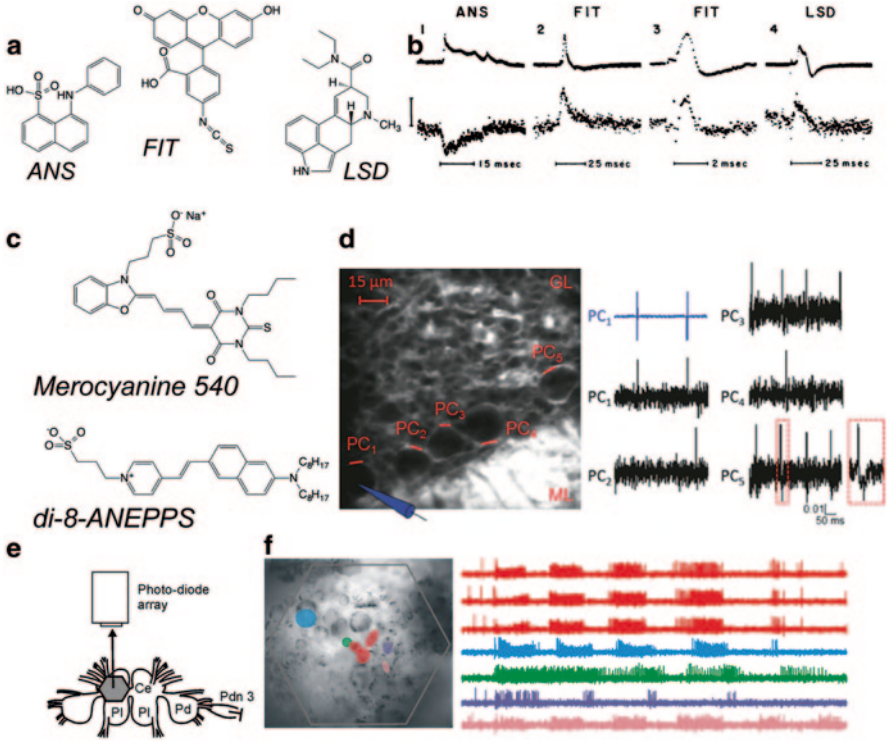

Fig. 4.2 Imaging neuronal activity with small-molecule voltage sensitive dyes. **a** Chemical structures of three, structurally unrelated fluorescent molecules that exhibit voltage sensitivity. *ANS* 8-anilinonaphthalene-1-sulfonate, *FIT* fluorescein isothiocyanate, *LSD* lysergic acid diethylamide. **b** Averaged fluorescence signals from squid giant axons (1, 3) and crab leg nerve (2, 4) loaded with the three different compounds. *Vertical bar* represents a fractional change of 4×10^{-4} (1), 4×10^{-5} (2), 6×10^{-5} (3), and 2×10^{-5} (4). **c** Chemical structures of representative merocyanine and hemicyanine VSDs. **d** Yan et al. [38] simultaneously imaged electrical activity in membrane regions (*red lines*) of several Purkinje cells (*PCs*) within an acute cerebellar slice using two-photon microscopy and the hemicyanine VSD di-4-AN(F)EPPTEA. Activity in *PC1* was simultaneously recorded using an extracellular electrode. *ML* molecular layer, *GL* granular layer. **e** Hill et al. [53] imaged activity in the dissected *Tritonia* swim network using absorbance measurements and the VSD RH-155. *Right panel* shows an absorbance image, in which several cellular ROIs are color-coded by neuron type. *Pl* pleural ganglion, *Pd* pedal ganglion, *Ce* cerebral ganglion. **f** An independent components analysis-based spike-sorting algorithm allowed extraction of optical signals arising from the ROIs shown in **e**. Panel **b** is reproduced from Tasaki et al. [33]. Panel **d** is from Yan et al. [38]. Panels **e** and **f** are reproduced from Hill et al. [53]

A series of thoughtful engineering efforts improved upon the merocyanine indicators by shifting focus to hemicyanine or "styryl" dyes (Fig. 4.2c), in which fluorescence is modulated when the membrane's electric field redistributes charge within the dye [37]. Early insight into the mechanism of voltage sensitivity in these dyes enabled methodical improvements in their design. By 1985, this work had

produced a variant called di-4-ANEPPS [39] that exhibited fractional fluorescence changes of 10% over a 100 mV range in living cells [40]. This dye and its derivatives have been the standard for neuronal imaging ever since, and they continue to be improved [38].

4.2.3 Biological Insight from VSD Imaging

Now that we have had almost three decades of experience with synthetic dyes that have reasonably strong photophysical properties, what has been done with them? Advances in instrumentation and imaging techniques continue to drive a steady flow of proof-of-principle studies. But putting the inevitable improvement of these techniques aside, what have we actually learned from voltage imaging that we did not know before?

One context in which voltage-sensitive dyes (VSDs) have been truly useful is as a readout of averaged, population activity. While the relatively low-voltage sensitivity of these dyes makes it difficult to resolve single action potentials in single cells in tissue, they provide a reasonably robust means to measure the summed activity of many neurons at once. Multiple groups have used this approach to characterize synchronized network phenomena such as cortical gamma oscillations [41], very fast oscillations and gamma rhythms in cerebellum [42], and the coordinated spread of activity in hippocampal slices [43]. Others have used bulk VSD imaging to observe how arousal state affects such network oscillations [44]. In all of these studies, the kinetics of current VSDs enabled observation of network phenomena that happen faster than a calcium readout would allow, while retaining spatial information about its structure.

Bulk VSD imaging has provided crucial information about other aspects of mesoscale network function as well. Blasdel and Salama [45] used the merocyanine dye NK2367 to monitor visually evoked activity in primate cortex and revealed a previously unappreciated spatial linkage of orientation selectivity and ocular dominance across large areas of the brain. More recently, Lim et al. [46] and Mohajerani [47] combined optogenetic stimulation using ChR2 with bulk VSD imaging to map neuronal connectivity in cortex. Because the VSD used in those studies has a significantly red-shifted activation wavelength, the authors were able to avoid cross-excitation of the dye with the ChR2 pulse and vice versa, an issue that has confounded similar connectivity mapping experiments using GECIs [48].

Dye-based voltage imaging has been similarly useful in studies of neuronal cell biology, particularly in dissociated cell culture models. Grinvald and colleagues [49] used voltage imaging to describe the propagation of action potentials across single cultured neurons and directly measured the electrical conduction velocity. Another early study directly observed and quantified the spread of an applied potential from the Purkinje cell soma into distal areas of its dendrites [50]. Others have combined VSDs with calcium imaging to describe the relationship between calcium transients and voltage in specific subcellular regions, such as the dendritic spine

[38]. In each of these cases, the use of an optical readout enabled a description of the subcellular characteristics of neuronal activity, which is typically quite difficult to achieve through electrode-based means.

Even the kind of measurement that is the ultimate goal of modern systems neuroscience, in which every cell in a network is simultaneously imaged with single-cell and single-spike resolution, has long been achievable in certain reduced preparations. These have typically been invertebrate ganglia, where the measurements are not complicated by the need for precise optical sectioning. In studies of the *Aplysia* abdominal ganglion, Wu et al. [51] used VSD imaging to characterize the network activity underlying a variety of gill movement behaviors and provided some of the first direct evidence that the distributed, combinatorial pattern of activity within a network, rather than the dedicated activity of neurons within labeled lines, can be an important determinant of behavior. Stadele and colleagues used ANEPPS imaging in the stomatogastric ganglion to identify pattern-generating neurons [52], and Hill et al. [53] applied absorption-based imaging to show that stereotyped neurons in a *Tritonia* locomotor circuit can participate variably during defined behaviors (Fig. 4.2e, f). These studies illustrate the potential strengths that could be offered by network-level voltage imaging with single-cell resolution, were the techniques mature enough to work in more complex preparations.

Despite significant progress in the development of VSDs with favorable photophysical properties, small-molecule dyes suffer from fundamental shortcomings that will continue to limit their use, particularly *in vivo*. Delivery to a target tissue requires invasive manipulations, and the dyes cannot be loaded specifically into neurons of a particular type. Toxicity is also significant, as many VSDs perturb cell health over time and must be imaged immediately to ensure the competency of the prep. Even if the cells are not killed by dye loading, the addition of very high numbers of charge carriers to the plasma membrane, which is typical for VSDs, can cause substantial capacitive loading effects and alter or suppress action potentials. Due to these and other concerns, the bulk of recent attention has been devoted to creating protein-based tools.

4.3 Genetically Encoded Indicators

The development of GFP as a genetically encoded fluorescent reporter [54] has motivated most of the major developments in biological imaging over the last 20 years, and voltage imaging is certainly no exception. The ability to specifically target a genetically defined population of cells is a huge experimental advantage. In contrast to electrode-based recordings, where little or no concrete information is available about cellular identity, genetically encoded indicators allow one to draw conclusions about a well-defined population of neurons even in cases where morphology and location within the brain fail to provide definitive classifiers. Furthermore, because the tools and techniques involved in creating and modifying genetic reagents fall within the expertise of any lab that performs molecular biology, the

advent of GFP allowed researchers with little background in chemistry or physics to begin developing reagents that suited their particular needs. This broadening of the community of tool builders has led to an explosion of new fluorescent reporters for a wide variety of biological phenomena. While the practical utility of these tools has not always met the lofty predictions that were made at the time of their invention, the collective enterprise of creating and improving on genetically encoded, fluorescent sensors over the last couple of decades is truly inspiring and has put us on the path to solving many significant technical challenges once and for all. Voltage imaging is one of these challenges.

4.3.1 Early Work: FlaSh, SPARC, and VSFP

The first genetically encoded voltage indicator (GEVI) came soon after GFP itself. Since the only genetically encoded fluorophores available in the late 1990s were GFP and its derivatives, using one of these proteins as the starting material in an effort to make a voltage sensor was an obvious choice. The less obvious decision was how to engineer in voltage sensitivity. By itself, cytoplasmically localized GFP is not voltage sensitive. However, GFP and its spectral variants have several photochemical properties that might potentially be modulated by an applied electric field, including intrinsic sensitivities to pH [55, 56] and chloride ions [57]. Electric field fluctuations across a cell membrane can be very large in magnitude (approximately 9×10^7 V/m for a 90 mV action potential and a 10-nm-thick membrane) but are extremely localized, having a Debye length of roughly 1 nm [58]. This requires any candidate sensor to be targeted at least near the cell surface, and preferably within the lipid bilayer itself. Because the structure of GFP is incompatible with membrane insertion, a means of anchoring it to the cell surface was a key requirement.

Siegel and Isacoff [59] addressed the problems of membrane targeting and voltage sensitivity simultaneously by rigidly fusing GFP into the juxtamembrane region of the voltage-gated Shaker potassium channel (Fig. 4.3a). Because this channel undergoes significant conformational changes in response to fluctuations in transmembrane potential, the authors reasoned that voltage transients might cause it to significantly change either GFP's local chemical environment or its intrinsic photophysical properties. The precise source of voltage sensitivity remains unclear. However, their sensor, which they called "FlaSh," did indeed show significant changes in fluorescence intensity when subjected to applied voltage waveforms in the *Xenopus* oocyte membrane (Fig. 4.3b). Interestingly, the kinetics of its fluorescence response were substantially slower than those of the applied membrane potential and the conformational change itself, suggesting that the conformational change triggered some biochemical process that reached equilibrium after a relatively long delay.

FlaSh was problematic in its kinetics (Table 4.1; Fig. 4.3b) and in the fact that its fluorescence saturates at transmembrane potentials above −20 mV, which limited its dynamic range relative to that of the neuronal action potential. A recent attempt to improve on the original design substituted a different potassium channel, KV1.4,

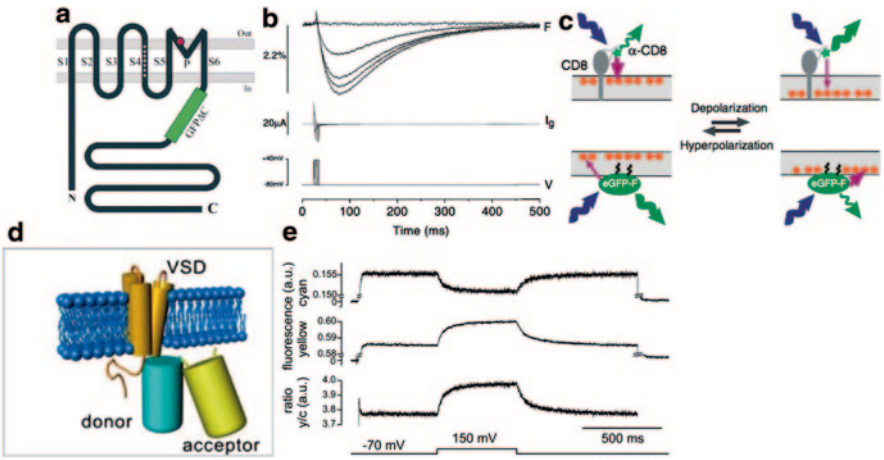

Fig. 4.3 Genetically encoded voltage indicators have diverse structural and photophysical properties. **a** FlaSh incorporates a truncated GFP (GFPΔC) into a juxtamembrane region of the Shaker potassium channel, where structural and charge rearrangements driven by changes in transmembrane potential modulate fluorescence intensity. **b** FlaSh responds to brief membrane depolarizations with slow and persistent decreases in GFP intensity. Each trace represents the average of 25 trials at a stimulus duration of 1.25, 3.75, 6.25, 8.75, or 11.25 ms. *Top*, fluorescence; *middle*, gating current; *bottom*, command potential. **c** Principles of hVOS operation. In one test configuration (*top*), a fluorescent antibody directed against the extracellular portion of the CD8 protein is quenched by DPA molecules in the membrane's outer leaflet. The quencher molecules redistribute during membrane depolarization, causing an increase in fluorescence. In the more typical hybrid configuration, a genetically encoded fluorophore (here, a farnesylated EGFP) attached to the intracellular leaflet is increasingly quenched upon depolarization. **d** Principles of VSFP operation. In VSFP2.1, a FRET donor–acceptor pair is linked in tandem at a juxtamembrane position to the voltage-sensing domain of Ci-VSP. Membrane depolarizations drive structural rearrangements in the VSD that changes the proximity of the two fluorophores, leading to **e** quenching of the donor (*cyan*), an increase in acceptor signal (*yellow*) and an increase in the ratio of *yellow* to cyan. Panels **a** and **b** reproduced from Siegel and Isaacoff [59]; Panel **c** from Chanda et al. [65]; Panels **d** and **e** from Dimitrov et al. [70]

for the Shaker channel, under the assumption that its higher voltage gating threshold would be reflected in a shift of the fluorescence versus voltage curve [60]. This proved correct and yielded a new variant called Flare that has been used to read out evoked sensory activity in rodent cortex *in vivo* by multiphoton microscopy. Fluorescence signals were quite small in those studies, requiring averaging across multiple trials to enable their detection, and only occurred in a small subset of neurons. A third permutation of this basic approach inserted wild-type GFP into an intracellular loop of a voltage-gated sodium channel from skeletal muscle [61]. While the resulting indicator, called SPARC, had faster kinetics than any previous tool, it exhibited just a 0.5% fractional change in fluorescence intensity per 100 mV and has not seen practical use. Similar issues limited the adoption of a FRET-based tool,

Table 4.1 Voltage-sensing properties of representative GEVIs. Indicator kinetics are given as a response half-time (tau) for a step in applied voltage. A range of values is given in cases where speed was reported to vary significantly under different experimental conditions, or when the off- and on-rates were markedly different. Both time constants are reported for indicators that had biphasic response profiles. Sensitivity is expressed in units of normalized fluorescence intensity change over a 100-mV step. Wherever possible, this corresponds to the nominal range of an action potential, from −70 to +30 mV. The sign of each indicator's response indicates whether membrane depolarization causes an increase (+) or decrease (−) in fluorescence intensity. "Ratiometric" indicators employ FRET schemes in which two fluorophores respond with opposite sign. All values are derived from the literature and are approximate

	τ (ms)	Δ F/F (%)	Sign of response
FlaSh	23–300	5	–
SPARC	>2	0.5	–
VSFP1	~1	6	Ratiometric
hVOS1	0.5	5–34	–
hVOS2	0.5	26	–
VSFP2.1	2–8 and 10–90 (biphasic)	2–5	Ratiometric
Mermaid	5–20	~5	Ratiometric
Arclight	10 and 50 (biphasic)	35	–
Chicken Arclight A173	4–9	9	–
ASAP1	2.1 and 71.5 (biphasic)	17.5	–
Arch(WT)	0.6	40	+
QuasAr1	0.05	35	+
QuasAr2	0.3 and 3.2 (biphasic)	90	+
MacQ-mOrange2	3 and 115 (biphasic)	15	–
QuasAr2-mOrange2	2.4 and 22 (biphasic)	10	–

called VSFP1, in which the degree of energy transfer between a CFP–YFP pair was modulated by an attached voltage-sensing domain from KV2.1 [62].

The lack of mechanistic understanding has been a recurring theme in voltage indicator design and has unfortunately slowed progress toward improved GEVIs. Some groups have worked on characterizing the biophysical mechanisms of voltage sensitivity in these first- and second-generation sensors [63, 64]. In some cases, relatively random manipulations that resulted in altered indicator properties also provided insight into the mechanisms of voltage sensing. However, we still know relatively little about how these tools work, and that has made rational design very difficult. Our failure to characterize the principles involved is understandable given the general difficulty of doing biochemistry on membrane proteins. As we learn more about the structure and dynamics of these sensors, it will become more obvious how to improve them.

4.3.2 Having it Both Ways with hVOS

The shortcomings of the early, voltage-gated channel-based tools, along with a general uncertainty about their biophysical mechanisms of action and resulting difficulty in improving their design, led several authors to consider alternative strategies. A technique called hVOS (hybrid voltage sensor) combined genetically encoded and small-molecule-based approaches [65] (Fig. 4.3c). The synthetic probe dipicrylamine (DPA) has the useful properties of intercalating into cell membranes, translocating between the inner and outer leaflets in response to applied voltage, and quenching GFP fluorescence. By targeting GFP to one face of the cell surface and simultaneously bath-applying DPA, the authors were able to read out transmembrane potential through the variable quenching of the GFP signal. This approach gave very high fluorescence dynamic range, voltage sensitivity, and kinetics when measured in cultured, nonneuronal cells, but carried significant concerns of phototoxicity owing to the DPA. The capacitive load introduced by adding massive numbers of mobile charge carriers to the membrane was also substantial, and in some cases appears to be high enough to inhibit action potentials [24, 65, 66]. While this issue has not been experimentally addressed for the fluorophore-channel fusion class of GEVIs, it is worth noting that the problem of capacitive shunting is expected to be even greater for those indicators owing to an increased charge density and steeper dependence of charge movement on transmembrane potential [65, 66]. In all, the hVOS class of sensors has been the best understood from the mechanistic level, and efforts to improve on the basic design have accordingly been the most productive, with versions that now report up to 34% fractional fluorescence intensity changes over the voltage range of an action potential [66, 67] (Table 4.1) and some reports of their use in a physiologically relevant context [68].

4.3.3 Ciona VSD-Based Indicators

A new direction in GEVI design was sparked by the discovery in 2005 of a lipid phosphatase, found in the sea squirt *Ciona intestinalis*, that possessed a voltage-sensitive enzymatic activity [69]. The VSD of this protein is homologous to motifs from voltage-sensitive ion channels but generated interest as the basis for a new class of GEVIs, in part because the native protein was assumed to exist as a monomer and thus lacks the requirement for higher order interactions that reduce surface expression of channel-based indicators. The first implementation of a *Ciona*-based GEVI, called VSFP2.1, attached a CFP–YFP FRET pair to the VSD core and exhibited modest voltage sensitivity and response times in the order of tens of milliseconds [70] (Table 4.1; Fig. 4.3d, e). The use of a dual-wavelength FRET readout increased signal-detection probability somewhat by allowing ratiometric measurements (Fig. 4.3e). Subsequent iterations of this tool improved substantially on its sensitivity by using novel FRET donors and acceptors, by repositioning them relative to the VSD, and by altering the sensor core to shift the detection threshold

[71–74]. These efforts have produced indicators such as VSFP Butterfly 1.2, which shows ratiometric fluorescence changes that are very sensitive to transmembrane potential and have been used to read out population activity and even under specific conditions that allow multitrial averaging, spikes in single neurons [75].

4.4 Recent Developments: Arch, Arclight, and ASAP1

A flurry of developments in the last few years has brought us to the cusp of fully realized optical voltage recordings in complex preprations. Three new indicator technologies motivated this leap forward, two of which were derived from the principles behind FlaSh- and VSFP-class tools, and a third that relied on a novel voltage sensing mechanism that is intrinsic to rhodopsin family proteins.

4.4.1 Rhodopsin-Based Sensors

The first significant improvement in GEVI design came unexpectedly from an academic subfield that has existed for nearly 140 years—the study of opsin biochemistry and photophysics. Franz Boll and Wilhelm Kuhne were the first to observe photochemical changes in isolated frog retina—namely, light-mediated bleaching and recovery of color—in the late 1800s [76]. The protein behind these effects turned out to be rhodopsin, and the discovery that the spectral properties of this photopigment change in response to light proved to be foundational to our understanding of how such proteins work. While the number of identified rhodopsin-superfamily members has grown to include thousands of proteins that are found in all kingdoms of biology [77], all of them share a fundamentally similar photocycle that is intimately linked to their function. Spectroscopic measurements on isolated rhodopsins have shown that, shortly after absorbing an excitation photon of the proper wavelength, these proteins cycle rapidly through a series of discrete photophysical states, each of which is characterized by a shift in absorption spectrum, and each of which corresponds to a functional intermediate in the protein's biochemical cycle [78].

Two essential features of the rhodopsin photocycle suggested that these proteins might be useful as the basis of a new class of GEVI. First, the spectral shifts induced by photoactivation can be quite large, spanning a range of well over 100 nm, such that the protein varies tremendously in its ability to absorb any given wavelength as it performs its biochemical function. Second, in many cases, spectral shifts are linked to the movement of charge within the protein (Fig. 4.4a). This makes sense given that all rhodopsins perform essentially the same biochemical function of transducing light energy into charge movement, whether pumping ions across the cell surface, as in the case of bacteriorhodopsin, or triggering conformational changes through the redistribution of charge, as in the case of the visual pigments. Together, these properties suggested a new means by which membrane potential

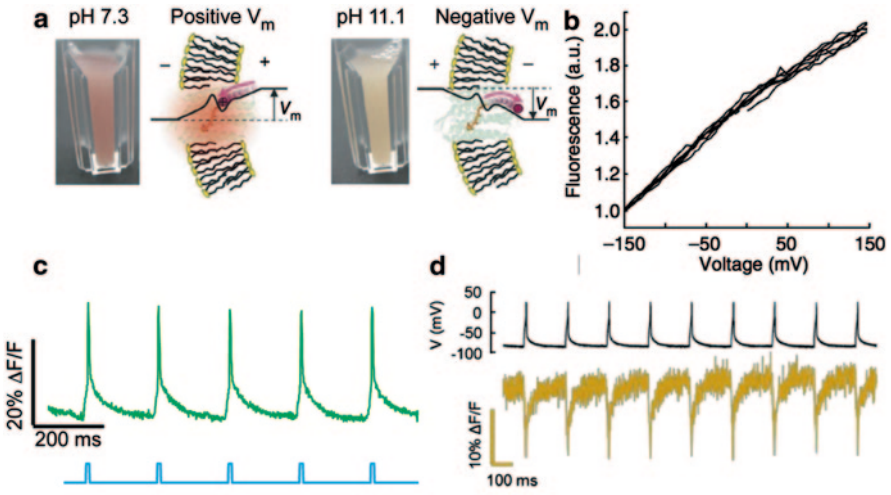

Fig. 4.4. Rhodopsin-based, genetically encoded voltage indicators. **a** Archaerhodopsin-3's photophysical properties are modulated by protonation of its retinal Schiff base. At a neutral pH (7.3), the chromophore is protonated and a solution of purified protein exhibits spectral properties that are distinct from those observed when it is deprotonated at pH 11.1. Because the Schiff base is accessible to solvent on the inside of the cell, membrane depolarization electrostatically increases the concentration of H+ in the vicinity of the chromophore and mimicks the neutral pH condition (*left diagram*). Negative membrane potentials decrease protonation and mimick the effects of high pH (*right diagram*). **b** Fluorescence from wild-type Arch expressed in HEK cells is linearly responsive to voltage across a wide range. **c** When co-expressed with the *blue*-activated channelrhodopsin variant CheRiff, the *red*-shifted emission wavelength and improved voltage-sensing properties of the Arch-derivative QuasAr2 enable visualization of single-trial, optogenetically evoked spikes in brain slice culture. *Blue* trace, CheRiff stimulus; *Green* trace, QuasAr2 fluorescence. **d** In the FRET variant QuasAr2-mOrange2, quenching of an attached donor fluorophore (mOrange2) by the rhodopsin inverts the sign of the voltage response and allows imaging of the substantially brighter donor signal. *Panels* show single-trial mOrange2 fluorescence (*orange trace*) and simultaneous patch-clamp recording from a dissociated hippocampal neuron. Panels **a** and **b** are reproduced from Kralj et al. [86]. Panel **d** is from Zou et al. [92]. Data in panel **c** courtesy of Daniel Hochbaum and Adam Cohen

might be transduced into an optical signal. By repositioning charge within the transmembrane segments of an opsin, variations in membrane potential might lead to detectable spectral shifts—essentially running the opsin in reverse. There was an overlooked precedent for this phenomenon in the literature, as Kolodner et al. [79] had demonstrated that bacteriorhodopsin in isolated membrane films showed 200 nm shifts in absorption wavelength when subjected to an applied electrical field, owing to charge movement in the vicinity of the retinal chromophore. The deep vein of biophysical research on these proteins also suggested a convenient mode of reading out such shifts, as studies from as early as the 1960s had observed fluorescence phenomena in purified visual pigments [80] that were later shown to occur in ion-pumping microbial opsins as well [81].

Intrinsic fluorescence was key, as a purely absorption-based measurement would suffer from the relatively low amounts of protein found in a cell membrane. While the intensity of fluorescence emitted from the rhodopsins was dim, having a quantum yield that was measured to be approximately 1/1000 that of EGFP, it was also markedly red-shifted [80, 81]. This partially alleviated concerns about brightness because cellular autofluorescence sources are most significant in blue-green wavelengths, making a high SNR potentially achievable even with dim fluorophores.

The first direct proof-of-concept experiments for these indicators came within the unexpected context of the bacterial cell membrane. Kralj and colleagues [82] took as their starting material a prokaryotic opsin called green proteorhodopsin (GPR; [83]), which normally functions as an outward-biased proton pump in response to green wavelengths of light. When expressed and imaged in *E. coli,* a mutant of GPR referred to as proteorhodopsin optical proton sensor (PROPS) exhibited dim, far-red fluorescence ($\lambda_{em} = 710$ nm, quantum yield $= 1 \times 10^{-3}$) that was nonetheless readily detectable by widefield epifluorescence microscopy using strong laser illumination and a sensitive camera. Upon the application of an external electric field, fluorescence was modulated rapidly and reversibly, with a sensitivity of $\Delta F/F = 150\%$ per 100 mV and a response time constant of 4.7 mV—a combination that was unmatched by previous indicators. Surprisingly, fluorescence in individual cells also showed spontaneous fluctuations indicating changes in transmembrane potential in the order of 100 mV. While the biological significance of these fluctuations is not completely clear, they highlight the exploratory utility of voltage imaging in contexts where electrode-based recordings are not feasible.

This initial success was followed by a set of unexpected difficulties in translating the indicators to a neuronal context. A human codon-optimized version of PROPS expressed at fairly high levels and exhibited fluorescence in mammalian (HEK) cells but was unfortunately mistargeted, with the vast majority of signal localizing to internal membranes and not the cell surface. Accordingly, PROPS-expressing cells showed no detectable fluorescence modulations in response to applied transmembrane potentials. While the addition of various membrane targeting motifs to certain archaeal rhodopsins has greatly improved their cell surface localization in eukaryotes [84], none of roughly 40 combinatorial permutations of such tags succeeded in redirecting PROPS to its appropriate location. It appears likely that certain prokaryotic membrane proteins are simply not well processed by eukaryotic cells.

As an alternative, the authors looked for similar opsins that were known to be trafficked appropriately in eukaryotic cells, and found one in the recently published optogenetic tool, archaerhodopsin-3 (Arch; [85]). Arch had been shown to be well tolerated by mammalian neurons and to mediate robust silencing when illuminated by green light, owing to its proton-pumping activity. Like PROPS, Arch was easily visualized in mammalian cells and showed voltage-dependent fluorescence, even when imaged in its unmodified state [86]. Arch was also extremely sensitive to voltage, exhibiting a fractional increase in fluorescence of 40% over the range of an action potential (Fig. 4.4b), and quite fast, responding within 600 μs of an applied voltage change. Most compellingly, Arch was the first GEVI to robustly report single-trial action potentials in cultured neurons, without temporal filtering. Simple

spike-finding algorithms identified over 99% of action potentials in single-trial fluorescence recordings, as verified against simultaneous patch measurements, and gave less than a 0.6% false-positive rate.

While wild-type Arch established a new benchmark for voltage imaging, it left significant room for improvement. The initial paper on Arch as a GEVI established the potential for engineering the properties of opsin-based GEVIs by mutating a single residue, Asp 95. Arch(D95N) showed dramatically increased voltage sensitivity and complete loss of light-activated proton pumping, at the cost of a significant reduction in speed. Subsequent work has used novel screening methods [87, 88] and directed engineering [89] to create a number of Arch variants with improved brightness and voltage sensitivities.

Despite these improvements, the most significant shortcoming of opsin-based GEVIs remains their relative dimness. While subsequent biophysical investigation showed that the fluorescence quantum yield of wild-type Arch is substantially higher than first appreciated, owing to a nonlinear fluorescence excitation process that had escaped notice [90], the brightness of this indicator under typical imaging conditions is still roughly 1/50 that of GFP. Even with the impressive progress in intensity, speed, and voltage sensitivity that was achieved in the recent "QuasAr" variants [87] (Fig. 4.4c), Arch's dim fluorescence is an obvious target for further engineering. A recently proposed alternative is to employ a FRET imaging scheme. By attaching a spectrally matched donor to Arch or to the related opsin, Mac, two groups have independently demonstrated that voltage-triggered changes in the opsin's absorption spectrum result in differential quenching of donor fluorescence via energy transfer [91, 92] (Fig. 4.4d). Since the donor fluorophores used in these probes are roughly as bright as EGFP, a loss of sensitivity when imaging the donor alone is compensated for by a significant increase in signal. This new class of derivatives is extremely promising and has been used to image voltage transients in the cerebellar Purkinje cells of live mice by epifluorescence microscopy [91].

While this rapidly evolving class of probes has yet to produce a canonical "best" tool for neuronal imaging, it has already proven its usefulness in a wide variety of experimental settings, including bacteria [82], cultured cell lines and dissociated neurons [86], brain slices [87], zebrafish heart [127], and, in one case, living mice [91]. The knowledge base provided by years of research on rhodopsin biochemistry and photophysics has been an extremely useful source of insight into the mechanisms of these indicators and should continue to produce useful reagents.

4.4.2 Arclight

Following shortly after the first publications on opsin-based GEVIs, a new indicator was derived from the *Ciona* VSD. Like VSFP-family indicators, this new tool, called Arclight, consists of the voltage-sensing domain from CiVSP fused to a fluorescent protein [93]. By linking the "ecliptic" form of a pH-sensitive GFP to the CiVSP voltage-sensing domain, the authors were able to achieve modest voltage

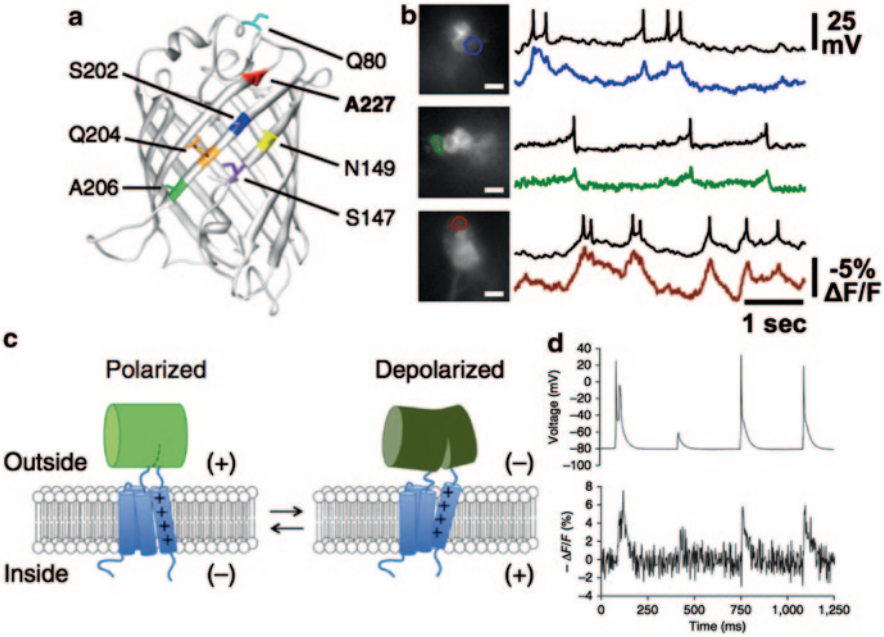

Fig. 4.5 Next-generation sensors based on the voltage-sensing domain of Ci-VSP. **a** Mutations at several sites on one side of the beta-barrel of a pH-sensitive GFP variant ("pHluorin") affect voltage sensitivity in GEVIs based on a fusion of this protein to the *Ciona* VSD. The resulting indicator, Arclight, robustly indicates single-trial action potentials. **b** Arclight enables accurate optical measurements of membrane potential, including spike identification, in whole-brain explants from *Drosophila*. *Black traces* show patch clamp records acquired simultaneously with the colored optical signals. Single neurons (colored ROIs) were imaged in sparsely labeled brains using epifluorescence microscopy. **c** ASAP1 mechanism. A circularly permuted GFP attached to an extracellular loop within the *Ciona* VSD undergoes conformational shifts in response to changes in transmembrane potential, decreasing its fluorescence during depolarization. **d** Epifluorescence imaging of ASAP1 in a layer 5 cortical neuron from an acute slice allows the identification of single spikes and subthreshold activity in single-trial data. The *bottom panel* shows the fluorescence record; *top*, simultaneous patch-clamp measurement. Panels **a** and **b** are reproduced from Jin et al. [93]. Panels **c** and **d** are from St-Pierre et al. [126]

sensitivity, in the order of 1.3 % ΔF/F per 100 mV. While this level of sensitivity has been far surpassed by other indicators, a fortuitous mutation in a derived HEK cell line produced an amino acid substitution (A227D) that increased sensitivity 14-fold. Subsequent permutations established that the same substitution in the "superecliptic" pH-GFP performed even better, as did constructs in which the fluorophore was positioned closer to the juxtamembrane domain of the VSD. While the authors performed a rigorous mutation analysis as part of their attempts to improve the protein's photophysical properties (Fig. 4.5a), it remains unclear exactly how pH sensitivity and the A227D mutation confer strong voltage-sensing properties upon these indicators. As with Arch, it is possible that local pH changes occurring within a Debye length or so of the intracellular membrane surface during depolarization directly affect protonation of a critical site within the fluorophore.

Despite such ambiguities, Arclight performs very well as a voltage indicator. It traffics well to the cell surface in neurons, is roughly as bright as EGFP, and readily reports action potentials and subthreshold depolarizations in single-trial data. It is relatively slow, having a biphasic voltage response with time constants of 10 and 50 ms (Table 4.1), but appears well suited to resolving spikes at relatively low frequencies. Most impressively, a subsequent paper used Arclight to read out single spikes, subthreshold activity, and barrages of odor-evoked spiking in whole-brain *Drosophila* explants and in living flies by epifluorescence microscopy [94] (Fig. 4.5b). The low-spatial resolution of this imaging technique precludes recording from many cells in parallel under most *in vivo* circumstances, but it appears quite possible that Arclight or one of its recent derivatives [95] (Table 4.1) will work with one of the rapidly developing, optical sectioning microscopies that are discussed in Sect. 5.

4.4.3 ASAP1

A third promising development has combined the principles behind VSD-based GEVIs and GCaMP-based calcium indicators. Termed Accelerated Sensor of Action Potentials 1 (ASAP1), this new indicator incorporates a cyclically permuted GFP (cpGFP). By engineering GFP to place the N and C termini near its chromophore, the creators of cpGFPs reasoned that differential movement at the termini might dramatically affect fluorescence [96]. This prediction has been well substantiated in the GCaMPs, where the cpGFP termini are fused to a calcium sensor that undergoes a dramatic conformational change upon binding calcium. The conformational change is propagated to the attached cpGFP, leading to changes in fluorescence. The creators of ASAP1 drew on structural data describing voltage-induced changes in the conformation of the *Ciona* VSD [97] to identify promising sites for fusing the cpGFP to create a new voltage indicator [126]. Since an extracellular loop between transmembrane helices S3 and S4 in this VSD appears to undergo significant reorganization upon depolarization, a cpGFP was attached in the corresponding region of the chicken VSD to create ASAP1 (Fig. 4.5c). The resulting probe was similar to Arclight in its sensitivity to voltage but was significantly faster, responding within 2 ms to pulse onset and offset (Table 4.1). Such kinetics still caused a filtering effect at high frequencies, but single action potentials were readily resolved in several experimental situations (Fig. 4.5d).

This nascent class of indicators is extremely promising, both in terms of what might be done with the first generation of tools and in terms of how they might be improved. As with opsin-based GEVIs, the mechanism of voltage sensitivity in ASAP1 is fairly well understood. The sole paper on this indicator examined an impressive set of systematic variations on the core design and identified several key properties that might be varied or conserved in future engineering efforts.

4.4.4 Which GEVI is Best?

This is an exciting time for GEVI development, but the pace at which new, seemingly useful tools are being created might be overwhelming for investigators who would just like to know which one to use in their experiments. We can certainly compare the standard benchmarks for GEVI performance among the various ASAP1, Arclight, and opsin-based voltage indicators [Table 4.1]. It seems clear that Arclight's relatively slow kinetics make it less well suited for resolving burst activity and that the low fluorescence intensity of the first generations of Arch-based indicators will limit their use with optically sectioning microscopies that collect photons from small subregions of a neuron. Other authors have presented detailed analyses of the SNR requirements for optically detecting single action potentials [24, 98]. However, there are several parameters that will significantly affect indicator selection, but that are either unknown, difficult to quantify, or become more or less important under different experimental settings.

- *Trafficking*. A primary reason that earlier GEVIs never saw widespread use was their mistargeting to internal membranes instead of the cell surface [99]. Localization within the cell ensures that the probe fails to experience evoked transmembrane potentials, and provides an additional source of nonresponsive background fluorescence that decreases SNR. While all three current classes of GEVI appear to be reasonably well enriched at the cell surface, this can vary based on cell type and the particular indicator version used. More extensive attempts to use each probe in a variety of biological contexts will clarify whether any of them suffers from trafficking defects.
- *Background fluorescence*. In general, cellular sources of autofluorescence emit green wavelengths of light, making red-shifted signals like those emitted intrinsically by opsin-class indicators potentially appealing. The decrease in noise in the far-red part of the spectrum is offset by the lower fluorescence intensity of these indicators. A direct comparison between Arclight and the recently developed "QuasAr" derivatives of Arch in HEK cells and neuronal cultures showed that the overall sensitivity, speed, and SNR of QuasAr imaging allowed more robust spike detection [87]. However, since the contribution of background signal will depend on experimental context, this might not be true in all applications.
- *Sign of response*. With the exception of intrinsic opsin fluorescence, all of the current indicators modulate their signals in inverse proportion to transmembrane potential. This is true for FRET-based donor fluorophore quenching in the recently created MacQ-FP and QuasAr-FP fusions as well. While the fluorescence intensities of all of these indicators are similarly high, the fact that they respond to action potentials by becoming dimmer is not optimal from a signal detection perspective, since it reduces the separation of signal from noise when a cell is firing. It also requires substantially higher illumination intensity throughout the experiment to minimize such SNR considerations, which increase the chance of photobleaching and phototoxicity effects. The direct relationship between voltage and fluorescence intensity in the intrinsic opsin signal is further reason to consider using these tools.

- *Multiphoton excitability*. All of these indicators are, in principle, excitable by a two-photon process and could be imaged by multiphoton microscopy as it is now commonly used in neuroscience. However, the efficiency of such excitation varies significantly for different fluorophores and can limit their practical use, as has been the case for several common red fluorescent proteins [100]. This consideration might be especially relevant for the opsin-based probes, which will presumably have longer 2P excitation wavelengths that might not be produced efficiently by currently available, femtosecond pulsed lasers.
- *Toxicity*. There is no such thing as a nonperturbative transgene, particularly if it is introduced using viral transduction methods. While none of these indicators are reported to be overtly toxic, it remains to be seen whether that is generally true across different model organisms, cell types, and expression systems.

The good news is that, from the figures of merit that we can measure, each of these indicator classes holds enormous promise for imaging in a variety of contexts. It simply remains to try.

4.5 Making it Work *in vivo*: Choosing an Imaging Mode

To date, very few single-cell voltage recordings have been made *in vivo*, despite the recent surge in *in vitro* GEVI performance. Because the justification for voltage imaging versus electrode-based techniques from the beginning has been to study electrical activity within ensembles of cells, making the jump into intact, functioning brains is an important barrier to clear. The essential problem in doing so is that voltage recordings must be performed at very high rates, which reduces the number of fluorescence photons sampled at each image frame. In cell culture and certain brain slice preparations, this can easily be compensated for by using wide-field imaging techniques that excite large areas of the cell simultaneously. Except under circumstances of sparse labeling or low neuronal density [94], *in vivo* recordings require the use of optical sectioning microscopies to eliminate background from out-of-focus areas of the brain, which can reduce the amount of light collected per pixel by multiple orders of magnitude. Sectioning microscopies are also generally slower than wide-field imaging. Careful consideration of imaging mode is therefore a crucial step in designing voltage imaging experiments. Fortunately, several recent developments in instrumentation make it easier to optically section the brain without discarding undue amounts of light, while achieving high sampling rates.

4.5.1 Scanning Two-Photon Microscopy

Two-photon laser scanning microscopy (TPLSM) has revolutionized *in vivo* imaging in complex, multicellular organisms. Where laser scanning confocal microscopy had achieved high spatial resolution and optical sectioning through the use of

conjugate sets of pinholes in the excitation and emission light paths, throwing out a large fraction of the fluorescence emitted by the sample, TPSLM relied instead on a nonlinear fluorescence excitation process to spatially restrict excitation to a small, subcellular volume, and collected all of the available fluorescent photons for routing to a PMT or other point detector [101, 102]. This advantage in its use of the available photon budget holds for GEVI imaging as well, as do its low phototoxicity, ability to image deep within tissue, and the relative maturity of the technique.

However, TPLSM and other point-scanning microscopies hold some serious drawbacks for voltage imaging. First is the reduction in speed that results from having to physically scan the excitation beam across the sample. While the incorporation of resonant scanners into two-photon microscopes has allowed imaging of large brain areas above video rate (30 Hz; [103–105]), this benchmark still falls far short of the >1 kHz rates needed to resolve single action potentials. The typical solution is to scan over a much smaller area, often a single line of pixels, but this greatly reduces the number of cells that can be recorded from simultaneously and so partly negates one of the key advantages of imaging. The second drawback is duty cycle. In scanning microscopies, a given pixel will be illuminated for only a small percentage of each frame acquisition period as the laser is moved across the sample, unlike in wide-field imaging, where all pixels are illuminated continuously. The result is an additional loss of photons in the case of TPLSM, which moves the measurement even closer to the noise floor.

Despite these disadvantages, several groups have used TPLSM to measure voltage in a variety of contexts. Akemann et al. [75] imaged both ensemble-averaged and single-cell electrical activities in mouse cortex by two-photon microscopy, using the VSFP variant Butterfly 1.2. Though they were not able to image fast enough to resolve single spikes, they did readily measure bursts of activity evoked by electrical stimulation or by sensory input. Another group exploited the second-harmonic generation (SHG) scattering signal generated by multiphoton illumination of an organic membrane dye to record rapid voltage transients in brain slices and cultured Aplysia neurons [106]. This method has not been used *in vivo* or with a GEVI, but is potentially interesting because of its selective excitation of fluorophores within the plasma membrane. A third study used a two-component dye system similar in principle to hVOS to image single-trial APs and subthreshold activity in single neurons using fixed-point illumination [107]. Last, using random-access line scans and a hemicyanine dye, Yan et al. simultaneously recorded activity in several cerebellar Purkinje cells in brain slices (Fig. 4.2d; YAN REF). From this work, it is clear that, given an indicator with appropriate photophysical properties, TPLSM can be used to read out electrical activity in complex preps. However, imaging many cells in parallel will require dramatic improvements in both scan hardware and detector efficiency.

4.5.2 Multifocal and WF-TeFo 2P Imaging

One way to increase the speed of point-scanning microscopies is to multiplex the illumination light. Scanning with multiple beams in parallel reduces the time required to acquire an image frame by a factor equal to the number of beams used (Fig. 4.6a).

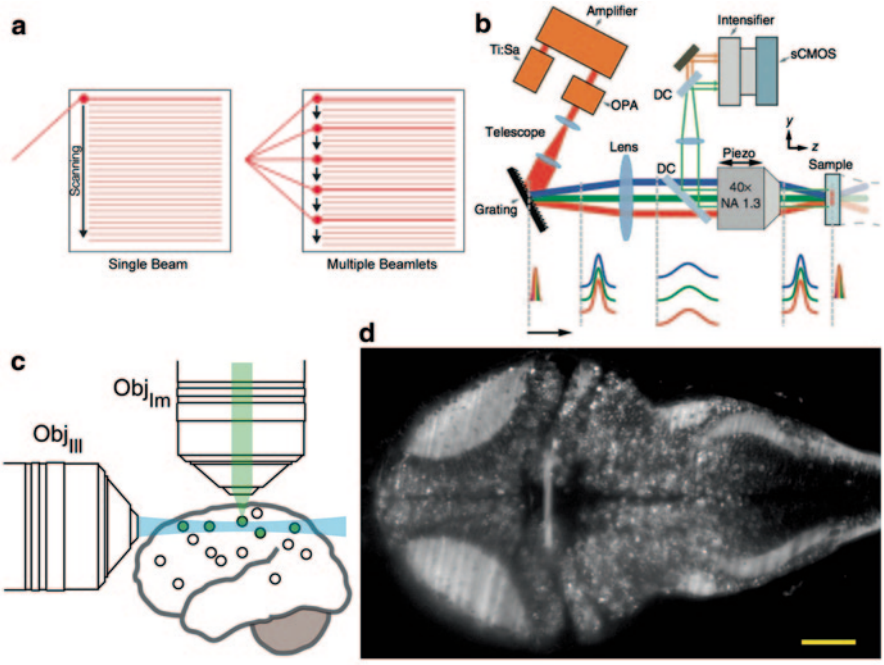

Fig. 4.6 Microscopy techniques for voltage imaging. **a** In simple DOE-based multifocal multiphoton illumination, the illumination source is split into multiple "beamlets" that are scanned in parallel at a fixed distance from one another. The resulting increase in sample coverage during a single scan decreases the time required to image a single frame. **b** In WF-TeFo, a diffraction grating is used to spatiotemporally disperse the chromatic components of a femtosecond pulsed laser beam in the illumination path. The pulses are recombined by the illumination objective only at the imaged focal plane, allowing optical sectioning with axial resolution similar to that of TPLSM. Colored traces at the *bottom* of the panel illustrate pulse dispersion at different points in the optical series. *OPA*, optical parametric amplifier; *DC*, dichroic mirror; *Ti:Sa*, titanium–sapphire oscillator. **c** In light-sheet microscopy, an illumination objective (Obj_{Ill}) creates a thin sheet of light (depicted from the side) that illuminates an entire field of view simultaneously. An orthogonally oriented imaging objective (Obj_{Im}) collects fluorescence signals from every cell lying within that plane simultaneously. **d** The resulting images—in this case, of Arch fluorescence throughout the entire lateral extent of a larval zebrafish brain—can be acquired very quickly (here, 10 ms) with axial resolution comparable to that of TPLSM. Scale bar = 100 μm. Panel **a** is from Watson et al. [111]. Panel **b** is from Schrodel et al. [116]

Permutations of this technique, referred to variously as multiline TPLSM, multifocal multiphoton fluorescence microscopy, or DOE scanning microscopy, employ a variety of techniques to split a high-intensity pulsed laser beam into a number of lower-intensity beamlets. Early permutations used microlens arrays [108] or combinations of high-reflection mirrors and 50–50 beamsplitters [109, 110] to create these beamlets. More recently, diffractive optical elements (DOEs) and spatial light modulators (SLMs) have been used to accomplish the same thing [111, 112]. In all cases, a detector with multiple, spatially separated sensors—such as a camera

or photodiode array—must be used to measure light from different sample locations simultaneously, in contrast to the single-element PMTs and photodiodes that are traditionally used in TPLSM. The improvement of electron multiplying charge-coupled device (EMCCD) and scientific complementary metal oxide semiconductor (sCMOS) cameras over the last decade has provided a number of options that are both fast and sensitive enough for voltage imaging [113]. Because the femtosecond lasers that are now common in multiphoton microscopy emit more than 100× the amount of light needed to excite a typical voxel, the beam can be split significantly. In combination with resonant scanning galvo mirrors, it is easily conceivable that this technique could enable fast voltage imaging with 100–200 line resolution.

A related and recently developed technique uses spatial light SLMs as the basis of a form of "scanless" multiphoton microscopy. SLMs essentially act as a dynamically shaped, two-dimensional diffraction grating, which allows one to sculpt the laser illumination source into arbitrary patterns that are then imaged onto the specimen without mechanical scanning. The elimination of scanning allows the acquisition rate to be determined entirely by the detector speed and the intensity of the fluorescence signal, and the ability to illuminate arbitrary patterns allows recordings to target only the desired regions of the sample, without subjecting irrelevant areas to unnecessary light exposure. Light intensity considerations are more significant than with static DOE imaging because of the typically greater degree of beam diffraction, but the technique has been used to dramatic effect in imaging calcium dynamics and precisely targeting multiple, spatially separated neurons for photoactivation in mouse brain slices [12, 114].

A second "scanless" form of multiphoton imaging, called wide-field temporal focusing (WF-TeFo), is based on the phenomenon of pulse dispersion. The lasers used in TPLSM emit light in discrete, high-frequency pulses of around 100 fs in duration, which are necessary to ensure a sufficiently high probability of individual fluorophores absorbing two photons simultaneously. These pulses can become temporally broadened due to interactions with incident surfaces in the illumination path of the microscope. This phenomenon, called dispersion, is an unavoidable and usually undesirable artifact of real optical elements that microscope designers make explicit efforts to compensate for. However, in WF-TeFo, dispersion is exploited to eliminate the need for scanning in multiphoton microscopy (Fig. 4.6b). Reflecting the illumination light off of a diffraction grating at a plane conjugate to the sample laterally disperses the spectral components of the beam and reduces their temporal overlap [115]. A lens recollimates the diffracted beam and relays it to the back aperture of the imaging objective. The spectral components are then recombined in space and time as they come to a focus at the sample plane. The resulting illumination pattern will have an approximately Gaussian profile with lateral dimensions that can be controlled by changing the initial beam size, and axial resolution similar to that of TPLSM. This technique has been used to rapidly image calcium signals throughout the entire *C. elegans* brain, employing a 60-μm-diameter illumination pattern and a fast camera [116]. In its published implementations, this technique has employed a regenerative amplifier and optical parametric amplifier to increase the peak pulse intensity and tune the illumination wavelength. It is not clear whether more conventional light sources would suffice.

4.5.3 Planar Illumination Microscopy

An imaging technique that has generated an enormous amount of recent interest is planar illumination microscopy. Variously referred to as single- or selective-plane illumination microscopy (SPIM), light-sheet microscopy, or by one of a host of acronyms denoting specialized implementations of the technique, the basic principles of this imaging modality are quite simple. In SPIM, the sample is illuminated using a thin sheet of light that is generated by an optical system oriented orthogonal to the microscope's imaging axis (Fig. 4.6c). This sheet can be created virtually, by rapidly scanning an illumination beam back and forth across the Y-axis of the image plane at several kilohertz or using cylindrical lenses. Its most important features are that it can be quite thin, in the order of a couple of microns at its waist, and that by illuminating an entire image plane simultaneously, the acquisition rate is again limited only photon budget and camera speed.

Planar illumination has been used most intensively in developmental biology experiments where the goal is to image an entire, developing organism over time with cellular resolution [117, 118]. Samples larger than a few hundred microns require significant modifications of the basic technique to combat the effects of scattering of the illumination beam and of the emitted light. These include sequential illumination and imaging from multiple angles [119], use of an angular positioner to rotate the sample into different orientations, and the use of two-photon [120] and/or Bessel beam [121] illumination. Bessel beam and Airy beam [122] illumination also extends the maximum field of view that can be imaged at one time. The images generated with these techniques are often spectacular and have deservedly prompted widespread adoption for fast, four-dimensional imaging in model organisms.

Neuroscience applications have included high-throughput morphological imaging of entire fixed and cleared mouse brains [123] and rapid calcium imaging in brain slices [124]. A recent paper used SPIM to record calcium dynamics in nearly every neuron in the larval zebrafish at the impressive rate of 0.8 Hz (i.e., for the entire brain; [125]). For spike-resolved voltage imaging, such volumetric recordings are clearly not achievable in the immediate future, but SPIM seems ideally suited to imaging high-speed electrical signals in single planes. We have built a SPIM microscope that applies both single-photon and 2P illumination to functional imaging in transgenic zebrafish, and we are optimistic about its potential to resolve single action potentials in cells throughout the brain (Fig. 4.6d). Unfortunately, it is not clear how useful this imaging method will be for *in vivo* mammalian experiments, where the presence of the skull and the large size of the brain make orthogonal illumination difficult.

4.6 Conclusions—Why it is Worth the Effort

Voltage imaging techniques have clearly been the subject of an extreme amount of effort over the last several decades. For all that, it is worth reflecting on the reasons it has commanded such sustained interest, and why it is worth our collective energy to push these last few steps toward widespread adoption.

For many practical reasons, calcium imaging will continue to be the de facto mode of optical activity recording in the immediate future. Some of this is due to simple inertia, as it takes time for new molecular reagents to be disseminated and utilized across the various subfields of neuroscience, and for microscope vendors to develop "turnkey" systems that allow users to avoid investing their time in instrumentation and technique development. It is also true that, unlike with calcium imaging, where the GCaMP family of reporters has become the undisputed standard set of reagents, we have yet to settle on a "best" voltage indicator. Many researchers are simply waiting to see which reagents gain widespread adoption before committing to a given method. A more fundamental issue, however, is that from an optical standpoint, calcium imaging is simply a better choice for most applications. The signals generated by the current generation of GCaMPs are much easier to detect than those of the latest Arch, Arclight, and ASAP-derived tools. For instance, the "slow" version of GCaMP6 exhibits a peak dF/F of nearly 30% in response to a single spike in a cultured neuron, with temporally filtered kinetics that eliminate the need to image at high frame rates [15]. The response increases to nearly 500% for a burst of 10 action potentials. Additionally, as variants of GFP, these indicators are readily compatible with all standard forms of fluorescence microscopy and require little in the way of instrumentation to employ on existing setups. If one's biological interest is simply in whether or not a given neuron fires under certain conditions, chances are good that calcium imaging is the best approach to use.

While that level of analysis suffices for many areas of investigation, there are of course many questions that require more detail. Calcium flux is an imperfect proxy for electrical activity. Not all neurons exhibit measurable calcium transients during an action potential, and most forms of subthreshold activity do not result in measurable calcium influx. Calcium falls especially short in reporting inhibitory activity, as membrane hyperpolarization will only be apparent if it causes a reduction in spike rates on the timescale of the recording. Low baseline firing rates may make it impossible to detect such changes. Last, while indicator kinetics are still a major source of temporal filtering in calcium imaging, the nature of the calcium transient itself ensures that very high-speed information about neuronal spiking will never be captured well by calcium imaging [14].

If the experimental question requires information about activity that does not result in a calcium spike, or about a neuron's fast electrical dynamics, then the methodological choice is between voltage imaging and an electrode-based measurement. The parallelism enabled by imaging creates a number of intriguing possibilities as large-ensemble voltage recordings become a reality. First, it will allow us to study in great detail network oscillations and other fast, coordinated phenomena. Second, it will allow direct measurement of temporally precise plasticity mechanisms such as spike-timing-dependent plasticity, and experimental evidence for how the large number of interacting neurons in a network work together to regulate such processes. Third, it will dramatically increase the precision with which connectivity can be inferred from population recordings, both from correlation analyses and in pump-probe experiments involving the simultaneous use of photoactivation and population imaging. And fourth, it will allow us to better define the physiology of

such interactions by learning whether they are excitatory, inhibitory, or modulatory in nature. Together, these types of measurements will fundamentally change the way we study the brain. Electrical activity might be just one facet of neuronal function, but it is certainly an important one.

References

1. Cohen, L. B., Keynes, R. D., & Hille, B. (1968). Light scattering and birefringence changes during nerve activity. *Nature, 218,* 438–441.
2. Boyden, E. S., Zhang, F., Bamberg, E., Nagel, G., & Deisseroth, K. (2005). Millisecond-timescale genetically targeted optical control of neural activity. *Nature Neuroscience, 8,* 1263–1268.
3. Miesenbock, G., De Angelis, D. A., & Rothman, J. E. (1998). Visualizing secretion and synaptic transmission with pH-sensitive green fluorescent proteins. *Nature, 394,* 192–195.
4. Fenno, L., Yizhar, O., & Deisseroth, K. (2011). The development and application of optogenetics. *Annual Review of Neuroscience, 34,* 389–412.
5. Klapoetke, N. C., et al. (2014). Independent optical excitation of distinct neural populations. *Nature Methods, 11,* 338–346.
6. Lin, J. Y., Knutsen, P. M., Muller, A., Kleinfeld, D., & Tsien, R. Y. (2013). ReaChR: A red-shifted variant of channelrhodopsin enables deep transcranial optogenetic excitation. *Nature Neuroscience, 16,* 1499–1508.
7. Prakash, R., et al. (2012). Two-photon optogenetic toolbox for fast inhibition, excitation and bistable modulation. *Nature Methods, 9,* 1171–1179.
8. Berndt, A., Yizhar, O., Gunaydin, L. A., Hegemann, P., & Deisseroth, K. (2009). Bi-stable neural state switches. *Nature Neuroscience, 12,* 229–234.
9. Gunaydin, L. A., et al. (2010). Ultrafast optogenetic control. *Nature Neuroscience, 13,* 387–392.
10. Berndt, A., Lee, S. Y., Ramakrishnan, C., & Deisseroth, K. (2014). Structure-guided transformation of channelrhodopsin into a light-activated chloride channel. *Science, 344,* 420–424.
11. Wietek, J., et al. (2014). Conversion of channelrhodopsin into a light-gated chloride channel. *Science, 344,* 409–412.
12. Packer, A. M., et al. (2012). Two-photon optogenetics of dendritic spines and neural circuits. *Nature Methods, 9,* 1202–1205.
13. Miyawaki, A., et al. (1997). Fluorescent indicators for Ca2+ based on green fluorescent proteins and calmodulin. *Nature, 388,* 882–887.
14. Looger, L. L., & Griesbeck, O. (2012). Genetically encoded neural activity indicators. *Current Opinion in Neurobiology, 22,* 18–23.
15. Chen, T. W., et al. (2013). Ultrasensitive fluorescent proteins for imaging neuronal activity. *Nature, 499,* 295–300.
16. Akerboom, J., et al. (2013). Genetically encoded calcium indicators for multi-color neural activity imaging and combination with optogenetics. *Frontiers in Molecular Neuroscience, 6,* 2.
17. Wu, J., et al. (2013). Improved orange and red Ca(2)+/− indicators and photophysical considerations for optogenetic applications. *ACS Chemical Neuroscience, 4,* 963–972.
18. Ponsioen, B., et al. (2004). Detecting cAMP-induced Epac activation by fluorescence resonance energy transfer: Epac as a novel cAMP indicator. *EMBO Reports, 5,* 1176–1180.
19. Klockow, J. L., Hettie, K. S., & Glass, T. E. (2013). ExoSensor 517: A dual-analyte fluorescent chemosensor for visualizing neurotransmitter exocytosis. *ACS Chemical Neuroscience, 4,* 1334–1338.

20. Marvin, J. S., et al. (2013). An optimized fluorescent probe for visualizing glutamate neurotransmission. *Nature Methods, 10,* 162–170.
21. Carter, M. E., Soden, M. E., Zweifel, L. S., & Palmiter, R. D. (2013). Genetic identification of a neural circuit that suppresses appetite. *Nature, 503,* 111–114.
22. Lammel, S., et al. (2012). Input-specific control of reward and aversion in the ventral tegmental area. *Nature, 491,* 212–217.
23. Stuber, G. D., et al. (2011). Excitatory transmission from the amygdala to nucleus accumbens facilitates reward seeking. *Nature, 475,* 377–380.
24. Sjulson, L., & Miesenbock, G. (2007). Optical recording of action potentials and other discrete physiological events: A perspective from signal detection theory. *Physiology, 22,* 47–55.
25. Hill, D. K., & Keynes, R. D. (1949). Opacity changes in stimulated nerve. *The Journal of Physiology, 108,* 278–281.
26. Cohen, L. B., & Keynes, R. D. (1969). Optical changes in the voltage-clamped squid axon. *The Journal of Physiology, 204,* 100P+.
27. Kim, G. H., Kosterin, P., Obaid, A. L., & Salzberg, B. M. (2007). A mechanical spike accompanies the action potential in Mammalian nerve terminals. *Biophysical Journal, 92,* 3122–3129.
28. Altig, J. A., Wesenberg, G. E., & Vaughan, W. E. (1986). Dielectric behavior of polyelectrolytes. IV. Electric polarizability of rigid biopolymers in electric fields. *Biophysical Chemistry, 24,* 221–234.
29. Kosterin, P., Obaid, A. L., & Salzberg, B. M. (2010). Long-lasting intrinsic optical changes observed in the neurointermediate lobe of the mouse pituitary reflect volume changes in cells of the pars intermedia. *Neuroendocrinology, 92,* 158–167.
30. Salzberg, B. M., Muschol, M., Kosterin, P., & Obaid, A. L. (2012). Measuring intrinsic optical signals from mammalian nerve terminals. *Cold Spring Harbor protocols, 2012*(12), pdb.prot072355.
31. Tasaki, I., Watanabe, A., Sandlin, R., & Carnay, L. (1968). Changes in fluorescence, turbidity, and birefringence associated with nerve excitation. *Proceedings of the National Academy of Sciences of the United States of America, 61,* 883–888.
32. Cohen, L. B. (1973). Changes in neuron structure during action potential propagation and synaptic transmission. *Physiological Reviews, 53,* 373–418.
33. Tasaki, I. I., Carnay, L., & Watanabe, A. (1969). Transient changes in extrinsic fluorescence of nerve produced by electric stimulation. *Proceedings of the National Academy of Sciences of the United States of America, 64,* 1362–1368.
34. Davila, H. V., Salzberg, B. M., Cohen, L. B., & Waggoner, A. S. (1973). A large change in axon fluorescence that provides a promising method for measuring membrane potential. *Nature: New Biology, 241,* 159–160.
35. Salzberg, B. M., Davila, H. V., Cohen, L. B. (1973). Optical recording of impulses in individual neurones of an invertebrate central nervous system. *Nature, 246,* 508–509.
36. Dragsten, P. R., & Webb, W. W. (1978). Mechanism of the membrane potential sensitivity of the fluorescent membrane probe merocyanine 540. *Biochemistry, 17,* 5228–5240.
37. Loew, L. M., Bonneville, G. W., & Surow, J. (1978). Charge shift optical probes of membrane potential. Theory. *Biochemistry, 17,* 4065–4071.
38. Yan, P., et al. (2012). Palette of fluorinated voltage-sensitive hemicyanine dyes. *Proceedings of the National Academy of Sciences of the United States of America, 109,* 20443–20448.
39. Fluhler E, Burnham VG, Loew LM. (1985). Spectra, membrane binding, and potentiometric responses of new charge shift probes. *Biochemistry*. *24,* 5749–5755.
40. Loew LM, Cohen LB, Dix J, Fluhler EN, Montana V, Salama G, Wu JY. (1992). A naphthyl analog of the aminostyryl pyridinium class of potentiometric membrane dyes shows consistent sensitivity in a variety of tissue, cell, and model membrane preparations. *J Membr Biol. 130,* 1–10.
41. Khazipov, R., Minlebaev, M., & Valeeva, G. (2013). Early gamma oscillations. *Neuroscience, 250,* 240–252.

42. Middleton, S. J., et al. (2008). High-frequency network oscillations in cerebellar cortex. *Neuron, 58,* 763–774.
43. Airan, R. D., et al. (2007). High-speed imaging reveals neurophysiological links to behavior in an animal model of depression. *Science, 317,* 819–823.
44. Kuhn, B., Denk, W., & Bruno, R. M. (2008). In vivo two-photon voltage-sensitive dye imaging reveals top-down control of cortical layers 1 and 2 during wakefulness. *Proceedings of the National Academy of Sciences of the United States of America, 105,* 7588–7593.
45. Blasdel, G. G., & Salama, G. (1986). Voltage-sensitive dyes reveal a modular organization in monkey striate cortex. *Nature, 321,* 579–585.
46. Lim, D. H., et al.(2012). In vivo large-scale cortical mapping using channelrhodopsin-2 stimulation in transgenic mice reveals asymmetric and reciprocal relationships between cortical areas. *Frontiers in Neural Circuits, 6,* 11.
47. Mohajerani, M. H., et al. (2013). Spontaneous cortical activity alternates between motifs defined by regional axonal projections. *Nature Neuroscience, 16,* 1426–1435.
48. Lim, D. H., Ledue, J., Mohajerani, M. H., Vanni, M. P., & Murphy, T. H. (2013). Optogenetic approaches for functional mouse brain mapping. *Frontiers in Neuroscience, 7,* 54.
49. Grinvald, A., Ross, W. N., & Farber, I. (1981). Simultaneous optical measurements of electrical activity from multiple sites on processes of cultured neurons. *Proceedings of the National Academy of Sciences of the United States of America, 78,* 3245–3249.
50. Staub, C., De Schutter, E., & Knopfel, T. (1994). Voltage-imaging and simulation of effects of voltage- and agonist-activated conductances on soma-dendritic voltage coupling in cerebellar Purkinje cells. *Journal of Computational Neuroscience, 1,* 301–311.
51. Wu, J. Y., Cohen, L. B., & Falk, C. X. (1994). Neuronal activity during different behaviors in Aplysia: A distributed organization? *Science, 263,* 820–823.
52. Stadele, C., Andras, P., & Stein, W. (2012). Simultaneous measurement of membrane potential changes in multiple pattern generating neurons using voltage sensitive dye imaging. *Journal of Neuroscience Methods, 203,* 78–88.
53. Hill, E. S., Vasireddi, S. K., Bruno, A. M., Wang, J., & Frost, W. N. (2012). Variable neuronal participation in stereotypic motor programs. *PloS One, 7,* e40579.
54. Chalfie, M., Tu, Y., Euskirchen, G., Ward, W. W., & Prasher, D. C. (1994). Green fluorescent protein as a marker for gene expression. *Science, 263,* 802–805.
55. Brejc, K., et al. (1997). Structural basis for dual excitation and photoisomerization of the Aequorea victoria green fluorescent protein. *Proceedings of the National Academy of Sciences of the United States of America, 94,* 2306–2311.
56. Chattoraj, M., King, B. A., Bublitz, G. U., & Boxer, S. G. (1996). Ultra-fast excited state dynamics in green fluorescent protein: Multiple states and proton transfer. *Proceedings of the National Academy of Sciences of the United States of America, 93,* 8362–8367.
57. Griesbeck, O., Baird, G. S., Campbell, R. E., Zacharias, D. A., & Tsien, R. Y. (2001). Reducing the environmental sensitivity of yellow fluorescent protein. Mechanism and applications. *The Journal of Biological Chemistry, 276,* 29188–29194.
58. Carnie, S., & McLaughlin, S. (1983). Large divalent cations and electrostatic potentials adjacent to membranes. A theoretical calculation. *Biophysical Journal, 44,* 325–332.
59. Siegel, M. S., & Isacoff, E. Y. (1997). A genetically encoded optical probe of membrane voltage. *Neuron, 19,* 735–741.
60. Ahrens, K. F., Heider, B., Lee, H., Isacoff, E. Y., & Siegel, R. M. (2012). Two-photon scanning microscopy of in vivo sensory responses of cortical neurons genetically encoded with a fluorescent voltage sensor in rat. *Frontiers in Neural Circuits, 6,* 15.
61. Ataka, K., & Pieribone, V. A. (2002). A genetically targetable fluorescent probe of channel gating with rapid kinetics. *Biophysical Journal, 82,* 509–516.
62. Sakai, R., Repunte-Canonigo, V., Raj, C. D., & Knopfel, T. (2001). Design and characterization of a DNA-encoded, voltage-sensitive fluorescent protein. *The European Journal of Neuroscience, 13,* 2314–2318.
63. Kohout, S. C., et al. (2010). Electrochemical coupling in the voltage-dependent phosphatase Ci-VSP. *Nature Chemical Biology, 6,* 369–375.

64. Kohout, S. C., Ulbrich, M. H., Bell, S. C., & Isacoff, E. Y. (2008). Subunit organization and functional transitions in Ci-VSP. *Nature Structural & Molecular Biology, 15,* 106–108.
65. Chanda, B., et al. (2005). A hybrid approach to measuring electrical activity in genetically specified neurons. *Nature Neuroscience, 8,* 1619–1626.
66. Sjulson, L., & Miesenbock, G. (2008). Rational optimization and imaging in vivo of a genetically encoded optical voltage reporter. *The Journal of Neuroscience: The Official Journal of the Society for Neuroscience, 28,* 5582–5593.
67. Wang, D., Zhang, Z., Chanda, B., & Jackson, M. B. (2010). Improved probes for hybrid voltage sensor imaging. *Biophysical Journal, 99,* 2355–2365.
68. Wang, D., McMahon, S., Zhang, Z., & Jackson, M. B. (2012). Hybrid voltage sensor imaging of electrical activity from neurons in hippocampal slices from transgenic mice. *Journal of Neurophysiology, 108,* 3147–3160.
69. Murata, Y., Iwasaki, H., Sasaki, M., Inaba, K., & Okamura, Y. (2005). Phosphoinositide phosphatase activity coupled to an intrinsic voltage sensor. *Nature, 435,* 1239–1243.
70. Dimitrov, D., et al. (2007). Engineering and characterization of an enhanced fluorescent protein voltage sensor. *PloS One, 2,* e440.
71. Akemann, W., et al. (2012). Imaging neural circuit dynamics with a voltage-sensitive fluorescent protein. *Journal, of Neurophysiology, 108,* 2323–2337.
72. Mishina, Y., Mutoh, H., & Knopfel, T. (2012). Transfer of Kv3.1 voltage sensor features to the isolated Ci-VSP voltage-sensing domain. *Biophysical Journal, 103,* 669–676.
73. Perron, A., Mutoh, H., Launey, T., & Knopfel, T. (2009). Red-shifted voltage-sensitive fluorescent proteins. *Chemistry & Biology, 16,* 1268–1277.
74. Tsutsui, H., Karasawa, S., Okamura, Y., & Miyawaki, A. (2008). Improving membrane voltage measurements using FRET with new fluorescent proteins. *Nature Methods, 5,* 683–685.
75. Akemann, W., et al. (2013). Two-photon voltage imaging using a genetically encoded voltage indicator. *Scientific Reports, 3,* 2231.
76. Marmor, M. F., & Martin, L. J. (1978). 100 years of the visual cycle. *Survey of Ophthalmology, 22,* 279–285.
77. Zhang, F., et al. (2011). The microbial opsin family of optogenetic tools. *Cell, 147,* 1446–1457.
78. Spudich, J. L., Sineshchekov, O. A., & Govorunova, E. G. (2014). Mechanism divergence in microbial rhodopsins. *Biochimica et biophysica acta, 1837,* 546–552.
79. Kolodner, P., Lukashev, E. P., Ching, Y. C., & Rousseau, D. L. (1996). Electric-field-induced Schiff-base deprotonation in D85 N mutant bacteriorhodopsin. *Proceedings of the National Academy of Sciences of the United States of America, 93,* 11618–11621.
80. Guzzo, A. V., & Pool, G. L. (1968). Visual pigment fluorescence. *Science, 159,* 312–314.
81. Lenz, M. O., et al. (2006). First steps of retinal photoisomerization in proteorhodopsin. *Biophysical Journal, 91,* 255–262.
82. Kralj, J. M., Hochbaum, D. R., Douglass, A. D., & Cohen, A. E. (2011). Electrical spiking in Escherichia coli probed with a fluorescent voltage-indicating protein. *Science, 333,* 345–348.
83. Beja, O., Spudich, E. N., Spudich, J. L., Leclerc, M., & DeLong, E. F. (2001). Proteorhodopsin phototrophy in the ocean. *Nature, 411,* 786–789.
84. Gradinaru, V., et al. (2010). Molecular and cellular approaches for diversifying and extending optogenetics. *Cell, 141,* 154–165.
85. Chow, B. Y., et al. (2010). High-performance genetically targetable optical neural silencing by light-driven proton pumps. *Nature, 463,* 98–102.
86. Kralj, J. M., Douglass, A. D., Hochbaum, D. R., Maclaurin, D., & Cohen, A. E. (2012). Optical recording of action potentials in mammalian neurons using a microbial rhodopsin. *Nature Methods, 9,* 90–95.
87. Hochbaum, D. R., et al. (2014). All-optical electrophysiology in mammalian neurons using engineered microbial rhodopsins. *Nature Methods, 11,* 825–833.
88. Park, J., et al. (2013). Screening fluorescent voltage indicators with spontaneously spiking HEK cells. *PloS One, 8,* e85221.

89. Gong, Y., Li, J. Z., & Schnitzer, M. J. (2013). Enhanced archaerhodopsin fluorescent protein voltage indicators. *PloS One, 8,* e66959.
90. Maclaurin, D., Venkatachalam, V., Lee, H., & Cohen, A. E. (2013). Mechanism of voltage-sensitive fluorescence in a microbial rhodopsin. *Proceedings of the National Academy of Sciences of the United States of America, 110,* 5939–5944.
91. Gong, Y., Wagner, M. J., Zhong Li, J., & Schnitzer, M. J. (2014). Imaging neural spiking in brain tissue using FRET-opsin protein voltage sensors. *Nature Communications, 5,* 3674.
92. Zou, P., et al. (2014) Bright and fast multicoloured voltage reporters via electrochromic FRET. *Nature Communications, 5,* 4625.
93. Jin, L., et al. (2012). Single action potentials and subthreshold electrical events imaged in neurons with a fluorescent protein voltage probe. *Neuron, 75,* 779–785.
94. Cao, G., et al. (2013). Genetically targeted optical electrophysiology in intact neural circuits. *Cell, 154,* 904–913.
95. Han, Z., et al. (2013). Fluorescent protein voltage probes derived from ArcLight that respond to membrane voltage changes with fast kinetics. *PloS One, 8,* e81295.
96. Baird, G. S., Zacharias, D. A., & Tsien, R. Y. (1999). Circular permutation and receptor insertion within green fluorescent proteins. *Proceedings of the National Academy of Sciences of the United States of America, 96,* 11241–11246.
97. Li, Q., et al. (2014). Structural mechanism of voltage-dependent gating in an isolated voltage-sensing domain. *Nature, Structural & Molecular Biology, 21,* 244–252.
98. Knopfel, T., Diez-Garcia, J., & Akemann, W. (2006). Optical probing of neuronal circuit dynamics: Genetically encoded versus classical fluorescent sensors. *Trends in Neurosciences, 29,* 160–166.
99. Baker, B. J., et al. (2007). Three fluorescent protein voltage sensors exhibit low plasma membrane expression in mammalian cells. *Journal of Neuroscience Methods, 161,* 32–38.
100. Drobizhev, M., Makarov, N. S., Tillo, S. E., Hughes, T. E., & Rebane, A. (2011). Two-photon absorption properties of fluorescent proteins. *Nature Methods, 8,* 393–399.
101. Denk, W., Strickler, J. H., & Webb, W. W. (1990). Two-photon laser scanning fluorescence microscopy. *Science, 248,* 73–76.
102. Mainen, Z. F., et al. (1999). Two-photon imaging in living brain slices. *Methods, 18*(231–239), 181.
103. Bonin, V., Histed, M. H., Yurgenson, S., & Reid, R. C. (2011). Local diversity and fine-scale organization of receptive fields in mouse visual cortex. *The Journal of Neuroscience: The Official Journal of the Society for Neuroscience, 31,* 18506–18521.
104. Fan, G. Y., et al. (1999). Video-rate scanning two-photon excitation fluorescence microscopy and ratio imaging with cameleons. *Biophysical Journal, 76,* 2412–2420.
105. Nguyen, Q. T., Callamaras, N., Hsieh, C., & Parker, I. (2001). Construction of a two-photon microscope for video-rate Ca(2 +) imaging. *Cell Calcium, 30,* 383–393.
106. Dombeck, D. A., Sacconi, L., Blanchard-Desce, M., & Webb, W. W. (2005). Optical recording of fast neuronal membrane potential transients in acute mammalian brain slices by second-harmonic generation microscopy. *Journal of Neurophysiology, 94,* 3628–3636.
107. Fink, A. E., Bender, K. J., Trussell, L. O., Otis, T. S., & DiGregorio, D. A. (2012). Two-photon compatibility and single-voxel single-trial detection of subthreshold neuronal activity by a two-component optical voltage sensor. *PloS One, 7,* e41434.
108. Bewersdorf, J., Pick, R., & Hell, S. W. (1998). Multifocal multiphoton microscopy. *Optics Letters, 23,* 655–657.
109. Kurtz, R., Fricke, M., Kalb, J., Tinnefeld, P., & Sauer, M. (2006). Application of multiline two-photon microscopy to functional in vivo imaging. *Journal of Neuroscience Methods, 151,* 276–286.
110. Nielsen, T., Fricke, M., Hellweg, D., & Andresen, P. (2001). High efficiency beam splitter for multifocal multiphoton microscopy. *Journal of Microscopy, 201,* 368–376.
111. Watson, B. O., et al. (2010). Two-photon microscopy with diffractive optical elements and spatial light modulators. *Frontiers in Neuroscience, 4,* 29.

112. Watson, B. O., Nikolenko, V., & Yuste, R. (2009). Two-photon imaging with diffractive optical elements. *Frontiers in Neural Circuits, 3,* 6.
113. Lambert, T. J., & Waters, J. C. (2014). Assessing camera performance for quantitative microscopy. *Methods in Cell Biology, 123,* 35–53.
114. Gandolfi, D., et al. (2014). The spatiotemporal organization of cerebellar network activity resolved by two-photon imaging of multiple single neurons. *Frontiers in Cellular Neuroscience, 8,* 92.
115. Zhu, G., van Howe, J., Durst, M., Zipfel, W., & Xu, C. (2005). Simultaneous spatial and temporal focusing of femtosecond pulses. *Optics Express, 13,* 2153–2159.
116. Schrodel, T., Prevedel, R., Aumayr, K., Zimmer, M., & Vaziri, A. (2013). Brain-wide 3D imaging of neuronal activity in Caenorhabditis elegans with sculpted light. *Nature Methods, 10,* 1013–1020.
117. Huisken, J., Swoger, J., Del Bene, F., Wittbrodt, J., & Stelzer, E. H. (2004). Optical sectioning deep inside live embryos by selective plane illumination microscopy. *Science, 305,* 1007–1009.
118. Keller, P. J., Schmidt, A. D., Wittbrodt, J., & Stelzer, E. H. (2008). Reconstruction of zebrafish early embryonic development by scanned light sheet microscopy. *Science, 322,* 1065–1069.
119. Keller, P. J., & Stelzer, E. H. (2008). Quantitative in vivo imaging of entire embryos with digital scanned laser light sheet fluorescence microscopy. *Current Opinion in Neurobiology, 18,* 624–632.
120. Truong, T. V., Supatto, W., Koos, D. S., Choi, J. M., & Fraser, S. E. (2011). Deep and fast live imaging with two-photon scanned light-sheet microscopy. *Nature Methods, 8,* 757–760.
121. Planchon, T. A., et al. (2011). Rapid three-dimensional isotropic imaging of living cells using Bessel beam plane illumination. *Nature Methods, 8,* 417–423.
122. Vettenburg, T., et al. (2014). Light-sheet microscopy using an airy beam. *Nature Methods, 11,* 541–544.
123. Tomer, R., Ye, L., Hsueh, B., & Deisseroth, K. (2014). Advanced CLARITY for rapid and high-resolution imaging of intact tissues. *Nature Protocols, 9,* 1682–1697.
124. Holekamp, T. F., Turaga, D., & Holy, T. E. (2008). Fast three-dimensional fluorescence imaging of activity in neural populations by objective-coupled planar illumination microscopy. *Neuron, 57,* 661–672.
125. Ahrens, M. B., Orger, M. B., Robson, D. N., Li, J. M., & Keller, P. J. (2013). Whole-brain functional imaging at cellular resolution using light-sheet microscopy. *Nature Methods, 10,* 413–420.
126. St-Pierre F, Marshall JD, Yang Y, Gong Y, Schnitzer MJ, Lin MZ. (2014). High-fidelity optical reporting of neuronal electrical activity with an ultrafast fluorescent voltage sensor. *Nat Neurosci. 17,* 884–889.
127. Hou JH, Kralj JM, Douglass AD, Engert F, Cohen AE. (2014). Simultaneous mapping of membrane voltage and calcium in zebrafish heart in vivo reveals chamber-specific developmental transitions in ionic currents. *Front Physiol. 5,* 344.

Chapter 5
Discovery and Development of Spectrally Diverse Channelrhodopsins (ChR) for Neurobiological Applications

John Y. Lin, Per M. Knutsen and Arnaud Muller

Abstract Channelrhodopsins (ChR) have become important tools for neuroscientific research, and part of an optogenetic toolbox used to excite genetically targeted neurons with light to investigate their functional and behavioral roles. As light is relatively noninvasive and light-induced excitation only occurs in neurons expressing ChR, this approach can be used to perform circuit mapping experiments and modulate behavior in awake animals in ways not possible using pharmacological agents or electrical stimulation. The majority of current ChR experiments utilize blue-light-activated variants and short blue light pulses (1–10 ms) for excitation. The recent discovery and reengineering of red-shifted ChR variants have permitted excitation of neurons with orange and red light ($\lambda > 600$ nm). These developments have extended the utility of optogenetic experiments to permit novel, noninvasive behavioral screening and the investigation of complex neuronal circuit interactions. This chapter discusses recent developments and applications of red-shifted ChRs in neurobiological research and how these novel ChR variants are having an important impact on biological discovery.

J. Y. Lin (✉)
University of Tasmania, Private Bag 23, 7000 Hobart, Tasmania, Australia
e-mail: john.lin@utas.edu.au

P. M. Knutsen · A. Muller
Department of Physics, Section of Neurobiology, University of California, 9500 Gilman Drive, 92093-0374 San Diego, CA, USA
e-mail: pknutsen@physics.ucsd.edu

A. Muller
e-mail: amuller@physics.ucsd.edu

A. D. Douglass (ed.), *New Techniques in Systems Neuroscience,* Biological and Medical Physics, Biomedical Engineering, DOI 10.1007/978-3-319-12913-6_5

5.1 Introduction

5.1.1 Channelrhodopsin (ChR)-Based Optogenetics

The light-activated, nonselective cation channel channelrhodopsin (ChR) has become an important tool in neuroscience since its discovery in green algae [40, 41]. The ectopic expression of these channels renders neurons responsive to pulsed light, which can be used to trigger action potentials on a millisecond time scale [10, 40, 42]. This approach, along with other light-mediated tools for manipulating cellular activities, has been labeled optogenetics [39]. Optogenetic approaches using ChRs have been applied extensively to the study of neuronal circuit analysis [9, 22, 27, 32, 46, 65] and have also been adapted for the study of other electrically active biological systems [2, 11, 42].

The principal reason for the popularity of optogenetic strategies using ChRs is their relative simplicity. The general approach requires the expression of a single transgene that is under 1100 bps and produces a protein that is under 40 kDa (without a fluorescent protein marker) [40, 41]. In rodent models, this permits expression using recombinant viruses without the need to generate transgenic animals, which dramatically reduces investments in time and labor. Furthermore, supra-threshold excitation of neurons by ChRs can be achieved in the millisecond time range, much faster than pharmacological approaches, permitting investigation of fast synaptic and behavioral events. In mammalian tissues, the chromophore required for ChRs, all-trans retinal, is endogenously present as a retinoid (vitamin A). Although all-trans retinal may need to be introduced in *Drosophila melanogaster* [26] and *C. elegans* [42], this chromophore is commercially available at low cost. In comparison, the azobenzene-based MAG chromophore required for the alternative optogenetic excitatory LiGluR approach is not commercially available and needs to be synthesized for individual experiments [18, 52].

Although ChR technology is readily accessible, users need to be wary of important biophysical and photophysical properties of ChRs that will influence the outcome and appropriateness for any given experiment. Such properties include channel conductance, ion selectivity, channel kinetics, desensitization, and recovery from the desensitization (i.e., loss of response after initial stimulation and the recovery of the lost response), light sensitivity, spectral response, membrane trafficking, and expression [33]. Ideally, the ChR chosen for any given application has high conductance, specific ion selectivity, fast kinetics, high light sensitivity, a narrow and distinct spectral response, and good membrane trafficking and expression. Some of these properties are biophysically interrelated, and it may be difficult to select for one without compromising the others [33, 34]. While many of these properties are candidates for improvement, this chapter will focus on the recent discovery and development of unique spectral properties.

5.2 Performing Optogenetics with Blue Light

5.2.1 The Development of Blue-Light-Activated Channelrhodopsins (ChR)

The first ChR used in a neuroscientific application was ChR2 from the algae *Chlamydomonas reinhardtii* [40, 41]. The most common, engineered variant of ChR, denoted hChR2(HR) or hChR2(H134R), was subsequently generated by codon optimization and substitution of arginine for the histidine residue at position 134 (Fig. 5.1a, b, c, and d). Human codon optimization increased the expression of this ChR2 in mammalian cells [19], and the H134R mutation increased the photocurrent by altering ion selectivity [42] and reduced desensitization [34, 42]. However, this point mutation also slowed down the kinetics of the channel compared to the original ChR2 [34]. At present, the hChR2(HR) variant remains widely used despite improvements introduced by more recently developed tools [7, 34, 37]. Although hChR2(HR) is sufficient for most applications, its widespread adoption is also due in part to the commercial availability of viruses carrying the hChR2(HR) transgene at several vector core services, as well as the existence of transgenic animals [68] and extensive practical information on its use.

In addition to hChR2(H134R), there are several alternative ChR variants that offer specific improvements [6, 21, 30]. The ChETA [21] and CatCh [30] variants exhibit small improvements in kinetics and ion selectivity, respectively, but these advantages come at the cost of reduced photocurrent amplitude (ChETA) and slowed channel kinetics (CatCh) [34]. These tools have not been widely adopted, due to limited commercial availability of viral systems for their delivery as well as the limited benefits they provide over the first-generation ChRs. Although many variants are based on point mutations in the hChR2 template, versions based on chimeras of *Chlamydomonas* ChR1 and ChR2 tend to result in more significant biophysical changes [34, 58, 61]. One such chimera, ChIEF [34], exhibits improved membrane trafficking, reduced desensitization, as well as faster kinetics compared to hChR2(H134R) [34, 35, 37] (Fig. 5.1a, b, c, d). The non-codon-optimized ChIEF expresses at lower levels in mammalian neurons, but subsequent mammalian codon optimization (denoted oChIEF) has improved mammalian expression [35]. Several groups have been able to take advantage of these properties to study synaptic events and responses to stimulation at various temporal intervals. Applications that require high temporal fidelity are particularly suited for ChIEF/oChIEF as the reduced desensitization and fast kinetics of this channel yields consistent excitation in expressing terminals at different pulse intervals (Fig. 5.1a, b, d, e, f). Thus, observed synaptic facilitation or depression can be attributed to synaptic neurotransmitter release mechanisms rather than reduced excitation of presynaptic terminals due to desensitizing ChR responses. [5, 28, 59, 60, 63].

Spectrally, ChR variants based on ChR2 or ChR1/ChR2 chimeras respond to light with wavelengths below 550 nm, with optimal activation in the blue light

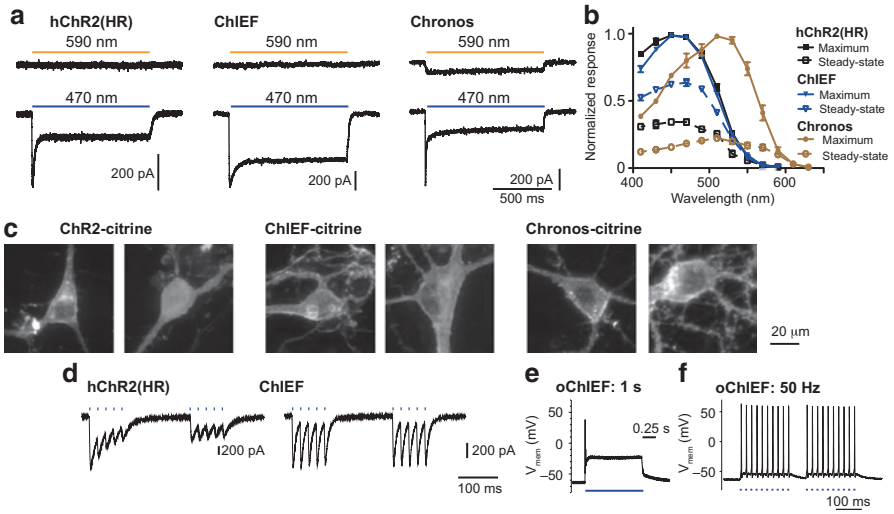

Fig. 5.1 Optimization of blue-light-activated channelrhodopsin (*ChR*) variants. **a** Examples of photocurrents of hChR2(*HR*), ChIEF, and Chronos in response to 1 s of 590 nm or 470 nm light measured under voltage-clamp recordings of HEK293 cells. The period of light illumination is indicated by *colored bars above* the photocurrent traces. *Downward* inflection of the traces indicates channel opening. Both hChR2(*HR*) and Chronos exhibit strong desensitization after the initial activation. **b** Summarized action spectra of hChR2(*HR*), ChIEF, and Chronos. "Maximum" values were measured when photocurrent amplitudes peaked in response to each wavelength, and "steady-state" responses were measured at 0.95—1 s after light onset. **c** Membrane expression of ChR2, ChIEF, and Chronos visualized with tethered fluorescent protein citrine in transfected primary cultured hippocampal neurons. In Chronos- and ChIEF-expressing cells, less cytosolic fluorescence signal is observed relative to membrane fluorescence, suggesting more efficient membrane trafficking of Chronos and ChIEF than ChR2 (see Lin et al. [35] for quantification). **d** Examples of light-evoked photocurrents of hChR2(*HR*) (*left*) and ChIEF (*right*) in response to 3 ms pulses of *blue* light (470 nm) presented in 50 Hz pulse trains with constant light intensity (*20 mW/mm*^{2}). Evoked responses of ChIEF have faster decay times and are more consistent in amplitudes during the pulse train. **e** In cultured neurons transfected with oChIEF, 1 s *blue* (*470 nm*) light induces strong depolarization (*upward inflection in the trace*) and action potential firing. **f** In cultured neuron expressing oChIEF, action potential firing can reliably follow 50 Hz pulse trains. (Figure modified from Lin et al. [34, 35])

range (450–470 nm [33, 34]. A recently described variant, Chronos [29], has a red-shifted spectral response that peaks at 510 nm but can still be strongly activated by 470 nm light (Fig. 5.1a, b). The spectral range of blue- and green-light-excitable ChRs permits wavelengths above 550 nm to be reserved for other optical techniques such as calcium imaging [13, 16], activation of other opsin tools [23, 66], intrinsic signal optical imaging [20], and imaging with red-shifted voltage sensors [17, 31]. The spectral peaks of these blue/green-light-activated variants also permit the use of commonly available light emitting diode (LEDs) and lasers that have strong light outputs in 470–488 nm range.

5.2.2 Application of Blue-Light-Activated Channelrhodopsins (ChRs) in Neurobiology

The principal application of blue-light-activated ChRs has generally been the fast activation of genetically targeted neurons, or presynaptic terminals, in brain slice preparations or in the intact brain *in vivo*. When ChRs are used to excite neurons, the kinetics of light-induced membrane depolarization is determined not only by intrinsic ChR properties but also by protein expression levels, membrane trafficking, and light intensity. In brain slices, ChR-expressing neurons are readily excited as high-intensity blue light can be either focused onto the preparation through the microscope's illumination path or delivered directly from a LED or optical fiber positioned in close proximity to the sample (Fig. 5.2a, b, c). When illuminating through the objective, it is possible to modulate the light spatially and achieve high light intensity at specific region of interests. To generate a spatially modulated illumination pattern, a digital mirror device (DMD) [48, 56] or computer-generated holography (CGH) can be used [1, 44, 47] (Fig. 5.2d). Although a DMD does not require a laser light source, lasers provide a more intense and coherent output compared to an arc lamp or a LED. While a DMD can generate 2-dimensional illumination patterns, a CGH approach with a spatial light modulator can generate a 3-dimensional illumination pattern [1, 44, 47]. The instrumentation for holography is, however, much more complex and costs are considerably higher. An alternative approach is to use galvanometric mirror-based laser scanning photostimulation (LSPS) where the laser beam is focused to a small point that sequentially scans an arbitrary path in the field of view [46] (Fig. 5.2e). LSPS illuminates with generally higher intensity as the laser light is focused onto a small point. Unlike DMDs, LSPS cannot simultaneously illuminate multiple regions of interest within the field of view, but with sufficiently fast galvanometric mirrors and laser pulse modulation, multiple regions can be illuminated with submillisecond delays. In experiments where a spatially defined illumination pattern is not required, excitation of ChR-expressing neurons can easily be achieved with light sources that are commonly used for epifluorescence imaging, such as arc lamps or LED light sources. Electronic shutter systems that can be externally controlled (mechanical shutters for arc lamps and externally modulated power supplies for LED) are preferred, as these permit precise temporal control of light illumination. If spatially modulated light patterns or uniform illumination of the field of view is not required, then light sources or fiber optic cables can be placed in close proximity to the specimen to directly excite ChR-expressing neurons [12].

ChRs have been used to interrogate neural circuits in awake animals during the performance of behavioral tasks [25, 43]. A major obstacle for *in vivo* activation in mammalian brains is the delivery of sufficient light to ChR-expressing neurons embedded within the tissue. Blue light is strongly absorbed and scattered by bone, blood, and skin [54]. When ChR-expressing neurons are located in superficial brain areas, the same technologies used for stimulating neurons in brain slices can be applied after removing or thinning the intervening tissue. Still, the spatial resolution

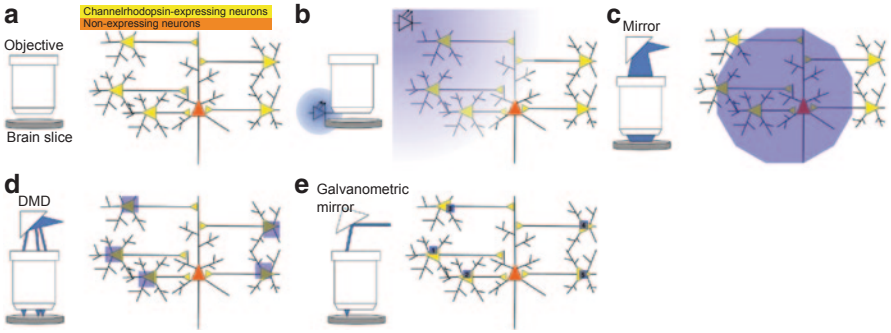

Fig. 5.2 Approaches for optical excitation of channelrhodopsin (*ChR*)-expressing neurons in *brain slices*. **a** *Left panel* schematic diagram showing *brain slices* (*gray*) with ChR-expressing neurons placed under a microscope objective. The panel on the *right* shows the field of view under the objective where *ChR-expressing neurons* (*yellow*) innervate the nonexpressing neuron of interest (*orange*). **b** ChR-expressing neurons and presynaptic terminals can be excited by a light source such as a LED or a laser/LED-coupled fiber placed near the *brain slice*. The neurons across the field of view are not illuminated uniformly. **c** ChR -expressing neurons and presynaptic terminals are excited by light guided through the microscope objective used for fluorescence imaging using an arc lamp, LED, or laser as a light source. In a system where the optical components are correctly aligned, the field of view can be uniformly illuminated. **d** A digital mirror device (*DMD*) can be placed in the light path to selectively illuminate specific pixels within the field of view simultaneously. **e** A focused light beam, from a LED or laser source, can be used to selectively illuminate specific points within the field of view sequentially with the use of galvanometric mirror to direct the position of the light beam. Computer-generated holographic illumination with a spatial light modulator is not illustrated in this figure

might be considerably lower due to light scattering [3, 24, 25]. When ChR-expressing neurons are embedded in deeper tissues, small optical fibers (typically 200 or 400 μm in diameter) can be acutely or chronically implanted to emit high-intensity light in close proximity to the expressing cells [51] (see also Fig. 5.4). These optical fibers are typically secured onto the skull of the animal and penetrate the tissues *en route* to the expressing neurons. Thus, simple optical fibers preclude using any kind of spatial modulation to target specific neurons.

5.3 Performing Optogenetics with Red Light

5.3.1 The Discovery and Development of Red-Light-Excitable Channelrhodopsins (ChRs)

Compared to blue-light-activated ChR variants, the development of red-light-excitable ChRs has progressed at a slower rate. Few naturally occurring red-shifted ChRs have been identified in the sequenced genomes of different organisms. VChR1 is a red-shifted ChR from *Volvox carteri* that was reported after the demonstration of

ChR2 in neurons [67]. VChR1 exhibits low expression levels and limited membrane trafficking in mammalian cells, restricting its use as an optogenetic tool [33, 35, 64]. Subsequent modification of VChR1 using a chimera approach generated the C1V1 and VCOMET variants [35, 64]. C1V1 and, particularly, VCOMET have improved membrane trafficking and higher expression levels compared to VChR1 in the neurons of both rodents and *Drosophila* [35, 26]. The improved membrane trafficking of C1V1 and VCOMET is mediated by an N-terminal sequence transferred from ChIEF/ChR1, which contains a membrane-targeting signal peptide. VCOMET additionally incorporates a transmembrane domain from the homologous VChR2, which enhanced expression levels in mammalian systems [35]. ReaChR is a VCOMET-based variant [35], which contains an additional point mutation that prolongs the lifetime of its red-shifted photocycle state. ReaChR thus exhibits a strong photoresponse to orange and red light above 600 nm (Fig. 5.3a, b). Although the channel kinetics of ReaChR at these longer wavelengths are slower than those of most blue-light-activated variants, ReaChR is effective when high-frequency stimulation (> 10 Hz) is not required and slower neuronal activation (> 3 ms) is acceptable [35].

Chrimson is a naturally occurring red-shifted ChR recently discovered in *Chlamydomonas noctigama*. Chrimson has a more red-shifted spectral response and faster kinetics at long wavelengths ($\lambda > 600$ nm) compared to ReaChR [29] (Fig. 5.3a, b). Both ReaChR and Chrimson are efficiently excited by visible light (λ 400–650 nm) although the biophysical characteristics of the two proteins differ as a function of wavelength [29, 35] (Fig. 5.3a, b, c, d, e, f).

5.3.2 Current and Future Applications of Red-Light-Activatable Channelrhodopsins (ChRs)

Although red-shifted ChRs have to date been applied in a limited number of studies, the recent progress in their discovery and engineering has circumvented prior limitations that hindered the wider adoption of tools such as VChR1. Working with efficient red-shifted ChRs, such as ReaChR or Chrimson, has some notable advantages. First, attenuation and scattering of light by biological tissues due to hemoglobin absorption and other processes is significantly reduced at wavelengths above 600 nm (orange/red) [54]. This allows orange/red light to penetrate neural tissue more readily and higher light intensities to be delivered at greater depths. Neurons can also be stimulated noninvasively through intact tissue. The need for highly invasive and damaging optic fiber implants, as well as open or thin-skull craniotomies, can then be eliminated. We have previously demonstrated that ReaChR-expressing motor neurons in deep layers of the cortex and brainstem of mice can be activated *in vivo* by externally positioned red LEDs (617–655 nm). Illumination of the expressing cells is then achieved through interposed fur, skin, and bone (Fig. 5.4) [35]. By activating ReaChR-expressing neurons transcranially, action potentials can be generated with high temporal fidelity and precise behaviors evoked in the head-fixed,

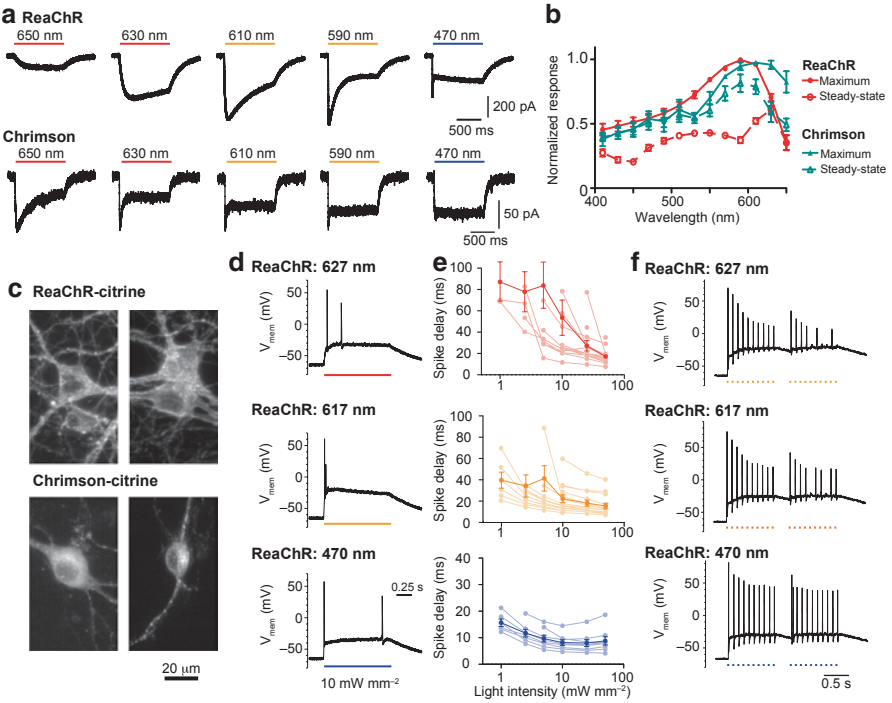

Fig. 5.3 Properties of the red-light-activatable ChR variants *ReaChR* and *Chrimson*. **a** Spectral response of red-shifted ChR variants *ReaChR* and *Chrimson*. Example photocurrent measurements of *ReaChR*- and *Chrimson*-expressing HEK293 cells to 650, 630, 610, 590, and 470 nm light stimulation. *Downward inflections* in the traces indicate channel opening induced by light illumination. Chrimson exhibits faster responses to light above 600 nm, although photocurrent amplitudes are significantly smaller at all wavelengths compared to ReaChR. **b** Spectral responses of *ReaChR* and *Chrimson*. "Maximum" values are peak photocurrent amplitudes measured at each wavelength, and "steady-state" values are the photocurrent amplitude measured at 0.95—1 s after light onset. **c** Membrane trafficking of *ReaChR* and *Chrimson* in primary cortical cultured neurons as visualized with the fluorescence of the tethered fluorescent protein citrine. ReaChR has a stronger, and more uniform, membrane expression throughout the cell soma and processes, whereas *Chrimson*–citrine fluorescence is strong in the cytoplasm but not on the membrane. **d** The membrane voltage response of *ReaChR*-expressing cultured neurons to 1 s of continuous 627, 617, or 470 nm light. Suprathreshold depolarization and light-induced spiking are observed at all three wavelengths. **e** Delay of light-induced spikes in *ReaChR*-expressing neurons at different illumination wavelengths and intensities. *Faint lines* indicate the results of individual neuron measurements, and the *darker lines* represent mean values. **f** Short (1 ms) pulses of 617, 627, or 470 nm light in 10 Hz trains trigger temporally precise spikes in *ReaChR*-expressing cultured hippocampal neurons. The slow kinetics of *ReaChR* can result in depolarization block that reduces spike fidelity later in the pulse train in some cells at longer wavelengths. Extra spikes are also observed in some cases (as seen with 470 nm light). See also Fig. 5.5 in Lin et al. [35] for comparable *in vivo* results. (Figure modified from Lin et al. [35])

awake mouse. With such transcranial light activation, high levels of light are typically needed to counteract attenuation arising from reflection off bone and the large distance between the light source and the ReaChR-expressing neurons (decrease

in light intensity is inversely proportional to distance squared). Thus, ambient illumination is not a concern. At present, it remains unclear whether a similar transcranial approach will work in species such as rats, where the skull is much thicker and less transparent than in mice. The removal of skin or thinning of the bone may still be required to achieve sufficient light delivery [15]. Optical fibers may also be advantageous in some cases when target neurons are located in very deep nuclei or if light needs to be focused at depth (for instance when combined with another ChR in a different region). A likely application of red-light-activated ChRs would be in experiments where the placement of optical fibers is difficult or undesirable, such as the brainstem or spinal cord. Regardless, red-light-excitable ChRs will be crucial for the adoption of optogenetics for clinical applications in which transcranial and transvertebral stimulation may allow treatments of neurological disorders and neuroprosthetic control.

Delivery strategies for introducing ectopic expression of red-shifted ChRs in mammalian neural tissue include targeted injections of lenti- and adeno-associated viruses to transduce local neurons. Transduction after such injections does not distinguish between subpopulations of similar neurons with different projection targets, which may be required for neural circuit analysis. Furthermore, local injections trigger inflammatory and immune responses and cause direct damage to the injected tissue. An alternative approach involves retrograde viral delivery systems, such as glycoprotein-deleted rabies virus [44], rabies glycoprotein-pseudotyped lentivirus [14], or AAV6 [53]. These viral delivery systems can target neurons that project to the site of virus injection and thus isolate specific neural circuits for testing functional connectivity between two regions. This approach potentially eliminates the need for craniotomies above areas where the expressing neurons are located since red light can be delivered transcranially, and combined with red-shifted ChRs, it will allow minimally invasive, optogenetic activation of long-distance circuits.

With red-shifted ChRs, it is also possible to stimulate central *Drosophila* neurons expressing ReaChR through the intact cuticle using an LED placed near the experimental arena [26]. Many GAL4 driver lines are available in *Drosophila,* and red-shifted ChR variants can easily be expressed in genetically defined cell groups. With appropriate behavioral assays, it is possible to screen the functional effects of activating different neuronal cell types (Fig. 5.5). Although similar experiments can be conducted with the thermosensitive TrpA channel by raising the ambient temperature, ChRs provide a complementary approach whereby neurons can be activated with a higher temporal and spatial fidelity. This approach also minimizes neuronal adaptation effects that can arise when TrpA is used to tonically modulate neuronal activity [26].

When neurons are activated with ChRs, it is always important to control for the behavioral effects caused by visual stimulation, which occur at wavelengths as long as 720 nm in *Drosophila* [29]. For this reason, experimenters may want to confirm results with thermogenetics and appropriate controls to avoid false-positive findings.

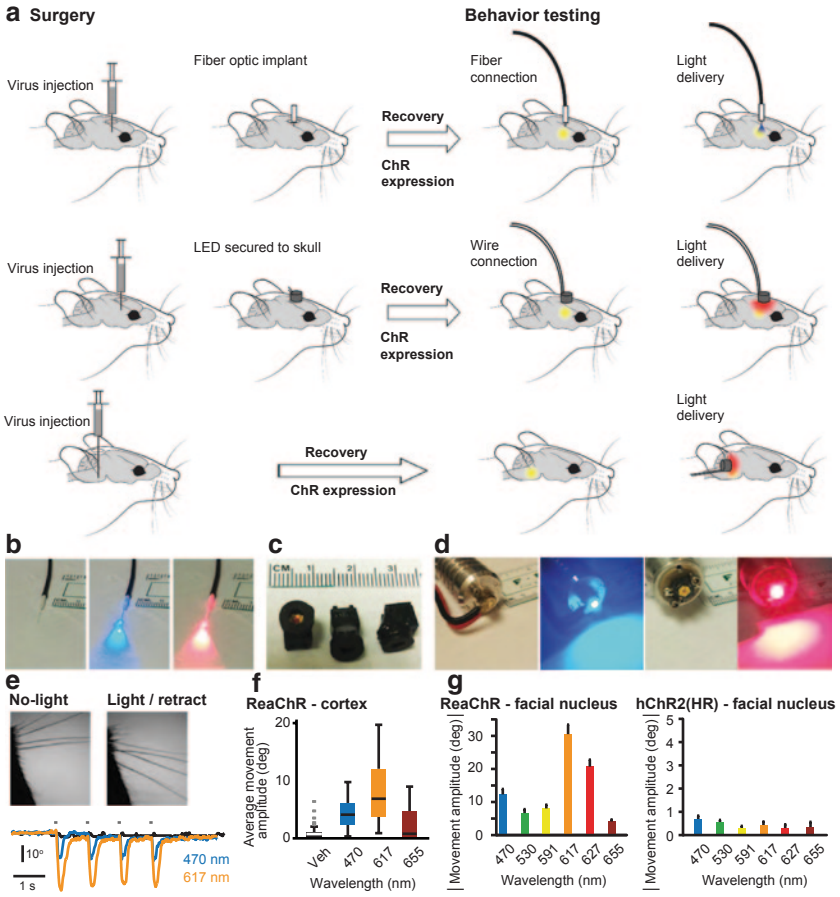

Fig. 5.4 *In vivo* activation of ChR-expressing neurons in the rodent brain. **a** Schematic diagrams illustrate different approaches for activating ChR-expressing neurons in the rodent brain. Recombinant virus with a ChR transgene is injected into the rodent brain for expression. In *A, top*, a fiber optic cannula is chronically implanted into the brain 2–3 weeks after initial transduction. During behavioral experiments, the cannula is connected to a flexible fiber optic patch cable that is coupled to a LED or laser light source. In *A, middle*, a small LED mount is secured onto the skull. On the day of the experiment, the LED is connected electrically and light is delivered through the healed tissue or a cranial window. In *A, bottom*, an external LED is placed noninvasively outside the head on the day of behavioral testing to activate ChR-expressing neurons. **b** Photographs of a fiber optic cannula coupled to a patch cable. The same fiber optic cannula can be used to deliver different wavelengths of light (*blue*/470 nm and *orange-red*/617 nm lights are shown here). **c** Photograph of custom-made small LED mounts that can be secured onto the skull of rodents to deliver light for neural activation. Electrical wires will be connected to the LED mount on the day of experiment. **d** Pictures of a LED attached to a metallic heat sink that can be used to deliver light externally for ChR activation, suitable for approach shown in *A, bottom*. The heat sink is often required due to the higher light levels and electrical currents required when LED illumination is provided externally. **e** Noninvasive activation of ReaChR-expressing neurons in the mouse brain (as in *A, bottom*) was used to trigger whisker movements with different wavelengths of light Lin et al. [35]. An example of reproducible whisker movements triggered by exciting

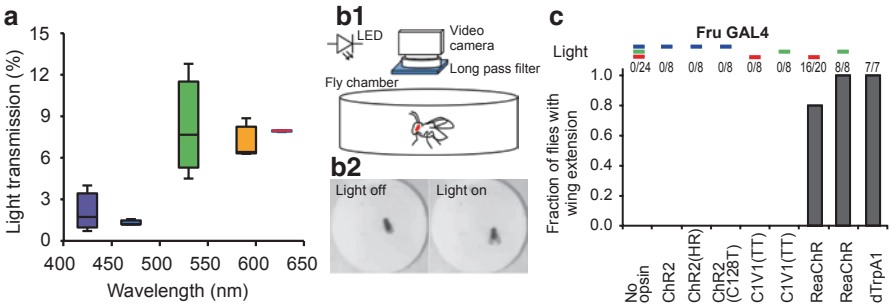

Fig. 5.5 Application of red-shifted ChR variant for screening of neural circuits controlling fly behavior. **a** Light transmission as a function of wavelength through *Drosophila melanogaster* cuticle (*447.5, 470, 530, 590, and 627 nm*). Light transmission through the cuticles increases dramatically above 500 nm. (*B, top*) A simplified schematic diagram showing the video monitoring system used for behavioral screening of ReaChR-expressing flies in Inangaki et al. 2014. The ChR-expressing fly was placed in a chamber with ambient illumination at 850 nm for video capture of behavior. A high-intensity LED was placed *above* the chamber to excite ChR-expressing neurons at distance. A video camera with a long-pass filter to block out LED light during ChR excitation was placed *above* the chamber. (*B, bottom*) An example of 627 nm light-induced wing extension courtship behavior in the fly when ReaChR is expressed in Fru neurons. **c** Fraction of flies with wing extension behavior during light illumination at a wavelength indicated by *horizontal colored bars* (*red: 627 nm, green: 53 nm, and blue: 470 nm*). Only ReaChR-expressing, but not ChR2(*HR*)-, ChR2(*C128T*)-, or C1V1(*TT*)-expressing flies, exhibited detectable light-inducible wing extension behavior during light illumination. The thermogenetic dTRPA1 also induces wing extension when the temperature in the chamber is raised. dTRPA1 animals were used as a positive control, confirming that activation of Fru neurons can be mediated by ReaChR excitation. (Figure modified from Inangaki et al. [26])

5.3.3 *Parallel and Independent Excitation of Multiple Neuronal Groups Using Blue- and Red-Light-Activatable Channelrhodopsins (ChRs)*

Since the first report of a red-shifted ChR, there have been several attempts to use blue and red light to independently activate spatially overlapping populations of neurons [29, 64, 67]. In principle, the approach is simple: light at one wavelength (e.g., blue) is used to activate one group and a second wavelength (e.g., red) is used to activate a second population, either simultaneously or sequentially. The ability to stimulate two spatially overlapping, but genetically distinct groups of neurons, will permit novel experiments to study the convergence of different neurotransmitter

ReaChR-expressing motoneurons located in the brainstem of an anesthetized adult mouse. The bottom traces display angle displacements of the whiskers during light pulses of 617 or 470 nm light. Larger movements were observed with 617 nm light consistent with a lower light absorption and scattering at longer wavelengths. **f** Comparison of evoked whisker movement triggered in ReaChR-expressing cortical motor neurons and **g** motoneurons of the facial nucleus in the brainstem as a function of illumination wavelength. No movement was observed when motoneurons in the brainstem expressed hChR2(*HR*). (Figure modified from Lin et al. [35])

outputs onto common target neurons and circuits involved in the generation of behaviors.

Unfortunately, available tools do not readily permit such experiments due to significant overlap in their action spectra [29, 35, 64, 67] (Fig. 5.1 and 5.3). Although red-light-excitable ChRs such as ReaChR and Chrimson can be activated at long wavelengths ($\lambda > 570$ nm) without concomitant activation of blue light ChRs [29, 64, 67], blue light (λ 400–500 nm) will strongly activate both types of ChR [29, 35, 64, 67]. The difficulty of achieving a two-color optogenetic system to excite two separate neuronal populations may be circumvented by careful calibration. For example, expression levels of the red-light-excitable ChRs may be attenuated such that the blue photoactivation pulse does not produce suprathreshold photocurrents in those cells [29, 67]. Similarly, the blue-light-activated ChRs may be expressed in the target population at high levels to increase sensitivity. Additional control can be achieved by careful tuning light pulse duration and intensity, as was recently demonstrated with the blue- and red-light-excitable ChR variants Chronos and Chrimson [29]. This approach would require very delicate calibration, and expression levels of both opsins would need to be carefully controlled. Undue variability in expression levels between cells, or across experiments, could significantly disrupt experimental reproducibility.

For many practical purposes, however, current variants of spectrally separated ChRs could still prove useful for two-color activation of different target populations expressing comparable levels of ChR when the somas of the two populations are sufficiently spaced apart. When this is the case, a red-light-excitable ChR can be expressed in one group of neurons and a blue-light-excitable ChR in neurons with somas located in a different region. Excitation of the neurons expressing red-light-activatable ChR with orange/red light will then not activate neurons or terminals expressing blue-light-excitable ChRs, while somas of neurons expressing blue-light-excitable ChRs can be excited independently with blue light at sufficient distance apart from neurons expressing red-light-excitable ChR. This two-color approach does not require careful calibration of expression and trafficking levels and is relatively simple to achieve with a standard dual-viral delivery system. Activation of the two regions could be achieved *in vivo* by placing two fibers in the brain or by illuminating through open/thinned cranial windows with a focused LED or laser light.

5.4 Future Development of Novel and Improved Channelrhodopsin (ChR) Variants

Despite significant advances in ChR development and engineering since the discovery of ChR1 and ChR2 [40, 41], several outstanding issues with current ChR variants will need to be improved upon. Red-light-shifted variants such as ReaChR and Chrimson are still strongly activated by blue light. Chrimson additionally suffers

from relatively poor membrane trafficking in mammalian cells (Fig. 5.3c). Proven strategies exist that can improve membrane trafficking of ChR variants and microbial opsin pumps [7, 37, 35], and it is therefore feasible to improve the membrane trafficking and expression of Chrimson as it has been done with other optogenetic tools. In order to attenuate blue light excitability, significant modification of the template proteins will be necessary, and complete elimination of this phenomenon might not be possible due to ChR's complex photocycle states [4]. Alternative strategies might also be worth exploring, such as co-expression of optogenetic tools that can inhibit synaptic release with blue light [36].

Current ChR variants are highly effective at depolarizing neurons. In comparison, optogenetic approaches for suppressing neuronal activities or synaptic releases are far less effective [36, 37]. Converting cation-selective ChRs into anion-selective or potassium-selective channels could generate optogenetic tools that are more efficient inhibitors of neuronal activities than existing opsin pumps such as NpHR/halo, Arch, Mac, and ArchT [37, 65]. Two recent studies report the development of anion-conducting blue-light-activated ChR [8, 62]. However, these channels remain cation permeable and exhibit significantly reduced photocurrents compared to the cation-selective ChR variants they are based on. Additional engineering and modification of these proteins will be necessary to generate anion-selective ChR variants with high photocurrent conversion efficacy.

The discovery and development of novel ChR variants thus far has relied principally on three strategies. Most common is the generation of point mutations based on structural knowledge of microbial opsin pumps and ChR, as was the case for hChR2(HR), ChETA, step-function opsin, and CatCh [6, 10, 21, 30]. Second, novel ChRs such as ChEF, ChRGR, C1V1, and VCOMET were generated by chimeric fusion of related opsin variants [34, 35, 61, 64]. The chimeric approach exploits the modular nature of proteins and the fact that domain recombination can generate unique properties [55]. Third, genomic screening and testing of homologous proteins from a large number of species has accelerated the discovery and characterization of new opsins, such as Chronos, Chrimson, VChR1, and MChR1 [29]. While each approach will independently continue to generate useful ChR variants, the most productive strategies will likely apply all three of them in tandem with high-throughput functional screening in order to select variants with desirable properties, as it has been done for the engineering of fluorescent proteins [49, 57]. Low-throughput screening and an emphasis on individual variants often generate limited improvements that are offset by undesirable changes. Worse, reengineering may generate proteins that fail to fold and mature correctly. Protein engineering techniques such as DNA shuffling in combination with structure-guided mutagenesis [38, 50] and microfluidic or cytometry screening would likely contribute to accelerating the progress of ChR development in the future by enabling –"protein engineers" to generate high numbers of variants and select for the ones with useful properties.

5.5 Summary

The development of novel neurophysiological tools in the last 40 years has resulted in exciting progress throughout the neuroscience community. The inventions of patch-clamp recording, calcium-sensitive dyes, fluorescent proteins, genetic approaches, and modern optical approaches have provided scientists with revolutionary tools to study and understand neural activities and interactions both in vitro and *in vivo*. The recent development of optogenetic tools has provided neuroscientists with exciting and accessible ways to explore neural function and permits experimental perturbations that were previously impossible. While many technical aspects of these optogenetic tools can still be improved, the potential of our current reagents has not yet been fully exploited. The application of optogenetics in neuroscience will undoubtedly provide many intriguing insights in the years ahead.

References

1. Anselmi F., Ventalon C., Begue A., Ogden D., Emiliani V. (2011). Three-dimensional imaging and photostimulation by remote-focusing and holographic light patterning. *Proceedings of the National Academy of Sciences of the United States of America, 108*(49), 19504–19509. doi:10.1073/pnas.1109111108.
2. Arrenberg, A. B., Stainier, D. Y., Baier, H., & Huisken, J. (2010). Optogenetic control of cardiac function. *Science, 330*(6006), 971–974. doi:10.1126/science.1195929.
3. Ayling, O. G., Harrison, T. C., Boyd, J. D., Goroshkov, A., & Murphy, T. H. (2009). Automated light-based mapping of motor cortex by photoactivation of channelrhodopsin-2 transgenic mice. *Nature Methods 6*(3), 219–224. doi:10.1038/nmeth.1303.
4. Bamann, C., Kirsch, T., Nagel, G., & Bamberg, E. (2008). Spectral characteristics of the photocycle of channelrhodopsin-2 and its implication for channel function. *Journal of Molecular Biology, 375*(3), 686–694. doi:10.1016/j.jmb.2007.10.072.
5. Bell, K. A., Shim, H., Chen, C. K., & McQuiston, A. R. (2011). Nicotinic excitatory postsynaptic potentials in hippocampal CA1 interneurons are predominantly mediated by nicotinic receptors that contain alpha4 and beta2 subunits. *Neuropharmacology, 61*(8), 1379–1388. doi:10.1016/j.neuropharm.2011.08.024.
6. Berndt, A., Yizhar, O., Gunaydin, L. A., Hegemann, P., & Deisseroth, K. (2009). Bi-stable neural state switches. *Nature Neuroscience, 12*(2), 229–234. doi:nn.2247 [pii].
7. Berndt, A., Schoenenberger, P., Mattis, J., Tye, K. M., Deisseroth, K., Hegemann, P., & Oertner, T. G. (2011). High-efficiency channelrhodopsins for fast neuronal stimulation at low light levels. *Proceedings of the National Academy of Sciences of the United States of America, 108*(18), 7595–7600. doi:10.1073/pnas.1017210108.
8. Berndt, A., Lee, S. Y., Ramakrishnan, C., & Deisseroth, K. (2014). Structure-guided transformation of channelrhodopsin into a light-activated chloride channel. *Science, 344*(6182), 420–424. doi:10.1126/science.1252367.
9. Bi, A., Cui, J., Ma, Y. P., Olshevskaya, E., Pu, M., Dizhoor, A. M., & Pan, Z. H. (2006). Ectopic expression of a microbial-type rhodopsin restores visual responses in mice with photoreceptor degeneration. *Neuron, 50*(1), 23–33. doi:10.1016/j.neuron.2006.02.026.
10. Boyden, E. S., & Zhang, F., Bamberg, E., Nagel, G., Deisseroth, K. (2005). Millisecond-timescale, genetically targeted optical control of neural activity. *Nature Neuroscience, 8*(9), 1263–1268. doi:10.1038/nn1525.

11. Bruegmann, T., Malan, D., Hesse, M., Beiert, T., Fuegemann, C. J., Fleischmann, B. K., & Sasse, P. (2010). Optogenetic control of heart muscle in vitro and in vivo. *Nature Methods, 7*(11), 897–900. doi:10.1038/nmeth.1512.
12. Campagnola, L., Wang, H., & Zylka, M. J. (2008). Fiber-coupled light-emitting diode for localized photostimulation of neurons expressing channelrhodopsin –2. *Journal of Neuroscience Methods, 169*(1), 27–33. doi:10.1016/j.jneumeth.2007.11.012.
13. Carlson, H. J., & Campbell, R. E. (2013). Circular permutated red fluorescent proteins and calcium ion indicators based on mCherry. *Protein Engineering, Design & Selection (PEDS), 26*(12), 763–772. doi:10.1093/protein/gzt052.
14. Carpentier D. C., Vevis K., Trabalza A., Georgiadis C, Ellison S. M., Asfahani R. I., Mazarakis N. D. (2012). Enhanced pseudotyping efficiency of HIV-1 lentiviral vectors by a rabies/vesicular stomatitis virus chimeric envelope glycoprotein. *Gene Ther, 19*(7), 761–774.
15. Drew, P. J., Shih, A. Y., Driscoll, J. D., Knutsen, P. M., Blinder, P., Davalos, D., Akassoglou, K., Tsai, P. S., & Kleinfeld, D. (2010). Chronic optical access through a polished and reinforced thinned skull. *Nature Methods, 7*(12), 981–984. doi:nmeth.1530 [pii].
16. Egawa, T., Hanaoka, K., Koide, Y., Ujita, S., Takahashi, N., Ikegaya, Y., Matsuki, N., Terai, T., Ueno, T., Komatsu, T., & Nagano, T. (2011). Development of a far-red to near-infrared fluorescence probe for calcium ion and its application to multicolor neuronal imaging. *Journal of the American Chemical Society, 133*(36), 14157–14159. doi:10.1021/ja205809h.
17. Gong, Y., Li, J. Z., & Schnitzer, M. J. (2013). Enhanced Archaerhodopsin Fluorescent Protein Voltage Indicators. *PloS ONE, 8*(6), e66959. doi:10.1371/journal.pone.0066959.
18. Gorostiza, P., Volgraf, M., Numano, R., Szobota, S., Trauner, D., & Isacoff, E. Y. (2007). Mechanisms of photoswitch conjugation and light activation of an ionotropic glutamate receptor. *Proceedings of the National Academy of Sciences of the United States of America, 104*(26), 10865–10870. doi:10.1073/pnas.0701274104.
19. Gradinaru, V., Thompson, K. R., Zhang, F., Mogri, M., Kay, K., Schneider, M. B., & Deisseroth, K. (2007). Targeting and readout strategies for fast optical neural control in vitro and in vivo. The. *Journal of Neuroscience, 27*(52), 14231–14238. doi:10.1523/JNEUROSCI.3578-07.2007.
20. Grinvald, A., Lieke, E., Frostig, R. D., Gilbert, C. D., & Wiesel, T. N. (1986). Functional architecture of cortex revealed by optical imaging of intrinsic signals. *Nature, 324*(6095), 361–364. doi:10.1038/324361a0.
21. Gunaydin, L. A., Yizhar, O., Berndt, A., Sohal, V. S., Deisseroth, K., & Hegemann, P. (2010). Ultrafast optogenetic control. *Nature Neuroscience, 13*(3), 387–392. doi:nn.2495 [pii].
22. Gunsalus, C. K., Bruner, E. M., Burbules, N. C., Dash, L., Finkin, M., Goldberg, J. P., Greenough, W. T., Miller, G. A., & Pratt, M. G. (2006). Mission creep in the IRB world. *Science, 312*(5779), 1441. doi:10.1126/science.1121479.
23. Han, X., & Boyden, E. S. (2007). Multiple-color optical activation, silencing, and desynchronization of neural activity, with single-spike temporal resolution. *PloS ONE, 2*(3), e299. doi:10.1371/journal.pone.0000299.
24. Harrison, T. C., Ayling, O. G., & Murphy, T. H. (2012). Distinct cortical circuit mechanisms for complex forelimb movement and motor map topography. *Neuron, 74*(2), 397–409. doi:10.1016/j.neuron.2012.02.028.
25. Huber, D., Petreanu, L., Ghitani, N., Ranade, S., Hromadka, T., Mainen, Z., & Svoboda, K. (2008). Sparse optical microstimulation in barrel cortex drives learned behaviour in freely moving mice. *Nature, 451*(7174), 61–64. doi:10.1038/nature06445.
26. Inagaki, H. K., Jung, Y., Hoopfer, E. D., Wong, A. M., Mishra, N., Lin, J. Y., Tsien, R. Y., & Anderson, D. J. (2014). Optogenetic control of Drosophila using a red-shifted channelrhodopsin reveals experience-dependent influences on courtship. *Nature Methods, 11,* 325–332. doi:10.1038/nmeth.2765
27. Ishizuka, T., Kakuda, M., Araki, R., & Yawo, H. (2006). Kinetic evaluation of photosensitivity in genetically engineered neurons expressing green algae light-gated channels. *Neuroscience Research, 54*(2), 85–94. doi:10.1016/j.neures.2005.10.009.

28. Jurgens, C. W., Bell, K. A., McQuiston, A. R., & Guido, W. (2012). Optogenetic stimulation of the corticothalamic pathway affects relay cells and GABAergic neurons differently in the mouse visual thalamus. *PloS ONE, 7*(9), e45717. doi:10.1371/journal.pone.0045717.
29. Klapoetke, N. C., Murata, Y., Kim, S. S., Pulver, S. R., Birdsey-Benson, A., Cho, Y. K., Morimoto, T. K., Chuong, A. S., Carpenter, E. J., Tian, Z., Wang, J., Xie, Y., Yan, Z., Zhang, Y., Chow, B. Y., Surek, B., Melkonian, M., Jayaraman, V., Constantine-Paton, M., Wong, G. K., & Boyden, E. S. (2014). Independent optical excitation of distinct neural populations. *Nature Methods, 11,* 338–346. doi:10.1038/nmeth.2836
30. Kleinlogel, S., Feldbauer, K., Dempski, R. E., Fotis, H., Wood, P. G., & Bamann, C., Bamberg, E. (2011). Ultra light-sensitive and fast neuronal activation with the Ca(2)+ -permeable channelrhodopsin CatCh. *Nature Neuroscience, 14*(4), 513–518. doi:nn.2776 [pii]
31. Kralj, J. M., Douglass, A. D., Hochbaum, D. R., Maclaurin, D., & Cohen, A. E. (2012). Optical recording of action potentials in mammalian neurons using a microbial rhodopsin. *Nature Methods, 9*(1), 90–95. doi:10.1038/nmeth.1782
32. Li, X., Gutierrez, D. V., Hanson, M. G., Han, J., Mark, M. D., Chiel, H., Hegemann, P., Landmesser, L. T., & Herlitze, S. (2005). Fast noninvasive activation and inhibition of neural and network activity by vertebrate rhodopsin and green algae channelrhodopsin. *Proceedings of the National Academy of Sciences of the United States of America, 102*(49), 17816–17821. doi:10.1073/pnas.0509030102.
33. Lin, J. Y. (2011). A user's guide to channelrhodopsin variants: Features, limitations and future developments. *Experimental Physiology, 96*(1), 19–25. doi:expphysiol.2009.051961 [pii].
34. Lin, J. Y., Lin, M. Z., Steinbach, P., & Tsien, R. Y. (2009). Characterization of engineered channelrhodopsin variants with improved properties and kinetics. *Biophysical Journal, 96*(5), 1803–1814. doi:S0006–3495(09)00016-2 [pii].
35. Lin, J. Y., Knutsen, P. M., Muller, A., Kleinfeld, D., & Tsien, R. Y. (2013a). ReaChR: A red-shifted variant of channelrhodopsin enables deep transcranial optogenetic excitation. *Nature Neuroscience, 16*(10), 1499–1508.
36. Lin, J. Y., Sann, S. B., Zhou, K., Nabavi, S., Proulx, C. D., Malinow, R., Jin, Y., & Tsien, R. Y. (2013b). Optogenetic inhibition of synaptic release with chromophore-assisted light inactivation (CALI). *Neuron, 79*(2), 241–253. doi:10.1016/j.neuron.2013.05.022.
37. Mattis, J., Tye, K. M., Ferenczi, E. A., Ramakrishnan, C., O'Shea, D. J., Prakash, R., Gunaydin, L. A., Hyun, M., Fenno, L. E., Gradinaru, V., Yizhar, O., & Deisseroth, K. (2012). Principles for applying optogenetic tools derived from direct comparative analysis of microbial opsins. *Nature Methods, 9*(2), 159–172. doi:10.1038/nmeth.1808.
38. Meyer, M. M., Hochrein, L., & Arnold, F. H. (2006). Structure-guided SCHEMA recombination of distantly related beta-lactamases. *Protein Engineering, Design & Selection (PEDS), 19*(12), 563–570. doi:10.1093/protein/gzl045.
39. Miller, G. (2006). Optogenetics. Shining new light on neural circuits. *Science, 314*(5806), 1674–1676. doi:10.1126/science.314.5806.1674.
40. Nagel, G., Ollig, D., Fuhrmann, M., Kateriya, S., Musti, A. M., Bamberg, E., & Hegemann, P. (2002). Channelrhodopsin-1: A light-gated proton channel in green algae. *Science, 296*(5577), 2395–2398. doi:10.1126/science.1072068.
41. Nagel, G., Szellas, T., Huhn, W., Kateriya, S., Adeishvili, N., Berthold, P., Ollig, D., Hegemann, P., & Bamberg, E. (2003). Channelrhodopsin-2, a directly light-gated cation-selective membrane channel. *Proceedings of the National Academy of Sciences of the United States of America, 100*(24), 13940–13945. doi:10.1073/pnas.1936192100.
42. Nagel, G., Brauner, M., Liewald, J. F., & Adeishvili, N., Bamberg, E., Gottschalk, A. (2005). Light activation of channelrhodopsin-2 in excitable cells of Caenorhabditis elegans triggers rapid behavioral responses. Current Biology (CB)*, 15*(24), 2279–2284. doi:10.1016/j.cub.2005.11.032.
43. O'Connor, D. H., Hires, S. A., Guo, Z. V., Li, N., Yu, J., Sun, Q. Q., Huber, D., & Svoboda, K. (2013). Neural coding during active somatosensation revealed using illusory touch. *Nature Neuroscience, 16*(7), 958–965. doi:10.1038/nn.3419.

44. Osakada F., Mori T., Cetin A. H., Marshel J. H., Virgen B., Callaway E. M. (2011). New rabies virus variants for monitoring and manipulating activity and gene expression in defined neural circuits. *Neuron, 71*(4), 617–631.
45. Papagiakoumou, E., Anselmi, F., Begue, A., de Sars V., Gluckstad, J., Isacoff, E. Y., & Emiliani, V. (2010). Scanless two-photon excitation of channelrhodopsin-2. *Nature Methods, 7*(10), 848–854. doi:10.1038/nmeth.1505.
46. Petreanu, L., Huber, D., Sobczyk, A., & Svoboda, K. (2007). Channelrhodopsin-2-assisted circuit mapping of long-range callosal projections. *Nature Neuroscience, 10*(5), 663–668. doi:10.1038/nn1891.
47. Reutsky-Gefen, I., Golan, L., Farah, N., Schejter, A., Tsur, L., Brosh, I., & Shoham, S. (2013). Holographic optogenetic stimulation of patterned neuronal activity for vision restoration. *Nature Communications, 4,* 1509. doi:10.1038/ncomms2500.
48. Sakai, S., Ueno, K., Ishizuka, T., & Yawo, H. (2013). Parallel and patterned optogenetic manipulation of neurons in the brain slice using a DMD-based projector. *Neuroscience Research, 75*(1), 59–64. doi:10.1016/j.neures.2012.03.009.
49. Shaner, N. C., Lin, M. Z., McKeown, M. R., Steinbach, P. A., Hazelwood, K. L., Davidson, M. W., & Tsien, R. Y. (2008). Improving the photostability of bright monomeric orange and red fluorescent proteins. *Nature Methods, 5*(6), 545–551. doi:10.1038/nmeth.1209.
50. Smith, M. A., Romero, P. A., Wu, T., Brustad, E. M., & Arnold, F. H. (2013). Chimeragenesis of distantly-related proteins by noncontiguous recombination. *Protein Science (A Publication Of The Protein Society), 22*(2), 231–238. doi:10.1002/pro.2202.
51. Sparta, D. R., Stamatakis, A. M., Phillips, J. L., Hovelso, N., van Zessen R., & Stuber, G. D. (2012). Construction of implantable optical fibers for long-term optogenetic manipulation of neural circuits. *Nature Protocols, 7*(1), 12–23. doi:10.1038/nprot.2011.413.
52. Szobota, S., Gorostiza, P., Del Bene, F., Wyart, C., Fortin, D. L., Kolstad, K. D., Tulyathan, O., Volgraf, M., Numano, R., Aaron, H. L., Scott, E. K., Kramer, R. H., Flannery, J., Baier, H., Trauner, D., & Isacoff, E. Y. (2007). Remote control of neuronal activity with a light-gated glutamate receptor. *Neuron, 54*(4), 535–545. doi:10.1016/j.neuron.2007.05.010.
53. Towne, C., Montgomery, K. L., Iyer, S. M., Deisseroth, K., & Delp, S. L. (2013). Optogenetic control of targeted peripheral axons in freely moving animals. *PloS ONE, 8*(8), e72691. doi:10.1371/journal.pone.0072691.
54. Tromberg, B. J., Shah, N., Lanning, R., Cerussi, A., Espinoza, J., Pham, T., Svaasand, L., & Butler, J. (2000). Non-invasive in vivo characterization of breast tumors using photon migration spectroscopy. *Neoplasia (New York, N. Y.), 2*(1–2), 26–40.
55. Trudeau, D. L., Smith, M. A., Arnold, F.H. (2013). Innovation by homologous recombination. *Current Opinion In Chemical Biology, 17*(6), 902–909. doi:10.1016/j.cbpa.2013.10.007.
56. Tsuda, S., Kee, M. Z., Cunha, C., Kim, J., Yan, P., Loew, L. M., & Augustine, G. J. (2013). Probing the function of neuronal populations: combining micromirror-based optogenetic photostimulation with voltage-sensitive dye imaging. *Neuroscience Research, 75*(1), 76–81. doi:10.1016/j.neures.2012.11.006.
57. Wang, L., Jackson, W. C., Steinbach, P. A., & Tsien, R. Y. (2004). Evolution of new non-antibody proteins via iterative somatic hypermutation. *Proceedings of the National Academy of Sciences of the United States of America, 101*(48), 16745–16749. doi:10.1073/pnas.0407752101.
58. Wang, H., Sugiyama, Y., Hikima, T., Sugano, E., Tomita, H., Takahashi, T., Ishizuka, T., & Yawo, H. (2009). Molecular determinants differentiating photocurrent properties of two channelrhodopsins from chlamydomonas. *The Journal of Biological Chemistry, 284*(9), 5685–5696. doi:10.1074/jbc.M807632200.
59. Wang, K., Liu, Y., Li, Y., Guo, Y., Song, P., Zhang, X., Zeng, S., & Wang, Z. (2011). Precise spatiotemporal control of optogenetic activation using an acousto-optic device. *PloS ONE, 6*(12), e28468. doi:10.1371/journal.pone.0028468.
60. Watanabe, S., Liu, Q., Davis, M. W., Hollopeter, G., Thomas, N., Jorgensen, N. B., & Jorgensen, E. M. (2013). Ultrafast endocytosis at Caenorhabditis elegans neuromuscular junctions. *eLife, 2,* e00723. doi:10.7554/eLife.00723.

61. Wen, L., Wang, H., Tanimoto, S., Egawa, R., Matsuzaka, Y., Mushiake, H., Ishizuka, T., & Yawo, H. (2010). Opto-current-clamp actuation of cortical neurons using a strategically designed channelrhodopsin. *PloS ONE, 5*(9), e12893. doi:e12893 [pii].
62. Wietek, J., Wiegert, J. S., Adeishvili, N., Schneider, F., Watanabe, H., Tsunoda, S. P., Vogt, A., Elstner, M., Oertner, T. G., & Hegemann, P. (2014). Conversion of channelrhodopsin into a light-gated chloride channel. *Science, 344*(6182), 409–412. doi:10.1126/science.1249375.
63. Xu, W., & Sudhof, T. C. (2013). A neural circuit for memory specificity and generalization. *Science, 339*(6125), 1290–1295. doi:10.1126/science.1229534.
64. Yizhar, O., Fenno, L. E., Prigge, M., Schneider, F., Davidson, T. J., O'Shea, D. J., Sohal, V. S., Goshen, I., Finkelstein, J., Paz, J. T., Stehfest, K., Fudim, R., Ramakrishnan, C., Huguenard, J. R., Hegemann, P., & Deisseroth, K. (2011). Neocortical excitation/inhibition balance in information processing and social dysfunction. *Nature, 477*(7363), 171–178. doi:10.1038/nature10360.
65. Zhang, Y. P., & Oertner, T. G. (2007). Optical induction of synaptic plasticity using a light-sensitive channel. *Nature Methods, 4*(2), 139–141. doi:10.1038/nmeth988
66. Zhang, F., Wang, L. P., Brauner, M., Liewald, J. F., Kay, K., Watzke, N., Wood, P. G., Bamberg, E., Nagel, G., Gottschalk, A., & Deisseroth, K. (2007). Multimodal fast optical interrogation of neural circuitry. *Nature, 446*(7136), 633–639. doi:10.1038/nature05744.
67. Zhang, F., Prigge, M., Beyriere, F., Tsunoda, S. P., Mattis, J., Yizhar, O., Hegemann, P., & Deisseroth, K. (2008). Red-shifted optogenetic excitation: A tool for fast neural control derived from Volvox carteri. *Nature Neuroscience, 11*(6), 631–633. doi:nn.2120 [pii].
68. Zhao, S., Ting, J. T., Atallah, H. E., Qiu, L., Tan, J., Gloss, B., Augustine, G. J., Deisseroth, K., Luo, M., Graybiel, A. M., & Feng, G. (2011). Cell type-specific channelrhodopsin-2 transgenic mice for optogenetic dissection of neural circuitry function. *Nature Methods, 8*(9), 745–752.

Chapter 6
Optogenetics in *Drosophila melanogaster*

Sung Soo Kim, Romain Franconville, Dan Turner-Evans and Vivek Jayaraman

Abstract The increasing popularity of the fruit fly, *Drosophila melanogaster*, in systems neuroscience can be attributed to the widespread availability of powerful genetic reagents that make efforts at understanding its numerically simple brain tractable, revealing the neural basis of a rich repertoire of behaviors. These tools allow exogenous labels, indicators, activators, and inhibitors of neural activity to be expressed in sparse sets of identified neurons in the brain, enabling specific, targeted neural recording and manipulation. In particular, thermogenetic reagents for activation and silencing, such as dTrpA1 and Shibire^{ts1}, have helped researchers identify circuits involved in a range of fly behaviors. However, temperature-sensitive reagents are slow to activate, and induce complicated behavioral artifacts in ectothermic animals such as flies. Early optogenetic reagents, such as channelrhodopsin2 and halorhodopsin, enabled temporally precise neural perturbation and had an almost immediate impact on mammalian neuroscience. Their use in intact flies was, however, hindered by the fact that blue and green excitation light does not efficiently penetrate adult fly cuticle, and the use of high-intensity light introduces artifacts, such as increased body temperature and photoreceptor-triggered behavioral responses. In this article, we discuss advances in the use of optogenetics in flies, with a special emphasis on recently developed bistable opsins and red-activated channelrhodopsins, CsChrimson, and ReaChR. Using a combination of genetic tools and an appropriate light delivery strategy, these optogenetic reagents allow precise spatial and temporal manipulation of neural activity in the fly while minimizing thermally and visually induced artifacts. We also consider some applications of optogenetics in flies, including testing for the role of identified neurons in the brain of tethered and freely behaving flies and, in combination with genetically encoded calcium indicators, mapping coarse functional connectivity between specific neurons.

V. Jayaraman (✉) · S. S. Kim · R. Franconville · D. Turner-Evans
Howard Hughes Medical Institute, Janelia Farm Research Campus, Ashburn, VA, USA
e-mail: vivek@janelia.hhmi.org

A. D. Douglass (ed.), *New Techniques in Systems Neuroscience,* Biological and Medical Physics, Biomedical Engineering, DOI 10.1007/978-3-319-12913-6_6

6.1 Introduction

Optogenetic tools such as channelrhodopsins and halorhodopsins [9, 54, 98, 110], are widely used to manipulate neural activity in the mammalian brain. Unfortunately, their application in the fruit fly, *Drosophila melanogaster*, has been limited. Blue light that is used to activate most opsins does not efficiently penetrate fly cuticle. As a result, optogenetic applications in the intact fly have usually been restricted to neurons near the body surface, such as peripheral chemosensory neurons in the proboscis [25, 42, 72] and antennae [24, 95], or to neurons in larvae, whose cuticle is less light-reflective than adult cuticle [5, 37, 40, 73, 82, 90, 101, 115]. Stimulation of neurons in the brain through adult cuticle has been more challenging, though not impossible [17, 30]. Further, because fly photoreceptors are very sensitive to blue light, optogenetics has been successful only for behaviors that are unaffected by visual-system-mediated artifacts [106], in contexts in which blue light can be blocked from reaching the eyes [24, 30], or with blind flies [17].

Such shackles have been broken with the recent development of two red-shifted channelrhodopsin variants, ReaChR [43] and CsChrimson [48]. ReaChR is an engineered variant of a widely used channelrhodopsin (ChR2) [56], whereas CsChrimson is a membrane-trafficking-enhanced version of a newly extracted microbial opsin, Chrimson [48]. Genetic effector lines of these reagents are both more sensitive and more suitable for behavioral studies than any previously available optogenetic reagents, because of the better cuticle penetrance of red light (Fig. 6.1, [43]) and also because of greatly improved genetic expression [78] and membrane trafficking systems [26, 43, 48]. These reagents enable reliable activation of neurons in the central brain of intact flies with much weaker light than previously possible, making optogenetics truly usable for a wide array of applications in *Drosophila*.

There are already many genetic tools for flies of course, such as cell killers, inhibitors, and activators controlled by temperature or drugs (see [93, 100] for comprehensive reviews), which raises the question of why one might favor optogenetic

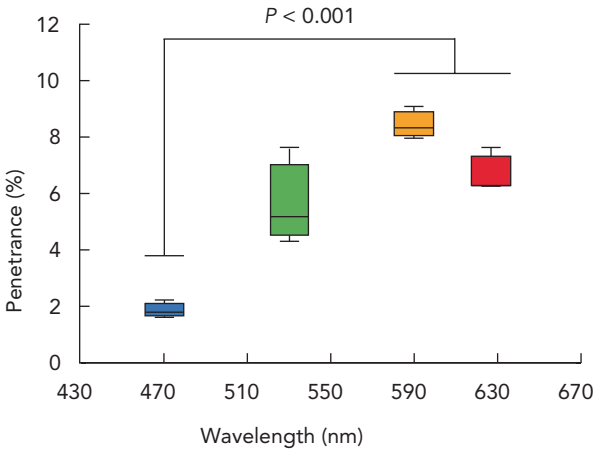

Fig. 6.1 Efficiency of light penetration through adult fly cuticle. (Source: [43])

tools over such alternatives. The obvious answer is the *temporal precision* of neural circuit manipulation that optogenetics provides. The genetic perturbation methods that are used most commonly within the fly community take minutes to hours to affect neural activity, whereas optogenetic tools act rapidly (milliseconds to seconds, at worst) and are quickly reversible. Further, with the Chrimson family of opsins (Chrimson, ChrimsonR, and CsChrimson), or ReaChR, thermally induced behavioral artifacts can be minimized or even completely eliminated, allowing cleaner experimental designs and requiring fewer temperature controls than are needed for dTrpA1 and Shibire^{ts}.

Here, we provide guidelines for the use of optogenetic tools in adult *Drosophila*, focusing primarily on red-shifted channelrhodopsins, but all the information in this chapter should apply to larval experiments as well [37, 48, 82]. We will first review progress in the development of optogenetic tools for *Drosophila*. Then, we will briefly describe how to control spatial and temporal expression of opsins in the nervous system. Light delivery methods and the mitigation of behavioral artifacts will be discussed next. Finally, we will provide examples of experimental applications and describe hardware setups that can be easily repurposed.

6.2 Early Optogenetics in Drosophila

The earliest application of optogenetics in any intact behaving animal came in *Drosophila* [53]. In these experiments, photostimulation was used to uncage ATP, thereby opening P2X2, an ATP-gated channel [10, 99] that was expressed in a subset of neurons including the escape-response-inducing giant fiber neuron. Although the imprecision and delay introduced by the injection and UV-uncaging of ATP to activate P2X2 has limited its use in behavioral studies, the basic scheme of using P2X2 with ATP stimulation has proved useful in physiological experiments [38, 39, 103, 109].

6.3 Microbial Opsins Available in Drosophila

In contrast to P2X2, which was first expressed and tested in *Drosophila*, subsequent optogenetic tools have first been developed in other species before being transferred to the fly. A major advance in the reliability, ease of use, and temporal precision of these tools came with the introduction of single-component reagents, such as ChR2 [9], eNpHR [112], and VChR1 [114]. Among these, the original channelrhodopsin2 [9, 40] has been the most widely used reagent within the fly community (see Fig. 6.6 for references). Other variants, such as C1V1 [111] and ET/TC [7], have been injected into flies but have found limited use, with the notable exception of the H134R mutant [43, 63, 68, 82]. In addition, a bistable ChR2 (C128S mutant) has been used to circumvent visual-system-mediated behavioral artifacts [30]. Among

inhibitors, only the halorhodopsin, eNpHR, has been used in flies [41, 105]. However, as mentioned previously, all of these opsins are problematic to use in *Drosophila* due to limited cuticle penetrance at the activation wavelengths and induced behavioral artifacts. In addition, if the proteins are expressed in the membrane at low levels, neural activation or inhibition requires intense illumination. High-intensity light generates undesirable heat and thus requires a cooling system in the behavior chamber and a complicated lighting system (for example, see Fig. 6.7d [24] and 6.7e [30]). Fortunately, ReaChR and CsChrimson address many of these concerns.

In this section, we briefly discuss the aforementioned opsins in *Drosophila*: ChR2, ChR2-H134R, ReaChR, CsChrimson, ChR2-C128S, and halorhodopsin (eNpHR). Much of the information provided here relies on both *Drosophila* experiments and those carried out in mammalian cell culture and slice.

6.3.1 Channelrhodopsin2 Variants: ChR2 and ChR2-H134R

ChR2 was the first channelrhodopsin successfully used to activate mammalian neurons [9]. Since then, many variants have been engineered. Some, including the original ChR2 and one of the variants, ChR2-H134R, have been injected in *Drosophila* and employed in many experiments. Figure 6.2a compares ChR2 and ChR2-H134R performance at the larval neuromuscular junction (NMJ) [82]. The opsins were expressed in motor neurons, and a 10 ms blue light pulse was delivered at different intensities to activate them. Neurons with ChR2-H134R were more reliably activated at lower light levels than those expressing ChR2. Because of its enhanced efficiency relative to ChR2, ChR2-H134R has found wide use [43, 63, 68, 82].

6.3.2 Red-Shifted Channelrhodopsins: ReaChR, CsChrimson, and ChrimsonR

ReaChR is a ChR2 engineered to be red-activatable [56]. ReaChR's activation spectrum peaks at ~530 nm with short light pulses (unpublished), but longer light pulses further red-shift the peak to ~590 nm and even 650 nm light can activate the channel (Figs. 6.2b and 6.3a, [48, 56]). ReaChR has been used to stimulate neurons in the brain of intact behaving flies with normal high-power LEDs, and can elicit reproducible patterns of spikes at relatively low light intensities (Fig. 6.4, [43]).

Chrimson is an even further red shifted channelrhodopsin (Fig. 6.2c). Extracted from the algae *Chlamydomonas noctigama* [48], it has a peak activation wavelength of ~590 nm (Fig. 6.3a). It is the first channelrhodopsin that can be driven by deep red light (720 nm, Fig. 6.5a, b). However, its off-kinetics are relatively slow (~21.4 ms, Fig. 6.3b).

Membrane trafficking of Chrimson is enhanced in the CsChrimson variant, which is a chimera between another activator, CsChR, and Chrimson (see [48] for more details). When combined with technical improvements in *Drosophila* genetics

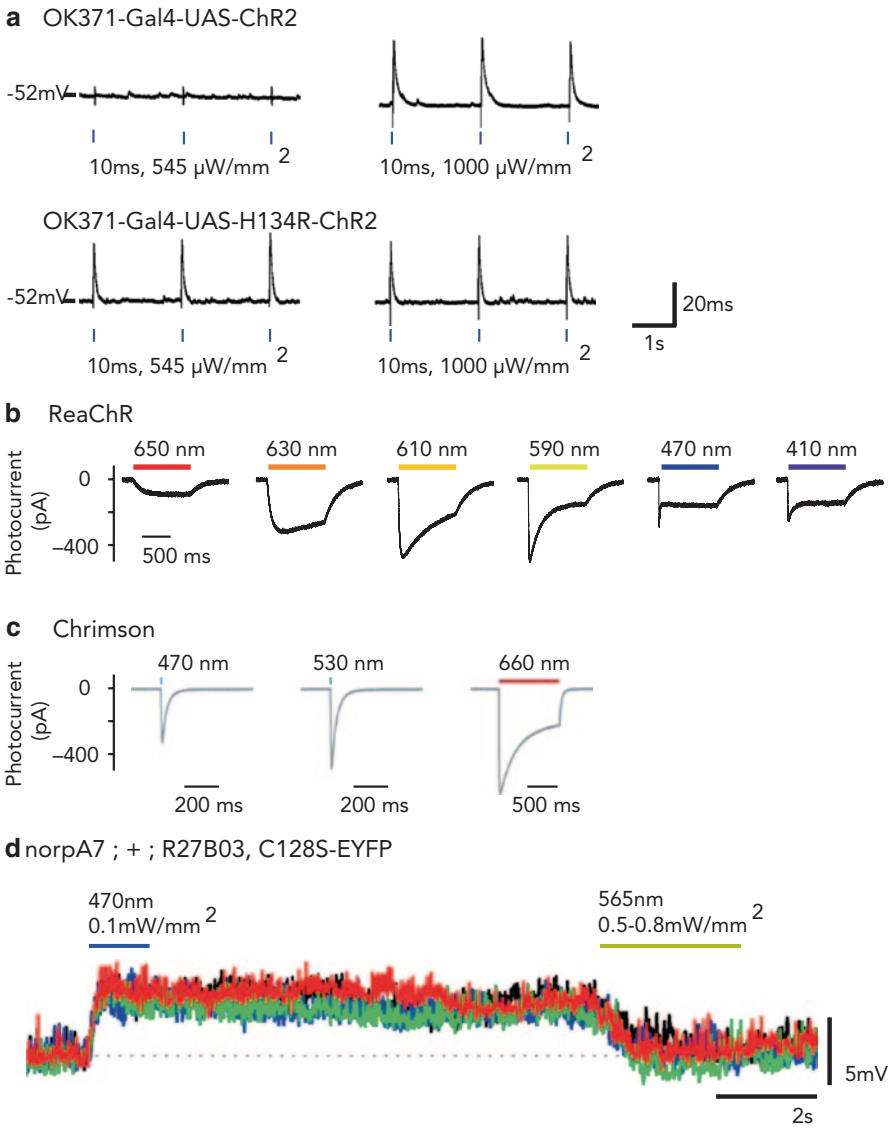

Fig. 6.2 **a** Thresholds for evoking single excitatory junction potentials (EJPs) at the m6 neuromuscular junction (NMJ) of *Drosophila* larvae for ChR2 and ChR2-H134R (Source: [82]). **b**. Light sensitivity of ReaChR measured by intracellular recording (HEK293 cells) with 1 s light stimulation across wavelengths (5.1×10^{16} photon/mm^2 s for all wavelengths tested, (Source: [56]). **c**. Representative voltage-clamp traces in cultured neurons expressing Chrimson (1 s, 10 mW/mm^2 for 660 nm, 5 ms, 3.66 mW/mm^2 for 530 nm, 5 ms, 4.23 mW/mm^2 for 470 nm, (Source: [48]). **d**. Whole-cell recordings of an HS LPTC, expressing a bistable step opsin, ChR2-C128S. *Blue* light (1 s) activated the bistable opsin, inducing a prolonged 2.5 mV depolarization that was deactivated by *yellow* light (3 s) (averages of five cells in blind norpA mutant flies. (Source: [30])

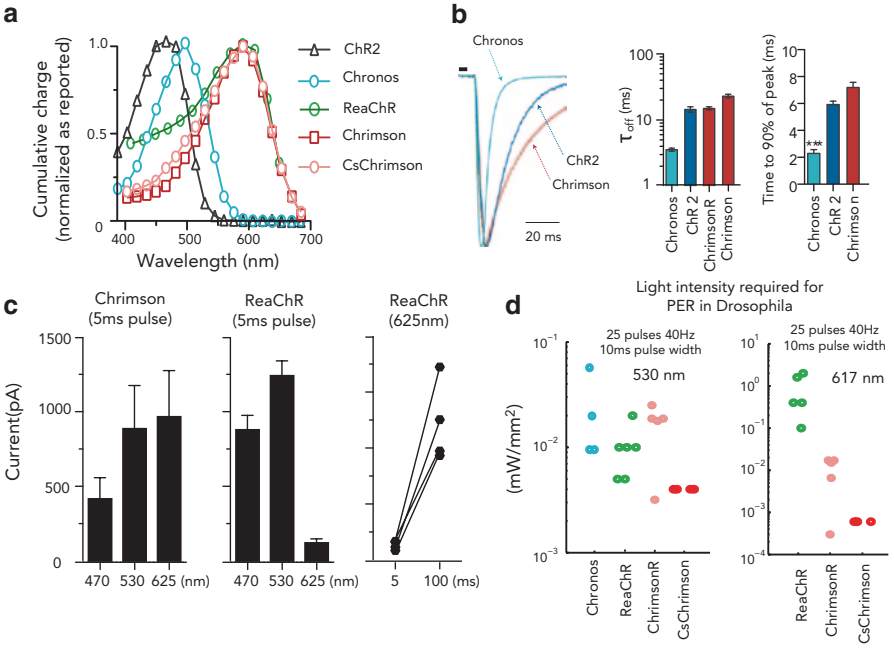

Fig. 6.3 **a** Channelrhodopsin action spectra (Source: [48, 56]). **b**. Channelrhodopsin properties in cultured neurons. τ_{off}: monoexponential fit of photocurrent decay (Source: [48]). See Fig. 6.5 for Chrimson variants. **c**. Comparison of Chrimson and ReaChR activation spectra ($n=5$ cells; 4.23 mW/mm^2 for 470 nm, 3.66 mW/mm^2 for 530 nm, 3.14 mW/mm^2 for 625 nm). With a 5 ms pulse, Chrimson shows maximum current at 625 nm. ReaChR shows maximum current at 530 nm with a 5 ms pulse, but current increases dramatically with 100 ms pulse (Source: [48]). **d**. Proboscis extension response (PER) of adult *Drosophila* expressing opsins in sweet taste receptor neurons (Gr64f.). Light pulses were presented with interstimulus intervals of 5 s. Light of a given intensity was presented five times, with a 1 min interval between presentations of different intensities. Tests started from the lowest possible intensities capable of driving the LED to avoid deactivation. Required light intensities for PER were determined as the lowest intensity that evoked reliable PER for all five consecutive trials

that boost expression [78], CsChrimson enables very sensitive optogenetic stimulation in flies (Fig. 6.5a, b).

A faster variant of Chrimson, ChrimsonR, also exists (K176R mutant, see [48] for more details). Although ChrimsonR proved less sensitive than CsChrimson when expressed in *Drosophila*, sweet taste receptor neurons for our proboscis extension reflex (PER) experiments (see caption of Fig. 6.5b for details), its off-kinetics are faster than CsChrimson (15.8±0.4 ms versus 21.4±1.1 ms, Fig. 6.3b, 6.5c, d, e, [48]), making it more attractive for applications where temporal precision is a high priority.

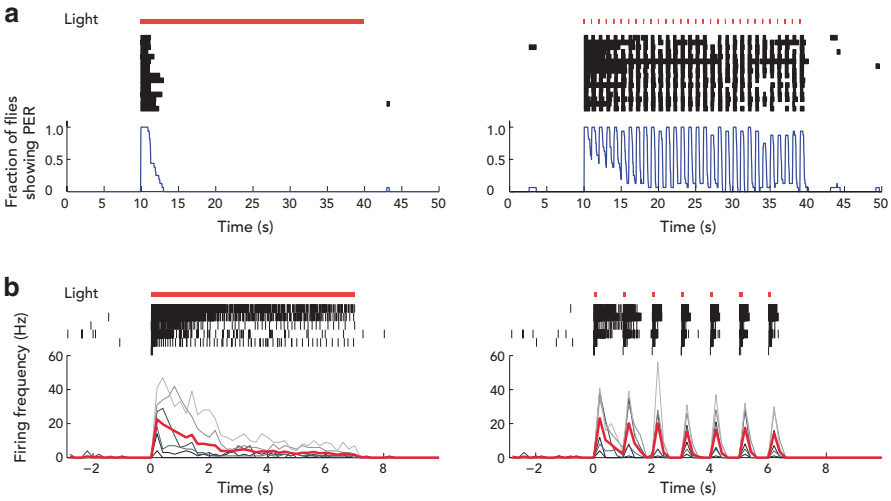

Fig. 6.4 Behavioral (**a**) and electrophysiological (**b**) responses to stimulation of ReaChR in sweet taste receptor neurons (Gr5a). *Red lines*: 627 nm 1.1 mW/mm^2. *Black tick marks*: PER responses (**a**) and spiking responses (**b**). *Blue traces*: fraction of flies showing PER (time bin = 1 s, $n = 16$). *Red traces*: spiking rates (time bin = 200 ms, $n = 6$). *Grey traces*: individual flies. Sustained stimulation (*left*) evoked only transient responses (both behaviorally and electrophysiologically), while 100 ms pulses at 1 Hz (*right*) produced reliable responses for over 30 s (Source: ([43]). Compare with Fig. 6.9b, and c, where light intensity was relatively low

6.3.2.1 Comparison Between ReaChR and CsChrimson

Both CsChrimson and ReaChR are red-shifted and can be effectively used in many applications, but they differ in their activation kinetics. ReaChR is maximally sensitive to red (>600 nm) light if the stimulation duration is long (~100 ms, Fig. 6.2b, 6.3a, c) and to green (~530 nm) light if the stimulation duration is short (<10 ms, Fig. 6.3c). Chrimson is maximally activated at red wavelengths (~600 nm, Fig. 6.3a, c) regardless of the stimulation pulse width [48]. Therefore, CsChrimson is likely to be more versatile than ReaChR for applications in which red light is preferred as an activation source, that is, for deep cuticle/brain penetrance and for minimization of visual system artifacts. However, currently available 20xUAS-CsChrimson versions are toxic with pan-neuronal Gal4 drivers (e.g., elav-gal4 or R57C10) unless all-*trans*-retinal is provided in the food (Karen Hibbard and Stefan Pulver, personal communication). Thus, if an application requires control experiments with pan-neuronal opsin expression in the absence of all-*trans*-retinal supplements, ReaChR would be a safer option, at least until weaker-expressing UAS-CsChrimson fly lines are validated.

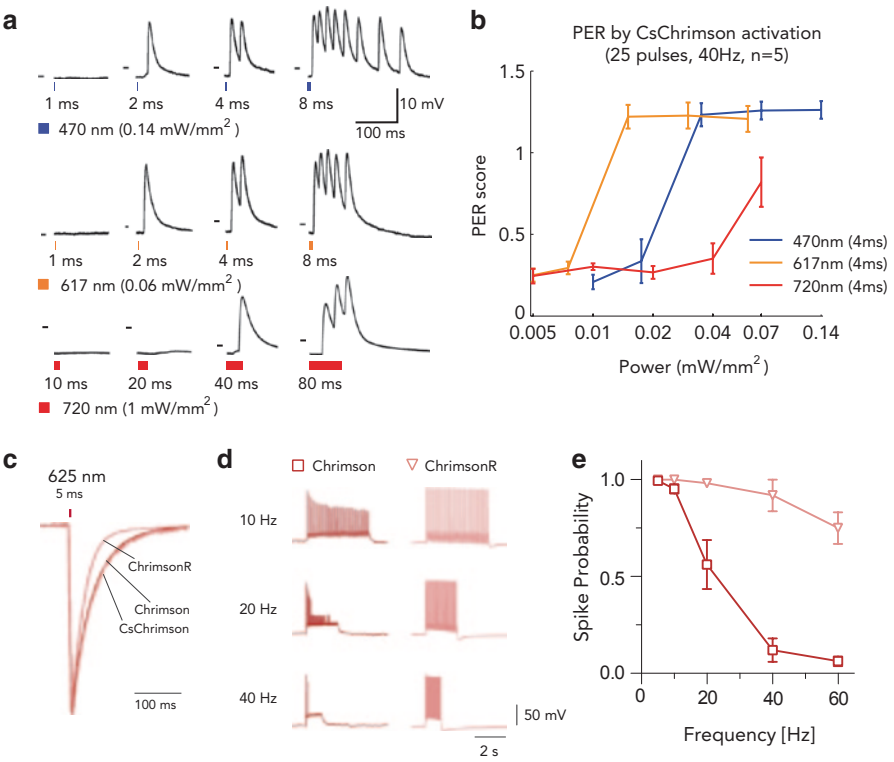

Fig. 6.5 **a** Intracellular recordings from m2 muscles in 3rd-instar larvae expressing CsChrimson in motor neurons. *Small horizontal dashes* in each subpanel indicate –50 mV. Two milliseconds pulse of weak *orange* light or *blue* light was sufficient to drive motor neurons. Longer light pulse induces barrage of EPSPs. Neurons were also driven by deep *red* light (720 nm). **b** PER of flies expressing CsChrimson in sweet taste receptor neurons (Gr64f.). PER score was defined by the distance from the center of head capsule to the tip of proboscis, scaled by the distance from the neck connective to the root of antennae. **c** Representative on- and off-kinetics for Chrimson, ChrimsonR, and CsChrimson. **d** Comparison of wild-type Chrimson and ChrimsonR high-frequency spiking in response to 625 nm light. **e** Population statistics: $n = 10$ for Chrimson, $n = 4$ for ChrimsonR, 40-pulse train, 2 ms pulse width, 5 mW/mm^2. (Source: [48])

6.3.3 *Fast Channelrhodopsin: Chronos*

Chronos is a fast new channelrhodopsin that is driven by blue and green light (peak sensitivity at ~500 nm, Fig. 6.3a). Our preliminary tests in *Drosophila* gustatory receptor neurons showed reliable PER with 530 nm light (Fig. 6.3d). The sensitivity of Chronos to green light (530 nm) was comparable to ReaChR or ChrimsonR (Fig. 6.3d). However, because it is not red-shifted (no activation at 617 nm, Fig. 6.3d), we expect significant visual-system-mediated behavioral artifacts,

unless a careful light delivery strategy is used, such as has been employed for ChR2 (see Light Delivery section below). Nevertheless, Chronos is the fastest of all available opsins (2.3 ± 0.3 ms on-time, 3.6 ± 0.2 ms off-time) and may prove useful in experiments that require precise high-frequency stimulation and are not affected by visual-system-mediated artifacts.

6.3.4 Bistable Channelrhodopsin: ChR2-C128S

ChR2 with a mutation at C128S [6] can be turned on with blue light (~450 nm) and turned off with yellow light (~550 nm). In Fig. 6.2d, ChR2-C128S was expressed in lobula plate tangential cells (LPTCs) of the horizontal system (HS), which respond to optic flow stimuli typically experienced by the fly during yaw rotation. The study used intracellular recordings to show that 1 s of exposure to blue light (blue bar) induced a sustained positive depolarization (~5 mV) in these graded-potential neurons, and three seconds of yellow light exposure reset the membrane potential. This feature of ChR2-C128S makes the opsin particularly useful when visual-system-mediated behavioral artifacts caused by optogenetic activation can critically impact the interpretation of experimental results. ChR2-C128S requires a very powerful LED or laser for activation, but an improved bistable opsin [3] may prove more sensitive.

6.3.5 Halorhodopsin: eNpHr

While cation channels (ChR2 and its variants, CsChrimson and ReaChR) are used for gain-of-function experiments, halorhodopsin (eNpHr), a light-gated chloride pump, has been used to perform loss-of-function optogenetic experiments [26, 27, 41, 105]. eNpHr has a yellow-shifted (540–580 nm) activation spectrum, allowing, to some degree, spectrally separated activation of ChR2 and eNpHr. However, it has not found widespread use in flies. In two studies, one demonstrating a significant behavioral effect of halorhodopsin activation in larvae [41] and the other a weak effect in adults [105], the intensity of activation light used was extremely high (7 ~ 20 mW/mm^2) when compared to the light intensity used in mammalian studies (~3.5 mW/mm^2) (also see [57], in which eNpHr had no effect in olfactory receptor neurons). Two alternatives, archaerhodopsin, a yellow-shifted proton pump [15], and Jaws, a red-shifted cruxhalorhodopsin [16], may find broader use. Preliminary data in *Drosophila* larvae suggests that they are both activated with prolonged illumination at a light intensity comparable to those used in mammalian studies (Stefan Pulver, personal communication).

6.3.6 Summary

A wide variety of opsins have been developed for the optogenetic tool kit. Figure. 6.6 shows light intensities and light wavelengths used to stimulate each of these opsins. It is not based on controlled comparison experiments, but rather on a survey of light intensities reported in published *Drosophila* optogenetics studies. We only include studies that report both the light intensities used and the stimulation protocols. The top panel shows the peak instantaneous light intensity. The vertical span of each marker covers the intensity range used in each study. The bottom plot (adjusted for intensity per second), from which efficiency can be inferred, shows the boosted performance of CsChrimson, which is likely due to trafficking enhancements and stronger expression.

6.4 Targeting Methods

While high sensitivity and specific functionality are essential to opsin performance, the ability to spatially and temporally target their expression broadens their usefulness. Below, we elaborate on techniques that allow for such targeting.

6.4.1 Spatial Targeting

Any application of optogenetics requires appropriate strategies to deliver proteins to the membrane of a specific population of neurons. In mammals, viral injection is the most widely used method [110] (also see [21]), but it comes with challenges in controlling expression levels. Transgenic animal lines can overcome such problems, but require considerable time, effort, and expense to generate and maintain (but see CRISPR/Cas9 system [88]). By comparison, the generation of transgenic lines in *Drosophila* is relatively fast, easy, and cheap. Furthermore, binary gene expression systems such as Gal4/UAS [11, 22] or LexA/Op [51, 96] allow for straightforward targeting of specific neurons [100]. In these binary systems, Gal4 or LexA driver or transactivator lines determine target cells. When the animal is crossed to a UAS or a LexAOp line, respectively, only the cells in the progeny targeted by Gal4 or LexA lines produce the desired proteins (reporter, activator, inhibitor, or some combination of those).

6.4.2 Temporal Targeting

Some applications require the timing of opsin expression in target cells to be controlled. There are three ways to achieve this goal. The simplest way is to exploit the all-*trans*-retinal deficiency in the *Drosophila* brain. In normal applications, all-

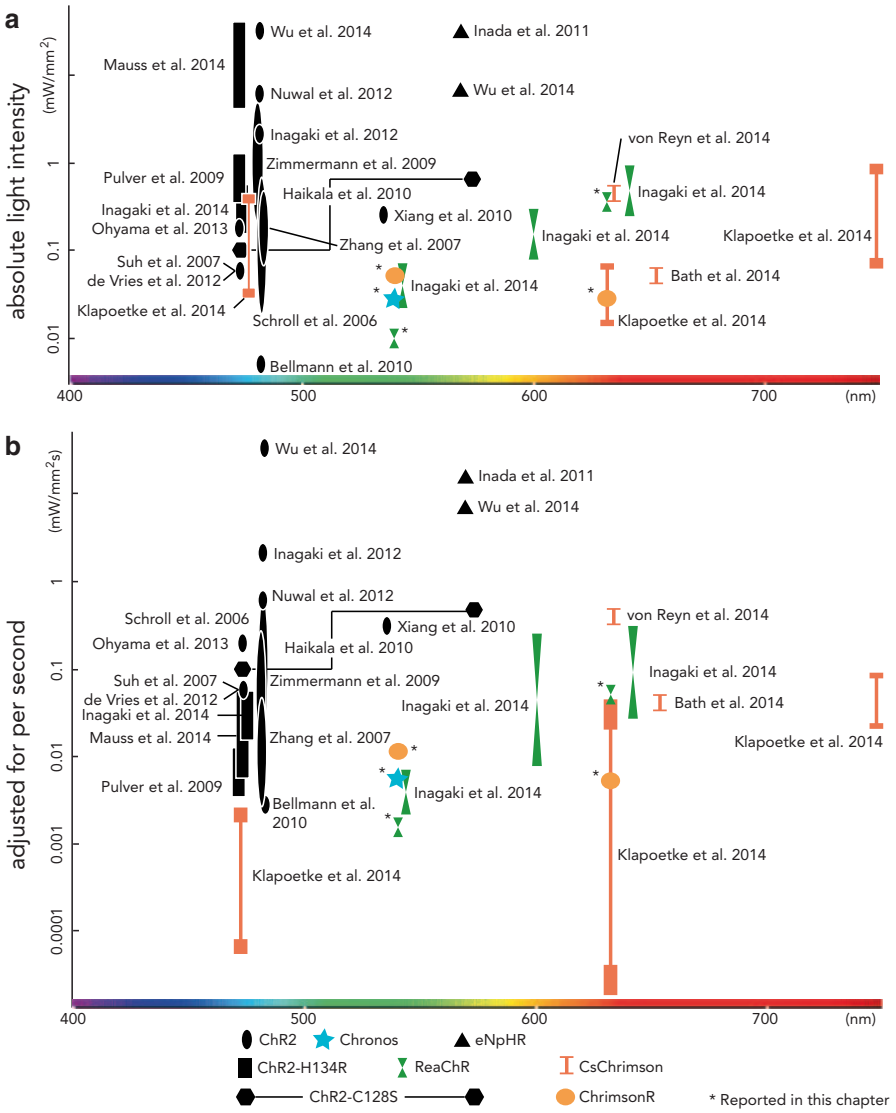

Fig. 6.6 Reported light power used to activate various opsins in *Drosophila*. **a** Instantaneous intensity of light sources. *Vertical span* covers the multiple intensities each study used. Temporal profiles were ignored. **b** Light intensities adjusted for per-second measures as a proxy for activation efficiency of each opsin

trans-retinal must be supplied in the food to make opsins functional in the fly brain. Therefore, controlling the timing of all-*trans*-retinal supply effectively controls the timing of opsin activation. For CsChrimson, we observed maximum excitability after ~5 days of supplying retinal-containing food (0.2 mM all-*trans*-retinal). It is also possible to control the timing of expression using a temperature-sensitive Gal80 repressor [64]. At 18 °C, Gal4 activity is suppressed by Gal80, whereas at

30 °C, Gal80 activity is inhibited and thus Gal4 is activated to express opsins. A minor problem with this method is stochastically leaky expression of Gal4. However, in practice, leaky expression of opsin is likely to be low enough not to generate significant neural activity. Finally, specific drugs can be used to activate an inducible Gal4 system. This method guarantees that Gal4 would not be activated during development, but only when flies are fed appropriate drugs [32, 69, 74, 84]. However, this is not a convenient method because drug-inducible Gal4 lines need to be re-established, that is, the rich library of existing Gal4 lines cannot be used [35, 44, 49, 78].

As an aside, we note that it is also possible to link opsin expression to neuronal activity [47, 60]. However, such methods have not yet found a foothold in flies.

6.5 Light Delivery

Just as expression of the opsins can be controlled in space and time, the delivery of light to activate them can also be manipulated in these regimes to control neural activity. In this section, we will discuss practical issues of light delivery, including the choice of wavelength, power, and homogenization as well as spatial and temporal patterning of beams.

6.5.1 Light Sources for Single Color Optogenetic Activation

The most commonly used light source for ChR2 excitation is a blue laser, which can deliver the high-intensity light required for opsin activation (typically more than 1 mW/mm^2 at 470 nm). LEDs, which are safer and simpler to set up, provide light at intensities sufficient to activate CsChrimson (< 0.5 mW/mm^2 at 617 nm) and ReaChR (< 1 mW/mm^2 at 530 nm). If visual-system-mediated behavioral artifacts need to be controlled, light at wavelengths longer than 700 nm can be used with CsChrimson. Unfortunately, reliable excitation at such long wavelengths requires much stronger light (typically > 10x; see the controlling artifacts section and [48] for more details), and therefore, a red laser may be a better option.

6.5.2 Two-Color Stimulation of Spatially Overlapping Populations

If two populations of neurons are functionally related and spatially overlapping, independent manipulation of each population can provide valuable information about how they interact. Independent stimulation can be achieved by using two opsins of sufficiently nonoverlapping excitation wavelengths. Methods using ChR2 and yellow-peaked opsins such as C1V1 are not free of cross-talk [19, 81, 110, 114], but

the recent characterization of Chronos and Chrimson variants provides a potentially more robust solution (Fig. 6.3a, ([48]). Unfortunately, no *Drosophila* application of two-color activation has been reported yet.

6.5.3 Light Homogenization

For reliable and repeatable stimulation of channelrhodopsins, it is important to maintain light intensity at the same level across trials. This is challenging for experiments in which flies need to be able to move around freely. Therefore, the light needs to be spatially homogenized. There are two methods to ensure a homogenous light profile: (1) collimation and (2) using a diffuser. Using a condenser lens, the light beam from a high power LED or a laser can be expanded and parallelized (Fig. 6.7a). This method is best used to illuminate a small nearby space (~1–2 cm^2), because even the strongest LED in the market cannot illuminate a large area with high enough light intensity. If the illuminated area is large (such as an entire Flybowl [12, 46]), using a diffuser with multiple LEDs presents a better option, as shown in Fig. 6.7b. This, however, may require a custom-designed LED array driver (Fig. 6.7b, c).

6.5.4 Spatially Nonhomogeneous Light

In some cases, it is desirable to stimulate a specific subset of opsin-expressing neurons. To achieve this selectivity, a spatially nonhomogeneous light pattern is required. In most mammalian experiments, mechanical and optical tools can be made small enough relative to the neural structures of interest that careful positioning of a physical device can suffice to achieve local stimulation. However, the *Drosophila* brain is tiny compared to most such tools. Nevertheless, fiber optics have been used to limit the spread of light during stimulation in tethered flies to achieve asymmetric stimulation, as shown in Fig. 6.7d [24], and Fig. 6.7e [30], evoking turning behaviors. Additionally, macroscale illumination of different body part is also possible for freely behaving flies using the flyMAD system, as shown in Fig. 6.7f [4]. However, neither system addresses the problem of shaping emitted light for microscale spatial light control. To address this problem, the light pattern must be sculpted before delivery. Possibilities here include: (1) Digital micromirror devices (DMDs), which can be used to create high-resolution, custom light patterns [2, 20, 29, 52, 85], (2) mirrors driven by galvanometers or AODs to steer light from a one-photon laser to small regions [58], and (3) a similar approach using a two-photon laser to stimulate a highly focused region in 3D without much scattering [1, 59, 62, 66, 70, 71, 76, 77, 80, 83, 108]

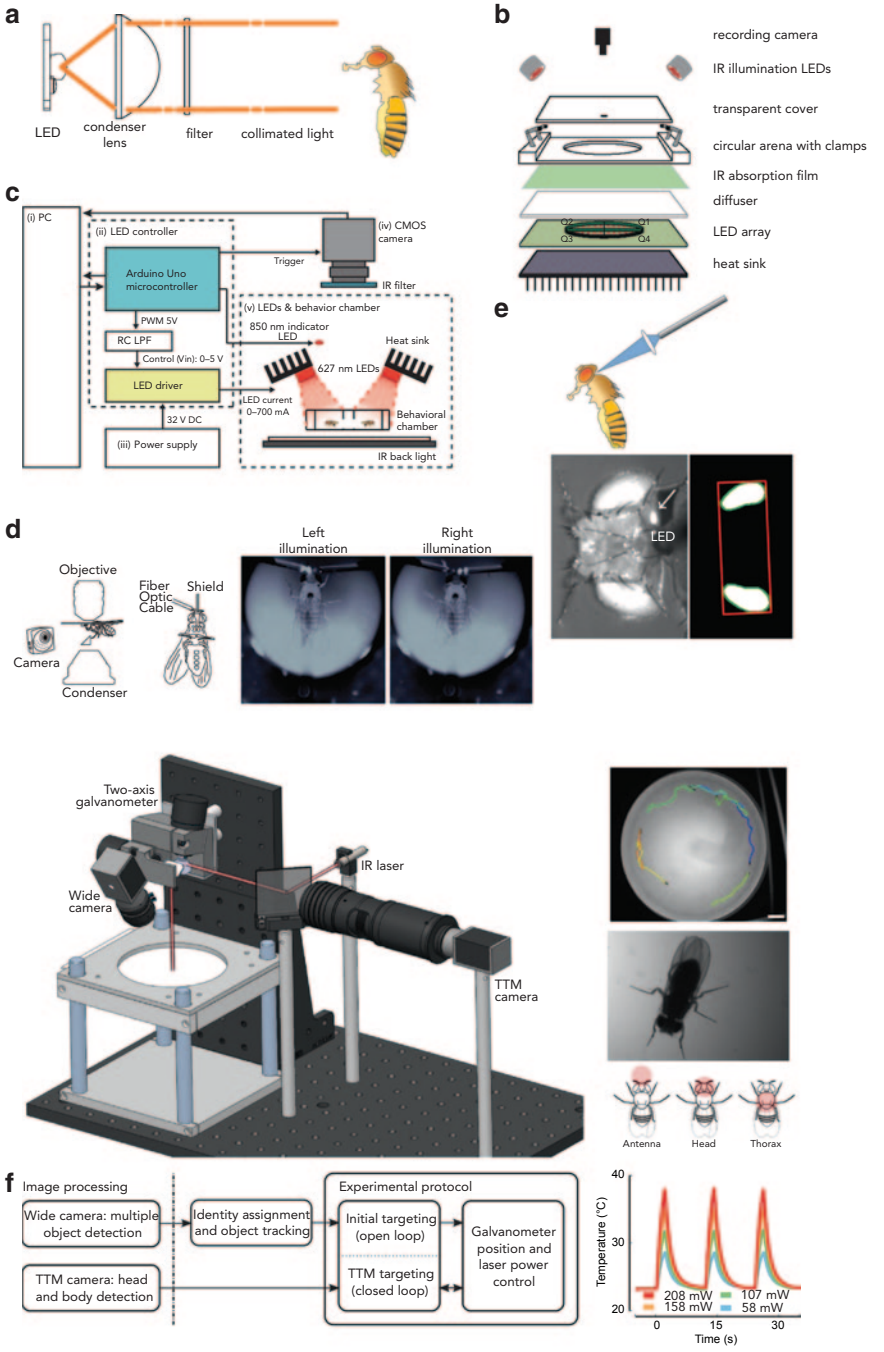

Fig. 6.7 Lighting setups. **a** LED collimation. An aspheric condenser lens provides evenly distributed light. Depending on the power of light source, optics, and opsin expression level in the fly, working distance from the collimated light source to fly may vary allowing flexibility of

6.5.5 *Temporal Patterning of Light Delivery*

The major advantage of optogenetic tools over thermogenetic tools is their temporal precision. Accordingly, most optogenetic applications have focused on neural stimulation on a millisecond time scale. For such stimulation, a relatively high-intensity light is typically delivered as a series of pulses of a few milliseconds (for example, see Fig. 6.3d and 6.4d). Note that, because of the slow off-kinetics of CsChrimson [48] and ReaChR [56], even a short-duration stimulation is likely to generate prolonged firing, as in the larval neuromuscular junction (Fig. 6.5a). In cases where such prolonged activation is undesirable, ChrimsonR may be preferable.

While fast stimulation provides millisecond-level precision, many fly experiments require an increase in neural activity that lasts many seconds or even minutes. Many labs have used thermogenetic tools such as dTrpA1 for that purpose [93, 100]. However, they require an increase in temperature that induces behavioral artifacts. Also, direct body heating using a laser takes at least 500 ms [4] and heating the entire behavioral arena can take even longer (~2–5 s) [43]. Fortunately, CsChrimson and ReaChR can be activated with weak continuous light, as exemplified by Fig. 6.9b, c in the Application section, which demonstrates reliable light-driven CO_2 avoidance behavior and repeated wing-extension bouts driven by prolonged pIP10 stimulation (compare with Fig. 6.4 where the light intensity was relatively high). However, it is important to find the right light intensity that reliably increases baseline activity, yet does not deplete opsins nor increase the temperature of the body or the environment. If the level of CsChrimson or ReaChR expression in a given neuron is low, this strategy is challenging to use.

experimental setup (size of fly exaggerated). b Wide-field illumination with LED arrays. The LED array is placed underneath a circular arena with a layer of a *white* plastic diffuser. The LED array is divided into four quadrants (Q1~Q4). See [48] and Applications (Fig. 6.9c) for more details. **c** Another wide-field illumination with LED arrays. Light is directed from above the arena. See [43] and Applications (Fig. 6.9b) for more details. **d** Small-field illumination with fiber optics. A prism was used to monitor the fly from both the front and the beneath. 50 μm bare fiber was used to deliver *blue* light to stimulate one antenna, while a foil shield was positioned between two antennae to block the light from reaching the other side. The fly stood on a spherical treadmill, and two fiber optic filaments were positioned laterally. The eyes and ocelli were painted *black* to avoid visual-system-mediated artifacts. See [24] and Applications (Fig. 6.9a) for more details. **e** Small-field illumination with focused light: 50 μm fiber optics and a focusing lens were used to stimulate spatially limited sets of neurons by focusing the light on a small area on the back of the head capsule. See [30] and Applications (Fig. 6.10) for more details. **f** Real-time fly position tracking and stimulation (FlyMAD): A fly is placed in a circular arena and allowed to move freely. A wide-field camera detects the rough position of the fly, and a high-magnification camera closely follows the fly using a through-the-mirror (TTM) tracking system, which also directs the stimulation light to the center of imaging area to selectively activate reagents in different parts of the fly body. Sample views from the wide-field camera and the high-magnification camera are shown. Note that the change of body temperature by laser stimulation is slow. See [4] and Applications (Fig. 6.9d) for more details

6.6 Controlling Artifacts

Light for opsin stimulation can also activate photosensitive organs such as eyes and ocelli [87, 91, 104]. High-intensity light can induce tissue damage [79] or heat the cuticle, exciting thermoreceptors, and, if the heated areas release odors (e.g., cuticular hydrocarbons), potentially even odorant receptors [23, 31, 89]. Such unintended activation of sensory organs can lead to behavioral responses that may affect the interpretation of an optogenetic experiment. In this section, we discuss visual-system-mediated and thermal artifacts, as well as toxicity and depolarization block induced by stimulation.

The original channelrhodopsin, ChR2 [9, 113], required continuous blue light of very high-intensity (460∼480 nm and up to 1 mW/mm^2) for activation in *Drosophila* (see Fig. 6.6), thereby inducing several undesired behavioral artifacts, as listed above. Such problems have largely limited the application of the original ChR2 in intact flies to those behaviors in which the artifacts did not significantly affect experimental interpretations.

CsChrimson and ReaChR solve many of these issues, because the low light intensity required for activation does not significantly increase body temperature. The most likely heat source in the setup would be from the LED driver circuit, which can be easily cooled down with a basic fin shaped heat sink (Fig. 6.7b, c). Also, red light is much more efficient for cuticle penetrance (Fig. 6.1). Thus, the only artifact left to control is the visual-system-mediated behavior caused by weak red light.

Red light is outside the normal absorption spectra of fly visual pigments [86, 107]. Although photoreceptor signal cascades induced by light longer than 700 nm have not been carefully characterized, a controlled startle assay in darkness showed that wild-type flies could easily detect up to 720 nm light [18, 33, 48]. The tail of the Rh1 photoreceptor light absorption spectrum extends to ∼670 or 680 nm [86], but does not appear to go over 700 nm. The spectrum of the Rh6 photoreceptor might have an even longer tail because it is more sensitive to longer wavelengths than Rh1 [34, 107], but, once again, no activation has been observed when they are stimulated by light of wavelengths above 700 nm. However, spectroscopy of Rh1 receptors suggests that they do absorb some energy from red light near 700 nm, which may well evoke stochastic activation [86], and Rh5 microspectrophotometry shows a nonzero difference of spectra between rhodopsin and metarhodopsin above 700 nm [86]. Thus, we speculate that metarhodopsin, which is not supposed to contribute to the normal signaling pathway, may in fact have some contribution because its absorption spectra extends to at least 680 nm [65]. Regardless, we were unable to completely inhibit red-light-induced behavioral artifacts. Thus, none of the currently available optogenetic tools can entirely eliminate visual-system-mediated behaviors.

Such caveats aside, flies are certainly less sensitive to red light than blue light. Indeed, dim wide-field blue light, such as that used to present visual stimuli, can be used to mask the flash of deep red light (720 nm, but not 617 nm) used for CsChrimson activation and entirely eliminates behavioral artifacts in the startle

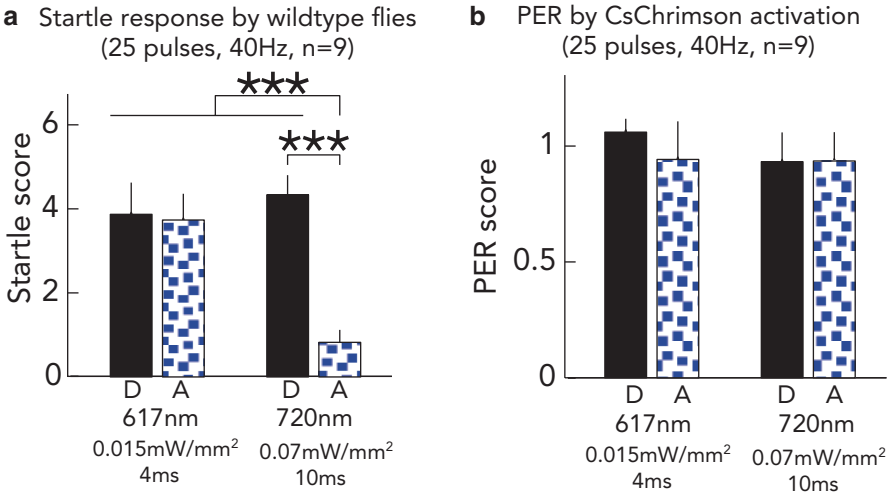

Fig. 6.8 Inhibition of visual-system-mediated behavioral artifacts. Startle response of wild-type flies by stimulation pulses of 720 nm light was inhibited when flowing *blue random dots* are presented together (**a**). The light level reliably induced PER response in flies expressing CsChrimson in sweet taste neurons (**b**, Gr64f.). Inhibition of startle response was not observed with 617 nm light. (Source: [48])

assay. However, 720 nm is at the tail end of the CsChrimson activation spectrum and thus needs to be delivered at significantly higher intensity for reliable stimulation (0.07 mW/mm^2, 10 ms pulses vs. 0.015 mW/mm^2, 4 ms pulses for 617 nm excitation, Fig. 6.8). Nevertheless, the intensity required is low enough to not build up any heat or cause photo-damage.

It should be noted that extended exposure to light can cause a reduction of activity [43, 82], or even unwanted inhibition of neural activity because of depolarization block [36, 61]. In many cases, slow opsins tend to saturate with high-frequency light stimulation and cannot follow fast modulation. The specific performance will depend on neuronal biophysics, expression level, and light protocol [36], underlining the importance of testing different light intensities and temporal profiles for any new set of neurons before finalizing the experimental procedure.

In summary, for deep red (720 nm) stimulation with CsChrimson, particularly if accompanied by blue-green visual stimuli, the only major concern is heat generated from LED driver circuits if they are physically close to flies. If neurons are stimulated with orange (~617 nm, ~630 nm) or green (~530 nm) light with CsChrimson or ReaChR (i.e., when visually induced behavioral artifacts do not significantly affect the experiment), using minimal light intensity and simple passive cooling for the LEDs may suffice (Fig. 6.7b, c). If only a single LED is used to stimulate a single tethered fly (Fig. 6.7a) or light is delivered directly on neurons in an exposed brain (see Applications), the LED can be placed far from the fly (10~30 cm) and no careful cooling is necessary.

6.7 Applications

In this section, we introduce three applications. First, we describe behavioral assays in which CsChrimson and ReaChR present a higher-temporal-precision alternative to thermogenetic tools. Second, we highlight an application in which the minimization of visual-system-mediated artifacts was crucial. Finally, we discuss how channelrhodopsins can be combined with calcium imaging and electrophysiology to map functional connectivity between neurons.

6.7.1 Stimulating Neurons in the Central Brain of Freely Behaving Flies

The most commonly used genetic tool to activate neurons in the fly brain is dTrpA1, a temperature-sensitive channel, but its temporal precision is limited because of inherently slow dynamics of temperature manipulation [4, 43]. Furthermore, even small changes in temperature affect the behavior of flies, which are ectothermic [23, 31, 89]. Highly sensitive optogenetic tools that can be activated at low light levels address both these concerns.

The original blue-light-activated ChR2 has been used effectively in situations that permit shielding of the light from photoreceptors. One study used the reagent to show that *Drosophila* can lateralize odors despite the fact that olfactory receptor neurons (ORNs) in each of their antennae send axons bilaterally. The authors expressed ChR2 in a specific type of ORN and delivered light locally to individual antennae (Fig. 6.7d) to show that flies consistently turned in response to such unilateral ORN stimulation (Fig. 6.9a). Importantly, light was delivered using optical fibers and was prevented from reaching either the other antenna or the fly's photoreceptors.

Red-shifted opsins permit behavioral experiments in which light can be delivered without such shielding. Figure 6.9b shows courtship behavior (wing-extension) induced by stimulation of ReaChR expressing pIP10 neurons, descending neurons in the courtship pathway [4, 43, 102]. This experiment highlights the utility of ReaChR for prolonged neural activation: the duration of the light pulse (green rectangles) is 30 s, and the wing-beat extension bout repeats during the whole stimulation period and quickly stops after the light is turned off.

In a different experiment depicted in Fig. 6.9c, flies moved freely in a circular arena (Fig. 6.7b). CsChrimson was expressed in a set of olfactory projection neurons of the V glomerulus, which is known to be selectively responsive to CO_2, an aversive odor stimulus for flies [45, 50, 55, 92, 94, 95]. A weak continuous 617 nm light was used to optogenetically evoke reliable avoidance behaviors (Fig. 6.9c). Control flies (i.e., those without CsChrimson) did not show any light-induced avoidance or attraction response.

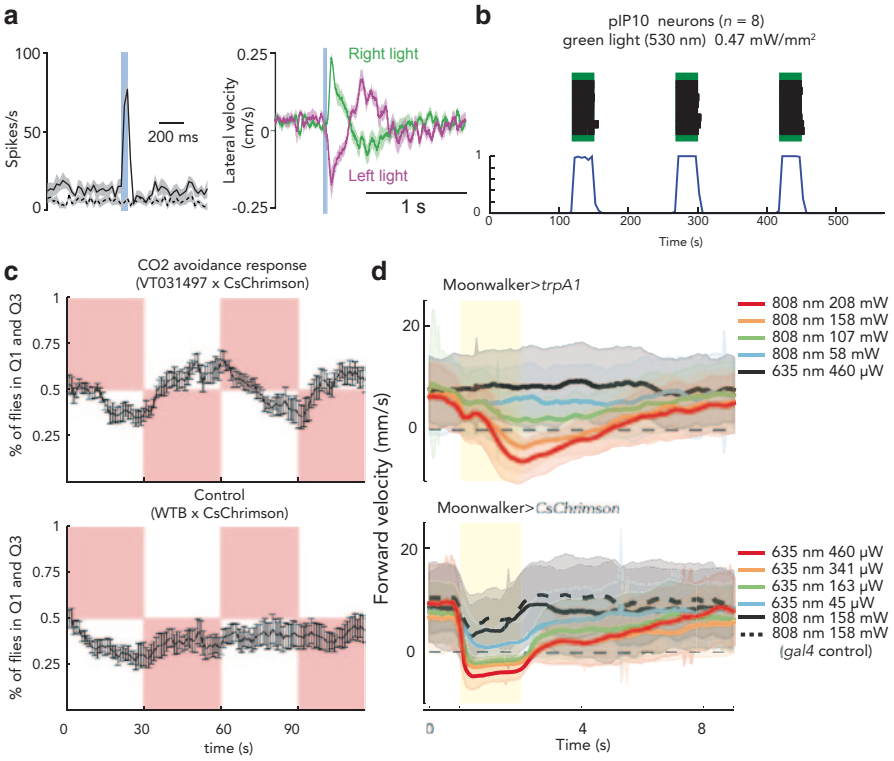

Fig. 6.9 **a** *Left*: ChR2 was expressed in olfactory receptor neurons in DM1 glomeruli (DM1 ORNs). *Blue* light stimulation induced robust responses in ChR2-expressing DM1 ORNs (*solid line*) but not in other ORNs (*dashed line*). *Right*: Time course of mean lateral velocity during activation of ChR2-expressing DM1 ORNs. (Source: [24]). **b** Activation of pIP10 neurons (VT40556/UAS > mCherry > ReaChR(attP40);fru-FLP) with *green* light (530 nm, 0.47 mW/mm^2). *Top*: raster plot representing wing extension bouts ($n = 8$). *Green shades*: 30 s continuous photostimulation trials with 120 s intertrial intervals. *Bottom*: fraction of flies showing wing extension (time bin: 5 s, Source: ([43]). **c** Two opposing quadrants (Q1 and Q3, or Q2 and Q4) of the arena (Fig. 6.7b) were illuminated for 30 s (0.015 mW/mm^2) and the illumination switched to the other two quadrants for the next 30 s. Switching protocol was repeated three times for a total video recording of 120 s. For each session (total of 9 sessions for each group), 10 ~ 20 flies were put in the arena. *Top*: Fraction of flies in Q1 and Q3 for the experimental group in which CsChrimson was expressed in CO_2-sensitive neurons in v-glomerulus. If Q1 and Q3 are illuminated, *red square* shade is drawn on the *top half* of the plot. *Bottom*: Result of a control group (Source: [48]). **d** Stimulation of Moonwalker neurons (*yellow shade*) induced backward walking. Note that CsChrimson required lower light power and showed smaller response latency than dTrpA1. (Source: [4])

Figure 6.9d [4] shows a direct comparison between dTrpA1 and CsChrimson. Each activator was individually expressed in a set of neurons known to induce backward walking if activated (a.k.a. moonwalker neurons VT50660-Gal4, [8]). These neurons in freely moving intact flies were optically stimulated using the flyMAD system (Fig. 6.7f). Note that CsChrimson required 2–3 orders of magnitude lower light intensity than dTrpA1 and induced behavioral responses almost immediately.

The above results demonstrate that red-shifted channelrhodopsins can successfully replace thermogenetic activators for experiments in freely behaving flies. Likewise, it should also be possible to use red-shifted channelrhodopsins to stimulate other kinds of neurons, such as those involved in neuromodulation (e.g., DA, OA, and 5HT) to induce learning, or sensory neurons, such as sweet-taste receptors or bitter-taste receptors [67], as potential unconditioned stimuli for learning paradigms.

6.7.2 Optogenetic Stimulation in the Visual System

For obvious reasons, it is particularly important to minimize visual-system-mediated behavioral artifacts when the neurons targeted for optogenetic stimulation are naturally responsive to visual stimuli.

Figure 6.10a demonstrates an application of CsChrimson to a visually driven behavior, showing the escape response of flies when two giant fiber neurons (GFs) are activated with CsChrimson [103]. When a looming stimulus is presented, flies try to escape either through a coordinated sequence of body posture changes (long escape) or by kicking away without such a preparatory motor sequence (short escape). When GFs were activated using CsChrimson, flies showed the short escape phenotype, which, together with other results from silencing experiments, suggested exclusive GF involvement in the short escape mode.

The above example suggests that photoreceptor activation with red light does not present insurmountable problems for the use of CsChrimson, even in the context of visually driven behavior. But the problem can be entirely circumvented by using bistable opsins, such as ChR2-C128S, which is activated by a short pulse of blue light (~470 nm), and deactivated by a short pulse of yellow light (~565 nm) [3, 6, 30].

When the ChR2-C128S was expressed in HS LPTCs, whole-cell recordings (Fig. 6.2d) showed robust depolarization of HS neurons (~2.5 mV) after 1 s of blue light excitation (470 nm, 0.1 mW/mm^2), with the membrane potential falling back to baseline after 3 s of yellow light illumination (565 nm, 0.5~0.8 mW/mm^2). Figure 6.7e shows the experiment setup, which allows monitoring of the behavior of tethered flies. The fly was placed in a visual arena and a fiber optic was used for light delivery. Light was focused on the back of the fly's head capsule. The total light power (50 μm diameter) was 10 μW (~1.27 mW/mm^2) for blue light and 6 μW (~0.76 mW/mm^2) for yellow light. A protocol that involved 1 s of blue light excitation of one side of the fly's head induced significant head turning and wing beat bias in blind flies (Fig. 6.10b, [30]).

Although bistable opsin requires a relatively high level of light intensity compared to CsChrimson or ReaChR, it is entirely free of visual-system-mediated artifacts outside the initial excitation/deactivation lighting periods. Improved versions have the potential to be applicable to an even broader range of experiments [3].

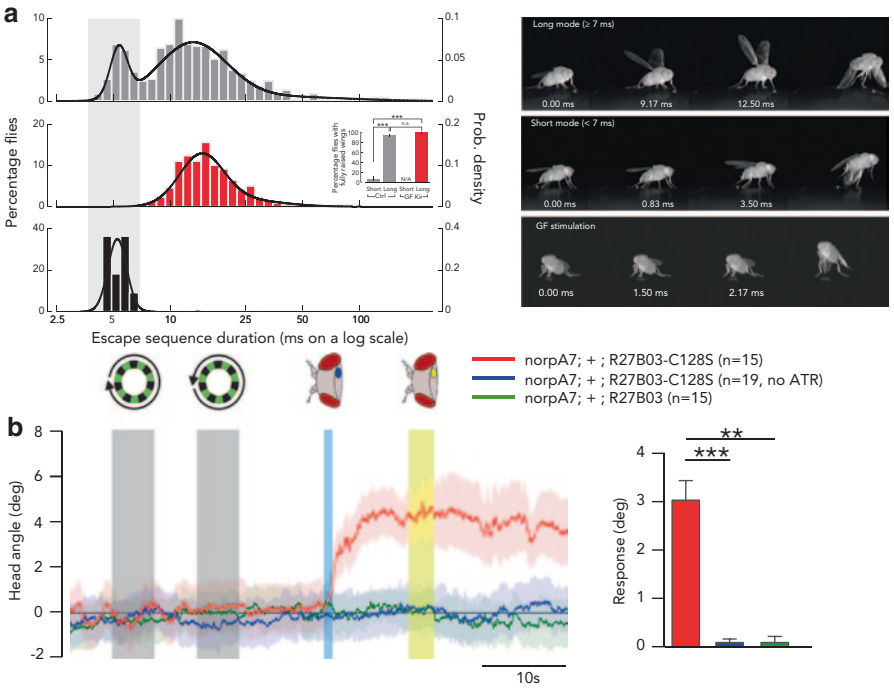

Fig. 6.10 **a** *Left top*: Two escape modes (short and long modes, shown as two peaks of the histogram) induced by looming stimulus. *Left center*: Inhibition of short escape mode by GF silencing. *Left bottom*: Induced jumping similar to short escape mode by activation of CsChrimson-expressing GF. *Right*: From *top* to *bottom*, long escape mode (note the complex motion sequence including the preparatory wing raise and body posture adjustment > 7 ms), short escape mode (simple leg kicking, no wing extension, short motion sequence of < 7 ms), and induced jump by GF stimulation (Source: [103]). **b** Effect of asymmetric HS LPTC activation on head rotation. Bistable opsin was expressed in HS cells of blind flies. Moving grating bars did not induce any head direction change in blind flies (*grey shades*), but asymmetric *blue* light activation of bistable opsins in HS cells induced strong head rotation. Head direction was sustained even after *yellow* light exposure. (Source: [30])

6.7.3 Mapping Coarse Functional Connectivity

A complete understanding of neural circuit function requires that we know how different circuit elements interact with each other. In mammals, viral synaptic tracing techniques are a standard way of getting at structural connectivity [13, 75]. These tools, for unknown reasons, have not produced satisfying results in flies. Instead, alternative methods have been developed, trying to exploit the huge libraries of genetic transformants. EM reconstruction combined with a characterization of the transmitter and receptor profiles of different neurons will ultimately provide a detailed structural connectome for the fly brain [97], but this requires enormous

time and effort and does not provide information about the strength of the individual synaptic connections or the way postsynaptic cells integrate their inputs.

Functionally connected pairs of cell classes can be more quickly discovered by expressing a neural activator in a potential presynaptic neuronal population while recording the activity of the hypothesized target neurons. One effector used in flies for that purpose is the P2X2 ATP receptor. As there are no endogenous ATP-gated conductances in the fly brain, expressing P2X2 receptors in a restricted set of neurons renders this set specifically activatable upon ATP application. Functional connectivity can then be quickly assessed by monitoring the candidate postsynaptic neurons with calcium indicators [109]. In their study, Yao et al. applied ATP through the saline, perfusing the entire brain (such experiments are more easily done in an isolated brain preparation). In our hands, more reliable results were obtained by puffing ATP directly on the presynaptic terminals through a glass pipette inserted inside the brain: the timing of ATP delivery is then faster, more local and more precise, and can be monitored if a red fluorophore is added to the ATP solution. An alternative that may provide still greater temporal precision is to use caged ATP and a UV laser to uncage it at the desired target [53].

Opsins have also been used for functional connectivity experiments [28, 63]. Gruntman et al. expressed ChR2 in a set of antennal lobe projection neurons (PNs) and stimulated them with blue light, while recording the activity of a Kenyon cell (KC) in the mushroom body using whole-cell patch-clamp. As shown in Fig. 6.11, KC activity was tightly locked to the blue light stimulation with very short latency, suggesting that it receives monosynaptic connections from the stimulated PNs. The experiment can be further simplified by monitoring postsynaptic calcium activity with indicators such as GCaMP6 [14]. In our experience, this was somewhat unreli-

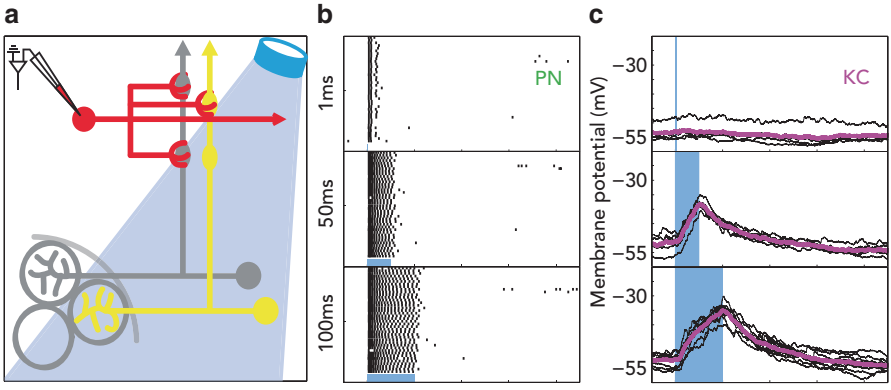

Fig. 6.11 **a** ChR2 was expressed in projection neurons innervating 3 of the 54 total glomeruli. Whole-cell recording of Kenyon cell was performed during *blue* light stimulation of projection neurons. **b** Projection neuron spiking responses to photostimulation with different light stimulation periods. **c** Postsynaptic responses of an example Kenyon cell. *Black traces* represent examples of membrane potential. *The magenta trace* represents the average. *Blue shades* represent photostimulation period. (Source: [28])

able when combined with ChR2 in the fly lines we have tried, but using CsChrimson as a presynaptic activator allowed us to reliably detect connected pairs. We found that for the strongest connections, a mere 2 ms pulse of 617 nm light with an intensity of 0.04 mW/mm^2 was sufficient to drive the presynaptic neuron and reproducibly generated a measurable postsynaptic calcium response (unpublished). The combination of CsChrimson and GCaMP6 presents a number of advantages. First, stimulation of presynaptic neurons and recording of postsynaptic neurons are both optical, making the whole process easier than other methods, permitting tests of dose/response and the use of pharmacology on a single brain. Second, compared to puffing ATP in P2X2 experiments, in which the amount of ATP arriving at the presynaptic terminal cannot be carefully controlled, the light intensity/number of light pulses can potentially be adjusted to explore the properties of a connected pair. Finally, the orange light used for stimulation does not leak into the green fluorescence channel of the microscope. However, care must be taken to avoid imaging areas that include the CsChrimson-expressing pattern, because the 2-photon scanning light may be sufficient to activate the opsin expressing neurons, albeit weakly (unpublished; also reported in [43]). For all methods that combine an activator with GCaMP, the main limitations are the same: (1) Monosynaptic connectivity cannot be proven; (2) An absence of responses does not rule out the existence of a weak connection; (3) Inhibitory connections can be difficult to detect. Nevertheless, the purpose here is to rapidly build coarse connectivity maps that can be refined via other techniques.

6.8 Conclusion

The advantage of *Drosophila melanogaster* in neuroscience is that genetically identified individual neurons can be repeatedly studied across animals allowing interrogation of neural mechanisms underlying complex behaviors. However, previously available tools for neural manipulation were slow (thermogenetic tools), difficult to use (whole-cell recording), or suffered from a risk of producing artifacts (ChR2), making it challenging to control the fine temporal dynamics of neural circuits. In this chapter, we summarized recent development and applications of optogenetic tools that offer better spatiotemporal control of neural manipulation with fewer undesired artifacts. Combined with emerging and existing tools, these opsins are poised both to generate new questions in Drosophila neuroscience and to help answer them.

Acknowledgements The ReaChR flies we tested were a generous gift from D. Anderson. We are grateful to K. Hibbard and S. Pulver for sharing unpublished information about CsChrimson and Jaws flies. We thank the Howard Hughes Medical Institute for support.

References

1. Andrasfalvy, B. K., Zemelman, B. V., Tang, J., & Vaziri, A. (2010). Two-photon single-cell optogenetic control of neuronal activity by sculpted light. *Proceedings of the National Academy of Sciences of the United States of America, 107,* 11981–11986.
2. Arrenberg, A. B., Stainier, D. Y., Baier, H., & Huisken, J. (2010). Optogenetic control of cardiac function. *Science, 330,* 971–974.
3. Bamann, C., Gueta, R., Kleinlogel, S., Nagel, G., & Bamberg, E. (2010). Structural guidance of the photocycle of channelrhodopsin-2 by an interhelical hydrogen bond. *Biochemistry, 49,* 267–278.
4. Bath, D. E., Stowers, J. R., Hormann, D., Poehlmann, A., Dickson, B. J., & Straw, A. D. (2014). FlyMAD: Rapid thermogenetic control of neuronal activity in freely walking Drosophila. *Nature Methods, 11,* 756–762.
5. Bellmann, D., Richardt, A., Freyberger, R., Nuwal, N., Schwarzel, M., Fiala, A., & Stortkuhl, K. F. (2010). Optogenetically induced olfactory stimulation in Drosophila larvae reveals the neuronal basis of odor-aversion behavior. *Frontiers in Behavioral Neuroscience*, 4, 27
6. Berndt, A., Yizhar, O., Gunaydin, L. A., Hegemann, P., & Deisseroth, K. (2009). Bi-stable neural state switches. *Nature Neuroscience, 12,* 229–234.
7. Berndt, A., Schoenenberger, P., Mattis, J., Tye, K. M., Deisseroth, K., Hegemann, P., & Oertner, T. G. (2011). High-efficiency channelrhodopsins for fast neuronal stimulation at low light levels. *Proceedings of the National Academy of Sciences of the United States of America, 108,* 7595–7600.
8. Bidaye, S. S., Machacek, C., Wu, Y., & Dickson, B. J. (2014). Neuronal control of Drosophila walking direction. *Science, 344,* 97–101.
9. Boyden, E. S., Zhang, F., Bamberg, E., Nagel, G., & Deisseroth, K. (2005). Millisecond-timescale, genetically targeted optical control of neural activity. *Nature Neuroscience, 8,* 1263–1268.
10. Brake, A. J., Wagenbach, M. J., & Julius, D. (1994). New structural motif for ligand-gated ion channels defined by an ionotropic ATP receptor. *Nature, 371,* 519–523.
11. Brand, A. H., & Perrimon, N. (1993). Targeted gene expression as a means of altering cell fates and generating dominant phenotypes. *Development, 118,* 401–415.
12. Branson, K., Robie, A. A., Bender, J., Perona, P., & Dickinson, M. H. (2009). High-throughput ethomics in large groups of Drosophila. *Nature Methods, 6,* 451–457.
13. Callaway, E. M. (2008). Transneuronal circuit tracing with neurotropic viruses. *Current Opinion in Neurobiology,* 18, 617–623.
14. Chen, T. W., Wardill, T. J., Sun, Y., Pulver, S. R., Renninger, S. L., Baohan, A., Schreiter, E. R., Kerr, R. A., Orger, M. B., Jayaraman, V., Looger, L. L., Svoboda, K., & Kim, D. S. (2013). Ultrasensitive fluorescent proteins for imaging neuronal activity. *Nature, 499,* 295–300.
15. Chow, B. Y., Han, X., Dobry, A. S., Qian, X., Chuong, A. S., Li, M., Henninger, M. A., Belfort, G. M., Lin, Y., Monahan, P. E., & Boyden, E. S. (2010). High-performance genetically targetable optical neural silencing by light-driven proton pumps. *Nature, 463,* 98–102.
16. Chuong, A. S., Miri, M. L., Busskamp, V., Matthews, G. A., Acker, L. C., Sorensen, A. T., Young, A., Klapoetke, N. C., Henninger, M. A., Kodandaramaiah, S. B., Ogawa, M., Ramanlal, S. B., Bandler, R. C., Allen, B. D., Forest, C. R., Chow, B. Y., Han, X., Lin, Y., Tye, K. M., Roska, B., Cardin, J. A., & Boyden, E. S.. (2014). Noninvasive optical inhibition with a red-shifted microbial rhodopsin. *Nature Neuroscience, 17,* 1123–1129.
17. de Vries S. E., & Clandinin TR. (2012). Loom-sensitive neurons link computation to action in the Drosophila visual system. *Current Biology, 22,* 353–362.
18. Dobzhansky, T., Judson, C. L., & Pavlovsky, O. (1974). Behavior in different environments of populations of Drosophila, pseudoobscura selected for phototaxis and geotaxis. *Proceedings of the National Academy of Sciences of the United States of America, 71,* 1974–1976.

19. Erbguth, K., Prigge, M., Schneider, F., Hegemann, P., & Gottschalk, A. (2012). Bimodal activation of different neuron classes with the spectrally red-shifted channelrhodopsin chimera C1V1 in Caenorhabditis elegans. *PLoS ONE,* 7, e 46827.
20. Farah, N., Reutsky, I., & Shoham, S. (2007). Patterned optical activation of retinal ganglion cells. Conference proceedings:... Annual International Conference of the IEEE Engineering in Medicine and Biology Society. IEEE Engineering in Medicine and Biology Society. Conference, 6368–6370.
21. Fenno, L. E., Mattis, J., Ramakrishnan, C., Hyun, M., Lee, S. Y., He, M., Tucciarone, J., Selimbeyoglu, A., Berndt, A., Grosenick, L., Zalocusky, K. A., Bernstein, H., Swanson, H., Perry, C., Diester, I., Boyce, F. M., Bass, C. E., Neve, R., Huang, Z. J., & Deisseroth, K. (2014). Targeting cells with single vectors using multiple-feature Boolean logic. *Nature Methods, 11,* 763–772.
22. Fischer, J. A., Giniger, E., Maniatis, T., & Ptashne, M. (1988). GAL4 activates transcription in Drosophila. *Nature, 332,* 853–856.
23. Gallio, M., Ofstad, T. A., Macpherson, L. J., Wang, J. W., & Zuker, C. S. (2011). The coding of temperature in the Drosophila brain. *Cell, 144,* 614–624.
24. Gaudry, Q., Hong, E. J., Kain, J., de Bivort B. L., & Wilson, R. I. (2013). Asymmetric neurotransmitter release enables rapid odour lateralization in Drosophila. *Nature, 493,* 424–428.
25. Gordon, M. D., & Scott, K. (2009). Motor control in a Drosophila taste circuit. *Neuron, 61,* 373–384.
26. Gradinaru, V., Thompson, K. R., & Deisseroth, K. (2008). eNpHR: A Natronomonas halorhodopsin enhanced for optogenetic applications. *Brain Cell Biology, 36,* 129–139.
27. Gradinaru, V., Zhang, F., Ramakrishnan, C., Mattis, J., Prakash, R., Diester, I., Goshen, I., Thompson, K. R., & Deisseroth, K. (2010). Molecular and cellular approaches for diversifying and extending optogenetics. *Cell, 141,* 154–165.
28. Gruntman, E., & Turner, G. C. (2013). Integration of the olfactory code across dendritic claws of single mushroom body neurons. *Nature Neuroscience,* 16, 1821–1829.
29. Guo, Z. V., Hart, A. C., & Ramanathan, S. (2009). Optical interrogation of neural circuits in Caenorhabditis elegans. *Nature Methods, 6,* 891–896.
30. Haikala, V., Joesch, M., Borst, A., & Mauss, A. S. (2013). Optogenetic control of fly optomotor responses. *The Journal of Neuroscience: The Official Journal of the Society for Neuroscience, 33,* 13927–13934.
31. Hamada, F. N., Rosenzweig, M., Kang, K., Pulver, S. R., Ghezzi, A., Jegla, T. J., & Garrity, P. A. (2008). An internal thermal sensor controlling temperature preference in Drosophila. *Nature, 454,* 217–220.
32. Han, D. D., Stein, D., & Stevens, L. M. (2000). Investigating the function of follicular subpopulations during Drosophila oogenesis through hormone-dependent enhancer-targeted cell ablation. *Development, 127,* 573–583.
33. Hanai, S., Hamasaka, Y., & Ishida, N. (2008). Circadian entrainment to red light in Drosophila: Requirement of Rhodopsin 1 and Rhodopsin 6. *Neuroreport, 19,* 1441–1444.
34. Hardie, R. (1979). Electrophysiological analysis of fly retina. I: Comparative properties of R1-6 and R 7 and 8. *Journal of Comparative Physiology. B, Biochemical, Systemic, and Environmental Physiology, 129,* 19–33.
35. Hayashi, S., Ito, K., Sado, Y., Taniguchi, M., Akimoto, A., Takeuchi, H., Aigaki, T., Matsuzaki, F., Nakagoshi, H., Tanimura, T., Ueda, R., Uemura, T., Yoshihara, M., & Goto, S. (2002). GETDB, a database compiling expression patterns and molecular locations of a collection of Gal4 enhancer traps. *Genesis, 34,* 58–61.
36. Herman, A. M., Huang, L., Murphey, D. K., Garcia, I., & Arenkiel, B. R. (2014). Cell type-specific and time-dependent light exposure contribute to silencing in neurons expressing Channelrhodopsin-2. *eLife, 3,* e 01481.
37. Honjo, K., Hwang, R. Y., & Tracey, W. D., Jr. (2012). Optogenetic manipulation of neural circuits and behavior in Drosophila larvae. *Nature Protocols, 7,* 1470–1478.

38. Hu, A., Zhang, W., & Wang, Z. (2010). Functional feedback from mushroom bodies to antennal lobes in the Drosophila olfactory pathway. *Proceedings of the National Academy of Sciences of the United States of America, 107,* 10262–10267.
39. Huang, J., Zhang, W., Qiao, W., Hu, A., & Wang, Z. (2010). Functional connectivity and selective odor responses of excitatory local interneurons in Drosophila antennal lobe. *Neuron, 67,* 1021–1033.
40. Hwang, R. Y., Zhong, L., Xu, Y., Johnson, T., Zhang, F., Deisseroth, K., & Tracey, W. D. (2007). Nociceptive neurons protect Drosophila larvae from parasitoid wasps. *Current Biology: CB, 17,* 2105–2116.
41. Inada, K., Kohsaka, H., Takasu, E., Matsunaga, T., & Nose, A. (2011). Optical dissection of neural circuits responsible for Drosophila larval locomotion with halorhodopsin. *PLoS ONE, 6,* e 29019.
42. Inagaki, H. K., Ben-Tabou†de-Leon, S., Wong, A. M., Jagadish, S., Ishimoto, H., Barnea, G., Kitamoto, T., Axel, R., & Anderson, D. J. (2012). Visualizing neuromodulation in vivo: TANGO-Mapping of dopamine signaling reveals appetite control of sugar sensing. *Cell, 148,* 583–595.
43. Inagaki, H. K., Jung, Y., Hoopfer, E. D., Wong, A. M., Mishra, N., Lin, J. Y., Tsien, R. Y., & Anderson, D. J. (2014). Optogenetic control of Drosophila using a red-shifted channelrhodopsin reveals experience-dependent influences on courtship. *Nature Methods, 11,* 325–332.
44. Jenett, A., Rubin, G. M., Ngo, T. T., Shepherd, D., Murphy, C., Dionne, H., Pfeiffer, B. D., Cavallaro, A., Hall, D., Jeter, J., Iyer, N., Fetter, D., Hausenfluck, J. H., Peng, H., Trautman, E. T., Svirskas, R. R., Myers, E. W., Iwinski, Z. R., Aso, Y., Depasquale, G. M., Enos, A., Hulamm, P., Lam, S. C., Li, H. H., Laverty, T. R., Long, F., Qu, L., Murphy, S. D., Rokicki, K., Safford, T., Shaw, K., Simpson, J. H., Sowell, A., Tae, S., Yu, Y., & Zugates, C. T. (2012). A GAL4-driver line resource for Drosophila neurobiology. *Cell Reports, 2,* 991–1001.
45. Jones, W. D., Cayirlioglu, P., Kadow, I. G., & Vosshall, L. B. (2007). Two chemosensory receptors together mediate carbon dioxide detection in Drosophila. *Nature, 445,* 86–90.
46. Kabra, M., Robie, A. A., Rivera-Alba, M., Branson, S., & Branson, K. (2013). JAABA: Interactive machine learning for automatic annotation of animal behavior. *Nature Methods, 10,* 64–67.
47. Katzel, D., Zemelman, B. V., Buetfering, C., Wolfel, M., & Miesenbock, G. (2011). The columnar and laminar organization of inhibitory connections to neocortical excitatory cells. *Nature Neuroscience, 14,* 100–107.
48. Klapoetke, N. C., Murata, Y., Kim, S. S., Pulver, S. R., Birdsey-Benson, A., Cho, Y. K., Morimoto, T. K., Chuong, A. S., Carpenter, E. J., Tian, Z., Wang, J., Xie, Y., Yan, Z., Zhang, Y., Chow, B. Y., Surek, B., Melkonian, M., Jayaraman, V., Constantine-Paton, M., Wong, G. K., & Boyden, E. S. (2014). Independent optical excitation of distinct neural populations. *Nature Methods, 11,* 338–346.
49. Kvon, E. Z., Kazmar, T., Stampfel, G., Yanez-Cuna, J. O., Pagani, M., Schernhuber, K., Dickson, B. J., & Stark, A. (2014). Genome-scale functional characterization of Drosophila developmental enhancers in vivo. *Nature, 512,* 91–95.
50. Kwon, J. Y., Dahanukar, A., Weiss, L. A., & Carlson, J. R. (2007). The molecular basis of CO2 reception in Drosophila. *Proceedings of the National Academy of Sciences of the United States of America, 104,* 3574–3578.
51. Lai, S. L., & Lee, T. (2006). Genetic mosaic with dual binary transcriptional systems in Drosophila. *Nature Neuroscience, 9,* 703–709.
52. Leifer, A. M., Fang-Yen, C., Gershow, M., Alkema, M. J., & Samuel, A. D. (2011). Optogenetic manipulation of neural activity in freely moving Caenorhabditis elegans. *Nature Methods, 8,* 147–152.
53. Lima, S. Q., & Miesenbock, G. (2005). Remote control of behavior through genetically targeted photostimulation of neurons. *Cell, 121,* 141–152.
54. Lin, J. Y. (2011). A user's guide to channelrhodopsin variants: Features, limitations and future developments. *Experimental Physiology, 96,* 19–25.

55. Lin, H. H., Chu, L. A., Fu, T. F., Dickson, B. J., & Chiang, A. S. (2013). Parallel neural pathways mediate CO2 avoidance responses in Drosophila. *Science, 340,* 1338–1341.
56. Lin, J. Y., Knutsen, P. M., Muller, A., Kleinfeld, D., & Tsien, R. Y. (2013b). ReaChR: A red-shifted variant of channelrhodopsin enables deep transcranial optogenetic excitation. *Nature Neuroscience, 16,* 1499–1508.
57. Liu, W. W., & Wilson, R. I. (2013). Transient and specific inactivation of Drosophila neurons in vivo using a native ligand-gated ion channel. *Current Biology: CB, 23,* 1202–1208.
58. Losonczy, A., Zemelman, B. V., Vaziri, A., & Magee, J. C. (2010). Network mechanisms of theta related neuronal activity in hippocampal CA1 pyramidal neurons. *Nature Neuroscience, 13,* 967–972.
59. Lutz, C., Otis, T. S., DeSars, V., Charpak, S., DiGregorio, D. A., & Emiliani, V. (2008). Holographic photolysis of caged neurotransmitters. *Nature Methods, 5,* 821–827.
60. Madisen, L., Mao, T., Koch, H., Zhuo, J. M., Berenyi, A., Fujisawa, S., Hsu, Y. W., Garcia, A. J. 3rd, Gu, X., Zanella, S., Kidney, J., Gu, H., Mao, Y., Hooks, B. M., Boyden, E. S., Buzsaki, G., Ramirez, J. M., Jones, A. R., Svoboda, K., Han, X., Turner, E. E., & Zeng, H. (2012). A toolbox of Cre-dependent optogenetic transgenic mice for light-induced activation and silencing. *Nature Neuroscience, 15,* 793–802.
61. Mattis, J., Tye, K. M., Ferenczi, E. A., Ramakrishnan, C., O'Shea, D. J., Prakash, R., Gunaydin, L. A., Hyun, M., Fenno, L. E., Gradinaru, V., Yizhar, O., & Deisseroth, K. (2012). Principles for applying optogenetic tools derived from direct comparative analysis of microbial opsins. *Nature Methods, 9,* 159–172.
62. Maurer, C., Khan, S., Fassl, S., Bernet, S., & Ritsch-Marte, M. (2010). Depth of field multiplexing in microscopy. *Optics Express, 18,* 3023–3034.
63. Mauss, A. S., Meier, M., Serbe, E., & Borst, A. (2014). Optogenetic and pharmacologic dissection of feedforward inhibition in Drosophila motion vision. *The Journal of neuroscience: The Official Journal of the Society for Neuroscience, 34,* 2254–2263.
64. McGuire, S. E., Le, P. T., Osborn, A. J., Matsumoto, K., & Davis, R. L. (2003). Spatiotemporal rescue of memory dysfunction in Drosophila. *Science, 302,* 1765–1768.
65. Minke, B., & Kirschfeld, K. (1979). The contribution of a sensitizing pigment to the photosensitivity spectra of fly rhodopsin and metarhodopsin. *The Journal of General Physiology, 73,* 517–540.
66. Mohanty, S. K., Reinscheid, R. K., Liu, X., Okamura, N., Krasieva, T. B., & Berns, M. W. (2008). In-depth activation of channelrhodopsin 2-sensitized excitable cells with high spatial resolution using two-photon excitation with a near-infrared laser microbeam. *Biophysical Journal, 95,* 3916–3926.
67. Montell, C. (2009). A taste of the Drosophila gustatory receptors. *Current Opinion in Neurobiology, 19,* 345–353.
68. Nagel, G., Brauner, M., Liewald, J. F., Adeishvili, N., Bamberg, E., & Gottschalk, A. (2005). Light activation of channelrhodopsin-2 in excitable cells of Caenorhabditis elegans triggers rapid behavioral responses. *Current Biology: CB, 15,* 2279–2284.
69. Nicholson, L., Singh, G. K., Osterwalder, T., Roman, G. W., Davis, R. L., & Keshishian, H. (2008). Spatial and temporal control of gene expression in Drosophila using the inducible GeneSwitch GAL4 system. I. Screen for larval nervous system drivers. *Genetics, 178,* 215–234.
70. Nikolenko, V., Watson, B. O., Araya, R., Woodruff, A., Peterka, D. S., & Yuste, R. (2008). SLM Microscopy: Scanless two-photon imaging and photostimulation with spatial light modulators. *Front Neural Circuits, 2,* 5.
71. Nikolenko, V., Peterka, D. S., & Yuste, R. (2010). A portable laser photostimulation and imaging microscope. *Journal of Neural Engineering, 7,* 045001.
72. Nuwal, N., Stock, P., Hiemeyer, J., Schmid, B., Fiala, A., & Buchner, E. (2012). Avoidance of heat and attraction to optogenetically induced sugar sensation as operant behavior in adult Drosophila. *Journal of Neurogenetics, 26,* 298–305.

73. Ohyama, T., Jovanic, T., Denisov, G., Dang, T. C., Hoffmann, D., Kerr, R. A., & Zlatic, M. (2013). High-throughput analysis of stimulus-evoked behaviors in Drosophila larva reveals multiple modality-specific escape strategies. *PLoS One, 8,* e 71706.
74. Osterwalder, T., Yoon, K. S., White, B. H., & Keshishian, H. (2001). A conditional tissue-specific transgene expression system using inducible GAL4. *Proceedings of the National Academy of Sciences of the United States of America, 98,* 12596–12601.
75. Oztas, E. (2003). Neuronal tracing. *Neuroanatomy, 2,* 2–5.
76. Packer, A. M., Peterka, D. S., Hirtz, J. J., Prakash, R., Deisseroth, K., & Yuste, R. (2012). Two-photon optogenetics of dendritic spines and neural circuits. *Nature Methods, 9,* 1202–1205.
77. Papagiakoumou, E., Anselmi, F., Begue, A., de Sars V., Gluckstad, J., Isacoff, E. Y., & Emiliani, V. (2010). Scanless two-photon excitation of channelrhodopsin-2. *Nature Methods, 7,* 848–854.
78. Pfeiffer, B. D., Ngo, T. T., Hibbard, K. L., Murphy, C., Jenett, A., Truman, J. W., & Rubin, G. M. (2010). Refinement of tools for targeted gene expression in Drosophila. *Genetics, 186,* 735–755.
79. Post, J. N., Lidke, K. A., Rieger, B., & Arndt-Jovin, D. J. (2005). One-and two-photon photoactivation of a paGFP-fusion protein in live Drosophila embryos. *FEBS Letters, 579,* 325–330.
80. Prakash, R., Yizhar, O., Grewe, B., Ramakrishnan, C., Wang, N., Goshen, I., Packer, A. M., Peterka, D. S., Yuste, R., Schnitzer, M. J., & Deisseroth, K. (2012). Two-photon optogenetic toolbox for fast inhibition, excitation and bistable modulation. *Nature Methods, 9,* 1171–1179.
81. Prigge, M., Schneider, F., Tsunoda, S. P., Shilyansky, C., Wietek, J., Deisseroth, K., & Hegemann, P. (2012). Color-tuned channelrhodopsins for multiwavelength optogenetics. *Journal of Biological Chemistry,* 287*,* 31804–31812.
82. Pulver, S. R., Pashkovski, S. L., Hornstein, N. J., Garrity, P. A., & Griffith, L. C. (2009). Temporal dynamics of neuronal activation by Channelrhodopsin-2 and TRPA1 determine behavioral output in Drosophila larvae. *Journal of Neurophysiology, 101,* 3075–3088.
83. Rickgauer, J. P., & Tank, D. W. (2009). Two-photon excitation of channelrhodopsin-2 at saturation. *Proceedings of the National Academy of Sciences of the United States of America, 106,* 15025–15030.
84. Roman, G., Endo, K., Zong, L., & Davis, R. L. (2001). P[Switch], a system for spatial and temporal control of gene expression in Drosophila melanogaster. *Proceedings of the National Academy of Sciences of the United States of America, 98,* 12602–12607.
85. Sakai, S., Ueno, K., Ishizuka, T., & Yawo, H. (2013). Parallel and patterned optogenetic manipulation of neurons in the brain slice using a DMD-based projector. *Neuroscience Research, 75,* 59–64.
86. Salcedo, E., Huber, A., Henrich, S., Chadwell, L. V., Chou, W. H., Paulsen, R., & Britt, S. G. (1999). Blue-and green-absorbing visual pigments of Drosophila: Ectopic expression and physiological characterization of the R8 photoreceptor cell-specific Rh5 and Rh6 rhodopsins. *The Journal of Neuroscience: The Official Journal of the Society for Neuroscience, 19,* 10716–10726.
87. Salomon, C. H., & Spatz, H. C. (1983). Colour vision in *Drosophila melanogaster*: Wavelength discrimination. *Journal of Comparative Physiology. B, Biochemical, Systemic, and Environmental Physiology, 150,* 31–37.
88. Sander, J. D., & Joung, J. K. (2014). CRISPR-Cas systems for editing, regulating and targeting genomes. *Nature Biotechnology, 32,* 347–355.
89. Sayeed, O., & Benzer, S. (1996). Behavioral genetics of thermosensation and hygrosensation in Drosophila. *Proceedings of the National Academy of Sciences of the United States of America, 93,* 6079–6084.
90. Schroll, C., Riemensperger, T., Bucher, D., Ehmer, J., Voller, T., Erbguth, K., Gerber, B., Hendel, T., Nagel, G., Buchner, E., & Fiala, A.. (2006). Light-induced activation of distinct modulatory neurons triggers appetitive or aversive learning in Drosophila larvae. *Current Biology, 16,* 1741–1747.

91. Schümperli, R. (1973). Evidence for colour vision inDrosophila melanogaster through spontaneous phototactic choice behaviour. *Journal of Comparative Physiology. B, Biochemical, Systemic, and Environmental Physiology, 86,* 77–94.
92. Semmelhack, J. L., & Wang, J. W. (2009). Select Drosophila glomeruli mediate innate olfactory attraction and aversion. *Nature, 459,* 218–223.
93. Simpson, J. H. (2009). Mapping and manipulating neural circuits in the fly brain. *Advances in Genetics, 65,* 79–143.
94. Suh, G. S., Wong, A. M., Hergarden, A. C., Wang, J. W., Simon, A. F., Benzer, S., Axel, R., & Anderson, D. J. (2004). A single population of olfactory sensory neurons mediates an innate avoidance behaviour in Drosophila. *Nature, 431,* 854–859.
95. Suh, G. S., Ben-Tabou de Leon, S., Tanimoto, H., Fiala, A., Benzer, S., & Anderson, D. J. (2007). Light activation of an innate olfactory avoidance response in Drosophila. *Current Biology: CB, 17,* 905–908.
96. Szuts, D., & Bienz, M. (2000). LexA chimeras reveal the function of Drosophila Fos as a context-dependent transcriptional activator. *Proceedings of the National Academy of Sciences of the United States of America, 97,* 5351–5356.
97. Takemura, S. Y., Bharioke, A., Lu, Z., Nern, A., Vitaladevuni, S., Rivlin, P. K., Katz, W. T., Olbris, D. J., Plaza, S. M., Winston, P., Zhao, T., Horne, J. A., Fetter, R. D., Takemura, S., Blazek, K., Chang, L. A., Ogundeyi, O., Saunders MA, Shapiro V, Sigmund C, Rubin G. M, Scheffer L. K, Meinertzhagen I. A., & Chklovskii D. B. (2013). A visual motion detection circuit suggested by Drosophila connectomics. *Nature, 500,* 175–181.
98. Tye, K. M., & Deisseroth, K. (2012). Optogenetic investigation of neural circuits underlying brain disease in animal models. *Nature Reviews Neuroscience, 13,* 251–266.
99. Valera, S., Hussy, N., Evans, R. J., Adami, N., North, R. A., Surprenant, A., & Buell, G. (1994). A new class of ligand-gated ion channel defined by P2X receptor for extracellular ATP. *Nature, 371,* 516–519.
100. Venken, K. J. T., Simpson, J. H., & Bellen, H. J. (2011). Genetic manipulation of genes and cells in the nervous system of the fruit fly. *Neuron, 72,* 202–230.
101. Vogelstein, J. T., Park, Y., Ohyama, T., Kerr, R. A., Truman, J. W., Priebe, C. E., & Zlatic, M. (2014). Discovery of brainwide neural-behavioral maps via multiscale unsupervised structure learning. *Science, 344,* 386–392.
102. von Philipsborn A. C., Liu, T., Yu, J. Y., Masser, C., Bidaye, S. S., & Dickson, B. J. (2011). Neuronal control of Drosophila courtship song. *Neuron, 69,* 509–522.
103. von Reyn C. R., Breads, P., Peek, M. Y., Zheng, G. Z., Williamson, W. R., Yee, A. L., Leonardo, A., & Card, G. M. (2014). A spike-timing mechanism for action selection. *Nature Neuroscience, 17,* 962–970.
104. Wardill, T. J., List, O., Li, X., Dongre, S., McCulloch, M., Ting, C. Y., O'Kane, C. J., Tang, S., Lee, C. H., Hardie, R. C., & Juusola, M. (2012). Multiple spectral inputs improve motion discrimination in the Drosophila visual system. *Science, 336,* 925–931.
105. Wu, M. C., Chu, L. A., Hsiao, P. Y., Lin, Y. Y., Chi, C. C., Liu, T. H., Fu, C. C., & Chiang, A. S. (2014). Optogenetic control of selective neural activity in multiple freely moving Drosophila adults. *Proceedings of the National Academy of Sciences of the United States of America, 111,* 5367–5372.
106. Xiang, Y., Yuan, Q., Vogt, N., Looger, L. L., Jan, L. Y., & Jan, Y. N. (2010). Light-avoidance-mediating photoreceptors tile the Drosophila larval body wall. *Nature, 468,* 921–926.
107. Yamaguchi, S., Desplan, C., & Heisenberg, M. (2010). Contribution of photoreceptor subtypes to spectral wavelength preference in Drosophila. *Proceedings of the National Academy of Sciences of the United States of America, 107,* 5634–5639.
108. Yang, S., Papagiakoumou, E., Guillon, M., de Sars V., Tang, C. M., & Emiliani, V. (2011). Three-dimensional holographic photostimulation of the dendritic arbor. *Journal of Neural Engineering, 8,* 046002.
109. Yao, Z., Macara, A. M., Lelito, K. R., Minosyan, T. Y., & Shafer, O. T. (2012). Analysis of functional neuronal connectivity in the Drosophila brain. *Journal of Neurophysiology, 108,* 684–696.

110. Yizhar, O., Fenno, L. E., Davidson, T. J., Mogri, M., & Deisseroth, K. (2011a). Optogenetics in neural systems. *Neuron, 71,* 9–34.
111. Yizhar, O., Fenno, L. E., Prigge, M., Schneider, F., Davidson, T. J., O'Shea, D. J., Sohal, V. S., Goshen, I., Finkelstein, J., Paz, J. T., Stehfest, K., Fudim, R., Ramakrishnan, C., Huguenard, J. R., Hegemann, P., & Deisseroth, K. (2011b). Neocortical excitation/inhibition balance in information processing and social dysfunction. *Nature, 477,* 171–178.
112. Zhang, F., Wang, L. P., Brauner, M., Liewald, J. F., Kay, K., Watzke, N., Wood, P. G., Bamberg, E., Nagel, G., Gottschalk, A., & Deisseroth, K. (2007a). Multimodal fast optical interrogation of neural circuitry. *Nature, 446,* 633–639.
113. Zhang, W., Ge, W., & Wang, Z. (2007b). A toolbox for light control of Drosophila behaviors through Channelrhodopsin 2-mediated photoactivation of targeted neurons. *The European Journal of Neuroscience, 26,* 2405–2416.
114. Zhang, F., Prigge, M., Beyriere, F., Tsunoda, S. P., Mattis, J., Yizhar, O., Hegemann, P., & Deisseroth, K. (2008). Red-shifted optogenetic excitation: A tool for fast neural control derived from Volvox carteri. *Nature Neuroscience, 11,* 631–633.
115. Zimmermann, G., Wang, L. P., Vaughan, A. G., Manoli, D. S., Zhang, F., Deisseroth, K., Baker, B. S., & Scott, M. P. (2009). Manipulation of an innate escape response in Drosophila: photoexcitation of acj6 neurons induces the escape response. *PLoS ONE, 4,* e 5100.

Chapter 7
Optically Monitoring and Manipulating Brain and Behavior in *C. elegans*

Linjiao Luo, Quan Wen and Aravinthan D. T. Samuel

Abstract Small animals such as the nematode *C. elegans* offer the possibility of understanding how an integrated nervous system in a live animal drives complex behaviors. The last decade has seen rapid progress in fluorescent genetically encoded optical probes of neuronal activity. These now permit physiological analysis of worm neural circuits using light microscopy, ideal for the small, transparent, genetically tractable nematode. *C. elegans* researchers can now dissect the activity patterns of virtually any cell in live animals. Here, we review progress on microscopy and instrumentation that allow one to use genetically encoded probes to connect brain and behavior in *C. elegans.*

The nematode *C. elegans* has long been an ideal model system for light microscopy. Its optical transparency and small size (the adult is only ~1 mm long and ~0.1 mm in diameter) put every cell within the depth of field of ordinary microscope objectives. These features allowed the complete cell lineage from fertilization to adulthood to be mapped using Nomarski differential interference contrast microscopy by visually following the division, migration, and death of every cell [54, 55]. The small size and stereotypy of the 302-neuron nervous system allow each neuron to be identified based on its position, and single cell laser ablation has long been used to evaluate the contribution of each neuron or group of neurons to nematode behaviors [4, 8, 16]. However, determining how the activity of each cell is related to behavior requires direct measurements or manipulations of cellular activity. Electrophysiology of individual neurons and muscle cells in *C. elegans* is possible, but requires

A. D. T. Samuel (✉)
Department of Physics and Center for Brain Science, Harvard University, 02138 Cambridge, MA, USA
e-mail: samuel@physics.harvard.edu

L. Luo
Key Laboratory of Modern Acoustics, Ministry of Education, Department of Physics, Nanjing University, 210093 Nanjing, China

Q. Wen
Department of Neurobiology and Biophysics, School of Life Sciences, University of Science and Technology of China, Hefei, Anhui Province, China

A. D. Douglass (ed.), *New Techniques in Systems Neuroscience,* Biological and Medical Physics, Biomedical Engineering, DOI 10.1007/978-3-319-12913-6_7

rupturing the cuticle, precluding the use of this technique in intact, behaving animals [19, 49]. Optical methods were needed to begin the era of neurophysiology in *C. elegans*.

In the last decade, neurophysiology has been transformed by the development of genetically encoded probes for imaging the activity patterns of excitable cells [37]. These probes typically comprise green fluorescent protein (GFP)-based fluorescent probes fused to proteins that are directly responsive to physiological signals such as intracellular calcium or membrane potential. A more recent development is optogenetics, a set of genetically encoded light-activated channels and pumps that allow specific cells to be activated or inactivated upon exposure to light of specific wavelengths, as well as genetically encoded photosensitizers that allow light-induced killing of specific cells [6, 21, 48, 61, 63]. *C. elegans* has been an ideal platform to apply and develop these methods, as its powerful genetic toolkit enables rapid creation of transgenic lines that express any of these genetically encoded reagents in specific cells, allowing neurophysiology studies to complement well-established methods for genetic analysis, laser ablation, and behavioral quantification.

The utility of genetically encoded reagents to study neuronal activities has been greatly augmented by parallel advances in instrumentation. Other recent reviews take inventory of and discuss the growing toolbox of genetically encoded reagents themselves [15, 37]. Here, we will discuss the advances in methodology and instrumentation that have allowed genetically encoded reagents to be adapted to *C. elegans* neurophysiology.

7.1 Calcium Imaging in Immobilized Worms

The invention of the genetically encoded calcium indicator cameleon opened the possibility of optical neurophysiology using *C. elegans* [42]. Cameleons are chimeric proteins composed of multiple domains: in the original probe these were cyan fluorescent protein (CFP), calmodulin, the M13 calmodulin binding domain, and yellow fluorescent protein (YFP) (Fig. 7.1a). When calmodulin binds free calcium, it also binds M13, bringing CFP and YFP into proximity for enhanced fluorescence resonance energy transfer from CFP to YFP. Thus, increases or decreases in the ratio between YFP and CFP fluorescence when excitation is fixed at a wavelength that efficiently excites CFP alone signify higher or lower levels of intracellular calcium, respectively. Ratiometric indicators such as cameleon are ideal for measurements in live animals like worms, as they are less sensitive to variations in total fluorescence intensity caused by movement, allowing the reliable detection of genuine calcium transients even with the low signal strengths of the earliest calcium reporters.

Cameleon was first used in *C. elegans* to reveal changes in intracellular calcium levels in spontaneously contracting pharyngeal muscles [31]. A number of studies rapidly followed, largely focusing on sensory encoding of various stimuli delivered through mechanical, thermal, and chemical modalities [7, 12, 23, 32, 56, 58]. The first technical challenge that had to be solved in conducting these studies was

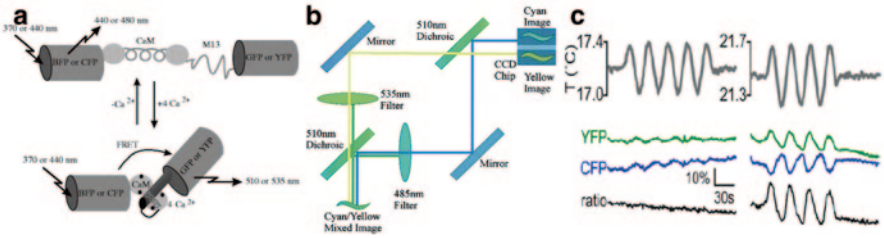

Fig. 7.1 Calcium imaging in immobilized worms, using cameleons as a calcium indicator. **a** Schematic structures of cameleons. It shows how the ratiometic measurement between YFP and CFP can indicate the levels of intracellular calcium (Adapted from Miyawaki et al. [43]). **b** Simultaneous recording of both cyan and yellow emission using dichroic mirrors to split the images (Adapted from Kerr et al. [31]). **c** Calcium activity in the AFD thermal sensory neuron. Worms grown at 20 °C were glued on an agar pad and subjected to sinusoidal temperature variations (*gray line*). YFP and CFP emission were simultaneously monitored so the ratio can be calculated (*black line*). It shows AFD responds to temperature variations near 21 °C (near or above the cultivation temperature), but not to temperature variations near 17 °C (below the cultivation temperature). For more details, see Clark et al. [12]

restraining the worm, to eliminate motion artifacts arising from behavior or from stimulus artifacts. Cyanoacrylate glue, which was earlier used to immobilize worms for surgery for electrophysiology, worked well. Much of an adult worm could be attached to a hydrated agar pad, leaving segments of the worm open to sensory stimulation such as gentle touch applied by a moving glass rod, the flow of chemical attractants or repellants applied by perfusion from nearby pipettes, or variations in ambient temperature provided by underlying metal plates (Fig. 7.2b).

The imaging technology that characterized most early optical neurophysiology using cameleons (and which remains adequate for many studies) was wide-field fluorescence microscopy. To be used as a ratiometric indicator, cameleons require simultaneous imaging of both cyan and yellow emission. This can easily be done with a single CCD camera, using dichroic mirrors to split the cyan and yellow image channels onto two halves of a CCD array, and using software to superimpose, align, and calculate the intensity ratios of the two signals (Fig. 7.1b). When single neurons can be labeled, using cell-specific promoters to drive cameleon expression, wide-field fluorescence microscopy may, in fact, be superior to more sophisticated and expensive techniques such as confocal or two-photon imaging. Improved optical sectioning along the z-axis becomes unnecessary when imaging one neuron at a time. Moreover, wide-field fluorescence microscopy effectively integrates signal along the z-axis, collecting more photons to improve signal-to-noise and reducing sensitivity to motion artifacts. In fact, going to the limits of low resolution, low-magnification wide-field fluorescence microscopy, now possible because of the most recently improved and brightest calcium indicators, allows one to image neuronal activity in freely moving worms with minimal motion artifacts (see below).

In most cases, calcium imaging using wide-field fluorescence microscopy measures fluorescence emission from the entire cell body of the targeted neuron. In this way, the neuronal activity patterns that characterize stimulation of numerous

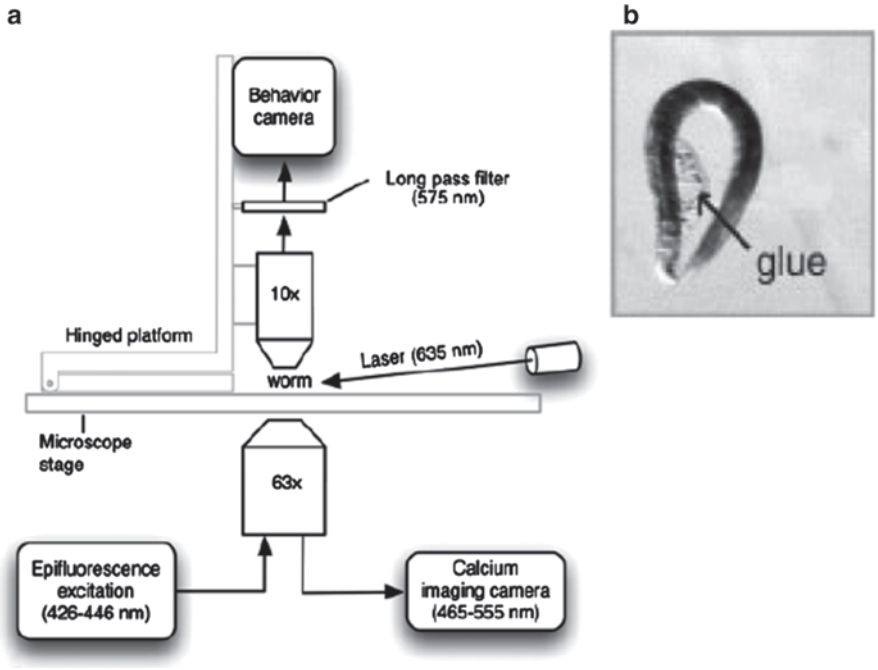

Fig. 7.2 A dual-camera system to simultaneously monitor calcium activities and behavior in partially glued worms. **a** Schematic diagram of the dual-camera system. The 63× objective and calcium imaging camera monitor specific neurons in the nerve wring at high magnification. The 10× objective and behavior camera monitor the entire worm body at low magnification (Adapted from Faumont et al. [17]). **b** Sample image of a worm glued at its neck region, leaving the rest of the body free to move

sensory neurons—for example, the ASH polymodal neuron, mechanosensory neurons, the AFD thermosensory neuron, AWC olfactory neuron, ASE chemosensory neurons—have been successfully characterized [7, 12, 23, 32, 57, 58]. However, the cell bodies of interneurons that are downstream of sensory neurons sometimes do not exhibit detectable calcium transients. For example, the AIY interneuron, a major downstream partner of both the AFD thermosensory neuron and the AWC olfactory neuron, has consistently failed to generate somatic calcium transients in response to thermal or olfactory cues when recorded with either cameleon or the single-wavelength indicator GCaMP [5, 7, 12]. Calcium activity in the AIY interneuron can be reliably recorded along the axon, suggesting compartmentalized calcium dynamics [35]. Neurons whose calcium activities can only be recorded in their neuronal processes, but not in their cell bodies, present a significant complication for functional imaging. Nerve fibers are small in diameter (<0.1 μm) and tightly packed together, so that activity patterns will be below the resolution limit of light microscopy when several cells are labeled. Panneuronal imaging methods that are now being applied in *C. elegans* (see below) will thus not be able to resolve neuronal activity patterns

that are localized to densely labeled processes. Single-unit recording with cell-specific promoters will continue to be needed to characterize activity patterns in the axonal compartments of important interneurons like AIY.

7.2 Calcium Imaging in Restrained Worms

The trouble with gluing an animal along its entire length is that it eliminates the possibility of correlating neuronal activity with locomotor behavior. The compactness of signaling in the worm nervous system—sensory neurons are separated from motor neurons by only ~2 layers of interneurons—means that sensory representations must be rapidly transformed into motor representations [28, 60]. To use optical neurophysiology to characterize the neuronal correlates of complex behaviors beyond the first steps of sensory representation, it became necessary to develop new techniques.

The first technique to simultaneously monitor neuronal activity at high resolution and motile behavior at low resolution used a dual-camera system, imaging the animal from both top and bottom (Fig. 7.2a). An animal was glued at its neck, leaving the body and tail free to move [17]. One camera visualized the entire worm body at low magnification, such that periods of movement could be observed and quantified. A second camera, using wide-field fluorescence, recorded the nerve ring at high magnification, monitoring calcium dynamics in specific chemosensory neurons. This approach allowed direct correlation of activity in ASH (which detects chemical repellants) and the triggering of backward movement.

While glue provides an effective restraint to fully or partially immobilize an animal for physiological analysis, it is difficult to use reproducibly in each experiment. Glue also keeps parts of the worm from moving, thereby disrupting important feedback loops that might modulate neural circuit activities through proprioceptive or stretch-sensory feedback. Thus, the use of microfabrication techniques to create devices to restrain or manipulate the bodies of individual worms was a significant step forward [10]. These devices are typically constructed using soft lithography, molding silicone elastomer into two-dimensional fluid-filled geometries within which worms can be manipulated through liquid flow.

Microfluidic channels that are slightly larger in diameter than the worm body allow the animal to propagate undulatory waves without allowing it to advance or retreat, making it possible for neurons that represent forward and backward movement to be identified through correlation of their activity with the behavior (Fig. 7.3a). Using microfluidic chips with optimally designed channel parameters, the activity patterns of the AVA command motor neuron were shown to be correlated with backward movement [10]. It had previously been shown that ablation of the AVA neuron caused defects in generating backward movement [8], but microfluidics combined with high-resolution imaging of AVA activity showed that this key command motor neuron is specifically active during the appropriate phase of behavior.

Worms do not regulate locomotion solely by transitioning between forward and backward states. Recent work in chemotaxis and thermotaxis has uncovered direct

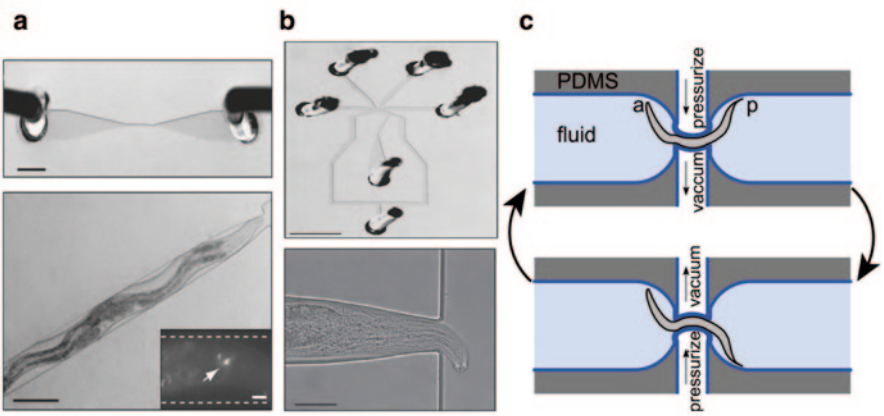

Fig. 7.3 Sample microfluidic devices for calcium imaging in restrained worms. **a** The behavior chip designed by Chronis et al. [10]. The *top* image shows the whole chip. Scale bar, 1 mm. The *bottom* image shows part of the channel with a trapped worm. Scale bar 100 μm. **b** The olfactory chip designed by Chronis et al. [10]. The *top* image shows the whole chip with four liquid channels for delivering odor and one worm channel for holding the worm. Scale bar 2 mm. The *bottom* image shows a higher magnification photograph of the worm channel with a trapped animal. Scale bar 30 μm. **c** Schematic of the pneumatic microfluidic device designed by Wen et al. [59] for manipulating body curvature. The worm is trapped in a channel flanked by two chambers. The curvature of the trapped part can be controlled by pressurizing one chamber and vacuuming the other chamber

steering mechanisms in worm navigation [3, 26, 29, 38, 39, 41]. In addition to regulating the frequency of reorientation maneuvers, sharp turns, and reversals, the worm also regulates the depth of head bending during periods of continuous forward movement to gradually orient itself toward favorable environments. Microfluidic environments that permit the observation of head bending in response to defined gradients of sensory input have allowed rigorous quantification of steering mechanisms (also called klinotaxis or weathervaning) [3, 41]. These devices allow worms to bend their heads into distinct fluid streams, permitting direct behavioral analysis of the klinotaxtic component of spatial orientation behavior.

Dissection of the neural regulation of head bending activity is enabled with microfluidic devices that allow the head to move freely while imaging specific neurons. This approach has been used to help understand the complex role played by the RIA interneuron in head movement. RIA is a major hub of synaptic wiring in the *C. elegans* nervous system, which lies downstream of many sensory pathways and has many reciprocal connections to head motor neurons [60]. By monitoring calcium dynamics in the RIA during head bending, it was shown that compartmentalized activities in regions of the RIA axon encode the direction of head bending owing to cholinergic input from head motor neurons, representing an efference copy by which information about the motor output is relayed to higher layers of the worm nervous system [22]. This result has two major implications (and cautions) for functional imaging in *C. elegans*. First, it suggests that powerful feedback loops

continuously send information about motor state to upstream interneurons in the nerve ring, and thus the activity patterns of the nerve ring are unlikely to exhibit activity patterns that represent normal behavior unless normal movements are allowed to occur. Second, it underscores and amplifies the point that activity patterns that reflect information processing in interneurons layers are likely to be restricted to compartmentalized portions of their nerve fibers.

Feedback loops between movement and neuronal activity also occur within the motor circuit itself. Dynamic microfluidic devices that trapped portions of the worm body and subjected them to user-controlled bending were used to investigate activity patterns in the motor circuit [59]. These devices allowed individual segments of the worm body to be subjected to imposed ventral and dorsal bends, while calcium dynamics in individual motor neurons within those segments were simultaneously monitored. The adult worm motor circuit has only three major types of cell: A-type excitatory cholinergic motor neurons that drive undulatory waves during backward movement, B-type excitatory cholinergic neurons that drive undulatory waves during forward movement, and D-type inhibitory GABAergic neurons that allow muscle cells to relax [52]. Pathways for sensory feedback that are ordinarily required to organize locomotor gait—for example, specific proprioceptive neurons and interneurons that relay information about animal movement to motor neurons—are not suggested by the wiring of the motor circuit. However, by systematically imaging motor neurons during imposed bending, B-type motor neurons were discovered to have a direct proprioceptive role. Imposing a ventral bend activates B-type neurons that innervate the ventral muscles; imposing a dorsal vend activates B-type neurons that innervate the dorsal muscle. This positive feedback loop plays an essential role in propagating an undulatory wave that starts at the head along the body to the tail during forward movement. This discovery also has a major implication for the experimental measurement of neural dynamics and behavior in *C. elegans*: single neurons can contain entire sensorimotor loops, compressing the role of sensory neuron, interneuron, and motor neuron into one.

7.3 Calcium Imaging in Unrestrained Worms

Microfluidics, while a powerful tool for neurophysiological analysis, also limits what the worm can do. With the recent improvement in the signal-to-noise ratio of genetically encoded calcium indicators, it has become possible to perform functional imaging without any restraint at all. For example, the YC3.60 version of cameleon allowed activity patterns in the AFD thermosensory neuron to be recorded when unrestrained adult worms freely navigated spatial temperature gradients [13]. In this setup, a user monitoring the movements of the AFD neuron visualized on a CCD camera dynamically adjusted the stage position and focus to keep the neuron centered in the field of view. After the experiment, the trajectory of the navigating animal could be reconstructed from the history of stage movements combined with the centroid position of the imaged neuron in each video frame (Fig. 7.4a).

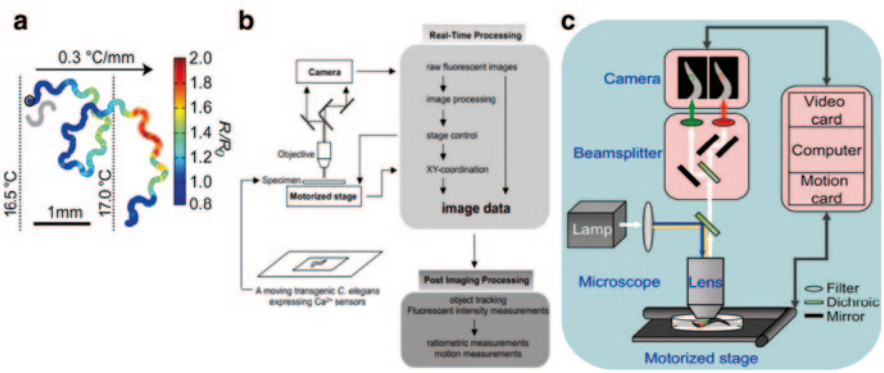

Fig. 7.4 Calcium imaging in unrestrained worms at high magnification. **a** AFD neuronal activity in an unrestrained worm navigating a spatial thermal gradient starting from the black circle. The color represents the ratiometric emission signal. The worm's head was imaged with a 20× objective and manually recentered with a joystick-controlled motorized stage. For more details, see Clark et al. [13]. **b** Schematic of an automatic imaging and tracking system developed by Kawano et al. [30]. In-house-developed software was used to do real-time image processing and automatically recenter the target during recordings. **c** Schematic of another automatic system simultaneously images calcium dynamics and worm behavior developed by Piggott et al. [46]

Manually recentering the image of a neuron in the field of view using a motorized stage can be difficult when neurons move quickly or when microscope objectives with the highest magnifications and numerical apertures are used. To solve this problem, the first fully automated imaging system was developed by analyzing the positions of imaged neurons in each captured video frame, and using the measured position to continuously recenter the neuron through stage movements [13] (Fig. 7.4b). With this system, key gap-junction mediated signaling relationships between the command motor neurons for driving backward and forward movement and the motor neurons that generate turning could be carefully dissected and resolved. A similar setup using image-based correction of stage position to keep specific neurons centered in the field of view was also used to dissect circuits that initiate spontaneous and nose-touch-mediated reversals [46] (Fig. 7.4c).

The feedback loop between image acquisition by CCD camera, image analysis, and stage control, limited by the frame rate of the camera and digital signal processing, can be slow. This makes it difficult to track individual neurons using the high-magnification, high-NA objectives that would provide the best resolving power. In a freely moving worm, individual neurons can move several micrometers between image captures of a standard video rate camera. To keep the neuron in the field of view, either lower magnification or faster feedback loops are needed. Much faster signal processing can be done without cameras. An image-free setup was shown to be effective for automated neuronal tracking by projecting the neuronal fluorescence signal onto the surface of a quadrant photomultiplier tube [18]. The relative activities from the four quadrants of the PMT provided a difference signal that was analyzed by analog signal processing to indicate the direction of movement at 2 ms

intervals. In principle, this allows fast, automated tracking in even much larger and faster animals such as *Drosophila* larva.

A solution at the other extreme for tracking neuronal activity in freely moving animals is to use such low magnifications that the whole animal never leaves the field of view, making any stage positioning unnecessary [35]. This is now possible because of parallel improvements in the signals emitted by new GCaMP indicators as well as high signal-to-noise EMCCD and scientific CMOS cameras. These advances make it possible to image neuronal activities in single or sparsely labeled neurons (>20 microns apart) in a freely behaving worm with low magnification and low numerical aperture objectives (2×—5×, NA=0.1–0.28). Under low magnification, recentering a worm within the field of view becomes much easier, and by restricting the animals' movement to a defined area, high-throughput calcium imaging of neuronal activities from multiple worms can also be achieved. Moreover, low numerical aperture objectives have high depths of field (~50 micron at NA=0.1) and thus can effectively collect fluorescence signals from within the entire body volume and reduce imaging artifacts arising from movement along the z-axis (Fig. 7.5). Indeed, a low NA objective is more effective for imaging calcium transients emitted from thin axons and dendrites (<1 micron in diameter) in a freely behaving worm [35], whereas imaging neuronal processes with a high NA objective is more susceptible to focal drift and motion artifact.

At low NA and low magnification, excitation light intensity is significantly lower and when coupled with rapid illumination pulses, this method reduces photo-toxicity and allows continuous neural recordings for hours. The ability to sample chronic neural responses from a large population of animals to a large number of stimuli becomes important when studying stochastic or variable processes, which include externally stimulated responses by most interneurons and some sensory neurons.

7.4 Multineuronal Imaging

Calcium imaging of single neurons with wide-field fluorescence microscopy can effectively probe the dynamic encoding of external sensory stimuli and correlations between single neuron activity and worm behavior. However, each neuron is only one component embedded in a network. Understanding the operating principles of a neural circuit, in particular, in cases where any stochasticity or variability is evident in single neuron responses, requires measuring the dynamics of several neurons at once. The compactness of the *C. elegans* nervous system offers both advantages and challenges for multineuron imaging in an intact and behaving animal.

In *C. elegans*, roughly two-third of its 302 neurons are packed in a small volume (50 μm × 100 μm × 50 μm) that can be imaged within the field of view of a high NA objective. The brightest genetically encoded calcium indicator (i.e., GCaMP6) can be expressed in all *C. elegans* neurons, and this opens the door for "whole-brain" imaging of neuronal activities with single-cell resolution. However, the small size of individual cell bodies and the compact spatial arrangement of neuropil in the

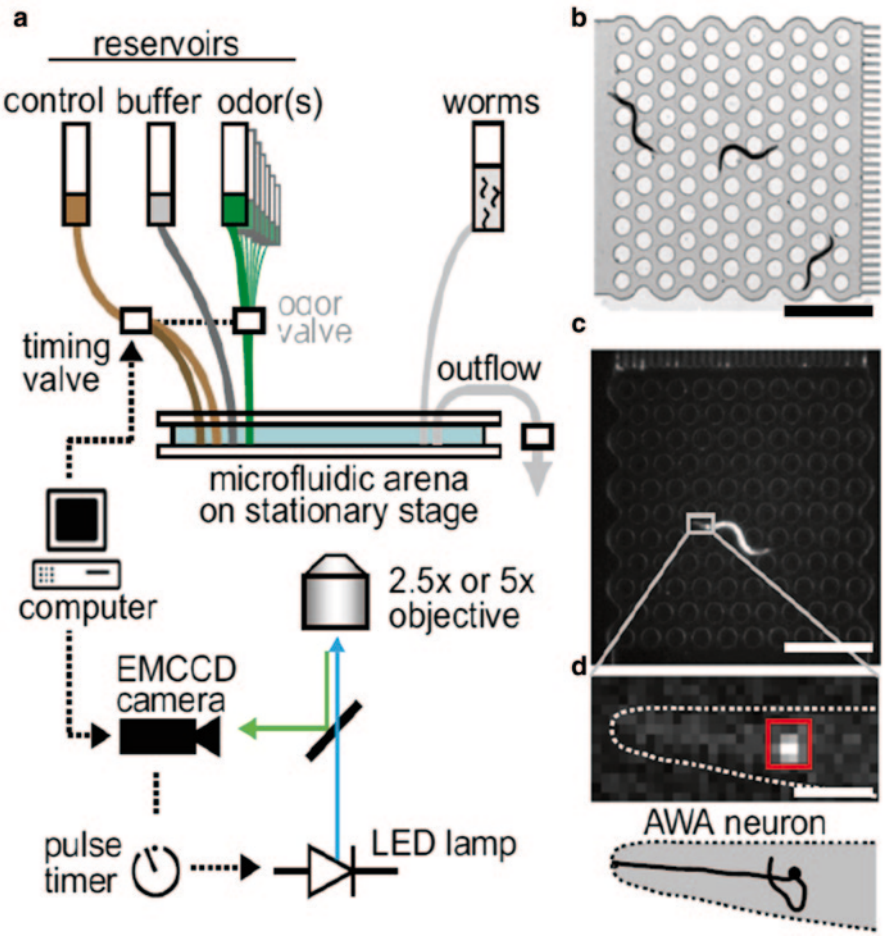

Fig. 7.5 Wide-field calcium imaging in freely moving worms at low magnification. **a** Schematic of the automated wide-field imaging system with microfluidic chemical stimulation. No motorized stage is needed with low-magnification objectives (Adapted from Larsch et al. [35]). **b** Image of the microfluidic arena with three worms moving freely in the channels (*gray areas*) around the microposts (*white circles*). Scale bar 1 mm. **c** Full-frame image of a freely behaving worm expressing GCaMP2.2b in the AWA neurons. Scale bar 1 mm. **d** Magnified view of the grey box in C. Scale bar 50 μm

head ganglion impose challenges for measuring neuronal activities in nearby neurons. This problem can be simplified by using nuclear-localized genetically encoded calcium indicators [50]. When this is done, fluorescence signals emitted from neighboring neurons are separated by distances larger than the diffraction limit and can be resolved. However, nuclear calcium dynamics must be interpreted with caution. A lack of nuclear calcium signal does not necessarily suggest the absence of electrical activities in a neuron: several *C. elegans* neurons have been shown to exhibit distinct compartmentalized calcium activities within axons and/or dendrites, signals that will not be detected from nucleus calcium imaging.

Laser scanning methods such as confocal or two-photon microscopy are the workhorses of optical neurophysiology, providing deep penetration and high resolution of image volumes. However, because traditional setups typically use single channel photon detectors (photomultiplier tubes or photodiodes), LSM is slowed by the need to move a single focal point throughout the regions of interest in an image volume. The speed of LSM setups can be enhanced by strategies such as random-access 2PLSM to more rapidly move the beam to only selected regions of interest, or multiplexing several beams to interrogate several regions of the sample at once.

The advent of cameras with ultrahigh quantum efficiency, such that individual pixels can be recorded with the sensitivity of the best single channel photon detectors, has created many new alternatives to capture image volumes at high resolution without sacrificing speed. One such alternative is planar illumination microscopy. Here, optical sectioning is achieved by illuminating an entire focal plane with a sheet of light, using a cylindrical lens that delivers light orthogonal to the microscope objective itself. Thus, an entire focal plane can be imaged at once. Planar illumination microscopy has proved to be an effective strategy for imaging large volumes, for example in tissue slices or brainwide imaging in zebrafish [2, 24]. Planar illumination microscopy has been used in *C. elegans* to image neuronal development at unprecedented temporal and spatial resolution, and, in principle, could be used for functional imaging of neural activity with immobilized worms [62]. However, planar illumination microscopes would be challenging to apply to freely moving worms, as the constantly changing shape of the animal would be likely to cause significant aberrations of the illumination beam from image volume to volume.

Illumination of an entire focal plane can be achieved through the microscope objective itself, for example with a spinning disk confocal microscope. Here, a series of pinholes in a spinning disk is used to scan an entire focal plane, achieving the sub-micrometer resolution of a confocal microscope but at the video-rate speed enabled by using a high-speed/high-sensitivity camera to simultaneously record all pixels in the field of view. A new technique called wide-field temporal focusing (WF-TeFo) enables two-photon excitation of an entire ~0.1 mm diameter field of view by spatially and temporally sculpting a femtosecond-pulsed laser beam, capturing the emitted photons with a high-speed/high-sensitivity camera [50] (Fig. 7.6). Volumetric imaging is performed in either spinning disk confocal microscopy or WF-TeFo by scanning in the axial direction using a piezo-driven microscope objective. WF-TeFo was recently used to record neuronal activity patterns in the head ganglion of an immobilized worm at 6 Hz with a lateral spatial resolution of ~0.3 μm and axial resolution of ~2 μm. Similar imaging acquisition rate and resolution could also be achieved by using a commercial spinning-disk confocal microscope.

Methods to illuminate single focal planes, while much faster than point scanning methods, are ultimately limited by the need to move the focal plane through a sample to capture an image volume. Two new multifocus methods recently applied to the *C. elegans* nervous system—aberration-corrected multifocus microscopy (MFM) [1] and light-field microscopy (LFM) (2014)–now allow truly simultaneous image capture at different depths in an image volume. Both methods introduce excitation light into the entire volume of a sample via conventional wide-field illumination,

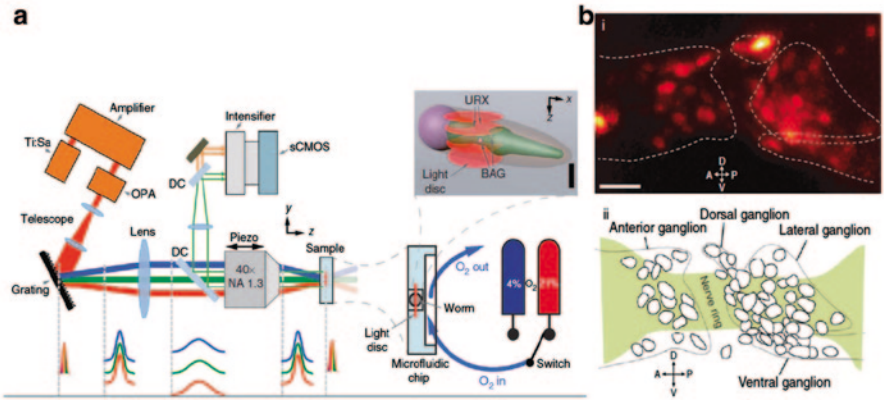

Fig. 7.6 Multineuron calcium imaging techniques. **a** Schematic of the two-photon light-sculpting microscope. The pulses at the *bottom* show the geometric dispersion in temporal focusing. The worm trapped in the microfluidic sample holder was subjected to change of environmental oxygen concentration (*bottom right*). Two neuron classes URX and BAG (*pink dots* in *top right*) showed response (Adapted from Schrodel et al. [50]). **b** Wide-field temporal focusing imaging of the head region of a worm expressing NLS-GCaMP driven by the unc-31 promoter (*top*) and schematic of the left anterior head ganglia (*bottom*)

but sort the emitted photons using customized optics on the basis of the focal plane from which they originate.

MFM produces an instant stack of 2D images at different focal planes simultaneously displayed on different portions of a single camera [1]. So far, nine focus-shifted images at up to 2 μm axial separation have been shown to be generated using custom diffraction gratings. By carefully designing the grating and by adding chromatic correction grating and prism, it is possible to significantly reduce the depth-induced aberration and chromatic dispersion, enabling simultaneous multicolor imaging of multiple focal planes with a lateral spatial resolution comparable with that of a conventional wide-field microscopy. In principle, many more than nine focal planes can be achieved with this strategy. The region of the camera that can be devoted to each image plane is inversely proportional to the total number of focal planes that will be imaged. However, this trade-off can be partially offset by using high-pixel density cameras.

The LFM uses a microlens array between the sample and camera to effectively allow sensor pixels to encode both the 2D location and 2D angle of incident light [47]. After collecting all of the information across the sensor array, a three-dimensional image can be computationally reconstructed using deconvolution [47]. An LFM setup and associated deconvolution algorithms have been demonstrated to capture activity patterns throughout the nervous system of *C. elegans* and larval zebrafish with 1–2 μm lateral spatial resolution and rates up to 20 Hz. Unlike the MFM technique, which instantaneously delivers focused images at multiple planes, the high spatial resolution of the LFM requires substantial postprocessing that can take several minutes per frame. However, the LFM technique does not have the

same trade-off between xy resolution and z resolution that occurs with the MFM technique, where different focal planes are separately tiled on distinct portions of the sensory pixel array.

7.5 Optogenetics

In addition to genetically encoded calcium indicators, genetically encoded, light-activated channels and pumps have provided a rich optogenetic toolbox for interrogation of the nervous system in an intact and behaving animal. The first uses of channelrhodopsin-2 (ChR2), a light-gated ion channel that depolarizes neurons, and halorhodopsin (NpHR), a light-gated chloride (Cl^-) pump that hyperpolarizes neurons, in a freely behaving animal were actually performed in *C. elegans* [6, 21, 45, 63]. In the presence of *all-trans* retinal, blue (for ChR2) or green (for NpHR) illumination will trigger the activity of these molecules to modulate membrane voltage. In *C. elegans*, light-gated ion channels were first expressed in cells by which light illumination could induce robust and readily observable behavioral changes. Using the *mec-4* promoter, ChR2 was expressed in six "gentle-touch" mechanosensory neurons. Blue light illumination of these cells induced rapid escape responses by which worms reversed direction and reoriented their movement [45]. By expressing ChR2 and/or NpHR in muscle cells or motor neurons, blue or yellow light illumination has also been used to induce rapid paralysis [45, 63].

Several new optogenetic proteins for activation and inhibition have since been reported—for example, archaerhodopsin (ArchT), a green light-gated proton pump for inactivating cells [9]; ReaChR, Chronos, and Chrimson, red-shifted channelrhodopsin variants [27, 33]; and Jaws, a red-shifted microbial rhodopsin variant for inactivating cells [11]. Additional probes for light-activated perturbation of neural circuits include KillerRed [61] and miniSog [48], ablative proteins that cause cells to rapidly deteriorate upon exposure to intense red or green light, respectively. In principle, the broadening palette of optogenetic proteins makes it possible to simultaneously manipulate and measure different aspects of neuronal activity using different parts of the spectrum, but care must be taken to avoid problems with spectral overlap.

The simplest hardware configuration for optogenetic manipulation in *C. elegans* is achieved by whole field illumination of an entire worm with high-intensity ($\sim$1 mW/mm^2) mercury or LED light sources. For many neurons in *C. elegans*, particularly sensory neurons and some interneurons, cell-specific promoters are available to restrict optogenetic activation to specific cells during whole animal illumination. New genetic techniques including DNA recombinase systems (Flp-*FRT* and Cre-*LoxP*) provide new ways to regulate the expression of engineered transgenes by manipulating regulatory elements [14, 40]. Recently, the Q system, a repressible binary expression system invented in *Drosophila*, has been shown to control transgenes in *C. elegans* with high spatial and temporal resolution.

In cases where light-activated proteins are broadly expressed within the nervous system—for example, in the motor circuit where the proximity of many neurons

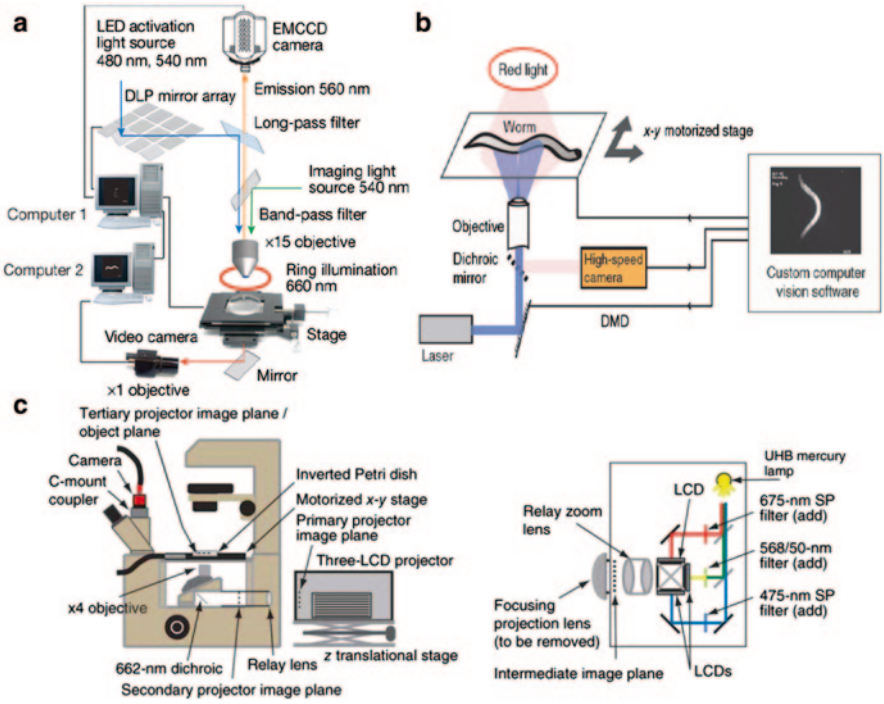

Fig. 7.7 Targeted optogenetic illumination of freely behaving worms. **a** Schematic of a closed-loop system for single-neuron stimulation developed by Kocabas et al. [34]. **b** Schematic of a closed-loop system for high-resolution optogenetic control of freely moving worms developed by Leifer et al. [36]. **c** A strategy for closed-loop optogenetic control using a video projector developed by Stirman et al. [53]

of a given class is unlikely to allow spatially distinguishable gene expression patterns—many groups have developed spatially targeted illumination methods. A common approach is to use a digital micromirror device (DMD) to achieve spatial specificity for optogenetic manipulation (Fig. 7.7a). DMDs, which contain hundreds of thousands of independently controllable micromirrors, have been widely used in digital projectors to generate arbitrary patterns of light. LCD projectors provide an alternative way of delivering structured illumination that is easier to use and far less expensive, although with less spatial and temporal resolution than can be achieved with the DMD approach [25]. Patterned illumination was first applied to activate a ChR2-expressing nociceptive neuron (ASH) in an immobilized worm [20]. Nociceptive stimuli normally induce avoidance responses. Whereas light-evoked behavioral output could not be observed in this preparation due to the animal's immobilization, it was inferred from simultaneous calcium imaging of a downstream command interneuron AVA, which controls backward locomotion.

Several closed-loop systems have been developed for targeted optogenetic stimulation in freely behaving worms. One of these, called COLBERT (Controlling Locomotion and Behavior in Real Time), uses online machine vision algorithms to

accurately measure the worm's outline and posture. This anatomical information can then be used to track the animal's movement, to generate illumination patterns for targeting defined body regions, and to quantify worm's locomotor behaviors (Fig. 7.7b). Because the relative position of a targeted neuron is invariant within the body, it is possible to quickly update (< 10 ms delay) the illumination pattern based on the worm's posture. A similar approach using feedback-controlled DMD-based illumination patterns used direct measurement of the fluorescence signal emitted from the targeted neuron [34].

In a more recent development, by integrating DMD-based illumination with calcium imaging, it is now possible to optically stimulate, inhibit, and image spatially separated (> 20 microns) neurons in a freely behaving *C. elegans* [51]. The illumination pattern generated by the DMD can be independently tuned to activate light-gated ion channels expressed in some neurons and to excite genetically encoded calcium indicators in others. For example, using this setup, one can optogenetically activate the mechanosensory neuron ALM while simultaneously performing calcium imaging in a downstream interneuron AVA that controls reversal during the escape response.

7.6 Outlook

C. elegans researchers often cite the small size and known wiring diagram of their animal's nervous system as motivations for its study. We think that models of this nervous system that span entire circuits, from sensory input to motor output, might be possible. For decades, this conviction was little more than an expression of faith, especially as the resolution and extent of neurophysiology in *C. elegans* significantly lagged that of other model systems. Optical neurophysiology is now allowing our field to catch up. To do this, hardware—new microscopes and other optical tools—is being engineered and adapted to the unique features of the *C. elegans* nervous system and its body plan. What might be called "systems neuroscience" in *C. elegans* is still in its early stages, but nevertheless circuit-level understanding of behavior has become a reality. And, when combined with unique strengths in our understanding of *C. elegans* genetics, molecular biology, and development, optical neurophysiology will create opportunities for mechanistic understanding of animal behavior that will be hard to match anytime soon in larger animals.

References

1. Abrahamsson, S., Chen, J., Hajj, B., et al. (2012). Fast multicolor 3D imaging using aberration-corrected multifocus microscopy. *Nature Methods, 10,* 60–63. doi:10.1038/nmeth.2277.
2. Ahrens, M. B., Orger, M. B., Robson, D. N., et al. (2013). Whole-brain functional imaging at cellular resolution using light-sheet microscopy. *Nature Methods, 10,* 413–420. doi:10.1038/nmeth.2434.

3. Albrecht, D. R., & Bargmann, C. I. (2011). High-content behavioral analysis of Caenorhabditis elegans in precise spatiotemporal chemical environments. *Nature Methods, 8,* 599–605. doi:10.1038/nmeth.1630.
4. Bargmann, C. I., & Horvitz, H. R. (1991). Chemosensory neurons with overlapping functions direct chemotaxis to multiple chemicals in *C. elegans*. *Neuron, 7,* 729–742. doi:10.1016/0896-6273(91)90276-6.
5. Biron, D., Shibuya, M., Gabel, C., et al. (2006). A diacylglycerol kinase modulates long-term thermotactic behavioral plasticity in *C. elegans*. *Nature Neuroscience, 9,* 1499–1505. doi:10.1038/nn1796.
6. Boyden, E. S., Zhang, F., Bamberg, E., et al. (2005). Millisecond-timescale, genetically targeted optical control of neural activity. *Nature Neuroscience, 8,* 1263–1268. doi:10.1038/nn1525.
7. Chalasani, S. H., Chronis, N., Tsunozaki, M., et al. (2007). Dissecting a circuit for olfactory behaviour in Caenorhabditis elegans. *Nature, 450,* 63–70. doi:10.1038/nature06292.
8. Chalfie, M., Sulston, J. E., White, J. G., et al. (1985). The neural circuit for touch sensitivity in Caenorhabditis elegans. *Journal of Neuroscience, 5,* 956–964.
9. Chow, B. Y., Han, X., Dobry, A. S., et al. (2010). High-performance genetically targetable optical neural silencing by light-driven proton pumps. *Nature, 463,* 98–102. doi:10.1038/nature08652.
10. Chronis, N., Zimmer, M., & Bargmann, C. I. (2007). Microfluidics for in vivo imaging of neuronal and behavioral activity in Caenorhabditis elegans. *Nature Methods, 4,* 727–731. doi:10.1038/nmeth1075.
11. Chuong, A. S., Miri, M. L., Busskamp, V., et al. (2014). Noninvasive optical inhibition with a red-shifted microbial rhodopsin. *Nature Neuroscience, 17,* 1123–1129. doi:10.1038/nn.3752.
12. Clark, D. A. (2006). The AFD sensory neurons encode multiple functions underlying thermotactic behavior in caenorhabditis elegans. *Journal of Neuroscience, 26,* 7444–7451. doi:10.1523/JNEUROSCI.1137-06.2006.
13. Clark, D. A., Gabel, C. V., Gabel, H., & Samuel, A. D. T. (2007). Temporal activity patterns in thermosensory neurons of freely moving caenorhabditis elegans encode spatial thermal gradients. *Journal of Neuroscience, 27,* 6083–6090. doi:10.1523/JNEUROSCI.1032-07.2007.
14. Davis, M. W., Morton, J. J., Carroll, D., & Jorgensen, E. M. (2008). Gene activation using FLP recombinase in *C. elegans*. *PLoS Genetics, 4,* e1000028. doi:10.1371/journal.pgen.1000028.
15. Deisseroth, K. (2010). Optogenetics. *Nature Methods, 8,* 26–29. doi:10.1038/nmeth.f.324.
16. Fang-Yen, C., Gabel, C. V., Samuel, A. D. T., et al. (2012). Laser microsurgery in caenorhabditis elegans. In: J. H. Rothman & A. Singson (Eds.), *Caenorhabditis elegans: Cell biology and physiology* (pp 177–206). Waltham: Elsevier.
17. Faumont, S. (2006). The awake behaving worm: simultaneous imaging of neuronal activity and behavior in intact animals at millimeter scale. *Journal of neurophysiology, 95,* 1976–1981. doi:10.1152/jn.01050.2005.
18. Faumont, S., Rondeau, G., Thiele, T. R., et al. (2011). An image-free opto-mechanical system for creating virtual environments and imaging neuronal activity in freely moving caenorhabditis elegans. *PLoS ONE, 6,* e24666. doi:10.1371/journal.pone.0024666.
19. Goodman, M. B., Hall, D. H., Avery, L., & Lockery, S. R. (1998). Active currents regulate sensitivity and dynamic range in *C. elegans* neurons. *Neuron, 20,* 763–772.
20. Guo, Z. V., Hart, A. C., & Ramanathan, S. (2009). Optical interrogation of neural circuits in Caenorhabditis elegans. *Nature Methods, 6,* 891–896. doi:10.1038/nmeth.1397.
21. Han, X., & Boyden, E. S. (2007). Multiple-color optical activation, silencing, and desynchronization of neural activity, with single-spike temporal resolution. *PLoS ONE, 2,* e299. doi:10.1371/journal.pone.0000299.
22. Hendricks, M., Ha, H., Maffey, N., & Zhang, Y. (2012). Compartmentalized calcium dynamics in a *C. elegans* interneuron encode head movement. Nature. doi:10.1038/nature11081.
23. Hilliard, M. A., Apicella, A. J., Kerr, R., et al. (2004). In vivo imaging of *C. elegans* ASH neurons: Cellular response and adaptation to chemical repellents. *The EMBO Journal, 24,* 63–72. doi:10.1038/sj.emboj.7600493.

24. Holekamp, T. F., Turaga, D., & Holy, T. E. (2008). Fast three-dimensional fluorescence imaging of activity in neural populations by objective-coupled planar illumination microscopy. *Neuron, 57,* 661–672. doi:10.1016/j.neuron.2008.01.011.
25. Husson, S. J., Gottschalk, A., & Leifer, A. M. (2013). Optogenetic manipulation of neural activity in C. elegans: From synapse to circuits and behaviour. *Biology Cell, 105,* 235–250. doi:10.1111/boc.201200069.
26. Iino, Y., & Yoshida, K. (2009). Parallel use of two behavioral mechanisms for chemotaxis in caenorhabditis elegans. *Journal of Neuroscience, 29,* 5370–5380. doi:10.1523/JNEUROSCI.3633-08.2009.
27. Inagaki, H. K., Jung, Y., Hoopfer, E. D., et al. (2014). Optogenetic control of Drosophila using a red-shifted channelrhodopsin reveals experience-dependent influences on courtship. *Nature Methods, 11,* 325–332. doi:10.1038/nmeth.2765.
28. Jarrell, T. A., Wang, Y., Bloniarz, A. E., et al. (2012). The connectome of a decision-making neural network. *Science, 337,* 437–444. doi:10.1126/science.1221762.
29. Kato, S., Xu, Y., Cho, C. E., et al. (2014). Temporal responses of *C. elegans* chemosensory neurons are preserved in behavioral dynamics. *Neuron, 81,* 616–628. doi:10.1016/j.neuron.2013.11.020.
30. Kawano, T., Po, M. D., Gao, S., et al. (2011). An imbalancing act: Gap junctions reduce the backward motor circuit activity to bias *C. elegans* for forward locomotion. *Neuron, 72,* 572–586. doi:10.1016/j.neuron.2011.09.005.
31. Kerr, R., Lev-Ram, V., Baird, G., et al. (2000). Optical imaging of calcium transients in neurons and pharyngeal muscle of C. elegans. *Neuron, 26,* 583–594. doi:10.1016/S0896-6273(00)81196-4.
32. Kimura, K. D., Miyawaki, A., Matsumoto, K., & Mori, I. (2004). The *C. elegans* thermosensory neuron AFD responds to warming. *Current Biology, 14,* 1291–1295. doi:10.1016/j.cub.2004.06.060.
33. Klapoetke, N. C., Murata, Y., Kim, S. S., et al. (2014). Independent optical excitation of distinct neural populations. *Nature Methods, 11,* 338–346. doi:10.1038/nmeth.2836.
34. Kocabas, A., Shen, C.-H., Guo, Z. V., & Ramanathan, S. (2012). Controlling interneuron activity in Caenorhabditis elegans to evoke chemotactic behaviour. *Nature, 490,* 273–277. doi:10.1038/nature11431.
35. Larsch, J., Ventimiglia, D., Bargmann, C. I., & Albrecht, D. R. (2013). High-throughput imaging of neuronal activity in Caenorhabditis elegans. *Proceedings of the National Academy of Sciences of the United States of America, 110,* E4266–E4273. doi:10.1073/pnas.1318325110.
36. Leifer, A. M., Fang-Yen, C., Gershow, M., Alkema, M. J., & Samuel, A. D. T. (2011). Optogenetic manipulation of neural activity in freely mov*ing* Caenorhabditis elegans. *Nat Meth, 8*(2), 147–152. doi: 10.1038/nmeth.1554.
37. Looger, L. L., & Griesbeck, O. (2012). Genetically encoded neural activity indicators. *Current Opinion in Neurobiology, 22,* 18–23. doi:10.1016/j.conb.2011.10.024.
38. Luo, L., Cook, N., Venkatachalam, V., et al. (2014a). Bidirectional thermotaxis in Caenorhabditis elegans is mediated by distinct sensorimotor strategies driven by the AFD thermosensory neurons. *Proceedings of the National Academy of Sciences of the United States of America, 111,* 2776–2781. doi:10.1073/pnas.1315205111.
39. Luo, L., Wen, Q., Ren, J., et al. (2014b). Dynamic encoding of perception, memory, and movement in a *C. elegans* chemotaxis circuit. *Neuron, 82,* 1115–1128. doi:10.1016/j.neuron.2014.05.010.
40. Macosko, E. Z., Pokala, N., Feinberg, E. H., et al. (2009). A hub-and-spoke circuit drives pheromone attraction and social behaviour in C. elegans. *Nature, 458,* 1171–1175. doi:10.1038/nature07886.
41. McCormick, K. E., Gaertner, B. E., Sottile, M., et al. (2011). Microfluidic devices for analysis of spatial orientation behaviors in Semi-Restrained caenorhabditis elegans. *PLoS ONE, 6,* e25710. doi:10.1371/journal.pone.0025710.

42. Miyawaki, A., Griesbeck, O., Heim, R., & Tsien, R. Y. (1999). Dynamic and quantitative Ca2 + measurements using improved cameleons. *Proceedings of the National Academy of Sciences of the United States of America, 96,* 2135–2140. doi:10.1073/pnas.96.5.2135.
43. Miyawaki, A., Llopis, J., Heim, R., McCaffery, J. M., Adams, J. A., Ikura, M., & Tsien, R. Y. (1997). Fluorescent indicators for Ca2+based on green fluorescent proteins and calmodulin. *Nature, 388*(6645), 882–887.
44. Miyawaki, A., Llopis, J., Heim, R., et al. (2007). Fluorescent indicators for Ca2 + based on green fluorescent proteins and calmodulin. *Nature, 388,* 882–887. doi:10.1038/42264.
45. Nagel, G., Brauner, M., Liewald, J. F., et al. (2005). Light activation of channelrhodopsin-2 in excitable cells of caenorhabditis elegans triggers rapid behavioral responses. *Current Biology, 15,* 2279–2284. doi:10.1016/j.cub.2005.11.032.
46. Piggott, B. J., Liu, J., Feng, Z., et al. (2011). The neural circuits and synaptic mechanisms underlying motor initiation in C. elegans. *Cell, 147,* 922–933. doi:10.1016/j.cell.2011.08.053.
47. Prevedel, R., Yoon, Y.-G., Hoffmann, M., Pak, N., Wetzstein, G., Kato, S., . . . Vaziri, A. (2014). Simultaneous whole-animal 3D imaging of neuronal activity using light-field microscopy. *Nat Meth, 11*(7), 727–730. doi: 10.1038/nmeth.2964.
48. Qi, Y. B., Garren, E. J., Shu, X., et al. (2012). Photo-inducible cell ablation in Caenorhabditis elegans using the genetically encoded singlet oxygen generating protein miniSOG. *Proceedings of the National Academy of Sciences of the United States of America, 109,* 7499–7504. doi:10.1073/pnas.1204096109.
49. Richmond, J. E., & Jorgensen, E. M. (1999). *Nature Neuroscience, 2,* 791–797. doi:10.1038/12160.
50. Schrödel, T., Prevedel, R., Aumayr, K., et al. (2013). Brain-wide 3D imaging of neuronal activity in Caenorhabditis elegans with sculpted light. *Nature Methods, 10,* 1013–1020. doi:10.1038/nmeth.2637.
51. Shipley, F. B., Clark, C. M., Alkema, M. J., & Leifer, A. M. (2014). Simultaneous optogenetic manipulation and calcium imaging in freely moving C. elegans. *Front Neural Circuits, 8,* 28. doi:10.3389/fncir.2014.00028.
52. Stetina Von, S. E., Treinin, M., & Miller, D. M. III. (2005). The motor circuit. In E. J. Aamodt (Ed.), *The neurobiology of C. elegans* (pp. 125–167). San Diego: Elsevier.
53. Stirman, J. N., Crane, M. M., Husson, S. J., Wabnig, S., Schultheis, C., Gottschalk, A., & Lu, H. (2011). Real-time multimodal optical control of neurons and muscles in freely behaving Caenorhabditis elegans. *Nat Meth, 8*(2), 153–158. doi: 10.1038/nmeth.1555.
54. Sulston, J. E., & Horvitz, H. R. (1977). Post-embryonic cell lineages of the nematode, Caenorhabditis elegans. *Developmental Biology, 56,* 110–156. doi:10.1016/0012-1606(77)90158-0.
55. Sulston, J. E., Schierenberg, E., White, J. G., & Thomson, J. N. (1983). The embryonic cell lineage of the nematode Caenorhabditis elegans. *Developmental Biology, 100,* 64–119. doi:10.1016/0012-1606(83)90201-4.
56. Suzuki, H., Kerr, R., Bianchi, L., et al. (2003a). In Vivo Imaging of *C. elegans* mechanosensory neurons demonstrates a specific role for the MEC-4 Channel in the process of gentle touch sensation. *Neuron, 39,* 1005–1017. doi:10.1016/j.neuron.2003.08.015.
57. Suzuki, H., Kerr, R., Bianchi, L., et al. (2003b). In Vivo Imaging of *C. elegans* mechanosensory neurons demonstrates a specific role for the MEC-4 channel in the process of gentle touch sensation. *Neuron, 39,* 1005–1017. doi:10.1016/j.neuron.2003.08.015.
58. Suzuki, H., Thiele, T. R., Faumont, S., et al. (2008). Functional asymmetry in Caenorhabditis elegans taste neurons and its computational role in chemotaxis. *Nature, 454,* 114–117. doi:10.1038/nature06927.
59. Wen, Q., Po, M. D., Hulme, E., et al. (2012). Proprioceptive coupling within motor neurons drives *C. elegans* forward kocomotion. *Neuron, 76,* 750–761. doi:10.1016/j.neuron.2012.08.039.
60. White, J. G., Southgate, E., Thomson, J. N., & Brenner, S. (1986). The structure of the nervous system of the nematode caenorhabditis elegans. *Philosophical Transactions of the Royal Society of London B Biological Science, 314,* 1–340. doi:10.1098/rstb.1986.0056.

61. Williams, D. C., Bejjani El, R., Ramirez, P. M., et al. (2013). Rapid and permanent neuronal inactivation in vivo via subcellular generation of reactive oxygen with the use of KillerRed. *Cell Reports, 5,* 553–563. doi:10.1016/j.celrep.2013.09.023.
62. Wu, Y., Ghitani, A., Christensen, R., et al. (2011). Inverted selective plane illumination microscopy (iSPIM) enables coupled cell identity lineaging and neurodevelopmental imaging in Caenorhabditis elegans. *Proceedings of the National Academy of Sciences of the United States of America, 108,* 17708–17713. doi:10.1073/pnas.1108494108.
63. Zhang, F., Wang, L.-P., Brauner, M., et al. (2007). Multimodal fast optical interrogation of neural circuitry. *Nature, 446,* 633–639. doi:10.1038/nature05744.

Chapter 8
Sensorimotor Integration in the Spinal Cord, from Behaviors to Circuits: New Tools to Close the Loop?

Claire Wyart and Steven Knafo

Abstract Sensorimotor behaviors are by definition "closed-loop" processes in which sensory feedback modulates behavioral output. Sensory feedback can be provided by visual, auditory, and vestibular inputs or direct proprioceptive inputs from muscle contraction. Although sensory feedback is not necessary for oscillation underlying locomotion to occur, there is evidence in the cat that sensory feedback can initiate locomotion [128] or reset the rhythm [183]. The contribution of sensory feedback to active locomotion is however difficult to estimate for technical reasons. Indeed, most physiological studies of genetically identified cells in spinal circuits involved in sensorimotor integration rely on preparations where mechano-muscles are paralyzed or dissected out, and are therefore deprived of sensory feedback.

In this chapter, we will first explain closed-loop processes, and we will review the precious information obtained using "open-loop" experimental paradigms on how spinal neurons generate the neural rhythms that are at the basis of locomotion [82]. Optical and genetics techniques offer today alternatives to electrophysiology for monitoring neuronal activity from genetically defined populations of spinal neurons. We will then discuss how innovative tools for monitoring and manipulating neural activity, together with conducting sophisticated behavioral analysis, have provided exciting opportunities for "closing the loop" in genetically accessible model organisms with a special emphasis on zebrafish.

C. Wyart (✉) · S. Knafo
Institut du Cerveau et de la Moelle épinière (ICM), 83 boulvard de l'hopital, 75013 Paris, France
e-mail: claire.wyart@icm-institute.org

A. D. Douglass (ed.), *New Techniques in Systems Neuroscience,* Biological and Medical Physics, Biomedical Engineering, DOI 10.1007/978-3-319-12913-6_8

8.1 A Closed-Loop Approach to Sensorimotor Behaviors

8.1.1 Defining Sensorimotor Behaviors

8.1.1.1 Eliciting Sensory Input

A fly approaching a fruit odor is a rich example of sensorimotor integration [188]: the fly must first detect the odor [32], extract information regarding its environmental relevance, and adapt its course to approach the fruit. All those steps have to be achieved while the animal is moving, thus adjusting its locomotor output to changing visual, olfactory, and mechanosensory feedback [67]. Combining multiple sensory modalities and their closed-loop feedbacks is critical to adapt to a noisy sensory environment and enhances the robustness of the behavioral output [67]. Multisensory processing relies on interdependent sensory signals, allowing for increased efficiency during sensorimotor tasks compared to unimodal sensory stimuli [127].

In mammals, it has long been clear that "high-level" cortical areas, such as parietal and prefrontal cortices, are able to integrate multiple sensory modalities. However, increasing evidence suggests that multisensory integration also occurs in "low-level" cortices that were previously thought to be unisensory [71, 185]. Studying sensorimotor integration, even at a relatively low level, thus requires one to reproduce a behaviorally relevant multisensory environment. However, practical considerations often make this difficult.

One solution proposed by the field of neuroethology [49] is to consider that neural circuits can be experimentally understood in the context of the animal's natural behavior. By focusing on innate behaviors in which the animal extracts critical sensory inputs to produce a behaviorally meaningful locomotor output, neuroethology has provided important models for sensorimotor integration. For instance, escape behaviors, by which an animal escapes from its predator, are a perfect example of a sensorimotor task that is crucial for the animal's survival. Escape responses can be found in many species, including *Drosophila* [36], *C. elegans* [160], and several fish species [186], allowing for comparative studies of sensorimotor integration across taxa.

Determining which sensory stimulus to control experimentally is a critical step of sensorimotor studies. We cannot reproduce the highly variable and multidimensional sensory inputs from the animal's natural environment, but we should at least choose a stimulus that replicates the minimum set of sensory cues necessary to elicit a behaviorally relevant and consistent motor output [39]. We also need to reliably record and quantify the locomotor output elicited by this sensory input.

8.1.1.2 Measuring Motor Output

The behavioral output of a sensorimotor transformation can be measured at different spatial and temporal scales, from the migration of an entire population of animals over several days to the analysis of single muscle fibers at millisecond

timescale [39]. Choosing the right scale for addressing the sensorimotor process of interest is not trivial.

At one extreme of this scale, "taxis" behaviors, such as chemotaxis in *Drosophila* [69] or rheotaxis in zebrafish [195], examine the cumulative change in spatial position of a group of animals over a relatively long period of time. It is also possible to look at the level of the individual in order to identify sequences of stereotyped behaviors such as mating in *C. elegans* [125]. Sequential analyses of canonical behaviors can allow the description of the complete locomotor repertoire for a given species, such as zebrafish [31]. Lastly, a more detailed kinematics analysis could measure the movements of individual joints and couple this analysis with muscle activity recordings, as has been done in rodents [41].

With the refinement of locomotor analysis, and the increasing set of kinematic parameters that can be measured simultaneously, automated tracking programs have become crucial to reliably quantify behavior. Such programs have been successfully applied to track individuals and classify behaviors in *C. elegans* [12], *Drosophila* [66], and zebrafish [141]. Automated tracking programs have also been used to identify interactions between populations of multiple animals [26, 141], characterize mutant behaviors and build behavioral phenotypes databases [210], and might be applied to high-throughput drug screening [141].

Analyzing complex datasets with multiple kinematic parameters per animal and several animals interacting simultaneously raises important technical challenges. Reducing the dimensionality of the behavioral dataset can be achieved either by arbitrarily focusing on a restricted number of kinematic parameters or though statistical dimensionality reduction as in principal component analysis (PCA) [145]. The main issue with dataset reduction is to determine and preserve the behavioral output related to the sensory stimulus of interest. This can be achieved by computing the level of prediction or correlation between the sensory input and motor output [28].

Although sensory input and motor output are the two ends and most accessible parts of a sensorimotor circuit, they are not sufficient to infer sensorimotor neural computation. Modulating inputs from "top-down" afferents or "bottom-up" feedback also heavily influence sensorimotor processing.

8.1.2 Modulating Sensorimotor Behaviors

8.1.2.1 Sensory Feedback

In the real world, sensorimotor integration is a dynamic process where the animal constantly updates its sensory inputs according to its behavioral output: as the fly approaches the fruit, olfactory and visual stimuli change continuously. By tracking these changes, the fly can adjust its flight to reach the target [67]. In an experimental setting, the animal must often be restrained or paralyzed to allow recording of neuronal activity. Such preparations are called "open-loop" because the motor output does not influence subsequent sensory input. But one might hypothesize that neuronal activity is not the same in the absence of sensory feedback.

"Closed loop" experiments, where new sensory information is acquired as the motor output is produced, can be obtained mainly through two complementary approaches: by attaching a miniaturized device onto a free moving animal interacting with a controlled environment or by providing simulated sensory inputs to a restrained animal. The developing field of brain-machine interfaces has provided key examples of how to go about this, for example in studies where cortical activity is recorded through chronically implanted electrode arrays and decoded in real time to control a motor effector, such as prosthetic limb [37]. It has also been possible to restore tactile sensation using a "brain-machine-brain interface," by providing a way to produce a virtual motor output and to generate the corresponding sensory feedback [157, 197].

Such tools make it possible to monitor neuronal activity while the animal is freely behaving, but they do not provide precise control over its sensory inputs. Virtual reality environments [50] reproduce a simulated sensory environment that is continuously updated based on the animal's behavior. Besides providing a better-controlled sensory input, virtual environments most importantly enable simultaneous neural recording by allowing the animal to perform a closed loop sensorimotor task while being physically restrained.

Combined with electrophysiology or genetically encoded calcium imaging, virtual environments have been applied in mice [87], *Drosophila* [190], and zebrafish [2, 161]. Notably, the zebrafish studies have shown that larvae were able to quickly modify their motor output in response to unexpected visual feedback (Fig. 8.1a) [161] and that this adaptive behavior correlated with state-dependent neural activity in a subset of brain areas identified using brain-wide calcium imaging [2].

8.1.2.2 Neuromodulation

State-dependent sensorimotor processing, in which the activity of a given population of neurons differs according to the behavioral state of the animal, is investigated within the larger framework of neuromodulation.

The core hypothesis underlying the concept of "multifunctional circuits" is that a given neural circuit should not be considered as a hard-wired diagram, activated during discrete states, but rather as a distributed network that is able to switch continuously between a variety of dynamical states to produce different patterns of activity, and eventually different behaviors [27]. In a multifunctional sensorimotor circuit, a given neuron can be active during multiple locomotor behaviors [179], producing different patterns of activity based on its modulatory inputs [27]. External parameters, such as modulatory neurotransmitters [129] or synaptic input, for example from sensory afferents [116], can control the transitions between these different phases.

The neuromodulatory functions of monoaminergic substances have been extensively studied in invertebrate sensorimotor models such as the crustacean somatogastric ganglion (STG) [130]. These central pattern generator (CPG) circuits can generate fictive locomotor patterns and are modulated by numerous substances, from neurotransmitters released locally by projecting sensory neurons to diffuse

hormones released at distance by secretory structures [20]. In rats with induced spinal cord injuries, the role of monoaminergic (in particular serotoninergic and dopaminergic) substances in modulating spinal locomotor circuits has been well documented [145]. Pharmacological manipulation, together with electrical spinal cord stimulation, could restore some locomotion independently of supraspinal input regeneration [42]. Such neuromodulatory-mediated functional recovery is also phase specific, that is, the observed recovery depends on the phase of the locomotor cycle during which it occurs, suggesting that different interventions facilitate distinct phases of the locomotor pattern [59]. This observation is in line with a multifunctional framework for the spinal sensorimotor circuits driving locomotion in spinal cord injured rats.

Intrinsic sensory states, that is neural dynamics that are not directly affected by an external physical stimulus, can also modulate multifunctional sensorimotor networks. One interesting example is the dual role of the gravimetric organ of the mollusk *Clione limacina*, which can switch between two very different rhythmic patterns, and associated behavioral outputs, depending on whether the animal is under control of a "hunting neuron" [116]. Another example of intrinsic sensory modulation is the feeding behavior of the *Aplysia californica*, where the same neurons drive both ingestion and rejection of food, but are differentially modulated by the coupling between the mouth muscles [209].

8.1.3 Modeling Sensorimotor Behaviors

8.1.3.1 Behavioral Computations

Analyzing sensorimotor transformations is more complicated than just correlating an observed motor output with an experimentally elicited sensory input. Computational models for sensorimotor integration have proven more and more helpful as the number of measured variables increased with the improvement of experimental techniques.

For any sensorimotor task, the underlying computation is complex and can be modeled on a coarse behavioral scale, or on a more refined neuronal scale. These approaches are complementary but have so far mostly been developed independently. The long-term objective is to map one onto the other.

One major issue when dealing with sensorimotor computation is that our motor system is highly nonlinear [65]. In a linear system, one can easily predict the behavioral response to a multisensory stimulus by calculating the sum of the motor outputs for each individual sensory stimulus. However, the force developed by a muscle in response to its nervous input largely depends on other variables such as muscle length, velocity, tendons, and joint positions, among others [211]. Similarly, multiple sensory inputs create combined representations that are more than merely the sum of the individual modalities [78].

Besides nonlinearity, many other issues increase the complexity of sensorimotor computations. For instance, noise limits our ability to perceive sensory inputs (e.g.,

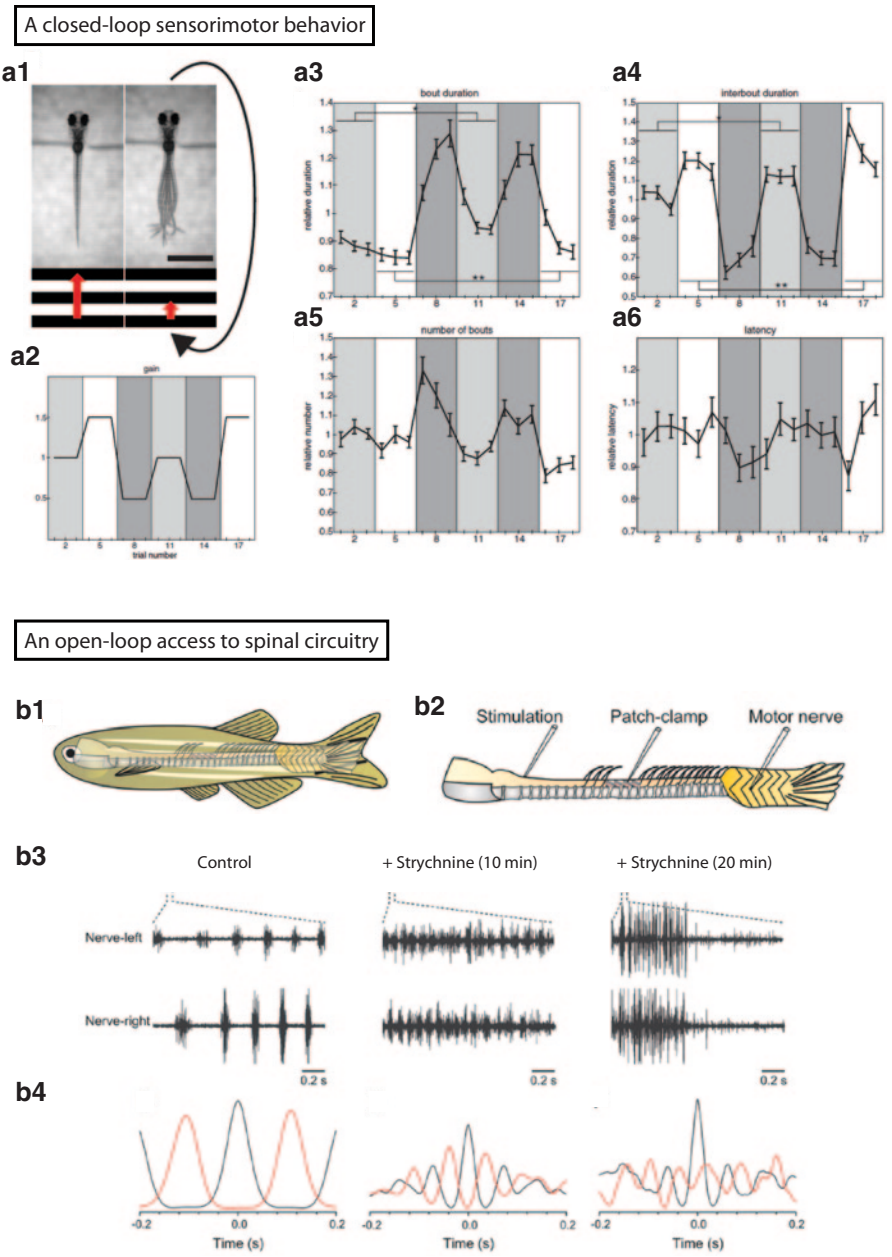

Fig. 8.1 Open loop and closed loop paradigms illustrated in zebrafish. A. A visual closed-loop virtual reality paradigm in the zebrafish larva. A moving visual stimulus is showed to a head-embedded larva (aged 6–7 days post-fertilization) while its behavior is monitored and its speed (*red arrow*) is modified by the swimming speed of the larva (A1). In this virtual visual closed-loop environment, a "gain" is used as a constant factor to adjust the grating speed to the larval swimming speed (A2). For three different gains, several kinematics parameters of the larvae locomotor output are modified consistently: bout duration (A3), interbout interval (A4), number of bouts

for our approaching fly, estimating the location of the fruit on the table) and to produce motor outputs precisely (e.g., adjusting speed by modifying wing movements to reach the target) [172]. Other issues include redundancy, that is the fact that multiple combinations of motor sequences can achieve the same behavioral task; nonstationarity, that is the fact that sensory and motor systems are modified throughout development and aging; sensory ambiguity, partial information; and even multiple and variable delays, whether due to sensory or motor processing [65].

One approach to resolve such complex sensorimotor computations is Bayesian decision theory [207]. Bayesian decision theory aims to produce, using a probabilistic reasoning, optimal inferences based on uncertain inputs by combining prior beliefs and multiple sensory modalities. Based on these inferences, decision theory is subsequently used to decide which action is more likely to achieve the task objectives [65]. In a Bayesian system, the probability of a sensory state being true (called the "posterior") is produced by combining the probability of receiving a set of sensory information if that state were true (the "likelihood") with the prior probability of that state (the "prior") [114].

Such Bayesian sensorimotor computation can be easily tested using a simple task where a subject is asked to reach a cursor in a virtual-reality environment. A discrepancy is introduced between the subject's actual and displayed hand positions [113]. The "prior" distribution can be experimentally set by varying the discrepancy, while the sensory feedback "likelihood" is adjusted by varying the degree of visual blur controls. Using this approach, the authors showed that subjects combined prior statistical distribution with sensory feedback likelihood in a Bayesian manner to optimize their performance during sensorimotor learning.

8.1.3.2 Circuit Computations

Mapping behavioral sensorimotor computations onto identified neural circuits requires knowing how those circuits process sensory inputs to produce a motor output at a cellular scale.

One important challenge for computing sensorimotor transformations, whether on a behavioral or cellular scale, is that they are mostly nonlinear. Geometrically, this means that modeling any neural network underlying a sensorimotor process requires at least a three-layered transformation, with an intermediate layer (referred

(A5) and latency (A6). *Adapted from Portugues et al. 2011.* **B.** An open-loop experimental fictive preparation for investigating with electrophysiology the role of spinal cells in the absence of mechanosensory feedback. To record from spinal neurons in a juvenile zebrafish (aged 8–15 weeks), the skin and muscles are dissected out to expose the isolated spinal cord (B1), and a stimulating electrode (1s, 40Hz) is placed at the junction with brainstem to elicit episodes of "fictive" swimming, while the motor output can be recorded from the ventral nerve root or from patched-clamp spinal neurons (B2). Bath application of pharmacological substances, such as the glycinergic antagonist strychnine, is used to modify the fictive motor output on the ventral nerve root recordings (B3). Short (10 minutes) application of strychnine results in increased swimming burst frequency, while longer application (20 minutes) leads to a decreased duration of the swimming episode as well as disruption of the left-right alternation (B4). *Adapted from Kyriakatos et al. 2011.*

to as the "hidden layer") used to recode sensory inputs before they are transformed into motor output. Such nonlinear transformations can be approximated using a linear combination of "basis functions" (such as sine and cosine functions in a Fourier transform) as the intermediate layer: this is a called the "basis function approach" [164].This basis function approach is particularly relevant in the context of sensorimotor transformations. For instance, if a subject wants to reach toward a visual target as in the previously described experiment, the motor command can be approximated by the weighted sum of several nonlinear basis functions of the visual and postural inputs [163]. On a cellular scale, this "intermediate layer" would be constituted by neurons whose firing properties, or "tuning curve," can be described as a basis function for both visual and postural sensory inputs. Such neurons whose gain is modulated by visual and postural inputs can actually be found in the parietal [6], occipital [202], and prefrontal [23] cortices.

Besides nonlinearity, another major concern when looking at sensorimotor transformations is variability. Most experiments, whether looking at sensorimotor processes or not, rely on mean statistics calculated from populations. However, it has been repeatedly shown that multiple physiological solutions can produce similar circuit outputs [129]. Even the most stereotyped motor behaviors such as rhythms generated by CPGs can be highly variable across animals [131]. The variability of the behavioral outputs evoked by similar sensory inputs is well known, although not always documented. Most studies describe the "typical" behavior of the system by a single model. One attempt to take into account variability in sensorimotor circuits models would be to construct of population of models reproducing the actual behavioral data rather than trying to use a single model to reproduce the generic behavior [131].

8.2 An Open-Loop Access to Sensorimotor Circuits in the Spinal Cord Across Vertebrates

In the particular case of spinal sensorimotor circuits, a great wealth of anatomical and electrophysiological data has been accumulated over the years. However, being able to elaborate broader models in order to fit those data onto observed behaviors still remains a challenge, largely due to the fact that available techniques have prevented us from monitoring sensory inputs concomitantly with motor outputs until recently.

8.2.1 Extrinsic Inputs to Spinal Sensorimotor Circuits

8.2.1.1 Descending Motor Control

Located in the periphery of the spinal cord, white matter tracts comprise both ascending fibers, mainly located dorsally and laterally, carrying sensory information, and descending axons, mainly located ventrolaterally and laterally, carrying motor information (Fig. 8.2a).

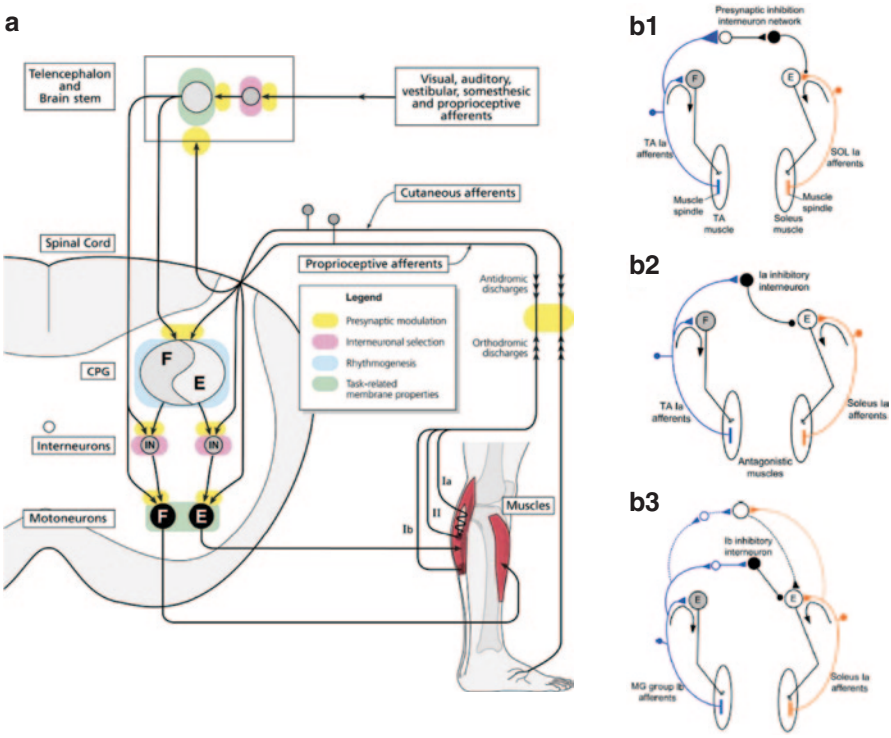

Fig. 8.2 Descending and ascending inputs to spinal circuits involved in sensorimotor reflexes. A. Motor and sensory inputs to spinal neurons and sites for sensorimotor integration. Descending motor control from the corticospinal and rubrospinal tracts in the dorsolateral funiculus) and reticulospinal and vestibulospinal tracts (in the the ventrolateral funiculus are integrated with ascending sensory inputs from proprioceptive afferents Ia and II from muscle spindles and Ib from Golgi tendon organs at various premotor locations. *Adapted from Rossignol et al. 2006.* **B.** Some spinal sensorimotor reflexes and underlying interneuronal networks. Presynaptic inhibition of sensory afferents by GABAergic premotor interneurons in the intermediate laminae of the spinal cord is a common control mechanism for filtering sensory inputs (B1). Reciprocal Ia inhibition by glycinergic interneurons allows for antagonist muscles inhibition during a flexion movement (B2). Non-reciprocal Ib inhibition facilitates synergist muscle contraction though polysynaptic pathways (B3).

Descending motor tracts mainly include corticospinal tracts, which forms monosynaptic connections between motoneurons located in the primary motor cortex and spinal motoneurons located in the anterior horn of the grey matter at each segment. Eighty to ninety percent of the corticospinal axons decussate to the contralateral side at the pyramid level in the medulla oblongata (hence the name "pyramidal tracts") and travel in the dorsolateral funiculus [83]. Corticospinal tracts are mostly involved in voluntary skilled movements.

Other descending motor tracts originate mainly in subcortical nuclei in the brainstem, and particularly in the reticular formation, and are called "extra-pyramidal tracts." Extra-pyramidal tracts are composed of the rubrospinal (located along the

corticospinal tract in the dorsolateral funiculus), vestibulospinal, tectospinal, and reticulospinal tracts (all three located in the ventrolateral funiculus) [19, 174].

Those descending inputs are mainly involved in autonomic functions, postural control, and locomotion. More specifically, they facilitate contralateral upper limb flexion (rubrospinal tract), neck and head motor control (tectospinal tract), autonomic functions (reticulospinal tract), and regulate ipsilateral extensors and antigravity muscles to control tone and posture (vestibulospinal tract) [83]. Extra-pyramidal tracts project mainly on premotor lamina (lamina VI–VIII) of the spinal cord grey matter at each segment [19].

The role of reticulospinal pathways originating from the brainstem in the initiation and control of locomotion has been extensively studied, leading to the concept that, while the spinal CPG produces the basic locomotor rhythm (see Sect. 8.2.2.1), brainstem structures are necessary to activate and regulate this structure [98, 205].

Numerous studies, mainly using decerebrate cat preparations, have identified several areas within the brainstem that can lead to the production of locomotion when activated, whether chemically or electrically. The mesencephalic locomotor region (MLR), first identified by Shik et al. [191], receives inputs from both the basal ganglia, the limbic system and the frontal cortex, and projects to neurons of the medial medullary reticular formation (MRF), and then on to interneurons in the spinal cord [205]. When stimulated electrically in decerebrate cats, the MLR can generate different gait patterns (walking, trotting, galloping) depending on the strength of the electrical stimulus [176]. Interestingly, after its initial description in cats, areas homologous to the MLR have been described in many vertebrate species, including the rat [70], lamprey [136], and monkey [60].

Other areas in the midbrain, such as the medial MLR, the pontomedullary locomotor strip (PLS) or areas in the subthalamic nucleus (subthalamic locomotor region), have been shown to be involved in the control of locomotion by projecting onto spinal circuits through reticulospinal pathways in rodents [205]. More recently, isolated spinal cord preparations from neonatal rats and mice have allowed the identification of various neurotransmitters (N-methyl-D-aspartate, 5-hydroxytryptamine, dopamine, noradrenaline) that can elicit locomotor rhythmic activity by stimulating the spinal CPG through descending reticulospinal pathways [99].

In nonmammalian vertebrates, the descending control of locomotion has been particularly well documented in the lamprey [52]. Trigeminal relay cells activate reticulospinal neurons in a “all-or-nothing” fashion to elicit escape responses in response to a mechanical cutaneous stimulus [203]. In contrast, MLR inputs to reticulospinal neurons initiate locomotion in a graded fashion through monosynaptic cholinergic and glutamatergic inputs, with the middle rhombencephalic reticular nucleus (RRN) being activated for low intensity stimulation, and the posterior RRN being activated as the stimulation strength increases [204] (Fig. 8.3a). Lastly, recent investigations in zebrafish larvae have demonstrated the role of descending reticulospinal neurons in the nucleus of the medial longitudinal fasciculus (nMLF) in the modulation of swimming speed [189] and swim posture [200].

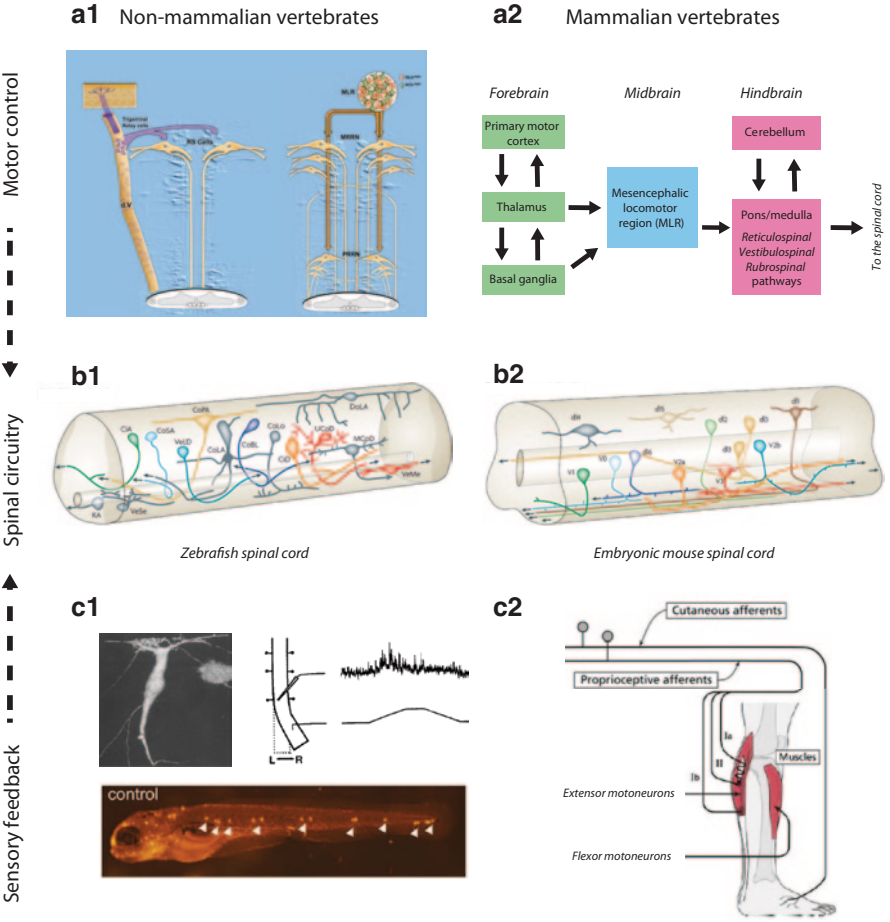

Fig. 8.3 Neural substrates of spinal sensorimotor integration across vertebrates. A. Descending motor control. In the lamprey, a mechanical stimulation to the head activates reticulospinal neurons through the trigeminal nerve, eliciting escapes reponses in an all-or-nothing fashion (A1 *left*). Swimming episodes can also be elicited by stimulating the Mesencephalic Locomotor Region (MLR), which projects onto reticulospinal neurons in the middle and posterior rhombencephalic reticular nuclei with a graded synaptic input (A1, *right*) *Adapted from Dubuc et al. 2008.* In mammalian vertebrates, forebrain regions such as the primary motor cortex can initiate locomotion by projection on the MLR, which in turn activate descending motor pathways that modulate the spinal circuitry (A2). *Adapted from Goulding, 2009.* **B.** Intraspinal circuitry. Based on this molecular homology, similar neuronal cell types can be identified in the zebrafish (B1) and mouse (B2) spinal cords, as indicated by the same color in the schematic. Zebrafish homologs of the mouse interneurons are: CoSA/MCoD (V0), CiA (V1), CiD (V2a), VeLD (V2b), UCoD/VeMe (V3). *Adapted from Goulding, 2009.* **C.** Ascending sensory feedback. In the lamprey, intraspinal stretch receptors called the "edge cells" are activated upon mechanical bending of the spinal cord and could serve as mechanoreceptor during swimming (C1, top. *Adapted from Grillner et al. 1984 and Di Prisco et al. 1990*). In the zebrafish, the lateral line can be used to sense the water flow and provide feedback for rheotaxis behavior. Ablation of the lateral line neuromasts results in the inability for the fish to successfully escape a suction source (percentage of larvae holding against the water flow in black) (C1, *bottom*. *Adapted from Olszewski et al. 2012*). In mammalian vertebrates, cutaneous and proprioceptive muscle receptors provide sensory feedback to the spinal circuitry and can modulate the motor output in a phase and state-dependent manner (C2. *Adapted from Rossignol et al. 2006*).

8.2.1.2 Ascending Sensory Feedback

While descending inputs schematically provide the motor command to spinal sensorimotor circuits, ascending afferents to the spinal cord mainly provide sensory information. In mammals, ascending sensory afferents include proprioceptive inputs (group Ia and II afferents from, respectively, primary and secondary endings of muscles spindles, and Ib afferents from Golgi tendon organs) and cutaneous inputs (chemosensitive group III/Aδ and group IV/C fibers from nociceptive receptors). These have been extensively studied in the context of local spinal reflex pathways [108, 176] (Fig. 8.2b).

The simplest, and fastest, somatic reflex is mediated by the monosynaptic pathway between primary sensory afferents from primary muscle spindles (Ia) and homonymous alpha motoneurons in the ventral horn of the corresponding segment grey matter. This drives the basic myotatic reflex that is elicited by a muscle stretch due to a tendon tap, but it is also involved in tonus and postural adjustments [83]. The experimental analog of the Ia reflex, the Hoffman reflex (H-reflex), where the mechanical stretch is replaced by a subthreshold electrical stimulation of the afferent nerve, has been extensively used to investigate spinal sensorimotor circuits, and in particular presynaptic and reciprocal inhibition [95, 108], see (Sect. 8.2.2.1).

Golgi tendon organs are force-sensitive receptors located at the muscle-tendon junction, which are activated by passive and active muscle force. The Ib reflex arc, also known as the "inverse myotatic reflex," is a disynaptic pathway by which group Ib sensory afferents from Golgi tendon organs inhibit alpha-motoneurons. This is the reflex arc responsible for the abrupt termination of the myotatic reflex, the well-known "clasp-knife" phenomenon [93]. Although stimulating the Golgi tendon organs at rest cannot induce any movement, the Ib reflex has been suggested to be important for regulating muscle stiffness [108].

While group Ib afferents from Golgi tendon organs provide information about the tension developed during muscle contraction, and group Ia afferents from primary muscle spindles inform spinal circuits about the dynamic of changes in muscle length, group II afferents from muscle spindle secondary endings provide information of muscle length itself [96]. Group Ia, Ib, and II muscle afferents taken together constitute what is generally termed the "proprioception" input. Together with cutaneous afferents from nociceptors (Aδ and C fibers) and other muscle afferents (thinly myelinated group III and unmyelinated group IV fibers), group II muscle afferents constitute the flexion reflex afferents (FRA) involved in the withdrawal reflex, by which a painful stimulus leads to withdrawal of the limb through ipsilateral flexion and contralateral extension [55]. This sensorimotor reflex, more sophisticated than the "myotatic" and "inverse myotatic" reflexes, involves at least to two interneurons that either activate or inhibit the ipsilateral flexor or extensor alpha-motoneurons over several spinal segments [83].

Sensory feedback pathways in nonmammalian vertebrates still remain unclear. Indeed, there is no clear equivalent to mammalian peripheral proprioceptive receptors in swimming vertebrates. However, in the lamprey, intraspinal mechanosensitive receptors called the "edge cells" [81] might provide movement-related sensory

feedback [48]. Interestingly, it has recently been proposed that edge cells could be modulated by GABAergic cerebrospinal fluid contacting neurons (CSF-cNs) [94]. Similar CSF-cNs, called "Kolmer-Agduhr" cells, have been described in the zebrafish and were able to modulate slow swimming upon optical activation [208]. Another sensory feedback pathway in larvae and adult zebrafish is the lateral line system [72]. Mechanosensory hair cells in the lateral line neuromasts provide information about the water flow, contributing to orientating the fish against the water, a behavior called "rheotaxis" [154] (Fig. 8.3c).

8.2.2 Intrinsic Spinal Sensorimotor Circuitry

8.2.2.1 Sensorimotor Interneuronal Networks

Presynaptic Inhibition As we have seen, spinal circuits are continuously provided with multiple ascending sensory inputs from various sources. This sensory feedback needs to be controlled to allow for the proper execution of a motor task [108]. One way to control this sensory input is through presynaptic inhibition of muscle afferents on alpha-motoneurons through GABAergic axo-axonal synapses [178] (Fig. 8.2b). A similar control can be achieved through primary afferent depolarization (PAD), and the two phenomena are now actually considered to be mediated by the same interneurons [95].

Initially described in relation to group Ia afferents from primary endings of muscle spindles [64], presynaptic inhibition through GABAergic interneurons has more recently also been described for group Ib and group II muscle afferents, as well as cutaneous and articular afferents [177]. Although it has traditionally been thought that different subgroups of interneurons mediate PAD of distinct muscle sensory afferents [95], it has also been demonstrated that the same interneurons, located within Rexed's laminae VI–VII of the spinal cord grey matter (*intermediate zone)*, could be coexcited by group Ia and group Ib afferents [62]. More surprisingly, even group Ib and group II inputs can be integrated by a common pool of interneurons, located within laminae V–VII [14]. These results led some authors to consider that all those subpopulations of interneurons (groups Ia, Ib and II) may actually operate as a single functional population with multisensory inputs from both several types of afferents and several muscles [96]. (Fig. 8.2b)

Reciprocal Ia Inhibition Considering that the same Ia muscle afferents innervate motoneurons belonging to many different motor pools, it has long been postulated that a neural pathway involving Ia afferents allowed for inhibition of alpha-motoneurons controlling antagonist muscles. The reciprocal Ia inhibition is mediated by a single glycinergic inhibitory interneuron activated by Ia afferents from a given flexor muscle, which in turn inhibits alpha-motoneurons controlling the antagonistic extensor muscle [58, 95]. As for PAD interneurons, it has later been showed that these reciprocal Ia inhibitory interneurons, located dorsomedially to the motor

nuclei in the ventral horn, actually also receive convergent inputs, both excitatory and inhibitory, from multiple descending and ascending sources, including Renshaw cells (see below) [92] (Fig. 8.2b).

Nonreciprocal Ib Inhibition Group Ib sensory afferents from Golgi tendon organs inhibit motoneurons projecting to synergist muscles and facilitate motoneurons projecting to antagonist muscles through di- or tri-synaptic pathways involving respectively one or two inhibitory glycinergic interneurons [57, 95]. As for Ia interneurons mediating reciprocal inhibition, Ib inhibitory interneurons exhibit a wide convergence of inputs from both descending inputs (excitatory corticospinal, rubrospinal, and inhibitory reticulospinal afferents) and ascending inputs (excitatory group Ia and Ib muscle afferents, as well as cutaneous and joint afferents) [92] (Fig. 8.2b).

Recurrent Inhibition Lastly, another sensorimotor interneuronal pathway involving an inhibitory interneuron is the one formed by Renshaw cells, located in the ventral horn (next to Ia reciprocal inhibitory interneurons) [166]. Renshaw cells are excited by cholinergic axonal collaterals from alpha-motoneurons and provide glycinergic recurrent inhibition to the same or synergistic muscles [56]. Again, as for other sensorimotor interneurons, Renshaw cells also receive inputs from other afferents, including ipsilateral group II and III muscle afferents, cutaneous afferents, and descending motor afferents, and project themselves not only to alpha-motoneurons but also to gamma-motoneurons, Ia reciprocal inhibitory interneurons, and other Renshaw cells within the same spinal segment [206].

8.2.2.2 Spinal Central Pattern Generator (CPG) Across Vertebrates

Along with this complex interplay between sensory afferents and sensorimotor interneuronal networks, a large amount of work has converged toward the identification of a spinal network able to generate the elementary patterns and rhythms of locomotion: the spinal CPG. First postulated from studies of decerebrated cats more than a century ago [29], extensive research in nonmammalian vertebrate species such as the lamprey [80] and the *Xenopus* tadpole [169] has provided many insights into the swimming CPG and its cellular mechanisms, leading to rapid advances in the understanding of the mammalian walking CPG [102].

Homology Across Vertebrates Interestingly, new insights into the genetic profiles of spinal interneurons have allowed direct comparison between different classes of interneurons across all vertebrates [76]. Based on the dynamic expression pattern of transcription factors, five major subclasses of spinal ventral interneurons have been described, called “V0, V1, V2, V3, and Hb9 interneurons” (Fig. 8.3). Each class being characterized by a specific transcription factor, such as “molecular code” opens the way for functional investigation of genetically targeted, rather than morphologically or electrophysiologically identified, spinal interneurons within the CPG (Fig. 8.3b).

Excitatory Rhythm-Generating Circuits Several lines of evidence suggest that the rhythmogenic neurons of the CPG are glutamatergic excitatory neurons projecting

ipsilaterally onto inhibitory left–right and flexor–extensor coordinating cells at each spinal segment [104]. Indeed, blocking inhibitory commissural or ipsilateral interneurons does not prevent rhythm generation, whether in the lamprey [35], rodent [22] or cat [100], therefore discarding the "half-center model" for CPG rhythm generation [102]. Various putative candidates for the role of "pacemakers" neurons have been recently investigated [103]. Among them, Hb9 [199] and V2a-Chx10 expressing interneurons [88] have been shown to have rhythmogenic properties in neonatal mouse models. Morphological homologs in the lamprey [80] and tadpole [123], and molecular homologs in zebrafish [139] support the hypothesis of a glutamatergic ipsilateral drive to the spinal CPG.

Flexor–Extensor Coordination Ipsilateral-projecting glycinergic inhibitory interneurons are known to be involved in alternation of extensor and flexor muscles activation, since flexor–extensor coordination is suppressed when glycinergic transmission is blocked but can persist in hemisected spinal preparations [22]. Putative candidate interneurons include Ia inhibitory interneurons and Renshaw cells (see Sect. 2.2.1), as both have been shown to fire rhythmically during locomotion and in opposing phases with respect to their flexor/extensor afferents [138].

However, a recent study challenged this assumption [74]. V1-derived interneurons expressing the transcription factor *Engrailed-1* (En1) are inhibitory ipsilaterally projecting interneurons that give rise to Renshaw cells and Ia inhibitory interneurons. Genetic knockout of En1-expressing neurons induced slower locomotor activity and increased step cycle, but did not suppress flexor–extensor coordination. This suggests the existence of other ipsilateral inhibitory interneurons, which might be specific to mammalian locomotor CPG [102].

Left–Right Coordination Coordination of left–right activity during locomotion is mainly achieved through commissural interneurons that cross the midline via the ventral commissure [102]. Experiments in mice have revealed a dual system for left/right coordination: (1) during alternative walking, inhibition of contralateral motoneurons is achieved either through mixed glycinergic and GABAergic inhibitory commissural interneurons that project monosynaptically to contralateral motoneurons, or excitatory commissural interneurons that project onto contralateral inhibitory premotor interneurons; (2) during synchronous "hopping," contralateral motoneurons are excited by glutamatergic commissural interneurons [165].

Candidate commissural interneurons for this dual model are derived from Dbx1 positive cells from the V0 transcription domain [115], in which about one-third of commissural interneurons are glutamatergic (Evx-1-positive, $V0_V$ interneurons) and two-thirds are inhibitory (Evx1-negative, $V0_D$ interneurons) [143]. A recent study [198] confirmed and further refined this hypothesis by showing that V0-ablated mice exhibited a hopping gait at all frequencies. Selective ablation of inhibitory V0 interneurons ($V0_D$) led to a lack of left–right alternation only at low frequencies, whereas selective ablation of excitatory V0 interneurons ($V0_V$) led to similar hopping gait but only at medium and high frequencies.

Neurons participating in the left–right alternation spinal network have also been identified in nonmammalian vertebrates. In the *Xenopus* tadpole, inhibitory gly-

cinergic commissural interneurons are responsible for mid-cycle reciprocal inhibition and are driven by descending glutamatergic interneurons [169]. In the lamprey, both inhibitory and excitatory commissural interneurons have been described with a left–right alternating pattern of activity [80]. Lastly, similar glycinergic inhibitory and glutamatergic excitatory commissural interneurons have been identified in the zebrafish, sharing molecular markers with the mouse V0 neurons, although the details of their network functions have not yet been worked out [61].

8.2.3 Dynamic Spinal Sensorimotor Interactions

8.2.3.1 Modulation of Spinal Circuitry from Extrinsic Inputs

Both descending motor inputs and ascending sensory feedback can modulate the activity of the spinal CPG. Dynamic sensorimotor interactions with both supraspinal and peripheral inputs continuously modulate CPG-generated activity patterns to achieve a flexible adaptation to the environment. Such interactions take place in a phase-dependent (swing/stance) and state-dependent (forward/backward) manner, such that extrinsic inputs will result in different modulations depending on the ongoing phase of the locomotor cycle [176].

As discussed in Sect. 2.1.1, supraspinal pathways, such as the MLR and its projections through the reticulospinal tract, can induce locomotion in "fictive preparations" such as isolated spinal cord or decerebrated adult cat. However, descending pathways, whether carrying sensory or motor information, can also modulate ongoing locomotion. This can be achieved either though modulation of brainstem command circuitry or through the direct modulation of spinal circuitry [137].

Vestibular inputs (relaying information about balance and posture) phasically modulate the activity of reticulospinal neurons during fictive locomotion in lampreys, thereby avoiding a counteractive drive from reticulospinal neurons during ongoing locomotion [34]. A recent study in zebrafish larvae suggested that vestibular inputs are able to differentially recruit dorsal and ventral premotor spinal microcircuits during postural correction, possibly prefiguring the mammalian modular organization of spinal flexor/extensor microcircuits [13]. The influence of visual feedback on the control of locomotion can be experienced on a daily basis when one needs to anticipate and adjust his gait to avoid an obstacle [173]. New experimental paradigms, such as the optomotor response in zebrafish [155], have started to shed light on the neural circuitry responsible for visually induced locomotion.

Besides descending inputs, ascending sensory feedback, from either proprioceptive or cutaneous inputs, can also modulate the activity of the spinal CPG. Cutaneous inputs (C and A fibers, see Sect. 2.1.2) are mainly involved in correcting the steps in response to external perturbations, such as an uneven floor, during the different phases of the step cycle [137, 176]. Interestingly, the same cutaneous stimulus can lead to responses in flexor or extensor muscles depending on the initial position of the limb, thereby exciting a given muscle group in one locomotor phase, and the antagonist muscles in the opposite phase, a phenomenon termed "reversal" [175].

Proprioceptive feedback also has an important role in modulating ongoing locomotion, in particular by adjusting the duration of, and facilitating the switch between, the different phases of the step cycle, therefore setting the frequency of locomotion [176]. In decerebrate cat preparations, stimulation of group Ib afferents from the Golgi tendon organs of extensor muscles can reset the locomotor cycle by abruptly terminating the ongoing fictive flexor activity and initiating a new burst in the extensor recording [40]. Similarly, stretch-evoked Ia inputs can increase the duration of the stance phase, but only when stimulated during flexor activity [84].

In all, patterns of fictive locomotion produced by the spinal CPG should not be considered the fixed output of a hard-wired circuit, but should be viewed rather as a dynamic multimodal process whose output is dramatically modulated by sensory experience.

8.2.3.2 Implications for Plasticity After Spinal Cord Injury

The emerging concept that intrinsic spinal circuits can produce adaptive locomotion through modulation by sensory feedback, and do so independently, at least to some extent, from supraspinal inputs, bears important consequences for new neurorehabilitative strategies after spinal cord injury.

Experimental paradigms with adult cats walking on a treadmill have demonstrated that neither bilateral lesion of the dorsolateral spinal cord (interrupting cortico- and rubrospinal tracts) [97] nor bilateral lesion of the ventrolateral spinal cord (interrupting vestibulo- and reticulospinal tracts) [30] could permanently suppress quadrupedal locomotion. However, after unilateral complete hemisection at the lower thoracic (T13) level, interrupting both dorsal and ventral descending pathways, cats showed a complete paralysis of the ipsilateral hindlimb during the first 3 days, followed by a progressive recovery over the following 3 weeks [174]. Interestingly, this recovery was accompanied by a modification of the step cycle, forelimb/hindlimb, and left/right coordination [135]. These results suggest that the intrinsic spinal circuitry is able to produce locomotion even after removal of all supraspinal inputs and that this recovery is underpinned by extensive reorganization of the spinal sensorimotor network [134]. They also suggest that treadmill-induced locomotor training, by providing sensory feedback, is crucial to drive the reorganization of spinal circuits [174].

To test this hypothesis of a plastic spinal CPG, Rossignol et al. designed a dual-lesion paradigm in which a first hemisection performed at the T10/T11 spinal level is followed, after several weeks of locomotor training and complete recovery, by a complete spinal transection at the T13 level [15, 134]. The major finding was that cats regained full locomotor performance after only 24 h, without any training of pharmacological intervention [15], therefore indicating that intrinsic changes within the spinal CPG had indeed occurred during the rehabilitation period, and could be retained after the complete removal of supraspinal inputs.

Similar results have been obtained recently in rodents [59], in which recovery of coordinated hindlimbs locomotion on a treadmill could be achieved only 1 week

after complete thoracic (T7) spinal transection when combined lumbosacral electrical epidural stimulation (EES) and systemic application of serotoninergic agonists were applied [41]. Interestingly, removing peripheral sensory inputs by unilateral dorsal rhizotomy prevented EES-facilitated locomotor recovery after complete spinal transection, but only on the deafferented side, thereby confirming the hypothesis that sensory feedback drives the reorganization of intrinsic spinal circuitry [117].

However, those results only concerned treadmill-induced "automatic" locomotion. To what extent can we exploit the plasticity of spinal sensorimotor circuits to induce restoration of voluntary locomotion? This question was investigated by a recent study [25], in which the authors used a simultaneous dual hemisection paradigm in adult rats together with a so-called electrochemical neuroprosthesis (i.e., the combination of lumbosacral epidural electrical stimulation together with systematic administration of a cocktail of monoaminergic agonists). They observed that rats trained with a robotic postural interface encouraging supraspinally mediated locomotion could regain voluntary control through remodeling of corticospinal projections. A similar approach has even been used successfully in a paraplegic human subject, who could regain some voluntary control of one of his lower extremities after intensive rehabilitation and electrical epidural stimulation, although this recovery was very limited and observed in few individuals [7, 86].

These results have raised hopes that clinically significant locomotor recovery can be achieved through reorganization of intrinsic sensorimotor circuitry, facilitated by intensive training and electrical and/or chemical manipulation. However, one major issue of such studies is that they can probe changes in spinal circuitry only in a very indirect manner.

Indeed, until now, one had to choose whether to access spinal circuitry in open-loop "fictive" preparations, discarding sensory feedback in favor of identifying and recording from neurons within the spinal cord, or to preserve active locomotion and sensory feedback at the cost of having only limited and indirect access to spinal circuits. New tools and animal models might change this conundrum in a near future.

8.3 Closing the Loop? Optogenetic Manipulation of Spinal Sensorimotor Circuits in Zebrafish

8.3.1 Genetic Targeting of Spinal Sensorimotor Circuits in Zebrafish

8.3.1.1 Identified Sensorimotor Neurons in the Zebrafish Spinal Cord

"Closing the loop" in sensorimotor studies should involve the ability to easily target neuronal populations of interest and monitoring their activity *in vivo* while the sensorimotor integration actually occurs. Over the last 10 years, zebrafish has become an increasingly popular model organism for such studies, thanks to its genetic accessibility with numerous transgenic lines targeting specific subsets of

neurons being shared among the community [180, 187], its optical transparency allowing the use of the always expanding palette of optogenetic actuators and reporters [2, 51, 90, 208], and its relatively simple and stereotyped behavioral repertoire [31, 139, 141].

As in other vertebrates, neurons in the zebrafish spinal cord can be broadly classified as motoneurons, sensory neurons, and interneurons [119]. The recent development of genetic tools allowing specific targeting of subtypes of neurons has allowed marked progress in our understanding of their functional roles, and has led to a refined classification.

Sensory neurons within the spinal cord comprised mainly mechanosensitive Rohon-Beard cells, of which homologs can be found in most anamniotic vertebrates, such as *Xenopus* tadpoles and lampreys [167]. Rohon-Beard neurons are derived from the same neural plate domain that generates neural crest cells, and die during development to be replaced by dorsal root ganglion cells in adult zebrafish [119]. When stimulated optically, Rohon-Beard neurons are able to trigger escape responses [51, 208], through either direct excitation of reticulospinal cells [51] or activation of CoPA interneurons [159].

In larvae, both primary and secondary motoneurons (together with oligodendrocytes) are derived from the pMN transcription domain in the ventral spinal cord, are positive for *olig2* expression, and persist through adulthood [105, 119]. Primary motoneurons are located more dorsally (with subtypes according to their position from caudal to rostral: CaP, MiP, RoP), innervate fast muscles, and mediate fast swimming and the startle response, while secondary motoneurons are located more ventrally, innervate both slow and fast muscles, and are involved in slow swimming [119].

To explore the differences between slow swimming and escape spinal networks, Ritter et al. [168] used a head-embedded preparation in which they could elicit either slow swim by illuminating the head with a fiber optic, or escapes by tapping the head with a piezoelectric actuator. They simultaneously monitored the activity of morphologically identified interneurons in the embedded part of the tail using calcium imaging and recorded the movements of the caudal tail using a high-speed camera. They showed that "circumferential ipsilateral descending" (CiDs) interneurons were activated during escapes but not during slow swim movements, while excitatory glutamatergic "multipolar commissural and descending" (MCoDs) interneurons were, on the contrary, activated during swimming but not during escapes [168].

A subsequent study from the same group [18] combining calcium imaging and paired patch recording confirmed that CiDs were responsible for motoneuron excitation during escapes and showed that stronger escapes elicited by a head tap were associated with the recruitment of a larger number of CiDs than delayed escapes elicited by a tail tap, although the effect of the descending control from the hindbrain seems subject of debate [18, 126]. Interestingly, the same authors also demonstrated that reinnervation of CiDs by regenerating Mauthner axon, following injection of cAMP, was associated with improved locomotor performances [17].

Using isolated spinal cord from larval zebrafish, a "topographic map" of recruitment for motoneurons and premotor interneurons has been documented [139, 140].

MCoDs interneurons, located in the ventral spinal cord, provide a phasic drive to a subset of ventral contralateral motoneurons during slow swimming patterns. When the swimming frequency was increased, MCoDs were inhibited through glycinergic synapses, while CiDs interneurons became progressively activated along a dorsoventral gradient [140]. Of interest is the fact that CiDs interneurons are the fish homologs of the mouse V2a interneurons [5, 13, 106, 107] (see Sect. 2.2.2).

It has also been shown in adult zebrafish that different motoneuron pools exhibit different patterns of recruitment, with slow, intermediate, and fast secondary motoneurons being recruited progressively as the fictive locomotion frequency increased, while fast primary motoneurons were recruited only during presumed escapes. Moreover, the distribution of these different motoneurons pools also followed a ventro-dorsal gradient, from slow secondary motoneurons to fast primary motoneurons [5, 68].

Apart from premotor interneurons, other populations of interneurons are also rhythmically activated during fictive locomotion. Glycinergic "circumferential ascending (CiA) interneurons," that are *Engrailed-1* positive interneurons derived from the V0 transcription domain, monosynaptically inhibit "commissural primary ascending" (CoPA) interneurons during swimming [91]. Remarkably, CoPA interneurons are glutamatergic and relay excitation from Rohon-Beard sensory neurons, providing a connectivity pattern that would be consistent with a homologous sensorimotor gating pathway to that observed in the *Xenopus* tadpole [120, 121].

"Commissural local" (CoLo) interneurons are inhibitory glycinergic interneurons driven by gap junctional inputs from reticulospinal cells (Mauthner cells, see Sect. 3.3) that have been shown to exert monosynaptic inhibition on contralateral primary motoneurons during fast swimming, thereby enhancing the efficiency of the escape responses [180]. Lastly, Kolmer-Agduhr interneurons, which are GABAergic cells located next to the central canal and have cilia extending into the cerebrospinal fluid, have been shown to trigger slow swimming when optically stimulated [208].

Many other subtypes of spinal interneurons have been identified and classified, mainly according to their morphology and neurotransmitter phenotype [85, 181], but their involvement in sensorimotor circuits remains to be elucidated.

8.3.1.2 A Genetic Toolbox for Targeting Populations of Neurons

Considering the large number of cells involved in spinal sensorimotor circuits, even in a simple vertebrate such as the zebrafish, one crucial requirement for investigating their functional roles is to be able to specifically target the neural subpopulation of interest. Rather than relying on morphological cues, identification of specific promoters and new tools to efficiently generate and screen transgenic lines has recently allowed researchers to take full advantage of the optical and genetic accessibility of the zebrafish model.

The most straightforward approach to target a given neuronal population is to identify a specific gene with selective expression in the population of interest and generate a bacterial artificial chromosome (BAC) incorporating a reporter such as

green fluorescent protein (GFP) into the gene's genomic locus. Alternatively, if a minimal enhancer sequence can be identified, it can be subcloned into a smaller, plasmid-based expression system. The engineered construct is then microinjected into embryos at the single-cell stage to allow integration into the genome. Injected fish larvae are subsequently raised to adulthood and their offspring screened for fluorescence in order to establish the transgenic line [11]. Such an approach has been successfully used to produce transgenic lines labeling cranial motoneurons or trigeminal/Rohon-Beard sensory neurons with the *Islet-1* promoter [89]. Animals that transiently expressed channelrhodopsin-2 were also used to investigate the role of Rohon-Beard and trigeminal neurons in the sensorimotor escape circuitry [51].

This approach can be combined with the bipartite Gal4/UAS system, widely used in *drosophila*, which relies on the specific expression of the yeast Gal4 transcriptional activator to drive the expression of a reporter gene placed under the control of repetitive Gal4-responsive upstream activator sequences (UAS) [9, 44]. Enhanced reporter expression can be obtained using Gal4-VP16 [112] or Gal4FF [9] fusion sequences and multiple (14X) repeats of the UAS. Stable zebrafish transgenic lines using the Gal4/UAS system have been created using *Tol2*-mediated transposition. A plasmid carrying the *Tol2* transposon is injected in zebrafish embryos along with the *Tol2* transposase mRNA, generating insertions throughout the zebrafish genome [10, 101]. *Tol2*-mediated Gal4-UAS transgenesis has been used to successfully perform enhancer-trap screens, leading to identification of a large number of stable transgenic lines selectively labeling subsets of spinal neurons [1, 9, 181, 187].

Another recent approach for genetic targeting of neurons in zebrafish is to combine viral gene delivery, using for instance rabies of sindbis viruses, together with the Tet system [214]. The Tet system works in a similar fashion to the Gal4/UAS system, with the transactivator (itTA) binding to the tTA-responder element (Ptet) to drive transcription of the downstream gene [75]. However, the Tet system has the advantage of being regulated by exogenously administered doxycycline, which binds to tTA and dramatically reduces its affinity to Ptet, turning off the expression of the gene of interest [214]. Interestingly, such silencing can also be used to generate sparse labeling in pan-neuronal *HuC* transgenic lines [214]. Combing the Tet and Gal4 systems provide exciting opportunities for combinatorial gene targeting of several neuronal populations of interest in zebrafish.

8.3.2 Optogenetic Tools for Monitoring and Breaking Neural Circuits

8.3.2.1 Reporters: Monitoring Neural Circuits

Monitoring neural activity can be indirectly achieved by measuring the intracellular calcium levels, since action potentials typically lead to a calcium influx through voltage dependent calcium channels [79]. This strategy has led to the elaboration of a number of chemical and genetically encoded calcium indicators (GECIs) that have been successfully used in many different animal models [149, 201] (Fig. 8.4a).

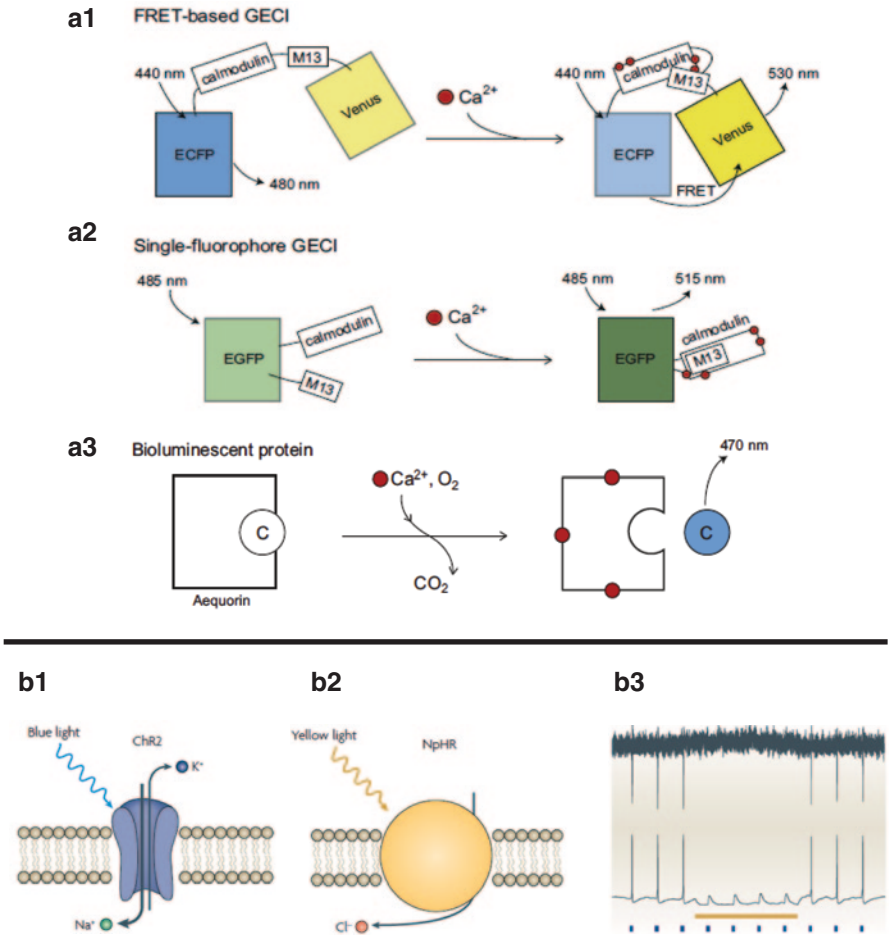

Fig. 8.4 Monitoring and manipulating neural circuits with genetically encoded reporters and actuators. A. Calcium indicators. Genetically encoded calcium indicators (GECIs) allows for monitoring neural activity through changes in intracellular calcium concentration. In a Förster resonance energy transfer (FRET)-based GECI (A1), such as *Cameleon,* a conformational change occurs after calcium ions binding between the two fluorescent proteins, leading to FRET, with a decrease in the 480 nm fluorescence and an increase in the 530 nm fluorescence. In a single-fluorophore GECI (A2), such as *GCaMP,* conformational modification upon calcium binding is intra-molecular, leading to an increase in the emitted fluorescence (515 nm). Bioluminescent GECIs, such as Aequorin, binding of calcium ions leads to oxidation of coelenterazine. Chemi-luminescence resonance energy transfer (CRET) between aequorin and GFP is responsible for the emission of a green photon. *Adapted from Grienberger et al., 2012.* **B.** Optogenetic actuators. Following illumination with blue light (470 nm, *blue* pulses in B3), channelrhodopsin-2 allows the entry of cations into the cell (B1), triggering action potentials in whole-cell current-clamp (B3). Following illumination with yellow light (580 nm, *yellow* line in B3), halorhodopsin pumps chloride anions in the cell (B2), leading to hyperpolarisation and silencing of neuronal activity (B3). *Adapted from Zhang et al. 2007*.

GECIs consist of engineered fluorescent proteins having two key features: their emission properties are modified depending upon the intracellular level of calcium, and their pattern of expression can be restricted genetically. They include either permutated single fluorescent proteins whose fluorescence properties are modified when calcium is bound to an attached Ca^{2+} recognition element—as with the GCaMP family of indicators [147]—or pairs of fluorescent proteins in which conformational changes induced by calcium binding lead to FRET (Förster Resonance Energy Transfer)-mediated modulation of fluorescence [142].

The transparency of the zebrafish larva and its genetic accessibility make it an ideal model to use such optical tools for monitoring neural activity. In the first zebrafish study using a GECI (*cameleon*), expressed under the *islet-1* promoter [89] (see Sect. 3.1.2), calcium transients could be observed within the spinal cord, in Rohon-Beard neurons activated by electrical cutaneous stimulation, and in motoneurons and CiD interneurons during escapes triggered by a mechanical head tap [90]. Since this first study, GECIs have been extensively used in zebrafish to monitor neural activity in various behavioral paradigms, including investigating the role of the optic tectum in prey capture [46], performing brain-wide monitoring of neural dynamics in a sensorimotor virtual environment [2] or testing neural coding of odors by the olfactory bulb [21]. Targeted mutagenesis and high-throughput screening have led to the continuous improvement of GECIs by optimizing their calcium affinity, kinetics, and dynamic range [3, 146, 149, 201]. From the first GCaMP [149] to the current GCaMP6 [38], and including the new generation of multicolor variants [4], the always improving GECI arsenal allows one to monitoring of neural activity under a wide range of conditions.

One major limitation of GECIs with particular relevance to the investigation of closed-loop sensorimotor behaviors *in vivo* is the need to provide focal excitation to the fluorescent proteins. This limitation implies constraining the neurons of interest (and therefore the animal itself) to a given location, either by partially embedding and/or paralyzing the animal. One alternative approach is to use the bioluminescent protein *aequorin-GFP*, derived from the jellyfish *Aequorea victoria* [192]. ApoAequorin, the naturally occurring complex of aequorin with GFP, binds to its substrate coelenterazine, which is then oxidized in the presence of calcium leading to the emission of a green photon by the GFP through chemiluminescence resonance energy transfer (CRET) [16]. Bioluminescence assays based on aequorin-GFP have been used not only for noninvasive monitoring of neural activity in vitro [170], but also in restrained flies [133] and freely behaving mice [171].

Taking advantage of this bioluminescence approach, neural activity in freely behaving zebrafish larvae has been monitored by genetically targeting the expression of aequorin-GFP to a specific subset of neurons and simultaneously counting the number of photons emitted over time while imaging locomotor activity [151]. Remarkably, the authors could monitor the activity of a small group of hypocretin-positive neurons in the hypothalamus over several days or combine a gated photomultiplier tube with stroboscopic illumination to record visually evoked behaviors [151]. While aequorin allows for noninvasive monitoring of an entire population of neurons in a moving animal, it does not provide any spatial information, thus making the specificity of genetic targeting a crucial limitation.

8.3.2.2 Actuators: Breaking Neural Circuits

Besides monitoring neural activity, the optical and genetic accessibility of the zebrafish larva also constitute an optimal playground for optogenetic actuators, making it possible to selectively activate or inhibit genetically targeted neurons [45, 162, 212] (Fig. 8.4b). Channelrhodopsin-2 (ChR2) is a light-gated channel derived from the unicellular alga *Chlamydomonas reinhardtii* that allows nonspecific influx of cations when illuminated with blue light [122, 148]. ChR2 can therefore be used to control a genetically targeted neuronal population with millisecond precision in a dynamic and reversible manner [24]. First tested in zebrafish to trigger escape responses by photoactivating Rohon-Beard neurons [51], ChR2 has subsequently been used to investigate diverse behaviors such as the optokinetic response [184] and modulation of odor responses [33]. Synthetic excitatory actuators that combine a chemical ligand with an ion channel, such as the light-gated ionotropic glutamate receptor (LiGluR, [73, 196]) and the light-gated metabotropic glutamate receptor (LimGluR2, [118]), have been successfully used to trigger neural activity in zebrafish. For instance, the potential role of Kolmer-Agduhr interneurons in modulating slow locomotion was investigated by combining LiGluR activation and Gal4/UAS enhancer-trap transgenics [208].

Optogenetics has also been used to selectively silence genetically targeted neurons in zebrafish, using the light-gated chloride pump halorhodopsin (NpHR), derived from the archaebacterium *Natronomonas pharaonis* [182, 194]. NpHR hyperpolarizes neurons by pumping chloride ions upon activation with yellow light, leading to optical silencing. Optical silencing with NpHR, and its improved variant eNpHR [77], can be combined with ChR2-mediated photoactivation to provide a versatile optogenetic toolbox to dissect circuits within the same animal [213].

Such a combined strategy has been successfully used in zebrafish to identify neurons in the hindbrain able to initiate locomotion through a rebound activity after eNpHR silencing [8], and for dissecting the mechanism of eye saccades during the optokinetic response [184]. In those two studies, light was delivered using optical fibers to achieve a high spatial selectivity in photoactivation. However, new microscopic techniques relying on light patterning with multimirror devices [21, 132] or temporal focusing of two-photon excitation [158] should allow for more complex 2D stimulation patterns. Lastly, 3D optical stimulation with a high spatiotemporal resolution could be achieved by combining digital holography and temporal focusing [156], opening the way for simultaneous imaging and neural manipulation in multiple planes *in vivo* [162].

8.3.3 The Escape Response as a Model for Sensorimotor Integration

8.3.3.1 The Escape Response and its Supraspinal Control

The “escape response” is a stereotyped sensorimotor behavior whereby an animal aims to avoid an approaching predator, which has been extensively described not only in many teleost fish species, including the goldfish and zebrafish [53], but also

in other anamniotic vertebrates such as the lamprey [43] and the *Xenopus* tadpole [169]. Escape responses in zebrafish can be elicited by several types of sensory stimuli, such as touch to the head or the tail [18], a water jet to the otic vesicle [110] or an auditory-vestibular stimulus produced by a sound vibration [180]. In zebrafish larvae aged 6–9 days post-fertilization (dpf), the escape behavior typically consists of an initial, fast "C-shaped" bend, followed by a counter-bend in the opposite direction, and lastly a burst swim [31]. Typical kinematics parameters for escapes in zebrafish larvae are a mean angular velocity of 21.2°/ms, a mean duration until completion of the first bend of 10.4 ms, and a mean counter-bend angle of 125.1 [31].

The roles played by reticulospinal neurons, and in particular the "Mauthner cell" (M-cell), in the initiation of escape responses have been extensively documented, initially in the goldfish [54, 111]. The M-cell and its homologs MiD2 cm and MiD3 cm are paired reticulospinal neurons, located respectively in hindbrain rhombomeres 4 and 6, sending their descending axons to the contralateral spinal cord. The M-cells receive excitatory inputs from the auditory and vestibular branches of the VIIIth nerve, the posterior lateral line, and the optic tectum [150].

In head-embedded zebrafish larvae, monitoring of neural activity in reticulospinal cells by calcium imaging has demonstrated that, while M-cells are activated by mechanical stimulation of both the head and tail, its homologs MiD2 cm and MiD3 cm are only activated by head taps [153]. Ablation studies confirmed this result, showing that destruction of all three cell types delayed the escape responses elicited by both head and tail stimulation, while ablation of the M-cell alone specifically increased the latency of tail-induced escapes [126]. These results demonstrate significant functional overlap among the neurons that drive escape behavior.

Recent studies by the group of Oda [109, 110, 150] further refined our understanding of the descending control of this multimodal sensorimotor behavior. Using simultaneous calcium imaging of reticulospinal neurons and high-speed video recording of actual escapes elicited by a water jet to the otic vesicle, the authors demonstrated that activation of the Mauthner cell led to fast-onset (4–8 ms) escapes while activity in the MiD3 cm homolog gave rise to delayed escapes (8–12 ms), and that activation of these cells was mutually exclusive [109]. The authors subsequently showed that (1) before 75 h post-fertilization (hpf), suppression of auditory-vestibular inputs by selective ablation of the otic vesicle did not increase escape latency, whereas ablating the trigeminal ganglia responsible for relaying tactile input did; (2) after 90 hpf, eliminating auditory-vestibular inputs increased escape latency, whereas suppressing tactile input did not. These results therefore suggest a dual control of the escape behavior, switching during development from a preferentially touch-driven, long-latency, M-independent escape to a preferentially auditory-vestibular driven, short-latency, M-dependent pathway [110].

8.3.3.2 Monitoring Spinal Neurons During Active Locomotion

The ability to simultaneously record active locomotor behavior and monitor neural activity in partially restrained zebrafish has proven very valuable in dissecting the descending motor and sensory control of escape responses. Similar head-embed-

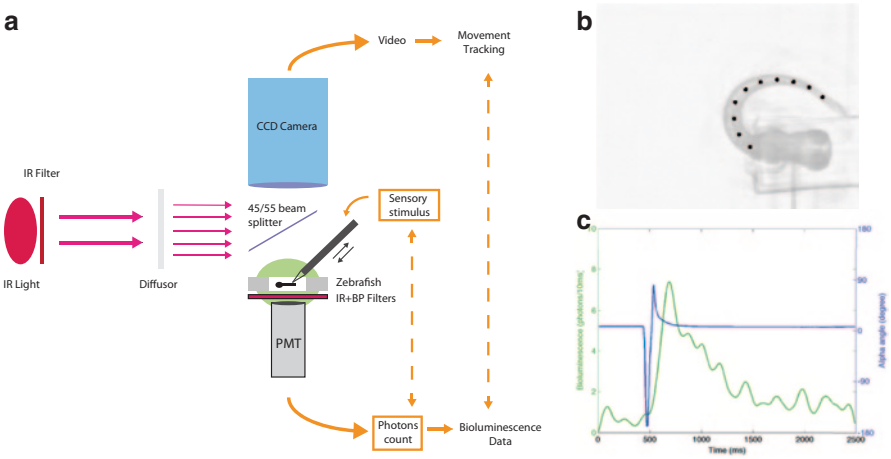

Fig. 8.5 Monitoring the activity of spinal neurons during active escape responses in zebrafish larva. A. A setup for simultaneously recording active locomotion using a high-speed camera. **B.** A custom tracking software detects the animal body movement while a PMT is counting photons emitted by spinal motoneurons during escape responses in the transgenic line s1020t:gal4/UAS:GFP-Aequorin. C. Signals of bioluminescence and tail angle are plotted simultaneously: in blue: tail angle (in degree) between the first and last points of the tail over time, superimposed with the bioluminescent signal in green (number of photons emitted /10 ms).

ded experimental paradigms have also been used to investigate the recruitment of spinal interneurons during active locomotion [18, 168] (see Sect. 3.1.1). Although studies based on calcium imaging of either hindbrain or spinal neurons in partially restrained animals have been an important step forward in the study of sensorimotor behaviors such as the escape response, they cannot provide information about neural activity in the moving tail of the fish and so fail to account for sensory feedback arising from locomotion itself.

New techniques such as aequorin-based bioluminescence recording (see Sect. 8.3.2.1) will allow monitoring of specific neurons in actively moving animals, whether head-restrained or freely swimming. Using an experimental setup adapted from Naumann et al. [151] in which escape responses are elicited in head-embedded zebrafish larvae either by a water jet to the otic vesicle or by an auditory-vestibular sound stimulus, we can simultaneously record detailed kinematic parameters and count photons emitted by the aequorin-GFP. Taking advantage of the Gal4/UAS system to restrict the expression of aequorin-GFP to motoneurons, we obtain bioluminescence signals that report the recruitment of spinal motoneurons (Fig. 8.5, Knafo et al. *unpublished*) during behavior. This approach could prove particularly useful in investigating the recruitment of sensory spinal neurons during active locomotion and determining how sensory feedback from the moving part of the tail modulates the recruitment of motoneurons.

8.4 Conclusion

The ability to monitor active behaviors *in vivo* with precise kinematics also provides a new framework in which results obtained from fictive recordings could be validated to confirm their environmental relevance. Moreover, the variability observed in real-world locomotor behaviors also questions whether "hard-wired" connectivity diagrams are actually the most suitable mean of modeling sensorimotor integration [131]. The emergence of multifunctional neuronal populations, that is. neurons that are recruited during multiple behaviors [124], as opposed to specialized neurons that are only active for a given motor output [180], will also benefit from *in vivo* studies involving active locomotion, in which multiple behaviors can be tested within the same animal [27].

The advances in genetic targeting and the identification of molecular markers to classify homologous populations of spinal neurons have allowed bringing together results obtained across animal models. However, the extent to which the walking CPG of mammalian vertebrates (such as rodents and cats) and the swimming CPG of nonmammalian vertebrates (such lampreys, zebrafish or tadpoles) can mutually inform each other remains unclear. In this regard, amphibian metamorphosis, during which the swimming CPG of a tadpole is transformed into a frog walking CPG, could provide an intriguing and unique model [193].

Sensorimotor behaviors are inherently a closed-loop process, where sensory feedback heavily influences the motor output. Although spinal networks do integrate this sensory information to modulate locomotion, detailed access to spinal sensorimotor circuitry has so far been only possible in open-loop preparations, where sensory feedback was not taken into account. New tools, such as optogenetic reporters and actuators, combined with genetically accessible animal models like zebrafish, should provide bright opportunities for monitoring targeted spinal sensorimotor neurons in actively moving animals and, possibly, closing the loop.

References

1. Abe, G., Suster, M. L., & Kawakami, K. (2011). *Tol2-mediated Transgenesis, gene trapping, enhancer trapping, and the Gal4-UAS System*. *Methods in cell biology* (3rd edn., Vol. 104, pp. 23–49). San Diego: Elsevier Inc. doi:10.1016/B978-0-12-374814-0.00002-1.
2. Ahrens, M. B., Li, J. M., Orger, M. B., Robson, D. N., Schier, A. F., Engert, F., et al. (2012). Brain-wide neuronal dynamics during motor adaptation in zebrafish. *Nature, 485*(7399), 471–477. doi:10.1038/nature11057.
3. Akerboom, J., Chen, T. W., Wardill, T. J., Tian, L., Marvin, J. S., Mutlu, S., et al. (2012). Optimization of a GCaMP calcium indicator for neural activity imaging. *The Journal of Neuroscience: The Official Journal of the Society for Neuroscience, 32*(40), 13819–13840. doi:10.1523/JNEUROSCI.2601-12.2012.
4. Akerboom, J., Carreras Calderón, N., Tian, L., Wabnig, S., Prigge, M., Tolö, J., et al. (2013). Genetically encoded calcium indicators for multi-color neural activity imaging and combination with optogenetics. *Frontiers in Molecular Neuroscience, 6,* 2. doi:10.3389/fnmol.2013.00002.

5. Ampatzis, K., Song, J., Ausborn, J., & Manira, El. A. (2013). Pattern of innervation and recruitment of different classes of motoneurons in adult zebrafish. *The Journal of Neuroscience: The Official Journal of the Society for Neuroscience, 33*(26), 10875–10886. doi:10.1523/JNEUROSCI.0896-13.2013.
6. Andersen, R. A., Essick, G. K., & Siegel, R. M. (1985). Encoding of spatial location by posterior parietal neurons. *Science , 230*(4724), 456–458.
7. Angeli, C. A., Edgerton, V. R., Gerasimenko, Y. P., & Harkema, S. J. (2014). Altering spinal cord excitability enables voluntary movements after chronic complete paralysis in humans. *Brain: A Journal of Neurology, 137*(Pt 5), 1394–409. doi:10.1093/brain/awu038.
8. Arrenberg, A. B., Del Bene, F., & Baier, H. (2009). Optical control of zebrafish behavior with halorhodopsin. *Proceedings of the National Academy of Sciences, 106*(42), 17968–17973. doi:10.1073/pnas.0906252106.
9. Asakawa, K., & Kawakami, K. (2009). The Tol2-mediated Gal4-UAS method for gene and enhancer trapping in zebrafish. *Methods, 49*(3), 275–281. doi:10.1016/j.ymeth.2009.01.004.
10. Asakawa, K., Suster, M. L., Mizusawa, K., Nagayoshi, S., Kotani, T., Urasaki, A., et al. (2008). Genetic dissection of neural circuits by Tol2 transposon-mediated Gal4 gene and enhancer trapping in zebrafish. *Proceedings of the National Academy of Sciences of the United States of America, 105*(4), 1255–1260. doi:10.1073/pnas.0704963105.
11. Asakawa, K., Abe, G., & Kawakami, K. (2013). Cellular dissection of the spinal cord motor column by BAC transgenesis and gene trapping in zebrafish. 1–14. doi:10.3389/fncir.2013.00100/abstract.
12. Baek, J.-H., Cosman, P., Feng, Z., Silver, J., & Schafer, W. R. (2002). Using machine vision to analyze and classify *Caenorhabditis elegans* behavioral phenotypes quantitatively. *Journal of Neuroscience Methods, 118*(1), 9–21. doi:10.1016/S0165-0270(02)00117-6.
13. Bagnall, M. W., & McLean, D. L. (2014). Modular organization of axial microcircuits in zebrafish. *Science, 343*(6167), 197–200. doi:10.1126/science.1245629.
14. Bannatyne, B. A., Liu, T. T., Hammar, I., Stecina, K., Jankowska, E., & Maxwell, D. J. (2009). Excitatory and inhibitory intermediate zone interneurons in pathways from feline group I and II afferents: Differences in axonal projections and input. *The Journal of Physiology, 587*(Pt 2), 379–399. doi:10.1113/jphysiol.2008.159129
15. Barrière, G., Leblond, H., Provencher, J., & Rossignol, S. (2008). Prominent role of the spinal central pattern generator in the recovery of locomotion after partial spinal cord injuries. *The Journal of Neuroscience: The Official Journal of the Society for Neuroscience, 28*(15), 3976–3987. doi:10.1523/JNEUROSCI.5692-07.2008.
16. Baubet, V. V., Le Mouellic, H. H., Campbell, A. K. A., Lucas-Meunier, E. E., Fossier, P. P., & Brúlet, P. P. (2000). Chimeric green fluorescent protein-aequorin as bioluminescent Ca^{2+} reporters at the single-cell level. *Proceedings of the National Academy of Sciences of the United States of America, 97*(13), 7260–7265.
17. Bhatt, D. H., Otto, S. J., Depoister, B., & Fetcho, J. R. (2004). Cyclic AMP-induced repair of zebrafish spinal circuits. *Science, 305*(5681), 254–258. doi:10.1126/science.1098439.
18. Bhatt, D. H., Mclean, D. L., Hale, M. E., & Fetcho, J. R. (2007). Grading movement strength by changes in firing intensity versus recruitment of spinal interneurons. *Neuron, 53*(1), 91–102. doi:10.1016/j.neuron.2006.11.011.
19. Bican, O., Minagar, A., & Pruitt, A. A. (2013). The spinal cord: A review of functional neuroanatomy. *Neurologic Clinics, 31*(1), 1–18. doi:10.1016/j.ncl.2012.09.009.
20. Blitz, D. M., & Nusbaum, M. P. (2011). Neural circuit flexibility in a small sensorimotor system. *Current Opinion in Neurobiology, 21*(4), 544–552. doi:10.1016/j.conb.2011.05.019.
21. Blumhagen, F., Zhu, P., Shum, J., Schärer, Y.-P. Z., Yaksi, E., Deisseroth, K., et al. (2012). Neuronal filtering of multiplexed odour representations. *Nature, 479*(7374), 493–498. doi:10.1038/nature10633.
22. Bonnot, A., Whelan, P. J., Mentis, G. Z., & O'Donovan, M. J. (2002). Locomotor-like activity generated by the neonatal mouse spinal cord. *Brain Research Reviews, 40*(1–3), 141–151.
23. Boussaoud, D., Barth, T. M., & Wise, S. P. (1993). Effects of gaze on apparent visual responses of frontal cortex neurons. *Experimental Brain Research (Experimentelle Hirnforschung. Expérimentation Cérébrale), 93*(3), 423–434.

24. Boyden, E. S., Zhang, F., Bamberg, E., Nagel, G., & Deisseroth, K. (2005). Millisecond-timescale, genetically targeted optical control of neural activity. *Nature Neuroscience, 8*(9), 1263–1268. doi:10.1038/nn1525.
25. Brand, R. V. D., Heutschi, J., Barraud, Q., DiGiovanna, J., Bartholdi, K., Huerlimann, M., et al. (2012). Restoring voluntary control of locomotion after paralyzing spinal cord injury. *Science, 336*(6085), 1182–1185. doi:10.1126/science.1217416.
26. Branson, K., Robie, A. A., Bender, J., Perona P., & Dickinson, M. H. (2009). High-throughput ethomics in large groups of *Drosophila*. *Nature Methods, 6*(6), 451–457. doi:10.1038/nmeth.1328.
27. Briggman, K. L., & Kristan, W. B. (2008). Multifunctional pattern-generating circuits. *Annual Review of Neuroscience, 31,* 271–294. doi:10.1146/annurev.neuro.31.060407.125552.
28. Briggman, K. L., Abarbanel, H. D. I., & Kristan, W. B. (2006). From crawling to cognition: Analyzing the dynamical interactions among populations of neurons. *Current Opinion in Neurobiology, 16*(2), 135–144. doi:10.1016/j.conb.2006.03.014.
29. Brown, T. G. (1911). The intrinsic factors in the act of progression in the mammal. *Proceedings of the Royal Society B: Biological Sciences, 84*(572), 308–319. doi:10.1098/rspb.1911.0077.
30. Brustein, E., & Rossignol, S. (1998). Recovery of locomotion after ventral and ventrolateral spinal lesions in the cat. I. Deficits and adaptive mechanisms. *Journal of Neurophysiology, 80*(3), 1245–1267.
31. Budick, S. A., & O'Malley, D. M. (2000). Locomotor repertoire of the larval zebrafish: Swimming, turning and prey capture. *Journal of Experimental Biology, 203*(17), 2565–2579.
32. Budick, S. A., & Dickinson, M. H. (2006). Free-flight responses of *Drosophila melanogaster* to attractive odors. *Journal of Experimental Biology, 209*(15), 3001–3017. doi:10.1242/jeb.02305.
33. Bundschuh, S. T., Zhu, P., Schärer, Y.-P. Z., & Friedrich, R. W. (2012). Dopaminergic modulation of mitral cells and odor responses in the zebrafish olfactory bulb. *The Journal of Neuroscience: The Official Journal of the Society for Neuroscience, 32*(20), 6830–6840. doi:10.1523/JNEUROSCI.6026-11.2012.
34. Bussières, N., & Dubuc, R. (1992). Phasic modulation of transmission from vestibular inputs to reticulospinal neurons during fictive locomotion in lampreys. *Brain Research, 582*(1), 147–153.
35. Cangiano, L. (2005). Mechanisms of rhythm generation in a spinal locomotor network deprived of crossed connections: The lamprey hemicord. *The Journal of Neuroscience: The Official Journal of the Society for Neuroscience, 25*(4), 923–935. doi:10.1523/JNEUROSCI.2301-04.2005.
36. Card, G. M. (2012). Escape behaviors in insects. *Current Opinion in Neurobiology, 22*(2), 180–186. doi:10.1016/j.conb.2011.12.009.
37. Carmena, J. M., Lebedev, M. A., Crist, R. E., O'Doherty, J. E., Santucci, D. M., Dimitrov, D. F., et al. (2003). Learning to control a brain–machine interface for reaching and grasping by primates. *PLoS Biology, 1*(2), e2. doi:10.1371/journal.pbio.0000042.
38. Chen, T.-W., Wardill, T. J., Sun, Y., Pulver, S. R., Renninger, S. L., Baohan, A., et al. (2013). Ultrasensitive fluorescent proteins for imaging neuronal activity. *Nature, 499*(7458), 295–300. doi:10.1038/nature12354.
39. Clark, D. A., Freifeld, L., & Clandinin, T. R. (2013). Mapping and cracking sensorimotor circuits in genetic model organisms. *Neuron, 78*(4), 583–595. doi:10.1016/j.neuron.2013.05.006.
40. Conway, B. A., Hultborn, H., & Kiehn, O. (1987). Proprioceptive input resets central locomotor rhythm in the spinal cat. *Experimental Brain Research (Experimentelle Hirnforschung. Expérimentation Cérébrale), 68*(3), 643–656.
41. Courtine, G., Gerasimenko, Y., Brand, R. V. D., Yew, A., Musienko, P., Zhong, H., et al. (2009a). Transformation of nonfunctional spinal circuits into functional states after the loss of brain input. *Nature Neuroscience, 12*(10), 1333–1342. doi:10.1038/nn.2401.
42. Courtine, G., Gerasimenko, Y., Brand, R. V. D., Yew, A., Musienko, P., Zhong, H., et al. (2009b). Transformation of nonfunctional spinal circuits into functional states after the loss of brain input. *Nature Neuroscience, 12*(10), 1333–1342. doi:10.1038/nn.2401.

43. Currie, S. N. (1991). Vibration-evoked startle behavior in larval lampreys. *Brain, Behavior and Evolution, 37*(5), 260–271.
44. Davison, J. M., Akitake, C. M., Goll, M. G., Rhee, J. M., Gosse, N., Baier, H., et al. (2007). Transactivation from Gal4-VP16 transgenic insertions for tissue-specific cell labeling and ablation in zebrafish. *Developmental Biology, 304*(2), 811–824. doi:10.1016/j.ydbio.2007.01.033.
45. Del Bene, F., & Wyart, C. (2012). Optogenetics: A new enlightenment age for zebrafish neurobiology. *Developmental Neurobiology, 72*(3), 404–414. doi:10.1002/dneu.20914.
46. Del Bene, F., Wyart, C., Robles, E., Tran, A., Looger, L., Scott, E. K., et al. (2010). Filtering of visual information in the tectum by an identified neural circuit. *Science, 330*(6004), 669–673. doi:10.1126/science.1192949.
47. Descending control of swim posture by a midbrain nucleus in zebrafish (2014). Descending control of swim posture by a midbrain nucleus in zebrafish. *Neuron, 83*(3), 679–691. doi:10.1016/j.neuron.2014.04.018.
48. Di Prisco, G. V., Wallén, P., & Grillner, S. (1990). Synaptic effects of intraspinal stretch receptor neurons mediating movement-related feedback during locomotion. *Brain Research, 530*(1), 161–166.
49. Dickinson, M., & Moss, C. F. (2012). Neuroethology. *Current Opinion in Neurobiology, 22*(2), 177–179. doi:10.1016/j.conb.2012.03.001.
50. Dombeck, D. A., & Reiser, M. B. (2012). Real neuroscience in virtual worlds. *Current Opinion in Neurobiology, 22*(1), 3–10. doi:10.1016/j.conb.2011.10.015.
51. Douglass, A. D. A., Kraves, S. S., Deisseroth, K. K., Schier, A. F. A., & Engert, F. F. (2008). Escape behavior elicited by single, channelrhodopsin-2-evoked spikes in zebrafish somatosensory neurons. *Current Biology: CB, 18*(15), 5–5. doi:10.1016/j.cub.2008.06.077.
52. Dubuc, R., Brocard, F., Antri, M., Fénelon, K., Gariépy, J.-F., Smetana, R., et al. (2008). Initiation of locomotion in lampreys. *Brain Research Reviews, 57*(1), 172–182. doi:10.1016/j.brainresrev.2007.07.016.
53. Eaton, R. C., Bombardieri, R. A., & Meyer, D. L. (1977). The Mauthner-initiated startle response in teleost fish. *Journal of Experimental Biology, 66*(1), 65–81.
54. Eaton, R. C., Lee, R. K., & Foreman, M. B. (2001). The Mauthner cell and other identified neurons of the brainstem escape network of fish. *Progress in Neurobiology, 63*(4), 467–485.
55. Eccles, R. M., & Lundberg, A. (1958). Significance of supraspinal control of reflex actions by impulses in muscle afferents. *Experientia, 14*(6), 197–199.
56. Eccles, J. C., Eccles, D. M., & Fatt, P. (1956). Pharmacological investigations on a central synapse operated by acetylcholine. *Journal of Physiology, 131*(1), 154–169.
57. Eccles, J. C., Eccles, R. M., & Lundberg, A. (1957a). Synaptic actions on motoneurones caused by impulses in Golgi tendon organ afferents. *Journal of Physiology, 138*(2), 227–252.
58. Eccles, J. C., Eccles, R. M., & Lundberg, A. (1957b). The convergence of monosynaptic excitatory afferents on to many different species of alpha motoneurones. *Journal of Physiology, 137*(1), 22–50.
59. Edgerton, V. R., Courtine, G., Gerasimenko, Y. P., Lavrov, I., Ichiyama, R. M., Fong, A. J., et al. (2008). Training locomotor networks. *Brain Research Reviews, 57*(1), 241–254. doi:10.1016/j.brainresrev.2007.09.002.
60. Eidelberg, E., Walden, J. G., & Nguyen, L. H. (1981). Locomotor control in macaque monkeys. *Brain: A Journal of Neurology, 104*(4), 647–663.
61. Fetcho, J. R., & Mclean, D. L. (2010). Some principles of organization of spinal neurons underlying locomotion in zebrafish and their implications. *Annals of the New York Academy of Sciences, 1198,* 94–104. doi:10.1111/j.1749-6632.2010.05539.x.
62. Fetz, E. E., Jankowska, E., Johannisson, T., & Lipski, J. (1979). Autogenetic inhibition of motoneurones by impulses in group Ia muscle spindle afferents. *Journal of Physiology, 293,* 173–195.
63. Flexor reflex afferents reset the step cycle during fictive locomotion in the cat (1998). Flexor reflex afferents reset the step cycle during fictive locomotion in the cat. *Experimental Brain Research (Experimentelle Hirnforschung. Expérimentation Cérébrale), 122*(3), 339–350.

64. Frank, K., & Fuortes, M. (1959). Presynaptic and postsynaptic inhibition of monosynaptic reflexes. *Federation Proceedings, 16,* 39–40.
65. Franklin, D. W., & Wolpert, D. M. (2011). Computational mechanisms of sensorimotor control. *Neuron, 72*(3), 425–442. doi:10.1016/j.neuron.2011.10.006.
66. Fry, S. N., Rohrseitz, N., Straw, A. D., & Dickinson, M. H. (2008). TrackFly: Virtual reality for a behavioral system analysis in free-flying fruit flies. *Journal of Neuroscience Methods, 171*(1), 110–117. doi:10.1016/j.jneumeth.2008.02.016.
67. Frye, M. A. (2010). Multisensory systems integration for high-performance motor control in flies. *Current Opinion in Neurobiology, 20*(3), 347–352. doi:10.1016/j.conb.2010.02.002.
68. Gabriel, J. P., Ausborn, J., Ampatzis, K., Mahmood, R., Eklöf-Ljunggren, E., & Manira, El. A. (2011). Principles governing recruitment of motoneurons during swimming in zebrafish. *Nature Publishing Group, 14*(1), 93–99. doi:10.1038/nn.2704.
69. Gao, X. J., Potter, C. J., Gohl, D. M., Silies, M., Katsov, A. Y., Clandinin, T. R., et al. (2013). Specific kinematics and motor-related neurons for aversive chemotaxis in Drosophila. *Current Biology: CB, 23*(13), 1163–1172. doi:10.1016/j.cub.2013.05.008.
70. Garcia-Rill, E., Kinjo, N., Atsuta, Y., Ishikawa, Y., Webber, M., & Skinner, R. D. (1990). Posterior midbrain-induced locomotion. *Brain Research Bulletin, 24*(3), 499–508.
71. Ghazanfar, A. A., & Schroeder, C. E. (2006). Is neocortex essentially multisensory? *Trends in Cognitive Sciences, 10*(6), 278–285. doi:10.1016/j.tics.2006.04.008.
72. Ghysen, A. A., & Dambly-Chaudière, C. C. (2007). The lateral line microcosmos. *Genes & Development, 21*(17), 2118–2130. doi:10.1101/gad.1568407.
73. Gorostiza, P., Volgraf, M., Numano, R., Szobota, S., Trauner, D., & Isacoff, E. Y. (2007). Mechanisms of photoswitch conjugation and light activation of an ionotropic glutamate receptor. *Proceedings of the National Academy of Sciences of the United States of America, 104*(26), 10865–10870. doi:10.1073/pnas.0701274104.
74. Gosgnach, S., Lanuza, G. M., Butt, S. J. B., Saueressig, H., Zhang, Y., Velasquez, T., et al. (2006). V1 spinal neurons regulate the speed of vertebrate locomotor outputs. *Nature, 440*(7081), 215–219. doi:10.1038/nature04545.
75. Gossen, M., & Bujard, H. (1992). Tight control of gene expression in mammalian cells by tetracycline-responsive promoters. *Proceedings of the National Academy of Sciences of the United States of America, 89*(12), 5547–5551.
76. Goulding, M. (2009). Circuits controlling vertebrate locomotion: Moving in a new direction. *Nature Reviews Neuroscience, 10*(7), 507–518. doi:10.1038/nrn2608.
77. Gradinaru, V., Thompson, K. R., & Deisseroth, K. (2008). eNpHR: A natronomonas halorhodopsin enhanced for optogenetic applications. *Brain Cell Biology, 36*(1–4), 129–139. doi:10.1007/s11068-008-9027-6.
78. Green, A. M., & Angelaki, D. E. (2010). Multisensory integration: Resolving sensory ambiguities to build novel representations. *Current Opinion in Neurobiology, 20*(3), 353–360. doi:10.1016/j.conb.2010.04.009.
79. Grienberger, C., & Konnerth, A. (2012). Imaging calcium in neurons. *Neuron, 73*(5), 862–885. doi:10.1016/j.neuron.2012.02.011.
80. Grillner, S. (2003). The motor infrastructure: From ion channels to neuronal networks. *Nature Reviews Neuroscience, 4*(7), 573–586. doi:10.1038/nrn1137.
81. Grillner, S., Williams, T., & Lagerbäck, P. A. (1984). The edge cell, a possible intraspinal mechanoreceptor. *Science, 223*(4635), 500–503.
82. Grillner, S., Manira, El. A., Kiehn, O., Rossignol, S., & S G Stein, P. (2008). Networks in motion. *Brain Research Reviews, 57*(1), 1. doi:10.1016/j.brainresrev.2007.11.005.
83. Guertin, P. A. (2013). Central pattern generator for locomotion: Anatomical, physiological, and pathophysiological considerations. 1–15. doi:10.3389/fneur.2012.00183/abstract.
84. Guertin, P., Angel, M. J., Perreault, M. C., & McCrea, D. A. (1995). Ankle extensor group I afferents excite extensors throughout the hindlimb during fictive locomotion in the cat. *Journal of Physiology, 487*(Pt 1), 197–209.
85. Hale, M. E. M., Ritter, D. A. D., & Fetcho, J. R. J. (2001). A confocal study of spinal interneurons in living larval zebrafish. *The Journal of Comparative Neurology, 437*(1), 1–16. doi:10.1002/cne.1266.

86. Harkema, S., Gerasimenko, Y., Hodes, J., Burdick, J., Angeli, C., Chen, Y., et al. (2011). Effect of epidural stimulation of the lumbosacral spinal cord on voluntary movement, standing, and assisted stepping after motor complete paraplegia: A case study. *Lancet, 377*(9781), 1938–1947. doi:10.1016/S0140-6736(11)60547-3.
87. Harvey, C. D., Collman, F., Dombeck, D. A., & Tank, D. W. (2010). Intracellular dynamics of hippocampal place cells during virtual navigation. *Nature, 461*(7266), 941–946. doi:10.1038/nature08499.
88. Hägglund, M., Borgius, L., Dougherty, K. J., & Kiehn, O. (2010). Activation of groups of excitatory neurons in the mammalian spinal cord or hindbrain evokes locomotion. *Nature Neuroscience, 13*(2), 246–252. doi:10.1038/nn.2482.
89. Higashijima, S., Hotta, Y., & Okamoto, H. (2000). Visualization of cranial motor neurons in live transgenic zebrafish expressing green fluorescent protein under the control of the islet-1 promoter/enhancer. *The Journal of Neuroscience: The Official Journal of the Society for Neuroscience, 20*(1), 206–218.
90. Higashijima, S.-I., Masino, M. A., Mandel, G., & Fetcho, J. R. (2003). Imaging neuronal activity during zebrafish behavior with a genetically encoded calcium indicator. *Journal of Neurophysiology, 90*(6), 3986–3997. doi:10.1152/jn.00576.2003.
91. Higashijima, S.-I., Masino, M. A., Mandel, G., & Fetcho, J. R. (2004). Engrailed-1 expression marks a primitive class of inhibitory spinal interneuron. *The Journal of Neuroscience: The Official Journal of the Society for Neuroscience, 24*(25), 5827–5839. doi:10.1523/JNEUROSCI.5342-03.2004.
92. Hultborn, H. (1972). Convergence on interneurones in the reciprocal Ia inhibitory pathway to motoneurones. *Acta Physiologica Scandinavica (Supplementum), 375,* 1–42.
93. Hultborn, H. (2006). Spinal reflexes, mechanisms and concepts: From Eccles to Lundberg and beyond. *Progress in Neurobiology, 78*(3–5), 215–232. doi:10.1016/j.pneurobio.2006.04.001.
94. Jalalvand, E., Robertson, B., Wallén, P., Hill, R. H., & Grillner, S. (2014). Laterally projecting cerebrospinal fluid-contacting cells in the lamprey spinal cord are of two distinct types. *The Journal of Comparative Neurology*. doi:10.1002/cne.23542.
95. Jankowska, E. (1992). Interneuronal relay in spinal pathways from proprioceptors. *Progress in Neurobiology, 38*(4), 335–378.
96. Jankowska, E., & Edgley, S. A. (2010). Functional subdivision of feline spinal interneurons in reflex pathways from group Ib and II muscle afferents; an update. *European Journal of Neuroscience, 32*(6), 881–893. doi:10.1111/j.1460-9568.2010.07354.x.
97. Jiang, W., & Drew, T. (1996). Effects of bilateral lesions of the dorsolateral funiculi and dorsal columns at the level of the low thoracic spinal cord on the control of locomotion in the adult cat. I. Treadmill walking. *Journal of Neurophysiology, 76*(2), 849–866.
98. Jordan, L. M., Liu, J., Hedlund, P. B., Akay, T., & Pearson, K. G. (2008a). Descending command systems for the initiation of locomotion in mammals. *Brain Research Reviews, 57*(1), 183–191. doi:10.1016/j.brainresrev.2007.07.019.
99. Jordan, L. M., Liu, J., Hedlund, P. B., Akay, T., & Pearson, K. G. (2008b). Descending command systems for the initiation of locomotion in mammals. *Brain Research Reviews, 57*(1), 183–191. doi:10.1016/j.brainresrev.2007.07.019.
100. Kato, M. (1987). Motoneuronal activity of cat lumbar spinal cord following separation from descending or contralateral impulses. *Central Nervous System Trauma: Journal of the American Paralysis Association, 4*(4), 239–248.
101. Kawakami, K., Shima, A., & Kawakami, N. (2000). Identification of a functional transposase of the Tol2 element, an Ac-like element from the Japanese medaka fish, and its transposition in the zebrafish germ lineage. *Proceedings of the National Academy of Sciences of the United States of America, 97*(21), 11403–11408. doi:10.1073/pnas.97.21.11403.
102. Kiehn, O. (2006). Locomotor circuits in the mammalian spinal cord. *Annual Review of Neuroscience, 29*(1), 279–306. doi:10.1146/annurev.neuro.29.051605.112910.
103. Kiehn, O. (2011). Development and functional organization of spinal locomotor circuits. *Current Opinion in Neurobiology, 21*(1), 100–109. doi:10.1016/j.conb.2010.09.004.

104. Kiehn, O., Quinlan, K. A., Restrepo, C. E., Lundfald, L., Borgius, L., Talpalar, A. E., et al. (2008). Excitatory components of the mammalian locomotor CPG. *Brain Research Reviews, 57*(1), 56–63. doi:10.1016/j.brainresrev.2007.07.002.
105. Kimmel, C. B., Warga, R. M., & Kane, D. A. (1994). Cell cycles and clonal strings during formation of the zebrafish central nervous system. *Development, 120*(2), 265–276.
106. Kimura, Y. (2006). Alx, a Zebrafish homolog of chx10, marks ipsilateral descending excitatory interneurons that participate in the regulation of spinal locomotor circuits. *The Journal of Neuroscience: The Official Journal of the Society for Neuroscience, 26*(21), 5684–5697. doi:10.1523/JNEUROSCI.4993-05.2006.
107. Kimura, Y., Satou, C., Fujioka, S., Shoji, W., Umeda, K., Ishizuka, T., et al. (2013). Hindbrain V2a neuronsin the excitation of spinal locomotor circuits during zebrafish swimming. *Current Biology, 23*(10), 843–849. doi:10.1016/j.cub.2013.03.066.
108. Knikou, M. (2008). The H-reflex as a probe: Pathways and pitfalls. *Journal of Neuroscience Methods, 171*(1), 1–12. doi:10.1016/j.jneumeth.2008.02.012.
109. Kohashi, T., & Oda, Y. (2008). Initiation of Mauthner- or non-Mauthner-mediated fast escape evoked by different modes of sensory input. *The Journal of Neuroscience: The Official Journal of the Society for Neuroscience, 28*(42), 10641–10653. doi:10.1523/JNEUROSCI.1435-08.2008.
110. Kohashi, T. T., Nakata, N. N., & Oda, Y. Y. (2012). Effective sensory modality activating an escape triggering neuron switches during early development in zebrafish. *The Journal of Neuroscience: The Official Journal of the Society for Neuroscience, 32*(17), 5810–5820. doi:10.1523/JNEUROSCI.6169-11.2012.
111. Korn, H., & Faber, D. S. (2005). The mauthner cell half a century later: A neurobiological model for decision-making? *Neuron, 47*(1), 13–28. doi:10.1016/j.neuron.2005.05.019.
112. Koster, R. W., & Fraser, S. E. (2001). Tracing transgene expression in living zebrafish embryos. *Developmental Biology, 233*(2), 329–346.
113. Körding, K. P., & Wolpert, D. M. (2004). Bayesian integration in sensorimotor learning. *Nature, 427*(6971), 244–247.
114. Körding, K. P., & Wolpert, D. M. (2006). Bayesian decision theory in sensorimotor control. *Trends in Cognitive Sciences, 10*(7), 319–326. doi:10.1016/j.tics.2006.05.003.
115. Lanuza, G. M., Gosgnach, S., Pierani, A., Jessell, T. M., & Goulding, M. (2004). Genetic identification of spinal interneurons that coordinate left-right locomotor activity necessary for walking movements. *Neuron, 42*(3), 375–386.
116. Latorre, R., Levi, R., & Varona, P. (2013). Transformation of context-dependent sensory dynamics into motor behavior. *PLOS Computational Biology*. doi:10.1371/journal.pcbi.1002908.s002.
117. Lavrov, I., Courtine, G., Dy, C. J., Brand, R. V. D., Fong, A. J., Gerasimenko, Y., et al. (2008). Facilitation of stepping with epidural stimulation in spinal rats: Role of sensory input. *The Journal of Neuroscience: The Official Journal of the Society for Neuroscience, 28*(31), 7774–7780. doi:10.1523/JNEUROSCI.1069-08.2008.
118. Levitz, J., Pantoja, C., Gaub, B., Janovjak, H., Reiner, A., Hoagland, A., et al. (2013). Optical control of metabotropic glutamate receptors. *Nature Neuroscience, 16*(4), 507–516. doi:10.1038/nn.3346.
119. Lewis, K. E., & Eisen, J. S. (2003). From cells to circuits: Development of the zebrafish spinal cord. *Progress in Neurobiology, 69*(6), 419–449.
120. Li, W.-C., Soffe, S. R., & Roberts, A. (2002). Spinal inhibitory neurons that modulate cutaneous sensory pathways during locomotion in a simple vertebrate. *The Journal of Neuroscience: The Official Journal of the Society for Neuroscience, 22*(24), 10924–10934.
121. Li, W.-C., Soffe, S. R., & Roberts, A. (2004). Dorsal spinal interneurons forming a primitive, cutaneous sensory pathway. *Journal of Neurophysiology, 92*(2), 895–904. doi:10.1152/jn.00024.2004.
122. Li, X., Gutierrez, D. V., Hanson, M. G., Han, J., Mark, M. D., Chiel, H., et al. (2005). Fast noninvasive activation and inhibition of neural and network activity by vertebrate rhodopsin and green algae channelrhodopsin. *Proceedings of the National Academy of Sciences of the United States of America, 102*(49), 17816–17821. doi:10.1073/pnas.0509030102.

123. Li, W.-C. W., Roberts, A. A., & Soffe, S. R. S. (2010). Specific brainstem neurons switch each other into pacemaker mode to drive movement by activating NMDA receptors. *The Journal of Neuroscience: The Official Journal of the Society for Neuroscience, 30*(49), 16609–16620. doi:10.1523/JNEUROSCI.3695-10.2010.
124. Liao, J. C., & Fetcho, J. R. (2008). Shared versus specialized glycinergic spinal interneurons in axial motor circuits of larval zebrafish. *The Journal of Neuroscience: The Official Journal of the Society for Neuroscience, 28*(48), 12982–12992. doi:10.1523/JNEUROSCI.3330-08.2008.
125. Liu, K. S., & Sternberg, P. W. (1994). Sensory regulation of male mating behavior in Caenorhabditis elegans. *Neuron, 14*(1), 79–89. doi:10.1016/0896-6273(95)90242-2.
126. Liu, K. S., & Fetcho, J. R. (1999). Laser ablations reveal functional relationships of segmental hindbrain neurons in zebrafish. *Neuron, 23*(2), 325–335. doi:10.1016/S0896-6273(00)80783-7.
127. Loquet, G. (2013). Multisensory integration in non-human primates during a sensory-motor task. 1–15. doi:10.3389/fnhum.2013.00799/abstract.
128. Lundberg, A. (1979). Multisensory control of spinal reflex pathways. *Progress in Brain Research, 50,* 11–28. doi:10.1016/S0079-6123(08)60803-1.
129. Marder, E. (2011). Variability, compensation, and modulation in neurons and circuits. *Proceedings of the National Academy of Sciences of the United States of America, 108*(Suppl. 3), 15542–15548. doi:10.1073/pnas.1010674108.
130. Marder, E. (2012). Neuromodulation of neuronal circuits: Back to the future. *Neuron, 76*(1), 1–11. doi:10.1016/j.neuron.2012.09.010.
131. Marder, E., & Taylor, A. L. (2011). Multiple models to capture the variability in biological neurons and networks. *Nature Neuroscience, 14*(2), 133–138. doi:10.1038/nn.2735.
132. Martial, F. P., & Hartell, N. A. (2012). Programmable Illumination and high-speed, multi-wavelength, confocal microscopy using a digital micromirror. *PloS ONE, 7*(8), e43942. doi:10.1371/journal.pone.0043942.
133. Martin, J.-R., Rogers, K. L., Chagneau, C., & Brûlet, P. (2007). In vivo Bioluminescence imaging of Ca^{2+} signalling in the brain of drosophila. *PloS ONE, 2*(3), e275. doi:10.1371/journal.pone.0000275.s009.
134. Martinez, M., & Rossignol, S. (2013). A dual spinal cord lesion paradigm to study spinal locomotor plasticity in the cat. *Annals of the New York Academy of Sciences, 1279*(1), 127–134. doi:10.1111/j.1749-6632.2012.06823.x.
135. Martinez, M., Delivet-Mongrain, H., Leblond, H., & Rossignol, S. (2012). Incomplete spinal cord injury promotes durable functional changes within the spinal locomotor circuitry. *Journal of Neurophysiology, 108*(1), 124–134. doi:10.1152/jn.00073.2012.
136. McClellan, A. D., & Grillner, S. (1984). Activation of "fictive swimming" by electrical microstimulation of brainstem locomotor regions in an in vitro preparation of the lamprey central nervous system. *Brain Research, 300*(2), 357–361.
137. McCrea, D. A. (2001). Spinal circuitry of sensorimotor control of locomotion. *Journal of Physiology, 533*(1), 41–50.
138. McCrea, D. A., Pratt, C. A., & Jordan, L. M. (1980). Renshaw cell activity and recurrent effects on motoneurons during fictive locomotion. *Journal of Neurophysiology, 44*(3), 475–488.
139. Mclean, D. L., Fan, J., Higashijima, S.-I., Hale, M. E., & Fetcho, J. R. (2007). A topographic map of recruitment in spinal cord. *Nature, 446*(7131), 71–75. doi:10.1038/nature05588.
140. Mclean, D. L., Masino, M. A., Koh, I. Y. Y., Lindquist, W. B., & Fetcho, J. R. (2008). Continuous shifts in the active set of spinal interneurons during changes in locomotor speed. *Nature Neuroscience, 11*(12), 1419–1429. doi:10.1038/nn.2225.
141. Mirat, O., Sternberg, J. R., & Severi, K. E. (2013). ZebraZoom: An automated program for high-throughput behavioral analysis and categorization. Frontiers in Neural. doi:10.3389/fncir.2013.00107/abstract.
142. Miyawaki, A., Llopis, J., Heim, R., McCaffery, J. M., Adams, J. A., Ikura, M., et al. (1997). Fluorescent indicators for Ca^{2+} based on green fluorescent proteins and calmodulin. *Nature, 388*(6645), 882–887. doi:10.1038/42264.

143. Moran-Rivard, L., Kagawa, T., Saueressig, H., Gross, M. K., Burrill, J., & Goulding, M. (2001). Evx1 is a postmitotic determinant of v0 interneuron identity in the spinal cord. *Neuron, 29*(2), 385–399.
144. Multisensory control of spinal reflex pathways (1979). Multisensory control of spinal reflex pathways. *Progress in Brain Research, 50,* 11–28. doi:10.1016/S0079-6123(08)60803-1.
145. Musienko, P., Brand, R. V. D., Märzendorfer, O., Roy, R. R., Gerasimenko, Y., Edgerton, V. R., et al. (2011). Controlling specific locomotor behaviors through multidimensional monoaminergic modulation of spinal circuitries. *The Journal of Neuroscience: The Official Journal of the Society for Neuroscience, 31*(25), 9264–9278. doi:10.1523/JNEUROSCI.5796-10.2011.
146. Muto, A., Ohkura, M., Kotani, T., Higashijima, S., Nakai, J., & Kawakami, K. (2011). Genetic visualization with an improved GCaMP calcium indicator reveals spatiotemporal activation of the spinal motor neurons in zebrafish. *Proceedings of the National Academy of Sciences of the United States of America, 108*(13), 5425–5430. doi:10.1073/pnas.1000887108/-/DCSupplemental.
147. Nagai, T., Sawano, A., Park, E. S., & Miyawaki, A. (2001). Circularly permuted green fluorescent proteins engineered to sense Ca^{2+}. *Proceedings of the National Academy of Sciences of the United States of America, 98*(6), 3197–3202.
148. Nagel, G., Szellas, T., Huhn, W., Kateriya, S., Adeishvili, N., Berthold, P., et al. (2003). Channelrhodopsin-2, a directly light-gated cation-selective membrane channel. *Proceedings of the National Academy of Sciences of the United States of America, 100*(24), 13940–13945. doi:10.1073/pnas.1936192100.
149. Nakai, J., Ohkura, M., & Imoto, K. (2001). A high signal-to-noise $Ca^{(2+)}$ probe composed of a single green fluorescent protein. *Nature Biotechnology, 19*(2), 137–141. doi:10.1038/84397.
150. Nakayama, H. H., & Oda, Y. Y. (2004). Common sensory inputs and differential excitability of segmentally homologous reticulospinal neurons in the hindbrain. *The Journal of Neuroscience: The Official Journal of the Society for Neuroscience, 24*(13), 3199–3209. doi:10.1523/JNEUROSCI.4419-03.2004.
151. Naumann, E. A., Kampff, A. R., Prober, D. A., Schier, A. F., & Engert, F. (2010). Monitoring neural activity with bioluminescence during natural behavior. *Nature Neuroscience, 13*(4), 513–520. doi:10.1038/nn.2518.
152. Neural control and modulation of swimming speed in the larval zebrafish (2014). Neural control and modulation of swimming speed in the larval zebrafish. *Neuron, 83*(3), 692–707. doi:10.1016/j.neuron.2014.06.032.
153. O'Malley, D. M. D., Kao, Y. H. Y., & Fetcho, J. R. J. (1996). Imaging the functional organization of zebrafish hindbrain segments during escape behaviors. *Neuron, 17*(6), 1145–1155. doi:10.1016/S0896-6273(00)80246-9.
154. Olszewski, J., Haehnel, M., Taguchi, M., & Liao, J. C. (2012). Zebrafish larvae exhibit rheotaxis and can escape a continuous suction source using their lateral line. *PloS ONE, 7*(5), e36661. doi:10.1371/journal.pone.0036661.g004.
155. Orger, M. B., Kampff, A. R., Severi, K. E., Bollmann, J. H., & Engert, F. (2008). Control of visually guided behavior by distinct populations of spinal projection neurons. *Nature Neuroscience, 11*(3), 327–333. doi:10.1038/nn2048.
156. Oron, D., Papagiakoumou, E., Anselmi, F., & Emiliani, V. (2012). Two-photon optogenetics. *Progress in Brain Research, 196,* 119–143. doi:10.1016/B978-0-444-59426-6.00007-0.
157. O'Doherty, J. E., Lebedev, M. A., Ifft, P. J., Zhuang, K. Z., Shokur, S., Bleuler, H., et al. (2012). Active tactile exploration using a brain–machine–brain interface. *Nature, 479*(7372), 228–231. doi:10.1038/nature10489.
158. Papagiakoumou, E., Anselmi, F., Bègue, A., de Sars, V., Glückstad, J., Isacoff, E. Y., et al. (2010). Scanless two-photon excitation of channelrhodopsin-2. *Nature Methods, 7*(10), 848–854. doi:10.1038/nmeth.1505.
159. Pietri, T., Manalo, E., Ryan, J., Saint-Amant, L., & Washbourne, P. (2009). Glutamate drives the touch response through a rostral loop in the spinal cord of zebrafish embryos. *Developmental Neurobiology, 69*(12), 780–795. doi:10.1002/dneu.20741.

160. Pirri, J. K., & Alkema, M. J. (2012). The neuroethology of *C. elegans* escape. *Current Opinion in Neurobiology, 22*(2), 187–193. doi:10.1016/j.conb.2011.12.007.
161. Portugues, R. (2011). Adaptive locomotor behavior in larval zebrafish. 1–11. doi:10.3389/fnsys.2011.00072/abstract.
162. Portugues, R., Severi, K. E., Wyart, C., & Ahrens, M. B. (2013). Optogenetics in a transparent animal: Circuit function in the larval zebrafish. *Current Opinion in Neurobiology, 23*(1), 119–126. doi:10.1016/j.conb.2012.11.001.
163. Pouget, A., & Snyder, L. H. (2000). Computational approaches to sensorimotor transformations. *Nature Neuroscience, 3 Suppl*(supp), 1192–1198. doi:10.1038/81469.
164. Pouget, A. A., Deneve, S. S., & Duhamel, J.-R. J. (2002). A computational perspective on the neural basis of multisensory spatial representations. *Nature Reviews Neuroscience, 3*(9), 741–747. doi:10.1038/nrn914.
165. Quinlan, K. A., & Kiehn, O. (2007). Segmental, synaptic actions of commissural interneurons in the mouse spinal cord. *The Journal of Neuroscience: The Official Journal of the Society for Neuroscience, 27*(24), 6521–6530. doi:10.1523/JNEUROSCI.1618-07.2007.
166. Renshaw, B. (1946). Central effects of centripetal impulses in axons of spinal ventral roots. *Journal of Neurophysiology, 9,* 191–204.
167. Reyes, R., Haendel, M., Grant, D., Melancon, E., & Eisen, J. S. (2003). Slow degeneration of zebrafish Rohon-Beard neurons during programmed cell death. *Developmental Dynamics: An Official Publication of the American Association of Anatomists, 229*(1), 30–41. doi:10.1002/dvdy.10488.
168. Ritter, D. A., Bhatt, D. H., & Fetcho, J. R. (2001). In vivo imaging of zebrafish reveals differences in the spinal networks for escape and swimming movements. *The Journal of Neuroscience: the Official Journal of the Society for Neuroscience, 21*(22), 8956–8965.
169. Roberts, A. A., Li, W.-C. W., & Soffe, S. R. S. (2009). How neurons generate behavior in a hatchling amphibian tadpole: An outline. *Frontiers in Behavioral Neuroscience, 4,* 16–16. doi:10.3389/fnbeh.2010.00016.
170. Rogers, K. L., Stinnakre, J., Agulhon, C., Jublot, D., Shorte, S. L., Kremer, E. J., et al. (2005). Visualization of local Ca^{2+} dynamics with genetically encoded bioluminescent reporters. *European Journal of Neuroscience, 21*(3), 597–610. doi:10.1111/j.1460-9568.2005.03871.x.
171. Rogers, K. L., Picaud, S., Roncali, E., Boisgard, R., Colasante, C., Stinnakre, J., et al. (2007). Non-invasive in vivo imaging of calcium signaling in mice. *PloS ONE, 2*(10), e974. doi:10.1371/journal.pone.0000974.
172. Rohrseitz, N., & Fry, S. N. (2010). Behavioural system identification of visual flight speed control in *Drosophila melanogaster*. *Journal of the Royal Society Interface, 8*(55), 171–185. doi:10.1038/417359a.
173. Rossignol, S. (1996). Visuomotor regulation of locomotion. *Canadian Journal of Physiology and Pharmacology, 74*(4), 418–425.
174. Rossignol, S., & Frigon, A. (2011). Recovery of locomotion after spinal cord injury: Some facts and mechanisms. *Annual Review of Neuroscience, 34,* 413–440. doi:10.1146/annurev-neuro-061010–113746.
175. Rossignol, S., & Gauthier, L. (1980). An analysis of mechanisms controlling the reversal of crossed spinal reflexes. *Brain Research, 182*(1), 31–45.
176. Rossignol, S., Dubuc, R., & Gossard, J.-P. (2006). Dynamic sensorimotor interactions in locomotion. *Physiological Reviews, 86*(1), 89–154. doi:10.1152/physrev.00028.2005.
177. Rudomin, P. (2009). In search of lost presynaptic inhibition. *Experimental Brain Research (Experimentelle Hirnforschung. Expérimentation Cérébrale), 196*(1), 139–151. doi:10.1007/s00221-009-1758-9.
178. Rudomin, P., & Schmidt, R. F. (1999). Presynaptic inhibition in the vertebrate spinal cord revisited. *Experimental Brain Research (Experimentelle Hirnforschung. Expérimentation Cérébrale), 129*(1), 1–37.
179. Sankrithi, N. S., & O'Malley, D. M. (2010). Activation of a multisensory, multifunctional nucleus in the zebrafish midbrain during diverse locomotor behaviors. *Neuroscience, 166*(3), 970–993. doi:10.1016/j.neuroscience.2010.01.003.

180. Satou, C., Kimura, Y., Kohashi, T., Horikawa, K., Takeda, H., Oda, Y., et al. (2009). Functional role of a specialized class of spinal commissural inhibitory neurons during fast escapes in zebrafish. *The Journal of Neuroscience: The Official Journal of the Society for Neuroscience, 29*(21), 6780–6793. doi:10.1523/JNEUROSCI.0801-09.2009.
181. Satou, C., Kimura, Y., Hirata, H., Suster, M. L., Kawakami, K., & Higashijima, S.-I. (2013). Transgenic tools to characterize neuronal properties of discrete populations of zebrafish neurons. *Development, 140*(18), 3927–3931. doi:10.1242/dev.099531.
182. Schobert, B., & Lanyi, J. K. (1982). Halorhodopsin is a light-driven chloride pump. *The Journal of Biological Chemistry, 257*(17), 10306–10313.
183. Schomburg, E. D., Petersen, N., Barajon, I., & Hultborn, H. (1998). Flexor reflex afferents reset the step cycle during fictive locomotion in the cat. *Experimental Brain Research. Experimentelle Hirnforschung. Expérimentation Cérébrale, 122(3), 3*39–350.
184. Schoonheim, P. J., Arrenberg, A. B., Del Bene, F., & Baier, H. (2010). Optogenetic localization and genetic perturbation of saccade-generating neurons in zebrafish. *The Journal of Neuroscience: The Official Journal of the Society for Neuroscience, 30*(20), 7111–7120. doi:10.1523/JNEUROSCI.5193-09.2010.
185. Schroeder, C. E., & Foxe, J. (2005). Multisensory contributions to low-level, "unisensory" processing. *Current Opinion in Neurobiology, 15*(4), 454–458. doi:10.1016/j.conb.2005.06.008.
186. Schuster, S. (2012). Fast-starts in hunting fish: Decision-making in small networks of identified neurons. *Current Opinion in Neurobiology, 22*(2), 279–284. doi:10.1016/j.conb.2011.12.004.
187. Scott, E. K., Mason, L., Arrenberg, A. B., Ziv, L., Gosse, N. J., Xiao, T., et al. (2007). Targeting neural circuitry in zebrafish using GAL4 enhancer trapping. *Nature Methods, 4*(4), 323–326. doi:10.1038/nmeth1033.
188. Seelig, J. D., & Jayaraman, V. (2011). Studying sensorimotor processing with physiology in behaving *drosophila*. *International Review of Neurobiology, 99,* 169–189. doi:10.1016/B978-0-12-387003-2.00007-0
189. Severi, K. E., Portugues, R., Marques, J. C., O'Malley, D. M., Orger, M. B., & Engert, F. (2014). Neural control and modulation of swimming speed in the larval zebrafish. *Neuron, 83*(3), 69*2–707. doi:10.1016*/j.neuron.2014.06.032
190. Seelig, J. D., Chiappe, M. E., Lott, G. K., Dutta, A., Osborne, J. E., Reiser, M. B., et al. (2010). Two-photon calcium imaging from head-fixed *Drosophila* during optomotor walking behavior. *Nature Methods, 7*(7), 535–540. doi:10.1038/nmeth.1468.
191. Shik, M. L., Severin, F. V., & Orlovsky, G. N. (1969). Control of walking and running by means of electrical stimulation of the mesencephalon. *Electroencephalography and Clinical Neurophysiology, 26*(5), 549.
192. Shimomura, O., Johnson, F. H., & Saiga, Y. (1962). Extraction, purification and properties of aequorin, a bioluminescent protein from the luminous hydromedusan, Aequorea. *Journal of Cellular and Comparative Physiology, 59,* 223–239.
193. Sillar, K. T., Combes, D., Ramanathan, S., Molinari, M., & Simmers, J. (2008). Neuromodulation and developmental plasticity in the locomotor system of anuran amphibians during metamorphosis. *Brain Research Reviews, 57*(1), 94–102. doi:10.1016/j.brainresrev.2007.07.018.
194. Slimko, E. M., McKinney, S., Anderson, D. J., Davidson, N., & Lester, H. A. (2002). Selective electrical silencing of mammalian neurons in vitro by the use of invertebrate ligand-gated chloride channels. *The Journal of Neuroscience: The Official Journal of the Society for Neuroscience, 22*(17), 7373–7379.
195. Suli, A., Watson, G. M., Rubel, E. W., & Raible, D. W. (2012). Rheotaxis in larval zebrafish is mediated by lateral line mechanosensory hair cells. *PloS ONE, 7*(2), e29727. doi:10.1371/journal.pone.0029727.g003.
196. Szobota, S. S., Gorostiza, P. P., Del Bene, F. F., Wyart, C. C., Fortin, D. L. D., Kolstad, K. D. K., et al. (2007). Remote control of neuronal activity with a light-gated glutamate receptor. *Neuron, 54*(4), 11–11. doi:10.1016/j.neuron.2007.05.010.

197. Tabot, G. A., Dammann, J. F., & Berg, J. A. (2013). Restoring the sense of touch with a prosthetic hand through a brain interface. Presented at the Proceedings of the United States of America. doi:10.1073/pnas.1221113110/-/DCSupplemental.
198. Talpalar, A. E., Bouvier, J., Borgius, L., Fortin, G., Pierani, A., & Kiehn, O. (2013). Dual-mode operation of neuronal networks involved in left-right alternation. *Nature, 500*(7460), 85–88. doi:10.1038/nature12286.
199. Tazerart, S., Vinay, L., & Brocard, F. (2008). The persistent sodium current generates pacemaker activities in the central pattern generator for locomotion and regulates the locomotor rhythm. *The Journal of Neuroscience: The Official Journal of the Society for Neuroscience, 28*(34), 8577–8589. doi:10.1523/JNEUROSCI.1437-08.2008.
200. Thiele, T. R., Donovan, J. C., & Baier, H. (2014). Descending control of swim posture by a midbrain nucleus in zebrafish. *Neuron, 83*(3), 679–691. doi:10.1016/j.neuron.2014.04.018
201. Tian, L., Hires, S. A., Mao, T., Huber, D., Chiappe, M. E., Chalasani, S. H., et al. (2009). imaging neural activity in worms, flies and mice with improved GcamP calcium indicators. *Nature Methods, 6*(12), 875–881. doi:10.1038/nmeth.1398.
202. Trotter, Y., & Celebrini, S. (1999). Gaze direction controls response gain in primary visual-cortex neurons. *Nature, 398*(6724), 239–242. doi:10.1038/18444.
203. Viana Di Prisco, G., Ohta, Y., Bongianni, F., Grillner, S., & Dubuc, R. (1995). Trigeminal inputs to reticulospinal neurones in lampreys are mediated by excitatory and inhibitory amino acids. *Brain Research, 695*(1), 76–80.
204. Wannier, T., Deliagina, T. G., Orlovsky, G. N., & Grillner, S. (1998). Differential effects of the reticulospinal system on locomotion in lamprey. *Journal of Neurophysiology, 80*(1), 103–112.
205. Whelan, P. J. (1996). Control of locomotion in the decerebrate cat. *Progress in Neurobiology, 49*(5), 481–515.
206. Windhorst, U. (2007). Muscle proprioceptive feedback and spinal networks. *Brain Research Bulletin, 73*(4–6), 155–202. doi:10.1016/j.brainresbull.2007.03.010.
207. Wolpert, D. M. (2007). Probabilistic models in human sensorimotor control. *Human Movement Science, 26*(4), 511–524. doi:10.1016/j.humov.2007.05.005.
208. Wyart, C., Del Bene, F., Warp, E., Scott, E. K., Trauner, D., Baier, H., et al. (2009). Optogenetic dissection of a behavioural module in the vertebrate spinal cord. *Nature, 461*(7262), 407–410. doi:10.1038/nature08323.
209. Ye, H., Morton, D. W., & Chiel, H. J. (2006). Neuromechanics of multifunctionality during rejection in *Aplysia californica*. *The Journal of Neuroscience: The Official Journal of the Society for Neuroscience, 26*(42), 10743–10755. doi:10.1523/JNEUROSCI.3143-06.2006.
210. Yemini, E., Jucikas, T., Grundy, L. J., Brown, A. E. X., & Schafer, W. R. (2013). A database of Caenorhabditis elegans behavioral phenotypes. *Nature Methods, 10*(9), 877–879. doi:10.1038/nmeth.2560.
211. Zajac, F. E. (1989). Muscle and tendon: Properties, models, scaling, and application to biomechanics and motor control. *Critical Reviews in Biomedical Engineering, 17*(4), 359–411.
212. Zhang, F., Aravanis, A. M., Adamantidis, A., de Lecea, L., & Deisseroth, K. (2007a). Circuit-breakers: Optical technologies for probing neural signals and systems. *Nature Reviews Neuroscience, 8*(8), 577–581. doi:10.1038/nrn2192.
213. Zhang, F., Wang, L.-P., Brauner, M., Liewald, J. F., Kay, K., Watzke, N., et al. (2007b). Multimodal fast optical interrogation of neural circuitry. *Nature, 446*(7136), 633–639. doi:10.1038/nature05744.
214. Zhu, P., Narita, Y., Bundschuh, S. T., Fajardo, O., Schärer, Y.-P. Z., Chattopadhyaya, B., et al. (2009). Optogenetic dissection of neuronal circuits in zebrafish using viral gene transfer and the Tet system. *Frontiers in Neural Circuits, 3,* 21. doi:10.3389/neuro.04.021.2009.

Chapter 9
Patterned Photostimulation in the Brain

Francesca Anselmi, Arkarup Banerjee and Dinu F. Albeanu

Abstract Photostimulation has been instrumental in the past two decades for studying the structural synaptic plasticity and functional connectivity of neuronal circuits. With the advent of optogenetic strategies, this approach has been further expanded and used to identify the neuronal substrates of behavior via monitoring and modulating the activity of specific neuronal types *in vivo*. To date, however, photostimulation has been mainly implemented via full-field illumination and laser scanning protocols, which suffer from limited selectivity and stop short of generating asynchronous and spatially distributed neuronal firing patterns, characteristic for brain activity.

In this chapter, we discuss advances in using novel light patterning techniques which allow shaping illumination to create flexible spatiotemporal photostimulation profiles over large ensembles of neurons, as well as onto subcellular compartments. Specifically, we describe two light patterning strategies implemented through intensity and phase modulation, respectively. We illustrate the underlying physical principles, their applications to date, and the scope and limitations of each method, in an attempt to bridge the gap between the development of optical techniques and their use for neuroscience experiments.

9.1 Introduction

A central goal of systems neuroscience is to describe behaviors in terms of the neuronal circuits that control them. This is particularly challenging in the mammalian brain because behaviors are thought to rely on widely distributed neuronal representations that are technically difficult to monitor at large scales, or to

D. F. Albeanu (✉) · F. Anselmi · A. Banerjee
Cold Spring Harbor Laboratory, Cold Spring Harbor, NY 11724, USA
e-mail: albeanu@cshl.edu

A. Banerjee · D. F. Albeanu
Watson School of Biological Sciences, Cold Spring Harbor, NY 11724, USA

A. D. Douglass (ed.), *New Techniques in Systems Neuroscience,* Biological and Medical Physics, Biomedical Engineering, DOI 10.1007/978-3-319-12913-6_9

manipulate at cellular resolution. Understanding the function of neuronal circuits requires monitoring large populations of neurons in the intact brain, while simultaneously perturbing specific circuit elements. This is a hard problem since functional imaging and electrophysiology studies have revealed that neuronal representations of sensory-motor information in many brain regions are spatially distributed and asynchronous. In addition, the spatial and temporal scales of physiological phenomena vary widely. Depending upon the question of interest, one may need to probe neuronal activity at micrometric scale, at the network level, or across brain regions, over milliseconds to several days.

In the past two decades, due to its noninvasive nature, light has been used as a tool to monitor the structure and activity of neuronal systems [1]. The flexibility in design of functional imaging setups, together with the diversity of available chemical and genetically encoded calcium [2–4] and voltage [5–7] indicators, have allowed researchers to address a wide range of issues ranging from structural synaptic plasticity [8, 9], dendritic integration [10–14], and functional connectivity [15–18] to circuit dynamics and the neuronal substrates of behavior [19–21].

As a complement to functional imaging, photostimulation techniques can be used to probe brain circuits by specifically manipulating neuronal activity. In particular, the advent of optogenetic actuators, allowing bidirectional control of neuronal firing [22–24], has made it feasible to map functional connectivity across the brain and assess the roles of genetically identified neuronal types in network computations [25]. Furthermore, this approach has advanced our understanding of brain architecture and function by relating anatomical structures to their roles in behavior. Commonly used photostimulation techniques have the advantage of simplicity, as they rely on genetic targeting to determine the specificity of stimulation and on the use of full-field illumination (mostly through optical fibers) to deliver light into brain preparations [26, 27]. Technical accessibility has, indeed, been an important factor in ensuring the fast spread and success of optogenetic manipulations.

However, of late scientists have started investigating the potential of more sophisticated optical techniques to overcome some limitations of full-field light stimulation [28, 29]. We describe in this chapter, two innovative optical methods referred to as *light patterning techniques* that enable simultaneous stimulation of multiple neuronal targets by flexibly shaping the illumination. Patterned illumination strategies allow the generation of flexible spatial and temporal photostimulation profiles, which, in combination with multiphoton imaging of neuronal activity, electrophysiological recordings, and optogenetic manipulations, provide an ideal framework toward achieving optical control of neuronal activity.

9.1.1 Why Do We Need Light Patterning?

Until recently, targeted photostimulation and imaging of multiple neuronal structures have been almost exclusively performed by sequential scanning. In this approach, a *collimated* laser beam is either focused by an objective lens in a *diffraction-limited*

volume or sent into the sample as a pencil of parallel light and steered through the field of stimulation by galvanometric mirrors. Laser scanning photostimulation has been successfully used in conjunction with uncaging of neurotransmitters [30–35] and in optogenetic experiments that map functional connectivity in [36–38]. The major limitation of this approach lies in the need to sequentially stimulate multiple targets. Although recent techniques such as resonant scanning [39, 40] and acousto-optical deflectors (AODs) [41–44] have allowed scanning at high frequencies (hundreds of Hz to KHz), the actual number of targets that can be stimulated within a physiologically relevant time window (a few milliseconds) remains constrained by the dwell time at each site. In turn, the dwell time is determined by the specifics of the excitation process and the photochemical properties of light-sensitive compounds. In the case of optogenetic actuators (opsins), these also include activation time and single-channel conductance [45, 46]. Thus, sequential approaches become unfavorable in experiments where a large number of sites needs to be probed and when the necessary dwell time is on the order of a millisecond or longer [47]. Under these conditions, patterned illumination techniques that shape the stimulation light in order to target multiple structures simultaneously provide a valuable alternative.

9.1.2 General Principles of Light Patterning

A simple example of light patterning is a configuration where the sample is illuminated by an array of *micro-LEDs* (Fig. 9.1a). The illumination light path in the microscope can be set up such that an image of the array is formed at the *focal plane* of the objective lens (Sect. 9.2.1). In this case, by switching ON and OFF any micro-LED in the array, the user can gate the illumination within corresponding regions in the sample (Fig. 9.1a). This principle of operation is general in light patterning techniques, where the illumination of the sample is shaped by an array of discrete actuators, generally referred to as spatial light modulator (SLM), placed in a remote location, but optically coupled to the focal plane of the microscope objective.

To understand the physical principles behind different types of light patterning strategies, it is convenient to introduce a formal notation, which describes light as an oscillating electromagnetic field. The light electromagnetic field, as any other propagating wave (Box 1), is a function of both space and time (imagine ripples in a pond). However, in the context of light patterning, the temporal dimension can be discarded, as if taking a snapshot at a particular moment, and light can be described as an electromagnetic field oscillating in space. Along the same lines, it is sufficient to represent light as an oscillating electric field:

$$E(\vec{r}) = A(\vec{r})e^{i\psi(\vec{r})} \tag{9.1}$$

where $A(\vec{r})$ is the maximum amplitude of the oscillation in a given location $\vec{r}$ and $\psi(\vec{r})$ is its phase, that is the angle within the oscillation cycle (Box 1).

BOX 1: Wave Propagation

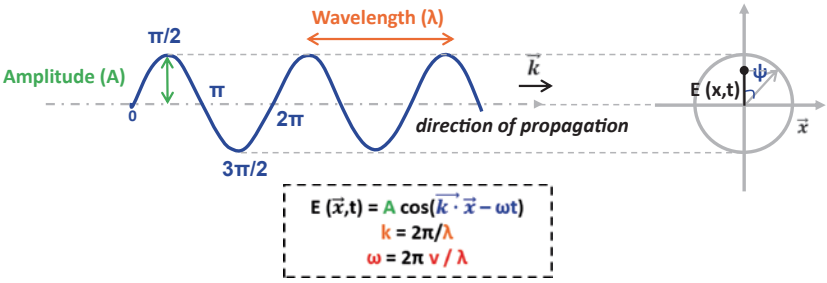

The amplitude of a wave propagating in one dimension (x) can be represented as a periodic function described in terms of sines and/or cosines. For example:

$$E\left(\vec{k}\vec{x}\right) = A\cos\left(\vec{k},\vec{x}\right), \tag{9.14}$$

where, A is the maximum amplitude of the oscillation and $\vec{k}$ is the wave vector of magnitude 2π/λ, whose direction corresponds to the propagation direction. To describe a propagating wave with velocity $\vec{v}$, Eq. (9.14) is modified to include a constant (a) (ω, angular velocity) denoting how much the wave has travelled in a time interval, t.

$$E\left(\vec{x},t\right) = A\cos\left(\vec{k}\cdot\left(\vec{x}-\vec{v}t\right)\right) = A\cos\left(\vec{k}\cdot\vec{x}-\omega t\right) = A\cos\psi \tag{9.15}$$

The argument of the cosine term (ψ) denotes the relative position within the oscillation cycle, also known as phase.

The above equation can be rewritten in terms of exponentials using the Euler's formula:

$$Ae^{i\psi} = A\cos\psi + iA\sin\psi, \tag{9.16}$$

where

$$Real\left(Ae^{i\psi}\right) = \mathrm{A}\cos\psi \tag{9.17}$$

For mathematical convenience, usually the imaginary part is also included in the equation which can be written in an exponential form:

$$E(x,t) = \cos\psi + i\sin\psi = Ae^{i\psi} \tag{9.18}$$

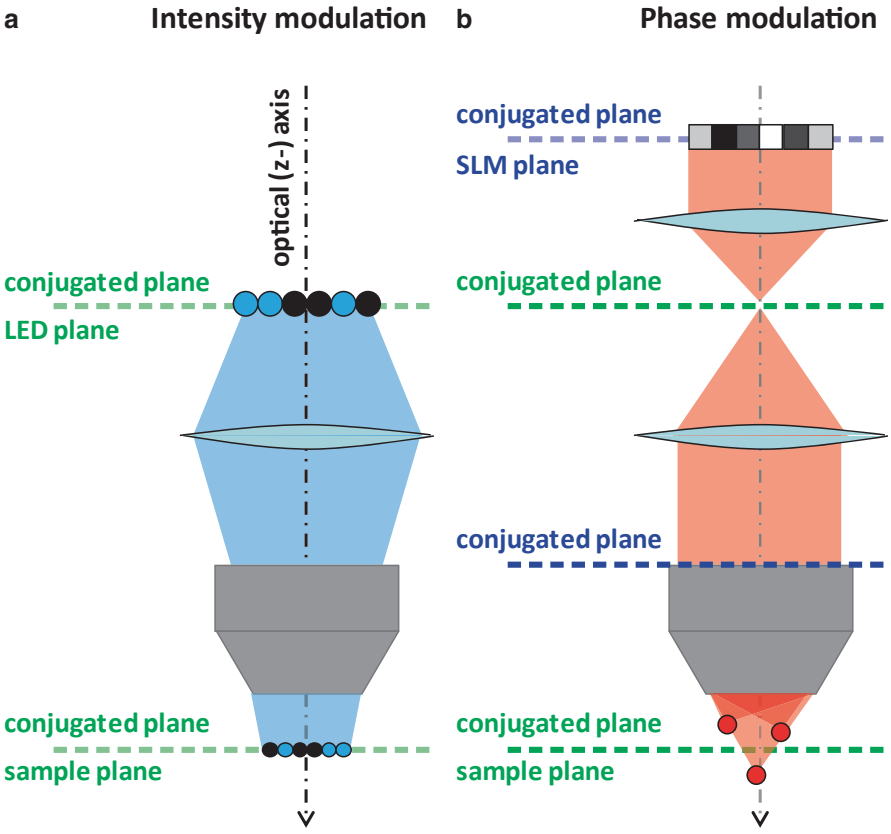

Fig. 9.1 Light patterning. Cartoon schematics illustrating the general principle of intensity (**a**) and phase (**b**) modulation. **a** Intensity modulation is obtained by placing a digital micromirror devices (DMD) or an LED array in a plane conjugated with the sample plane, such that the intensity pattern generated by the DMD/LED is imaged into the sample. **b** Phase modulation is obtained by placing an SLM in a plane conjugated with the back focal plane of the microscope objective. The phase profiles generated by the SLM are transformed by the objective lens into the desired intensity pattern at the sample

In order to perform light patterning, the amplitude of the light electric field at the sample $\left(E(\vec{r})\right)$ needs to be modulated. This is implemented by modifying either the intensity $\left(I(\vec{r}) \propto (\vec{r})^2\right)$ or the phase $\left(\psi(\vec{r})\right)$ of the light electric field at a remote location using an SLM. One very convenient remote location is a plane *conjugated* to the front focal plane of the microscope objective. An SLM placed at this particular location will be imaged at the sample (the front focal plane of the objective, Fig. 9.1a). If the maximum amplitude of the light electric field $\left(A(\vec{r})\right)$ is modulated at the SLM plane, the same modulation will apply to all conjugated planes, one of which is the sample plane. This strategy is extensively used in "intensity-modulation" light patterning techniques, described in Sect. 9.2. However,

this is not the only option. Another possibility is to modulate the phase of the light electric field $\left(\psi(\vec{r})\right)$ in order to create specific interference patterns that generate the desired light intensity pattern at the sample (Fig. 9.1b). This strategy is adopted in "phase-modulation" light patterning techniques, such as digital holography described in Sect. 9.3.

As defined above, the term SLM applies to any device used for either intensity or phase-modulation light patterning techniques. However, numerous studies in the field use it to refer specifically to phase-modulation devices, as we will also do throughout this chapter.

9.2 Light Patterning by Intensity Modulation

9.2.1 General Principle

A simple way of achieving light patterning is by using a light source composed of discrete actuators that can be individually turned ON and OFF. If such a source is imaged onto the sample (Fig. 9.1a), this results in a 2D pixelated illumination profile, which can be flexibly shaped. A common way of implementing this idea is to place a micro-LED array at a plane conjugated to the objective plane. LED arrays are cheap and illumination patterns can be modified at kHz rate [48]. In biological applications to date, the maximum available power is limited [48], and the number of mini-actuators used is generally small (64×64) [48], restraining the number of possible light patterns. However, new developments in microfabrication technologies allow the construction of more powerful high-density micro-LED arrays [49].

Alternatively, digital light processing (DLP) technology can be used as a means of generating and displaying precise spatiotemporal light patterns. DLP was invented by Larry Hornbeck at Texas Instruments in 1987. This is the basis of all the digital projector systems, including those used today to screen motion pictures in the USA. At the heart of this technology lies a digital micromirror device (DMD) which consists of a large number of independently controllable micrometer-scale mirrors (e.g., 1024×768), each one representing one pixel at the sample. A CMOS chip placed underneath each micromirror stores one bit of information (1 or 0) translated into the ON/OFF position. When the DMD chip is illuminated by an external source, the light reflected by each micromirror in the ON position is directed toward the optical path, whereas the light reflected by micromirrors in the OFF position is physically blocked. Each micromirror can be independently switched ON/OFF at microsecond timescale to create arbitrary light patterns. A DMD device can be used to project not only binary patterns, but also graded ones. The brightness of any pixel at the sample can be modulated by the duty cycle (ratio of ON vs. OFF states per unit time) of the corresponding micromirror. For example, in an 8-bit system, one can achieve 255 shades of grey [50].

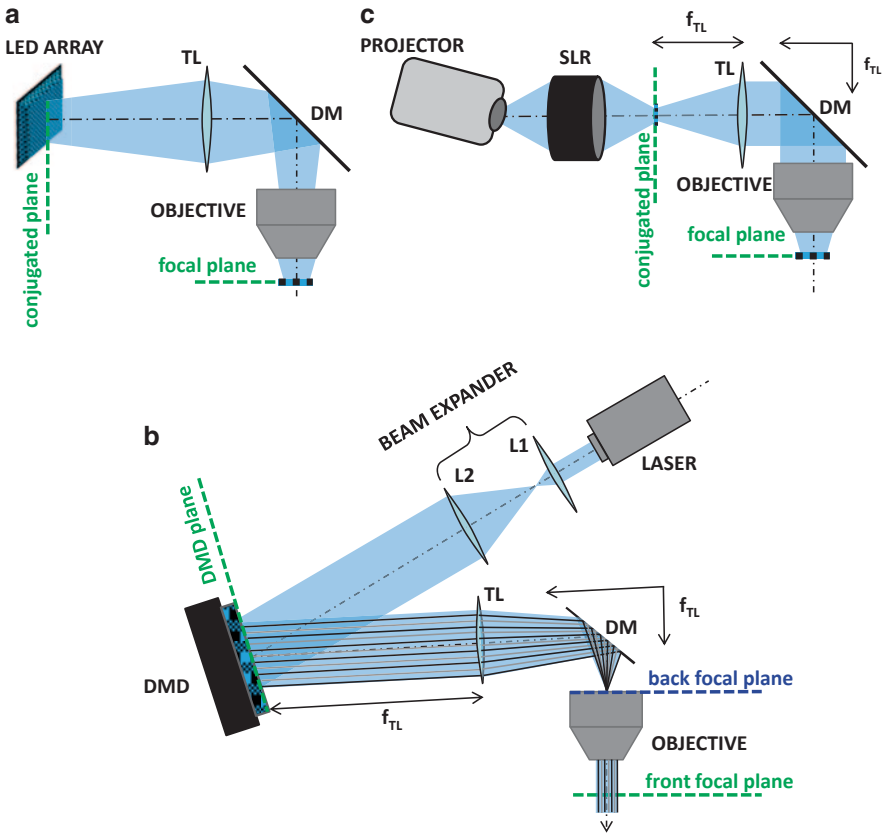

Fig. 9.2 Light patterning by intensity modulation—optical configurations. **a** An LED array is imaged into the sample using a telescope formed by the tube lens (*TL*) and the microscope objective. **b** A beam expander formed by lenses L1-L2 magnifies a laser beam to illuminate the DMD chip. The light reflected by the DMD is projected into the sample via a TL and the microscope objective, resulting in a pencil of parallel light carrying the desired pattern. **c** The output of a DLP projector is imaged onto an intermediate plane using an SLR lens. This intermediate pattern is further imaged into the sample with a telescope formed by the TL and the objective. In all configurations, a dichroic mirror (*DM*) is placed above the objective to rotate the illumination beam so that it impinges perpendicularly onto the back aperture of the objective

9.2.2 Optical Configurations

The LED array/DMD is imaged onto the sample using a pair of lenses (a telescope). Generally, the lens closest to the sample is the objective, while the other one is called the "tube" lens (TL—because traditionally it was placed in a tubular holder) (Fig. 9.2a). A convenient configuration consists in placing the LED array/DMD at the focal plane of the tube lens (i.e., at a distance equal to the tube lens focal length, f_1), while ensuring that the distance between the tube lens and the objective

is the sum of their focal lengths ($f_1 + f_2$). What determines the choice of the lenses? The ratio of the focal lengths (f_2/f_1) is the demagnification ratio and sets the size of the field of stimulation (FoS). Depending upon the desired FoS size and given the focal length of the objective, the required focal length of the tube lens can be calculated using Eq. 9.2:

$$FoS\ size = \frac{f_2}{f_1} Object\ size \tag{9.2}$$

In case of DMD chips, an additional telescope (called the beam expander) is used to bring the LASER/LED light to the DMD and to expand it to match the size of the chip (Fig. 9.2b). Since the intensity of light from extended sources such as arc lamps/LED decreases steeply with distance, it is desirable to place the light source as close as possible to the DMD. This is not necessary if the light source is a collimated laser beam.

Another possible configuration involves a commercial projector, which comes with its own DMD chip along with an internal light source and an output lens (Fig. 9.2c). Since the projector output beam is tilted with respect to the optical axis (~ 10–20°), the projector should be placed on a stage such as to compensate for this angular displacement and ensure that light comes out parallel to the optical axis. A second lens is further needed to collimate (as much as possible) the beam. Since the projector output beam is highly divergent, it is advisable to place this lens as close as possible to the projector to minimize power loss. Single light reflex (SLR) camera lenses have wide acceptance angles and are therefore ideally suited for such high-divergence conditions. In addition, they are corrected for coma and spherical aberrations, which can otherwise significantly distort the projected patterns. The SLR lens creates an image of the DMD chip at an intermediate position which can be further treated as a new object to be imaged at the sample using a tube lens and an objective as described above (Fig. 9.2c). Within this configuration, it is important to choose the tube lens with a short focal length to minimize light loss due to high divergence. Note that usage of a short focal length tube lens also increases the size of the FoS for a fixed objective. Therefore, a trade-off must be reached between the desired size of FoS and the focal length of the tube lens. To achieve a large FoS, a typical microscope objective can also be replaced with an SLR lens. The temporal resolution is limited by the refresh rate of the projector, usually in the range of 60–360 Hz. In single-chip projectors, rapidly spinning a color wheel to combine appropriate RGB components for each pixel creates the illusion of color to the human eye. To utilize the full refresh rate of single-chip projectors, it is therefore useful to remove the color wheel from the optical path (complete disconnect usually has undesired effects). The output color can be modified for a variety of optogenetic actuators by placing excitation filters in the optical path.

Examples of light patterns obtained with a DMD setup similar to the one described in Fig. 9.2b are shown in Fig. 9.3.

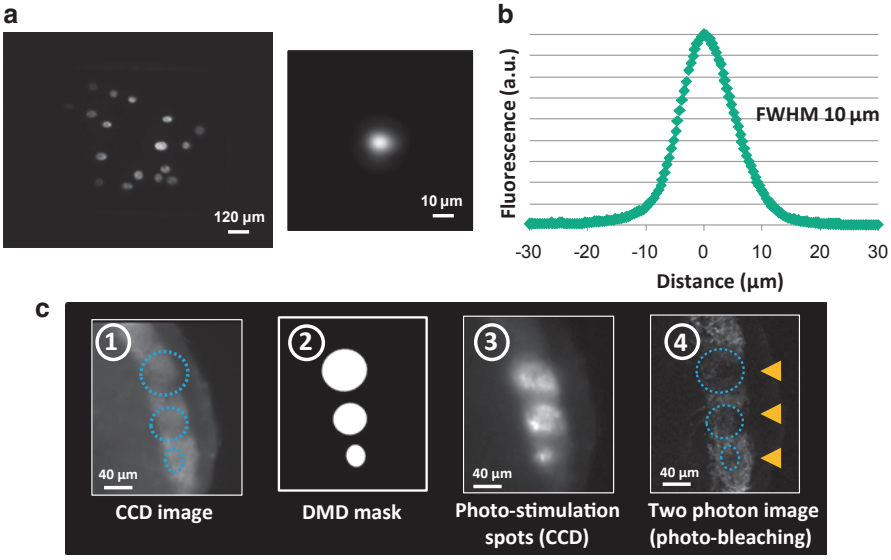

Fig. 9.3 Example DMD patterns. **a** DMD spots reproducing the shape of glomeruli in the olfactory bulb, projected onto a thin (1 µm) fluorescent layer and imaged with a CCD camera. **b** *Left:* image of a 20-µm-diameter spot projected with a DMD. *Right:* Lateral intensity profile for the spot shown on the left. **c** *(1–2)* Three DMD spots were targeted into the glomerular layer of a sagittal olfactory bulb slice, from a transgenic mouse expressing ChR2-YFP in the olfactory sensory neurons. *(3)* Wide-field images of the emitted florescence from regions in the sample illuminated by the DMD spots. *(4)* Two-photon image of the same slice: photobleached regions indicate the location of the DMD spots previously shown. Note the precise spatial correspondence between the desired and actual location of the projected photostimulation patterns

9.2.3 Choice of the Light Source

The choice of light source is critical and has important consequences for photostimulation experiments. A simple and cheap solution is to use LEDs (a *noncoherent* source), which come in different colors and have high luminance for effective optogenetic manipulations. Since noncoherent light cannot be perfectly collimated, the effective power decreases steeply with distance from the light source, imposing constraints in the ability to stimulate opsins [26].

Other noncoherent light sources, including the arc lamps found inside projectors, have generally high power and a wide wavelength spectrum, thus permitting multicolor excitation.

If power is still limiting (for example, when photostimulating multiple large regions), lasers can be used as light sources for a DMD. Laser light is coherent and propagates through space with minimal power loss, which makes it possible to place the light source farther from the DMD. Additionally, the photostimulation pattern at the sample has higher contrast between its ON and OFF pixels compared to noncoherent sources. This is due to the fact that it is impossible to focus noncoherent

light from an extended source (such as a lamp or an LED) to a diffraction-limited spot or equivalently to create sharp edges in the pattern. The disadvantage is that laser light will produce higher-order diffraction replicas of the pattern (*ghosts*) from the physical edges of the micromirrors. To get rid of the ghost patterns, a variable aperture diaphragm can be placed in the optical path.

9.2.4 Trade-off Between Field of Stimulation Size and Resolution

The use of a telescope to image the DMD or LED array into the sample determines the size of the FoS, as well as of individual excitation spots (pixels). The latter is defined as the theoretical resolution of the photostimulation system. The size of individual pixels and of the FoS is determined by the ratio of the focal lengths of the objective and the tube lens (demagnification, Eq. 9.2). There is, thus, a trade-off between the maximum size of the FoS and the resolution. For example, let us consider a gallium arsenide LED array (64×64, 20 μm diameter, 50 μm spacing) [48] imaged onto the sample with a 1:1 size ratio (using same focal length lenses). This results in an FoS of $\sim 3 \times 3$ mm^2. The theoretical resolution in this case is simply the size of an individual LED (~ 20 μm). To obtain a better resolution (e.g., ~ 2 μm), the entire LED array needs to be demagnified 10 times at the sample using appropriate lenses, which also results in 10 times smaller size of the FoS ($\sim 0.3 \times 0.3$ mm^2). For the same reasons, in case of a DMD, the size of an individual pixel at the sample and the size of the FoS are inversely related. Since DMD devices have large number of micromirrors, it is theoretically possible to have a much smaller excitation spot (~ 1 μm) at a reasonable FoS size (~ 1 mm) (Table 9.1). However, in practice, this is a lower bound, since the actual photostimulation resolution is constrained by scattering in the sample.

9.2.5 Applications

Over the past decade, DMDs have been used not only as projection systems, but also in a wide variety of other applications. In epifluorescence microscopes, DMDs have been placed in the illumination path to shape the excitation beam. DMDs have also been integrated in confocal microscopes to achieve spatial discrimination in the absence of a pinhole [51].

Patterned illumination strategies using DMDs for optogenetic stimulation are becoming increasingly popular. Initially, such approaches were successfully used to stimulate light-sensitive ionotrophic glutamate receptors in cultured neurons [52] and ChR2-expressing ganglion cells in retinal explants [53]. DMD technology has been used to deliver light to select regions of the spinal cord in zebrafish [54, 55] and in immobilized *C-elegans* [56]. Recently, behavioral tracking of locomoting *C-elegans* was combined with DMD technology to illuminate target sites in a closed-loop design [57, 58].

DMD-based optogenetic stimulation has been effectively combined with neuronal readout methods, such as extracellular or patch clamp recordings. A commercial projector system was used to excite input nodes called glomeruli (one at a time) in the olfactory bulb (OB) of genetically engineered mice that express ChR2 in the terminals of olfactory sensory neurons (OSNs) [59, 60]. Simultaneous extracellular recordings from pairs of output neurons (mitral/tufted cells) enabled the investigation of the interplay between common input and lateral local signals within the circuit [59] and temporal integration rules in different brain regions [60]. In zebrafish, DMD technology coupled to optogenetic activation was used to excite ensembles of mitral cells [61], as well as genetically targeted interneurons in the OB [62]. Varying the distribution of pixels in the ON vs. OFF states (at a carrier frequency of 20 Hz) allowed the manipulation of the synchrony of neuronal ensemble activation. Simultaneous intracellular recordings in a cortical target region allowed them to investigate the role of input synchrony in determining the firing rate/spike timing of target cells [61].

Further, DMD stimulation can be coupled with two photon microscopy to read out activity patterns from a large number of cells as opposed to one or a few cells accessed by electrical recordings (Sect. 9.3.11).

All these studies demonstrate the effectiveness and the potential of using DMD-based approaches for optogenetic manipulation of neuronal ensembles coupled to various readout methods for studying neuronal circuit dynamics.

9.2.6 Limitations

Light propagating deep into biological tissues is subjected to scattering. This is an important constraint for one-photon light patterning techniques (Table 9.1), since scattering deteriorates the spatial precision of stimulation and causes ballistic power loss (that is loss of nonscattered photons). For example, the *mean free path* in brain slices for light of 405 nm is 25 μm [63]. This corresponds to a residual power of $<2\,\%$ at a depth of 100 μm from the surface of the slice. Because of the use of longer excitation wavelengths and its nonlinear nature, two-photon illumination is more resistant to scattering and thus the technique of choice to image and photostimulate deeper in the brain [64, 65]. Unfortunately, two-photon stimulation requires high power exactly due to nonlinear absorption processes. This approach is not compatible with intensity-modulation techniques since light patterning is obtained by blocking the illumination light in pixels corresponding to off-target locations at the sample, which results in substantial power loss. Within these constraints, a more efficient strategy is shaping the illumination such that all available light is redirected toward the targets in the sample. In phase-modulation light patterning techniques, this is achieved by modifying the phase of the illumination light using an SLM device as described in Sect. 9.3.

Table 9.1 Comparison of intensity and phase based patterned illumination techniques

	Intensity modulation techniques	Phase-modulation techniques
Size of FoS	~ several mm^2	< 400 x 400 x 400 μm^3 (2p)
Spatial resolution	x-y ~ 1–10 μm; z ~ 1–100 μm	Superior, x-y and z ~ 1 μm (2p)
Tissue axial penetrance	Poor, < 100 μm	Superior, < 500 μm (2p)
Temporal resolution	60 Hz–5 KHz	Nematic LC-SLM, 60–200 Hz
Number of targets	Tens-hundreds	Few tens (2p)
Coupling to imaging/ ephys readout methods	Easy to implement	Easy to implement

9.3 Light Patterning by Phase Modulation

9.3.1 General Principle

The *phase* of a wave can be defined as the fraction of the oscillation cycle that the wave has travelled at a particular time point. Referring back to Eq. (9.1), describing the electric field oscillating in space at a given time, the phase is given by the angle ψ:

$$E(\vec{r}) = A(\vec{r})e^{i\psi(\vec{r})} \tag{9.1}$$

It is helpful to introduce the concept of *wavefront*, as the spatial envelope of all points where the light electric field has the same phase at a given time. For example, a collimated laser beam has a planar wavefront, since the light electric field at all the points in any plane perpendicular to the direction of propagation has the same phase (Fig. 9.4a). Modulating the phase of a light beam can thus be thought of as changing the shape of its wavefront. This is a recurring event in any optical setup. For example, a lens focusing a collimated laser beam into a point is an SLM that changes a planar wavefront into a spherical one (Fig. 9.4a), while a *diffraction grating* is an SLM that produces a phase gradient equivalent to a tilted wavefront (Fig. 9.4b). The shape of the wavefront impinging on a lens (e.g., on the microscope objective) determines the light distribution beyond that lens. For example, a collimated laser beam (planar wavefront) will be focused at the focal point of the objective. However, a divergent laser beam (convex wavefront) will be focused beyond the focal plane, and a convergent beam (concave wavefront) will be focused before the focal plane (Fig. 9.4c). Introducing a tilt in the wavefront at the back aperture of the objective displaces the focused point laterally in the front focal plane of the objective: the larger the tilt, the bigger the lateral displacement (Fig. 9.4d).

Thus, through simple modifications (curvature, tip, or tilt) of the wavefront shape at the back focal plane of the microscope objective, the intensity distribution can be altered at the sample and the focused laser point can be displaced in 3D. By implementing more elaborate modulations of the wavefront, arbitrary intensity patterns can be obtained, including multiple spots in 2D and 3D, as well as light

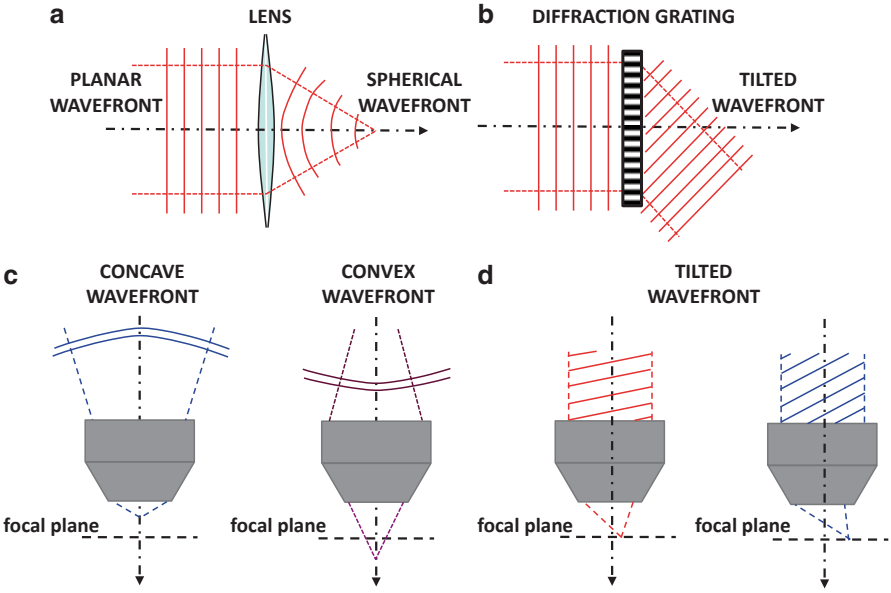

Fig. 9.4 Wavefronts. **a** A planar wavefront propagating parallel to the optical axis is transformed by a lens into a spherical wavefront. The light is focused into a diffraction-limited spot at the focal point of the lens. **b** The propagation direction of a planar wavefront is changed by a diffraction grating. Note that, for simplicity, only the +1 diffraction order is represented. **c** Examples of concave (*left*) and convex (*right*) wavefronts impinging onto the back aperture of a microscope objective. Light is focused by the objective in a point above and below the focal plane, respectively. **d** Example of tilted wavefronts impinging onto the back aperture of a microscope objective. Light is focused into a diffraction-limited spot laterally displaced from the focal point of the objective. A steeper tilt (*right*) causes larger displacement

profiles reproducing the shape of biological objects (i.e., cell bodies, dendritic or axonal branches). This principle constitutes the basis of phase-modulation light patterning techniques such as digital holography [66–68], described in this section.

9.3.2 Optical Configuration

In digital holography, light patterning at the sample is obtained by modulating the phase of a collimated laser beam at the back focal plane of the microscope objective. Since the back focal plane of the objective is not physically accessible, phase modulation is implemented by placing an SLM in a conjugated plane. The SLM is composed of a 2D matrix of ~500,000 liquid crystals, hence its name—liquid crystal spatial light modulator (LC-SLM, Box 2). Each LC-pixel can be independently controlled to introduce a desired phase delay to the incident light. The overall wavefront modulation is the envelope of the individual LC-pixel contributions.

Box 2: Technical Specification of DMD and LC-SLM Chips

Digital Micromirror Device

The digital micromirror device (DMD), as the name suggests, is an array of aluminium micromirrors manufactured by Texas Instruments. It comes in various array sizes such as extended graphics array (XGA, 1024×768), super-extended graphics array (SXGA+, 1400×1050), etc, each micromirror dimension being either 13.7 or 10.8 μm. The reflectivity is usually high for a broad range of visible wavelengths (400–700 nm). Each micromirror can be tilted at an angle of $-12°$ or $+12°$, with respect to the normal (perpendicular to the DMD plane), by a hinge that runs diagonally. Each mirror is electronically controlled to switch between ON ($+12°$) or OFF ($-12°$) positions independently. A CMOS static random access memory (SRAM) cell underneath each mirror determines the direction of the tilt by electrostatically pulling either of its two free corners. The process of loading the memory cell with a 1 or a 0 is decoupled from the physical movement of the micromirrors, which is synchronized to a separate clock signal. This signal can be applied to specific sectors, or to the whole chip all at once. The optomechanics are robust enough to avoid hysteresis in the movement of the micromirrors. Under normal operation, the mirrors must sit at either of the two tilts and can only return to rest (0°) when the array is set into the "parked" mode. The time it takes for the entire array to refresh is ~150 μs, making it ideal for fast and precise temporal control. Basic functions to operate the DMD via control boards can be implemented in software available from the manufacturers in conjunction with LABVIEW or C/C++.

Liquid Crystal Spatial Light Modulator

Each pixel in a *liquid crystal spatial light modulator* (LC-SLM) chip is composed of a layer of liquid crystals (LC) sandwiched between the two poles of a transparent electrode. LC are birefringent materials characterized by a molecular anisotropy, resulting in perpendicular axes of symmetry with different associated refractive indices (ordinary and extraordinary): The actual refractive index experienced by light travelling through the LC depends on the relative orientation between these axes and the polarization plane of the incident laser beam [72]. A change in the applied voltage causes the LC molecules to reorient, triggering a change in refractive index.

Since the amount of phase delay experienced by light in a medium is proportional to the refractive index, spatial phase modulation can be achieved by varying the voltage applied within each pixel of the SLM. The relationship

between the applied voltage and the resulting phase modulation (lookup table, LUT) is typical of each instrument and generally provided by the manufacturer. Often, instead of the actual voltage value, the LUT is specified in terms of number of bits (which express the grey levels) sent to the computer interface performing the digital-to-analog (D/A) conversion.

The velocity of re-orientating the LC molecules within each pixel depends on the LC material, on the thickness of the LC layer, and on the type of voltage signal applied to the electrode [72]. These parameters, together with the choice of the D/A interface, determine the maximum refresh rate of the LC-SLM (Sect. 9.3.6).

In reflective LC-SLMs, a dielectric mirror is mounted behind the LC layer. In order to minimize light loss, the reflectivity of the mirror needs to be high (>90%) for the wavelength of interest. This requires the mirror to be appropriately coated. It is possible to coat the mirror with multiple layers in order to achieve high reflectivity for a wider range of wavelengths at the expense of potentially compromising the flatness of the mirror, a key parameter to assure uniform phase modulation across the LC-SLM chip.

A schematic of a typical setup for digital holography is represented in Fig. 9.5. A collimated laser beam is used as the illumination source, to ensure that a planar wavefront impinges onto the SLM plane. The beam is first magnified by a beam expander (L1-L2 in the figure), in order to fully illuminate the LC-SLM chip. The beam is then reflected by the LC-SLM onto a second telescope (L3-L4) that produces an image of the LC-SLM chip in the back focal plane of the microscope objective. This telescope must be aligned in a *4 f configuration*, meaning that its composing elements (LC-SLM, L3, L4, objective back aperture) are at focal distances from one another (Fig. 9.5). This configuration is convenient, since it allows access to two fundamental planes of the optical system: a plane conjugated to the back focal plane of the objective (Fig. 9.5*, blue*), where the LC-SLM chip sits and where the phase modulation occurs, and a plane conjugated to the front focal plane of the objective (the sample plane, Fig. 9.5, *green*). Within this configuration, a real magnified image of the actual pattern projected into the sample is formed around the L3 front focal plane, allowing rapid visual inspection.

9.3.3 Algorithms for Digital Holography

The main goal of digital holography is to establish what phase distribution at the back focal plane of the microscope objective (and hence at the LC-SLM) will result in the desired light intensity distribution into the sample. The back focal plane of the objective (also called pupil plane) sits inside the lens and is not directly accessible, but, for practical purposes, it can be approximated by the back aperture. Determin-

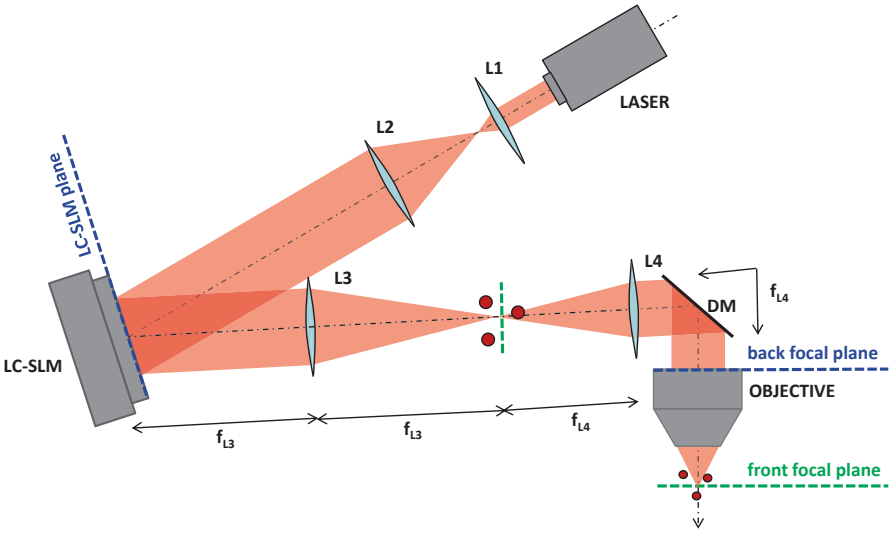

Fig. 9.5 Digital holography—optical configuration. A beam expander formed by lenses L1-L2 magnifies a laser beam to illuminate the LC-SLM chip. A telescope formed by lenses L3-L4 images the LC-SLM chip onto the back aperture (*back focal plane*) of the microscope objective. The objective transforms the phase profile implemented by the LC-SLM into the desired intensity pattern at the sample. Note that a magnified replica of this pattern is formed at the front focal plane of L3. A dichroic mirror (DM) placed above the objective rotates the illumination beam, so that it impinges perpendicularly onto the back aperture of the objective

ing the phase profile at the back focal plane can be solved computationally, and many algorithms have been developed to generate phase profiles (masks) that result in 2D or 3D light patterns of choice. A complete review of these algorithms [69–72] is beyond the scope of this chapter. However, it is important to illustrate some basic strategies which may help the reader understand the physical principles underlying digital holography.

Generating a 3D Distribution of Diffraction-Limited Spots One can place a diffraction-limited spot in 3D by creating an appropriate phase profile at the back aperture of the objective. In order to analytically determine this phase profile, the phase (ψ) at each point of the back aperture needs to be expressed as a function of the spot position in the sample space $(\vec{r}(x_r, y_r, z_r))$. By describing the phase at the back aperture in polar coordinates, ϕ (azimuth angle) and ρ (normalized radius), the phase profile generating the target spot can be written as follows (for derivation, see Botcherby et al. [73]):

$$\psi\left(\rho,\phi,\vec{r}_p\right) \approx n\frac{2\pi}{\lambda}\left(x_p\rho\sin\alpha\cos\phi + y_p\rho\sin\alpha\sin\phi + z_p\sqrt{1-\rho^2\sin^2\alpha}\right), \quad (9.3)$$

where λ is the wavelength of the light and $n*\sin\alpha$ is the numerical aperture (NA) of the objective. The lateral displacement of the target spot is controlled by the first

two terms of the equation, which depend on ϕ and describe a tip (x displacement) and tilt (y displacement) in the phase. The axial (z) displacement (lens effect) of the target spot is controlled by the last term in the equation. The electric field generating the target spot can then be obtained by substituting the phase ψ into Eq. (9.1):

$$E_p\left(\rho,\phi,\overrightarrow{r_p}\right) = A_0 e^{i\psi\left(\rho,\phi,\overrightarrow{r_p}\right)} \tag{9.4}$$

The principle of superposition of waves allows one to calculate the total electric field resulting in a 3D distribution of multiple spots by simply summing the electric fields corresponding to each independent spot:

$$E_{TOT} = \sum\nolimits_p E_p = \sum\nolimits_p A_0 e^{i\psi\left(\rho,\phi,\overrightarrow{r_p}\right)} \tag{9.5}$$

To reconstruct exactly E_{TOT} at the back aperture of the microscope objective, modulation of both the phase and the amplitude of the electric field is required (Eq. 9.5). However, 3D spot patterns can still be generated by modulating only the phase. An easy way is to calculate E_{TOT}, but consider only the resulting phase modulation as the LC-SLM mask, discarding the intensity component (*superposition of prisms and lenses*) [74]. This algorithm is fast and directs light to the target spots rather efficiently [69]. However, since the algorithm neglects the intensity component, the light distribution among different spots is not uniform, especially if the desired photostimulation pattern contains symmetrical arrangements of spots. Adding a random term to the phase of individual spots improves the uniformity of the intensity pattern in the sample (*random superposition*) [75]:

$$E_{TOT} = \sum\nolimits_p E_p = \sum\nolimits_p A_0 e^{i\psi\left(\rho,\phi,\overrightarrow{r_p}\right)} e^{i\psi random} \tag{9.6}$$

Neuronal targets are often not symmetric, in which case the random superposition algorithm might be good enough for practical purposes. Efficiency and uniformity can be further improved using iterative algorithms, such as *Gerchber-Saxton* [76] and *weighted Gerchber-Saxton* [69, 77], at the expense of computational load.

Generating Arbitrary 2D Patterns When aiming at photostimulating neuronal cell bodies and projections, one needs to generate extended 2D patterns, shaped on the target structures. Creating these patterns by placing multiple individual spots next to each other is computationally expensive [72]. A shortcut has been used for calculating extended patterns in the front focal plane of the microscope objective. This strategy exploits a fundamental property of light diffraction, namely the fact that the light electric field at the back focal plane of a lens is the Fourier transform (FT) of the light electric field at its front focal plane [78]. Knowing the desired intensity distribution at the front focal plane of the microscope objective, it is then possible to

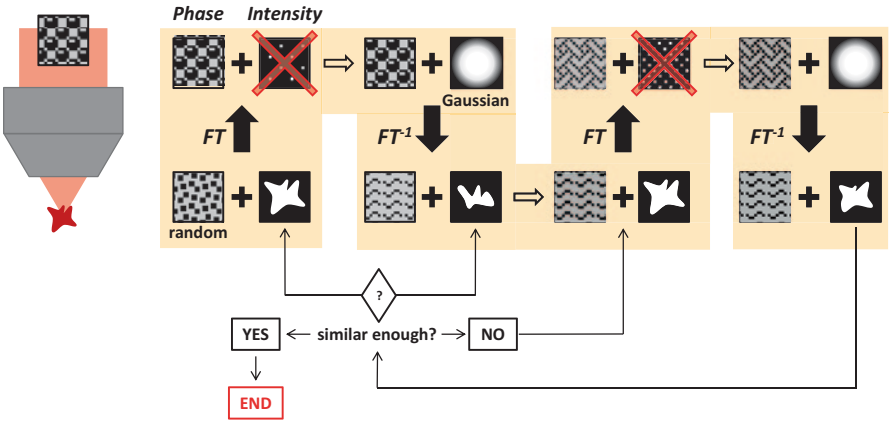

Fig. 9.6 Iterative Fourier transform algorithm (*IFTA*). Schematic of the IFTA algorithm used to generate 2D holographic patterns, as described in Sect. 9.3.3

derive the corresponding electric field at the back focal plane by simply taking the FT. Importantly, an exact solution of the FT requires modulation of both intensity and phase. One way around this problem is, again, to discard the intensity modulation of the light electric field at the back focal plane of the objective and use an iterative algorithm to generate an optimized phase mask.

An example is the *iterative Fourier transform algorithm* [66, 79], based on the *Gerchber-Saxton* routine [76] (Fig. 9.6). Briefly, an initial electric field is calculated at the front focal plane of the objective, combining the desired amplitude distribution with a random phase:

$$E_0(x,y) = A_D(x,y)e^{i\psi_0(x,y)random} \tag{9.7}$$

A first iteration is performed by:

a. calculating the FT of E_0, which corresponds to the electric field at the back focal plane of the objective (as if virtually propagating $E_0(x, y)$ from the front to the back focal plane of the objective):

$$G_0(x',y') = FT\,E_0(x,y) \tag{9.8}$$

where x', y' are the coordinates for a given point in the back focal plane;

b. discarding the amplitude of G_0 and substituting it with the amplitude profile of the laser beam impinging on the LC-SLM (generally a 2D Gaussian):

$$G_1(x',y') = A_G e^{i\psi_1(x',y')} \tag{9.9}$$

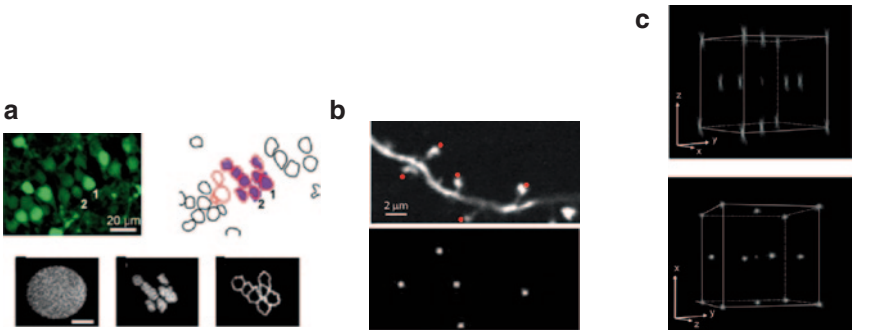

Fig. 9.7 Example holographic patterns. **a** Holographic spots were targeted onto CA1 neurons in a hippocampal slice (*top*). Images of the holographic patterns projected onto a thin (1 μm) fluorescent layer (*bottom*) (Adapted from Zahid et al. [82]). **b** *Top*: two-photon fluorescent image of a dendrite of a pyramidal neuron in a mouse cortical slice. *Red dots* indicate desired positions for the photostimulation spots. *Bottom*: Image of the photostimulation spots generated by digital holography (Adapted from Nikolenko et al. [67]). **c** 3D distribution of holographic spots (*top*: y–z projection; *bottom*: x–y projection) (Adapted from Yang et al. [77])

c. applying an inverse FT (FT^{-1}) to G_1, thus obtaining an updated value for the desired electric field at the front focal plane of the objective (as if virtually propagating $G_1(x', y')$ from the back to the front focal plane of the objective):

$$E_1(x, y) = FT^{-1}G_1(x', y') \tag{9.10}$$

The intensity distribution at the sample is calculated as the squared amplitude of $E_1(x, y)$ and then compared with the desired intensity pattern. If the two are sufficiently similar (least square minimization), the algorithm ends here. If further improvement is required, the amplitude of $E_1(x, y)$ is discarded and substituted with the desired amplitude distribution, while the phase is conserved:

$$E_2(x, y) = A_D(x, y)e^{i\psi_1(x,y)} \tag{9.11}$$

A *second iteration* cycle begins. The algorithm rapidly converges to an optimal solution, after ~8 iterations [66].

Examples of 2D and 3D patterns obtained by the algorithms described above and imaged on a thin fluorescent cover slip are shown in Fig. 9.7.

9.3.4 Resolution and Precision of Stimulation

In intensity modulation techniques, theoretical resolution is determined by the size of the micromirror in a DMD, or miniaturized light source in an LED array im-

aged at the sample. This one-to-one correspondence between SLM actuators and illumination pixels in the sample is lost in digital holography, where the LC-SLM is placed in a plane conjugated to the back focal plane of the microscope objective. As a result, the light diffracted by every actuator (pixel) of the LC-SLM contributes to all points of the pattern in the sample.

The theoretical resolution of a digital holography system is generally defined as the size of the smallest diffraction-limited spot generated at the front focal plane of the microscope objective. This, in turn, is determined by the numerical aperture (NA) of the objective. Specifically, if the back aperture of the objective is completely filled by the holographic beam, the resolution is equal to the objective resolution (Abbe limit) at the chosen illumination wavelength, just as in imaging systems:

$$x_{min} = y_{min} = \frac{0.61\lambda}{NA} \quad \text{and} \quad z_{min} = \frac{2\lambda n}{NA^2}, \tag{9.12}$$

where λ is the wavelength of the illumination light, NA is the numerical aperture of the microscope objective, and n is the refractive index. In experimental configurations where the back aperture of the objective is underfilled, the resolution depends on the actual numerical aperture ($NA = f_{obj}/r$, where f_{obj} is the focal length of the objective and r is the radius of the holographic beam at the back aperture).

To maintain maximum resolution when placing spots in 3D, it is important to take into account spherical aberration. Indeed, microscope objectives perform as ideal (aberration free) imaging systems only at the focal plane (sine configuration), while the image (in this case the holographic pattern) is rapidly degraded by spherical aberration as it is displaced away from the focal plane [73]. Luckily, it is possible to use the LC-SLM to compensate for spherical aberration [77, 80].

Note that in digital holography, extended spots are generated by shaping the illumination wavefront (iterative Fourier transform algorithm), without underfilling the back aperture of the microscope objective. This results in an improvement of both lateral and axial precisions with respect to spots of the same size obtained by underfilling the back aperture of the objective with a Gaussian beam (Fig. 9.8) [66]. For example, for a 0.8 NA objective, the axial resolution (measured as full-width half maximum of the light intensity profile) of a holographic spot scales as 2× the diameter of the spot (as opposed to the square of the diameter for *Gaussian spots*) [66]. The precision further improves in two-photon photostimulation (Sect. 9.3.7), due to nonlinear effects and the axial resolution (for similar NA objective) is comparable to the spot diameter [81]. For currently available opsins and caged compounds, a single-cell body can be efficiently stimulated with a spot of 10–15 μm diameter [66, 82–84], which corresponds to an axial precision of 20–30 μm or 10–15 μm for one-photon and two-photon digital holography, respectively. In many cases, this precision is sufficient for simulation of single cells, when working at a minimum (but reliable) light power regime [66, 82].

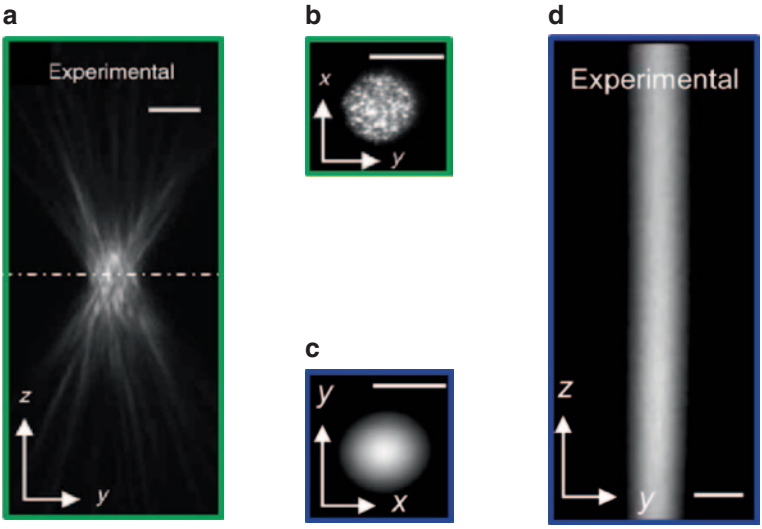

Adapted from Lutz et al. 2008

Fig. 9.8 z-profile of holographic spots. Images of a holographic (**a, b**) and a Gaussian spot (**c, d**) of the same diameter. Lateral (**b, c**) and axial projections are compared (Adapted from Lutz et al. [66])

9.3.5 Trade-off Between FoS Size and Resolution

In digital holography, the FoS cannot be thought of simply as a scaled version of the LC-SLM chip. However, a relationship between the size and number of the LC-SLM pixels and the extent of the FoS can be derived following the laws of diffraction.

For determining the 2D FoS, one can exploit, once again, the fact that the front and back focal planes of the objective are related by an FT. A first step is to calculate the actual electric field at the back focal plane, which is the electric field at the LC-SLM, spatially magnified by a telescope (L3-L4 in Fig. 9.5). This electric field can be described as the continuous holographic profile broken up into discrete units, each corresponding to individual pixels of the LC-SLM (Fig. 9.9a). Mathematically, the LC-SLM chip imaged in the back aperture of the objective is represented as the convolution of a *comb function* with periodicity equal to the interpixel distance and a *rectangular (rect) function* representing the shape of individual pixels. These functions, when multiplied by the electric field corresponding to the holographic phase profile, give the actual electric field at the back focal plane of the objective.

The second step consists in propagating the discretized electric field thus calculated to the front focal plane by inverse FT. The result is illustrated in Fig. 9.9b: note how FT converts multiplications into convolutions and vice versa. Importantly, the resulting light pattern at the front focal plane of the objective is filtered (convolved)

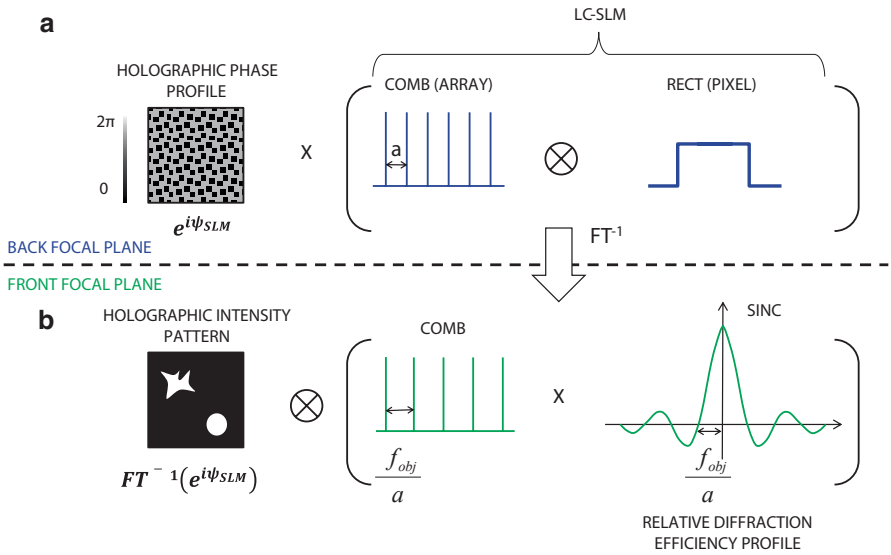

Fig. 9.9 Inverse Fourier transform of the light electric field between the back and the front focal plane of the objective in digital holography. **a** Back focal plane: The image of the LC-SLM at the back focal plane of the objective is the convolution of a comb function with periodicity equal to the interpixel distance, and a rect function representing the shape of an individual pixel. This function is multiplied by the electric field corresponding to the holographic phase profile. **b** Front focal plane: The inverse Fourier transform (FT^{-1}) performed by the objective converts convolution into multiplication and vice versa. As a consequence, the desired holographic intensity pattern is convolved by the product of a comb function with a sinc function (FT^{-1} of the LC-SLM comb function and the pixel rect function, respectively). ψ_{SLM} : phase profile at the LC-SLM/back focal plane; a : pixel size at the back focal plane; λ : wavelength of the illumination light; f_{obj} : focal length of the microscope objective

by a sinc function arising as the inverse FT of the pixel rect function. This transformation results in an inhomogeneous, bell-shaped lateral intensity profile of the following form [71, 77]:

$$\frac{I_{spot}}{I_0} = \left(\frac{\sin x^*}{x^*}\right)^2 \left(\frac{\sin y^*}{y^*}\right)^2, \; with \; x^* = \left(\frac{\pi a}{\lambda f_{obj}} x\right) \; and \; y^* = \left(\frac{\pi a}{\lambda f_{obj}} y\right) \quad (9.13)$$

(I_{spot}: intensity of a holographic spot at any location in the focal plane of the objective; I_0: intensity of a spot at the focal point of the objective; a: size of the image of one pixel of the LC-SLM at the back aperture of the objective; f_{obj}: focal length of the objective; x, y: coordinates at the sample plane).

The ratio (I_{spot}/I_0) is referred to as relative diffraction efficiency of the system. Most of the available power (>90%) is contained in the first order of the sinc function, whose first zero values at $x_0 = y_0 = \lambda f_{obj}/a$ define the accessible FoS. In many applications, the FoS is further limited to the region where relative diffraction

efficiency is ≥50%, which ensures higher uniformity of intensity and avoids ghost spots (Sect. 9.3.8).

Note that the extent of the illumination field is inversely proportional to the size of the LC-SLM pixel imaged at the back focal plane of the objective. As a consequence, the resolution and extent of the FoS are not independent. In fact, maximal resolution requires that the image of the LC-SLM chip fills the back aperture of the objective. For a given number of pixels in the chip of the LC-SLM, this sets the size of the pixel imaged at the back aperture (a) and thus the extent of the FoS. Larger FoS can be obtained by underfilling the back aperture (smaller a), at the expense of resolution.

In the axial direction, the relative diffraction efficiency also decreases as the stimulation point is moved away from the focal plane of the objective [71, 77]. Indeed, the LC-SLM behaves as a diffraction grating of periodicity equal to the interpixel distance. Light diffracted from a single LC-SLM pixel propagates from the pupil of the objective to the sample within a cone of half angle $\theta = \lambda/2a$. This limits the extent of the axial region illuminated by LC-SLM pixels imaged at the border of the objective back aperture and causes a decrease in relative diffraction efficiency for points farther away from the focal plane [77]. The maximal achievable axial displacement of a holographic point is limited by the numerical aperture of the microscope objective to $\sim \lambda n f_{obj} / 2aNA$ [72, 77]. The bell-shaped profile of the relative diffraction efficiency can be computed numerically, by adding the contribution of all LC-SLM pixels to a stimulation point in the sample at different positions along the optical (z-) axis [77].

As an example, for an illumination wavelength of 1060 nm, considering a typical pixel size at the back focal plane of the objective of ~20 μm and a 20×, 1.0 NA objective with focal length 9 mm, the 3D FoS of digital holography is $\sim 400 \times 400 \times 400\ \mu m^3$ (Table 9.1).

9.3.6 Dynamical Alternation of Patterns

Different phase profiles can be sequentially displayed by LC-SLMs, resulting in dynamical alternation of light patterns at the sample. However, the refresh rate is limited by the response time of the liquid crystals (LC), the properties of the electronic circuit driving the chip, and the type of interface between the LC-SLM and the computer.

Different types of LC have specific response times. Ferroelectric LCs can alternate phase profiles at KHz rates, but they are limited to a binary phase modulation [85]. This greatly reduces diffraction efficiency (to a theoretical upper limit of 40% and often a lower actual value) [71].

Nematic LCs are more commonly used to build LC-SLMs for digital holography, since they allow finer phase modulation (typically 8-bit, 256 values for a full 2π phase modulation) and better diffraction efficiency (>85%, for a diffraction-limited point near the center of the FoS) [85, 86]. However, their increased viscosity

reduces the response time by an order of magnitude. Moreover, both the response time and the maximum amount of phase delay introduced by a nematic LC-SLM are proportional to the thickness of the LC layer. Reflective LC-SLMs, where incident light travels twice through the LC layer, are almost always preferred to transmission ones, since they allow a better compromise between the maximum phase delay and the refresh rate [70]. Nematic LC-SLM models available on the market (Hamamatsu, Boulder) have refresh rates on the order of 60 Hz, if coupled to a DVI computer interface, and >100 Hz (Table 9.1) with a PCIe interface. Phase profiles can generally be pre-calculated and loaded into the interface, while the timing of presentation is controlled by an internal clock.

9.3.7 Two-Photon Digital Holography

The basic alignment of a digital holography setup does not change between one-photon and two-photon systems, apart from the need for specific reflective coatings on the LC-SLM and the other optical elements (lenses, mirrors), which should match the appropriate wavelength range.

Effects of scattering on two-photon excitation of a small diffraction limited spot have been extensively characterized in the framework of two-photon imaging [65, 87, 88] and are mostly limited to loss of ballistic power. Recent work also explored the propagation of holographic patterns deep into brain tissue. Experimental data and computer simulations showed that holographic patterns are more robust to scattering than Gaussian spots of comparable size and maintain their x–y spatial coherence, as well as z-confinement up to a depth of ~250 μm (λ = 800 nm) [84, 89]. The robustness to scattering is due to the much broader angular spectrum (i.e., spatial frequency) content of a holographic beam compared to a low-NA, Gaussian beam, which must underfill the back aperture of the objective in order to generate a spot of comparable size. The broad angular content makes the holographic beam less sensitive to small perturbations in spatial frequency induced by scattering in the tissue, allowing nearly undistorted propagation of the holographic pattern. The depth penetrance of holographic beams can be further increased (up to 500 μm, Table 9.1) by coupling digital holography with temporal focusing [81, 84, 90, 91].

Temporal focusing [90, 91] utilizes a diffraction grating to disperse the spectral components of the laser pulse, thereby widening the temporal profile of the illumination beam. The separated frequencies travel different paths through the tissue and recombine only in the front focal plane of the objective. As a result, the laser pulse reaches its minimum duration only in the focal plane allowing maximal probability for two-photon absorption. This confines the two-photon excitation to a few micrometers (~5 μm) [81] above and below the focal plane, significantly improving the z-confinement of the holographic pattern. Temporal focusing also improves the spatial homogeneity of the holographic pattern when propagating through scattering samples [84, 89]. Importantly, while temporal focusing allows deeper penetration, it is associated with power loss at the diffraction grating (~20%). Therefore,

when implementing this strategy, power loss due to the combined effects of optics and scattering must be first characterized in order to estimate the number of targets that can be modulated optically in the deep layers.

One disadvantage of two-photon versus one-photon excitation is the higher power requirement, due to the dependence of two-photon absorption probability on the squared intensity of the illumination light. This limits the number of targets that can be stimulated simultaneously by two-photon digital holography. In digital holography, the available power is split among the illuminated spots, proportionally to their area. Thus, for a constant illumination power, the intensity in a circular area of radius R will be about fourfold lower than that in a spot of radius R/2, and the two-photon absorption probability will decrease by 16-fold. On the other hand, larger spots are often more efficient at stimulating neurons. Opsins such as Channelrhodopsin 2 (ChR2) have a relatively large two-photon *cross-section*, but a low single-channel conductance [45]. Thus, a neuron expressing ChR2 is optimally activated by a low-intensity (>0.2 mW/μm^2) spot, covering the entire cell body [83, 84]. 2D extended patterns can be used to activate multiple neurons simultaneously, with stimulation pulses of a few milliseconds [84, 89, 92].

An alternative solution is to rapidly scan a small diffraction-limited two-photon excitation spot across a neuronal cell body, recruiting multiple opsin molecules sequentially [45]. This approach is particularly efficient for ChR variants with increased single-channel conductances and longer off-time kinetics [93, 94]. In one implementation of this strategy, a 3D distribution of diffraction-limited holographic spots is generated to target multiple neuronal cell bodies. The holographic beam is then scanned by galvanometric mirrors, such that all the spots are simultaneously steered through the target cell bodies. This approach has the potential to allow simultaneous activation of a larger number of cells, at the expense of longer simulation times (tens of milliseconds, with the currently available ChR variants) [93].

To date, a study assessing the maximum number of neurons that can be activated simultaneously by two-photon digital holography is still lacking. Given currently available laser technology, opsin variants, and constraints imposed by tissue photodamage, a reasonable estimate for the number of neurons that can be simultaneously modulated using two-photon digital holography is in the range of a few tens [47, 84, 93].

9.3.8 Caveats

Zeroth Diffraction Order and Ghost Spots The LC-SLM behaves as a diffraction grating. As such, it modulates a fraction of the incident light to form a first diffraction order (the desired spot pattern). However, an important fraction of incident light, corresponding to the constant component of the electric field (zeroth diffraction order), remains unmodulated and is focused into a diffraction-limited spot at the sample. Yet another fraction of the incident light is lost as ghost spots, fainter replicas of the desired spot pattern.

There are two sources of ghost spots. One set of ghosts is generated by the phase-only modulation algorithm, as higher harmonics (higher diffraction orders) of the basic frequency in the LC-SLM diffraction grating. Another set of ghosts results from the pixelated nature of the LC-SLM (Fig. 9.9). At the front focal plane of the objective, a replica of the spot pattern is generated periodically due to the convolution of the spot pattern with the comb function arising from the pixelated nature of the LC-SLM. The period of these ghost spots is given by $\lambda f_{obj}/a$ (a, SLM pixel size imaged at the back aperture of the objective) and is equal to the half-width of the bell-shaped relative diffraction efficiency profile (Sect. 9.3.5, Eq. 9.13). Hence, by reducing the effective FoS ($FoS=2\lambda f_{obj}/a$) by half, these ghosts spots can be prevented from reaching the sample [71]. This can be easily achieved by placing a variable aperture diaphragm in a plane conjugated with the sample plane (e.g., focal plane of L3, Fig. 9.5). In the same plane, it is convenient to insert a small block (as simple as a black-painted aluminium foil glued on a glass cover slip) to mask the focused zeroth-order component [66]. If blocking part of the field of view to eliminate the zeroth-order and the undesired diffraction components is not feasible, alternative strategies can achieve the same effect [71, 82, 95]. Finally, an appropriate choice of the LC-SLM helps reduce the amount of light directed into the zeroth-order and ghost spots (Sect. 9.3.9). Corrections to the basic digital holography algorithms discussed in Sect. 9.3.3 also improve efficiency in directing light toward the desired spots [69, 70, 86].

High Frequency Spatial Intensity Inhomogeneities Figures 9.7 and 9.8 show examples of extended 2D holographic patterns, imaged on a thin fluorescent layer. It is immediately apparent that the intensity of the patterns is not homogeneous, but rather characterized by high-frequency inhomogeneities (speckles). The origin of speckles is the IFTA algorithm used to generate the holographic patterns (Sect. 9.3.3), since the phase at the front focal plane of the objective is treated as a free parameter. As a consequence, overlapping points in the pattern can have completely different phases, interacting constructively (bright speckles) or destructively (dark speckles) [96]. The effect is particularly evident for two-photon excitation, given that the quadratic dependence of the emitted fluorescence on the light intensity accentuates the brightness differences between neighboring speckles.

Speckle patterns are generally only a minor problem for photostimulation experiments, because diffusion of the active molecules in the extracellular and intracellular space (caged compounds), or horizontal diffusion in the cellular membrane (optogenetic actuators), even out any inhomogeneities in the illumination profile. Smoother patterns may however be desirable for targeting smaller structures (average dendrite width is comparable to the diameter of a single speckle) and in cases when light patterning by phase modulation is used for optical imaging experiments. Indeed, smoother patterns can be achieved using modified digital holography methods [79, 96–99] or other phase-modulation techniques such as generalized phase contrast [100, 101].

9.3.9 Tips for Practical Implementation

Choice of the Light Source Unlike intensity modulation, phase-modulation light patterning techniques require the use of coherent light sources (laser illumination), which generate a planar wavefront, allowing effective phase modulation unattainable via incoherent light sources. For the same reason, phase-modulation techniques cannot be coupled with light guides that do not preserve phase information (such as many optical fibers).

For one-photon stimulation, relatively cheap lasers producing a 50–100 mW continuous output can be used. In two-photon digital holography, femtosecond oscillators should be used. The probability of two-photon absorption is proportional to the peak light intensity [64], so this parameter (together with photodamage) ultimately determines the maximum number of targets that can be stimulated simultaneously. Titanium–sapphire lasers have been effectively used for multipoint photo-uncaging [67], but their power decreases steeply at wavelengths >950 nm. For red-shifted optogenetic actuators, single-line femtosecond oscillators [93] and regenerative amplifiers [102] are more powerful choices.

Choice and Alignment of the LC-SLM The choice of the LC-SLM, as well as its characterization and alignment, is critical to a successful implemention of digital holography.

One important characteristic of the LC-SLM is the diffraction efficiency, calculated as the percentage of the incident light that is redirected to the first diffraction order (useful signal). For fine phase modulation, it is key to achieve good diffraction efficiency. In this respect, nematic LCs allowing multilevel phase modulation are preferable to binary ferroelectric LCs (Sect. 9.3.6). In addition, the actual number of achievable phase levels depends on the type of digital–analog interface (8-bit or 16-bit). The shape of the lookup table (LUT, Box 2) also influences the degree of phase modulation, a linear LUT being preferable to a nonlinear one. Another important parameter is the fill factor of the LC-SLM chip, accounting for the space between the LC pixels, where no phase modulation occurs.

If high diffraction efficiency is critical for the success of an experiment, more advanced characterization of the LC-SLM may be required. Measuring a regional LUT (within different sectors of the LC-SLM) can help compensate for inhomogeneous phase modulation across the LC-chip [85]. Furthermore, it is convenient to use a wavefront analyzer to measure the actual phase of the holographic beam when a flat phase profile is applied to the LC-SLM. If any distortion of the wavefront is observed, a compensatory mask can be applied to the LC-SLM [82]. Finally, diffraction efficiency can be improved by compensating for the electrical crosstalk between adjacent pixels [86].

For experiments targeting multiple neurons in a circuit, a large FoS is convenient. In this scenario, LC-SLMs with a larger number of pixels allow for a better compromise between the extent of the FoS and the resolution (Sect. 9.3.5).

Choice of the Lenses In digital holography, the choice of lenses focal length determines the performance of the setup in terms of available power at the sample, quality of resolution, and extent of the FoS. A first telescope (L1-L2 in Fig. 9.5) is used to expand the laser beam impinging on the LC-SLM. The best configuration for uniform illumination is to choose the telescope magnification such that the beam slightly overfills the longer dimension of the LC-SLM chip. The choice of the second telescope, imaging the LC-SLM into the back aperture of the microscope objective, is more critical, since it sets the trade-off between resolution and FoS (Sect. 9.3.5): Overfilling the back aperture assures maximum resolution, while underfilling it allows for a larger FoS.

Integrating Digital Holography Setup in Commercial Systems Digital holography can be assembled in a custom-made setup, but is also easily coupled into commercial microscopes. For this purpose, it is convenient to mount the holographic setup (Fig. 9.5) horizontally on a breadboard, at a height slightly above the back aperture of the objective. A dichroic mirror can be used to rotate the horizontal holographic beam by 45°, so that it impinges vertically on the back aperture of the objective. In upright microscopes, a dichroic module can be mounted right below the epifluorescence arm [66]. Alternatively, the imaging tube lens of the microscope can be used as the last lens of the holographic setup (L4). This imposes some additional constraints on the choice of focal lengths for the other lenses in the setup. Moreover, the user should make sure that the tube lens is placed at a distance from the back aperture of the objective equal to the focal length of the tube lens itself (which is not always the case in commercial systems).

Combining Digital Holography and Imaging The easiest configuration is to implement 2D digital holography and imaging in the same plane [82, 103]. This is achieved by coupling both the imaging and the photostimulation light paths onto the same microscope objective. The two paths can use different light wavelengths, which can be combined with a dichroic mirror above the microscope objective. Alternatively, if the absorption spectra of photosensitive actuators are compatible and the available power is sufficient, the same laser source can also be split between the imaging and digital holography paths. For example, polarizing beam splitters can be used for both separating and recombining the two illumination lines.

In neuronal circuits where the input and the output layers are well defined, it is possible to use digital holography to stimulate in one layer, while imaging in another layer [47]. Generally, the imaging plane is defined by the axial position of the microscope objective through focusing (moving the objective) and coincides with the focal plane of the objective itself. In order to displace the photostimulation pattern to a different plane, a curvature can be introduced in the phase pattern at the LC-SLM to compensate for the axial movement of the objective [104]. If an LC-SLM is introduced in the imaging laser path, the same method can be used to displace the imaging plane, without changing the axial position of the objective [105, 106]. Thus temporally, this approach is not limited by the inertia of the objective, but only by the refresh rate of the LC-SLM (>100 Hz). Moreover, the use of a LC-SLM allows compensating for spherical aberration that would otherwise deteriorate the image

quality. Remote focusing [73, 80, 107] is an alternative aberration-free method that can be used to modify the imaging plane (by axial shift or tilt) without moving the principal microscope objective.

Introducing a variable wavefront curvature selectively in the imaging path could potentially be also achieved using a deformable mirror [108], a variable focus lens [109, 110], or acousto-optical deflectors [31, 44, 111].

Note that these methods are also compatible with intensity modulation techniques (Sect. 9.2).

9.3.10 Applications

Digital holography was first used in biology in the context of optical tweezers [68, 112]. Here the electric field generated by focused light beams is used to "trap" and manipulate microscopic particles and microspheres, as well as viral particles and bacteria. The first implementation of digital holography created multisite 3D light traps [68, 112]. Later, the technique was used in neuroscience, where simultaneous illumination of extended 2D patterns or multiple spots in 3D allowed multisite neurotransmitter uncaging [66, 67]. The ability of digital holography to generate extended 2D light patterns was exploited to target individual [66] and multiple [82, 103] neurons simultaneously in brain cell cultures and slices, as well as neuronal compartments, such as dendritic branches [66]. Fast holographic illumination was also applied to photostimulate retinal ganglion cells in genetically or pharmacologically blind retinas [113]. Recently, focal 3D multipoint uncaging was used to study dendritic integration and neuronal signal propagation [80, 114, 115].

Importantly, almost from the start, digital holography was extended to two-photon illumination allowing patterned photostimulation in scattering brain samples [67, 81]. Preliminary studies on two-photon stimulation of ChR-expressing neurons in brain slices [84, 93] open exciting venues for future *in vivo* applications. Finally, digital holography is not limited to photostimulation experiments, but it has also been successfully implemented for multiplexed two-photon imaging [67, 103, 105, 116, 117].

Despite these exciting developments, the potential of light patterning by intensity or phase modulation in neuroscience remains vastly unexplored. Further developments will benefit from reducing the gap between developers and endusers and from pursuing a systematic approach to iteratively test, adapt, and optimize these novel techniques by going back and forth between the optical bench and "real-life" experiments in slice preparations, anesthetized and awake behaving animals.

Acknowledgement We would like to thank Aurélien Bègue, Adriana 'Dăbâcan', Priyanka Gupta, and Matthew Koh for constructive critique and comments. This work was supported by an EMBO Long-Term Fellowship and a Swartz Foundation Fellowship (FA), and CSHL start-up funds and a Louis and Gertrude Feil Foundation Fellowship (DFA).

Glossary

1. *4f configuration*: an optical configuration involving two lenses of focal length 'f'. The object is placed at focal length distance from the first lens and the distance between the two lenses is 2f. This configuration ensures that the distance between the object and its image is 4f. Even when two lenses of different focal lengths are used (f1 and f2), the configuration is still commonly referred to as a 4f. system.
2. *Absorption cross-section*: a proportionality constant that determines the probability of a photon being absorbed by an absorber molecule. It has the units of area, which is why it is known as cross-section and can be imagined to be a perfectly absorbing disk of that area.
3. *Collimated beam*: a beam of light with near-zero divergence that propagates through a given medium. Lasers are highly collimated, but light from extended sources like lamps and LEDs is not.
4. *Comb function*: a periodic function composed of individual delta functions repeated at a particular interval. Also known as impulse train or sampling function in engineering. The Fourier transform of the comb function is another comb function with different periodicity.
5. *Conjugate plane*: if all points residing in a given plane P are imaged onto another plane P' by a lens, then P and P' are said to be conjugate planes of each other. In an optical system with more than one lens, changes in the amplitude or phase at any given plane propagate to all other conjugated planes.
6. *Diffraction grating*: an optical component with periodic variation of phase across the surface that causes constructive/destructive interference to produce characteristic diffraction patterns.
7. *Diffraction-limited spot*: the theoretical minimum spot size that can be achieved after focusing a coherent light beam using a lens. The size of the spot at the focal plane is proportional to the wavelength of light and inversely proportional to the numerical aperture of the lens. The function that describes the intensity distribution of a diffraction-limited spot in 3D is known as the point-spread function.
8. *Focal plane*: the point where rays parallel to the optical axis converge after passing through a lens is called the focus. The plane perpendicular to the optical axis containing the focus is called the focal plane (technically the front focal plane). Back focal plane refers to the image plane of an object placed at infinity and is located at a focal distance from the center of the lens, but symmetrically opposite from the front focal plane.
9. *Gaussian spot*: a spot generated by a Gaussian beam when focused, whose intensity profile can be fitted with 2D Gaussian function in the lateral plane.
10. *Ghost-replicas*: the higher-order diffraction patterns (low-intensity repeats) of a light mask when using a coherent light source.

11. *LED (Light-emitting diodes)*: a small semiconductor device made up of a pn-junction diode that emits photons (whose energy correspond to the band gap) when an electric potential is applied.
12. *Mean free path*: the average distance travelled by light (photons) between successive collisions (scattering) in the propagating medium.
13. *Rectangular (rect) function*: a step function of a particular duration. Its Fourier transform is a sinc function, whose un-normalized form matches the diffracting pattern from a single-slit (rect function) experiment.
14. *Temporal coherence*: two waves are coherent if they have a constant phase difference between them. For light sources, it is a condition where all the individual light emitters (electron transitions in atoms at the source) have a constant phase difference between themselves, as is the case of LASERs.
15. *Wavefront*: the spatial envelope of all the points in a wave that have the same phase.

References

1. Yuste, R., Konnerth, A., & Masters, B. R. (2006). Imaging in neuroscience and development, a laboratory manual. *Journal of Biomedical Optics, 11,* 019902.
2. Looger, L. L., & Griesbeck, O. (2012). Genetically encoded neural activity indicators. *Current Opinion in Neurobiology, 22,* 18–23.
3. Stosiek, C., Garaschuk, O., Holthoff, K., & Konnerth, A. (2003). In vivo two-photon calcium imaging of neuronal networks. *Proceedings of the National Academy of Sciences of the United States of America, 100,* 7319–7324.
4. Minta, A., Kao, J. P. Y., & Tsien, R. Y. (1989). Fluorescent indicators for cytosolic calcium based on rhodamine and fluorescein chromophores. *The Journal of Biological Chemistry, 264,* 8171–8178.
5. Hochbaum, D. R., et al. (2014). All-optical electrophysiology in mammalian neurons using engineered microbial rhodopsins. *Nature Methods, 11,* 825–833. doi:10.1038/nmeth.3000.
6. St-Pierre, F., et al. (2014). High-fidelity optical reporting of neuronal electrical activity with an ultrafast fluorescent voltage sensor. *Nature Neuroscience, 17,* 884–889.
7. Jin, L., et al. (2012). Single action potentials and subthreshold electrical events imaged in neurons with a fluorescent protein voltage probe. *Neuron, 75,* 779–785.
8. Trachtenberg, J. T., et al. (2002). Long-term in-vivo imaging of experience-dependent synaptic plasticity in adult cortex. *Nature, 420,* 788–794.
9. Grutzendler, J., Kasthuri, N., & Gan, W. B. (2002). Long-term dendritic spine stability in the adult cortex. *Nature, 420,* 812–816.
10. Svoboda, K., Denk, W., Kleinfeld, D., & Tank, D. W. (1997). In vivo dendritic calcium dynamics in neocortical pyramidal neurons. *Nature, 385,* 161–165.
11. Helmchen, F., Svoboda, K., Denk, W., & Tank, D. W. (1999). In vivo dendritic calcium dynamics in deep-layer cortical pyramidal neurons. *Nature Neuroscience, 2,* 989–996.
12. Euler, T., Detwiler, P. B., & Denk, W. (2002). Directionally selective calcium signals in dendrites of starburst amacrine cells. *Nature, 418,* 845–852.
13. Charpak, S., Mertz, J., Beaurepaire, E., Moreaux, L., & Delaney, K. (2001). Odor-evoked calcium signals in dendrites of rat mitral cells. *Proceedings of the National Academy of Sciences of the United States of America, 98,* 1230–1234.

14. Branco, T., & Häusser, M. (2011). Synaptic integration gradients in single cortical pyramidal cell dendrites. *Neuron, 69,* 885–892.
15. Ohki, K., Chung, S., Ch'ng, Y. H., Kara, P., & Reid, R. C. (2005). Functional imaging with cellular resolution reveals precise micro-architecture in visual cortex. *Nature, 433,* 597–603.
16. Ohki, K., et al. (2006). Highly ordered arrangement of single neurons in orientation pinwheels. *Nature, 442,* 925–928.
17. Hofer, S. B., et al. (2011). Differential connectivity and response dynamics of excitatory and inhibitory neurons in visual cortex. *Nature Neuroscience, 14,* 1045–1052.
18. Ko, H., et al. (2011). Functional specificity of local synaptic connections in neocortical networks. *Nature, 473,* 87–91.
19. Komiyama, T., et al. (2010). Learning-related fine-scale specificity imaged in motor cortex circuits of behaving mice. *Nature, 464,* 1182–1186.
20. Petreanu, L., et al. (2012). Activity in motor-sensory projections reveals distributed coding in somatosensation. *Nature, 489,* 299–303.
21. Orger, M. B., Kampff, A. R., Severi, K. E., Bollmann, J. H., & Engert, F. (2008). Control of visually guided behavior by distinct populations of spinal projection neurons. *Nature Neuroscience, 11,* 327–333.
22. Nagel G, Szellas T, Huhn W, Kateriya S, Adeishvili N, Berthold P, Ollig D, Hegemann P, Bamberg E. (2003). Channelrhodopsin-2, a directly light-gated cation-selective membrane channel. *Proc Natl Acad Sci, 100*(24), 13940–13945.
23. Boyden, E. S., Zhang, F., Bamberg, E., Nagel, G., & Deisseroth, K. (2005). Millisecond-timescale, genetically targeted optical control of neural activity. *Nature Neuroscience, 8,* 1263–1268.
24. Zhang, F., et al. (2011). The microbial opsin family of optogenetic tools. *Cell, 147,* 1446–1457.
25. Yizhar, O., Fenno, L. E., Davidson, T. J., Mogri, M., & Deisseroth, K. (2011). Optogenetics in neural systems. *Neuron, 71,* 9–34.
26. Aravanis, A. M., et al. (2007). An optical neural interface: In vivo control of rodent motor cortex with integrated fiberoptic and optogenetic technology. *Journal of Neural Engineering, 4,* 143–156.
27. Cardin, J. A., et al. (2010). Targeted optogenetic stimulation and recording of neurons in vivo using cell-type-specific expression of Channelrhodopsin-2. *Nature Protocols, 5,* 247–254.
28. Packer, A. M., Roska, B., & Häusser, M. (2013). Targeting neurons and photons for optogenetics. *Nature Neuroscience, 16,* 805–815.
29. Papagiakoumou, E. (2013). Optical developments for optogenetics. *Biology of the Cell/Under the Auspices of the European Cell Biology Organization, 105,* 443–464.
30. Shepherd, G. M. G., Pologruto, T. A., & Svoboda, K. (2003). Circuit analysis of experience-dependent plasticity in the developing rat barrel cortex. *Neuron, 38,* 277–289.
31. Shoham, S., O'Connor, D. H., Sarkisov, D. V., & Wang, S. S.-H. (2005). Rapid neurotransmitter uncaging in spatially defined patterns. *Nature Methods, 2,* 837–843.
32. Bureau, I., von Saint Paul, F. & Svoboda, K. (2006). Interdigitated paralemniscal and lemniscal pathways in the mouse barrel cortex. *PLoS Biology, 4,* e382.
33. Gasparini, S., & Magee, J. C. (2006). State-dependent dendritic computation in hippocampal CA1 pyramidal neurons. *The Journal of Neuroscience, 26,* 2088–2100.
34. Branco, T., Clark, B. A., & Häusser, M. (2010). Dendritic discrimination of temporal input sequences in cortical neurons. *Science, 329,* 1671–1675.
35. Callaway, E. M., & Katz, L. C. (1993). Photostimulation using caged glutamate reveals functional circuitry in living brain slices. *Proceedings of the National Academy of Sciences of the United States of America, 90,* 7661–7665.
36. Wang, H., et al. (2007). High-speed mapping of synaptic connectivity using photostimulation in Channelrhodopsin-2 transgenic mice. *Proceedings of the National Academy of Sciences of the United States of America, 104,* 8143–8148.
37. Petreanu, L., Huber, D., Sobczyk, A., & Svoboda, K. (2007). Channelrhodopsin-2-assisted circuit mapping of long-range callosal projections. *Nature Neuroscience, 10,* 663–668.

38. Petreanu, L., Mao, T., Sternson, S. M., & Svoboda, K. (2009). The subcellular organization of neocortical excitatory connections. *Nature, 457,* 1142–1145.
39. Glickfeld, L. L., Andermann, M. L., Bonin, V., & Reid, R. C. (2013). Cortico-cortical projections in mouse visual cortex are functionally target specific. *Nature Neuroscience, 16,* 219–226.
40. Bonin, V., Histed, M. H., Yurgenson, S., & Reid, R. C. (2011). Local diversity and fine-scale organization of receptive fields in mouse visual cortex. *The Journal of Neuroscience, 31,* 18506–18521.
41. Bullen, A., Patel, S. S., & Saggau, P. (1997). High-speed, random-access fluorescence microscopy: I. High-resolution optical recording with voltage-sensitive dyes and ion indicators. *Biophysical Journal, 73,* 477–491.
42. Salomé, R., et al. (2006). Ultrafast random-access scanning in two-photon microscopy using acousto-optic deflectors. *Journal of Neuroscience Methods, 154,* 161–174.
43. Losavio, B. E., Iyer, V., Patel, S., & Saggau, P. (2010). Acousto-optic laser scanning for multi-site photo-stimulation of single neurons in vitro. *Journal of Neural Engineering, 7,* 045002.
44. Katona, G., et al. (2012). Fast two-photon in vivo imaging with three-dimensional random-access scanning in large tissue volumes. *Nature Methods, 9,* 201–208.
45. Rickgauer, J. P., & Tank, D. W. (2009). Two-photon excitation of channelrhodopsin-2 at saturation. *Proceedings of the National Academy of Sciences of the United States of America, 106,* 15025–15030.
46. Berndt, A., et al. (2011). High-efficiency channelrhodopsins for fast neuronal stimulation at low light levels. *Proceedings of the National Academy of Sciences of the United States of America, 108,* 7595–7600.
47. Oron, D., Papagiakoumou, E., Anselmi, F., & Emiliani, V. (2012). Two-photon optogenetics. *Progress in Brain Research, 196,* 119–143.
48. Grossman, N., et al. (2010). Multi-site optical excitation using ChR2 and micro-LED array. *Journal of Neural Engineering, 7,* 16004.
49. Liu, J., et al. (2014). Random nanolasing in the Anderson localized regime. *Nature Nanotechnology, 9,* 285–289.
50. James, E. L. (2011). *Fifty shades of grey*. New York: Vintage Books.
51. Bansal, V., & Saggau, P. (2013). Digital micromirror devices: Principles and applications in imaging. *Cold Spring Harbor Protocols, 2013,* 404–411.
52. Wang, S., et al. (2007). All optical interface for parallel, remote, and spatiotemporal control of neuronal activity. *Nano letters, 7,* 3859–3863.
53. Farah, N., Reutsky, I., & Shoham, S. (2007). Patterned optical activation of retinal ganglion cells. *Conference Proceedings Annual International Conference of the IEEE Engineering in Medicine and Biology Society,* 2007*,* 6368–6370.
54. Wyart, C., et al. (2009). Optogenetic dissection of a behavioural module in the vertebrate spinal cord. *Nature, 461,* 407–410.
55. Warp, E., et al. (2012). Emergence of patterned activity in the developing zebrafish spinal cord. *Current Biology, 22,* 93–102.
56. Guo, Z. V, Hart, A. C., & Ramanathan, S. (2009). Optical interrogation of neural circuits in Caenorhabditis elegans. *Nature Methods, 6,* 891–896.
57. Leifer, A. M., Fang-Yen, C., Gershow, M., Alkema, M. J., & Samuel, A. D. T. (2011). Optogenetic manipulation of neural activity in freely moving Caenorhabditis elegans. *Nature Methods, 8,* 147–152.
58. Shipley, F. B., Clark, C. M., Alkema, M. J., & Leifer, A. M. (2014). Simultaneous optogenetic manipulation and calcium imaging in freely moving C. elegans. *Frontiers in Neural Circuits, 8,* 28.
59. Dhawale, A. K., Hagiwara, A., Bhalla, U. S., Murthy, V. N., & Albeanu, D. F. (2010). Non-redundant odor coding by sister mitral cells revealed by light addressable glomeruli in the mouse. *Nature Neuroscience, 13,* 1404–1412.

60. Haddad, R., et al. (2013). Olfactory cortical neurons read out a relative time code in the olfactory bulb. *Nature Neuroscience, 16,* 949–957.
61. Blumhagen, F., et al. (2011). Neuronal filtering of multiplexed odour representations. *Nature, 479,* 493–498.
62. Zhu, P., Frank, T., & Friedrich, R. W. (2013). Equalization of odor representations by a network of electrically coupled inhibitory interneurons. *Nature Neuroscience, 16,* 1678–1686.
63. Trigo, F. F., Papageorgiou, G., Corrie, J. E. T., & Ogden, D. (2009). Laser photolysis of DPNI-GABA, a tool for investigating the properties and distribution of GABA receptors and for silencing neurons in situ. *Journal of Neuroscience Methods, 181,* 159–169.
64. Zipfel, W. R., Williams, R. M., & Webb, W. W. (2003). Nonlinear magic: Multiphoton microscopy in the biosciences. *Nature Biotechnology, 21,* 1369–1377.
65. Helmchen, F., & Denk, W. (2005). Deep tissue two-photon microscopy. *Nature Methods, 2,* 932–940.
66. Lutz, C., et al. (2008). Holographic photolysis of caged neurotransmitters. *Nature Methods, 5,* 821–827.
67. Nikolenko, V., et al. (2008). SLM microscopy: Scanless two-photon imaging and photostimulation with spatial light modulators. *Frontiers in Neural Circuits, 2,* 5.
68. Curtis, J. E., Koss, B. A., & Grier, D. G. (2002). Dynamic holographic optical tweezers. *Optics Communications, 207,* 169–175.
69. Di Leonardo, R., Ianni, F., & Ruocco, G. (2007). Computer generation of optimal holograms for optical trap arrays. *Optics Express, 15,* 1913–1922.
70. Spalding, G. C., Courtial, J., & Leonardo, R. Di. (Academic Press, 2008). Holographic optical tweezers. In D. L. Andrews (Ed.), *Structured Light and Its Applications,* (pp. 139–168).
71. Golan, L., Reutsky, I., Farah, N., & Shoham, S. (2009). Design and characteristics of holographic neural photo-stimulation systems. *Journal of Neural Engineering, 6,* 066004.
72. Maschio, M. D. (2014). Novel approaches for single molecule activation and detection. 7–26. doi:10.1007/978-3-662-43367-6.
73. Botcherby, E. J., Juškaitis, R., Booth, M. J., & Wilson, T. (2008). An optical technique for remote focusing in microscopy. *Optics Communications, 281,* 880–887.
74. Reicherter, M., Haist, T., Wagemann, E. U., & Tiziani, H. J. (1999). Optical particle trapping with computer-generated holograms written on a liquid-crystal display. *Optics Letters, 24,* 608–610.
75. Lesem, L. B., Hirsch, P. M., & Jordan, J. A. (1969). The kinoform: A new wavefront reconstruction device. *IBM Journal of Research and Developement, 13,* 150–155.
76. Gerchberg, R. W., & Saxton, W. O. (1972). A practical algorithm for the determination of phase from image and diffraction plane pictures. *Optik, 35,* 237–246.
77. Yang, S., et al. (2011). Three-dimensional holographic photostimulation of the dendritic arbor. *Journal of Neural Engineering, 8,* 046002.
78. Mahajan, V. N. (2011). *Optical imaging and aberrations: Part II*. Bellingham: SPIE. doi:10.1117/3.415727.
79. Wyrowski, F., & Bryngdahl, O. (1988). Iterative Fourier-transform algorithm applied to computer holography. *Journal of the Optical Society of America A, 5,* 1058.
80. Anselmi, F., Ventalon, C., Begue, A., Ogden, D., & Emiliani, V. (2011). Three-dimensional imaging and photostimulation by remote-focusing and holographic light patterning. *Proceedings of the National Academy of Sciences of the United States of America, 108,* 19504–19509.
81. Papagiakoumou, E., de Sars, V., Oron, D., & Emiliani, V. (2008). Patterned two-photon illumination by spatiotemporal shaping of ultrashort pulses. *Optics Express, 16,* 22039–22047.
82. Zahid, M., et al. (2010). Holographic photolysis for multiple cell stimulation in mouse hippocampal slices. *PLoS ONE, 5,* e9431.
83. Papagiakoumou, E., et al. (2010). Scanless two-photon excitation of channelrhodopsin-2. *Nature Methods, 7,* 848–854.
84. Bègue, A., et al. (2013). Two-photon excitation in scattering media by spatiotemporally shaped beams and their application in optogenetic stimulation. *Biomedical Optics Express, 4,* 2869–2879.

85. Ambs, P., Otón, J., Millán, M. S., & Jaulin, A. (2007). Spatial light modulators for information processing: Applications and overview. AIP Conference Proceedings *949,* 226.
86. Ronzitti, E., Guillon, M., de Sars, V., & Emiliani, V. (2012). LCoS nematic SLM characterization and modeling for diffraction efficiency optimization, zero and ghost orders suppression. *Optics Express, 20,* 17843–17855.
87. Oheim, M., Beaurepaire, E., Chaigneau, E., Mertz, J., & Charpak, S. (2001). Two-photon microscopy in brain tissue: Parameters influencing the imaging depth. *Journal of Neuroscience Methods, 111,* 29–37.
88. Beaurepaire, E., Oheim, M., & Mertz, J. (2001). Ultra-deep two-photon fuorescence excitation in turbid media. *Optics Communications, 188,* 25–29.
89. Papagiakoumou, E., et al. (2013). Functional patterned multiphoton excitation deep inside scattering tissue. *Nature Photonics, 7,* 274–278.
90. Oron, D., & Silberberg, Y. (2005). Spatiotemporal coherent control using shaped, temporally focused pulses. *Optics Express, 13,* 9903–9908.
91. Zhu, G., van Howe, J., Durst, M., Zipfel, W., & Xu, C. (2005). Simultaneous spatial and temporal focusing of femtosecond pulses. *Optics Express, 13,* 2153–2159.
92. Papagiakoumou, E., et al. (2010). Scanless two-photon excitation of channelrhodopsin-2. *Nature Methods, 7,* 848–854.
93. Packer, A. M., et al. (2012). Two-photon optogenetics of dendritic spines and neural circuits. *Nature Methods, 9,* 1202–1205.
94. Prakash, R., et al. (2012). Two-photon optogenetic toolbox for fast inhibition, excitation and bistable modulation. *Nature Methods, 9,* 1171–1179.
95. Polin, M., Ladavac, K., Lee, S.-H., Roichman, Y., & Grier, D. (2005). Optimized holographic optical traps. *Optics Express, 13,* 5831–5845.
96. Golan, L., & Shoham, S. (2009). Speckle elimination using shift-averaging in high-rate holographic projection. *Optics Express, 17,* 1330–1339.
97. Matar, S., Golan, L., & Shoham, S. (2011). Reduction of two-photon holographic speckle using shift-averaging. *Optics Express, 19,* 25891–25899.
98. Amako, J., Miura, H., & Sonehara, T. (1995). Speckle-noise reduction on kinoform reconstruction using a phase-only spatial light modulator. *Applied Optics, 34,* 3165–3171.
99. Jesacher A. (2008). Advanced shaping of light fields with cascaded spatial light modulators. PhD Thesis. Innsbruck Medical University.
100. Glückstad, J. (1996). Phase contrast image synthesis. *Optics Communications, 130,* 225–230.
101. Papagiakoumou, E., et al. (2010). Scanless two-photon excitation of channelrhodopsin-2. *Nature Methods, 7,* 848–854. doi:10.1038/nmeth.1505.
102. Theer, P., Hasan, M. T., & Denk, W. (2003). Two-photon imaging to a depth of 1000 microm in living brains by use of a Ti:Al2O3 regenerative amplifier. *Optics Letters, 28,* 1022–1024.
103. Dal Maschio, M., et al. (2010). Simultaneous two-photon imaging and photo-stimulation with structured light illumination. *Optics Express, 18,* 18720–18731.
104. Emiliani, V., et al. (2005). Wave front engineering for microscopy of living cells. *Optics Express, 13,* 1395–1405.
105. Dal Maschio, M., De Stasi, A. M., Benfenati, F., & Fellin, T. (2011). Three-dimensional in vivo scanning microscopy with inertia-free focus control. *Optics Letters, 36,* 3503–3505.
106. Quirin, S., Jackson, J., Peterka, D. S., & Yuste, R. (2014). Simultaneous imaging of neural activity in three dimensions. *Frontiers in Neural Circuits, 8,* 29.
107. Botcherby, E. J., et al. (2012). Aberration-free three-dimensional multiphoton imaging of neuronal activity at kHz rates. *Proceedings of the National Academy of Sciences of the United States of America, 109,* 2919–2924.
108. Kner, P., Sedat, J. W., Agard, D. A., & Kam, Z. (2010). High-resolution wide-field microscopy with adaptive optics for spherical aberration correction and motionless focusing. *Journal of Microscopy, 237,* 136–147.

109. Grewe, B. F., Voigt, F. F., van 't Hoff, M., & Helmchen, F. (2011). Fast two-layer two-photon imaging of neuronal cell populations using an electrically tunable lens. *Biomedical Optics Express, 2,* 2035–2046.
110. Fahrbach, F. O., Voigt, F. F., Schmid, B., Helmchen, F., & Huisken, J. (2013). Rapid 3D light-sheet microscopy with a tunable lens. *Optics Express, 21,* 21010–21026.
111. Kirkby, P. A., Srinivas Nadella, K. M. N., & Silver, R. A. (2010). A compact Acousto-Optic Lens for 2D and 3D femtosecond based 2-photon microscopy. *Optics Express, 18,* 13721–13745.
112. Dufresne, E. R., Spalding, G. C., Dearing, M. T., Sheets, S. A., & Grier, D. G. (2000). Computer-generated holographic optical tweezer arrays. *Review of Scientific Instruments, 72,* 1810–1816.
113. Reutsky-Gefen, I., et al. (2013). Holographic optogenetic stimulation of patterned neuronal activity for vision restoration. *Nature Communications, 4,* 1509.
114. Yang, S., et al. (2011). Three-dimensional holographic photostimulation of the dendritic arbor. *Journal of Neural Engineering, 8,* 046002.
115. Yang, S., Emiliani, V., & Tang, C.-M. (2014). The kinetics of multibranch integration on the dendritic arbor of CA1 pyramidal neurons. *Frontiers in Cellular Neuroscience, 8,* 127.
116. Watson, B. O., et al. (2010). Two-photon microscopy with diffractive optical elements and spatial light modulators. *Frontiers in Neuroscience, 4,* 1–8.
117. Ducros, M., Goulam Houssen, Y., Bradley, J., de Sars, V., & Charpak, S. (2013). Encoded multisite two-photon microscopy. *Proceedings of the National Academy of Sciences of the United States of America, 110,* 13138–13143.

Chapter 10
Beyond Localization of Function: Dissecting a Neural Code with Optogenetics

Matthew C. Smear

Abstract Neuroscientists want to know which neurons mediate which behaviors. Electrical microstimulation has a rich history of localizing behavioral functions to particular brain regions. Optogenetics has advanced this cause by enabling microstimulation that is cell type specific and less invasive. But localization does not complete our understanding. We also want to know how functionally relevant neurons communicate with each other—How do they encode and decode information? Electrophysiology and imaging can provide correlative evidence for neural coding hypotheses, but how can we know whether the brain reads its activity in the same way we do? To test whether a given pattern of neural activity is causally related to perception and behavior, we use optogenetics in the mouse olfactory system. The activity of olfactory sensory neurons (OSN) is patterned in space, amplitude, and time. We have dissected these cues and presented them in isolation in the context of an operant behavioral task. We show that mice can perceive all three of these olfactory coding features. This may enable mice to efficiently smell in natural olfactory scenes. Questions remaining to be answered include, what do these cues encode, in other words, what do they mean for perception? Further, how important are these cues to perception? In this chapter, we describe our previous findings and consider how ongoing technical innovations might allow us to progress beyond our current level of understanding.

10.1 Introduction

Microstimulation has long been a powerful technique for localization of function. Throughout the history of neuroscience, electrical microstimulation has provided causal evidence for the involvement of various brain areas in perception and behavior. In pioneering work, Penfield electrically stimulated somatosensory and motor cortex in awake neurological patients [53]. By carefully mapping which cortical stimuli evoked sensations or movements in specific parts of the body, he

M. C. Smear (✉)
Institute of Neuroscience, 1254 University of Oregon, Eugene, OR 97403-1254, USA
e-mail: smear@uoregon.edu

A. D. Douglass (ed.), *New Techniques in Systems Neuroscience,* Biological and Medical Physics, Biomedical Engineering, DOI 10.1007/978-3-319-12913-6_10

demonstrated a topographic relationship between cortical position and somatic location. He named this cortical map of the body the homunculus.

In more recent work, Newsome and colleagues applied microstimulation to cortical area MT (middle temporal) in behaving monkeys [60]. MT contains a topographic map of visual space, and neuronal responses are tuned to visual motion direction. Motion direction tuning is also mapped in MT, with nearby neurons preferring similar directions of motion. Salzmann et al. found that when they applied electrical microstimulation to a localized region of MT, they could bias the monkeys' perceptual reports toward the stimulated region's direction preference, but only in the region of visual space to which that area of MT was sensitive. These findings provided evidence that the position and motion direction maps in MT are causally related to motion perception.

These and many other studies demonstrate that electrical microstimulation is a powerful technique. However, electrical microstimulation has a fatal flaw: It indiscriminately activates all neurons within a localized region, as well as en passant axons. The neuronal populations within a given region are highly heterogeneous, with cell types of different function intermingled with each other. For example, inhibitory and excitatory neurons are neighbors in most regions of brain. Stimulating both populations simultaneously is unnatural and may give rise to unexpected effects. This indiscriminateness limits the interpretability of electrical microstimulation experiments.

Optogenetic techniques enable us to overcome this limitation. With optogenetics, microstimulation can be performed with unprecedented cell type specificity, which has revolutionized our ability to localize functions to neuronal subpopulations within a brain region of interest. For example, in a study of the hypothalamic control of feeding, Aponte et al. [4] investigated the effects of stimulating two intermingled neuronal populations, one defined by expression of the agouti-related peptide (AGRP) and the other by pro-opiomelanocortin (POMC). They found that stimulation of AGRP neurons instigated voracious feeding, while POMC neuron activation reduced feeding. Localizing these feeding functions to specific cell types interspersed within the same structure has only now become possible.

Thanks to optogenetics, we are gaining a finer and finer-grained understanding of which neurons do what jobs. Localizing a behavioral function to a population of neurons is an essential step in understanding that function's neural basis, but once this is accomplished, there remains further work to be done. To really understand how a group of neurons mediate a particular function, we must also decipher how these neurons communicate with the rest of the brain. How do neurons encode information and what aspects of their activity are decoded by their synaptic partners?

Neural coding can be defined as "the representation and transformation of information in the nervous system" [54]. As much as our understanding of neural coding has advanced [11, 37, 56], the vast majority of studies operate at the level of correlation. For example, one approach in this area is to compare neuronal responses with behavioral performance [7]. I would argue that the next step is to ask what response features are read out by downstream neurons and which manifest themselves in perception and behavior. We took advantage of the cell type specificity and high

temporal resolution of optogenetics to dissect and isolate putative neural coding features and test their behavioral relevance.

10.2 Olfactory Coding

10.2.1 Spatial Properties

Coding in the olfactory system has several interesting features. The spatial structure of olfactory representations is set by the projection pattern of olfactory sensory neurons (OSNs) onto the olfactory bulb (OB), the first olfactory processing center of the brain [47, 49]. Each OSN expresses one out of over 1000 odorant receptor (OR) genes. All OSNs expressing a given OR project their axons to one glomerulus, which is a spherical structure in which OSN axons form synapses with interneurons and projection neurons of the OB. This arrangement of axonal projections gives rise to a map of receptor activation in the glomerular layer of the OB.

How is this glomerular map organized functionally? There is some rough organization of odorant ligand preference, corresponding to the axonal projection patterns of OSNs expressing different classes of OR gene [6, 36]. There are three known classes of OR gene, and each prefers a different kind of ligand [36, 52]. What about at a finer scale of organization? Early imaging studies suggested that neighboring glomeruli might have similar odorant preferences, giving rise to a chemotopic map [48, 59]. However, more recent work using more sensitive imaging techniques and a larger number of stimuli gives a different answer. These studies indicate that the odor tuning of neighboring glomeruli is uncorrelated and is equally correlated with distant glomeruli [67]. Thus, there may be no fine-scale place code for odor space. Rather, the spatial coding of odor stimuli consists of a combinatorial population code.

10.2.2 Temporal Properties

In addition to this spatial organization, it has long been recognized that the brain's responses to odor are temporally structured at a finer timescale than are odor stimuli [2]. (Adrian 1953). This temporal patterning seems to be evolutionarily conserved, having been demonstrated across a broad range of animal phyla [22, 24, 32, 39]. In mammalian olfactory responses, a particularly conspicuous temporal feature is the phase of the response relative to the sniff cycle. Sniffing parses olfactory scenes into discrete samples every few hundred milliseconds. Despite this slow sampling rate, responses in olfactory receptor neurons [68] and bulb [15, 18, 43, 62] contain odor-specific temporal structure at a finer timescale, on the order of tens of milliseconds. The temporal microstructure of spike timing relative to sniff onset has been proposed to contribute to olfactory perception [8, 28, 44]. Such coding by time relative to sampling behavior has been hypothesized in other sensory modalities [72],

including vision [23, 25, 55], somatosensation [19, 31], and electrosensation [27, 70]. Away from the sensory periphery, timing relative to internally generated oscillations has been proposed as a coding feature in higher-level brain regions involved in navigation [10, 30, 51] and working memory [63]. The similarity of these observations across diverse neural systems hints that phase coding may be a powerful and flexible representational strategy useful in various neural computations [28, 54].

10.3 Using Optogenetics to Determine the Importance of Phase Coding

As is true of most of these "phase coding" schemes, the hypothesis that sniff phase contributes to odor coding had been supported only by correlative evidence. Thus, sniff phase structure may be superfluous for odor coding, merely an epiphenomenon that conveys no information higher up in the olfactory pathway [41]. However much information may be contained in fast temporal patterning of olfactory responses, it can only enter olfactory perception if downstream neurons possess mechanisms to read it. To test whether the mouse's brain has such mechanisms, we have used optogenetics [64].

We sought to dissect and isolate the sniff phase cue and ask whether mice can discriminate spatially identical olfactory activation patterns applied at different phases of the sniff cycle. To decouple olfactory stimulation from nasal airflow, which might not be possible with odorant stimuli, we made a mouse line with light-sensitive OSNs.

10.3.1 Experimental Setup

To do this, we knocked in the coding sequence for ChR2 fused to the yellow fluorescent protein (ChR2-YFP) at the olfactory marker protein (OMP) locus (Fig. 10.1a). OMP is expressed in all OSNs and is thought to function in odor transduction [9, 33]. In OMP-ChR2 mice, ChR2-YFP is expressed in all mature OSNs and glomeruli of the OB (Fig. 10.1b). ChR2 replaces the OMP sequence in OMP-ChR2 mice, and OMP null mice are known to have physiological and behavioral phenotypes [9, 40], so all experiments were conducted in heterozygous animals. Preliminary electrophysiological recordings from OMP-ChR2 mice confirmed that light responses could be evoked in neurons in the olfactory epithelium and bulb.

We surgically prepared OMP-ChR2 mice for light stimulation, sniff measurement, and head-fixed behavior (Fig. 10.1c). Our goal for light stimulation was to activate the same OSNs on every trial. To do this, we implanted an optical fiber stub into the nasal cavity, where OSN somata and axons could be illuminated. The optical fiber was cemented in place in order to stimulate a fixed set of OSNs. The fiber stub was coupled to another fiber from which photostimuli from a laser could

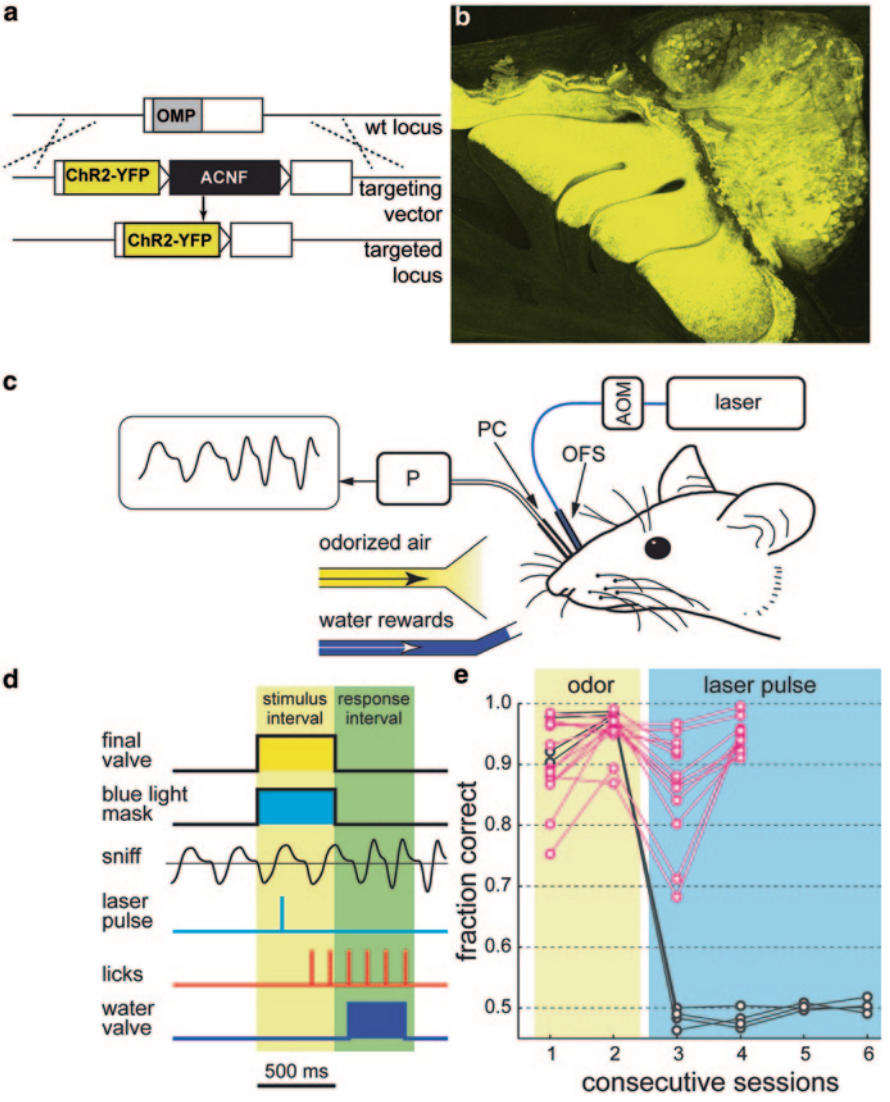

Fig. 10.1 Stimulating the olfactory system optogenetically. **a** Schematic of the gene knock-in strategy. The *ChR2-YFP* sequence (*yellow box*) is knocked into the olfactory marker protein (*OMP*) locus. (*gray box*). **b** Whole mount from olfactory epithelium (*OE*) and olfactory bulb (*OB*) in OMP-ChR2 mice. ChR2-YFP labels OSNs and their axons in OB. **c** Diagram of experimental setup. Mice were implanted with a nasal optical fiber stub (*OFS*) to photostimulate the OE with light. An acousto-optic modulator gated a laser to deliver light stimuli. A nasal pressure cannula (*PC*) and a pressure sensor (*P*) were used to monitor sniffing. Intranasal pressure signal at *top left*. **d** Behavioral trial structure. Each trial is composed of a stimulus interval (*yellow shading*) and a response interval (*green*). **e**, Performance of OMP-ChR2 mice (*pink circles*; $n=12$) and +/+ littermate controls (*black circles*; $n=4$) in odor detection sessions (*yellow shading*), followed by light detection sessions (*blue shading*). ([64] with permission from Nature Publishing Group)

be delivered. Contralateral to the optic fiber stub, we implanted a stainless steel cannula in the nasal cavity for sniff measurement. During experiments, the cannula was connected via a polyethylene tube to a pressure sensor. The pressure sensor gives a fast, faithful reading of the mouse's respiration. Lastly, a headbar was affixed to the skull so that the mouse could be tested in a head-fixed behavioral paradigm.

10.3.2 Initial Training

Mice were then trained to report their perception in a go/no-go task. After recovering from surgery, the mice were first given two daily sessions in which they received water while head-fixed. This served to acclimate the mice to being head-fixed in the behavioral setup. We then began training in the go/no-go paradigm (Fig. 10.1d). Go/no-go sessions were broken into trials, each consisting of a 500-ms stimulus period and a 500 -ms response period. During the stimulus period, a stimulus or a blank would be presented. The mice respond during the response period by licking or not licking. Licking is the correct response on go trials, while withholding licking is the correct response on no-go trials. In the first go/no-go sessions, the mice performed an odor detection task, with an odor stimulus presented on go trials and a blank presented on no-go trials. Mice learn to lick appropriately in this task very quickly, always achieving well above chance performance (50%) in the first session, followed by near-perfect performance in subsequent sessions. Mice were given two to four of these odor detection sessions (Fig. 10.1e). This initial training with odor was intended to familiarize the mice with the rules of the go/no-go task.

10.3.3 Light Detection

After they performed the odor detection task, we next trained the mice at light detection (Fig. 10.1e). Mice were to lick when a light stimulus was presented and to not lick when no light was presented. Pilot experiments determined a light intensity range in which wild-type mice, implanted with optical fibers identically to OMP-ChR2 mice, did not detect the light stimulus. Based on these initial experiments, the light stimulus power was set at 5 mW, measured at the ferrule that coupled to the ferrule implanted on the mouse, and the stimulus duration was 1 ms. To counter the possibility that the mice would see the light stimulus and base behavioral performance on this, we set up a masking light. Two bright blue LEDs, positioned on both sides of the mouse's face, were activated throughout the stimulus period (500 ms) in every trial. In this paradigm, OMP-ChR2 mice detected the stimulus quite well, achieving performance well above chance in the first session and near-perfect performance in subsequent sessions (Fig. 10.1e). By contrast, wild-type mice, which had previously performed well on the odor detection task, were unable to detect the light, with performance at 50% correct (Fig. 10.1e). Taken together, these results demonstrate that ChR2 is required for behavioral detection of nasal light stimuli and that the animals are not detecting the stimulus via vision or thermosensation.

10.3.4 Sniff Phase Perception

Having established that we can stimulate OSNs with light in OMP-ChR2 mice, we were able to ask whether the mouse olfactory system reads a temporal coding cue. To do this, we triggered light stimuli using the sniff signal recorded from the intranasal cannula (Fig. 10.2a, Top). The pressure sensor signal reads negative when the mice are inhaling and positive when the mice are exhaling. By convention, we display the signal with the sign reversed. Therefore, the onset of inhalation occurs at a positive-going zero-crossing, while exhalation begins at a negative-going zero-crossing. We thus used the sniff signal to test whether the mice could discriminate light stimuli delivered at inhalation onset from stimuli delivered at exhalation onset. On go trials, light stimuli were triggered by inhalation, and on no-go trials, stimuli were triggered by exhalation (Fig. 10.2a, Top). Mice were trained to perform this discrimination after they had reached a high performance level at light detection. We found that all mice attained above-chance performance by the second day of training and gave high performance on subsequent days (Fig. 10.2a, Bottom). We

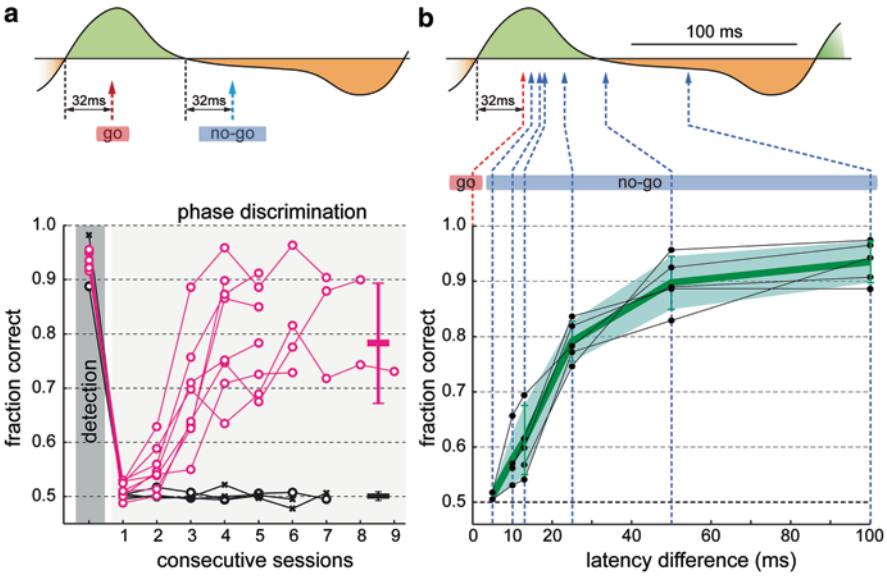

Fig. 10.2 OMP-ChR2 mice perceive sniff phase. **a** Top, schematic of the sniff phase discrimination task. Laser pulses shown relative to a sniff waveform. Inhalation is shaded *green*, and exhalation is shaded *orange*. Light was delivered 32 ms after inhalation onset (*red arrow*) in "go" trials or 32 ms after exhalation onset (*blue arrow*) in "no-go" trials. *Bottom*, performance of OMP-ChR2 mice (*pink circles*; $n=8$) for their last light detection session, followed by phase discrimination sessions. *Black lines* show click detection (*gray shading*) and click phase discrimination performance for OMP-ChR2 (*black circles*, $n=2$) and wild type (*black asterisks*, $n=2$). Phase discrimination performance for light (*pink*; $n=30$ sessions) and click (*black*; $n=19$ sessions) stimuli (*Horizontal dashes; mean s.d.*) **b** Fraction correct as a function of latency difference. *Top*, as **a**. *Bottom*, Performance of individual OMP-ChR2 mice (*black circles*) and mean±s.d. (*green line and shaded region*; $n=5$). ([64] with permission from Nature Publishing Group)

performed a control experiment to determine to what extent this ability to perceive the timing of a stimulus relative to sniff was unique to the olfactory system. We attempted to train mice to discriminate clicks based on their timing in the sniff cycle. Mice that had previously acquired the sniff phase discrimination task were given click stimuli that occurred at inhalation (go) or exhalation (no-go). Unlike OSN stimulation, mice were unable to discriminate click timings based on timing relative to sniff (Fig. 10.2a, Bottom). This indicates that the ability to time stimuli relative to sniff might be unique to olfaction.

These results demonstrate that the mouse's brain can read a temporal coding cue: the sniff phase of OSN activation. We next asked how acute this sense of timing is. To do this, we triggered from inhalation onset and delivered stimuli with different latencies (Fig. 10.2b, Bottom). We measured the animal's behavioral accuracy as a function of latency difference. The mice maintained high performance down to a latency difference of 25 ms and performed above chance for a latency difference of 10 ms. Thus, mice can sense very small temporal differences.

This observation is in striking agreement with other work from the Rinberg laboratory, in which we recorded odor responses in the OB of awake mice [62]. In this study, we reported that excitatory odor responses are highly precise: The standard deviation of onset times relative to inhalation onset was on average 10 ms, in the same range as the temporal acuity we found in our optogenetic work. In summary, olfactory neuronal responses have precise temporal structure, and our work suggests that the olfactory system decodes temporal structure at this precise scale.

10.3.5 Sniff Phase Encoding in the OB

To mediate the behavioral performance we observe the olfactory system must have the following properties. First, it must be able to precisely follow and faithfully preserve the timing of the light stimulus. Second, the timing of the stimulus must be compared to an internal representation of the sniff. To ask whether the olfactory system meets these requirements, we performed electrophysiological recordings in the OB. We implanted OMP-ChR2 mice chronically with 32-channel silicon probe microelectrode arrays. We stimulated mice that were awake but not performing a task. In these recording sessions, we delivered stimuli at six latencies relative to sniffing: 32, 62, and 92 ms after inhalation onset and 32, 62, and 92 ms after exhalation onset (Fig. 10.3a). We recorded from 86 putative mitral and tufted cells (MT cells), the projection neurons of the OB. Of these cells, 26 gave excitatory spiking responses and 23 gave inhibitory responses.

Excitatory responses to light stimuli were brief and tightly locked to stimulus onset (Fig. 10.3a). To quantify the temporal precision of these responses, we fit a Gaussian to the peristimulus time histogram of each cell's responses and took the width (σ) and latency (τ) of this Gaussian as our measure of temporal precision. The values of both parameters were tightly distributed around short values of response duration and onset jitter (Fig. 10.3b, c). The distributions of these temporal parameters demonstrate that the responses of OB neurons faithfully transmit the timing of light stimuli.

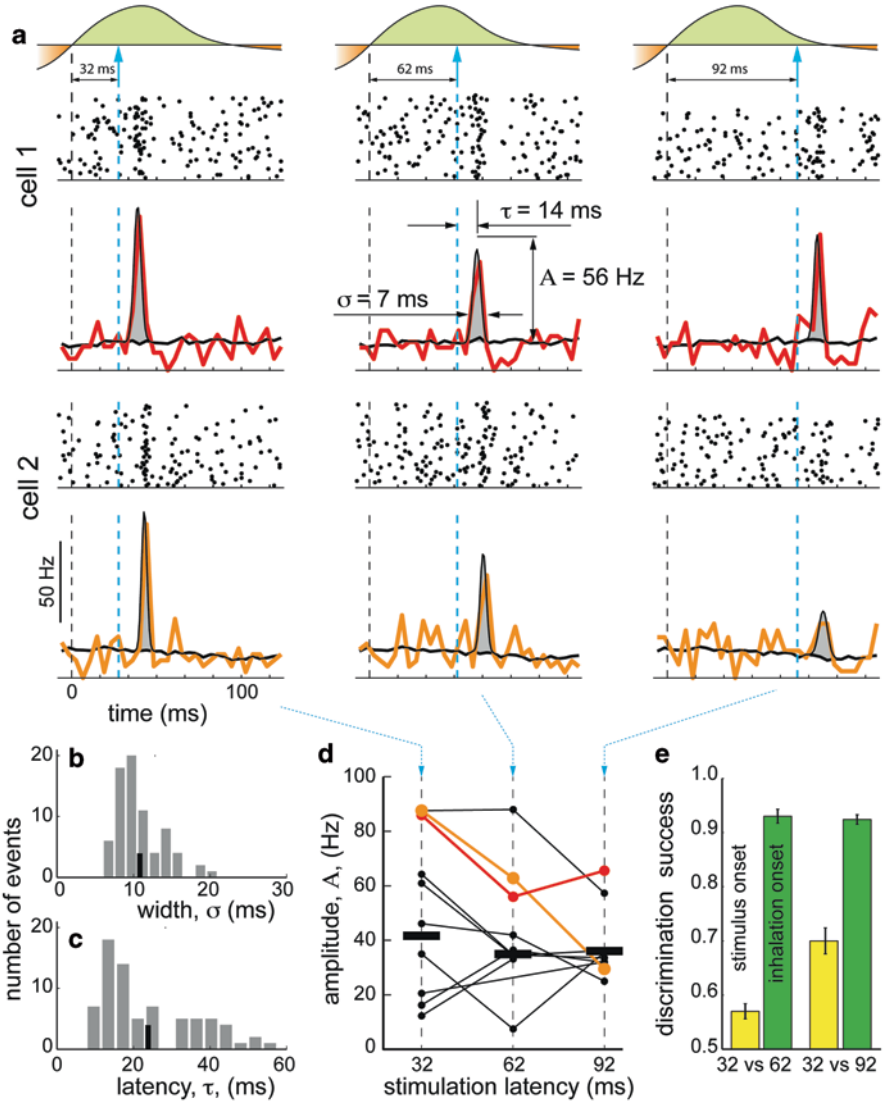

Fig. 10.3 Light-evoked responses of olfactory bulb (*OB*) cells. **a** *Top*, timing of light application relative to sniff. *Middle and bottom*, raster plots± peristimulus time histogram (*PSTH*) for two cells' responses (*cell 1, top; cell 2, bottom*) to light at three latencies (*32 ms, left; 62 ms middle; 92 ms, right*) after inhalation onset. PSTHs for light responses (*colored lines*) and spontaneous activity (*thick gray lines*). Gaussian fit of the difference between PSTHs for stimulated and unstimulated sniffs (*thin black lines*). The fit parameters give values for response width (σ), latency (τ), and amplitude (A). **b** Distribution of response widths (σ, *top*) and latencies (τ, *bottom*). *Gray bars*, data; *thick black line*, mean. **c** Response amplitudes (A) from individual cells (*connected filled circles; red and orange dots show respectively cells 1 and 2*), with the across-cell mean (*blue line*). **d** Classification performance for the neuronal population response (*mean ± s.d. across repeated permutations*) discriminating between 32- and 62-ms and between 32- and 92-ms light stimulation latencies. Responses were aligned to the stimulus onset (*yellow*) or inhalation onset (*green*). ([64] with permission from Nature Publishing Group)

As stated above, the olfactory system must compare the precise timing of the light stimulus with an internal representation of the sniff. We wondered whether we could find evidence of such a comparison in the responses of OB neurons. Indeed, we found that many OB neurons gave different amplitudes of light responses as a function when in the sniff cycle they were stimulated (Fig. 10.3d). In other words, the sniff phase cue of the stimulus is partly transformed into a spike rate cue, which itself carries information about stimulus timing.

Thus, neurons downstream of the OB have two potential cues with which to discriminate stimulus timings: the precise timing of the response relative to sniff and the amplitude of the spike rate response. We evaluated the amount of information these cues carry using a classification algorithm (Fig. 10.3e). Basically, this algorithm compares each individual trial's response to the across-trial mean response for two stimulus conditions. For a given trial, the algorithm determines to which stimulus condition's mean the given trial's response is more similar and assigns each trial to one stimulus condition or the other. The fraction of correct assignments gives a measure of how much information the neuronal response cues contain. In our case, the classifier attempts to discriminate different stimulus latencies (in our case, 32-ms latency to 62 or 92 ms latency). To estimate the relative contribution of the two cues, timing and amplitude, we ran the classification with the data aligned in two different ways. If we align to inhalation onset, both the sniff timing and the amplitude cue are available. If instead we align to stimulus onset, the sniff timing cue is omitted, and the classifier must discriminate solely on the basis of response amplitudes. When the data are aligned to inhalation onset, the classifier discriminates at a rate of over 90% correct (Fig. 10.3e). When alignment is to stimulus onset, the classifier performs worse, but still well above chance (about 70% for a 60-ms latency difference; about 60% for a 30-ms latency difference). These results imply that both timing and amplitude cues carry information that the mouse's brain may use to discriminate stimulus timings.

10.3.6 Sniff Phase Coding: Possible Meanings and Mechanisms

Stimulus-dependent phase or latency patterns are present in a functionally and phylogenetically broad range of neural correlates. Whether this rhythmic patterning enters perception has seldom been tested directly. To our knowledge, the only example comes from mormyrid electric fish, whose electroreceptors encode current amplitudes with first-spike latency [70]. In a psychophysical assay using fictive electric organ discharge [27], these fish could detect differences in latency relative to motor command. While the necessary degree of temporal stimulus control inheres in studies of electrosensation, odor stimuli are notoriously sluggish and difficult to control. Optogenetics allowed us to circumvent this obstacle and control the underlying circuit activity with a high degree of temporal precision.

We show that mice perceive the sniff phase of olfactory input, but what might this cue "mean" to the animal? According to an appealingly simple theory, sniff latency encodes the intensity of receptor activation [8, 28, 45]. Similar relationships between

intensity and latency have been observed in vision [55] and electrosensation [70]. The intensity of a receptor neuron's activation depends on the concentration of the odorant and its affinity for the olfactory receptor protein expressed by the OSN. Concentration-to-time coding, in which raising odor concentration shifts activation to earlier times in the sniff cycle, has been observed in OSNs [68] and MT cells [12, 44]. Further, an affinity-to-time coding scheme, where a neuron's response latency is proportional to its affinity for an odorant, can explain the odor specificity of sniff phase coding [28, 34, 45]. An inherent benefit of such an intensity-to-time representation is speed [28, 61, 72]. Psychophysical studies demonstrate that rodent olfaction is indeed fast: A single sniff can suffice for odor discrimination [1, 57, 71, 73].

The mechanism for these intensity-to-time transformations may reside in the transduction kinetics of OSNs, which predict that response latency shortens for a stronger stimulus [50, 58]. This shift in latency would be propagated to downstream neurons in the OB. At the level of MT cells, timing may also be shaped by sniff-locked oscillations [12, 44], which can transform intensity into timing by modulating excitability [28]. Whether encoded by these or other mechanisms, the resultant mapping of intensity onto time can be decoded by timing-sensitive mechanisms in downstream neurons [14, 46]. Sniffs may be represented by broadly patterned activity in the OB. Many OSN terminals [13] and MT cells [16, 62] modulate their activity with the sniff cycle in the absence of overt odor stimulation. This modulation may originate from responses of OSNs to airflow or background odor in the nose [26, 66], or from an efferent source, for example, if respiratory motor commands are copied to the bulb.

Finally, our results exclude the possibility that differences in the spatial input patterns at the receptor level are necessary for stimulus discrimination, which has been suggested previously [21, 41]. That said, our results in no way contradict the well-established importance of spatial coding in olfaction. Coding by spatial patterns of glomerular activation and coding by sniff phase are not mutually exclusive. Instead, spatial and temporal coding, working in concert, may optimize olfactory processing in any number of ways.

10.4 Using Optogenetics to Probe the Signaling Capacity of a Single Glomerulus

10.4.1 Are Glomeruli Binary?

For our next studies, we investigated the signaling capacity of a single glomerulus [65]. As stated above, mice have over a thousand OR genes and consequently over a thousand types of glomerulus [49]. This endows the olfactory system with an enormous coding capacity—even if glomeruli are binary, signaling in an all-or-none fashion, such a combinatorial code could represent an astronomical number of odor states: 2^1000 [38]. Can the mouse's brain exploit the capacity of this combinatorial code? Is it fully available to perception?

Furthermore, are glomeruli indeed binary, or do they have dynamic range? From imaging studies, we know that glomeruli can give different amplitudes of response depending on odor identity and concentration [5], and as discussed above, glomeruli and the postsynaptic neurons to which they are connected fire at different times in the sniff cycle, again as a function of odor identity and concentration [69]. Can the mouse's brain read different signals from a single glomerulus and use them to guide behavior?

10.4.2 Experimental Strategy

We could not pursue these questions using odor stimuli, because odors typically activate many glomeruli. Instead, we turned again to optogenetics, in this case to deliver stimuli to a genetically defined glomerulus. We generated a mouse line in which ChR2 expression is limited to a single-glomerulus type: the M72 glomerulus. M72 is an OR gene for which we know the ligand specificity (see below). To drive expression in M72-positive cells, we engineered a transgene consisting of the M72 ORF followed by the ChR2 sequence. In between the two genes, an internal ribosomal entry site (IRES) was interposed, which enables two transcripts to be generated from a single gene locus (Fig. 10.4a). In this way, M72-expressing sensory neurons would retain their normal ligand preferences, while adding light sensitivity. This transgene was knocked into the M72 locus, expression from which faithfully recapitulates the normal M72 distribution pattern. The axons of M72- and ChR2-positive OSNs form 4 glomeruli (one medial and one lateral glomerulus on each hemisphere of the OB) in the normal locations in the OB (Fig. 10.4b). Importantly, the lateral glomeruli in each bulb are conveniently located on the dorsal surface of the bulb, where light can be delivered relatively easily.

As in the study described above, we surgically prepared these mice for light stimulation, sniff measurement, and head-fixed behavior. To deliver light stimuli to the M72-ChR2 glomerulus, we again used optical fiber stubs, but in this case the fiber was affixed directly above the glomerulus in question. We thinned the bone overlying a M72-ChR2 glomerulus (always the lateral glomerulus in the right hemisphere of the OB) and glued the tip of the optical fiber to the overlying bone (Fig. 10.4b). As a control, we affixed another fiber to thinned bone posterior to the OB, above frontal cortex (Fig. 10.4b). The fiber stubs were then stabilized with dental cement. Sniff cannulae and headbars were implanted as above.

10.4.3 Light Detection Through a Single Glomerulus

These mice were then trained on the go/no-go task as above, first training on the simple odor detection task. After high performance was achieved in this task, we began to train the mice at light detection. Almost all mice (10 of 11) were able to report detection of the light stimulus (Fig. 10.4c). The mice that were able to detect

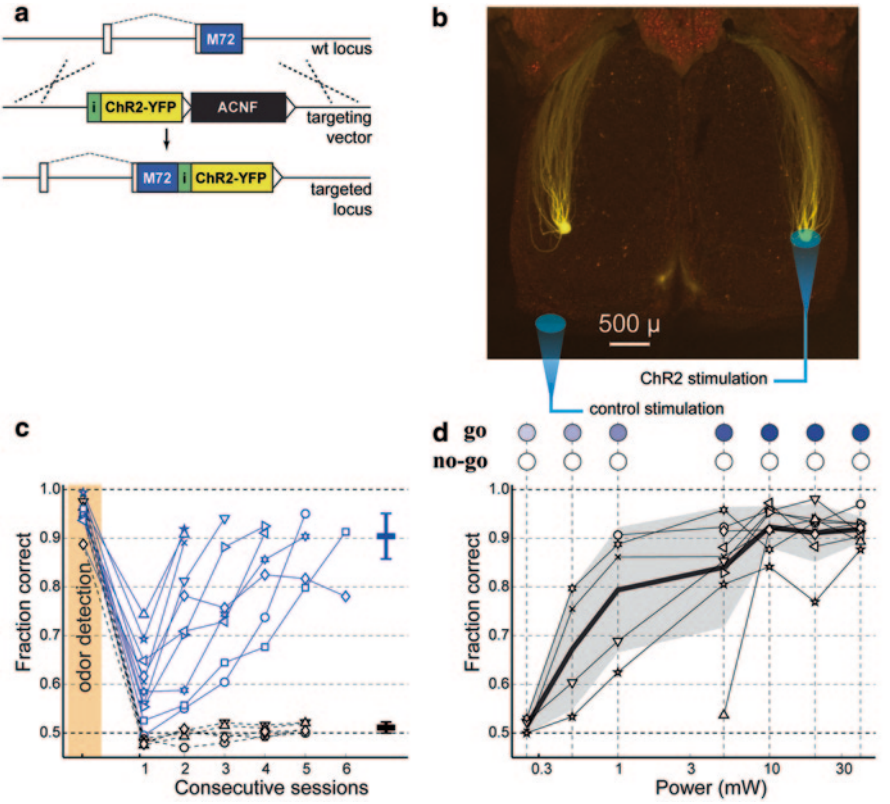

Fig. 10.4 Light stimulating an olfactory glomerulus. **a** Diagram of the gene-targeting strategy. An internal ribosome entry site (*IRES, green box*) was appended to the sequence for the odorant receptor (*OR*) *M72* just after the unmodified receptor coding sequence. The IRES was followed by the coding sequence for *ChR2-YFP* (*yellow box*). **b** Convergence of *M72* axons into single glomerulus. The *overlaid diagram* shows the optical fiber placement. **c** Performance of M72-ChR2 mice in one odor detection session, followed by light detection sessions (*blue symbols*, $n=10$ mice) and control stimulation sessions (*black circles*, $n=5$ mice). Symbols at *far right* represent across-mouse mean ± s.d. **d** Different stimulus powers evoke varying levels of detection success. Performance of individual M72-ChR2 mice (*black symbols*), and mean ± s.d. for all mice (*green line and shaded area* $n=9$) is shown. ([64] with permission from Nature Publishing Group)

the stimulus reached high performance quickly, after 2–5 sessions. In contrast, when we stimulated the same mice on their control fiber, they were unable to detect the stimulus. This demonstrates that mice can detect activation of a single glomerulus.

We next asked how detection performance varies as a function of the power of the light stimulus. Importantly, we found a range of stimulus powers that elicited a high, asymptotic level of detection success, a range of powers that evoked intermediate performance (~75%), and a power at which the mice were unable to detect the stimulus (Fig. 10.4d).

10.4.4 Detecting One Glomerulus in the Presence of Other Activated Glomeruli

At this point, we had shown that mice can detect stimulation of a single glomerulus in isolation. But this is an unnatural condition—odors typically activate many glomeruli. To better approximate a natural stimulus, we next presented odor and light stimuli simultaneously. In a previous study, the Bozza laboratory had performed electrophysiology on isolated M72-expressing OSNs while stimulating them with a large panel of odorants [74]. From this work, we knew which odorants were M72 ligands and which were not. We reasoned that M72 ligands should be able to mask light stimuli, rendering them less detectable, while non-M72 ligands should leave light detection unaffected (Fig. 10.5a).

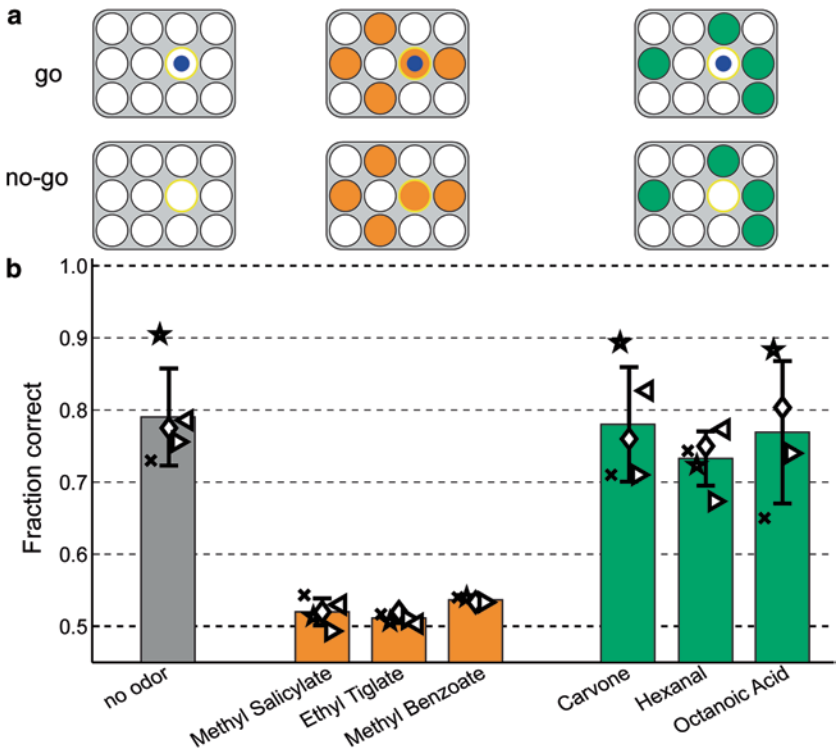

Fig. 10.5 Detecting single-glomerulus stimulation in the presence of odor. **a** Diagram of the glomerular array's (*circles*) responses to paired odor and light stimulation. The M72-ChR2 glomerulus is colored *yellow,* and the *blue dot* indicates photostimulation. M72 ligands activate many glomeruli, including the M72 glomerulus (*orange-filled circles*). Non-M72 ligands stimulate other glomeruli (*green-filled circles*), but not the M72-ChR glomerulus. **b** Light detection performance in the presence of odors—for individual mice (*black symbols*) and across-mouse mean ± s.d. (*bars* ± *error bars*). Colors indicate the presence of no odor (*gray*), M72 ligands (*orange*) and M72 non-ligands (*green*). (Smear et al. 2013 with permission from Nature Publishing Group)

To test this prediction, we tested the mice in an odor+light condition. In odor sessions, an odor was presented on each trial, and whether that trial was a go or a no-go was determined by the presence or absence of the light stimulus. The light stimulus power we used for these experiments was adjusted to evoke ~75% performance in the absence of odor. We used 6 odors totally, 3 M72 ligands (ethyl tiglate, methyl salicylate, and methyl benzoate) and 3 M72 non-ligands (carvone, hexanal, and octanoic acid). In each odor session, only one of these odors was used. Daily odor sessions alternated with no-odor sessions, so the sequence was (1) ligand odor session, (2) no-odor session, (3) non-ligand odor session, and (4) no-odor session. By repeating this sequence, we cycled through all 6 odors.

We found that the presence of M72 ligands reduced detection of light stimuli to chance or near-chance levels (Fig. 10.5b). In contrast, the non-M72 ligands had no effect on light detection performance. Taken together, the odor specificity of these results further supports the assertion that our light stimuli are detected via ChR2 expressed in M72-positive OSNs. Furthermore, activation of a single glomerulus can be detected on a background of many odor-activated glomeruli. Thus, the smallest possible change in the ensemble of activated glomeruli is perceptible.

10.4.5 Amplitude Discrimination

We next investigated whether glomeruli are binary. Can different amplitudes of glomerular stimulation be discriminated? To answer this question, we referred to the power detection function I discussed above. Specifically, we worked within the laser power range in which detection performance of the mice was high and asymptotic, and we tested whether mice could discriminate among intensities in this range (Fig. 10.6a, Top). Since we know that even the lowest power of stimulation was easily perceptible, we ensure that we are not merely using subthreshold stimuli for the low intensity. In other words, we know that the mice must be performing a discrimination and not a detection task. We found that mice could indeed discriminate among light powers down to a twofold difference (Fig. 10.6b, Bottom). Thus, an individual glomerulus' contribution to perception is not binary in the amplitude domain. Amplitude-of-activation coding can drive olfactory perception.

10.4.6 Sniff Phase Discrimination

Another variable for which a single glomerulus' perceptual contribution may not be binary is in the time domain, specifically in sniff phase. Previously we had shown that mice can discriminate different sniff phases of activation when many OSNs are activated. Can mice discriminate sniff phases when only one glomerulus is activated? To test this, we repeated the sniff phase discrimination paradigm we had used with OMP-ChR2 mice: A stimulus early in the sniff cycle defines a go trial, while the stimulation occurs later in the sniff cycle in no-go trials (Fig. 10.6b, Top). We

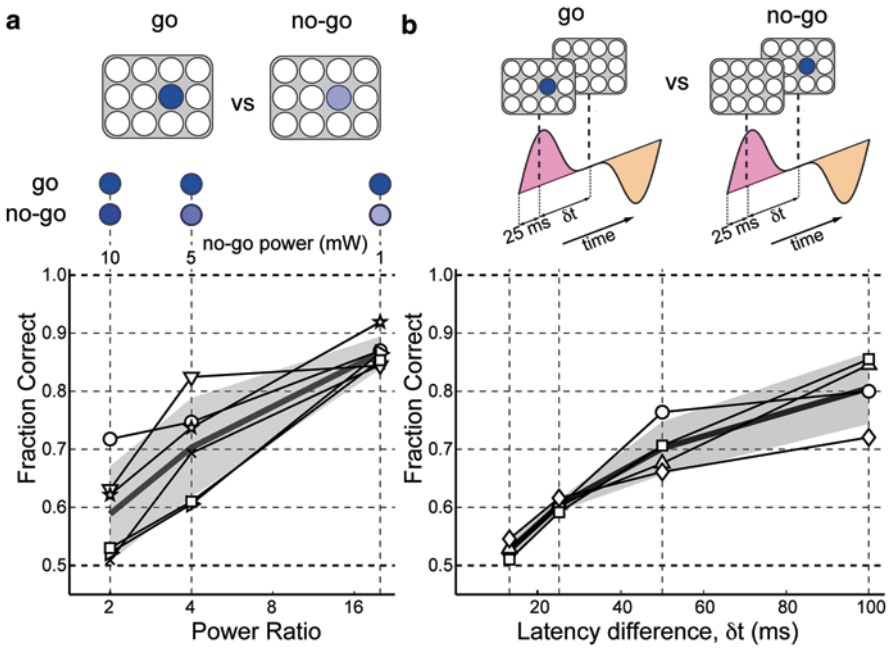

Fig. 10.6 Amplitude and timing differences discriminated through a single glomerulus. **a** Amplitude discrimination. Mice discriminated a high stimulus power (*dark blue, go stimulus*) from lower stimulus powers (*light blue, no-go stimulus*). Performance of individual mice as a function of the ratio between high and low powers (*black symbols*), and mean ± s.d. (*thick black line and shaded region*; $n = 5$ mice) are shown. **b** Latency discrimination. The diagram shows light timing relative to the sniff cycle. Inhalation (*pink*) and exhalation (*orange*) are indicated. Mice discriminated laser pulses delivered early in the sniff cycle (*go*) from pulses that occurred later (*no-go*). Performance of individual mice (*black symbols*; $n = 4$ mice) and mean ± s.d. (*thick black line and shaded region*). (Smear et al. 2013 with permission from Nature Publishing Group)

found that even with only one glomerulus, mice are able to discriminate different timings in the sniff cycle, down to a 25-ms latency difference (Fig. 10.6b, Bottom). This is not as small a latency difference as is discriminable by OMP-ChR2 mice (10 ms), but still quite acute. This demonstrates that another coding variable, sniff phase, is not binary, but can signal through different discriminable timings.

10.4.7 Multiple Perceptible Signals Through One Glomerulus

Our results demonstrate that a single glomerulus can send multiple signals to perception. The large size of the OR gene family and the concomitantly large number of glomeruli in the OB endow a glomerular identity code with an enormous combi-

natorial capacity. Our results in the odor + light experiments strongly pertain to this point, especially the lack of masking we observed in the experiments in which non-M72 ligand odors were combined with photostimulation. We showed that a large array of active glomeruli can be discriminated solely on the basis of the presence or absence of activity in one glomerulus. Mice can perceive the smallest possible change in the glomerular identity code, which indicates that circuits downstream of the glomeruli can use the full combinatorial capacity of the glomerular array.

We also have shown that a glomerulus can signal more than its identity—its signaling capacity is more than all or nothing. It has long been known that glomeruli can activate with different amplitudes [5, 59] and timings [13, 68] depending on stimulus properties. Our demonstration, that mice can discriminate different amplitudes and timings, guarantees that circuits in the bulb and beyond can read these neural coding parameters.

These results raise a perplexing question: when there are so many glomeruli, why should one be so powerful? We can only speculate here, but the answer likely lies in the fact that natural olfactory scenes are complex. In a single sniff, a mouse may take in hundreds of volatile molecules emitted by several environmental sources. Furthermore, the temporal structure with which different odors hit the nose is complex, since odor propagation depends on convection and turbulent flow.

An olfactory function for which high-capacity glomeruli would be especially useful is the "olfactory cocktail party problem," the challenge of parsing the different molecules entering the nose simultaneously into distinct odor sources [29]. One example of this problem is detecting a faint odor in the presence of multiple background odors. If even one glomerulus can make a perceptual contribution, then it will be less likely for background odors to "occlude" a less concentrated odor of interest. Furthermore, having graded signaling capacity in individual glomeruli may improve the animal's ability to navigate to an odor source. To navigate, the animal needs to be able to discern concentration differences at different points in space and time. Sensing concentration differences may be, at least in part, mediated by graded signaling in single glomerulus [28, 45]. If so, an animal could track an odor source even when very few glomeruli are uniquely activated by the odor of interest.

Neural activity in the olfactory system and the rest of the brain is structured in space and time. By analyzing different features of this spatiotemporal structure, researchers can infer what that activity represents. Such inferences are inherently limited. How can we know that the brain decodes neuronal activity the same way that we do? Here I have demonstrated one approach to this question. We have used optogenetics to dissect the activity patterns of OSNs into putative coding variables (identity, amplitude, and sniff phase) and asked whether an animal can perceive these features in isolation. Our demonstration that each of these cues is perceptible shows that circuits downstream of the OSNs possess mechanisms to preserve the information they encode and ultimately to transform this information into a perceptual report.

10.5 Dissecting Neural Codes Outside the Olfactory System

This strategy should be generalizable to other neural structures or systems. For example, our approach could enable testing of various other phase/latency coding hypotheses [72], especially in sensory systems where the timing of neuronal activity relative to sampling behavior might be relevant, as in vibrissal somatosensation [17, 20] or visual latency coding [23, 25, 55]. Beyond the sensory periphery, our strategy may also help dissect putative temporal cues in central systems, for example, in the phase precession of hippocampal place cells [10, 30, 51].

10.5.1 Neural code Dissection—Extensions of the Strategy

Can our approach "solve" a neural code? Not on its own. There are two major limitations in interpreting this type of experiment. The first pertains to the choice of behavioral tasks. Using operant behavior in detection or discrimination tasks can tell us that an animal can discern some coding cue, but tells us nothing about what the cue "means" to the animal. To close this gap, we could attempt to mimic one of these cues as the animal performs some natural behavior. For example, when activity is advanced earlier in the sniff cycle, what changes in the animal's perception? Above, I presented evidence in favor of the idea that sniff phase encodes the intensity of receptor activation [28, 61, 72]. This would therefore be a candidate mechanism through which the animal encodes the concentration of incoming odor stimuli. Olfactory navigation, a natural behavior, is based on measurement of concentration differences across space (in this case, a difference across the nostrils) and time (through differences across consecutive sniffs). We could therefore attempt to create fictive navigation, in which we mimic the sniff phase cue, giving stimuli at progressively earlier sniff phase as the animal gets closer to a fictive odor source. If we can guide an animal to such a fictive odor source solely with phase coding, this would be strong evidence that sniff phase indeed encodes the intensity of receptor activation.

The second limitation to this type of experiment is that it is essentially a sufficiency test. We can show that the animal can perceive an experimentally manipulated coding feature. Whether that feature is actually used in perceiving natural stimuli remains an open question. What is needed to complement our strategy is a necessity test: selectively take away some aspects of the code and characterize the extent to which behavioral performance suffers in its absence. For example, in the case of sniff phase coding in the olfactory system, we would want to selectively disrupt the temporal pattern of activity, while preserving the amount and spatial pattern of that activity. We would examine the effect of this disruption on performance in some olfactory behavioral task. Such a manipulation would be very difficult, but perhaps possible now that red-shifted opsins are becoming available [35, 42]. Simultaneously expressing spectrally separated optogenetic actuators and inhibitors

may enable us to insert and remove spikes from a given neuronal population. This could provide the necessity test that neural code dissection needs.

References

1. Abraham, N. M., Spors, H., Carleton, A., Margrie, T. W., Kuner, T., & Schaefer, A. T. (2004). Maintaining accuracy at the expense of speed: Stimulus similarity defines odor discrimination time in mice. *Neuron, 44,* 865–876.
2. Adrian, E. D. (1953). Sensory messages and sensation; the response of the olfactory organ to different smells. *Acta Physiol Scand 29,* 5–14.
3. Adrian, E. (1954). Sensory messages and sensation. The response of the olfactory organ to different smells. *Acta Physiologica Scandinavica, 29,* 5–14.
4. Aponte, Y., Atasoy, D., & Sternson, S. M. (2010). AGRP neurons are sufficient to orchestrate feeding behavior rapidly and without training. *Nature Neuroscience, 14,* 351–356.
5. Bozza, T., McGann, J. P., Mombaerts, P., & Wachowiak, M. (2004). In vivo imaging of neuronal activity by targeted expression of a genetically encoded probe in the mouse. *Neuron, 42,* 9–21.
6. Bozza, T., Vassalli, A., Fuss, S., Zhang, J.-J., Weiland, B., Pacifico, R., Feinstein, P., & Mombaerts, P. (2009). Mapping of class I and class II odorant receptors to glomerular domains by two distinct types of olfactory sensory neurons in the mouse. *Neuron, 61,* 220–233.
7. Britten, K. H., Shadlen, M. N., Newsome, W. T., & Movshon, J. A. (1992). The analysis of visual motion: A comparison of neuronal and psychophysical performance. *The Journal of Neuroscience, 12,* 4745–4765.
8. Brody, C. D., & Hopfield, J. J. (2003). Simple networks for spike-timing-based computation, with application to olfactory processing. *Neuron, 37,* 843–852.
9. Buiakova, O. I., Baker, H., Scott, J. W., Farbman, A., Kream, R., Grillo, M., Franzen, L., Richman, M., Davis, L. M., Abbondanzo, S., et al. (1996). Olfactory marker protein (OMP) gene deletion causes altered physiological activity of olfactory sensory neurons. *Proceedings of the National Academy of Sciences of the United States of America, 93,* 9858–9863.
10. Buzsáki, G. (2002). Theta oscillations in the hippocampus. *Neuron, 33,* 325–340.
11. Buzsáki, G. (2010). Neural syntax: Cell assemblies, synapsembles, and readers. *Neuron, 68,* 362–385.
12. Cang, J., & Isaacson, J. S. (2003). In vivo whole-cell recording of odor-evoked synaptic transmission in the rat olfactory bulb. *Journal of Neuroscience, 23,* 4108–4116.
13. Carey, R. M., Verhagen, J. V., Wesson, D. W., Pirez, N., & Wachowiak, M. (2008). Temporal structure of receptor neuron input to the olfactory bulb imaged in behaving rats. *Journal of Neurophysiology, 101,* 1073–1088.
14. Carr, C. E. (2007). Processing of temporal information in the brain. *Annual Review of Neuroscience, 16,* 1–23.
15. Chaput, M., & Holley, A. (1980). Single unit responses of olfactory bulb neurones to odour presentation in awake rabbits. *Journal de Physiologie (Paris), 76,* 551–558.
16. Chaput, M. A., Buonviso, N., & Berthommier, F. (1992). Temporal patterns in spontaneous and odour-evoked mitral cell discharges recorded in anaesthetized freely breathing animals. *The European Journal of Neuroscience, 4,* 813–822.
17. Curtis, J. C., & Kleinfeld, D. (2009). Phase-to-rate transformations encode touch in cortical neurons of a scanning sensorimotor system. *Nature Neuroscience, 12,* 492–501.
18. Cury, K. M., & Uchida, N. (2010). Robust odor coding via inhalation-coupled transient activity in the mammalian olfactory bulb. *Neuron, 68,* 570–585.
19. Diamond, M. E., von Heimendahl, M., Knutsen, P. M., Kleinfeld, D., & Ahissar, E. (2008). 'Where' and 'what' in the whisker sensorimotor system. *Nature Reviews Neuroscience, 9,* 601–612.

20. Fee, M. S., Mitra, P. P., & Kleinfeld, D. (1997). Central versus peripheral determinants of patterned spike activity in rat vibrissa cortex during whisking. *Journal of Neurophysiology, 78,* 1144–1149.
21. Fleischmann, A., Shykind, B. M., Sosulski, D. L., Franks, K. M., Glinka, M. E., Mei, D. F., Sun, Y., Kirkland, J., Mendelsohn, M., Albers, M. W., et al. (2008). Mice with a "Monoclonal Nose": Perturbations in an olfactory map impair odor discrimination. *Neuron, 60,* 1068–1081.
22. Friedrich, R. W., & Laurent, G. (2001). Dynamic optimization of odor representations by slow temporal patterning of mitral cell activity. *Science, 291,* 889–894.
23. Gawne, T. J., Kjaer, T. W., & Richmond, B. J. (1996). Latency: Another potential code for feature binding in striate cortex. *Journal of Neurophysiology, 76,* 1356–1360.
24. Gelperin, A., & Tank, D. W. (1990). Odour-modulated collective network oscillations of olfactory interneurons in a terrestrial mollusc. *Nature, 345,* 437–440.
25. Gollisch, T., & Meister, M. (2008). Rapid neural coding in the retina with relative spike latencies. *Science, 319,* 1108–1111.
26. Grosmaitre, X., Santarelli, L. C., Tan, J., Luo, M., & Ma, M. (2007). Dual functions of mammalian olfactory sensory neurons as odor detectors and mechanical sensors. *Nature Neuroscience, 10,* 348–354.
27. Hall, C., Bell, C., & Zelick, R. (1995). Behavioral evidence of a latency code for stimulus intensity in mormyrid electric fish. *Journal of Comparative Physiology, 177,* 29–39.
28. Hopfield, J. J. (1995). Pattern recognition computation using action potential timing for stimulus representation. *Nature, 376,* 33–36.
29. Hopfield, J. J. (1999). Odor space and olfactory processing: Collective algorithms and neural implementation. *Proceedings of the National Academy of Sciences of the United States of America, 96,* 12506–12511.
30. Jensen, O., & Lisman, J. E. (2000). Position reconstruction from an ensemble of hippocampal place cells: Contribution of theta phase coding. *Journal of Neurophysiology, 83,* 2602–2609.
31. Johansson, R. S., & Birznieks, I. (2004). First spikes in ensembles of human tactile afferents code complex spatial fingertip events. *Nature Neuroscience, 7,* 170–177.
32. Junek, S., Kludt, E., Wolf, F., & Schild, D. (2010). Olfactory coding with patterns of response latencies. *Neuron, 67,* 872–884.
33. Kass, M. D., Moberly, A. H., & McGann, J. P. (2013). Spatiotemporal alterations in primary odorant representations in olfactory marker protein knockout mice. *PLoS ONE, 8,* e61431.
34. Kepecs, A., Uchida, N., & Mainen, Z. F. (2006). The sniff as a unit of olfactory processing. *Chemical Senses, 31,* 167–179.
35. Klapoetke, N. C., Murata, Y., Kim, S. S., Pulver, S. R., Birdsey-Benson, A., Cho, Y. K., Morimoto, T. K., Chuong, A. S., Carpenter, E. J., Tian, Z., et al. (2014). Independent optical excitation of distinct neural populations. *Nature Methods, 11,* 338–346.
36. Kobayakawa, K., Kobayakawa, R., Matsumoto, H., Oka, Y., Imai, T., Ikawa, M., Okabe, M., Ikeda, T., Itohara, S., Kikusui, T., et al. (2007). Innate versus learned odour processing in the mouse olfactory bulb. *Nature, 450,* 503–508.
37. Konishi, M. (1999). Deciphering the brain's codes. Neural Codes and Distributed Representations.
38. Koulakov, A., Gelperin, A., & Rinberg, D. (2007). Olfactory coding with all-or-nothing glomeruli. *Journal of Neurophysiology, 98,* 3134–3142.
39. Laurent, G., Stopfer, M., Friedrich, R. W., Rabinovich, M. I., Volkovskii, A., & Abarbanel, H. D. (2001). Odor encoding as an active, dynamical process: Experiments, computation, and theory. *Annual Review of Neuroscience, 24,* 263–297.
40. Lee, A. C., He, J., & Ma, M. (2011). Olfactory marker protein is critical for functional maturation of olfactory sensory neurons and development of mother preference. *Journal of Neuroscience, 31,* 2974–2982.
41. Leon, M., & Johnson, B. A. (2009). Is there a space-time continuum in olfaction? *Cellular and Molecular Life Sciences: CMLS, 66,* 2135–2150.
42. Lin, J. Y., Knutsen, P. M., Muller, A., Kleinfeld, D., & Tsien, R. Y. (2013). Technical reports. *Nature Neuroscience, 16,* 1499–1508.

43. Macrides, F., & Chorover, S. L. (1972). Olfactory bulb units: Activity correlated with inhalation cycles and odor quality. *Science, 175,* 84–87.
44. Margrie, T. W., & Schaefer, A. T. (2003a). Theta oscillation coupled spike latencies yield computational vigour in a mammalian sensory system. *The Journal of Physiology, 546,* 363–374.
45. Margrie, T. W., & Schaefer, A. T. (2003b). Theta oscillation coupled spike latencies yield computational vigour in a mammalian sensory system. *The Journal of Physiology, 546,* 363–374.
46. Mauk, M. D., & Buonomano, D. V. (2004). The neural basis of temporal processing. *Annual Review of Neuroscience, 27,* 307–340.
47. Mombaerts, P., Wang, F., Dulac, C., Chao, S. K., Nemes, A., Mendelsohn, M., Edmondson, J., & Axel, R. (1996). Visualizing an olfactory sensory map. *Cell, 87,* 675–686.
48. Mori, K. (1999). The olfactory bulb: Coding and processing of odor molecule information. *Science, 286,* 711–715.
49. Mori, K., & Sakano, H. (2011). How is the olfactory map formed and interpreted in the Mammalian brain? *Annual Review of Neuroscience, 34,* 467–499.
50. Nagel, K. I., & Wilson, R. I. (2011). Biophysical mechanisms underlying olfactory receptor neuron dynamics. *Nature Neuroscience, 14,* 208–216.
51. O'keefe, J., & Recce, M. L. (1993). Phase relationship between hippocampal place units and the EEG theta rhythm. *Hippocampus, 3,* 317–330.
52. Pacifico, R., Dewan, A., Cawley, D., Guo, C., & Bozza, T. (2012). An olfactory subsystem that mediates high-sensitivity detection of volatile amines. *Cell Reports, 2,* 76–88.
53. Penfield, W., & Boldrey, E. (1937). Somatic motor and sensory representation in the cerebral cortex of man as studied by electrical stimulation. *Brain: A Journal of Neurology, 60,* 389–443.
54. Perkel, D. H., & Bullock, T. H. (1968). Neural coding. *Neurosciences Research Program Bulletin, 6,* 221–348.
55. Reich, D. S., Mechler, F., & Victor, J. D. (2001). Temporal coding of contrast in primary visual cortex: When, what, and why. *Journal of Neurophysiology, 85,* 1039–1050.
56. Rieke, F., Warland, D., de Ruyter van Steveninck, R., & Bialek, W. (1997). *Spikes: Exploring the neural code (computational neuroscience)*. Massachusetts: MIT Press.
57. Rinberg, D., Koulakov, A., & Gelperin, A. (2006). Speed-accuracy tradeoff in olfaction. *Neuron, 51,* 351–358.
58. Rospars, J. P., Krivan, V., & Lánský, P. (2000). Perireceptor and receptor events in olfaction. Comparison of concentration and flux detectors: A modeling study. *Chemical Senses, 25,* 293–311.
59. Rubin, B. D., & Katz, L. C. (1999). Optical imaging of odorant representations in the mammalian olfactory bulb. *Neuron, 23,* 499–511.
60. Salzman, C. D., Britten, K. H., & Newsome, W. T. (1990). Cortical microstimulation influences perceptual judgements of motion direction. *Nature, 346,* 174–177.
61. Schaefer, A. T., & Margrie, T. W. (2007). Spatiotemporal representations in the olfactory system. *Trends in Neuroscience, 30,* 92–100.
62. Shusterman, R., Smear, M. C., Koulakov, A. A., & Rinberg, D. (2011). Precise olfactory responses tile the sniff cycle. *Nature Neuroscience, 14,* 1039–1044.
63. Siegel, M., Warden, M. R., & Miller, E. K. (2009). Phase-dependent neuronal coding of objects in short-term memory. *Proceedings of the National Academy of Sciences of the United States of America, 106,* 21341–21346.
64. Smear, M. C., Shusterman, R., O'Connor, R., Bozza, T. C., & Rinberg, D. (2011). Perception of sniff phase in mouse olfaction. *Nature, 479,* 397–399.
65. Smear, M. C., Resulaj, A., Zhang, J., Bozza, T. C., & Rinberg, D. (2013). Multiple perceptible signals from a single olfactory glomerulus. *Nature Neuroscience, 16,* 1687–1691.
66. Sobel, E. C., & Tank, D. W. (1993). Timing of odor stimulation does not alter patterning of olfactory bulb unit activity in freely breathing rats. *Journal of Neurophysiology, 69,* 1331–1337.
67. Soucy, E. R., Albeanu, D. F., Fantana, A. L., Murthy, V. N., & Meister, M. (2009). Precision and diversity in an odor map on the olfactory bulb. *Nature Neuroscience, 12,* 210–220.

68. Spors, H., & Grinvald, A. (2002a). Spatio-temporal dynamics of odor representations in the mammalian olfactory bulb. *Neuron, 34,* 301–315.
69. Spors, H., & Grinvald, A. (2002b). Spatio-temporal dynamics of odor representations in the mammalian olfactory bulb. *Neuron, 34,* 301–315.
70. Szabo, T., & Hagiwara, S. (1967). A latency-change mechanism involved in sensory coding of electric fish (mormyrids). *Physiology & Behavior, 2,* 331–335.
71. Uchida, N., & Mainen, Z. F. (2003). Speed and accuracy of olfactory discrimination in the rat. *Nature Neuroscience, 6,* 1224–1229.
72. VanRullen, R., Guyonneau, R., & Thorpe, S. J. (2005). Spike times make sense. *Trends in Neuroscience, 28,* 1–4.
73. Wesson, D. W., Carey, R. M., Verhagen, J. V., & Wachowiak, M. (2008). Rapid encoding and perception of novel odors in the rat. *PLoS Biology, 6,* e82.
74. Zhang, J., Huang, G., Dewan, A., Feinstein, P., & Bozza, T. (2012). Uncoupling stimulus specificity and glomerular position in the mouse olfactory system. *Molecular and Cellular Neurosciences, 51,* 79–88.

Index

A. D. Douglass (ed.), *New Techniques in Systems Neuroscience,* Biological and Medical Physics, Biomedical Engineering, DOI 10.1007/978-3-319-12913-6